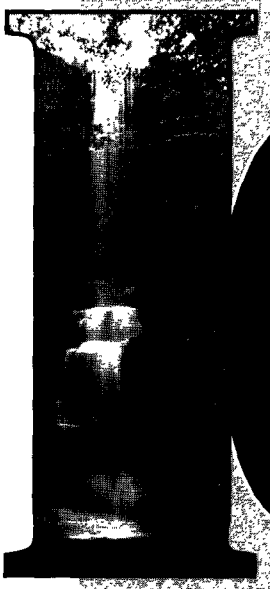

ICANS-XIV

The Fourteenth Meeting of the International Collaboration on Advanced Neutron Sources

June 14-19, 1998
Starved Rock Lodge
Utica, Illinois

Volume I

ANL-98/33
ISSN 1560-859X

Argonne National Laboratory, with facilities in the states of Illinois and Idaho, is owned by the United States government, and operated by The University of Chicago under the provisions of a contract with the Department of Energy.

DISCLAIMER

This report was prepared as an account of work sponsored by an agency of the United States Government. Neither the United States Government nor any agency thereof, nor any of their employees, makes any warranty, express or implied, or assumes any legal liability or responsibility for the accuracy, completeness, or usefulness of any information, apparatus, product, or process disclosed, or represents that its use would not infringe privately owned rights. Reference herein to any specific commercial product, process, or service by trade name, trademark, manufacturer, or otherwise, does not necessarily constitute or imply its endorsement, recommendation, or favoring by the United States Government or any agency thereof. The views and opinions of authors expressed herein do not necessarily state or reflect those of the United States Government or any agency thereof.

Reproduced from the best available copy.

Available to DOE and DOE contractors from the
Office of Scientific and Technical Information
P.O. Box 62
Oak Ridge, TN 37831
Prices available from (423) 576-8401

Available to the public from the
National Technical Information Service
U.S. Department of Commerce
5285 Port Royal Road
Springfield, VA 22161

ICANS XIV

Proceedings of the 14th Meeting of the International Collaboration on Advanced Neutron Sources

Starved Rock Lodge
Utica, Illinois
U.S.A.

June 14-19, 1998

Volume I

Editors
J.M. Carpenter
C.A. Tobin

Intense Pulsed Neutron Source
Argonne National Laboratory
9700 South Cass Avenue
Argonne, IL 60439
U.S.A.

ICANS XIV
Volume I
ISSN 1560-859X
ANL-98/33

Cover Design by:
Argonne National Laboratory
Information and Publishing Division

This publication is available from:
Argonne National Laboratory
Intense Pulsed Neutron Source
J.M. Carpenter
9700 South Cass Avenue
Argonne, Illinois, USA 60439
Phone: 630-252-5519
FAX: 630-252-4163
E-mail: jmcarpenter@anl.gov

TABLE OF CONTENTS

VOLUME I

FOREWARD ..... *i*

IN MEMORIAM MOTOHARU KIMURA ..... *iii*

ICANS XIV AGENDA ..... *vii*

STATUS REPORTS 1

Status of IPNS
B. S. Brown, J. Carpenter, R. Kent Crawford, G. McMichael and W. Ruzicka 3

SINQ as of 1998 (Status Report)
G. S. Bauer 10

News from Moscow Meson Factory
S.F Sidorkin 19

Status of Neutron Scattering Facility in JAERI Neutron Science Project
Y. Oyama, R. Hino, N. Watanabe, M. Mizumoto and T. Mukaiyama 22

A Progress Report on the Spallation Neutron Source
B.R. Appleton 32

The IBR-2 Fast Pulsed Reactor: Present and Future
V.L. Aksenov, V.D. Ananiev, A.V. Belushkin and A.V. Vinogradov 41

Status Report of KENS
H. Ikeda 46

Progress at ISIS
A.D. Taylor and W.G. Williams 51

Current Status of JHF N-arena Development
M. Furusaka and H. Ikeda 56

BNL Activities in Advanced Neutron Source Development: Past and Present
J.B. Hastings, H. Ludewig, P. Montanez, M. Todosow, G.C. Smith and J.Z. Larese 57

AUSTRON Progress Report
E. Jericha, H. Rauch, M. Regler and H. Weber 61

SPECIAL TOPICS PRESENTATIONS 69

Front End and Linac Developments for the Spallation Neutron Source
J.R. Alonso 71

Ring Developments Relevant to Short-Pulse Spallation Neutron Sources
R.J. Macek 84

Report on the International Workshop on Cold Moderators for Pulsed Neutron Sources
J. M. Carpenter 98

The ACoM Collaboration: An International Effort to Develop Advanced Cold Moderators
G. S. Bauer 101

Neutron Scattering Instruments

INSTRUMENTATION AND TECHNIQUES 111

Backscattering Spectroscopy with 2 μeV Resolution at Pulsed Spallation Sources
F. Mezei and G. Zsigmond 113

Experimental Test of Constant q Single Crystal Spectroscopy on a Time-of-Flight Spectrometer
S. Schorr and F. Mezei 119

INSTRUMENTATION AND TECHNIQUES (cont'd)
Experimental Studies on Cold Neutron Beam Focusing by Magnetic Field
Y. Kiyanagi, Y. Suda, H. Nakagawa, T. Kamiyama, Y. Ogawa, H. Iwasa, H.M. Shimizu, H. Kato, T. Oku and T. Wakabayashi 125
Enhancement of Reflectivity of Short D-Spacing Multilayer Mirrors by Ion Polishing in Combination with Ion Beam Sputtering Deposition
K. Soyama, W. Ishiyama and K. Murakami 132
General Time-Focusing of the Pulsed Source Crystal Analyzer Spectrometer
J. M. Carpenter 144
Extending the Domain of Time-of-Flight Powder Diffraction Techniques
P.G. Radaelli 159
Polarisation Modulated Crosscorrelation Neutron Spectroscopy Using ^{3}He Polarising Filters on a Pulsed Source
W.G. Williams 169
New Horizons with Position Sensitive ^{3}He Detectors
C.D. Frost, R.S. Eccleston, J. Norris, N.J. Rhodes and D.J. White 184

COMPUTER SOFTWARE 193
Remote Data Collection and Analysis
T.G. Worlton 195
Report on the Workshop on Monte Carlo Simulation of Neutron Scattering Instruments
R. K. Crawford 201
The Neutron Instrument Monte Carlo Library MCLIB: Recent Developments
P. A. Seeger, L.L. Daemen, R.P. Hjelm, Jr. and T.G. Thelliez 202

INSTRUMENT SUITES 219
Neutron Scattering Instruments for the Spallation Neutron Source (SNS)
R. K. Crawford, K.W. Herwig and T. Fornek 221

LIQUID TARGET SYSTEMS 227
Heat Deposition in Mercury by 24 GeV Protons
G. S. Bauer, H. Spitzer, G. von Holzen, L. Ni and J. Hastings 229
Measurement of Pressure Wave in Mercury Target
M. Futakawa, K. Kikuchi, H. Conrad and H. Stechemesser and ASTE Collaboration 244
Spallation Target Development at JAERI
R. Hino, M. Kaminaga, T. Aso, H. Kogawa, S. Ishikura, A. Susuki, A. Terada, H. Kinoshita and K. Haga 252
Thermal and Hydraulic Design of Mercury Target -Cross Flow Type-
M. Kaminaga, R. Hino, A. Susuki, M. Sakashita, F. Nakamura and H. Tagawa 269
Preliminary Design of Mercury Target -Return Flow Type-
R. Hino, M. Kaminaga, S. Ishikura, I. Yanagisawa, M. Uzawa, K. Kurosawa, K. Ikeda and S. Uchida 278
Analyses on Pressure Wave Propagation and Dynamic Stress in Mercury Targets
S. Ishikura, M. Kaminaga, A. Susuki, R. Hino, I. Harada, K. Kamba and M. Sakashita 288
Opportunities for Irradiation Studies of Structural Materials for Neutron Sources at the Proton Beam-Stop of Moscow Meson Factory
S.F. Sidorkin, G. S. Bauer, Y. Dai, M.I. Grachev, L.V. Kravchuk and Y.I. Orlov 301
Flow Study of JHF N-arena Liquid Target
J. Sakakibara, T. Ino and Y. Takeda 320

LIQUID TARGET SYSTEMS (cont'd)
Flow Measurement in a SINQ Mockup Target Using Mercury
Y. Takeda, H. Kikura and G. Bauer 321
Flow Study on the ESS Target Water Model
K. Haga, Y. Takeda, G. Bauer and B. Guttek 329

SOLID TARGET SYSTEMS 343
Engineering Design of the Lujan Center Target
N.K. Bultman 345
Target Materials Development for SINQ and Out of Beam Testing
A. Malik, G. Bauer and G. Heidenreich 361
Lessons Learned From the First 500 mAh of Beam on SINQ
H. Heyck, B. Amrein, G.S. Bauer and K. Geissmann 374
Measurements of Heat Transfer at the Beam Window in a Mockup Target for SINQ Using Mercury
I. Platnieks, G.S. Bauer, O. Lielausis and Y. Takeda 382
Heat Transfer and Thermomechanic Analyses on the Test Rods in the SINQ-Target Mark 2 for SINQ Using Mercury
L. Ni and G.S. Bauer 396
Thermal Hydraulic Design Concept of the N-Arena Solid Target System
K. Mishima, Y. Saito and T. Hibiki 411
Discussion on the Thickness Optimization of the Water Cooled Solid Target for N-arena
N. Takenaka, Y. Hayashida, R. Yasumura, T. Fujii, N. Hata,
Y. Ogawa and Y. Kiyanagi 424

AUTHOR INDEX

VOLUME II

TABLE OF CONTENTS

Neutron Scattering Instruments (cont'd)

NEUTRON PRODUCTION AND TARGET PHYSICS 439
Radiation Physics Experiments to Develop the Target-Moderator-Reflector System for ESS (European Spallation Neutron Source)
R.-D. Neef 441
Measurement and Analysis of Reaction Rate Distributions in a Lead Assembly Containing Tungsten Target with 500 MeV Proton Bombardment
H. Takada, S. Meigo, T. Sasa and K. Tsujimoto 448
Measurement of Incident Proton Beam Characteristics for AGS Spallation Target Experiment
H. Nakashima, H. Takada, S. Meigo, Y. Kasugai, Y. Ikeda, Y. Oyama,
N. Watanabe and ASTE Collaboration 457
Measurements of Reaction Rate Distributions on a Mercury Target Bombarded with High Energy Protons
H. Takada, Y. Kasugai, H. Nakashima, Y. Ikeda, Y. Oyama,
N. Watanabe, M. Arai, Y. Kiyanagi and ASTE Collaboration 468
Proton Energy Dependence of Reflector Effect on a Beam Intensity from a Decoupled Water Moderator
R. Takagi and Y. Kiyanagi 478

MODERATOR PHYSICS AND PERFORMANCE 487
A Ring Moderator Concept for a Long-Pulse Source
E.J. Pitcher, G.J. Russell and P.D. Ferguson 489
On Radiation Effects in Water Ice at Low Temperatures
E.P. Shabalin 497
Cryogenic Moderator Simulations: Confronting Reality
E.B. Iverson and J.M. Carpenter 507
Use of a Cold Beryllium Reflector-Filter to Enhance Cold Source Brightness at Long Wavelengths
E.J. Pitcher, G.J. Russell and P.D. Ferguson 524
Thermal Neutron Scattering Kernels for Moderator Materials: Comparison of NJoy Results from a Synthetic Model and Its Standard Library
M.M. Sbaffoni, V.H. Gillette, M.E. Pepe and J.R. Granada 533
Development of a Cold Methane Pellet Moderator for ESS
H. Barnert-Wiemer, K. Döring and H. Stechemesser 557
Comparison of Decoupled Cryogenic Moderators for High Resolution Experiments
Y. Ogawa, M. Konno, H. Iwasa, T. Kamiyama, Y. Kiyanagi, M. Furusaka and N. Watanabe 569

NEW INSTRUMENTS AND EQUIPMENT 579
HET II: A Proposed Upgrade for HET, the High Energy Chopper Spectrometer at ISIS
R.S. Eccleston, S. Foster and R.I. Bewley 581
The Backscattering Spectrometer HERMES: Design Issues
J.Z. Larese, L. Daemen, P.A. Seeger, J. Eckert and T.O. Brun 586
HELIOS: A High Intensity Chopper Spectrometer at LANSCE
T.E. Mason, C. Broholm, B. Fult, R. Osborn, R.A. Robinson, G. Aeppli, H.A. Mook, S.E. Nagler, B. Keimer and S. Kern 598
A Design for a High Resolution Very-Low-Q Time-of-Flight Diffractometer
R.P. Hjelm, P.A. Seeger, P. Thiyagarajan, L. Assoufid, L.R. Bertolini and B. Heuser 628
Optimisation of PRISMA at ISIS for Cold Neutron Single Crystal Spectroscopy
M. Bull, M. Harris, M. Hagen, U. Steigenberger, C. Petrillo, F. Sacchetti and K. McEwen 642
Recent Developments of Neutron Diffraction Instruments at the IBR-2 Pulsed Reactor
A.M. Balagurov 650
Design and Placement Considerations for Propeller-Type T-Zero Choppers
R.A. Robinson 657

Targets and Moderators

TARGET AND MODERATOR NEUTRONICS 668
Comparisons of MCNP Thermal Scattering Kernels in a Calculation of the Spectrum from the RAL Liquid Hydrogen Moderator
D.J. Picton, T.D. Beynon and T.A. Broome 669
Progress Report: SNS Neutronics Studies
L.A. Charlton, J.M. Barnes, J.O. Johnson and T.A. Gabriel 678
A Modular Approach to the Design of Cold Moderators
A.T. Lucas 687
Target Options for SINQ-A Neutronic Assessment
G. S. Bauer, A. Dementyev and E. Lehmann 703

TARGET AND MODERATOR NEUTRONICS (cont'd)

Neutronic Aspects of the SINQ Mark 2 Target with Irradiation Test Samples
A. Dementyev, G. S. Bauer, Y. Dai and E. Lehmann 717
A Conceptual Design Study of Target-Moderator-Reflector System for JAERI 5 MW Spallation Source
N. Watanabe, M. Teshigawara, H. Takada, H. Nakashima, Y. Oyama, T. Nagao, T. Kai, Y. Ikeda and K. Kosako 728
Towards a High-Efficiency Pulsed Cold Neutron Source
N. Watanabe, M. Teshigawara, H. Takada, H. Nakashima, Y. Oyama, T. Kai, T. Nagao and K. Kosako 743
Neutron Production Enhancements for the Intense Pulsed Neutron Source
E.B. Iverson, J.M. Carpenter, T.L. Scott, M.E. Miller, L.D. Peters and M.W. Schlueter 751

POSTERS 759
The Iris 4.2 K Cold Graphite Analyser Design
M. Adams, J. Balchin, T. Broome, C. Carlile, D. Cragg, J. Tomkinson, C. Uden, ISIS ... 761
Membrane Windows with Get-Lost Tubes for Use at Small Scattering Angles in Neutron Spectrometers
H. Belch, R. Kleb, J. Carpenter, and K. Crawford, ANL 764
Development and Modernization of the System for the Diagnostics of the State of the Pulsed Neutron Source IBR-2
Yu.N Pepyolyshev, A.V. Belushkin and A.V. Vinogradov, JINR 768
Sample Environments at the Intense Pulsed Neutron Source (IPNS)
D. E. Bohringer and K. J. Volin, ANL 773
A "Hot Stage" Displex®: 20 - 800K in a Neutron Scattering Environment
K. J. Volin and D. E. Bohringer, ANL 783
The New Drive System for ISIS Disc Choppers
Z. Bowden, M. Fischer, P. Chorley; ISIS
B. Halls, Spectral Drives & Controls, Ltd 791
A New Scintillator for Neutron Scattering Instruments
J.B. Czirr, Mission Support, Inc. 792
Structural and Hydraulic Study on Cold Source Moderator
T. Aso, S. Ishikura, A. Terada, T. Kai, M. Teshigawara, M. Kaminaga, R. Hino, N. Watanabe, JAERI 804
Incident Spectrum Determination for Time-of-Flight Powder Neutron Diffraction Data Analysis
J. Hodges, J. Jorgensen, S. Short, D. Argyriou and J. Richardson Jr., ANL 813
Behavior of ^{7}Be in the Moderator Cooling System at the Pulsed Neutron Source, KENS
S. Itoh, T. Miura, M. Furusaka, S. Yasui, Y. Ogawa, Y. Kiyanagi, S. Sasaki, K. Iijima .. 823
The High-Resolution Medium-Energy Chopper Spectrometer (HRMECS): Instrumentation Upgrade and Future Scientific Opportunities
C. Loong, J. Hammonds, D. Yocum, J. Nipko, K. Takeuchi, D. Chen, L. Donley, G. Ostrowski, R. Crawford, H. Belch and R. Kleb, ANL 829
Material Development for Spallation Target at JAERI
K. Kikuchi, H. Kogawa, M. Futakawa, I. Ioka and R. Hino 830
Preliminary Design Studies for an Iridium Rod Target at the BNL-AGS
H. Ludewig, J. Hastings, P. Montanez, and M. Todosow 836
A Foil-less Charge Exchange Injection (LUCE) for the Intense Proton Storage Ring
Y. Suzuki (JAERI) (Presented by Y. Oyama) 847

POSTERS (cont'd)
Adjustable Collimation for the General Materials Diffractometer (GEM)
L.C. Perrott, S.A. Temple, and G. Thomas, ISIS 852
A New Polarized Neutron Reflectometer at KENS
M. Takeda, N. Toyoshima and Y. Endoh 855
Performance of the Small-Angle Diffractometer SAND at IPNS
P. Thiyagarajan, V. Urban, K. Littrell, C. Ku, D. G. Wozniak, H. Belch, R. Vitt, J. Toeller, D. Leach, J.R. Haumann, G.E. Ostrowski, L.I. Donley, J. Hammonds, J.M. Carpenter and R. K. Crawford, ANL 864

WORKING GROUP REPORTS 879
Working Group on Monte Carlo Simulation of Neutron Scattering Instruments
R.K. Crawford, Chair 881
Report on the Workshop Group Meeting on: Next Generation Powder Diffractometers
P. G. Radaelli, Chair 884
Report of the Workshop on Small-Angle and Reflectometry Instruments on Future Spallation Sources
P.A. Seeger, Chair 887
Working Group Report: Critical Heat Flux: Limitation to Solid Target?
Y. Takeda, Chair 889
Summary of the Objective Discussion of Solid and Liquid Targets for High-Power Sources
N. Watanabe and P. Ferguson, Co-Chairs 890
Summary Report for the Working Group "Needs for Target Systems and Instrument Materials, Beamline Components, Detectors, and Beamline Technology"
M. Furusaka, Chair 891
Working Group: Spectroscopy in Future Neutron Sources
C. Loong, Chair 894
Moderator Performance Enhancement and Development Activities: Progress and Needs
G. Russell, Chair and E. Pitcher, Co-Chairman 895

VENDOR PAPER
Equipment and Software for Research with Neutrons
H. Betzold 907

GROUP PHOTO

LIST OF ATTENDEES

VENDOR LIST

AUTHOR INDEX

FOREWORD

ICANS XIV, the fourteenth meeting of the International Collaboration on Advanced Neutron Sources, took place at Starved Rock Lodge, Utica, Illinois, June 14–19, 1998. Argonne's Intense Pulsed Neutron Source division served as host. The U.S. Department of Energy, The University of Chicago Board of Governors, Argonne National Laboratory, Los Alamos National Laboratory, Oak Ridge National Laboratory, and the Neutron Scattering Society of America sponsored the meeting. Jack Carpenter was conference chair and organizer, with Erik Iverson assisting, while Laura Miller, IPNS executive secretary, served as conference secretary. Beverly Marzec, Cathy Riblon, Carolyn Tobin, Ira Bresof, and Merle Faber, all of IPNS, ably and good-naturedly saw to all the needs of the attendees. One hundred twenty-seven participants registered for the meeting, representing 27 institutions and ten countries.

Starved Rock State Park was named for a grisly battle between American Indian tribes in the mid-18th century. We occupied the entire Lodge, a 1920s complex standing on a bluff above the Illinois River. Dann Sarro and Joanne Thomas of Argonne's Information and Publishing division created the conference logo, in which the ICANS "I" represents a picturesque waterfall in the park. Participants enjoyed nature walks in the nearby woods and visits to the small towns in the bucolic surrounding area.

The meeting began with a reception on Sunday evening. Monday's plenary sessions included status reports on the four operating spallation neutron sources, IPNS, ISIS, KENS, and the Lujan Center; on the INR source under construction at Troitsk; on the IBR-2 pulsed reactor at Dubna; and on proposals for five new installations. We also heard reports on spin-off activities: the ASTE tests (liquid mercury target tests at the AGS accelerator at Brookhaven), the ACoM activities (developments aimed to provide cold moderators suitable for high-power pulsed sources), and the International Workshop on Cold Moderators for Pulsed Neutron Sources, held in September 1997 at Argonne. Jose Alonso and Bob Macek delivered enlightening invited talks overviewing linear accelerators and rings for spallation neutron sources. The rest of the meeting was devoted to targets and moderators and to instrumentation in a normal rotation of ICANS topics. There were altogether 84 oral reports and 23 poster presentations.

On Tuesday and on Wednesday morning, we divided into separate series of sessions on Instrumentation and on Targets and Moderators. In the first, we had reports and discussions on instrumentation and techniques, on computer software, on instrument suites, and on new instruments and equipment. In the second series were sessions on liquid target systems, on solid target systems, on neutron production and target physics, on moderator physics and performance, and on target and moderator neutronics. The Tuesday evening meetings went on until 10:00, making for a 14-hour working day. That everyone willingly endured the long hours is a credit to the dedication of the attendees.

On Wednesday afternoon, we boarded buses for the 1-hour trip to Argonne, where attendees toured IPNS and the Advanced Photon Source. Returning to Starved Rock, we enjoyed boat rides on the Illinois River and then a barbecue banquet dinner at the Lodge.

All day Thursday and Friday morning, the attendees, in small working groups, discussed next-generation powder diffractometers, critical heat flux limitations on solid targets, monte carlo instrument simulation, prospects for high- and low-energy spectroscopy, small angle scattering and reflectometry, and the roles of solid and liquid targets in high-

power pulsed spallation sources. Representatives of the laboratories participating in ICANS met Thursday evening to discuss the outcome of ICANS XIV and to decide whether, where, and when the next meeting would take place. They agreed to meet again in about 2 years in Japan. After the lunch break on Friday, the working group chairs presented the findings of their groups to the participants in a final plenary session, and the meeting adjourned with good feelings of accomplishment.

A great deal has been achieved since the last ICANS meeting in 1995 at PSI in Switzerland, and much more is in progress. At this writing, the good news is that the Spallation Neutron Source project, SNS, at Oak Ridge National Laboratory in the United States, has received the official go-ahead, designated as a funded seven-year-long construction project with $130 million for the 1999 fiscal year (began October 1, 1998). The schedule calls for completion at the end of FY 2005. We hail this event and the wonderful progress made worldwide in the development of pulsed sources and accelerator-based neutron facilities.

We have reproduced the papers and reports essentially as they came to us, with only minor format changes. Carolyn Tobin and Beverly Marzec in the IPNS offices carried out the organization and collation of papers. Argonne's Information and Publishing Division produced these Proceedings, and ICANS XIV has a web site accessible through the IPNS home page at http://www.pns.anl.gov/.

I thank our sponsors, all those who worked so hard as hosts to our meeting and in preparation of the Proceedings, and the authors and participants whose cooperation with our manuscript requirements made the final task easier.

J. M. Carpenter
November 1998

IN MEMORIAM
MOTOHARU KIMURA

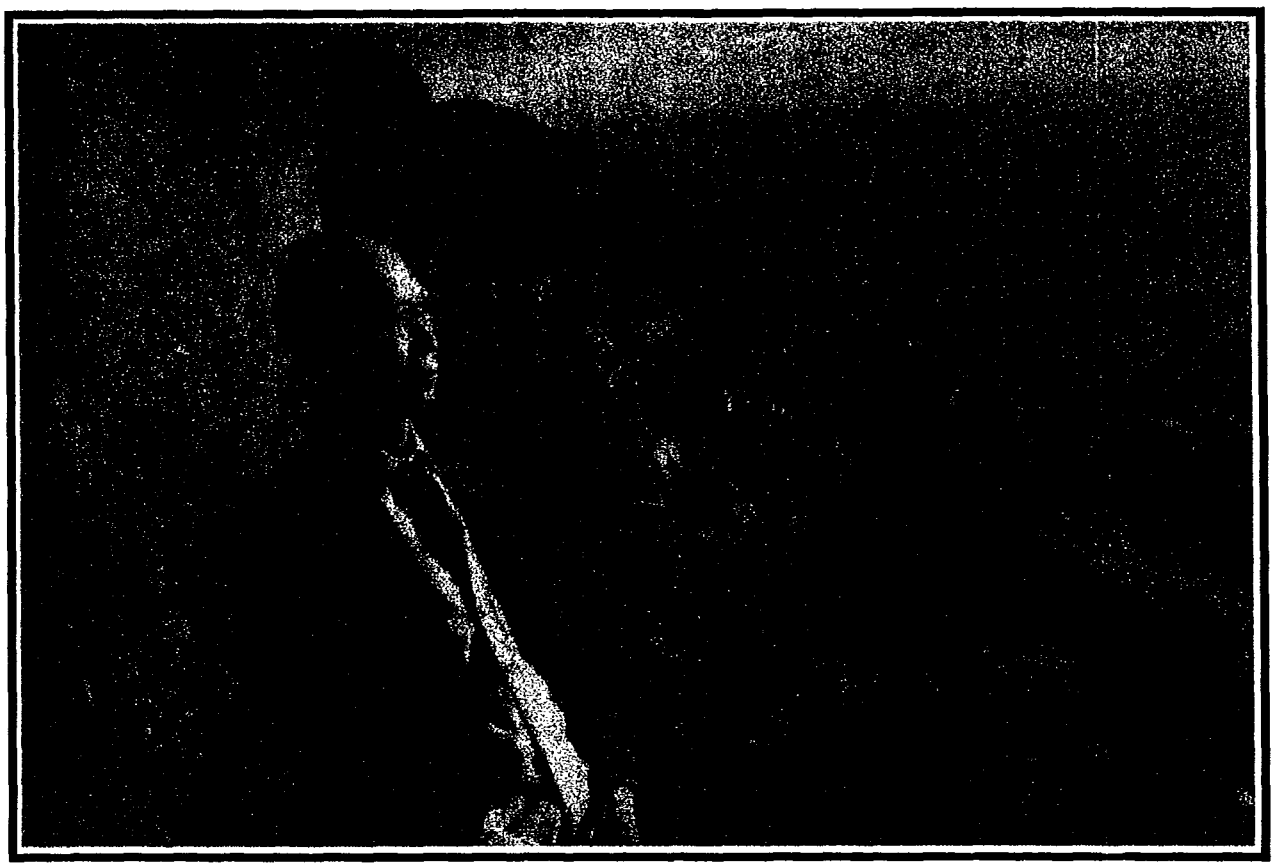

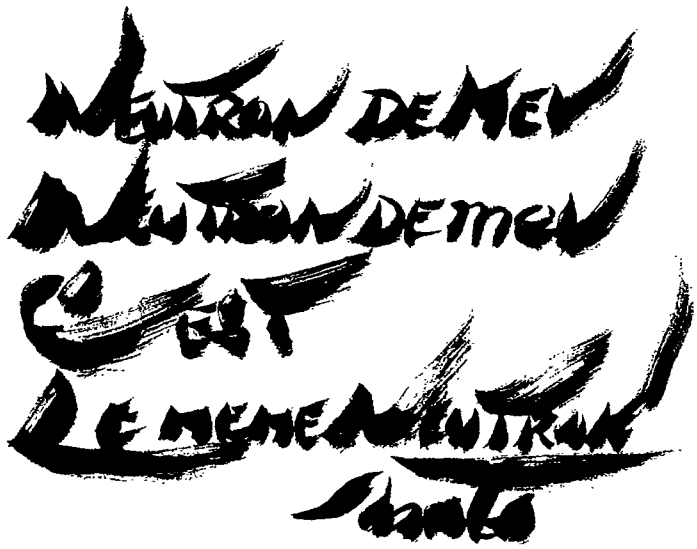

"Thermalization," a haiku by Motoharu Kimura

IN MEMORIAM

MOTOHARU KIMURA

Motoharu Kimura died at his home in Sendai on March 14, 1996, after an extended illness. He was 87. Kimura was one of the pioneers of neutron physics in Japan, beginning his work shortly after the discovery of the new particle in 1932, working with Shyoji Nishikawa in the RIKEN Laboratory of Yoshio Nishina at the University of Tokyo. It was Kimura who first conclusively determined that the awesome explosion over Hiroshima was of nuclear origin, and he was the first scientist with instruments to arrive there after the atomic bomb burst. He made important damage and radiation surveys and triangulated the hypocenter and altitude of the blasts at Hiroshima and Nagasaki. Kimura-sensei reestablished accelerator science in Japan during the reconstruction following the war and was one of the first to observe synchrotron light. He created an important center for electron scattering and time-of-flight slow neutron scattering based on the 300-MeV Tohoku University electron linear accelerator in the 1960s. He worked vigorously with us during the early years of pulsed spallation neutron source development at Argonne in the early 1970s and through the 1980s and was a cofounder of ICANS. Moto attended nearly all the ICANS meetings, where his energy and good spirit inspired us all. Kimura's technical contributions and encouragement were essential to the beginnings of the ICANS collaboration and of IPNS. The photograph shows Moto at the summit of Tsukuba Mountain at an outing during the Tsukuba ICANS-IV meeting in 1980. Moto also wrote and calligraphed the accompanying French-language *haiku*, which I have called "Thermalization."

From the rubble of Nagasaki's Uragami Cathedral, Kimura rescued a stone bust, the Uragami Angel's Head. That figure, an icon for peace, for many years inspired a small, quiet peace and disarmament movement, the Sendai International Brotherhood Society, SIBS, which he founded. The bust is now in the Hiroshima Peace Museum. He cultivated orchids and was an accomplished painter in the sumi-e style. In his later years, Kimura-sensei devoted his energies to peace, reconciliation, and disarmament. Scientist, teacher, artist, humanist, friend, this persistent, diligent, gentle, caring man was admired throughout the world.

J. M. Carpenter

ICANS-XIV Agenda
June 14-19, 1998

SUNDAY, JUNE 14, 1998

5:00-8:00 p.m. *REGISTRATION*
Room: Great Hall

5:00-8:00 p.m. *RECEPTION*
Room: Great Hall

8:00 p.m. *DINNER: No Host*

MONDAY, JUNE 15, 1998

7:00-8:30 a.m. *BREAKFAST: No Host*

8:30 a.m.-5:00 p.m.
PLENARY SESSIONS ONLY
Room: Starved Rock Room all day

8:30 *WELCOME: Bruce Brown*

8:45 *MEETING DETAILS: John M. Carpenter*

9:00-3:00 *STATUS REPORTS* (20 min. each):

9:00 Status of IPNS: *Bruce Brown*
9:30 Status of SINQ: *G. S. Bauer*
9:40 Status of Spallation Sources INR RAS: *S. Sidorkin*

10:00 *COFFEE BREAK*

10:30 Status of Neutron Scattering Facility in JAERI Neutron Science Project: *Y. Oyama*
10:50 A Progress Report on the Spallation Neutron Source (SNS) Project: *B. Appleton*
11:10 Review of the Present Status and Development Plans for IBR-2: *A. Belushkin*
11:30 Status Report of KENS: *M. Arai*
11:50 Recent Progress at the Lujan Center: *J. Roberts*

12:10 *LUNCH*

1:30 *CONTINUE STATUS REPORTS*

MONDAY, JUNE 15, 1998 (cont'd.)

1:30	*SPECIAL TOPIC PRESENTATION*
1:30	Front End and Linac Developments for Spallation Neutron Sources: *J. Alonso*
2:00	*CONTINUE STATUS REPORTS*
2:00	ISIS Status Report: *G. Williams*
2:20	Current Status of JHF N-arena Development: *M. Furusaka*
2:40	BNL Activities in Advanced Neutron Source Development: Past and Present: *J. Hastings*
3:00	Update on the AUSTRON Project: *G. S. Bauer*
3:20	*GROUP PHOTO*
3:40	*COFFEE BREAK*
4:00-5:50	*SPECIAL TOPICS PRESENTATIONS*
4:00	Ring Developments Relevant to Spallation Neutron Sources: *R. Macek*
4:30	The Cold Moderator Workshop: *J. M. Carpenter*
4:50	International Collaboration on Advanced Cold Moderators: *G. Bauer*
5:10	*IN MEMORIAM MOTOHARU KIMURA*
5:30	*ADJOURN*

POSTER DISPLAYS ALL DAY

VENDOR DISPLAYS ALL DAY

TUESDAY, JUNE 16, 1998

7:00-8:00 a.m. *BREAKFAST: No Host*

La Salle Room - Neutron Scattering Instruments

8:00-10:00	*INSTRUMENTATION AND TECHNIQUES*
8:00	Backscattering Spectroscopy with 2 μeV Resolution at Pulsed Spallation Sources: *F. Mezei*
8:20	Experimental Test of Constant q Single Crystal Spectroscopy on a TOF Spectrometer: *F. Mezei*
8:40	Prospects for Powder Diffraction Using a Solid Methane Moderator at IPNS: *J. Richardson*
9:00	Experimental Studies on Cold Neutron Beam Focusing by Magnetic Field: *Y. Kiyanagi*
9:20	Enhancement of Reflectivity of Short D-Spacing Multilayer Mirrors by Ion Polishing in Combination with Ion Beam Sputtering Deposition: *K. Soyama*
10:00	*COFFEE BREAK*
10:30	General Time-Focusing of the Pulsed Source Crystal Analyzer Spectrometer: *J. Carpenter*
10:50	Cold Neutron TOF Spectroscopy on LANSCE Coupled Moderator: A Breakthrough in Neutron Intensity: *F. Mezei*
11:10	Extending the Domain of Time-of-Flight Powder Diffraction Techniques: *P. Radaelli*
11:30	Polarization-Modulated Cross-Correlation Neutron Spectroscopy Using Helium-3 Filters on a Pulsed Source: *G. Williams*
11:50	New Horizons with Position Sensitive ^{3}He Detectors: *C. Frost*
12:00-1:30	*LUNCH*
1:30-3:00	*TOPICAL DISCUSSIONS - PREPARED TALKS*

TUESDAY, JUNE 16, 1998 (cont'd.)

1:30-3:00	*COMPUTER SOFTWARE*
1:30	Remote Display and Analysis of Neutron Scattering Data: *T. Worlton*
1:50	Toward an International Standard for a Library of Monte Carlo Subroutines for Neutron Scattering Instrument Design: *K. Crawford*
2:10	The Los Alamos Neutron Instrument Simulation Package: Recent Developments: *P. A. Seeger*
2:50	MC-Web: A WWW-based Application for NIS: *T. Thelliez*
3:10	*COFFEE BREAK*
3:40-5:30	*INSTRUMENT SUITES*
3:40	Call for Discussion on Selection of Instrument Suites for New Facilities: *U. Steigenberger*
3:50	Neutron Scattering Instruments for the Spallation Neutron Source: *K. Crawford*
5:30-7:30	*OPEN PERIOD AND DINNER*
7:30-10:00	Discussion on Selection of Instrument Suites for New Facilities: *U. Steigenberger*
10:00	*ADJOURN*

POSTER DISPLAYS ALL DAY

VENDOR DISPLAYS ALL DAY

TUESDAY, JUNE 16, 1998

7:00-8:00 a.m. *BREAKFAST: No Host*

Starved Rock Room – Targets and Moderators

8:00-10:00	*LIQUID TARGET SYSTEMS*
8:00	Heat Deposition in Mercury by 24 GeV Protons: *G. Bauer*
8:40	Measurement of Pressure Wave in Mercury Target: *K. Kikuchi*
	Spallation Target Development at JAERI: *R. Hino*
9:00	Thermal and Hydraulic Design of Mercury Target - Cross Flow Type: *M. Sakashita*
	Preliminary Design of Mercury Target – Return Flow Type: *I. Yanagisawa*
9:20	Analyses on Pressure Wave Propagation and Dynamic Stress in Mercury Target: *I. Harada*
9:40	Opportunities for Liquid Metal Irradiation at INR: *G. Bauer*
10:00	*COFFEE BREAK*
10:30	Flow Study for JHF N-arena Liquid Target: *T. Ino*
10:50	Flow Study on the ESS Target Water Model: *Y. Takeda*
	Flow Measurement in a SINQ Mockup target using Mercury: *Y. Takeda*
11:30-1:00	*LUNCH*
1:00-3:00	*SOLID TARGET SYSTEMS*
1:10	The Lujan Center Target Station: A Progress Report: *J. Donahue*
1:30	Engineering Design of the Lujan Center Target System: *N. Bultman*
1:50	Measurement of Temperature Distribution on the Window of SINQ Mockup Target: *Y. Takeda*
2:10	Target Materials Development for SINQ and Out of Beam Testing: *A. Malik*
2:30	Lessons Learned From the First 500 mAh of Beam on SINQ: *H. Heyck*
2:50	Thermal Structure Analyses on the Test Rods in the SINQ Target Mark 2 *G. Bauer*
	Thermal Hydraulic Design Concept of the N-arena Solid State System in JHF Project: *K. Mishima*
	Simple Thermal Hydraulic Discussion of the Thickness Optimization of the Water Cooled Solid Target for N-arena: *N. Takenaka*
3:10-3:40	*COFFEE BREAK*

TUESDAY, JUNE 16, 1998 (cont'd.)

3:40-5:30	*NEUTRON PRODUCTION AND TARGET PHYSICS*
3:40	Radiation Physics Experiments to Develop the Target-Moderator-Reflector System for ESS: *R. Neef*
4:00	Measurement and Analysis of Reaction Rate Distributions in a Lead Assembly Containing Target with 500 MeV Proton Bombardment: *H. Takada*
4:20	Measurement of Incident Proton Beam Characteristics for AGS Spallation Target Experiment: *H. Takada*
4:40	Measurements of Reaction Rate Distributions on a Mercury Target Bombarded with High Energy Protons: *H. Takada*
5:00	Proton Energy Dependence of Reflector Effect on a Beam Intensity From a Decoupled Water Moderator: *Y. Kiyanagi*
5:20	Experimental Study of the Combined W-Be Photoneutron Targets of 40 MeV Electrons: *V. Lomidze*
5:30-7:30	*OPEN PERIOD AND DINNER*
7:30-10:00	*MODERATOR PHYSICS AND PERFORMANCE*
7:30	Ring Moderator LPSS Target Station Design and Optimization: *E. Pitcher*
7:50	On Radiation Effects in Water Ice at Low Temperatures: *E. Shabalin*
8:10	Cryogenic Moderator Simulations: Confronting Reality: *E. Iverson*
8:30	Use of a Cold Beryllium Filter to Enhance Cold Source Performance: *E. Pitcher*
8:50	Thermal Neutron Scattering Kernels for Moderator Materials: Comparison of N-Joy Results from a Synthetic Model and Its Standard Library: *R. Granada*
9:10	Development of a Cold Methane Pellet Moderator for ESS: *H. Barnert-Wiemer*
9:30	Comparison of Decoupled Cryogenic Moderators for High Resolution Experiments: *Y. Kiyanagi*
9:50	*ADJOURN*

POSTER DISPLAYS ALL DAY

VENDOR DISPLAYS ALL DAY

WEDNESDAY, JUNE 17, 1998

7:00-8:00 a.m. *BREAKFAST: No Host*

La Salle Room - Neutron Scattering Instruments

8:00-12:00 *NEW INSTRUMENTS AND EQUIPMENT*

8:00 HET II: A Proposed High Intensity Chopper Spectrometer at ISIS: *R. S. Eccleston*
8:20 A 30-T Pulsed Magnet for Neutron Scattering: *R. Robinson*
8:40 The Backscattering Spectrometer HERMES: Design Issue: *L. Daemen*
9:00 HELIOS: A High Intensity Chopper Spectrometer at LANSCE: *T. Mason*
9:20 A Design for a High Resolution Very-Low-Q Time-of-Flight Diffractometer: *R. Hjelm*
9:40 Optimisation of PRISMA for Cold Neutron Single Crystal Experiments: *M. Bull*

10:00-10:10 *COFFEE BREAK*

10:10 Recent Developments of Neutron Diffraction Instruments at the IBR-2 Pulsed Reactor: *A. Balagurov*
10:30 Design and Placement Considerations for Propeller-Type T-Zero Choppers: *R. Robinson*
11:10 The High Pressure Preferred Orientation (HIPPO) Diffractometer: *J. Roberts*
11:30 The Future is SMARTS...Spectrometer for Materials Research at Temperature and Stress: *J. Roberts*

11:45-12:00 *PLENARY SESSION*
Starved Rock Room, Formation of Working Groups

12:00 p.m. *EXCURSION TO ARGONNE IPNS AND APS* (Box Lunch on Bus)

5:00, 6:00, 7:00 p.m.
RIVERBOAT TRIPS

8:00 *BARBECUE BANQUET*

POSTER DISPLAYS

VENDOR DISPLAYS

WEDNESDAY, JUNE 17, 1998

7:00-8:00 a.m. *BREAKFAST: No Host*

Starved Rock Room-Targets and Moderators

8:00-12:00 *TARGET AND MODERATOR NEUTRONICS*

8:00 Comparison of Hydrogen Kernels for a Calculation of the ISIS H2 Moderator Spectrum: *D. Picton*
8:20 SNS Neutronics Studies: *L. Charlton*
8:40 A Modular Approach to the Design of Cold Moderators: *T. Lucas*
9:00 Target Options for SINQ- A Neutronic Assessment: *G. Bauer*
Neutronic Aspects of the SINQ Mark 2 Target with Irradiation Test Samples: *G. Bauer*
9:20 A Conceptual Design Study of Target-Moderator-Reflector System for JAERI 5MW Spallation Source: *N. Watanabe*
9:40 Final Design Neutronic Performance Calculations for the Lujan Center Target System: *P. Ferguson*

10:00 *COFFEE BREAK*

10:30 Toward a High Efficiency Pulsed Cold Neutron Source: *M. Teshigawara*
10:50 Enhancements to the Target and Moderator System at the Intense Pulsed Neutron Source: *E. Iverson*

11:45-12:00 *PLENARY SESSION*
Starved Rock Room, Formation of Working Groups

12:00 PM *EXCURSION TO ARGONNE IPNS AND APS* (Box Lunch on Bus)

5:00, 6:00, 7:00 p.m.
RIVERBOAT TRIPS

8:00 *BARBECUE BANQUET*
POSTER DISPLAYS ALL DAY

VENDOR DISPLAYS ALL DAY

THURSDAY, JUNE 18, 1998

7:00-8:30 a.m. *BREAKFAST: No Host*

8:30-10:00 *WORKSHOP GROUP MEETINGS*

Needs for Target Systems and Instrument Materials, Beamline Components, Detectors, and Beamline Technology Development
Chairman: *M. Furusaka*
Room: Hennepin Room

Monte Carlo Simulation of Neutron Scattering Instruments
Chairman: *R. Kent Crawford*
Room: Utica Room

Combined Workshop:
Prospects for Spectroscopy in Future Neutron Sources (Low Energy, High Resolution; High Energy, Modest Resolution)
Chairman: *C. Loong*
Room: Peru Room

10:00-10:15 *COFFEE BREAK*

10:15 - 12:00

Critical Heat Flux Limitations on Solid Targets
Chairman: *Y. Takeda*
Room: Starved Rock Room

12:00-1:30 *LUNCH*

1:30-5:00

Moderator Development Activities: Needs and Work in Progress
Chairman: *G. Russell*
Room: La Salle Room

Next Generation Powder Diffractometers
Chairman: *P. Radaelli*
Room: Hennepin Room

Small Angle Scattering and Reflectometry at Future Pulsed Neutron Sources
Chairman: *P. Seeger*
Room: Utica Room

8:00-10:00 p.m.-*WORKSHOP GROUP MEETINGS cont'd*

Objective Discussion of Solid and Liquid Targets for High-Power Sources
Chairman: *N. Watanabe*
Co-chair: *P. Ferguson*
Room: La Salle Room

10:00 *ADJOURN*

FRIDAY, JUNE 19, 1998

7:00-8:00 a.m. *BREAKFAST: No Host*

8:00-12:00 *WORKSHOP GROUP MEETINGS*
REPORT PREPARATIONS

Rooms: Starved Rock Room
LaSalle Conference Room
Peru Conference Room
Utica Conference Room
Hennipen Conference Room

1:30-3:00 *WORKSHOP GROUP REPORTS*
SELF-REFLECTION ON ICANS
CLOSING REMARKS

Room: Starved Rock Room

3:00 *ADJOURN*

POSTERS

1. The Iris 4.2 K Cold Graphite Analyser
   M. Adams, J. Balchin, T. Broome, C. Carlile, D. Cragg, J. Tomkinson, C. Uden, ISIS
2. The Iris 4.2 K Cold Graphite Analyser (cont'd)
   M. Adams, J. Balchin, T. Broome, C. Carlile, D. Cragg, J. Tomkinson, C. Uden, ISIS
3. Membrane Windows with Get-Lost Tubes
   H. Belch, J. Carpenter, K. Crawford, R. Kleb, ANL
4. Reactor Parameters Monitoring System
   A. Belushkin, JINR
5. Sample Environments at the Intense Pulsed Neutron Source (IPNS)
   D. E. Bohringer and K. J. Volin, ANL
6. A "Hot Stage" Displex: 20 - 800K In A Neutron Scattering Environment
   K. J. Volin and D. E. Bohringer, ANL

POSTERS cont'd

7. A New Drive System for ISIS Disc Choppers
   Z. Bowden, ISIS
8. A New Scintillator for Neutron Scattering Instruments
   B. J. Czirr, Mission Support, Inc.
9. Design and Status of the Upgrade to the IPNS spectrometer, QENS
   K. W. Herwig, R. K. Crawford, F. R. Trouw, and H. A. Belch, ANL
10. Structural and Hydraulic Study on Cold Source Moderator
    T. Aso, S. Ishikura, A. Terada, T. Kai, M. Teshigawara, M. Kaminaga, R. Hino, N. Watanabe, JAERI
11. Incident Spectrum Determination for Time-of-Flight Neutron Diffraction Data
    J. Hodges, J. Jorgensen, J. Richardson Jr., S. Short and D. Argyriou, ANL
12. Behavior of ^{7}Be in the Moderator Cooling System at the Pulsed Neutron Source
    S. Itoh, T. Miura, M. Furusaka, S. Yasui, Y. Kiyanagi, Y. Ogawa, S. Sasaki, K.Iijima, KENS
13. The High-Resolution Medium-Energy Chopper Spectrometer (HRMECS): Instrumentation Upgrade and Future Scientific Opportunities
    C. Loong, J. Hammonds, D. Yocum, J. Nipko, K. Takeuchi, L. Donley, G. Ostrowski, R. Crawford and H. Belch, ANL
14. Material Development for Spallation Target at JAERI
    K. Kikuchi, H. Kogawa, M. Futakawa, I. Ioka and R. Hino, JAERI
15. IBR-2 Solid Methane Moderator: Design Features for Removal of Radiolytic Hydrogen
    V. Melikhov, A. Beljakov, I. Tretjakov, and E. Shabalin, JINR
16. Preliminary Design Study for an Ir Rod Target at the BNL AGS
    H. Ludewig, J.B. Hastings, Paul Montanez, and M. Todosow, BNL
17. IBR-2 Solid Methane Moderator: Design Features for Removal of Radiolytic Hydrogen
    V. Melikhov, A. Beljakov, I. Tretjakov, and E. Shabalin, JINR
18. A Foil-less Charge Exchange Injection (LUCE) for the Intense Proton Storage Ring
    Y. Suzuki (JAERI) (Presented by *Y. Oyama*)
19. GEM, A New Beamline for ISIS
    L. Perrott, ISIS
20. Recent Developments on the General Purpose Powder Diffractometer (GPPD) at IPNS
    J. W. Richardson, Jr., Brian J. Mitchell and Christopher D. Murphy, ANL
21. The IPNS Single Crystal Diffractometer: Capabilities and Recent Accomplishments
    A. J. Schultz, R. W. Henning, M. E. Miller and R. Vitt, ANL
22. Moderator Enhancements for the Intense Pulsed Neutron Source
    T. Scott, ANL
23. A New Polarized Neutron Reflectometer at KENS
    M. Takeda, N. Toyoshima and Y. Endoh, KENS
24. The Performance of the Small-Angle Diffractometer SAND at IPNS
    P. Thiyagarajan, R. K. Crawford, D. G. Wozniak, R. Kleb, C. Ku, V. Urban, K. Littrell, R. Vitt, H. Belch, J. Toeller and D. Leach, ANL
25. IPNS: Instruments, ANL
26. IPNS: General, ANL
27. IPNS: Neutrons and Materials, ANL

STATUS REPORTS

ICANS-XIV
14th Meeting of the International Collaboration on
Advanced Neutron Sources
June 14-19, 1998
Utica, IL USA

STATUS OF IPNS

B.S. Brown, J. Carpenter, R. Kent Crawford, G. McMichael, W. Ruzicka
Argonne National Laboratory
IPNS Division, Argonne, IL 60439
USA

Abstract

Under the Scientific Facilities Initiative, IPNS has increased the beam time for users by 50% and is operating 25 weeks/yr. We have added scientific and technical staff to support the greatly expanded user program. Projects are underway to increase the capabilities for most IPNS instruments and an upgraded quasielastic spectrometer (QENS) is under construction. IPNS has been given lead responsibility for the neutron scattering instruments for the Spallation Neutron Source to be built at Oak Ridge, for which instrument teams are being formed.

1. User Program

In 1995 the US national laboratories put forth a highly coordinated successful effort to obtain funding for a number of Department of Energy (DOE) facilities that were operating well below their optimum level. For a relatively small increase in operating funds, facilities for physical sciences, high energy physics and nuclear physics research significantly increased their operating effectiveness. IPNS, along with the other DOE neutron, synchrotron and electron microscope facilities, received a significant increase in funds starting in 1996. This resulted in our hiring 23 new staff, primarily for scientific support, and an increase of 50% for instrument beam time for users.

IPNS continues to run one of the most active user programs at a US neutron scattering source and to foster scientific interactions with the user community (see table below of recent meetings).

1.1 Recent Meetings Organized by IPNS

Materials Research Using Cold Neutrons at Pulsed Neutron Sources, Aug. 1997

International Workshop on Cold Moderators for Pulsed Neutron Sources, Sept. 1997

Monte Carlo Simulation of Neutron Scattering Instruments, Nov. 1997

ICANS XIV, June 1998

IPNS operates 25 weeks, with slightly more than 200 users coming to IPNS for one or more experiments each year. Eleven instruments are in the user program, two more are under development, and a total of 15 stations are active on 12 beamlines. The 31st round of approved user experiments will begin in July, 1998. The oversubscription ratio remains at more than 2. The table below shows the results of recent operation. The decrease in the number of

experiments performed following 1989-90 was due to the removal of the booster target and a decrease in operating time.

Table 1. IPNS User Program

	FY87	FY88	FY89	FY90	FY91	FY92	FY93	FY94	FY95	FY96	FY97
No. of Experiments Performed:	223	257	323	330	273	210	248	281	279	320	353
VISITORS TO IPNS FOR AT LEAST ONE EXPERIMENT:											
ANL	55	57	60	61	60	53	48	49	55	58	60
Other Gov. Labs.	15	18	16	19	15	14	18	13	16	18	29
Universities	78	89	94	120	92	62	64	63	83	85	91
Industry	24	20	24	36	18	20	16	15	12	7	6
Foreign	24	17	26	18	27	14	25	32	33	33	42
TOTAL	196	201	220	254	212	163	171	172	199	201	228

The results of the additional operation are reflected in the figures for publications:

Table 2. IPNS Publications (fiscal year)

1992	1993	1994	1995	1996	1997
121	124	112	115	140	170

The IPNS accelerator system has maintained its already excellent operating record and even improved upon it. Reliability and average current figures are shown below. Also shown below are historical records of time lost for various systems. Key to the outstanding and improving reliability is identifying the subsystems that are most responsible for the downtime so that the available effort can be concentrated where it may have the greatest effect. As can be seen from the figure, a few systems (kickers, linac, rf and source) have been responsible for most of the downtime and we are having some success in reducing these worst offenders.

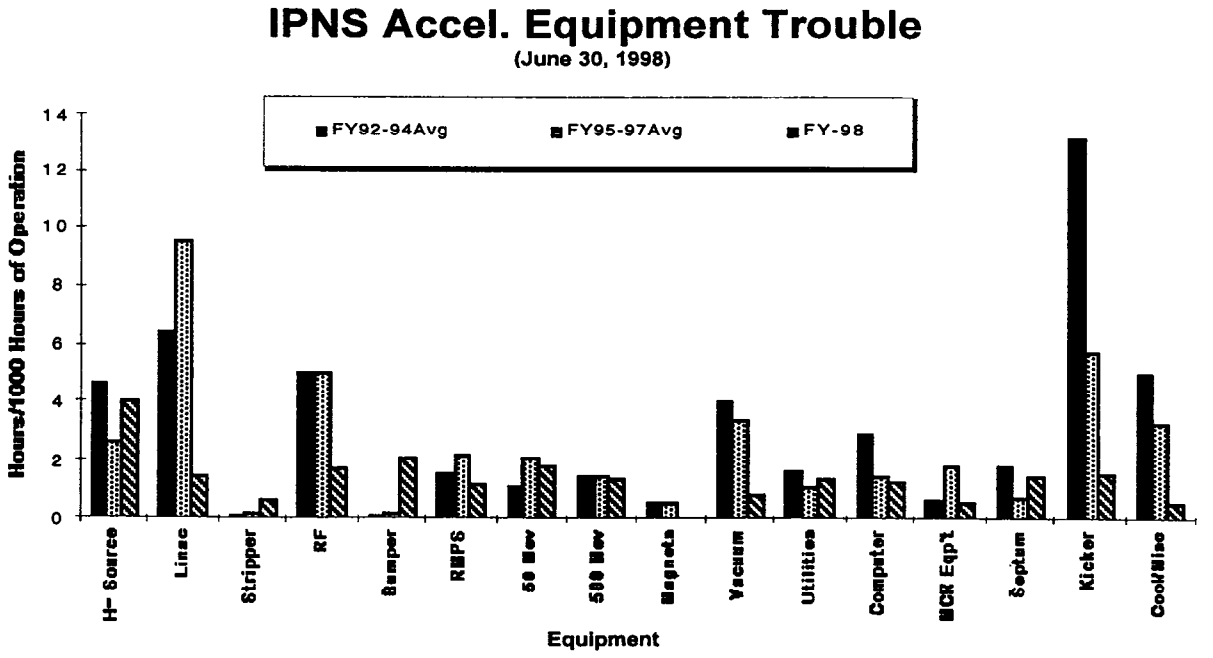

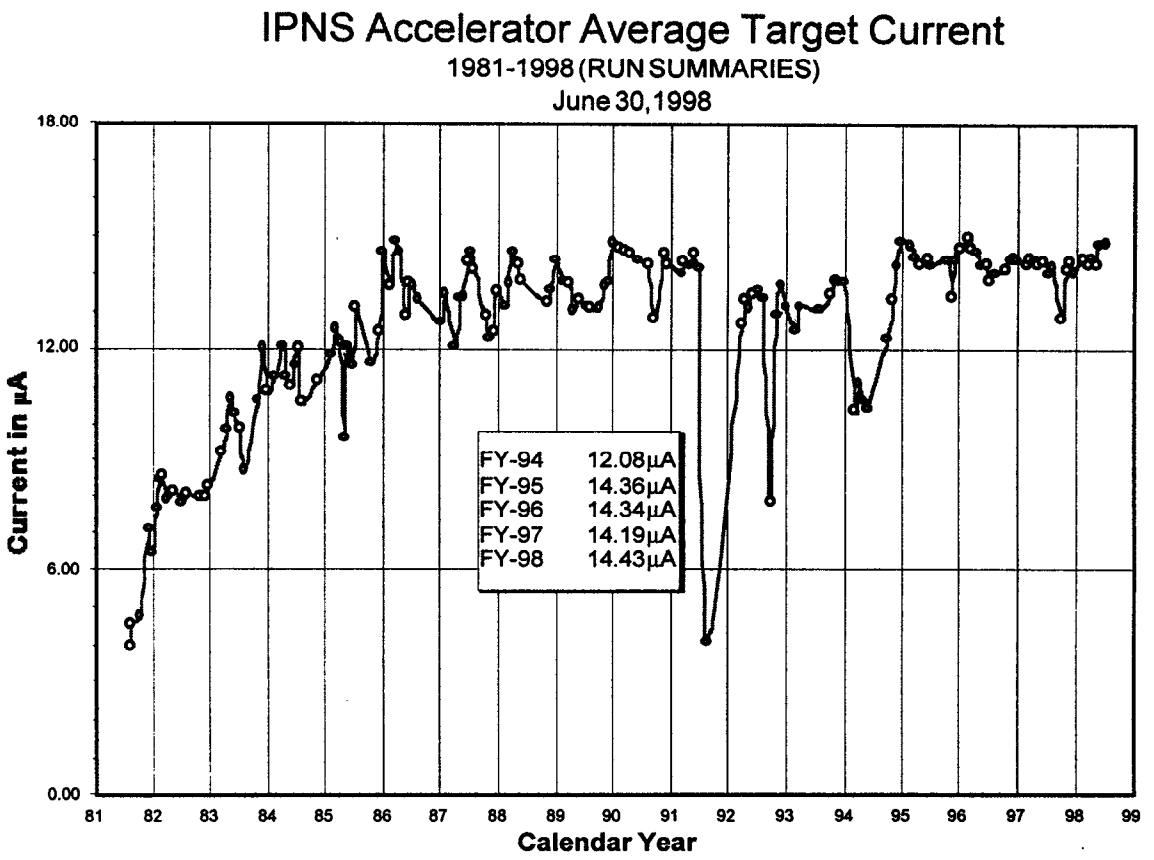
IPNS Accelerator Average Target Current
1981-1998 (RUN SUMMARIES)
June 30, 1998
Current in µA
18.00
12.00
6.00
0.00
FY-94 12.08µA
FY-95 14.36µA
FY-96 14.34µA
FY-97 14.19µA
FY-98 14.43µA
81 82 83 84 85 86 87 88 89 90 91 92 93 94 95 96 97 98 99
Calendar Year

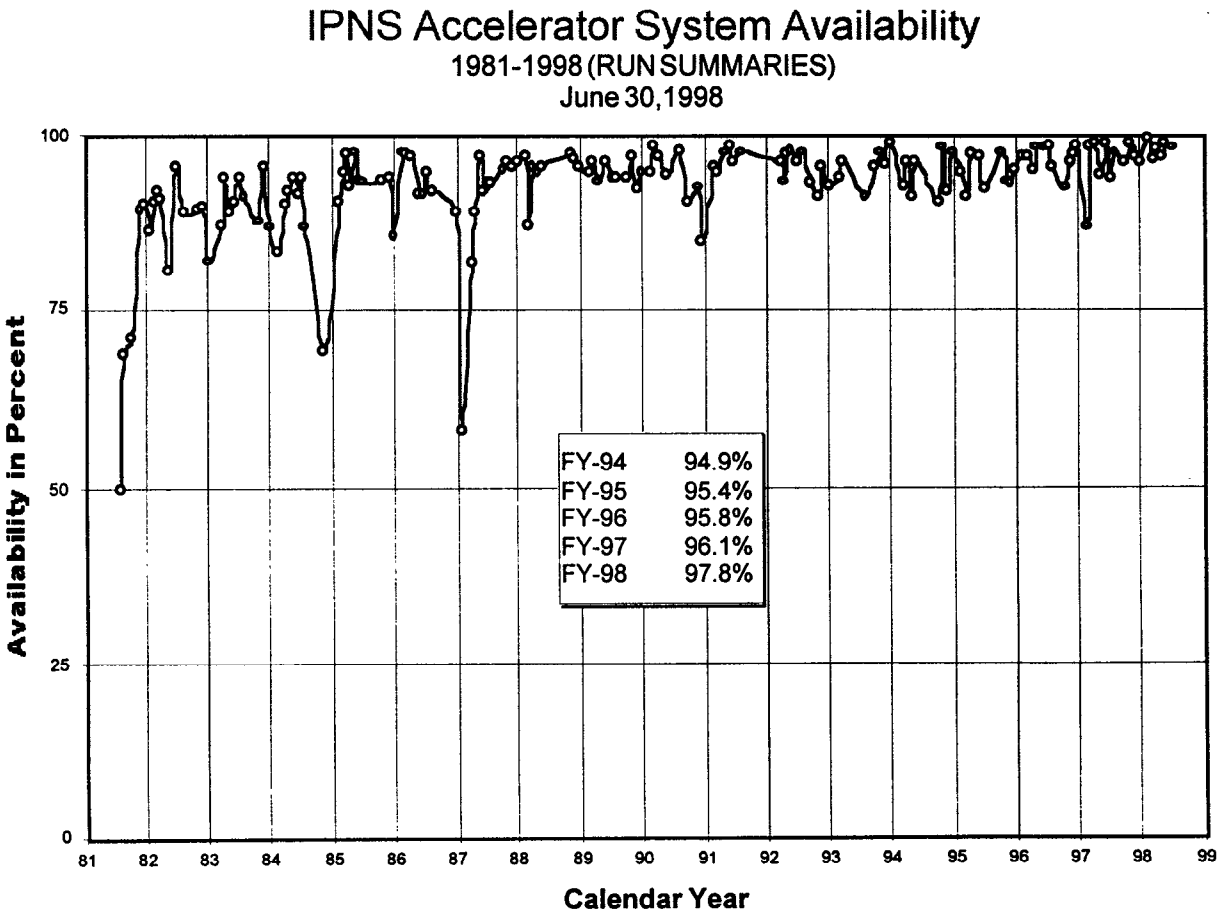
IPNS Accelerator System Availability
1981-1998 (RUN SUMMARIES)
June 30, 1998
Availability in Percent
100
75
50
25
0
FY-94 94.9%
FY-95 95.4%
FY-96 95.8%
FY-97 96.1%
FY-98 97.8%
81 82 83 84 85 86 87 88 89 90 91 92 93 94 95 96 97 98 99
Calendar Year

2. IPNS Enhancement Project

2.1 Instruments

Over the last 20 years, the United States has fallen alarmingly behind other nations in the availability to their scientific communities of up-to-date neutron sources and instrumentation. This is being addressed with the planned Spallation Neutron Source at Oak Ridge (discussed below and in other ICANS papers) and with the LANSCE enhancement, also discussed in these proceedings. We at IPNS asked what could be accomplished in the short term, 2-3 years, to increase our scientific productivity, and a number of projects have begun. Some immediate ("off the shelf") upgrades to existing IPNS Instruments are possible that can be done in 2 years with no technical risk that will have a significant impact on instrument performance.

Table 3

Instrument	Improvement
POWDER DIFFRACTOMETER (GPPD)	add 300 detectors (x3)
Chopper Spectrometer (HRMECS)	add 400 detectors (x2)
Glass and Liquids Diffractometer (GLAD)	add 180 detectors (x2)
Powder Diffractometer (SEPD)	add 50 detectors (x1.3)
Single Crystal Diffractometer (SCD)	add 2nd area detector

All upgrades can be done in 2 years with no technical risk.
All instruments will at least double their data rate and some (*) will have new capabilities

Table 4. Impacts of the IPNS Instrument Enhancement Project

Instrument	Data rate gain factor	Other new capabilities
QENS	10	All Q settings measured simultaneously
MIGS	---	New instrument, unique in the US
HRMECS	2	Continuous angle coverage, improved Q and E resolution
GPPD	2	Continuous angle coverage, improved ±90° resolution
SEPD	---	Improved low-angle resolution for magnetic scattering, large cells
GLAD	1.5	Range extended to higher Q
SCD	2	Capture larger volume of Q space

Funds have been limited for these improvements, but some changes have occurred since ICANS XIII in 1995:

Instrument	Improvement
HRMECS	-130 LPSDs purchased for low angles -moved low angle detectors to high angles -new DAS installed and in testing
SAND	-delayed neutron chopper is operational -high angle detector bank in commissioning -started doing user experiments
GLAD	-improved low angle window resulting in lower background
GPPD	-180 detectors purchased for high angle banks, to be installed in summer, 1998

2.2 QENS Upgrade

QENS is a crystal-analyzer spectrometer at IPNS optimized to provide ~70 μeV resolution for quasielastic scattering, but it also has very good resolution for chemical spectroscopy at excitation energies up to ~150 meV. The "white" beam from the source is incident on the sample, so a separate detector can be mounted to monitor diffraction from the sample. This allows a careful following of phase changes, in situ sample growth or modification, etc., concurrently with the quasielastic- and inelastic-scattering measurements. QENS has three focused-crystal-analyzer arms mounted on a rotating table so that a wide range of scattering angles can be covered. A recently accomplished modification has provided QENS a solid CH_4 moderator at 25K, and this has resulted in a factor of ~5 increase in data rate for most experiments, when compared to the previous liquid CH_4 moderator which operated at ~100K. This higher intensity has made the instrument even more attractive, and demand is rapidly increasing.

An upgrade of QENS, now in the construction stage, will replace the rotating instrument table having 3 detector banks with a fixed instrument having 20 analyzer-detector arms plus 2 diffraction detector banks. Quasielastic resolution will be kept at ~70 μeV for each of the banks. The incorporation of 20 analyzers will allow sampling of the full angular range (~15°- 165°) for inelastic scattering without rotating the instrument. Eliminating the need to rotate will allow the use of improved shielding and will simplify the types of sample environment required. The upgrade will also result in a factor of ~10 increase in the analyzer solid angle, leading to an additional factor of ~10 increase in useful data rate. QENS Upgrade is scheduled for installation in Dec. 1998.

2.3 Target and Moderator Systems

IPNS is currently operating with two solid CH_4 moderators (C and H positions) and a modified C with grooves in the vertical direction to better serve the POSY reflectometers will be installed soon. Plans are also underway to change the third moderator, currently liquid CH_4, to solid CH_4 in July 1999. Meanwhile, we have launched a program of calculations and measurement to evaluate a number of potential improvements to the IPNS target/moderator/reflector system. Improved computational capabilities support these efforts as does a program of measuring and benchmarking the intensity spectra and the wavelength-dependent pulse shapes of the existing moderators, which is described elsewhere in these proceedings. We coordinate these pursuits widely with workers at other laboratories. These collaborations are of great benefit to us, and, we hope, similarly beneficial to others. The paper by E. Iverson in these proceedings discusses further the IPNS moderators.

2.4 Accelerator System

A proposal was recently submitted to DOE for $1.9M for the addition of a second harmonic cavity to the IPNS synchrotron which would increase the current-handling capability by 30 to 40%. A test of the concept using laboratory discretionary funds (recently requested) would make use of existing cavity components, and would significantly reduce the risk for the full-scale DOE proposal.

A prototypic cathodefollimer (CF) amplifier and ferrite loaded cavity will be built using some existing parts, which includes ferrite for the cavity and a ceramic window and vacuum pipe assembly. The assembly will be bench tested, installed in an IPNS Rapid Cycling Synchrotron (RCS) straight section, and tested with beam. It will be possible to demonstrate capture and acceleration through a considerable part of the acceleration cycle using the system on the second harmonic frequency using the existing ferrite. At present, only computer calculations of beam performance exist for the RCS facility. This experimental test using the prototypic system will confirm these studies without large expenditures. Scientists from the Rutherford-Appleton Laboratory in England and the National Laboratory for High Energy Physics (KEK) in Japan are pursuing similar studies and seek to collaborate with ANL to further extend the study base and share resources. A CF amplifier model has been built in Japan and is being tested on a small ferrite cavity, but this model is not designed to go onto an accelerator. The English and Japanese propose to build a system for testing on the accelerator for the ISIS source.

As an additional benefit, the cavity and amplifier would be able to operate throughout the accelerating cycle at the fundamental frequency, providing an on-line spare if either of the existing cavities or amplifiers failed, and providing extra capability by permitting operation with three cavities (either at increased total voltage, or with the two present cavities operating at reduced voltage). This capability would enhance performance under normal operation, and provide another "knob" to adjust to optimize accelerator performance.

3. IPNS Involvement with the SNS

A 1 MW spallation neutron source upgradeable to higher power will be built at Oak Ridge National Laboratory, starting in Oct. 1998 and is scheduled for competition in 2005. Argonne has lead responsibility for the neutron scattering instruments and is forming a team of scientists and engineers under the leadership of Kent Crawford, the Senior Instrumentation Scientist at IPNS. Scientists are being hired by ORNL to work at IPNS during the R&D, design and procurement phases of the instruments; moving to ORNL with the instrument. Based on the fact that IPNS is the DOE's most active pulsed neutron user facility and technology center, we will continue the role of training the user community as we will lead in the development and construction of the neutron scattering instruments. K. Crawford's paper on SNS instruments in these proveedings provides more detail.

Argonne is also involved in the liquid Hg target and moderators. Jack Carpenter is a primary consultant for all target and moderator issues and serves as Senior Scientific Advisor to the project while Erik Iverson is participating in IPNS moderator tests and SNS moderator calculations. Argonne carried out a study of a solid metal back up target for SNS and frequent visits to ANL by ORNL engineers and moderator neutronics analysts are taking place.

4. Procedure for Fast Access to the IPNS Powder Diffractometers

IPNS implemented a procedure beginning in October, 1995 for obtaining fast turn-around on the Special Environment and General Purpose Powder Diffractometers. A small fraction of the

operating time on each of these instruments is available on a first-come first-served basis, without the need to write the standard four page proposal. A short, one-page form is all that needs to be completed, indicating any potential hazards. Interested users should contact the instrument scientists, J. Jorgensen (SEPD) or J. Richardson (GPPD), to learn the backlog for each instrument. Samples will be shipped to IPNS and data will be collected when time becomes available without requiring the user to come to IPNS. The raw data are then accessed on the instrument computer. Similar to other experiments performed at IPNS, users are responsible for data analysis. This service will be limited to short (less than one-day) experiments involving only room-temperature data collection for samples that present no special handling problems. The time allocated to a single user will be limited to allow access for as many different users as possible.

Jim Jorgensen
Phone: 708/252-5513
FAX: 708/252-7777
e-mail: Jim_Jorgensen@qmgate.anl.gov

Jim Richardson
Phone: 708/252-3554
FAX: 708/252-4163
e-mail: JWRichardson@anl.gov

5. Future plans

The IPNS user program will continue to grow as instrument capabilities are improved and operation will continue to increase as funds permit. The Enhancement Project continues to be our top equipment priority and instrument improvements are proceeding. An accelerator plan incorporating the rf 2nd harmonic (with an increase in current of ~40%) has been submitted to DOE and calculations and measurements will proceed in developing an improvement program for the target/moderator/reflector system.

Key to the future plans will be incorporation of the SNS instrument development into IPNS. The new scientists and instrument development will be closely integrated with existing IPNS developments, for example prototyping components will be tested on IPNS instruments and beamlines.

Acknowledgments

Almost all of the work discussed in this article and many of the words of the article are the result of effort by other members of IPNS, the neutron scattering group and the APS at Argonne. The operation of IPNS is funded by the U.S. Department of Energy, BES-Materials Science, under contract W-31-109-ENG-38, and the National Science Foundation (DMR-91-20000) through the Science and Technology Center for Superconductivity.

ICANS XIV
14th Meeting of the International Collaboration on Advanced Neutron Sources,
Starved Rock Lodge, Utica, Ill., USA
June 14-19, 1998

SINQ as of 1998 (Status Report)

G S. Bauer

Paul Scherrer Institut CH-5232 Villigen-PSI, Switzerland

Abstract

the Swiss spallation neutron source SINQ had first beam on target on Dec. 16, 1996 and reached its full current of 0.85 mA on the following day in a demonstration run. After a commissioning phase during the first half of 1997, in which the parameters of the source were studied, full current operation was resumed in the second half of the year with no technical problems. The first half of 1998 was characterised by an extensive accelerator shut down in which the splitter region that supplies beam to PSI's medical facility was completely rebuilt and which advantage was taken of by SINQ to open up two previously blocked beam ports for new instruments and to carry out the first target exchange. The user programme will start in July 1998 and by the end of the year it is expected to have 12 experimental facilities operational with five more under construction.

1. Introduction

SINQ at the Paul Scherrer Institut in Switzerland is the latest member in the family of operating spallation neutron sources. Being an add-on to an existing accelerator, a 590 MeV cyclotron, there was no choice on the time structure. Therefore SINQ is a continuous neutron source and hence plays in the competitive league of research reactors. Like a modern research reactor, it has a large D_2O tank where the beam tubes originate (Fig. 1) and is designed to permit access to the outside of the target biological shielding on all sides. This is accomplished by injecting the beam into the target from underneath; another feature which makes SINQ unique among its (unfortunately few) fellow spallation neutron sources.

Over the course of the years the beam current of the PSI ring cyclotron has been upgraded from its original design value of 100 μA to 1.5 mA, which makes this the world's highest time average proton current. Since the prime purpose of the accelerator used to be pion and muon generation, there are two targets in the beam upstream of SINQ, of which in particular the last one, "Target E", has a strong effect on the phase space distribution in the beam. After scraping the generated halo and reshaping and focusing the beam for further low loss transport, only 0.85 mA at 570 MeV are left to drive SINQ. Nevertheless, this is a serious power level to deal with and, in anticipation of future improvements, the SINQ target and its heat removal system have been

Keywords: SINQ, continuous spallation source, cold neutrons, supermirror guides

designed to handle 1 MW of beam power. During the design studies it was concluded that, in order to remove this power from a solid target and to avoid excessive stress which would shorten the life time unduly, a rod structure of the target and a hemispherical beam entry window were the best solution. Since its first day, SINQ has been operating on a target made up from 450 Zircaloy-2 rods of 10.8 mm diameter, arranged in a closely packed array with a pitch of 1.2 and cooled in a cross flow configuration. Since the neutronic performance of this target is not optimum, a development program is going on that aims at achieving a gain factor of at least two from using a higher yield target material. Several reports dealing with this work can be found in these proceedings.

2. SINQ - The Worst of Both Worlds or a Breakthrough?

"The worst of both worlds", this was the comment made when the then SIN (Swiss Institute of Nuclear Research) announced the intention to build a continuous spallation neutron source - meaning that this facility would suffer from the disadvantages but not benefit from the potential advantage of a spallation neutron source over reactors: the pulse structure.

Now, while the pulse structure is clearly missing, there are other advantages of spallation neutron sources that SINQ shares: the absence of criticality, the ease of shutdown in an emergency, the lower γ-ray production per neutron (and hence better conditions for cold moderators close to the primary source), the lower afterheat, etc. These features make it well worth-while to think about continuous neutron sources in the future which work on a beam power level pulsed sources will simply not be able to handle because of their very pulsed nature. In this sense, SINQ is a breakthrough: It is proof that continuous spallation neutron sources can be built and operated and can be competitive with research reactors. Of course, during the whole construction phase the question was in the air: "will we be able to control the fast neutron background?" Now, after half a year of experience at full beam power we know: we were! The overall radiation level in the SINQ target and neutron guide hall is as low or lower than on any reactor and our cold neutron beams are literally free of high energy neutron contamination. It is true, that special care was taken to accomplish this in designing the system and in assembling the shielding, but the success shows: it can be done. Also high energy neutron contamination in the beams did not turn out as a problem. Probably three design features of SINQ contributed to this:

a) The plane is which all beam tubes are located is perpendicular to the proton beam; in this way the more forewardly emitted high energy neutrons are not seen.

b) Within a distance of 1 m around the target no materials (such as steel or heavy metals) are located that would strongly interact with high energy neutrons and lead to large angle scattering.

c) The axes of the beam tubes and neutron guides are displaced by 25 resp. 40 cm from the proton beam axis and grazing incidence of high energy neutrons directly from the target into the beam tubes is much less likely than in pulsed spallation sources where this distance is of the order of 10 cm only. All taken together, we are happy to state that SINQ is much less severely hit by the worst of the spallation source world than one might have feared before trying.

SINQ is a breakthrough also in that sense. It is also a breakthrough in that almost its whole neutron guide system is built from supermirrors. It was clear from the very beginning that the emphasis of SINQ would be on cold neutrons. This was not only because a cold source could be placed more optimally in the reflector of a continuous neutron source than in that of a reactor; this is also because long wavelength neutrons have shown a steady growth in importance in the field of neutron scattering and continue to do so.

Besides their scientific merits cold neutrons also have the advantage that they are easy to transport over long distances in neutron guides. Development of efficient neutron guides was, therefore, an important part in the SINQ project and it was done successfully: all glass plates for the neutron guides of SINQ were coated with supermirrors in PSI's own facility following a recipee developed here. They were then individually examined for quality and were sorted such that poorer plates would not jeopardize the performance of those guides where the large beam divergence supermirrors provide was useful. In sorting the glass plates the future use of the guides were carried in mind. For example, the SANS instrument with its narrow collimation does not need high angles of total reflection on the guides. (Since the extra neutrons would only be a nuisance when they generate γ-rays upon absorption, the SANS guide is actually the exception to the supermirror rule at SINQ). Also other high resolution instruments with primary collimation cannot use the full divergence of an m=2 guide and the less perfect plates were used for those. It should be noted, however, that, since the angular divergence is proportional to wavelength, an important advantage of supermirror coating is that it shifts the cutoff wavelength of a guide with a given curvature and width to shorter wavelengths. Fig. 2 shows a spectrum measured at one of the SINQ guides. Relative to predictions made during the construction phase (curve C), this guide has about 50% more intensity in the long wavelength region and shows a spectral shift of about 0.5 Å to longer wavelengths at the short wavelength side. These two properties are attributed to uncertainties in predicting the performance of the cold moderator, which, in the case of SINQ, is a large liquid D_2 volume [1]. In the region below 6 Å the rugged appearance results from Bragg edges of the materials in the beam (Zircaloy-2 and Aluminum). Despite this "depression" one would expect to be able to fit the curve with a Maxwellian distribution, making allowance for the total transmission also shown in the figure. This turned out not to be possible; in fact a sum of three Maxwellians was required to obtain a reasonably good fit (curve 3M); the best fit found for two Maxwellians is represented by the curve labeled 2M. A detailed discussion of the spectral and intensity measurements carried out during the commissioning phase of SINQ may be found in ref. [2]. A direct comparison, also made in that paper, showed that even where the supermirrors don't help, namely in the SANS instrument, SINQ performs equally well as a recently upgraded 10 MW reactor.

An overview of the neutron currents measured at the various monochromator or sample positions of different instruments and other locations is shown in Fig. 3. Except where a narrow collimation or wavelength band or multiple gaps in the guide reduce the intensity, values between 2.5 to 3.2 x 10^8 $cm^{-2}s^{-1}mA^{-1}$ are found for the guides and around 10^8 for the beam tubes. These data are for 1 mA; presently only 850 μA are available (see below). The contamination with neutrons above 20 MeV measured with the ^{12}C (n2n) reaction was less than 10^{-4} in the thermal beams and not detectable at the neutron guides.

3. A Furious Start and a Slow Takeoff

SINQ holds a record not only for being, by a large margin, the world's most powerful spallation neutron source; also the speed at which it went from first beam on target to full power is unbeaten: on Dec. 6, 1996 the beam line between target E and SINQ was first tuned with protons at a current level of 20 μA. (This is also when the first neutrons generated were used to measure the ToF-spectrum shown in Fig. 2). Little more than 24 hours later the source had reached its full power and had exhausted the contingent of 2 mAh set by the licensing authorities as the charge limit for this first demonstration run.

Clearly, it was never intended to take off at full power from that moment on, because several weak points in the shielding that had been left until the amount of shielding necessary could be determined by measurement, needed to be fixed and other parameter studies had to be made to fully understand the system. Therefore, a three months commissioning phase at varying current levels had been planned to take place after the end of the annual accelerator shutdown in the first half of 1997. During that time also the first generation instruments were completed and commissioned at low intensity.

Following this, full power operation was to be scheduled according to demand. As can be seen from Fig. 4, this demand rose continuously during the second half of 1997, but problems with a beam splitter upstream in the proton beam line became more and more serious and the delivered beam fell increasingly behind the scheduled one, ending up at a total of 500 mAh in 1997. In order to cure the problem with the beam splitter, which supplies protons to the medical facility for treatment of human cancer patients, an extensive shut down was scheduled for the full first half of 1998. The splitter region was completely rebuilt and an new concept for the splitter was used. The hope is that, after restart at the beginning of July 1998, these problems will be solved and routine operation of SINQ will start. Apart from changing the target, the shutdown period was also taken advantage of to implement the overall control system which should allow the SINQ target station to operate without the control room being manned. This is a necessary condition for being able to come close to the goal of 140 days of running at full current in the second half of 1998.

Although there is clearly still some uncertainty attached to the SINQ schedule in the second half of 1998, a call for proposals was launched in February 1998 for those instruments that would be operational when the source restarts or would be completed during the rest of the year. Proposals for short term experiments as well as long term research programs were solicited. The result shown in Table 1 is very rewarding on the one hand but very obliging on the other. For SINQ to become a competitive player in the league of continuous neutron sources in Europe, we must achieve high availability and further improve the performance of the source. At the same time, more instruments will come on line. Apart from the neutron scattering instruments listed in Table 1, for which proposals have been solicited, SINQ currently hosts several other neutron facilities which will become available for users soon:

- a thermal neutron transmission radiography facility
- a cold neutron capture radiography facility
- an isotope production station
- a facility for neutron activation analysis
- a facility for prompt gamma emission studies
- a facility for fission product studies, using a thin uranium foil in the thermal flux.

Further instruments under construction or in the planning stage are
- a polarized neutron decay instrument (particle physics)
- an engineering strain scanner
- a high resolution crystal analyser time of flight spectrometer
- a phase space transformer for high resolution thermal neutron time-of flight

This large investment into the source utilization adds even more to the pressure to improve the performance of the source itself.

Table 1:

	Short term proposals		Long term proposals	
Instrument	Total days available	Total days requested	Total days available	Total days requested
AMOR (Reflectometer)	not sched.			
DMC (Cold n diffract.)	15	71	83	137
DrüChaL Cold n TAS)	31	56	167	228
FOCUS (cold n ToF)	0	38	49	126
HRPT (high res. Powder)	0	15	100	141
SANS (small angle scatt.)	21	55	147	375
TASP (pol. n TAS)	22	121	149	295
TOPSI (Test beam)	-			10
TRiCS (4 circle diffr.)	0	-	100	98

4. The Way to More Neutrons

For SINQ, the number of useful neutrons generated per unit time depends on four main factors:
- the average availability of the accelerator (currently > 85%)
- the fraction of the accelerator up time during which SINQ can receive beam (in competition with other modes of operation)
- the fraction of beam lost in the target E
- the neutronic performance of the SINQ target.

As for the availability (mAh delivered / mAh scheduled) of the accelerator, the current value of more than 85% includes, of course, periods where some problem anywhere along the beam line impedes operation. Transporting a 1.5 mA beam with low losses along most of the beam line is

not trivial. Even the target "E", which is a 6 cm long rotating and radiation cooled graphite ring and never used to cause problems, now must be replaced about twice a year because it deforms due to radiation damage. So, while some improvement may be possible, one will always have to be prepared to accept a certain amount of time lost. Even on good days, i.e. without major beam interruptions the users will be faced with and will have to adjust to a large number of short trips. An example of such a day is shown in Fig. 4. Although the beam delivered was 97% of what could be expected, many short interruptions occurred, often lasting less than 1 minute (lines not going all the way down to zero in Fig. 4, where the sampling time is 1 minute).

As far as other operating modes of the accelerator are concerned, there were two types of "single use" at low current in the past: (1) If human patients were being treated at the proton cancer therapy station and the splitter did not work reliably, it became necessary to run the whole facility at low current with direct injection to the medical facility. This will, hopefully, be solved with the new splitter. (2) Some particle and nuclear physics experiments used polarized protons which could only be supplied at low intensity from a special injector. This program will also come to an end soon, as the number of users not served while it is running has become too large.

Concerning the fraction of beam lost at target E, the possibility of shortening that target from 6 to 4 cm has been studied [3]. While some of the pion and muon experiments would not suffer from that move, others would lose 1/3 of their present flux. For SINQ it would, by the same token, mean a 50% gain, but would also require different tuning of the beam transport line, which can probably be done. Currently this issue is still being debated, but another development might make this move even a must: The accelerator group is looking into using copper cavities instead of the present aluminum cavities, which might allow to operate the accelerator at 2 mA. If this materializes, Target E must be shortened to keep the power deposition and activation from the lost beam in its environment at the present level. In this case the total gain for SINQ would be almost 70%, raising the beam power to over 800 kW (this is why the design power is 1 MW).

Finally, as far as the target itself is concerned, theoretical studies [4] showed that, in the optimum case, a factor of 2.7 in neutron yield could be gained if it was possible to realize a liquid lead-bismuth target of optimum thickness and with a low absorption container. Realistically a factor around 2.4 can be expected with a steel container. By improving the solid rod target through the use of clad lead rods - which is the more near term solution - the anticipated gain is about 1.6. Work towards this step is reported in other papers at this conference [5] [6] [7].

5. Conclusions

Since SINQ first became alive in Dec. 1996, it could be shown that the concept of a continuous spallation neutron source is not necessarily a stupid one. Its breadth of use ranging from isotope production and activation analysis via radiography all the way to high resolution neutron spectroscopy makes it competitive with existing research reactors and, in a different sense, also with pulsed spallation neutron sources. From the onset on the system performed well at full power and constituted a breakthrough in several respects. Especially the successful use of supermirror neutron guides, although not tied to any specific source type has opened up the possibility of designing for "all guide sources" in the future, also in the regime of thermal neutrons. Even, if these guides are designed without curvature, they would help to further reduce the high energy

neutron contamination at the monochromator position significantly below the level of 10^{-4} relative to the thermal flux which is currently measured at SINQ. This would eliminate practically completely the worst of the spallation source world and would allow to take full advantage of the best of the continuous source world, namely that the neutron flux per unit proton current is high and that the distance over which neutrons can be usefully transported by guides is not limited by frame overlap considerations. In view of the limitations on pulse power that can, at present, be handled with confidence and in view of the need for non-diffractive uses of neutrons which rely on high time average flux, the successful operation of SINQ may well mark a real breakthrough, and its further development may show a route to the future.

6. References

[1] Spitzer et al; "First Operation Experience with the Cryogenic Moderator at the SINQ Spallation Neutron Source" Int. Workshop on Cold Moderators for Pulsed Neutron Sources, Argonne Ill. Sept. 28 - Oct. 2, 1997

[2] W. Wagner, G.S. Bauer, J. Duppich, S. Janssen, E. Lehmann, M. Lüthy and H. Spitzer "Flux Measurements at the New Swiss Spallation Neutron Source SINQ" J. Neutron Research, Vol 6, pp249-278 (1998)

[3] F. Foroughi, G. Heidenreich, D. Herlach, C. Petitjean, U. Rohrer "Realisierbarkeit und Auswirkungen einer Verkuerzung von Target E zur Erhoehung des Protonenstroms auf SINQ" PSI-internal report TM-13-98-01 (1998)

[4] G.S. Bauer, A. Dementyev, E. Lehmann "Target Options for SINQ - A Neutronic Assessment", this conference

[5] L. Ni and G.S. Bauer "Heat Transfer and Thermomechanic Analyses on the Test Rods in the SINQ-Target Mark 2", this conference

[6] A. Dementyev et al., "Neutronic Aspects of the SINQ Mark 2 Target with Irradiation Test Samples" this conference

[7] A. Malik et al. "Target Materials Development for SINQ and Out of Beam Testing", this conference

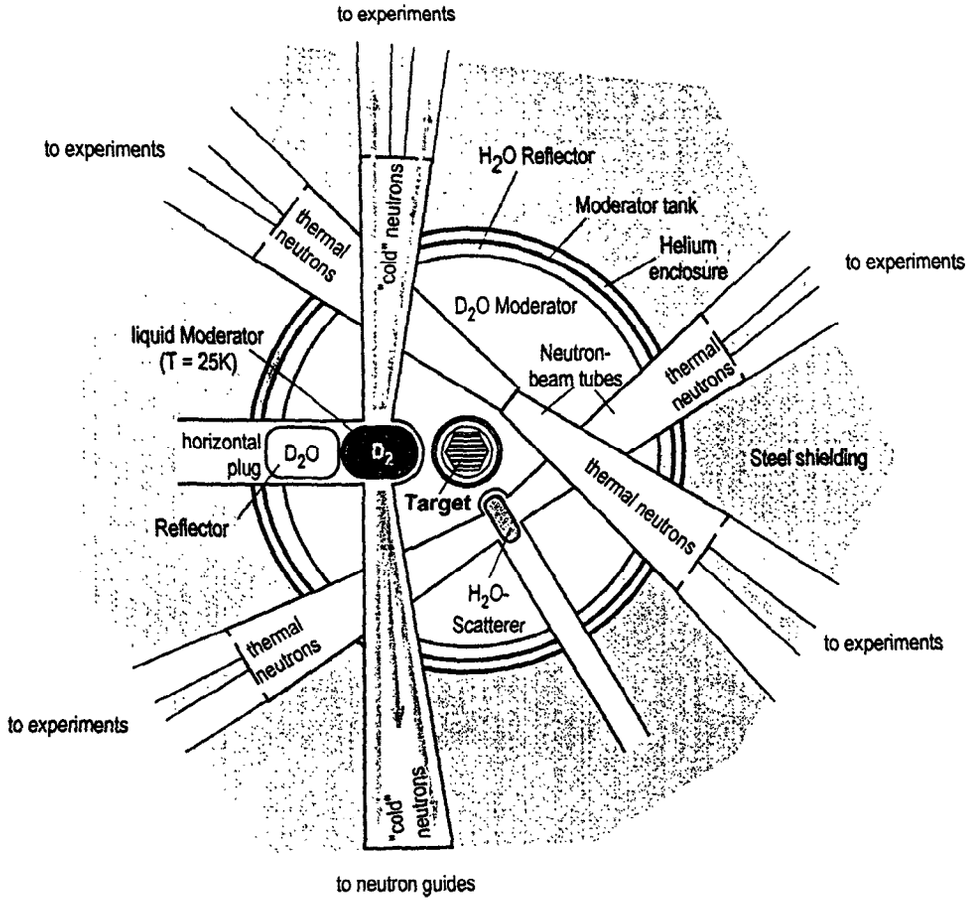

Figure 1: Schematic horizontal cut through the SINQ Target-moderator region

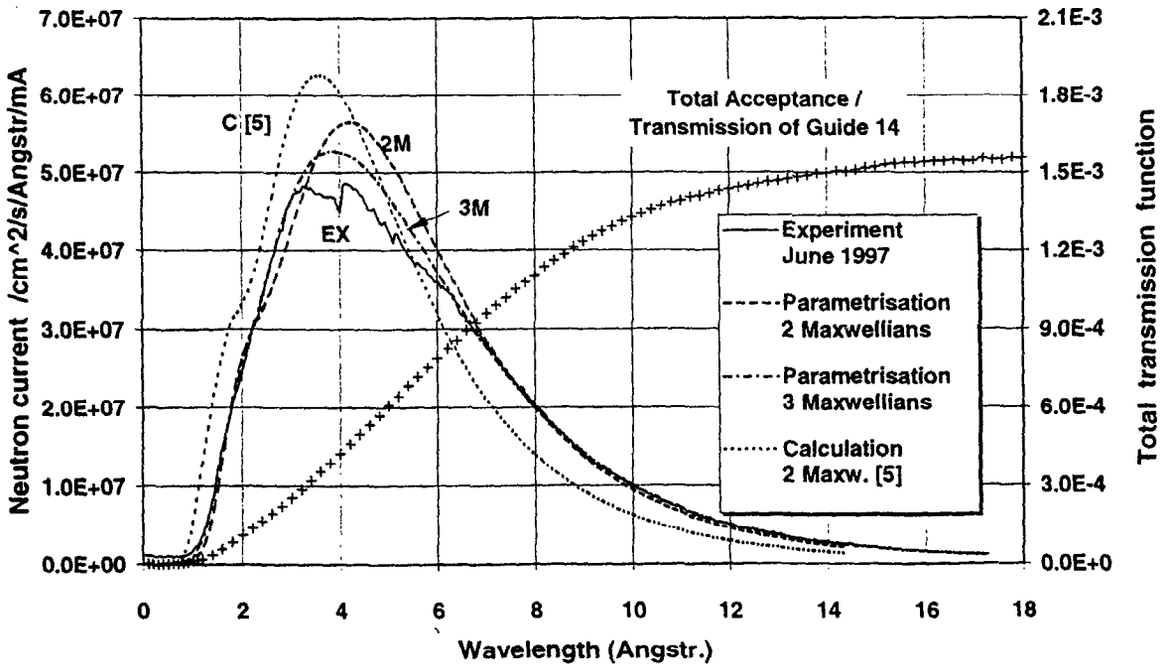

Figure 2: Cold neutron spectrum measured at the SINQ guide IRNR14 and calculated transmission function of that guide

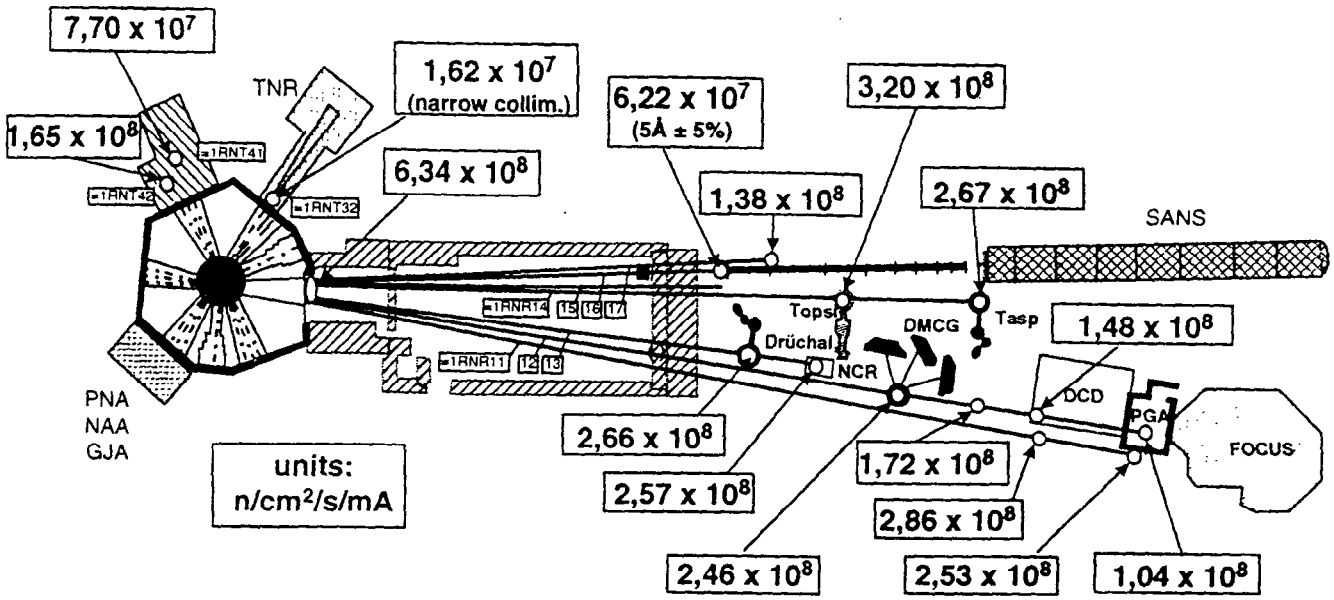

Figure 3: Measured neutron currents at various positions of the SINQ guide system and thermal neutron beams

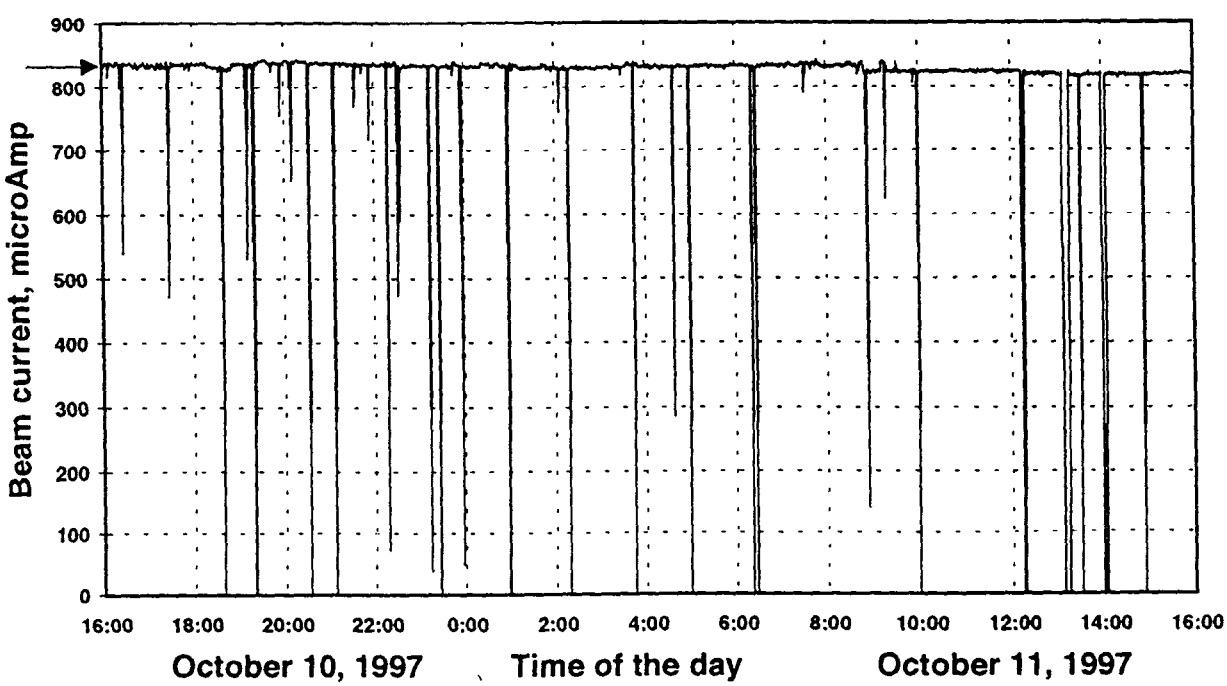

Figure 4: Example of the recorded proton current over a period of 24 hours with high accelerator availability but a large number of short trips. The total charge delivered during the period shown was 19.3 mAh; the integrated performance was 97.1 %.

ICANS-XIV
14th Meeting of the International Collaboration on Advanced Neutron Sources
June 14-19, 1998
Starved Rock Lodge, Utica Ill., USA

News from Moscow Meson Factory

S.F. Sidorkin
Institute for Nuclear Research of the Russian Academy of Sciences, 117312 Moscow, Russia

Moscow Meson Factory consists of linac accelerator, storage ring and experimental area with a complex of neutron sources (neutron source, beam stop, lead slowing-down neutron spectrometer). The defined progress in development of neutron source was made for past 2.5 years.

Accelerator

- The stability operation of the accelerator on a current 60 – 65 μA is reached at energy of protons 450 MeV. In separate sessions the current reached 70μA
- Maximum energy of protons is 502 MeV.
- Now accelerator mainly works on the isotope program (50μA,160 MeV). It is connected to an incompleteness of works in an experimental area, commercial obligations of INR and payment of the electric power.
- The preparation for operation of the accelerator on a current 120 μA is carried on. These parameters are planned to receive to an extremity of a current year after completion of debugging on RFQ – system.
- Project parameters of the accelerator - 600 MeV, 500μA.

PSR/MMF - Status of Construction

- The construction work in the building of PSR has been finished.
- Practically all necessary equipment for PSR has been produced.
- The assembly of PSR and tuning of equipment may have been finished during the next two years.
- Tuning of PSR after completing this work.
- Project pulse duration of a storage ring is 0.3 μs (600 MeV, 100Hz)

At the first stage, before the storage ring will be in operation, it is supposed to use the linac's proton beam with pulse duration 0.2-1 μs for nuclear physics studies and 30-50 μs for solid state physics studies. Pulse shaping is performed with the chopper in the linac injector.

The Experimental Area

- Mounting of the vacuum system and the beam line from an input of an experimental area up to the beam stop is completed.

- The first neutrons on the beam stop were received during a test short-term session.
- Mounting of shield around beam lines of beam stop and neutron source is completed.
- The mounting of accompanying systems (systems of cooling, power supply, etc.) is completed.

Neutron Source, Beam Stop and Lead Slowing-Down Neutron Spectrometer

The INR RAS Neutron Complex consist of the Pulsed Neutron Source, Beam Stop with the irradiation channel and the Lead Slowing-Down Neutron Spectrometer (LSNS).

Neutron source and beam stop with internal irradiation channel are executed under the uniform scheme, where basic elements are the tungsten plates covered with a titanium and cooled by water /1,2/. The cartridge with plates is in body made from an aluminum alloy. The density of tungsten plates is about 18.9 g/cm^3, the thickness – 5 and 10 mm. Tungsten elements with different coating have been tested in the core of the light-water research reactor. The zirconium and titanium coating have given the best results. Ti has smaller sensitivity to dissolved Oxygen in comparison with Zr, and it is also characterized by smaller irradiation growth. This is the reason that Ti was chosen as a material for the target plates coating.

State of Matters

- The beam stop and neutron source was assembled completely.
- The tests of the system of cooling were conducted.
- On the beam stop was conducted brief test beam seance and the first neutrons are received.
- The preparation of experiment on search of correlation between displacements of atoms during radiation damages and conductivity of a material at low temperatures carries out at present time.
- R&D of irradiation studies of structural materials for neutron sources at the proton beam-stop of Moscow meson factory is carried out /3,4/.
- The attempt was undertaken to direct a beam to a neutron source during the last seance of the accelerator. The beam was lead up to the last bending magnet. Debugging of a beam line was not possible because of a shortage of time and diagnostics completely. We hope that the following attempt will be successful.
- The technical actions for taking of a beam on a neutron source during an autumn seance of the accelerator are making now.
- The new tungsten and uranium neutron targets with beryllium reflector is under construction.
- At present, the experiments are conducted on the small-scale prototype lead slowing-down spectrometer (volume is about 1m^3 and weight 15 tons). The spectrometer places in the end of the linac's tunnel in a temporary experimental zone. Proton pulses with the duration 0.2 μs and average current up to 1μA is shaped by a chopper in the linac's injector. The LSNS carries the

research of neutron reactions with the microquantitative samples (for example, radioactive nuclei including isomers).

- The new generation of accelerator-driven LSNS, which is planned to place inside the experimental area of meson factory, will contain about 100 tons of lead /1/.

Instruments

Now, the Multi-purpose time of flight neutron spectrometer is created by joint group of Lebedev Physical Institute and INR /5/.

The Spectrometer consist of:

1. evacuated neutron guide tube (60 ×110 cm^2)
2. group of replaceable collimators and diaphragms
3. sample changer
4. high resolution powder diffractometer
5. high intensity diffractometer
6. quasi elastic spectrometer
7. high resolution inelastic and quasi elastic spectrometer
8. small-angle-neutron-scattering diffractometer
9. single crystal diffractometer
10. inelastic neutron scattering spectrometer (Be-filters)

The multi-purpose neutron spectrometer aimed for simultaneously study of structure and dynamics of condensed matters in the real time scale.
It is natural, that the allowing of a flexible unit is lower than at specialized spectrometers.
The three other channels is equip by spectrometers intended for physics of a condensed state and nuclear physics too.

References

1. Y.Y.Stavissky. Spallation Neutron Sources at the INR RAS: Present Status and Prospects. Meeting of the Inter. Collaboration on Advanced Neutron Sources (ICANS-13) PSI, Switzerland, p.63,1995.
2. A.V.Dementyev, V.G.Miroshnichenko, S.F.Sidorkin, N.M.Sobolevsky, Y.Y.Stavissky, I.I.Konovalov, A.A.Maslov, I.I.Tretyakov, V.I.Truskin, A.D.Rogov. Tungsten and Uranium target for Moscow Meson Factory. 13 th. Meeting of the Inter. Collaboration on Advanced Neutron Sources (ICANS-13) PSI, Switzerland, p.461, 1995.
3. S.F.Sidorkin, G.S.Bauer, Y.Dai, M.I.Grachev, L.V.Kravchuk, Y.I.Orlov. Oportunities for Irradiation Studies of Structural Materials for Neutron Sources at the Proton Beam-Stop of Moscow Meson Factory. (ICANS-14).
4. E.A.Koptelov, S.G.Lebedev, O.N.Smirnova, et al. Prospect for study of radiation damage at RADEX-15, radiation experiment facility, based on the beam stop of Moscow Meson Factory. Journal of Nuclear Materials 233-237 (1996) 1552-1556.
5. A.I.Isakov, S.N.Kuznetsov, A.D.Perekrestenko, N.I.Sapozhkov, S.F.Sidorkin, Yu.Ya.Stavissky. A multifunctional neutron spectrometer for the pulse neutron source of the Moscow meson factory. The preprint of Lebedev Institute N 18 (Solid physics, Neutron-physical department) 1994 (in Russian).

ICANS-XIV
14th Meeting of the International Collaboration
on Advanced Neutron Sources
June 14-19, 1998
Starved Rock Lodge, Utica, Illinois, USA

STATUS OF NEUTRON SCATTERING FACILITY IN JAERI NEUTRON SCIENCE PROJECT

Y. Oyama, R. Hino, N. Watanabe, M. Mizumoto and T. Mukaiyama

Center for Neutron Science
Japan Atomic Energy Research Institute
Tokai-mura, Naka-gun, Ibaraki-ken 319-1195, Japan

ABSTRACT

The JAERI Neutron Science Project is aiming at construction of high power and high energy proton accelerator for conducting both basic and nuclear energy researches. Neutron scattering facility is one of the high prioritized research facilities. A plan and R&D activities for the Neutron Science Project and the neutron scattering facility considered in the project are outlined in this paper.

1. INTRODUCTION

Neutron scattering research has achieved notable successes in recent years, such as studies on crystal structures and magnetism, and is now attracting biologists for large organic molecules such as proteins. However, a limiting factor for neutron scattering research, specially for biology, is due to the intensity of the neutron beams. High intensity of neutron beams extends research areas to the fields that have been impossible. For this context, in Europe, the European Spallation Source (ESS) with 5 MW proton beam power is under designing, and in the USA, Spallation Neutron Source (SNS) with 1 MW at the first stage (upgraded to 4 MW) is proposed by ORNL. In Japan, the High Energy Accelerator Research Organization (KEK) is designing a spallation neutron source with 0.6 MW proton beam power as a part of the Japan Hadron Facility (JHF) project. These spallation neutron sources are dedicated to basic science.

Since the middle of 1970's, JAERI has been carrying out R&D for the partitioning and transmutation of long-lived radio-nuclides which are produced in nuclear power generation. In 1988, the Atomic Energy Commission set the long term partitioning and transmutation R&D program "OMEGA", i.e., Options Making Extra Gain from Actinide and fission products. In the course of discussion on proton accelerator development for the OMEGA project, it was recognized that neutron scattering community desires to have very high neutron source strength, two order of magnitude stronger than that of existing ones. This future source is also discussed in conjunction with continuation of JAERI role as a supplier in

Keywords: Neutron Science Project, Linac, Storage Ring, Neutron Scattering Facility

future, because JAERI has been one of major neutron suppliers for basic science community in Japan with its research reactor JRR-3M.

Combining requirements of basic and nuclear sciences, JAERI had started the Neutron Science Project in 1996. The Neutron Science Project is preparing a conceptual design for a research complex utilizing spallation neutrons, including a high intensity pulsed and cw spallation neutron sources. [1] This paper is describing specially a plan of neutron scattering facility of the Neutron Science Project, as well as brief description of the project itself.

2. JAERI NEUTRON SCIENCE PROJECT

2.1 Scope of Neutron Science Project

The Neutron Science Project aims at pushing researches, utilizing neutrons, for basic science and technology development of accelerator transmutation. The projects includes R&D and construction of an 8 MW (1.5 GeV, 5.3 mA) super-conducting proton linac, a 5 MW target station with compression storage rings to allow short neutron pulses for neutron scattering research, and research facilities for transmutation engineering, neutron physics, material irradiation, medical isotopes production, spallation RI beam production for exotic nuclei investigation.

Basic science in the Neutron Science Project covers the fields of structural biology for investigating the structure and dynamics of biological molecules such as protein, advanced material science (e.g., under extreme conditions), high-energy neutron science (e.g., spallation phenomena), nuclear cross-section measurements for transmutation study, heavy-ion science for creating unstable heavy nuclei through spallation, and synthesis of super heavy extremely-neutron-rich nuclei.

Research facilities considered are classified into three groups on the basis of difference of pulse time duration, namely, a short pulse facility, a very short pulse facility, and a long pulse or continuous beam facility. Also, a direct use of proton beam of 100-200 MeV is considered for medical RI production. The preliminary layout of the facility complex is shown in Fig. 1.

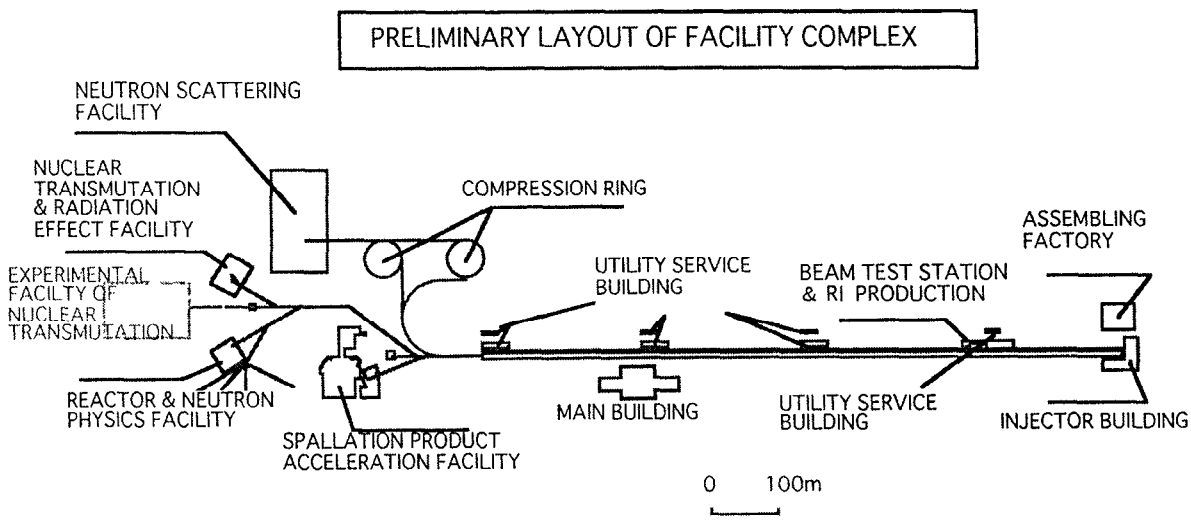

Fig. 1 Preliminary layout of facility complex

Neutron scattering facility requires short pulse of which time duration is shorter than 1 μs. Two storage rings act to compress the time duration of the output pulse of 2-3.7

ms from a super-conducting linac to be shorter than 1 μs. Very short pulse around 1 ns of time duration is required for such experiments with high time resolution as high energy neutron physics by neutron time-of-flight (TOF) spectrometers. Very short pulse beam is also required for low current duty in such low power experiments as spallation RI beam science. Various radioisotopes are produced by bombarding a target with 1.5 GeV protons through the spallation process. In this facility, the produced radioisotopes are separated with an ISOL (Isotope Separator On-line), and then accelerated by the existing Tandem Van de Graff accelerator. Extremely-neutron-rich nuclei are produced which change easily into many exotic nuclei, heavy and super-heavy nuclei. The material irradiation facility utilizes a long pulse beam or a continuous beam directly from the linac. The irradiation facility has a slender metal target to obtain high neutron flux of 2×10^{14} n/cm^2/s around the target by 1.5 MW. Possibility of a muon facility is also being considered.

In order to efficiently utilize the accelerator, it is preferable to carry out different kind of experiments in parallel. For the compression ring, negative hydrogen beam is suitable but negative hydrogen beam is not adequate for the experiments which require a small bending radius of proton beam line arrangement because of Lorenz charge stripping. In the latter case, positive hydrogen beam is better. In our accelerator, both positive and negative hydrogen ions are accelerated alternatively in successive bunches and these are separated by switching magnet. Negative hydrogen beam is introduced into the compression ring for neutron scattering and positive hydrogen beam to other facilities. Very short pulses can be switched out of the positive beam trains by a fast kicker magnet.

2.2 Proposed Accelerator Complex [2]

The Neutron Science Project of JAERI comprises very wide fields of basic science which utilizes the neutron as the probe to investigate materials of their structure and dynamics, and of nuclear technology. Various beam modes are required to fulfill the experimental requirements of these wide fields, namely, very short pulse for neutron physics, short pulse for neutron scattering, and continuous wave (cw) or long pulse mode for transmutation experiments and material irradiation.

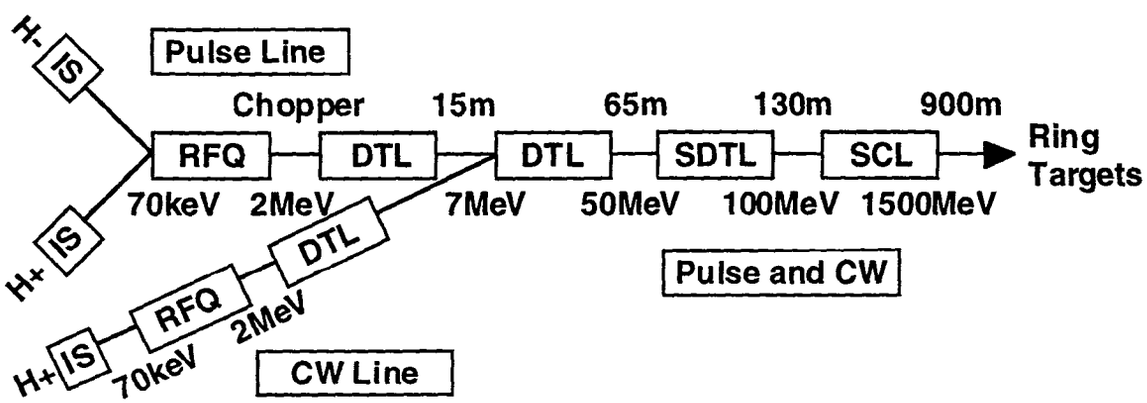

Fig. 2 Schematic diagram of the proposed accelerator system

The propose accelerator system is shown in Fig.2. The proton linac is designed to deliver 8 MW beam power and at the first stage is constructed at a power of 1.5 MW (1.5 GeV, 1 mA) with pulse operation, and then gradually is increased to 8 MW and cw operation as experience of high power accelerator operation being accumulated. At the final stage, both with pulse and cw modes will be achieved. Proposed accelerator complex consists of super-conducting cavity linac more than 800 m in length and two injectors both for pulse and cw operation. The injectors consist of RFQ and DTL, and connected to superdonducting linac. For neutron scattering facility, a high energy beam transport and one (finally two) compression storage ring are considered. A preliminary specification for the proton linac is given in Table 1. The beam power with pulse mode operation is shared with 5 MW for a neutron scattering target, 2 MW for transmutation experiments and 1 MW for other experiments, in parallel, within the total beam power of 8 MW. On the other hand, for cw mode operation, a beam of several MW is required for engineering tests of a thermo-hydraulic system and materials database for a demonstration facility development for transmutation system.

Table 1 A proposed specification of the linac complex

Total beam power at targets:	8 MW
Proton energy:	1.5 GeV
Ion source:	Negative/positive hydrogen ion sources (70 keV)
Average current:	5.33 mA
Peak current:	30 mA(pulse)/5 mA(cw)
Linac type	
RFQ:	2 MeV for pulse/cw operations (200 MHz)
Low β (2-100MeV) :	DTL/SDTL normal-conducting linac (200 MHz)
High β (0.1-1.5GeV):	Super-conducting linac (600 MHz)
Beam mode:	
First stage:	Pulse mode operation 2 ms
Second stage:	CW and pulse mode (3.7 ms) operations
Repetition rate:	50 Hz
Intermediate pulse width:	400 ns (interval 270 ns)
Chopping factor:	60%

The proton energy of 1.5 GeV was chosen considering the peak current limit of the ion source and the pulse width limit of the storage ring. The motivations for choosing a super-conducting cavity linac option are: 1) smaller beam hollow effect in large current acceleration because of large iris radius, 2) the cost reduction owing to the reduction of length of the linac which leads to the reduced investment costs and savings in operating costs, and 3) possibility for application of large current accelerator to the nuclear energy technology in future.

2.3 R&D for Accelerators

The major R&D efforts are presently: 1) the beam dynamic calculation including the high b linac, 2) the development of the negative ion source and the fabrication of high power test models with a cw-radio frequency for a quadrupole linac (RFQ) and a cw-drift tube linac (DTL), 3) the super-conducting cavity development, 4) the development of high intensity

proton beam storage ring, and 5) the optimization of the system design. In the course of the super-conducting cavity development, the vertical cavity test for β=0.5 (145 MeV) was successfully conducted in 1997 with the maximum field strength of 24 MV/m at 4.2K and 44 MV/m at 2.1K.

The proton storage ring is also one of the most important R&D items. The injection scheme is specially critical to compress the beam to shorter pulse less than 1 μs, because the conventional technology using charge stripping foil has a limit by heating up to accept the high current beam. This is the main reason to separate a ring to two rings in the most of designs for MW spallation source. In JAERI project, two ring scheme is considered for the reference design for 5 MW operation. However, the two ring increase the cost and makes another problem for fast beam switching and merging. To solve the problem of charge exchange foil, new charge exchange system, the LUCE method, the Laser Undurator Charge Exchange has been proposed.[3] The detailed proposed scheme is shown in Fig.3 and described in accompanying paper.[4] In this scheme, an undulator is used for a foil as a stripping magnet but a charge exchange is made by two steps from H^- to H^0 and H^0 to H^+. The first step stripping is made by the undulator for Lorenz stripping and in the second step, a resonance excitation by laser is used together with Lorenz stripping by the second undulator. The feasibilty study of this scheme is planned on an interanational collaboration.

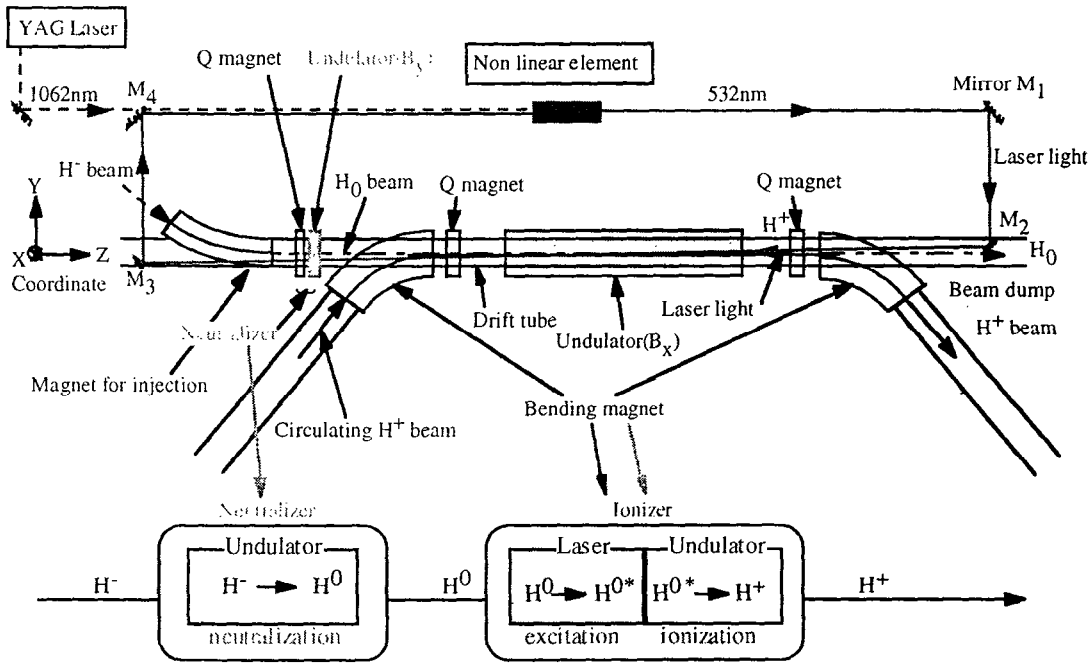

Fig.3 Proposed scheme of charge exchange system (LUCE method)

3. 5 MW NEUTRON SCATTERING FACILITY

3.1 Facility Design

The conceptual design of neutron scattering facility has been performed. The cutaway view of the facility is shown in Fig. 4. The target station is located in the center of the facility and has an independent building structure as a bone. The target station part includes a large crane with capacity of 100 ton, and therefore large open space is taken to hung up a shielding/reflector/moderator assembly and to carry it for a maintenance place. The wastes caused from the target system will be put in a storage inside the building with a water

cooling system. The experimental area is assumed to be controlled as a worker area for radiation safety, but one of beam lines is planned to be a controlled area of radioactivity for treating irradiated samples. On the other hand, the target station part is designed to be a radioactivity controlled area. The experimental area is separated from the target by the target shield that consists of an iron of 5.5-6 m in thickness and concrete of 1 m in thickness.

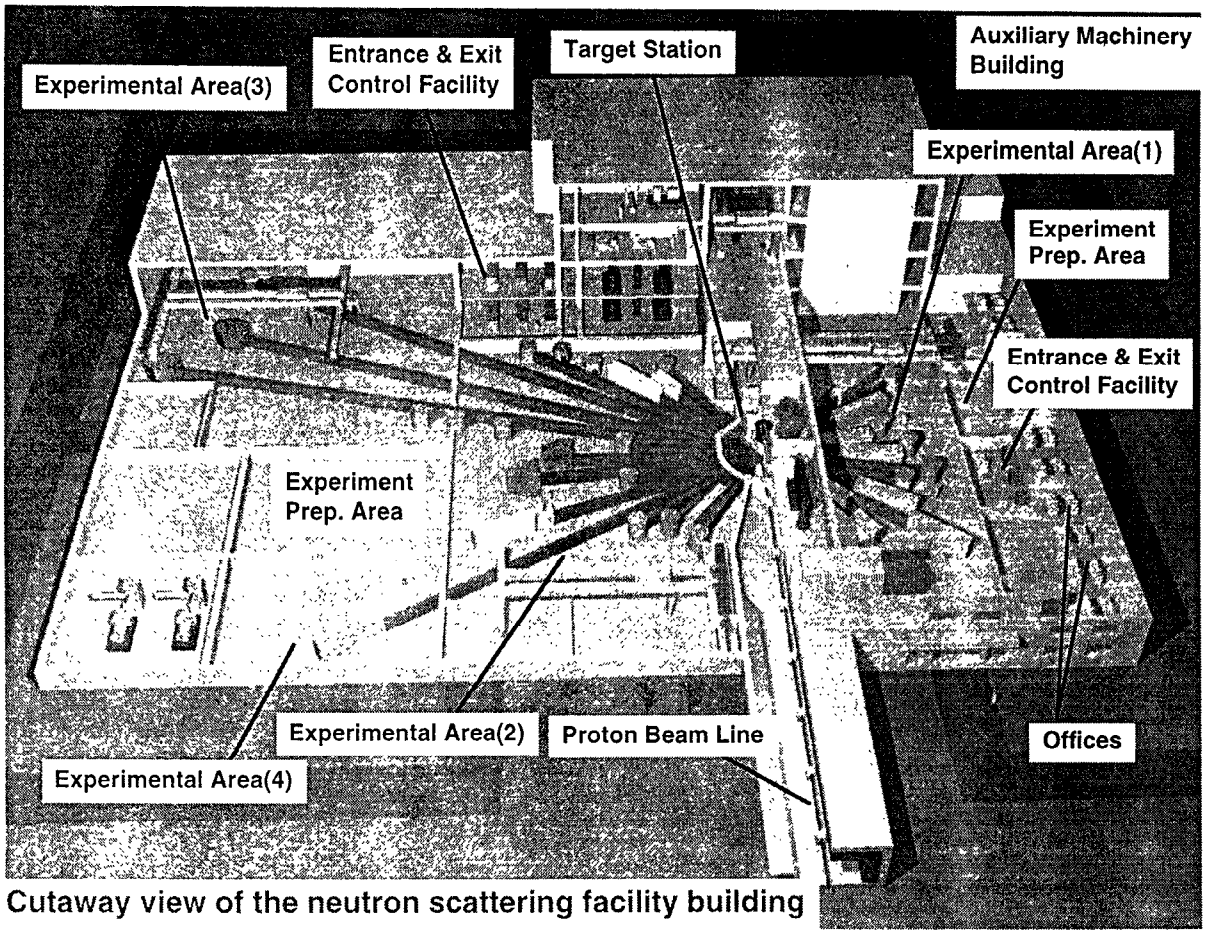

Fig.4 A Floor Plan of Neutron Scattering Facility in JAERI Neutron Science Project

3.2 Target/Moderator

The target is one of the key equipment at the facility and requires for extensive efforts to develop. It suffers from severe irradiation of high energy protons and neutrons, and thermal shocks by a pulsed operation. The detailed R&D strategy and status of the target/moderator development are reported separately in accompanying paper [5-8]. Two types of the target systems are considered corresponding to beam power and development stage. A solid system is used at low power up to 1.5 MW and at the initial stage and a liquid mercury system for high power stage at the goal. The moderator systems are also extensively designed including neutronics optimization study [9-12]. The present design considers two coupled liquid hydrogen moderators (20K) with water pre-moderator for cold neutron sources, one decoupled and poisoned liquid hydrogen moderator (20K) for thermal source and one decoupled water moderator (room temperature) for epithermal source, as listed in Table 2.

Table 2 Specification of Reference Moderators[9]

	Cold neutron	Thermal neutron	Epithermal neutron
Purpose	high resolution high intensity	high resolution	high resolution
Moderator type	Liq-H_2	Liq-H_2+ZrH_2 or H_2O particles + Liq-H_2	H_2O
Size (mm)	120x120x50	100x100x50	100x100x30
Temperature (K)	20	20	room temp.
Pre-moderator	H_2O(25mm thick)	none	none
Coupling	coupled	decoupled	decoupled
Cut-off energy (eV)	---	1	10
Angular coverage	50 degree	50 degree	50 degree
No. of viewed surfaces	1	2	2
No. of moderators	2	1	1

3.3 Proton Beam Specification

The proton beam injected on the target will be shaped by the transport optics using a octapole magnet system to make a rectangular foot print with 34.4 mm in height x 200 mm in width. The macro pulse length is 3.7 ms from the linac and the pulse repetition rate is 50 Hz at maximum. The pulse length at the target is designed to be 400 μs compressed by the storage ring, or according to the further study, it might be 800 μs depending on the beam merging method.

3.4 Instruments

Thirty two neutron beam lines are preliminary arranged around the target station based on the reference target/moderator arrangement, as shown in Fig. 5. The possible number of instruments is more than 40. The example of instrument types equipped at three kinds of neutron areas, cold, thermal and epithermal neutrons, are listed in Table 3. This number is very preliminary at present and should be discussed in the neutron scattering community in Japan for decision.

Table 3 Candidates of Instruments

Cold neutron	SANS, Reflectometer, IN5 type, IN10 type, TFXA, TAS, Spin echo, Interferometer, UCN
Thermal neutron	DCD, SXD, HRPD, HIPD, SEPD, Residual stress, TAS, MAPS type, MARI type, LAM-D type, TFXA, Hot sample
Epithermal neutron	SANDLAS type, Glass & Liquid, Epithermal chopper, eVs, PEN, Nuclear physics

At the same time that high intense neutron source is constructed, an effort of increase the efficiency of neutron transport to the instrument is very important to allow us to

arrange the instruments as much as possible. For that purpose, a fabrication techniques of high performance super-mirror neutron guide is also being developed in conjunction with upgrading the performance of JRR-3M instruments.[13]

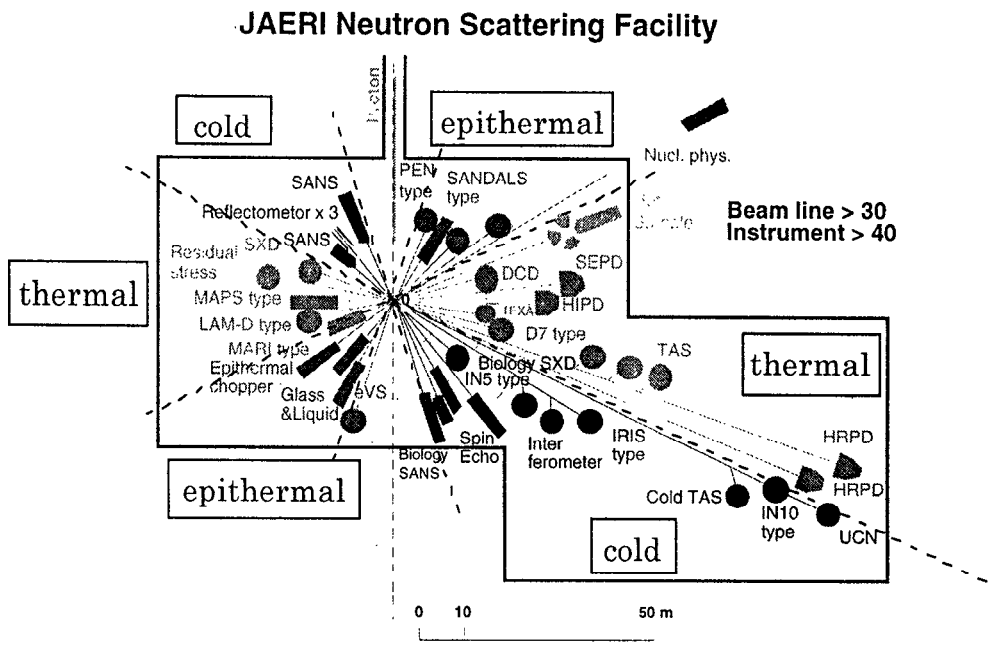

Fig. 5 Example of Instrument Arrangement

4. Time Scale

The R&Ds for both the accelerator and target are being progressed. The accelerator R&D was already performed for several years and achieved somehow the goal performance for low energy part, such as the positive ion source and the RFQ linac. Then the development

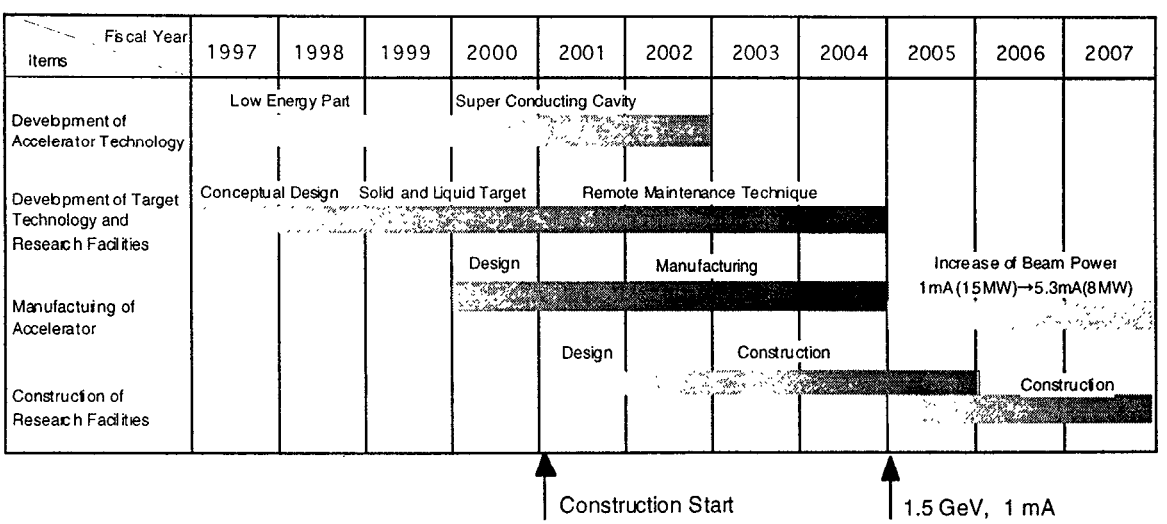

Fig. 6 Preliminary schedule of R&D and construction

R&D is continued to 2002, and the target R&D to 2004. The fabrication of the accelerator will start from 2001 for the low energy part, and complete in 2004. Then the low current beam test will be started and the current will be gradually increased to 5.3 mA , upgrading the RF power system. On the other hand, the neutron scattering facility will be equipped with the solid target system in 2004 for the beam test. The liquid system will be in a test phase at that time, and then replaced after confirmation. The facility will be fully opened for users in 2008.

ACKNOWLEDGMENTS

The authors would like to thank all the member of JAERI Neutron Science Project.

REFERENCES

[1] T. Mukaiyama, Y. Oyama, M. Mizumoto, T. Takizuka and R. Hino, "Neutron Science Project at JAERI," ANS Topical Meeting on Nuclear Applications of Accelerator Technology (ACCAPP'97), Nov. 16-20, 1997, Albuquerque.

[2] M. Mizumoto, J. Kusano, K. Hasegawa, N. Oguchi, H. Oguri, M. Kinsho, E. Chishiro, T. Tomisawa, Y. Touchi, Y. Honda, K. Mukugi, H. Ino, F. Noda, N. Asaoka, H. Kaneko and B. Fechner, " A Proton Accelerator for Neutron Science Project at JAERI," The 1st Asian Pacific Accelerator Conference, March 23-27, 1998, KEK, Tsukuba, Japan.

[3] Y. Suzuki, " A New Concept of Charge-Exchange injection for the High Intensity Proton Storage Ring of JAERI," ibid.

[4] Y. Suzuki, " A Foil-less Charge Exchange Injection (LUCE) for the Intense Proton Storage Ring," this meeting.

[5] R. Hino, M. Kaminaga, T. Aso, K. Kogawa, S. Ishikura, A. Susuki, A.Terada, H. Kinoshita and K. Haga, " Spallation Target Development at JAERI," ibid.

[6] M. Kaminaga, R. Hino, A. Susuki, M. Sakashita, H. Tagawa, and. Nakamura, " Thermal and Hydraulic Design of Mercury Target -Cross Flow Type-," ibid.

[7] R. Hino, K. Kaminaga, S. Ishikura, Y. Yanagisawa, M. Uzawa,K. Kurosawa, K. Ikeda and S. Uchida, "Preliminary Design of Mercury target - Return Flow Type-," ibid.

[8] S. Ishikura, K. Kaminaga, A. Susuki, R. Hino, I. Harada and M.Sakashita, " Analyses on Pressure Wave Propagation and Dynamic Stress in Mercury Target ," ibid.

[9] N. Watanabe, M. Teshigawara, K. Aizawa, J. Suzuki and Y. Oyama, " A Target-Moderator-Reflector Concept of the JAERI 5MW Pulsed Spallation Neutron Source," JAERI-Tech 98-011 (1998)

[10] N. Watanabe, M. Teshigawara, H. Takada, H. Nakashima, Y. Oyama, T. Nagao and T.

[10] N. Watanabe, M. Teshigawara, H. Takada, H. Nakashima, Y. Oyama, T. Nagao and T. Kai , Y. Ikeda and K. Kosako, " A Conceptual Design Study of Target-Moderator-Reflector System for JAERI 5MW Spallation Source", this meeting.

[11] N. Watanabe, M. Teshigawara, H. Takada, H. Nakashima, Y. Oyama, T. Nagao and T. Kai and K. Kosako, "Toward a High Efficiency Pulsed Cold Neutron Source", ibid.

[12] T. Aso, A. Terada, S. Ishikura, M. Kaminaga, R. Hino and N. Watanabe, " Structural and Hydraulic Study on Cold Source Moderator," ibid.

[13] K. Soyama , W. Ishiyama and K. Murakami, "Enhancement of Reflectivity of Small D-Spacing Multilayer Mirrors by Ion Polishing in Combination with Ion Beam Sputtering Deposition," ibid.

ICANS-XIV
14th Meeting of the International Collaboration on
Advanced Neutron Sources
June 14–18, 1998
Utica, Illinois

A Progress Report on the Spallation Neutron Source

Bill R. Appleton
for the
Spallation Neutron Source Project
Oak Ridge National Laboratory
Oak Ridge, Tennessee 37831, U.S.A.

Introduction

The neutron science community has been working to gain new neutron sources and improved instrumentation since the 1970s. In FY 1996, the Department of Energy (DOE) provided $8 million to initiate the R&D and conceptual design studies on a next-generation, accelerator-based spallation neutron source. This presentation is a brief overview of the status of the design and funding efforts on this new neutron source, which is called the Spallation Neutron Source (SNS).

The SNS Collaboration

Figure 1 is a schematic representation of the SNS. It also highlights the fact that the SNS will be designed and constructed by a collaboration of five DOE National Laboratories. The design selected for SNS is an H^- ion source, a 1-GeV conventional linac, an accumulator ring, and a mercury target with water and supercritical hydrogen moderators that provide pulsed neutrons to 18 beam lines.

When Oak Ridge National Laboratory (ORNL) was asked by DOE to assume responsibility for the design of SNS, we decided to establish a full collaboration that focussed the considerable expertise of the DOE National Laboratory system. Not only were we seeking to involve those laboratories with recognized expertise in accelerator/target/instrument technologies, but we sought laboratories that also were experienced in the operation and/or design of major neutron facilities. This added dimension enhanced our connection with the neutron science community, who are our ultimate customers, and provided an understanding of the essential elements of a successful neutron facility.

The Lawrence Berkeley National Laboratory is responsible for the front-end systems of SNS (H^- ion source, RFQ, and initial beam chopping). Los Alamos National Laboratory (LANL) is responsible for the conventional linac accelerator system, which accelerates the H^- ions to 1-GeV energy. LANL also directs the integrated controls systems effort for SNS. Brookhaven National Laboratory is responsible for the accumulator ring and

SPALLATION NEUTRON SOURCE

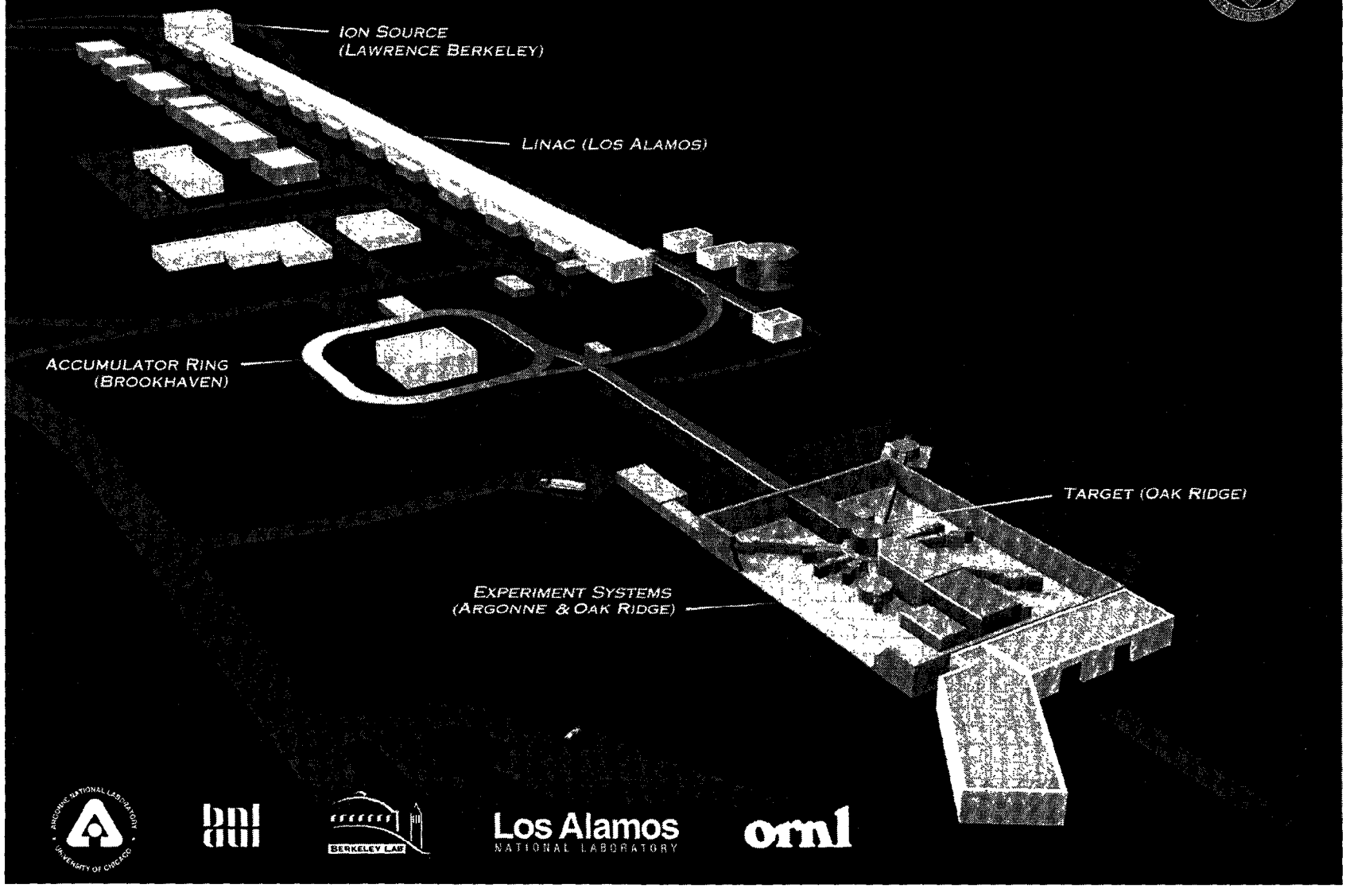

ARGONNE NATIONAL LABORATORY · UNIVERSITY OF CHICAGO

BNL

BERKELEY LAB

Los Alamos NATIONAL LABORATORY

ornl

the associated beam transport systems. Argonne National Laboratory is primarily responsible for instrument development. ORNL is responsible for developing the mercury target, conventional facilities, and overall project coordination and management. ORNL is also responsible for final operations of the SNS for the DOE and scientific community, and for establishing the staff and expertise for operating and upgrading the SNS in the future.

Reference Design

The schematic for the SNS reference design is shown in Figure 2. The 1-megawatt (MW) beam power is achieved by injecting ~1 ms pulses of H^- from the linac at 1 GeV, through a stripper foil, into the accumulator ring as H^+. The ring accumulates about 1200 linac pulses and compresses them into ~1 μs pulses, which are delivered to the mercury target at a frequency of 60 Hz. The H^+ beam is converted to neutrons as a result of the spallation nuclear reaction process; the neutrons are slowed in water, or supercritical hydrogen moderators, and directed to the instruments at the end of the beam lines.

The reference design parameters are listed in Figure 3. The SNS is designed to be upgradeable to significantly higher powers in the future. An initial upgrade to 2 MW requires only minor system improvements, but the ring and shielding are already capable of accommodating the increased powers. The design of the accelerator systems was made to be robust and flexible so that a variety of higher-power upgrades would be possible. This facilitates future upgrades that will be selected based on current technologies and neutron community needs at the time.

Since additional technical presentations in this meeting detail the capabilities and features of SNS, I will not elaborate further on those here.

The Joint Institute for Neutron Sciences

The SNS will be a designated user facility accessible to scientists and engineers from universities, industries, and government laboratories from all over the world. Based on user interests and needs, it is expected that 1000–2000 users will utilize SNS facilities each year. ORNL has 14 user facilities at present, including the High Flux Isotope Reactor (HFIR), which provides the highest thermal neutron flux of any research reactor for neutron scattering, and thus has a long history of user facility operation.

In order to facilitate user access to the SNS and HFIR, the state of Tennessee has provided $8 million for the construction of a Joint Institute for Neutron Sciences (JINS). The JINS is a joint venture between the University of Tennessee (UT) and ORNL. State funds will be provided to UT to construct the JINS facility on DOE land adjacent to SNS. The facility will be operated by ORNL and UT for the benefit of the neutron science user community.

ORNL 97-5016D/tcc

Spallation Neutron Source Reference Design

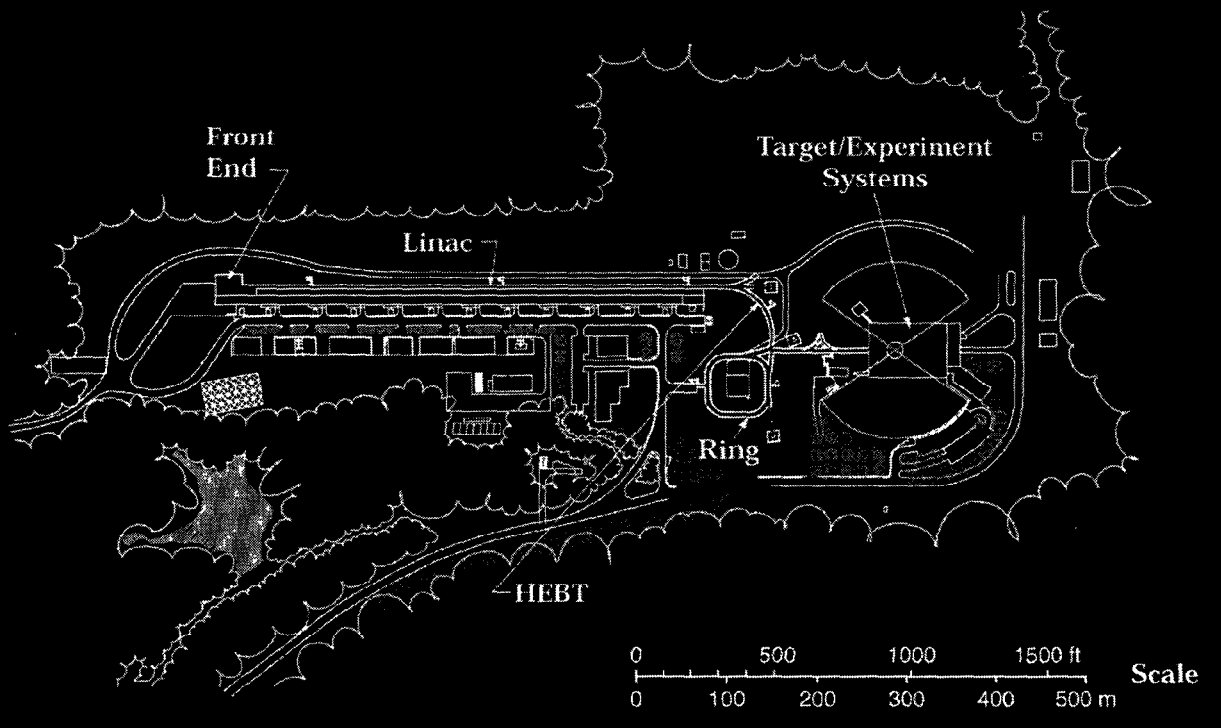

ORNL 98-3720A/jcp

Design Parameters

	Initial *1 MW*	Upgrade *to 2 MW*
Pulse repetition rate (Hz)	60	
Peak ion source H^- current (mA)	35	70
Front-end efficiency (%)	> 80	
Linac length (m)	493	
Linac capture-acceleration efficiency (%)	100	
Linac beam duty factor (%)	6	
Linac final beam energy (GeV)	1.0	
Accumulator ring circumference (m)	220.7	
Ring controlled injection loss (%)	< 4	
Ring orbit rotation time (ns)	841	
Pulse length at ring injection (ns)	546	
Kicker gap at ring injection (ns)	295	
Ring filling fraction (%)	65	
Number of injected turns	1158	
Ring filling time (ms)	0.97	
Protons per pulse on target	1.04×10^{14}	2.08×10^{14}
Protons per second on target	6.3×10^{15}	1.25×10^{16}
Time average beam current on target (mA)	1.0	2.0
Target	Hg	
Beam power on target (MW)	**1.0**	**2.0**

JINS will provide an intellectual focus for neutron science and a gateway for users of SNS and HFIR. It will provide teleconferencing facilities, conference rooms and meeting space, offices, laboratory space, education and training facilities, and a nucleus for all interested universities and industries wishing to utilize SNS.

Status of the SNS Project

The DOE Office of Energy Research (ER) provided $8 million in FY 1996 to initiate the R&D and conceptual design of the SNS. The five DOE National Laboratory Collaboration was formed to accomplish this. In FY 1997 the SNS requested $23 million and received $8 million to continue this design process. The result was the reference design discussed above and a comprehensive *Conceptual Design Report* (CDR). This design was guided by performance requirements provided by DOE and the neutron science community. The first neutron users meeting (User's Workshop on Instrumentation Needs and Performance Metrics) was held in Oak Ridge October 31–November 1, 1996, to define instrumentation needs for SNS.

In June 1997 the DOE ER held a comprehensive review of the CDR. A team of 60 external experts from other laboratories, universities, and industry spent a week examining the project cost, schedule, technical scope, and management structure. In addition, an Independent Cost Estimation (ICE) team from industry assessed the costing methodology. and cost. The SNS was approved to continue preparation for construction with recommendations to extend the schedule one year and enhance funding for instrument R&D, and the ICE team validated the cost to within 2% of the SNS estimate.

In FY 1998 the SNS requested $43 million and received $23 million to continue preparations for construction. These funds were used to prepare a request to DOE for a construction line item start in FY 1999, based on the funding profile and construction schedule shown in Figure 4 and Figure 5, respectively.

In June 1998 DOE held a second review of the technical progress, cost, schedule, and management readiness of SNS to proceed with the start of Title I design and construction activities. The work plans were presented for the first half of FY 1999, and the project was judged ready to initiate construction and design activities on October 1, 1998, pending approval of the construction line item request and funding from Congress.

In the deliberations of Congress on the FY 1999 budget, the following actions were taken. The Senate Appropriations Committee recommended the full funding requested by the project of $157 million in FY 1999 and a construction line item. The House recommended $100 million and a line item. In action by the Conference Committee on Appropriations, it was recommended that construction line item approval and $130 million be provided for the SNS Project. Both houses of congress have approved this recommendation, and the bill has been signed into law.

ORNL 97-127699D/djr

Financial Summary - Spallation Neutron Source

(Optimum Profiles for a 7 Year Schedule)

SNS SPALLATION NEUTRON SOURCE

Budget Authority (BA) in Actual Year Millions of Dollars

Fiscal Year	1996	1997	1998	1999	2000	2001	2002	2003	2004	2005	*Total*
TEC				128	197	255	253	185	78	43	1,139
R&D											
OPEX				26	15	12	8	4	3		68
Capital				2	1						3
Pre-Ops				1	1	1	2	6	16	57	84
Prior Year	8	8	23								39
Total	**8**	**8**	**23**	**157**	**214**	**268**	**263**	**195**	**97**	**100**	***1,333***

ORNL 97-127692c/djr

SNS Integrated Construction Schedule

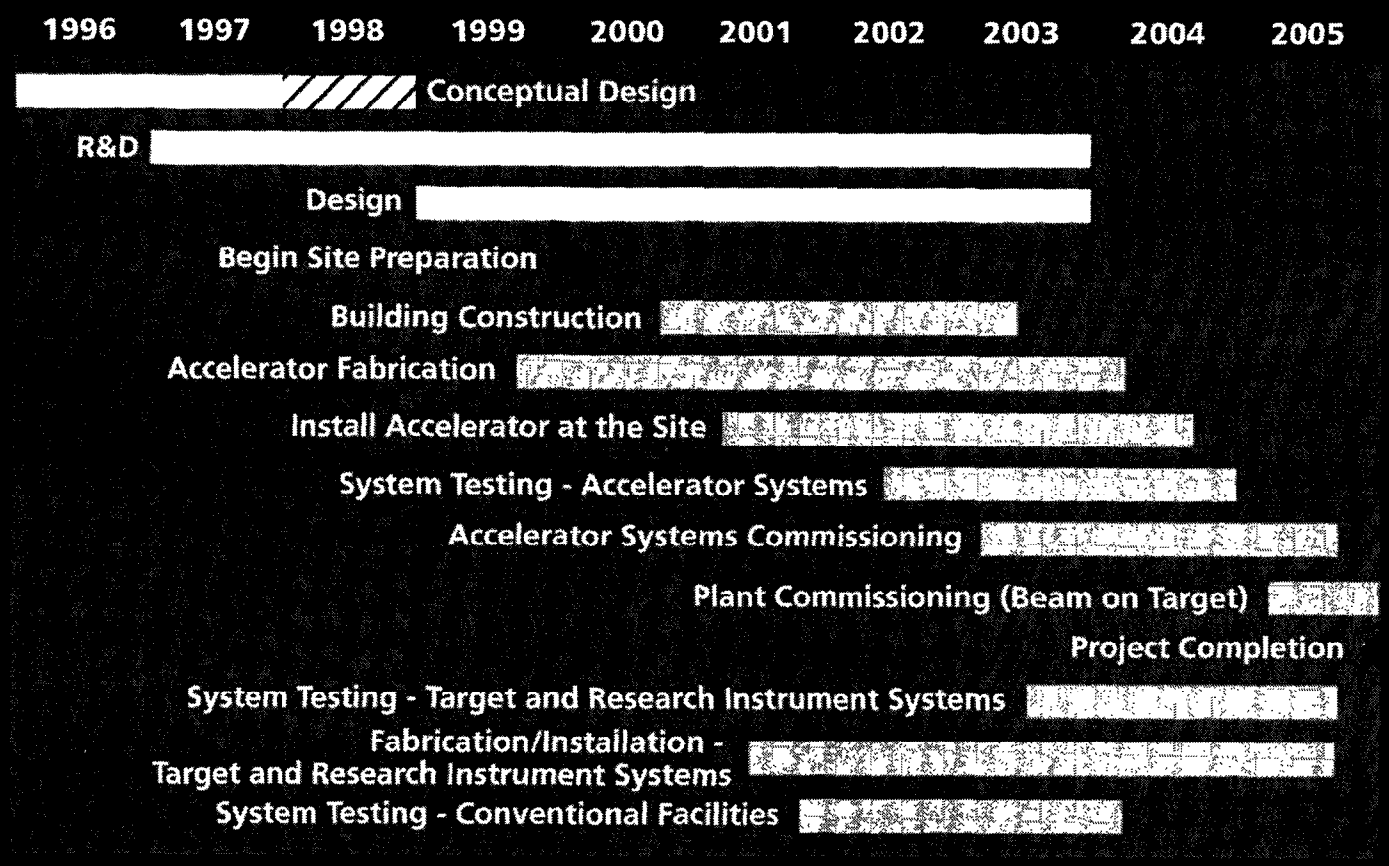

Progress on SNS

The SNS Project is ready to initiate Title I design and construction activities beginning in FY 1999. The project management systems, plans and schedules, technical baselines, and detailed work plans and schedules for FY 1999 are in place and have been approved by DOE. There are mechanisms in place to coordinate interface issues among the collaborating laboratories and agreements to accomplish the work. A second neutron user's meeting will be held November 9–11, 1998 in Oak Ridge to initiate a formal User's Group for SNS, and to engage the scientific community in the actual selection, design, and construction of the instruments that will be used on SNS. The initial design of SNS of 1 MW will deliver a beam 6–10 times more powerful than any existing pulsed neutron source. The design and flexibility built into the SNS means that it can be economically upgraded to significantly higher powers with the addition of experimental capability in the future. This should provide the needed capability to the neutron science community for an intense neutron source well into the next century.

Acknowledgements

I wish to acknowledge the members of the SNS collaboration for whom I am reporting. Although the members are too numerous to detail, I wish to acknowledge the laboratory groups by noting the Senior Team Leaders at each lab — Kent Crawford at Argonne National Laboratory; Bill Weng at Brookhaven National Laboratory; Rod Keller at Lawrence Berkeley National Laboratory; Dave Gurd and Bob Hardekopf at Los Alamos National Laboratory; and Tony Gabriel and Jim Lawson at Oak Ridge National Laboratory.

THE IBR-2 FAST PULSED REACTOR: PRESENT AND FUTURE

V.L.Aksenov, V.D.Ananiev, A.V.Belushkin, A.V. Vinogradov
Frank Laboratory of Neutron Physics (FLNP), Joint Institute for Nuclear Research (JINR),
141980, Dubna, Moscow Region, Russia.

1. Introduction

The IBR-2 fast pulsed reactor belongs to and is operating in the Frank Laboratory of Neutron Physics (FLNP) of the Joint Institute for Nuclear Research (JINR) in Dubna, Russia. JINR is an international research centre founded in 1956 and it includes seven laboratories with research programs in nuclear physics, condensed matter research and elementary particle physics.

At present, FLNP with a staff of 500 people has two pulsed neutron sources: the pulsed booster IBR-30 and the fast pulsed reactor IBR-2. The first is mainly used to perform experiments in the field of nuclear physics (physics of the neutron and study of nuclear reactions with neutrons). The second source is used for condensed matter research.

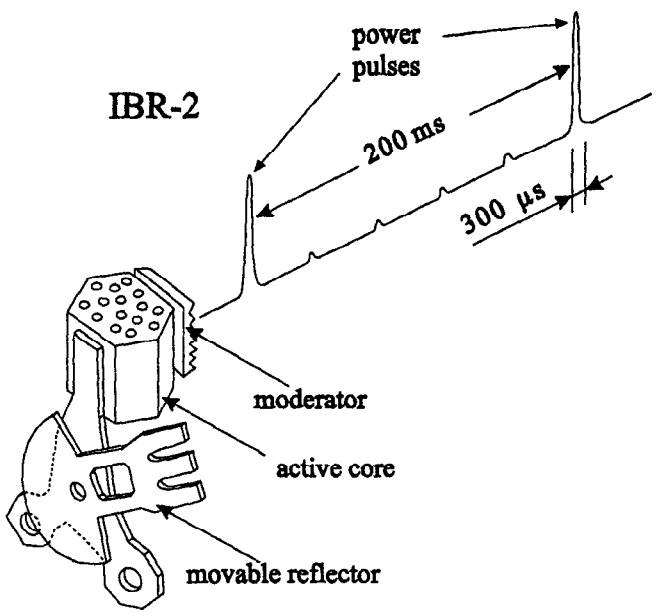

The principle of IBR-2 operation is schematically shown in the figure. The core of the reactor is composed of fuel element subassemblies (plutonium dioxide). The cooling system has three circuits and two loops. In the first and second circuits the coolant is liquid sodium and in the third it is air. The core is contained in a double-wall steel vessel and is surrounded by a stationary reflector with control and safety rods. Around the reactor, water moderators scanned by 14 horizontal channels for neutron extraction are located. Power pulses with a frequency of 5 Hz are generated by a movable reflector whose rotation ensures reactivity modulation of the reactor. When both rotating wheels of the reflector approach the core, a power pulse develops.

Some of the main IBR-2 working parameters are presented in Table 1.

Table 1. IBR-2 working parameters

N	Parameter	As of 01/04/98	Rated
1	Operation for physical experiment, h	33755	
2	Power operation time, MW·h	63358	85000
3	Operation time of movable reflector, h	8172	18000
4	Maximum fluence on reactor vessel in the center of core (10^{22} n/sm^2) for $E_n > 0.1$ MeV	2.79	3.72
5	Maximum fuel burn, %	5.09	6.5
6	Emergency shut-downs	395	550

2. Enhancement of the IBR-2 reactor utilization

The upgraded reactor will be given the name IBR-2M. By the year 2002, the principal parts of the reactor IBR-2 will have their radiation resource exhausted and will have to be replaced. In this connection a possibility appears to improve the characteristics of the reactor. The programme for upgrading the IBR-2 reactor has been elaborated for 10 years (1996-2005) and will be executed in three directions:

- improvement of the reactor parameters,
- increase in nuclear safety and reliability of the reactor,
- updating of the reactor systems.

The main stages of the IBR-2 modernization project:

- designing and manufacturing of the new equipment 1996-1998,
- assembly and tests of equipment,
  replacement of old equipment and fuel reloading 1999-2001,
- physical startup, energy startup 2002-2004,
- startup of IBR-2 for physical experiments 2005.

Improvement of the main parameters of the reactor, including an increase in the thermal neutron flux is connected with the realization of the new reactor core structure and the principally new design of the heterogeneous movable reflector. The expected increase in the thermal neutron flux in pulse is up to $(1.8\text{-}2)\cdot 10^{16}$ n/cm^2/s. The IBR-2 pre- and post-modernization parameters are illustrated in table 2.

Table 2. IBR-2 pre- and post-modernization parameters

N	Parameters	IBR-2	IBR-2M
1.	Average power, MW	2	2
2.	Fuel	PuO_2	PuO_2
3.	Number of fuel assemblies	78	69
4.	Maximum fuel burn, %	6.5	9
5.	Pulse repetition rate, Hz	5; 25	5; 10
6.	Pulse width, μs	215	200
7.	Revolution/minute		
	Main reflector (MR)	1500	600
	Auxiliary reflector (AR)	300	300
8.	MR and AR material	steel	nickel+steel
9.	Service life, h	20000	50000
10.	Background, %	6	7
11.	Number of satellites at 5 Hz	4	1

On a number of IBR-2 beams the flux in the cold neutron part of the spectrum will be essentially increased by using a new cryogenic moderator (CM) to be commissioned in 1999. In parallel with the manufacturing of CM, work to modernize the currently operating neutron moderators will be carried out.

Increasing the nuclear safety and reliability of the reactor involves a number of activities the most important of which are as follows:

1. Improvement of control systems for fuel elements tightness and vibration diagnostics of the movable reflector.
2. Startup of an automated system for measuring and control (ASMC). At present, some of ASMC subsystems are in the process of adjustment and tests are being carried out in order to start the ASMC test operation in 1998-1999. The execution of the ASMC project will provide the IBR-2 reactor with a branched diagnostics system and, thus, essentially increase the safety and reliability of the reactor. This is the PC-based (PC-Lab Standard) Control and Monitoring System. Work has continued to improve the IBR-2 control and monitoring system in a search for higher reliability of the control of the reactor state and the maintenance equipment. At

the same time, the system has been under constant development to increase the information capability on the basis of recent achievements in the field. This helps the staff to get adapted to the system and develop new, more convenient programs for the control of technological parameters, as well as the equipment of the reactor state control system and electronics to execute necessary logic operations of the reactor alerting and monitoring. At present, some ASMC subsystems are in the process of adjustment and resource tests are being carried out in order to start the ASMC test operation in 1998-1999. Unfortunately, the work is delayed due to insufficient financing.

3. Reconstruction of the IBR-2 power supply system. The IBR-2 operation experience showed that a considerable number of IBR-2 emergency shutdowns (about 20%) are connected with different interruptions in power supply caused by malfunctioning of the electric transmission substation. In 1990-1991, the project for switching the IBR-2 high voltage power supply system over to a separate transformer was developed. The reconstruction of the electric substation is to be completed before the year 2000.
4. The IBR-2 reserve control desk. In 1998-1999, in the frame of the project for the construction of the IBR-2 reserve control desk (as required by the State Atomic Inspection of Russian Federation) is to be completed.
5. Substantiation of the technological resource of the reactor. The work is being carried out by design institutes in accordance with the latest requirements of the State Atomic Inspection of Russian Federation.

The modernization of the main systems of the reactor is necessitated by nearly exhausted radiation and mechanical resources of a number of reactor blocks and the fuel burn.

The new movable reflector (PO-2RM). The resource of the currently operating movable reflector PO-2R will be exhausted in 7 years, by the beginning of the year 2002. By this time, the new reactivity modulator PO-2RM will be manufactured. According to the PO-2RM project this involves:

- construction of the main and auxiliary rotors from nickel alloy (nickel content is 70%);
- the main and auxiliary rotors rated speed of rotation is 600 and 300 rpm, respectively. The pulse duration of about 200 μsec is retained. The reactor reliability and the resource of the machine will considerably increase.

By now, the PO-2RM project has got experts approval from the State Atomic Inspection of Russian Federation

In 1998-1999, the first two movable reflectors, PO-1 and PO-2, will have to be removed from a temporary storage room which is 2/3 full at present. Because of high induced radioactivity of these devices, unique technologies will be used to accomplish the task.

Fuel reloading. By the year 2001 the existing active zone will exhaust its resource. Maintaining the current reactor operation schedule (2500 h a year at the power 2 MW) the energy generated by the end of the year 2001 will be 85000 MW-h and the maximum burn of fuel elements will be 6.5%.

In the period up to the year 2001 the operational reactivity resource, as well as replacement of separate fuel cassettes, if such a necessity appears, will be provided from the reserve. At the same time, the new plutonium dioxide fuel elements have to be created. To do this, it is necessary:

- to develop a technical project for fuel elements in a specialized institute,
- to conclude a contract for manufacturing with an appropriate Russian plant,
- in 1999, to start an investigation of two fuel cassettes currently working under greatest strain in the laboratory of the Ministry of Atomic Energy of Russian Federation to obtain necesseary data for designing the new core,
- to assemble the new core at FLNP.

The reactor jacket. By the end of the year 2001 the maximum fast neutron fluence will be $2.3 \cdot 10^{22}$ n/cm^2 for neutrons with an energy E > 0.5 MeV and $3.72 \cdot 10^{22}$ n/cm^2 for neutrons with an energy E > 0.1 MeV, and the number of emergency shutdowns will be 550, i.e., these parameters will reach the rated limiting values established by the new requirements for reactor safety and the calculation of the reactor jacket durability performed by the designer in 1994. In this connection, it seems expedient to simultaneously replace the reactor jacket, fuel, stationary reflectors, control and emergency system (CES) mechanisms and water moderators in the period from the year 2002 to the year 2004. The estimated IBR-2 modernization expenditures are summarized in table 3.

Table 3. Enhancement of the IBR-2 reactor utilization (estimated cost, k$)

	Stage 1 (designing, manufacturing, assembly and tests of new equipment)					Stage 2 (equipment replacement, physical startup, beginning work for physical experiments)				
Year	1998	1999	2000	2001	Total	2002	2003	2004	2005	Total
k$	1450	1700	1730	1150	6030	750	550	400	300	2000

Remark

1) Total for the period 1998-2005 - 8.03 k$.

2) Expenses for the period 1995-1997 - 0.7 k$.

3) Salary fund and business trip expenses are not included.

3. Scientific programme at IBR-2

A wide program of scientific investigations in different disciplines has been developed on the reactor beams. The following figure illustrates the distribution of beam time among scientific directions.

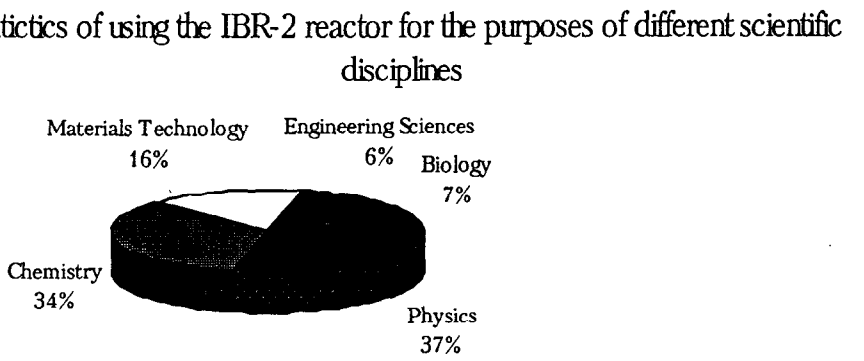

At present, the general trend in neutron scattering is the expansion of research in the fields of biology and engineering sciences. This tendency is also pursued at IBR-2. At the same time, other scientific directions develop very actively as well.

IBR-2 as a pulsed neutron source has some specific features. These are a low repetition rate and a very high neutron peak flux with a relatively large pulse duration. The first two were always considered as advantages because they allow one to investigate a broad Q range, study weakly scattering samples, and use very tight collimation to improve spatial resolution. Due to these, a lot of very interesting results were obtained during the last years.

Reflectometry with polarised neutrons is used to measure the magnetic field penetration depth in thin films of type-II superconductors and high-T_c superconductors. Very important results were obtained in the study of the magnetic properties of thin magnetic films and multilayer structures, polymer composites, thin films, etc.

In the field of small-angle neutron scattering intense activity goes in the study of self-organizing systems, model and biological membranes, structure of biological macromolecules.

Considerable progress has been made in the field of texture studies. Due to the startup of a new spectrometer constructed at IBR-2 by the German group for texture studies, investigations of complex multicomponent rock samples have become possible. This opens a new field of research – the study of the relationship between the texture of geological samples and the physical properties of the earth crust and the upper mantle.

During the last years, a very high pulsed neutron flux has made it possible to start a very pressing research program in the study of the structure and dynamics of condensed matter at very high pressures. The results for 9.5 GPa have been obtained and in the future, it is planned to increase the pressure up to 25 GPa or even higher. Very interesting experiments of high-T_c superconductors, metal hydrides and ammonium halides were performed.

The new spectrometer built for such kind of research allows simultaneous measurements of diffraction and inelastic scattering spectra. It can also be used for the study of the structure and dynamics of microsamples.

For many years a relatively large neutron pulse width has been considered as a natural disadvantage of IBR-2, because it limits the resolution of the instruments in the traditional approach. However, the implementation of the reverse time-of-flight Fourier technique and the construction of the high resolution Fourier diffractometer have completely changed the situation. At present, for a very broad range of scientific problems, at IBR-2, one can obtain structural results of the same quality as they can be achieved on the best powder diffractometers in the world. Also, this machine has a very good potential for stress/strain research as it was demonstrated in recent experiments.

Very good possibilities exist at IBR-2 for time-of-flight inelastic neutron spectroscopy. For example, the NERA high resolution inverted geometry neutron spectrometer makes it possible to obtain inelastic scattering data of the quality comparable with the best spectrometer of its type, TFXA, in the Rutherford Appleton Laboratory. The DIN direct geometry time-of-flight inelastic scattering spectrometer has very good parameters to study the dynamics of quantum and normal liquids.

The method of neutron activation analysis is presently applied very effectively to analytical work connected with the protection of the environment: biomonitoring of industrial areas, multielement analysis of aerosols etc.

The new direction in applied research is the testing of radiation hardness of various constituents of detectors for large hadron colliders. After some years of operation such detectors will get the neutron fluence of the order 10^{15} n/cm^2 and the gamma-dose 10 Mrad. The neutron and gamma-spectra, similar to the corresponding spectra from hadron colliders, can be easily formed at the reactor IBR-2 and at present, different electronics and construction elements created in the frame of the project ATLAS CERN are being tested.

At the present time, the cold methane moderator is being installated. The first experiments have shown that such moderator gives the gain of 20 times in the yield of cold neutrons (with E<1meV). In 1999, it is planned to move the cold moderator to its regular site at IBR-2.

4. Conclusion

The reactor has been operated for over 13 years without accidents. The years of continuous operation of IBR-2 have demonstrated that it is reliable in operation and is very effective for studies in condensed matter physics. It supplies neutron spectrometers with neutrons 110 days per year. The initial fuel charge ensures over 15 years of operation without fuel reloading. The liquid sodium loops are working reliably in the non-stop regime. A succesful implementation of the IBR-2 modernization program will extend its service life to the year 2030.

References

1. V.L.Aksenov / Update on pulsed reactor IBR-2 at Dubna, Physica B 174 (1991), 438-442
2. Yu.S.Yazvitskii / The pulsed reactor IBR-2 as a neutron source, (1977), Nuclear Structure Study with Neutrons, Publishing House of the Hungarian Academy of Sciences
3. I.M.Frank and P.Pacher / First experience on the high intensity pulsed reactor IBR-2, Physica 120 B (1983), 37-44
4. E.P.Shabalin / Fast Pulsed and Burst Reactor, Pergamon Press, Oxford, 1979
5. FLNP - Programme of Research and Development 1996-1998, ed. V.L. Aksenov and Yu. V. Taran (JINR, Dubna, 1995)
6. V.I. Luschikov, A.V. Vinogradov / Applied research at the IBR-2 fast pulsed reactor, IAEA International Seminar "Enhancement of the research reactors utilization", Bhabha, India (1996).

Status Report of KENS

Hironobu Ikeda

Neutron Science Laboratory,
High Energy Accelerator Research Organization
Oho 1-1, Tsukuba 305, Japan

1. JHF and the new Research Organization

Japan Hadron Facility (JHF) project is an interdisciplinary project among particle physics, nuclear science and material science, which utilizes world-most-intensive proton beam produced by synchrotron accelerators. The Institute of Nuclear Study of University of Tokyo (INS), which has been devoting to realize JHF for a long time, was merged to KEK in April 1997, and KEK was re-organized to be a new Research Institute, i.e. the High Energy Accelerator Research Organization (new KEK). The neutron science facility, so called Neutron-arena (N-arena) for material research and other related science will produce intensive pulsed neutron beam by 3GeV, 200μA proton synchrotron.

The formal Committee for discussing about the future of accelerator science in Japan, which was organized in April 1995 in MONBUSHO (Ministry of Education, Science, Sports and Culture), reported the decision of establishment of new organization, mentioned above, in 30th of April 1996. It says, " Under considering the evolution of accelerator science and scientific importance in particle physics, nuclear science, meson science, synchrotron radiation science and neutron science, it is decided to have a comprehensive research institute by combining the three laboratories, i.e. KEK, INS and the Meson Science Laboratory of University of Tokyo (UT-MSL), and reform them to make continuous development of the accelerator science and lead international initiative in the related scientific field." Hence two new institutes, i.e. the Institute of Particle and Nuclear Studies and the Institute of Materials Structure Science, were formed in the new KEK. These institutes share the backbone accelerators in collaborative fashion with keeping independent research scheme.

The budget proposal for the new organization was sent off to the Ministry of Finance from MONBUSHO in August 1996 and approved by the government in December 1996. Under the new KEK, the Neutron Science Laboratory is composed from four units for the neutron scattering research division and three units for the neutron target development division. (One unit contains three research staffs and one or two technical staffs.) The outline of the new organization is shown below. Total staffing at new KEK amounts to about 750 full-time permanent positions.

High Energy Accelerator Research Organization (new KEK)

- Institute of Particle and Nuclear Studies
- Institute of Materials Structure Science
  - Synchrotron Radiation Laboratory
  - Neutron Science Laboratory
  - Meson Science Laboratory
- Accelerator Laboratory
- Applied Research Laboratory
  - Radiation Science Center
  - Computer Science Center
  - Low Temperature Technology Center
  - Manufacturing Center

The one of the aims of the new organization is to realize JHF, which has been a long time dream of researchers in the related scientific fields, especially neutron scientists. The accelerator complex is composed from the 200MeV proton linac, the 3GeV proton booster synchrotron and the 50GeV synchrotron. 3GeV protons of 200μA (0.6MW, 25Hz) will be supplied for N-arena (neutron arena), M-arena (meson arena) and E-arena (exotic-nuclei science arena). 50GeV protons of 10μA will be supplied for K-arena (K-on, pi-meson, anti-protons, neutrino science arena). In order to reduce the construction costs, the existing tunnel for the present 12GeV proton synchrotron and infrastructure, such as the electric power facility, the cooling water facility and so on, will be refurbished and used for JHF. Figure 1 shows the outline of the JHF.

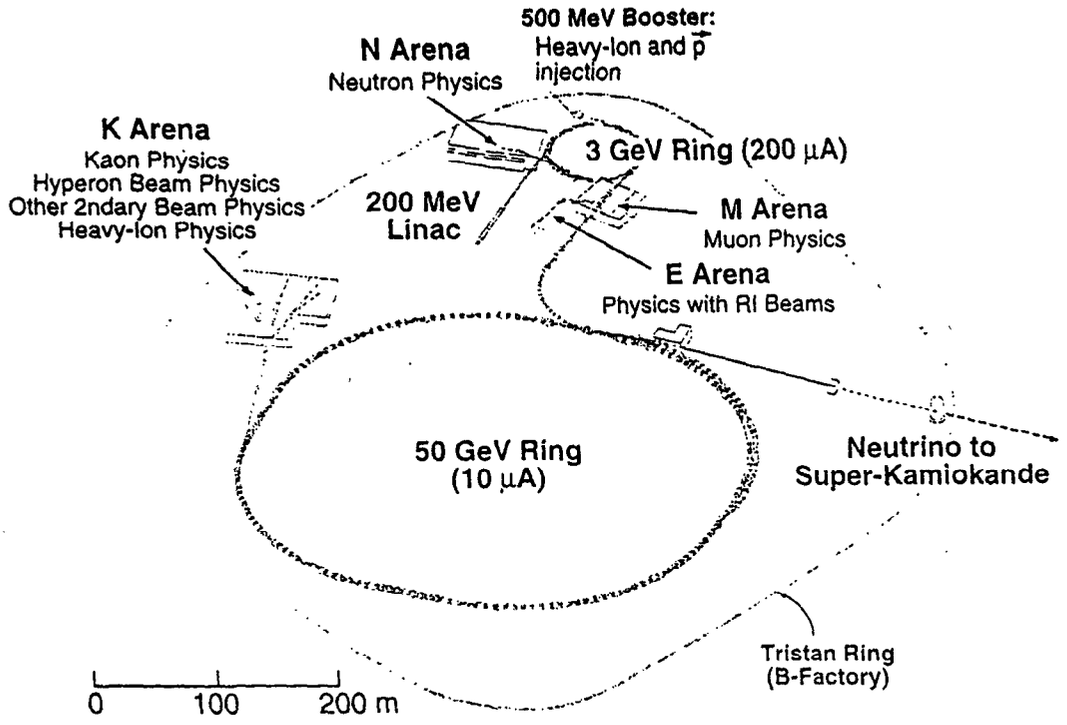

Fig.1 Proposed accelerator complex and experimantal areas for JHF

The N-arena is aimed at producing the world highest neutron flux by utilizing newly developed moderators. It is six times for thermal neutrons and 36 times for cold neutrons compared to those of the ISIS facility of the Rutherford Appleton Laboratory. Hence it is over 200 times of the present flux of the KENS facility, and a large number of fruitful scientific outputs are highly expected. In addition, for endowing further uniqueness to JHP, a possible research scheme of multi-beam experiment with using neutron, muon and synchrotron radiation, and development of high performance spectrometer are under consideration. In the N-arena more than twenty spectrometers will be installed. Those are small-angle scattering instrument, diffractometers, inelastic spectrometers, polarization analysis instruments, reflectometer and so on, which will be served for studying static and dynamic structure of materials including biological substances and basic nuclear science.

After realizing the performance of 0.6MW in the neutron source, there will be possible upgrading to 1.2MW by increasing the operational frequency of the accelerator to 50Hz. Further increase of the proton power can be achieved by improving the 200MeV lineac, which will reserve available site for this purpose. It is, however, indispensable to develop a component for high power accelerator and a new type of neutron target for high power neutron source, because even liquid metal target is not proved yet to be usable above a few MW. Those issues should be solved in the future by the related working force. Working for N-arena program is underway by the power users. The working group for target station is lead by Dr. M.Furusaka (KEK) and for spectrometers by Dr. M.Arai (KEK). The cost estimation for the target station of N-arena was already made and the gloss budget proposal was submitted to the government in July 1997, but the project was not officially approved because the Japanese Government started the reform of the Japanese financial systems.

The N-arena will be opened for the outside users after completion of the construction, and it will be also opened for international community. Hence it is important to consider the strategy of the management of the facility. KEK has been making collaboration with any foreign countries without collateral beam costs.

The development of target station, spectrometers, sample environments and data analysis software, the decision of the strategy of the management of the facility for achieving high performance, establishing the relation between foreign countries in competing way and collaborative way and improving research environment for in-house staff, those all should be well discussed and considered among neutron community to realize JHF, which will be really an important project for continuous development of the neutron science in the next century.

2. Activities at KENS

2.1 Facility Operation

At present, the high-energy pulsed neutrons are produced by the spallation reaction with the proton beam of 500MeV and 6μA, and are moderated by two moderators of the circulating water at ambient temperature and the solid methane at 20 K to the thermal and cold neutrons, respectively. These moderated neutrons are delivered to 17 neutron spectrometers through 11 neutron beam holes in the biological shield (see Fig.2).

In 1997, the construction of new spectrometers (SIRIUS: high-resolution powder diffractometer, TOP: polarized cold-neutron spectrometer, SWAN: small- and wide-angle scattering instrument) was completed and installed in the new cold-neutron experimental hall, which was built in 1996, and the instruments are now open for the use of external users. In 1998, the beam-time of about 70 days is allocated to the neutron scattering facility.

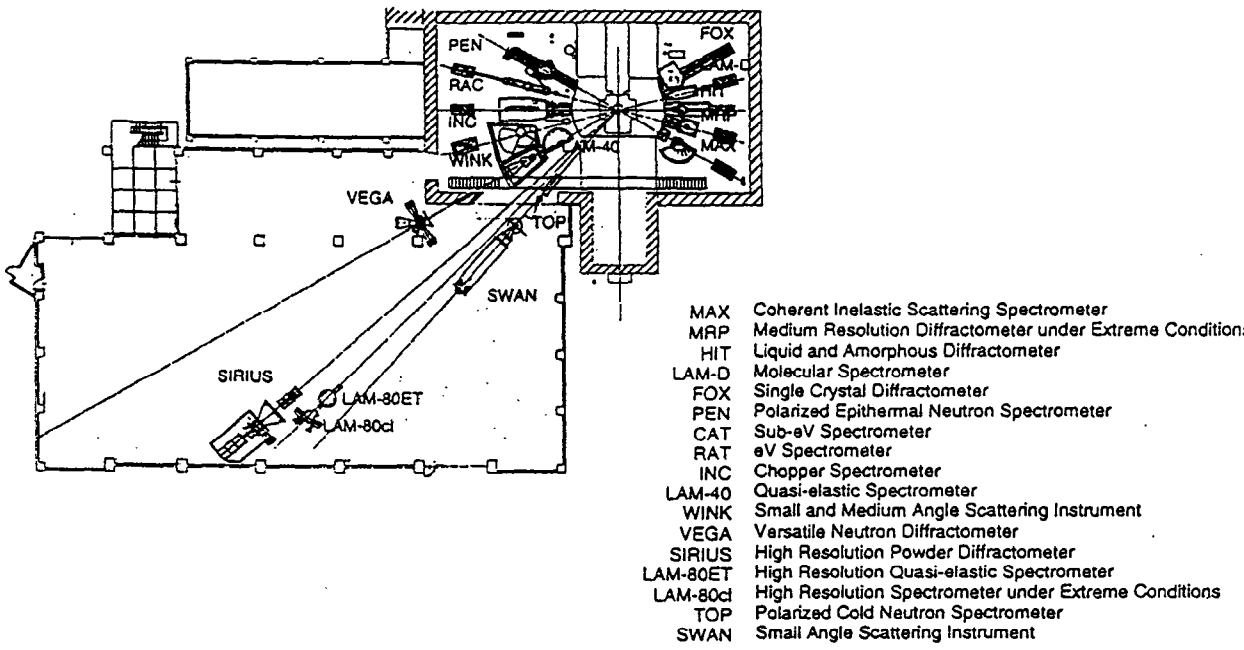

Fig.2 Layout of KENS instruments

2.2 Inter-University Program

99 scientific proposals have been submitted as the Inter-University Research Program at KENS for the year 1998. Among them, 80 proposals were accepted through peer review. About 400 researchers were registered as a radiation worker at KENS. About 60% of proposals are concerned with studies of crystal structure and excitations of materials including liquids and glasses.

2.3 Recent Progress of Scattering Experiments

There are increasing demands for higher resolution neutron powder-diffraction experiments at KENS. In order to satisfy the demands, a new high-resolution powder diffractometer (SIRIUS) was installed in the guide hall. Figure 3 shows a layout of SIRIUS. Because of the pulse width through the solid methane moderator at KENS, a flight path of about 40m is required to achieve a high resolution of $\Delta d/d=1\times10^{-3}$. A long flight path demands the use of a neutron guide tube to avoid a loss of intensity. If natural nickel is used for the coating materials of the guide tube, the intensity is very small at wavelengths shorter than 4Å. In order to gain more intensity at shorter wavelengths on SIRIUS, it was decided to use a guide tube comprising supermirrors with a beam cross section of 4cm × 5cm. In the case of a NiC/Ti-supermirror with a critical angle three-times larger than that of natural nickel, the intensity around 1Å is large. The guide tube started at 5.5m from the moderator, and the total length of the guide tube (28.5m) was chosen to meet the geometrical limitation. A collimator is installed between the end of the guide tube and the diffractometer chamber, and the resolution and intensity can be selected by changing its slit. An overall flight path of 39.5m enables a wavelength window of 5Å, which corresponds to the d-range of 2.5Å. Figure 3 illustrates the layout of SIRIUS with a large backward bank and a 90-degree bank comprising one-dimensional position sensitive detectors (PSD). Each PSD has a diameter of 1.27cm and an effective length of 60cm. The PSD-VME data-acquisition system, which has been developed at KENS, was adopted. The position encoding, data transfer and histograming are carried out by a Macintosh. The calculated ratio of the intensity of SIRIUS to that of

VEGA, the existing powder diffractometer at KENS, has been expected to be almost 15. It was confirmed in a recent experiment. Furthermore, it was found that SIRIUS realized the best resolution of $\Delta d/d=1\times10^{-3}$ by a measurement of the Bragg reflection from a single crystal of silicon.

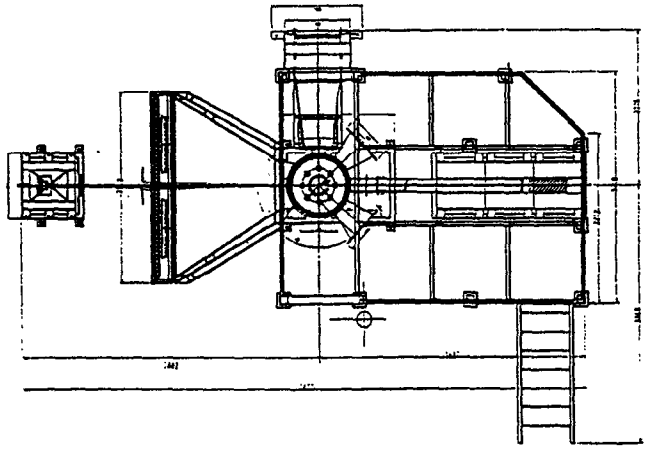

Fig.3 Layout of SIRIUS

SWAN has been designated as a small/wide-angle diffractometer to observe the structural changes in a wide momentum space. Figure 4 shows a layout of the SWAN. The SWAN has 48 3He position-sensitive detectors (PSD) in the small-angle detector bank, 48 conventional 3He detectors in the medium-angle detector bank, and 160 PSDs in the high-angle detector bank. It makes it possible to measure the structure in the very wide momentum transfer range 0.004-20 Å-1. The investigation of both microscopic and semi-macroscopic atomic structures can be performed simultaneously using the SWAN.

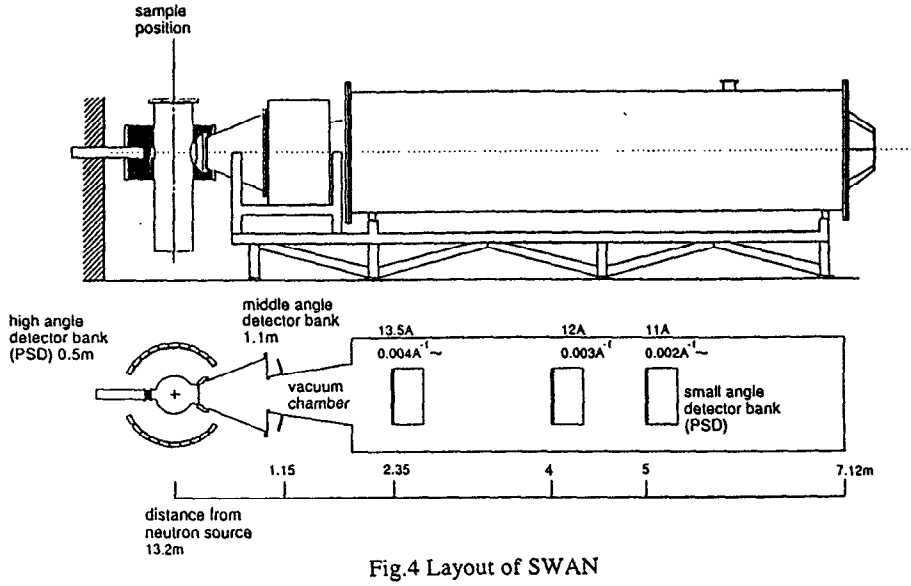

Fig.4 Layout of SWAN

Polarized neutron reflectometer, TOP, has been newly designed for the investigation of surface and interfacial magnetism in magnetic thin films and multilayers. The polarized neutron is much more sensitive to minute magnetic moments than unpolarized one. The advantage makes the polarized neutron reflectometer a very powerful tool for the investigation of such magnetism. Figure shows the reflectivities of a natural Ni mirror which is used for C2 cold neutron guide tube at KENS under a magnetic field of 300 Oe. The interference between reflected beam from the surface and the Ni - substrate interface makes many fringes of reflectivities. The reflectivities depend on the magnitude of magnetic moments of Ni and a relative angle between neutron spin and magnetization of Ni in the mirror. Figure 5 shows the parallel case (solid circles) and the antiparallel case (open circles). From the data Ni in the mirror was revealed to have very small magnetic moments of 0.06 (Bohr magneton / atom) which is only 10% of saturation magnetization. In other words, such small magnetic moments makes very clear difference of the reflectivities. This shows that the

polarized neutron reflectometry is a very promising tools for the investigation of surface and interfacial magnetism.

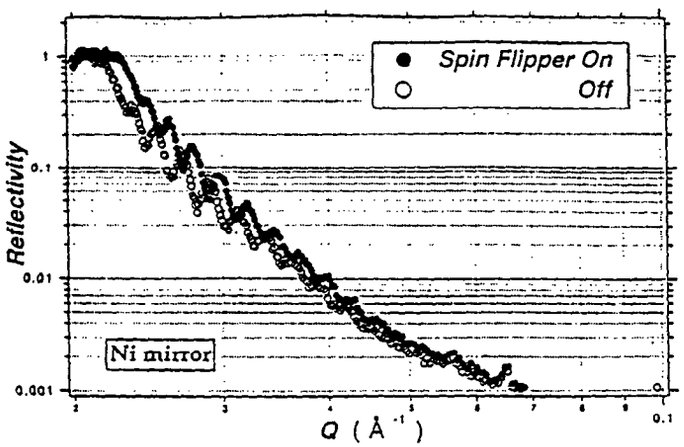

Fig.5 Reflectivities from the Ni mirror

ICANS-XIV
14th Meeting of the International Collaboration on
Advanced Neutron Sources
June 14-19 1998,
Starved Rock Lodge, Utica, Illinois, USA.

PROGRESS AT ISIS

A D Taylor and W G Williams

ISIS Facility, Rutherford Appleton Laboratory, Chilton, Didcot, Oxon, OX11 0QX

ABSTRACT

Recent progress at the ISIS pulsed neutron source is reviewed. Specific developments in instrumentation and source performance are described together with plans for the future development of the facility.

1 Introduction

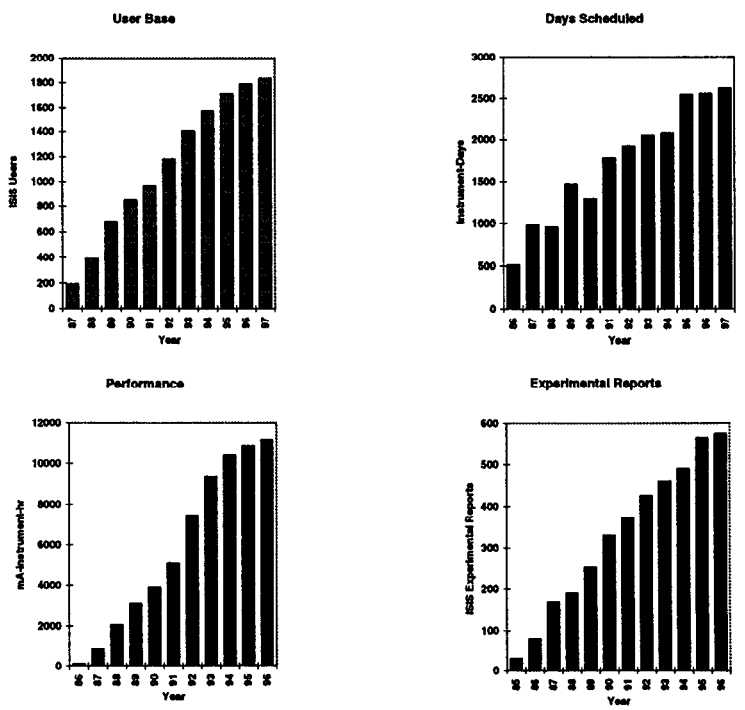

Figure 1. Measures of ISIS performance.

The last few years have seen ISIS continue to grow and develop as the world's most powerful pulsed neutron source. Instrument and source developments enable the facility to be increasingly productive, as indicated by some of the measures shown in figure 1. Investment for new instruments has come from UK research councils and international

partners over and above our normal budget. The main activities at ISIS are directed towards the users' scientific programmes, and the UK user community is rising to the challenge of the new access mechanism, known as the 'tickets' system, introduced by the funding U.K. Research Councils in 1996. Examples of instrument and source upgrades, and prospects for the future expansion of the facility, are described below.

2 Source

The performance of the ISIS accelerator in terms of the average daily current delivered is shown in figure 2. Despite running at low currents at the beginning of 1996 due to accumulated damage to RF screens in the main synchrotron dipoles, the accelerator recovered to produce average daily currents in excess of 200 μA, and the past year has seen the source running with greater than 90% reliability. Replacement of obsolete equipment and development of machine components continue with the aim of improving reliability and performance. Upgrade of the synchrotron diagnostics systems and the use of infrared thermography to locate potential trouble spots are improving source operations, and development continues to replace the Cockcroft-Walton pre-injector with a Radio Frequency Quadrupole to increase the Linac beam current. The tantalum neutron production target continues to give reliable performance after receiving over 4000 Coulombs of proton beam.

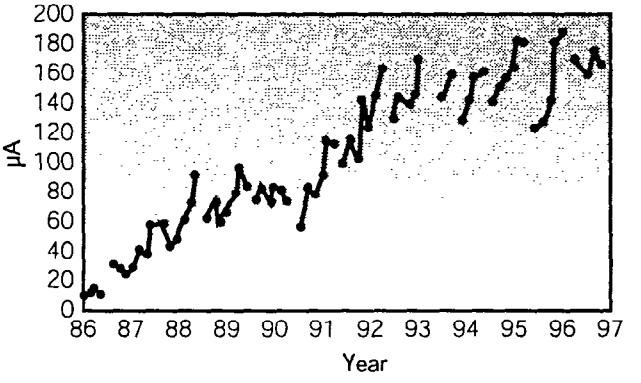

Figure 2. Average daily ISIS current since 1986.

3 Instrumentation Developments

Upgrades and development of ISIS instruments continue apace; the full instrument suite is shown in figure 3. Over the past year, two new spectrometers, OSIRIS and TOSCA, have been commissioned. OSIRIS is optimised for the use of cold neutrons, enabling high-resolution, long wavelength diffraction, high-resolution spectroscopy and polarisation analysis. The significant increase in flux compared with IRIS, produced by novel guide and supermirror designs, will open up the possibility of real-time phase transition studies. TOSCA is a development of the TFXA vibrational spectroscopy instrument. Phase I of this programme, a five-fold increase in the number of detectors, was completed this year with commissioning runs demonstrating the improved detected flux. Resolution improvements will be forthcoming when TOSCA is moved further

from the ISIS target in 2000; a background chopper and second analyser array will be installed at the same time.

The ISIS Pressure and Engineering Advanced Research Line (PEARL) has been significantly developed over the past year. Two dedicated stations are now available to the ISIS user community: HiPr, the High Pressure facility, and ENGIN, the Engineering science facility. Both facilities have seen improvements in terms of sample environment equipment (the ordering of a new Paris-Edinburgh pressure cell for HiPr, and a dedicated stress rig built for ENGIN), as well as improvements to the HiPr detector array. Other instruments have also received significant development: a new location and improved detector complement for POLARIS; a new high-angle detector bank for LOQ; the installation of state-of-the-art supermirrors and spin flippers for reflectometry studies using polarised neutrons on CRISP; and development of a source of slow muons for thin film and surface studies using the muon spin rotation/relaxation technique.

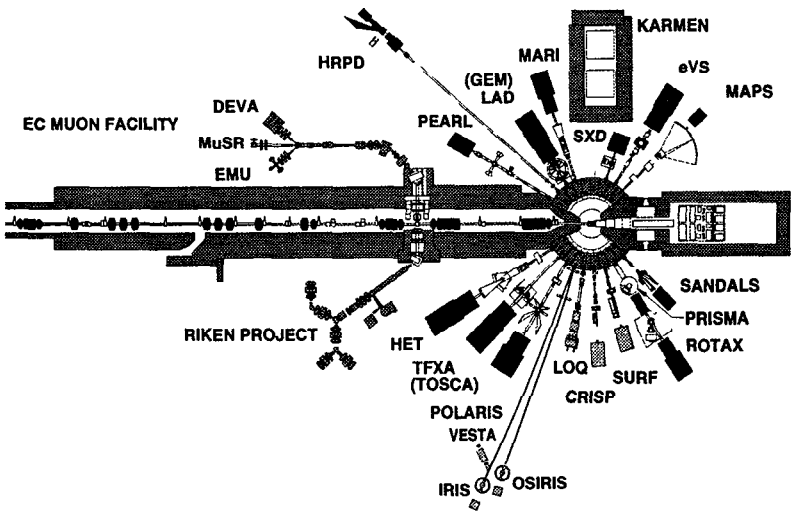

Figure 3. The ISIS instrument suite.

The MAPS spectrometer, optimised for measuring high energy coherent magnetic excitations in single crystals, will be the first ISIS instrument with detectors consisting entirely of position sensitive ^{3}He gas tubes (PSDs), arranged in an array covering an area of over 16m^2. The two huge detector tanks were delivered to ISIS in November 1997, and two PSD modules, based on the MAPS technology, were installed in summer 1997 on HET and are performing extremely well in terms of resolution, efficiency and stability. MAPs is expected to be ready for first neutrons before the end of 1998.

Design and construction of the new General Materials Diffractometer (GEM) continues. GEM will combine a high resolution over a wide Q range with the high count rate required to study samples under varying conditions such as temperature, pressure and chemical reaction. Its special features will include a large detector area, with high detector stability over a large solid angle; prototype detector modules constructed over the past year have achieved both the resolution and stability required. Installation of GEM is expected to be completed by August 1999.

And instrument developments continue into the foreseeable future. Funding was achieved this year for an upgrade to the eVS spectrometer for Neutron Compton Scattering, with realisation of this new instrument, VESUVIO, anticipated for the end of 2001.

4 Science

The range of science at ISIS continues to span Physics, Chemistry, Biology, Engineering, Materials and Earth Science. In-situ and real-time studies of complex systems are developing, whilst fundamental studies of materials with technological potential, for example giant magnetoresistance materials, spin valves, superconductors, polymers and surfactants, molecular materials and ionic conductors, continue. Full descriptions of science at ISIS can be found in the facilities annual reports (ISIS96-98).

5 Future Facility Developments

In addition to the upgrading of individual instruments, plans continue to progress for upgrades to the facility as a whole. The potential exists for an upgrade to the ISIS synchrotron to enable production of 300 μA beam currents, an increase of 50%, by addition of four RF cavities operating at twice the frequency of the existing cavities. The existing target station would require only minimal changes to its shielding and cooling to be made capable of handling the increased current, and the enhanced beam could be available by 2001.

The enhanced 300 μA current would enable pulse sharing of the proton beam to supply a second ISIS target station (figure 4). The addition of new instruments to the ISIS suite now requires the removal of existing instruments as all available ports from the ISIS target are occupied. But new instruments can be envisaged which would significantly improve upon existing instruments, or which would open up entirely new areas of science. The solution to this problem is the development of a second target station, which would be optimised for the production of cold neutron beams for high intensity, high resolution applications. The ISIS proton current would be pulse-shared between the two target stations, with the new station taking, for example, one pulse in five. This lower rate would open up the possibility of using uranium as the target material for the second station, and would enable the use of solid methane at 25K as a moderator. Such an assembly offers the prospect of pulse intensities an order of magnitude greater than that of the existing target station, and would open up opportunities in the fields of biological sciences (pharmaceuticals, membranes, proteins and food science), complex inorganic and organic assemblies such as clathrates, intercalates and zeolites, magnetic materials (systems with small moments, low magnetic exchange or long range structures), and surfaces, interfaces and soft condensed matter including magnetic thin films, polymers, colloids and surfactants. Such developments will provide exciting scientific opportunities in the short term, and will pave the way for the planned third generation European Spallation Source.

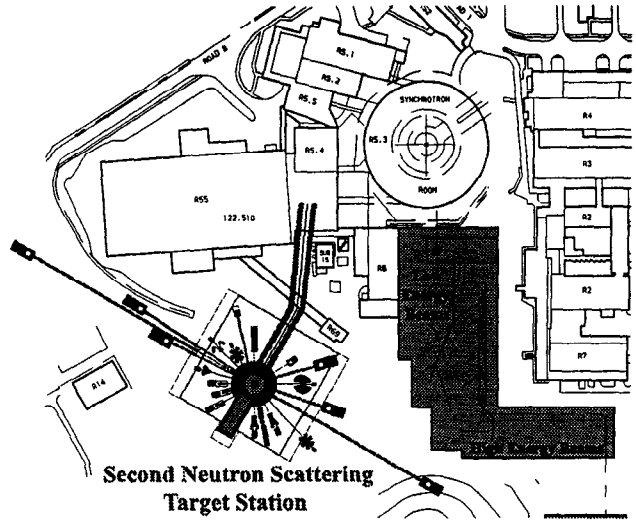

Figure 4. Layout of a second target station and a proposed radioactive beams facility, SIRIUS, at ISIS.

6 ISIS Review

1998 has seen an independent Review of the ISIS facility, chaired by Sir Michael Thompson, former Vice-Chancellor of Birmingham University. The Review was to consider the scientific output, the technical performance of the facility, and the scope for future improvements, and its report was presented to the Council of the CLRC, the U.K. Research Council with responsibility for ISIS, in September 1998. The Review concluded that neutron scattering is an important tool for basic, strategic and applied research; that ISIS has demonstrated the advantages of accelerator-based sources and that future sources are likely to build on the ISIS design; that the construction of a second target station at ISIS is essential and justified, and would ensure ISIS' place as *the* world centre for neutron scattering science; and that the second target station would pave the way for a Third Generation Neutron Source.

ICANS XIV
14th Meeting of the International Collaboration on
Advanced Neutron Sources
June 14-19, 1998
Starved Rock Lodge, Utica, IL

Current Status of JHF N-arena Development

M. Furusaka and H. Ikeda
Neutron Science Laboratory (KENS),
High Energy Accelerator Research Organization (KEK),
Tsukuba-shi 305, Japan

The Japan Hadron Facility Project (JHF) aims to advance the multi-disciplinary research fields, such as materials science, life science, and nuclear and particle physics, by using high intensity beams supplied by a proton accelerator complex. It consists of a 200-MeV linac, a 3-GeV-200 μA-25 Hz booster synchrotron and a 50-GeV-10 μA proton synchrotron. The pulsed spallation neutron source (SNS) facility N-arena is one of the four facilities in the JHF project. It will utilize proton beam from the 3-GeV booster synchrotron (0.6 MW for the first stage, 1.2 MW for the second stage).

For the first stage of the N-arena, a heavy-water cooled solid-metal target made of cladded-tungsten plates will be employed for the upstream part. For the down stream part, we are considering to put a liquid mercury "beam dump" to acquire experiences of handling the mercury system.

To design the solid-target system, we are performing a series of thermal-hydraulic experiments. From critical heat flux experiments we performed so far, we have confidence in making a solid-target system which could be used for the upgraded 1.2 MW source with reasonable performance. Mockup experiment of a water distributor for the target is also carrying out by a flow visualization technique using laser beam. We have only got preliminary results so far, but simple-shaped distributors seems to have enough performance. Continuing efforts to make an optimized distributor is underway.

Production of ^{7}Be and T by spallation process in the cooling water circuit could become a very severe problem. We are now performing test experiments to determine the production rate of both nuclei, deposition-rate and deposition-mechanism of ^{7}Be using the room-temperature water-moderator circuit at the KENS facility.

We are also developing a liquid-metal target system for the second stage of the project. We have done a mockup experiment using water in place of liquid-metal to optimize the flow of the system. Modified U-shaped target model shows consistent flow without any vertexes.

We have been carrying out extensive neutronic calculations as well as experiments using the Hokkaido university electron linac. From the results, we decided to have two liquid-hydrogen moderators with a premoderator, one coupled and one decoupled. Liquid-methane moderator is indispensable for high-resolution experiments, but it is well known from its radiation damage problems. Since no good substitution is found so far, we are trying to improve the life-time of the moderator. We are trying to evaluate the effect of putting a heavy-water premoderator for the reduction of damage. There are several other possibilities to reduce the damage, but if that fails, decoupled liquid-hydrogen moderator would be the only solution. For the reflector, lead seems to have better performance for decoupled moderators and beryllium for coupled one.

ICANS XIV
14th Meeting of the International Collaboration on
Advanced Neutron Sources
June 14-19, 1998
Starved Rock Lodge, Utica, IL

BNL Activities in Advanced Neutron Source Development: Past and Present

J.B. Hastings, H. Ludewig, P. Montanez, M. Todosow, G. C. Smith, and J.Z. Larese
Brookhaven National Laboratory

Introduction

Brookhaven National Laboratory has been involved in advanced neutron sources almost from its inception in 1947. These efforts have mainly focused on steady state reactors beginning with the construction of the first research reactor for neutron beams, the Brookhaven Graphite Research Reactor. This was followed by the High Flux Beam Reactor that has served as the design standard for all the subsequent high flux reactors constructed worldwide. In parallel with the reactor developments BNL has focused on the construction and use of high energy proton accelerators. The first machine to operate over 1 GeV in the world was the Cosmotron. The machine that followed this, the AGS, is still operating and is the highest intensity proton machine in the world and has nucleated an international collaboration investigating liquid metal targets for next generation pulsed spallation sources. Early work using the Cosmotron focused on spallation product studies for both light and heavy elements into the several GeV proton energy region. These original studies are still important today.

In the sections below we discuss the facilities and activities at BNL focused on advanced neutron sources. BNL is involved in the proton source for the Spallation Neutron source, spectrometer development at LANSCE, target studies using the AGS and state-of-the-art neutron detector development.

Proton sources

BNL has a long and internationally recognized involvement in high intensity proton sources. The AGS which presently operates mainly for high energy physics can provide single pulse energies approaching those of the most intense spallation neutron sources that are now being planned. BNL is also specifically responsible for the compressor ring construction for the Spallation Neutron Source (SNS) at Oak Ridge TN.

The proton beam intensity in the AGS has increased steadily over the 35 year existence of the AGS, but the most dramatic increase occurred over the last few years with the addition of the new AGS Booster. The AGS Booster has one quarter the circumference of the AGS and therefore allows four Booster beam pulses to be stacked in the AGS at an injection energy of 1.5 GeV. At this energy, space charge forces are much reduced and this in turn allowed for the dramatic increase in the AGS beam intensity.

The beam intensity in the Booster has surpassed the design goal of 1.5×10^{13} protons per pulse and has already reached a peak value of 2.2×10^{13} protons per pulse. The AGS itself also had to be upgraded extensively to be able to cope with the higher beam intensity. The peak beam intensity reached at the AGS extraction energy of 24 GeV is 6.3 10^{13} protons per pulse, also exceeding the design goal for this latest round of intensity upgrades. This represents a world record beam intensity for a proton synchrotron. This level of performance was reached quite consistently during the last AGS experimental run of 24 weeks during which more than 10^{20} protons were accelerated in the AGS to 24 GeV.

This performance is ideally matched to the R&D needs of the neutron spallation source community for high power targets for the next generation sources. To take advantage of this an international collaboration was formed. The partners include

Forschungzentrum Jülich and Paul Scherrer Institut with interests directed toward the European Spallation Source, the Japan Atomic Energy Research Institute (JAERI) with a proposal for a 5 MW short pulse source and Oak Ridge National Laboratory and Brookhaven National Laboratory who are partners in the SNS to be located in Oak Ridge, TN.

The AGS Spallation Target Experiment (ASTE) has made preliminary measurements of neutron production, power deposition and pressure wave phenomena on a mercury target in the summer of 1997. Initial results of these efforts are reported at ICANS XIV by the various participants.

Spectrometer development

The Department of Energy is investing in upgrades at LANSCE in both the source and instrumentation. As a part of the instrumentation upgrade several Spectrometer Development Teams have formed to provide new instrumentation. J. Z. Larese, BNL Chemistry, is leading an SDT for a crystal backscattering spectrometer (CBS) to be built at BNL and installed at LANSCE.

There is a need in the United States for a state-of-the-art, cold-neutron CBS designed to investigate the structure and dynamics of condensed matter systems by the simultaneous utilization of long wavelength elastic diffraction and high-energy-resolution inelastic scattering. Cold neutron spectroscopy with CBS-type instruments has already made many important contributions to the study of atomic and molecular diffusion in biomaterials, polymers, semiconductors, liquid crystals, superionic conductors and the like. Such instruments have also been invaluable for ultra high resolution investigations of the low-lying quantum tunneling processes that provide direct insight into the dynamical response of solids at the lowest energies. Until relatively recently, however, all such instruments were located at steady-state reactors. This proposal describes HERMES I (High Energy Resolution Machines I) a CBS intended for installation at the LANSCE pulsed neutron facility of Los Alamos National Laboratory

The need for such an instrument was originally demonstrated by the success of the IRIS CBS at the ISIS pulsed neutron facility of the Rutherford Appleton Laboratory which made it clear that pulsed neutron and steady-state sources are equally effective for cold neutron spectroscopy. Intended originally as a quasielastic spectrometer for the study of diffusional motions, IRIS has had a major impact on the field of low energy inelastic spectroscopy as well by combining high resolution with a wide-enough energy transfer range to permit access to very-low-lying excitations in ground-state systems. (This Q,ω range is not accessible in equivalent, direct-geometry instruments because the energy transfer range is coupled to the incident neutron energy.) In fact so heavy is the demand for IRIS (it is currently oversubscribed by more than a factor of five) that only a few days per year are available to investigate new possible applications.

Including a white beam diffraction detector in a CBS adds to such instruments the capability of simultaneous diffraction and inelastic spectroscopy, thus - as recently demonstrated by experiments on IRIS - further enhancing their utility. And because IRIS-type instruments use neutrons with wavelengths as long as 25 Å, they have the attractive feature of extending the range of diffraction studies to long range magnetic periodicities and other types of large-scale structural ordering.

We propose to construct an updated, high-performance CBS which incorporates neutron techniques developed during the decade since IRIS was built, i.e. improved supermirror technology, a larger area crystal analyzer and high efficiency wire gas detectors. The

instrument is designed in such a way as to be readily adaptable to future upgrades. HERMES I, we believe, will substantially expand the range and flexibility of neutron investigations in the United States and open new and potentially fruitful directions for condensed matter exploration. This document describes a implementation plan with a direct cost range between $4.5 to 5.6 M and scheduled duration of 39-45 months for identified alternatives.

Position sensitive thermal neutron detectors

Detector development for thermal neutron scattering experiments in the study of biological structures has been underway for some years at Brookhaven. The technology of choice has been the gas proportional detector, with ^{3}He as the neutron absorbing gas, because of several beneficial factors. These detectors offer superior efficiency to that of almost all other detectors, their maximum counting rate capability is adequate for that required in most reactor and spallation source applications, they can be built in a wide range of sizes, they are very insensitive to gamma radiation with appropriate choice of gas mixture, and their position stability is better than most other detectors. In single neutron counting mode, they offer infinite dynamic range for static experiments, while also offering the capability of performing dynamic studies with time frames below one second.

The reaction $^3He + n \rightarrow {}^3H + p + 0.764$ MeV represents the process by which neutrons interact with a helium three atom. The ionization centroid of the tracks of the two resultant particles is displaced from the interaction position because the proton is more heavily ionizing than the triton, and has a longer range. To a first approximation the FWHM position resolution is 0.8 times the proton range [1] and a quench gas such as propane is added the the helium in order to provide stopping power for the proton and triton. A resolution of about 1.5 mm FWHM can be achieved with 2.5 atm propane, a standard operating parameter in detectors with an active area of 20cm by 20cm. Combined with 4 or 5 atm ^{3}He, this results in a high resolution, high efficency detector which, with a suitable gas purification and circulating system [2], can operate for some years with no servicing. Other detectors of the same type that we have built are ones with a sensitive area of 50cm by 50cm, and one with 5cm by 5cm. The latter, because it is compact, can maintain a very high pressure. The propane in this device has a pressure of 6atm and the detector yields a resolution of less than 400 microns FWHM [3], the best resolution for a gas based neutron detector ever recorded.

Position information is obtained from the cross-wire cathodes that sandwich the anode plane. A readout has been developed in which the center of gravity of the induced cathode charge from a single event is determined from charge division between two, or at most three, closely spaced nodes [4]. Each cathode comprises about 20 nodes, providing a continuously sensitive readout, and permitting low readout noise with only a modest avalanche size, which is essential to the for the longevity of the detector.

A useful summary of operating characteristics of gas filled proportional chambers for thermal neutron detectors is given in table 1. It should be noted that not all the properties listed can necessarily be achieved in one detector at the same time. A set of detectors has been designed and fabricated which provide high resolution, stable, and reliable performance to a range of structural biology experiments. In this ongoing program, new devices and techniques are under development; for example, methods to minimize parallax errors in planar detectors for small angle experiments are being investigated, and large, curved detectors for crystallography experiments are being studied. Finally, it should be emphasized that the proportional detectors described here have one important advantage over competing devices such as image plates and phosphor/CCDs: the proportional detector, with sub-microsecond timing resolution, is the only device from

these three with adequate timing resolution for white beam experiments at spallation sources.

Table 1: Performance Figures

Position Resolution (FWHM)	<0.4 - 2 mm
Number of Resolution Elements	from 128×128 to 1024×1024
Size	from 5×5 cm^2 to 50×50 cm^2
Wavelength Range	1 - 20 Å
Detection Efficiency	50 - 80 %
Counting Rate (total)	10^5 - 5×10^5 sec^{-1} (single readout)
Counting Rate (single peak)	5×10^4 sec^{-1}
Integral non-linearity	2×10^{-4} to 10^{-3}
Absolute Position Accuracy	30-100 μm
Stability of Origin	<50 μm
Stability of Response (efficiency)	<1%
Differential non-linearity	±3%
Dynamic Range	Single Neutron Detection
Timing Resolution	~ 1 μs

References:

1. Fischer, J., Radeka, V. and Boie, R.A., 1983, High Position Resolution and Accuracy in He^3 Two-dimensional Thermal Neutron Detectors. *Workshop on The Position-Sensitive Detection of Thermal Neutrons, ILL, Grenoble, France 11-12 October 1982. Proceedings edited by P. Convert and J.B. Forsyth (Academic Press, London)*, p129.

2. Boie, R.A., et al., 1982, Two-Dimensional High Precision Thermal Neutron Detectors, *Nucl. Instrum. & Meth.* 200: 533-545.

3. Radeka, V., Schaknowski, N.A., Smith, G.C. and Yu, B. 1996, High Precision Thermal Neutron Detectors. In "Neutrons in Biology", ed B.P. Schoenborn and R.B. Knott, Plenum Press, 1996, 57-67.

4. Radeka, V. and Boie, R.A., 1980, Centroid Finding Method for Position-Sensitive Detectors, *Nucl. Instrum. & Meth.* 178: 543-554.

ICANS-XIV
14th Meeting of the International Collaboration on Advanced Neutron Sources
June 14-19, 1998
Starved Rock Lodge, Utica Ill., USA

AUSTRON Progress Report*

E. Jericha[1], H. Rauch[2], M. Regler[3], H. Weber[4]

[1]AUSTRON Koordinationsbüro, Atominstitut, Stadionallee 2, A-1020 Wien, Austria
[2]Atominstitut der Österreichischen Universitäten, Stadionallee 2, A-1020 Wien, Austria
[3]Institut für Hochenergiephysik, Nikolsdorferg. 18, A-1050 Wien, Austria
[4]AUSTRON Projektleitung, Wirtschaftskammer Österreich, Wiedner Hauptstr. 63, A-1045 Wien, Austria

* The paper was presented on behalf of the authors by
G. S.. Bauer, Paul Scherrer Institut, CH-5232 Villigen PSI, Switzerland,.

Abstract

The present status of the AUSTRON project is discussed. Updates are given on the AUSTRON accelerator and target design. A preliminary list of instruments under present discussion is introduced.

1. Background

AUSTRON is the project of a pulsed spallation source, which is foreseen to be built in Austria. At the last ICANS - Meeting a report [1] was given on the successful finalisation of a Feasibility Study [2]. We would now like to report on the progress of the project.

Two major events have added new elements to the project:
In 1996 a Med-AUSTRON Office was created. The city of Wiener Neustadt and the Bundesland Lower Austria are financing since then the elaboration of a Feasibility Study covering the Medical Part of AUSTRON. The Study will be finalised in early fall this year and describes a medical synchrotron aiming at proton and light ion (C) cancer therapy and research. The facility is planned as a stand alone project, which in case of being built at the same site and at the same time as AUSTRON will benefit from considerable

Keywords: AUSTRON, solid target, Rapid cycling synchrotron, Tungsten-Rhenium, Instruments, Instrument environment

synergies. The preliminary cost estimate for the Med-AUSTRON project sums up to some 800 million shillings (65 mill $). The light ions have a maximum nominal intensity of $5x10^8$ ions/fill (C) in case of single turn injection and a maximum nominal energy of 400 MeV/nucleon. Med-AUSTRON will be the world's best medical synchrotron enabling the cancer scientists and researchers to compare results of protons and ions under the same conditions.

The second important move was to present the AUSTRON Feasibility Study to the European Science Foundation (ESF) located in Strasbourg late 1996. In October 1997 the ESF returned its Assessment to the Austrian Ministry of Science and acknowledged the technical feasibility of the Study. The Austrian Minister of Science supported the idea to install a project group to enlighten the recommendations of the ESF until early September 1998. Based on the fact the Austrian government is prepared to finance up to a third of the total investment (400 mill $) transnational partners will have to co-finance the facility.

In their summary the ESF - Panel came forward essentially with the following assessment of the AUSTRON project:

* The AUSTRON feasibility study is recognised to be aiming at a high-performance research facility of medium to large scale that could serve science and research with high impact and satisfactory value.

* The R&TD fields served by neutron sources are, and will be in the long term, of high actuality and importance for fundamental and applied research in Europe.

* The users' clientele in the catchment area targeted by AUSTRON is large enough (some 940 users), and the facility's projected size in general appears to be adequate.

* The technical feasibility of the AUSTRON study is acknowledged, but a new cost analysis is needed to update the recommended 0.5 MW facility.

* The policy value and impact which a central facility of excellence like AUSTRON would have for the region and Austria is acknowledged.

According to the recommendations of the ESF the following chapters are elaborated by the AUSTRON - Project - Group (H. Rauch, M. Regler, P. Skalicky, H. Weber):

The positioning of AUSTRON in the landscape of other available neutron sources in Europe (ILL, ISIS, FRM2, SINQ, HMI, BNC).

The development of an instrumentation plan offering the possibility of unique experiments at AUSTRON.

Finalisation of the envisaged accelerator concept, leading to a spallation source of up to 0.5 MW at a pulse rate of 50 Hz. Thus AUSTRON will offer a neutron flux at the world-

wide highest level of a pulsed source before the European Spallation Source (ESS) presently under discussion would go into operation.

Since the AUSTRON project is aiming at a new and additional neutron source for transnational use in the context of the existing and future neutron facilities, and as the Austrian parties are aiming at a substantial financial inflow from the targeted transnational region, a diplomatic mission to confirm collaborations with partners is planned in fall 1998. The specific value of the projected AUSTRON facility and its specific features of merit within its regional context are the crucial issues which would be decisive for the projected transnational use.

2. Accelerator

A prominent feature of the AUSTRON project is the well-founded accelerator concept [3]. AUSTRON's power substantially exceeds that of the present world-leading facility. Based on custom-tailored solutions in known technologies, it could be built relatively quickly and with a ratio of cost to scientific and technological potential that is very favorable. Its design has been performed by the AUSTRON accelerator team hosted by CERN, under the leadership of P. Bryant.

With respect to the European Spallation Source (ESS), AUSTRON should be regarded as a second, and ESS as a third, generation facility that will be separated by a decade in time and an order of magnitude in beam power.

In the AUSTRON accelerator complex, the particles are accelerated through a series of accelerators of different types that are adapted to the changing energy and intensity. First, negative hydrogen ions (H-) are accelerated in a radio frequency quadrupole (RFQ), followed by a drift tube linac (DTL) which raises the energy to 130 MeV before injection into the rapid cycling synchrotron (RCS). The RCS is a strong focussing separate-function accelerator of 213 m circumference with a double pulse structure (h=2) that is capable of being cycled at 25 Hz (AUSTRON II) and 50 Hz (AUSTRON III, the final choice for AUSTRON). At injection into the RCS, the H- ions are stripped of their electrons by a thin foil (charge exchange injection, allowing a very high-intensity proton beam to be accumulated). After trapping, the proton bunches are accelerated to 1.6 GeV and ejected onto a spallation target, with 200–250 kW and 400-500 kW, respectively. In both cases an energy of about 10 kJ per pulse impinges on the spallation target.

A possible upgrade could be the addition of a storage ring, working as a bunch accumulator, in order to deposit 40-50 kJ with a frequency of 10 or 12.5 Hz on the target. This would, however, require a new RF design in order to operate the RCS at h = 1, a decision which will be taken right from the beginning.

3. Target

In the present concept of the target design a flat target geometry is proposed [1,4]. The target material under consideration is solid W-5%Re according to its excellent thermal and mechanical properties [4]. Dimensions of a target block are 10 x 30 x 60 cm^3 (Heigth x Width x Length) where, due to the edge-cooling concept, cooling channels are only installed within 2 cm from the top and bottom surface. Since the beam power on target was taken to be 250 kW (version AUSTRON II) for the initial target design and for material tests on W-5%Re a target group, coordinated by T. Schmeskal, Austria Research Centre Seibersdorf, has been nominated to clarify the impact of a 0.5 MW beam on a target of the proposed design.

Calculations of the temperature distribution in the target, based on the standard AUSTRON III conditions with source repetition rate 50 Hz, yield a temperature maximum of about 1250 °C. Cooling of a target under these conditions is possible within the edge-cooling concept and an improved cooling system has been designed for this task. Material properties of W-5%Re like ductility, thermal conductivity or self-healing after irradiation damage look favorable for the temperature range of AUSTRON III. However, to obtain reliable data about the properties of W-5%Re under the combined effects of high temperature and high irradiation, further test series will be necessary for the final target design. From the present point of view, metallurgy as well as cooling technology, a 50 Hz/0.5 MW solid W-5%Re target seems feasible.

The final target design will be mainly influenced by the actual neutron instrumentation set for AUSTRON. Even if a 50Hz/0.5 MW solid target is feasible it might be preferable to make the AUSTRON target of two target blocks situated above each other [1]. Moderators can be placed between the two target blocks or above the upper and below the lower block. At 50 Hz operation of the accelerator both target blocks can be operated alternately at 25 Hz or one at 12.5 Hz or 10 Hz and the other at 50 Hz with every fourth or fifth pulse missing. With one target block acting as an effective decoupler from the neutron flux of the other, the upper and lower moderators would eventually represent 50, 25, 12.5 or 10 Hz sources while the moderators in the middle would operate at 50 Hz always. The double target block design offers good flexibility for neutron instrumentation and reduced radiation and thermal load for a single target block. Cold moderators will be needed to fulfil the needs of most instruments.

The final decision on the target design will be made in agreement with the instrument development and after neutron flux calculations for the respective moderator configurations which will take place in the AUSTRON design phase immediately after approval of the AUSTRON project.

4. Instrumentation

The AUSTRON instrumentation is one of the chapters to be elaborated according to the ESF assessment. In a workshop held in Wien, May 1998, a preliminary list of instruments was compiled with the idea of a well-balanced set of instruments comprising state-of-the-art instrument design following concepts already exploited with tremendous success at pulsed neutron sources and new instrument ideas with concepts not yet transferred to actual instrument design. From the first point of view, instruments will gain by sheer increase of neutron flux compared to instruments at existing sources and by using state-of-the-art instrument components, especially advanced detector systems. The second point of view underlines the innovative aspect of instrument development at AUSTRON, also with respect to the instrumentation for future generation sources, like ESS.

With the proposals for the AUSTRON instrumentation it is also tried to find a balance in scientific coverage of the research fields which are expected to be served at a source like AUSTRON. A set of 18 instruments has been proposed and associated with the chapters of the report on scientific prospects for future neutron sources [5]. To each topic, a couple of representative instruments from the AUSTRON instrument list is assigned. This assignment is, of course, by no means exclusive and most of the instruments will find use in the fields of almost all cited subjects.

Clean room conditions and vibration isolated areas will cover about one quarter of the experimental hall. Neutron optics instruments, reflectometers and in-situ crystal growth inspection spectrometers will gain most from these advanced environmental conditions. In the field of neutron quantum optics a novel neutron optics research station is proposed under special environmental conditions. A neutron optics development beam line, e.g. for the development of an NMR guide tube resonator for travelling magnetic wave focusing is added. Within a perfect crystal resonator system a stationary flux equivalent to the peak flux of the pulsed source can be produced which can be used for advanced beam tailoring devices.

With the, now for neutron studies, traditional area of magnetism and superconductivity in condensed matter research we associated a chopper spectrometer for magnetic excitations and vibrational spectroscopy (with respectively extensive low and wide angle detector banks) and the development project of an instrument for spin-polarized neutron specular reflection (for model independent determination of layer and interface structures; to be situated in the specially controlled environment area).

For science on liquids and amorphous materials we propose a dedicated diffractometer with emphasis on low- and small-angle scattering but also sufficient high angle coverage and the development of a spin echo small-angle neutron scattering instrument.

An important instrument for polymers and soft matter research is a general purpose reflectometer (with flexible position and orientation of the sample and extensive sample environment; also located in the environmentally controled area). For soft matter

dynamics, a neutron spin echo spectrometer project, emphasizing its use on a pulsed source, is under discussion.

For biological studies, a general purpose small-angle instrument (optimised for pulsed source operation) is of general importance. Also assigned to this topic is a high resolution crystal analyzer spectrometer with an option for long d-spacing diffraction suited for large volume unit cells.

With the studies of new materials (especially, regarding their structural properties) in materials science we associated a general materials diffractometer (with large detector coverage and various possibilities for extreme sample environment conditions) and a general purpose single crystal diffractometer (also suited for large unit cell structures).

For dynamical studies in the area of chemical reactions, catalysis and electrochemistry we added a dedicated crystal analyzer molecular spectrometer (with large analyzer and detector area) and a multi-chopper TOF spectrometer with variable energy resolution.

In the upcoming fields, regarding neutron sources, of earth science and engineering a high resolution diffractometer (a flexible set-up to measure also textures, internal residual stress and phase analysis; which includes also a variety of extreme sample environment) and a radiography/tomography facility (exploiting the technique of time-gated energy selection) are listed.

Underlining the aspect of developing new instrumentation at AUSTRON, a phase-space transformation instrument project (aiming at high resolution spectroscopy studies) and a general development beam line (with various beam formation, manipulation and detection possibilities) are included in the AUSTRON instrumentation proposal.

This list of instruments is by all means preliminary. Scientific and technical goals and parameters for the AUSTRON instrumentation are worked out at present. Technical details and evaluation of performance and resolution by Monte Carlo techniques will be part of the above-mentioned AUSTRON design phase. All instruments are chosen due to their special performance on a pulsed neutron source, and there is yet no preference for an initial set of instruments.

5. Conclusion

The AUSTRON project represents now a short pulsed neutron spallation source with 0.5 MW design beam power. Two target configurations seem feasible for the initial target station. A second target station is planned as an option when the number of instruments is accordingly increased. Upgrading to a 1 MW spallation source is possible. A number of instruments has been defined for AUSTRON from which the initial set of instruments will be selected.

Acknowledgement

The support from the Austrian Ministry for Science and Transport for continuation of the AUSTRON project is gratefully acknowledged. The interest and support for the AUSTRON project from PSI is also acknowledged.

References

[1] M. Schuster, P.J. Bryant, ICANS-XIII, PSI-Proc. 95-02, Villigen (1995), p. 831

[2] P.J. Bryant, M. Regler, M. Schuster eds., AUSTRON Feasibilty Study, Wien (1994)

[3] P.J. Bryant, M. Schuster, M. Regler, Physica B 234-236 (1997) 1220

[4] M. Schuster, I. Smid, G. Leichtfried, Physica B 234-236 (1997) 1224

[5] ESF Framework Studies into Large Research Facilities, Scientific prospects for neutron scattering with present and future sources, Autrans (1996)

SPECIAL TOPICS PRESENTATIONS

ICANS-XIV
14th Meeting of the International Collaboration on
Advanced Neutron Sources
June 14-19, 1998
Starved Rock Lodge, Utica, Illinois, USA

Front End and Linac Developments for the Spallation Neutron Source*

Jose R. Alonso, for the SNS Collaboration
Oak Ridge National Laboratory
SNS – 104 Union Valley Road
Oak Ridge, TN 37831-8218

1. ABSTRACT

The Spallation Neutron Source (SNS) at the Oak Ridge National Laboratory will be the world-leading accelerator-based neutron-scattering research facility when it comes on line at the end of 2005 [1]. By providing 1-MW of beam power on a heavy-metal target in short (<1 μs) bursts of 1-GeV protons, intense neutron beams will be available at flux levels at least a factor of five over presently-operating spallation sources. This paper will address the requirements driving accelerator parameters for the SNS, and will discuss how the SNS design meets these requirements. As the ultimate power level for the SNS is expected to be significantly higher than 1 MW, the roadmap for achieving these higher powers and increased flexibility for users will also be addressed.

2. REQUIREMENTS

The chief advantage of accelerator-generated neutrons over those from a reactor is the ability to generate sharp "start" pulses of neutrons, to characterize velocity (hence wavelength) of the neutron by pure time-of-flight from the arrival of the proton pulse on the target. Parameters that need to be explored to set the baseline for accelerator performance are: efficiency of neutron production (conversion of proton beam power into neutron flux), the time-length of the proton pulse (how much contribution to the uncertainty in the "start" pulse can come from the accelerator pulse), and repetition rate.

2.1 Neutron Yield

The flux of neutrons emanating from the target depends on proton beam energy, total power deposited on the target, and the target material itself. As to the latter, common wisdom calls for a heavy metal, with the highest possible nuclear density commensurate with the ability to absorb the heat and radiation damage from intense proton bombardment. As is well know, these considerations have driven the SNS team to select liquid mercury as their target material [1]; this matter is discussed at substantial length in other parts of these proceedings.

A rather straightforward [2] relationship for neutron yield exists between beam energy and total power, as shown in Figure 1. The curve in this figure represents neutron yield versus beam energy, for a constant beam power. The curve shows neutron yields as being approximately equal for a 1 MW beam that could consist of, for instance, a 1 mA average beam current at 1 GeV, or a 0.5 mA, 2 GeV beam. As is seen, the curve is fairly flat, with an optimum range between 1 and 3 GeV. (For purposes of normalizing the curve, approximately 26 neutrons are produced per proton at 1 GeV on a

* This work is supported by the Director, Office of Science, Office of Basic Energy Sciences, of the US Department of Energy under Contract No. DE-AC05-96OR22464

mercury target.) Optimizing the choice of proton beam energy for the SNS is driven by cost and technology factors: the SNS team has selected a full-energy linac and an accumulator ring (AR) as the proton generator; cost optimization for this scenario drives design to a lower-energy, higher-current configuration. Were one to select a shorter linac and a rapid-cycling synchrotron (RCS) to accelerate the beam during each storage cycle, the better cost-performance tradeoff would occur for higher energies and lower currents. From the standpoint of neutron production alone, either configuration would be equally satisfactory. However, the SNS team strongly endorses the full-energy linac option in that it provides a better platform on which to build for higher powers, and although initially about 10-15% more costly than the RCS option, provides much lower technical risk towards achieving a reliable, user-friendly facility.

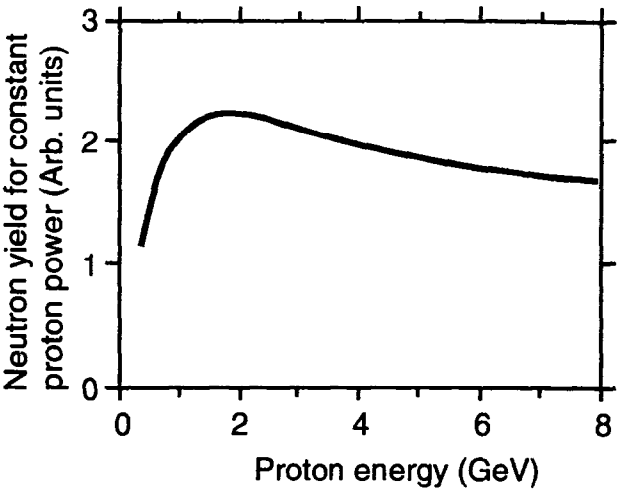

Figure 1. Neutron yield as a function of proton energy, for constant proton power deposition on target.

2.2 Timing Considerations

The sharpness of the "start" signal for the time-of-flight (TOF) measurement is dominated by the characteristics of the slow neutron pulse emerging from the moderators towards the measurement instruments. Although somewhere in the order of 10^9 reduction in neutron energy must be accomplished in the moderator (from MeV to meV), this takes place in a surprisingly small number of collisions, and a very small time period. Figure 2 shows calculations [3] for the full-width at half-maximum (listed as "W") of the neutron pulse emerging from an ambient (room-temperature) water moderator, assuming all neutrons entered the moderator at exactly the same time. The width of this pulse is thus a measure of the sharpness to which the neutron time-of-flight can be determined. While the sharpness of the pulse can be affected by coupling and poisoning the moderator (almost invariably a sharper pulse can be obtained at the expense of flux), natural widths for neutrons in the milli-electron volt range are in the tens-of-microseconds range. If an accelerator pulse were to be of the order of one microsecond, there would be very little contribution to the time-jitter from the width of the proton pulse on the target. It is not until one looks for neutrons at energies greater than a few 100 meV (e.g. a non-thermalized cut) that a 1 μs proton pulse might contribute to time uncertainty. Note that widths for cryogenic moderators are even larger, so again a 1 μs proton pulse contributes almost insignificantly to the time uncertainty for thermally-equilibrated neutrons from these moderators. General consensus is that a specification for proton beam width of "less than 1 μs" is appropriate. By a happy chance of nature, 1 μs is close to the revolution period of beam in an appropriately-sized 1 GeV accumulator ring, making this particular timing requirement on the beam a straightforward one to meet.

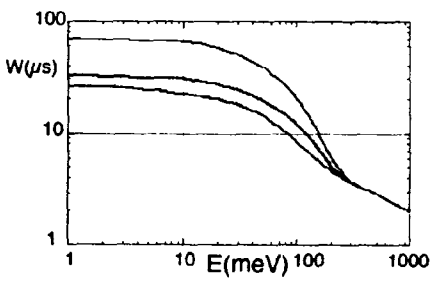

Figure 2. Time widths W (FWHM) of neutrons emerging from an example of a room-temperature water moderator, for (top-to-bottom) coupled, decoupled and decoupled-poisoned conditions.

An interesting constraint arises when considering the design of the overall timing system for

the accelerator. The expected scenario for the SNS' pulse-repetition rate (discussed in the following section) will be a multiple or subharmonic of 60 Hz. Efficient operation of the accelerator power systems indicate it best to synchronize the pulses with the AC line frequency, triggering off of a zero-crossing of one of the AC line phases. For most experimental conditions this is quite satisfactory; a beam-current transformer located in the beamline just upstream of the target produces a signal when the proton pulse passes through it on its way to the target, providing a clean "start" trigger for the TOF measurement. However, for instruments measuring inelastic scattering, where an initial neutron velocity determination is made by measuring the time between the beam arriving on target and the opening of a Fermi chopper window close to the sample, phase errors between the Fermi chopper and the AC line can produce potentially-unacceptable variations in the beam velocity measurement. This is likely to occur since variations in both long-term, and pulse-to-pulse reproducibility of both chopper revolution frequency and a typical AC line trigger can be many times greater than the acceptable accuracy limits. Achieving needed timing accuracy then suggests that the master accelerator timing signal for the accelerator beam be derived from the most critical (if there are more than one in operation) Fermi chopper. A sophisticated chopper drive system is required to ensure that all operating choppers run as closely as possible to the same revolution phase, and that this phase closely tracks variations in the AC line. Rotation frequency of the choppers must be adjusted at a slew rate commensurate with the inertia and drive-system capabilities of these choppers.

2.3 Pulse Repetition Rate

The best repetition rate for proton pulses is closely connected to the type of measurements to be made, to the velocity and flight-path-length of the neutron beams, and to the requirement for total neutron flux from the target. For the accumulator ring concept, total proton beam-power in a single pulse is a very steep function of dollars. For instance, the SNS design calls for 17 kJ of energy to be delivered in a single pulse, and while delivering less than this is relatively easy to do, any increase over the 17 kJ limit would require very significant and quite costly design modifications to the accelerator system. The result of this is that a (1 GeV) 1 MW facility based on 17 kJ pulses at a 60 Hz rate is a very different animal from a (1 GeV) 1 MW system running at 30 Hz that would require 34 kJ pulses. While it would be very easy to run the SNS accelerator complex at 30 Hz, the total power delivered would only be 500 kW. The initial capital investment is driven primarily by the power in each pulse, increasing the number of pulses comes at only a modest cost. Not to say that one would wish to run at 120 Hz, but it does imply that achieving the highest possible overall facility power for the lowest cost is achieved by designing for the highest practical repetition rate.

The design decision then to run the SNS at 60 Hz is based on the fact that a significant portion of the user community can utilize neutrons arriving at this rate. Note that it is very cost-effective to add a second target station that can operate at a lower repetition rate in concert with the high-rep-rate target, providing more optimal service to those users requiring longer flight-paths or slower neutrons.

Such a second target station also doubles the number of available beam ports, in addition to allowing for customization of moderator configurations for specifically tailored neutron spectra on both targets. The second target station is, as a consequence, the very first item on the priority list for facility upgrades.

2.4 Reliability and Availability

An extremely important requirement is the highest-possible reliability and availability. Neutron-scattering experiments are by nature short, and are typically planned far in advance. As a result, it is most important that when an experimental group comes to the facility, neutrons are available as promised. In short, the SNS must be a facility built for users, to ensure maximum experimental throughput and productivity, and is not to be a proving ground for development of new accelerator frontiers.

Reliability results from several factors: a) use of well-developed, mature technology, b) conservative design parameters with adequate performance margins to ensure that systems are not being stressed unduly, c) high-quality components that will not be likely to fail, and d) a highly-trained and motivated operations staff.

All of these factors, unfortunately, add to the facility cost. One must be extremely careful, in the inevitable cost-optimization processes that go on throughout the life of the construction project, that economies are not taken which introduce unacceptable risk to the operational reliability of the facility.

One specific area sets the SNS apart from other user-based accelerator facilities; the beam-currents are so high that extreme care must be taken to minimize beam losses during the acceleration and accumulation processes. The consequences of beam loss are either catastrophic failure of components that might be hit, in the event of accidental gross mis-steering of the beam, or activation of components in the accelerator tunnels to the point where access must be limited, and maintenance of accelerator systems becomes very difficult. Both will adversely impact machine availability. Typical fractional beam losses in existing high-power proton accelerators are significantly higher than can be tolerated in the SNS, leading to significant challenges to the design teams to understand mechanisms for beam loss in these existing accelerators, and to provide designs that will perform better. The goal of our design is between one and two orders of magnitude lower fractional beam losses than are presently experienced at commensurate accelerator systems of LANSCE, AGS or Fermilab.

Table 1. Design Parameters for the SNS

Beam Species on Target	Protons
Beam Species in Linac	H^-
Proton Beam Energy	1 GeV
Beam Current (average)	1 mA
Linac Duty Factor	6%
Pulse Repetition Rate	60 Hz
Pulse Width on Target	≈600 ns
Particles per Pulse on Target	1×10^{14}
Instantaneous Beam Energy on Target	17 kJ
Instantaneous Power on Target	≈30 GW

3. SPECIFICATIONS

Translating the above requirements into performance specifications for the SNS accelerator, we derive the operating parameters listed in Table 1. The biggest challenge lies in the large number of particles that must be delivered to the target in the very short time period. The best way of achieving this is to use well-established RF linear-accelerator technology, which can easily handle tens-of-milliamps of current, and to use a pulse-compression system such as an accumulator ring to build the peak current up to required levels.

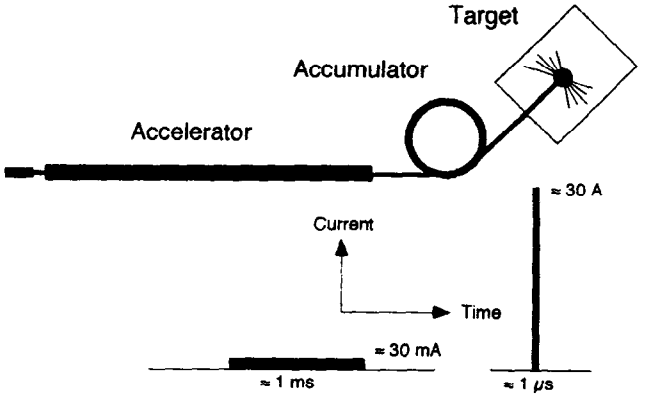

Figure 3. Configuration of a short-pulse spallation source, indicating the use of an accumulator ring to achieve the needed factor of 1,000 amplification in peak current.

The planned instantaneous current through the SNS RF linac structures is around 30 mA, driven both by ion-source performance at the emittance and brightness required, as well as by linac-structure sizes and costs. The instantaneous current delivered to the target, however, must be of the order of 30 amperes (to meet the criterion of 1 MW in 60 pulses of 1 μs duration). To produce this 30-A pulse, one wraps the beam from the linac many times around the circumference of the accumulator ring, then kicks this accumulated beam out in a single turn. By stacking 1000 turns into

the ring, the required instantaneous power amplification is achieved. Figure 3 shows a schematic for this configuration; the SNS design calls for the number of particles stored in the ring, around 1 x 10^{14}, to enter the ring as a low-current, long string and to leave as a short, high-current pulse.

In the context of minimizing beam losses, one of the most critical areas is the injection and stacking into the accumulator ring. The most important element in this regard is the absolute necessity of accelerating H^- ions in the linac. Charge-changing, by passing these negative ions through a thin stripper foil, is the most effective way of injecting protons into a ring, and is now used almost exclusively in the world's high-energy proton accelerator facilities. Increases in phase-space density are possible with this technique that are not possible using positive-ion injection, as the circulating beam can pass through the stripper foil used to convert the negative hydrogen into protons (by removal of the two electrons), with little consequences to the overall beam quality. A magnetic field, bending opposite charges in opposite directions, merges the two beams to a common point at the stripper foil. As both beams have the same charge following the foil, their orbits are now coincident. This is shown schematically in Figure 4. While this technique has allowed an efficiency increase in stacked and captured particles from the 70% typical for optimized positive-ion multi-turn injection to well over 90%, the required efficiency for the SNS of >99.9% has required added refinements to the concepts. These will be discussed briefly below.

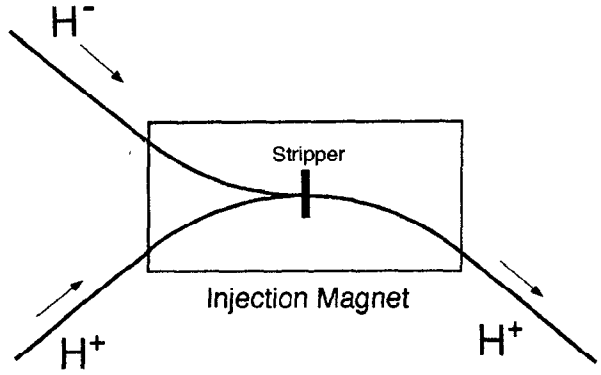

Figure 4. Schematic representation of charge-changing injection into a ring. The injection line (H^- beam) is bent upwards in the magnetic field, and merges with the circulating (H^+) beam that is bent downwards. The two orbits meet in the stripper foil. After the two electrons are removed from the incident ions, the two beams follow the same trajectory through the remainder of the magnet.

4. SNS BASELINE DESIGN

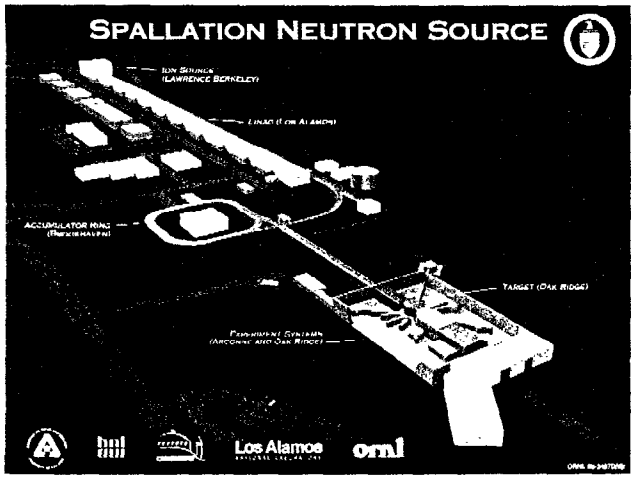

Figure 5. Schematic layout of the SNS Facility

The baseline design for the SNS is described in the Conceptual Design Report [1], and is shown in Figure 5. Although over a year old, the baseline design has changed little since this original study. The scope of this paper covers the Front End and Linac portions, only brief mention will be made of the components beyond the linac. The reader is referred to the Conceptual Design Report for in-depth descriptions of these components. In addition, ring issues (in the context of the LANSCE - PSR) are covered in R. Macek's paper in these proceedings.

4.1 Front End

Lawrence Berkeley National Laboratory is providing the "front end" of the SNS, consisting of components that produce the H^- beam and accelerate it to 2.5 MeV. Figure 6 shows a schematic of these components, including the ion source, LEBT (Low Energy Beam Transport), RFQ (Radio-Frequency Quadrupole) accelerator, and MEBT (Medium-Energy Beam Transport) line. The total length of the front end is around 10 meters. Although a very small fraction of the total system dimensions, the front end plays a crucial role in defining beam quality necessary to meet performance goals.

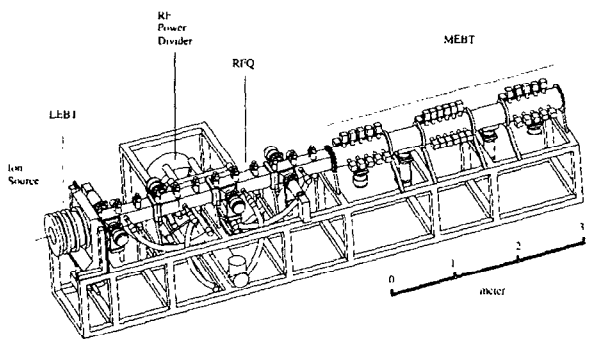

Figure 6. Schematic layout of Front End, showing ion source, LEBT, RFQ and MEBT

The ion source, a cesium-enhanced volume-production source is now a very mature technology that has been applied in many accelerators and other beam-forming applications. Plasma formed by a high-power (≈30 kw) RF discharge is contained by a multi-cusp magnetic field configuration of permanent magnets. Ions drift through a barrier field into a low ion-temperature region, where cesiated surfaces enhance the population of negative ions. Beam is extracted through a 6 mm diameter hole. A sophisticated magnetic-field configuration separates electrons extracted with the ions. Required peak beam current is 35 mA, this level has already been demonstrated in R&D sources operating without Cs. The introduction of Cs will increase current by about a factor of 3, allowing much lower RF discharge powers, significantly increasing source lifetimes and reliabilities.

The LEBT consists of a short (11 cm) column of electrostatic lenses which accelerate the extracted beam to 65 keV and match it to the RFQ. While traditional LEBTs are longer and employ solenoid-magnet focusing, the use of an all-electrostatic system eliminates problems associated with time-dependent space-charge neutralization that can arise with pulsed beams.

The RFQ, operating at 402.5 MHz, bunches the beam from the ion source into the packets that fit within the accelerating RF "buckets" (every 2.5 ns), and accelerate the beam to 2.5 MeV. Careful attention is paid to maximizing the efficiency of this bunching process, and ensuring that the emittance of the beam (its spatial and time characteristics) is preserved. This is particularly difficult because of the strong space-charge forces from the very high bunch densities that tend to drive the beam apart. RF quadrupoles have been long-used in mass spectrometry as strong-focusing transport channels, but by careful modulation of the shapes of the vane-tips (introducing "wiggles") selective longitudinal components to the strong transverse electric fields can be introduced which first bunch, then accelerate the beam. Again, this is now a very mature technology, with almost all of today's high-energy accelerators employing these structures for initial

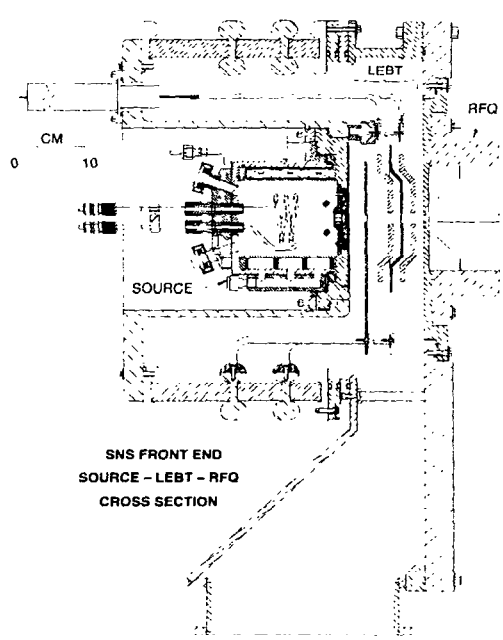

Figure 7. Cross section of ion source and LEBT. Large pumping port in base allows for handling of gas loads from ion source

stages of acceleration.

The MEBT serves as a 3.7 meter channel to transport the beam from the RFQ to the next stage of acceleration. While it is normally desired to close-couple each acceleration stage (butting the accelerating sections right up against each other), the SNS requires a sophisticated "beam-chopping" system that mandates the use of the long MEBT.

4.2 Beam Chopper

Three basic time scales can be identified for the beam in the linac: the 1 millisecond "macro-pulse" length providing all the particles that are compressed into the single very short pulse on the target, the RF bunches ("micro-pulses") that come every 2.5 nanoseconds, and the natural revolution frequency of the beam in the accumulator ring (AR), which introduces a time scale in the microsecond range.

As noted earlier, the 1 ms macro-pulse is wrapped into ≈1000 turns in the AR, and then is kicked out in a single turn. Thinking of the mechanics of the kicking process, which is performed by a fast "kicker magnet", one must ask how "fast" the fast kicker really can be. The best engineering designs, for a ring of the required aperture, indicate the quickest rise time could be around 200 nanoseconds. This is almost 25% of the ring revolution period. If any beam is in the kicker during the time the magnet is transitioning from "off" (beam circulating) to "on" (beam extracted), this beam will be sprayed into the region between the ring and the extraction channel. As the total beam power is 1 MW, this implies that approximately 250 kw of beam will be lost in this area, causing completely unacceptable activation and component damage.

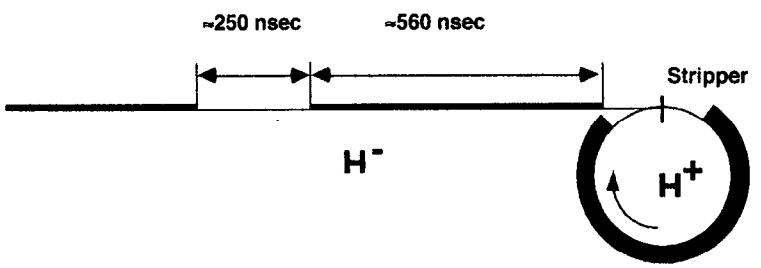

Figure 8. Schematic of beam chopper showing train of 560 ns pulses from linac stacked into accumulator ring.

To mitigate this problem, the linac beam is "chopped," placing 250 ns holes in the otherwise continuous macro-pulse that correspond to what is called the "extraction gap." By synchronizing the beam chopper with the ring circulation frequency, the overlap of all 1000 such holes is ensured. Chopping is performed by passing the beam through a set of parallel plates on which a high-voltage square-wave is placed. This pulse deflects the unwanted 250 ns of beam into a stopper, and allows the remaining 560 ns of beam to pass through undeflected. Most efficient chopping is performed at a low energy, where reasonable fields can cause adequate deflection of the beam, where beam power of the waste beam can be effectively absorbed, and where this waste beam will not produce neutrons. For these reasons, the 2.5 MeV point has been selected for beam chopping.

Several issues must be addressed: it is important that the rise-time of the square wave be very sharp, to separate adjacent RF micro-pulses. This would imply a better-than-2.5 ns rise-time. Any micro-pulse that is caught in the transition time of the square wave will be partially deflected, and at least a portion will miss the stopper, producing beam that might be transmitted off-center through the remaining accelerating components. These partially-chopped bunches might possibly lead to significant beam-loss problems at higher energies. For this reason, the MEBT is designed with an "anti-chopper" that is designed to bring any partially-chopped bunches back to the beam axis.

Another issue is that the chopper plates are about 50 cm in length, and the transit time of a 2.5 MeV beam through these plates is around 40 ns. It is important then that the plates be not continuous, but be segmented into a travelling-wave structure, so that the transitioning edges of the square wave can propagate down the length of the structure at the same velocity as the beam bunches. This complicates the design of the chopper, and increases the problem of maintaining the required very fast rise-time.

Nonetheless, a chopper with close to the required performance specifications has been in operation at LANSCE for many years, and Los Alamos will provide the SNS chopper system based on this experience.

4.3 Linacs

Three different linear-accelerator structures will be provided by Los Alamos National Laboratory for the main acceleration stages: a DTL, or Drift-Tube Linac brings the beam to 20 MeV, a CCDTL (Coupled-Cavity Drift-Tube Linac) takes the beamto 93 MeV, and a CCL (Coupled-Cavity Linac) completes the chain to 1 GeV. Many examples of DTL and CCL structures exist, designs are very well characterized and their performance is quite well understood. The CCDTL is a new concept, with excellent properties to provide gentle matching between the DTL and CCL structures, which produces, at least in simulations, very high quality beams. While no operating CCDTL exists, models have been constructed to verify field calculations, and prototypes are being built for both APT and SNS to ensure proper operating characteristics.

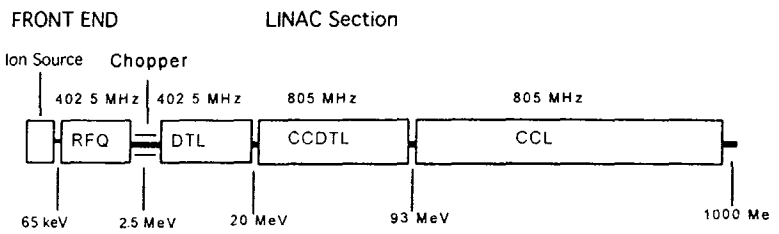

Figure 9. Schematic (not to scale!) of Front End and Linac elements.

The DTL, or Alvarez Linac, consists of a long tank (actually, the DTL is in two sections, so there will be two tanks) resonating at 402.5 MHz in a mode where the electric field parallels the beam direction. As the electric field switches directions every 2.5 ns, copper "drift tubes" are provided at appropriate intervals to shield the beam bunches from the adverse fields. Bunches emerge from the end of each tube to receive a kick before entering into the next tube. There are 84 drift tubes in the tanks, these tubes increase in length down the structure to match the increased beam velocity. Each tube also contains a quadrupole magnet (SmCo) to provide transverse beam focusing.

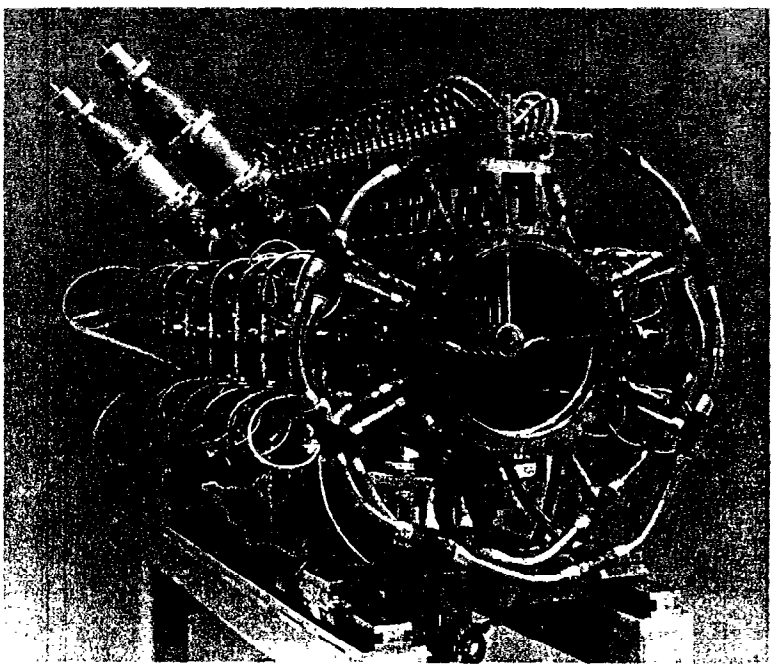

Figure 10. DTL structure built by LANL for the GTA program, very similar to design for SNS. Beam passes through small aperture in drift tubes.

The CCDTL structure is directly coupled to the end of the DTL, and operates at 805 MHz. The doubling of the operating frequency allows for more efficient size and shape of the accelerating structures, and as long as the designs are carefully done, the transition in frequency will have very little effect on the beam quality. It should be noted that LANSCE does not have this intermediate CCDTL

structure, but instead transitions directly from a 200 MHz DTL to an 800 MHz CCL. Addition of the new structure, and reduction in the frequency jump factor from 4 to 2 are expected to produce much higher quality beams than are currently available from LANSCE.

After approximately 68 meters of CCDTL structure, at the 93 MeV point, the CCL structure takes over bringing the beam, after an additional 473 meters, to its full energy of 1 GeV. The transition between these two structures occurs seamlessly, ensuring very smooth transitions in both longitudinal and transverse forces on the beam.

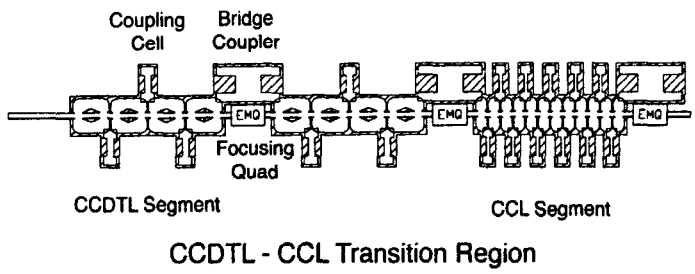

Figure 11. Schematic of CCDTL and CCL structures showing individual components

As seen schematically in Figure 11, the CCDTL and CCL structures externally look very similar: brazed segments approximately 1.5 meters in length each containing several accelerating cells, are mounted on strongbacks, with approximately 30 cm spacing between segments in which focusing magnets and beam diagnostics are placed. Segments along the 540 meter length of the two structures are grouped into 26 distinct RF "modules," each fed by two klystrons, the RF feed occurring in a bridge-coupler between two segments (at the 1/6 and 5/6 point of each module). RF energy is transferred between the individual cells by means of the coupling cells on the top or bottom of adjacent accelerating cells. Fields on the beam axis in the cells is parallel (or antiparallel) to the beam, phasing of the beam bunches is such that each sees an accelerating field as it traverses the cell and is in an inter-cell "bore tube" as the fields are reversing. Energy of the beam in the CCDTL is low enough that an additional drift tube must be inserted in each of the cells to ensure proper matching of structure geometry, resonant fields and beam velocity. Thus, each of the CCDTL cells will have two accelerating gaps.

4.4 Accumulator Ring, Target, Instruments

At the 1 GeV point, beam enters the HEBT (High-Energy Beam Transport), is bent through 90° to provide beam analysis and clean-up opportunities before reaching the ring injection point. An elaborate series of pulsed and fixed bump magnets provides flexibility for "painting" the 1000 turns as they are injected through the carbon stripper foil, to provide the best distribution of beam circulating in the ring. Optimization of this beam distribution can have significant impact on beam losses during the accumulation process, and also affects the distribution of beam density on the target, important for thermal and radiation-damage management on target

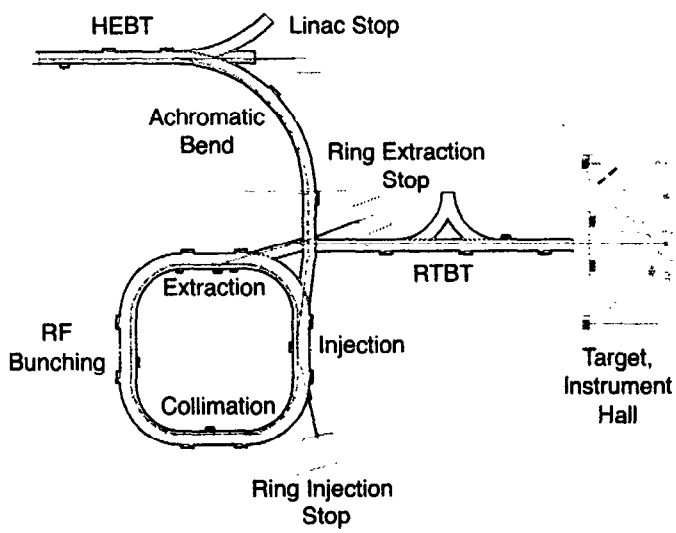

Figure 12. Simplified schematic of accumulator ring systems, including the HEBT transport from the linac to the ring, and the RTBT between the ring and the target building.

components.

A fast kicker bumps the beam up vertically into a special septum magnet that provides horizontal deflection into the RTBT (Ring-to-Target Beam Transport), the beam bunch is now 590 nanoseconds long. This beam is transported to the target, where it is spread out into a relatively-uniform rectangular distribution roughly 20 cm wide by 7 cm high. Again, because the beam is kicked out in a single turn, distribution on the target is closely related to the distribution of beam inside the ring, and hence to the injection painting scheme.

These systems will all be provided by the Brookhaven National Laboratory.

The mercury target, provided by the Oak Ridge National Laboratory converts proton power to neutrons via spallation reactions; intra- and inter-nuclear cascades yield approximately 26 neutrons for every incident 1 GeV proton. Liquid mercury has been selected to mitigate thermal shock effects from the ≈30 GW proton pulses that might cause unacceptable damage to solid target materials. These pulse loads will be substantially higher as well, once the SNS is upgraded to its higher-power operating levels.

Two room-temperature water moderators, and two supercritical hydrogen cryogenic moderators will deliver neutron beams to 18 beam lines, and an initial complement of 10 instruments will be built under the supervision of the Argonne National Laboratory as part of the SNS project line-item scope.

5. CONTROLLING BEAM LOSS

As has been mentioned before, a most important element of the SNS design is controlling beam losses. Particularly at the higher energies, beam that is lost will cause activation, or even component damage that can have severely deleterious effects on operational reliability and efficiency of maintenance activities. Mentioned above as well was that design requirements for beam loss for many of the systems employed in the SNS surpass by a large factor the base of current experience. As a consequence, very careful attention has been paid to parameters and designs to maximize the chances for controlling beam loss.

A very large experience base has been collected from the operation of the LANSCE linac, which has beam power capabilities very similar to SNS'. Although the power actually delivered to the neutron-production target in the Lujan Center is only about 80 kw, the total beam power available from the LANSCE linac is of the order of 1 MW. Typical losses experienced are of the order of 1 na/meter, producing dose rates in the vicinity of linac components of the order of 30 mr/hr. This level does not preclude hands-on maintenance, provided exposure times are kept to the barest minimum. As a matter of course, good engineering practice calls for accelerator component designs that allow for accomplishing required maintenance activities as rapidly and efficiently as possible.

It is anticipated that the SNS will operate at significantly lower beam loss levels than LANCE's. Since the original design of LANSCE, substantial experience has been gained in understanding of beam-loss mechanisms, particularly in mechanisms for driving beam particles into the wings of the transverse distributions that can yield orbits for particles that go beyond the containing boundaries of the beam pipe. In particular, ensuring smooth transitions between different accelerating structures is predicted to very significantly reduce population of beam halos. The size and extent of beam halos are also much better understood now, and required structure apertures to contain most readily-populated halo trajectories can be calculated. As a result, the SNS apertures are significantly larger than LANSCE's, and in addition the beam diameter is quite a bit smaller.

One area of linac engineering design that must receive careful attention is the vacuum system. For the H^- ions, interactions with residual gas atoms can strip electrons from the ions, leading to beam loss. Base pressures in the 10^{-8} torr range are required to keep these losses within acceptable limits. Such levels are achievable with proper attention to cleanliness, and good pumping systems.

There are several areas in the ring where beam losses could present significant problems. As mentioned earlier, the injection system must perform at new levels of efficiency. As a first step to achieving this, the HEBT is designed to ensure ample opportunities for cleaning halos and outlying particles from the beam prior to reaching the injection foil. In addition, specialized RF cavities in the

HEBT line can provide fine adjustments in beam characteristics to improve injection matching. Good simulation codes are also now available for modeling the injection process.

Of particular note is the atomic physics associated with the stripping process. Even at 1 GeV, the removal of both electrons from the H^- ion is not a completely trivial matter. Foils must be very thin, resulting in an appreciable percentage of the beam remaining in excited H° states. The interaction of these excited states with downstream magnetic fields can lead to high beam losses through Lorentz stripping. This is the dominant mechanism for beam loss in the LANSCE PSR, and has been one of the factors limiting performance of this facility. As a specific example, at 1 GeV, a 200 $\mu g/cm^2$ carbon stripper foil can leave almost 8% of the beam in various un-stripped states. While a 400 $\mu g/cm^2$ foil reduces this fraction to well-below 1%, the operating temperature of this foil may reach over 3000°, causing concern for foil lifetime and reliability. A novel layout for the injection region has been developed which is particularly effective in mitigating Lorentz stripping effects, allowing the use of foils thin enough to where thermal effects can be controlled. This, coupled with the better understanding of the physics of injection processes and improved simulation codes, gives us confidence that the SNS injection efficiency will be within specifications.

There are many other mechanisms that can cause orbits for beam particles in the accumulator ring to grow beyond the available machine aperture, many of them as yet not fully analyzed. However, a properly-designed collimator system capable of absorbing such tails, can keep the errant particles from activating portions of the machine where routine access for maintenance activities is required. As seen in Figure 12, the SNS ring is designed with four straight sections, one dedicated to collimation systems. The aperture in this region is by design smaller than other portions of the machine, so that any particles with aberrant orbits will be intercepted in this region. As a result, it is expected that the required specification of 1 part in 10^4 of *uncontrolled* beam loss can be satisfactorily met in the ring.

6. UPGRADE PATHS

The initial 1 MW operating level is considered the base starting point for the SNS performance. A clearly-stated requirement for the next-generation spallation source has been [4] that if the initial performance level was 1 MW, it must be upgradable to significantly higher powers. The Kohn report [5] drew a parallel between an accelerator-based spallation source and a top-class research reactor, stating that a rough measure of scientific productivity would equate the two were the power level for the spallation source to be 5 MW. As a consequence, plans have been formulated to ensure that an upgrade path to powers at least in the 4 to 5 MW range is clearly defined for the SNS.

6.1 Second Target Station

Recalling the discussion above on specifications for repetition rates for the SNS, it was concluded that the broader neutron-scattering community could be best served were the facility to include two target stations. The first would receive pulses at the basic 60 Hz SNS operating rate, while the second could be optimized for a lower repetition rate, of say 10 Hz. Such a configuration would not only allow for a doubling of available neutron ports, but would also double the number of moderators, and would enable the optimization of each moderator design to best suit the particular neutron spectral characteristics for instruments viewing that moderator. As a result, this item is clearly the highest priority for enhancing the overall capabilities of the SNS.

Space has been reserved on the proposed site (see Figure 13) to accommodate a second target hall, and a beamline from the RTBT to the second hall. The operating mode for the facility would not change the basic 60 Hz rate for pulses being produced by the SNS accelerator system, but every sixth pulse would be directed to the second target station. Note, any combination of the 60 pulses per second could be distributed between the two target stations, but it is expected that once optimization has occurred in target, moderator and instrument design, the utilization of this flexibility is unlikely.

6.2 Two MW Operating Level

Upgrade of the accelerator complex to deliver 2 MW is quite straightforward. All of the accelerator components are designed to handle this level of beam, only a few elements need to be upgraded to reach this level of performance.

Specifically, the ion source must be improved to deliver 70 mA of beam from its original 35 mA. This is not viewed as difficult: this type of ion source has performed at this current level already [6], but for lower duty factors, so only engineering enhancements are required for management of extra heat loads from the longer SNS duty factor. Beam dynamics simulations for the front end, linac and ring sections have verified that designs of these elements are suitable for accelerating and transporting 2 MW beam levels. The extra beam-loading will require some enhancements in the linac RF system, but a very efficient scheme for addition of extra klystrons has been developed which will accomplish this upgrade in a very straightforward manner. Some very minor improvements to the target thermal-management systems will be required, but basic shielding is designed to handle a full 4 MW of beam power.

It is anticipated that this upgrade will occur as a relatively routine extension of operations. It can probably be accomplished with very little if any disruption of service, and might even happen incrementally over the first few years of operation.

6.3 Four MW Operation Level

Upgrading to 4 MW is somewhat more involved, but is still of much smaller scope than the initial construction project. As the accumulator ring is designed for a maximum of 2 MW, a second ring will be required. Again, space has been reserved on the planned site for this ring, to be built in mirror-image position from the first ring. Building a separate tunnel, while adding to the costs of the upgrade (as opposed to placing the second ring in the same tunnel as the first ring), provides for continuing operation of the first ring during construction and installation. In addition, it also adds significant flexibility to the facility for operating modes (e.g. continuing operation of one ring while handling maintenance problem in the second ring), as well as for future upgrades (placing double rings in one or both tunnels).

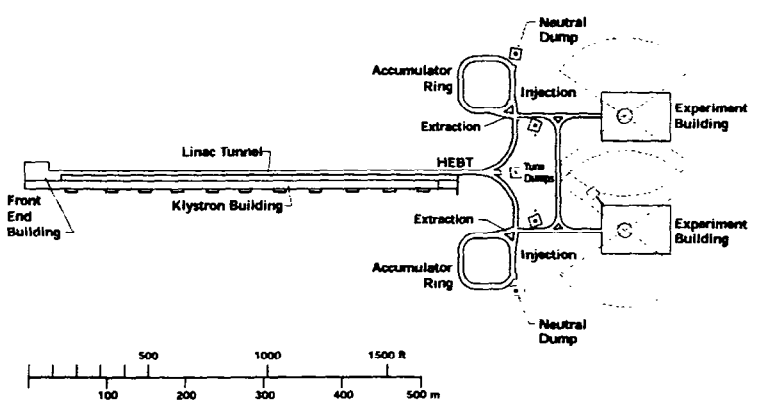

Figure 13. Footprint of SNS upgraded to 4 MW, with two target stations. Note second ring, and cross-over transport line to bring beam from both rings to either target station.

It is unlikely that a 140 mA ion source can be developed with suitable operating characteristics. As a result, the 4 MW upgrade plan calls for building a second front end system, up to and including a second DTL set. This second system would be placed parallel to the first, and a new merging section installed at the 20 MeV point to serve as a "funnel." As this is also the point where a frequency jump between 402.5 MHz and 805 MHz occurs, phasing of the two front ends will allow a doubling of the pulses accelerated in the 805 MHz section, hence a net doubling of the beam current. Note, that with only one front end operating at 402.5 MHz, only half of the available buckets in the 805 MHz section are utilized. The funnel will alternate pulses from the two front ends, filling all available buckets.

As was the case with the 2 MW upgrade, some further enhancements in the linac RF system will be needed to provide for the increased beam loading.

The switchyard will become more complex as well. The cross-over to the second target station will now become bi-directional, so that beam from either ring can be delivered to either of the two target stations. The operating mode will be as follows: the first 500 μs of the linac pulse will be used to load 2 MW of beam into one ring, the second 500 μs loads the second ring. Then the switchyard is set up for whichever target will receive the pulse, and both rings will be emptied into that target. This can be done in one of two ways: the first would have the tail of the pulse from the first ring immediately followed by the head of the second ring's pulse (with a 250 ns gap to allow for switching of the proper kicker). This would produce a pulse of almost 1.3 μs duration. A second method would be to have a parallel transport line into each target, so the heads and tails of pulses from both rings would be aligned. This would produce the shortest pulse, ≈590 ns, but would require a very sophisticated transport line design.

6.4 Further Power Increases

As mentioned earlier, having a full-energy, highly flexible linac as a base platform provides excellent opportunities for expansion of facility capabilities. The well-defined paths to 2 and 4 MW have been described, but in addition it is possible to consider inclusion of second rings in each tunnel, again doubling beam power. One could even contemplate using one of the accumulator rings as an injector for a higher-energy synchrotron that could deliver, say, 10 GeV protons to the target. While fraught with potential difficulties, the time scale for such a further enhancement is sufficiently far in the future that other projects may have paved new technology paths that would be applicable for either this scenario, or for as-yet unanticipated designs.

7. SUMMARY

The design requirements for the SNS are very well understood, and a well-conceived design has been developed which is expected to meet the required specifications with very conservative safety margins. The technologies selected are well established, leading to an overall level of technical risk which is substantially lower than normally expected for a project of this magnitude. Areas where extrapolations are called for, such as the very tight specifications on beam loss, are believed to be well understood. Extra conservatism has been incorporated into designs affected by these areas.

An overriding criterion is designing for reliability. Engineering specifications and analyses to ensure meeting this goal are an important part of the design effort. It is our goal to produce the best facility in the world for neutron scattering!

It should be noted that at the time this manuscript was prepared, construction approval for the SNS has been granted, and an allocation of $130M has been made by the United States Congress for the first year of construction. (The author is particularly grateful for the patience of the ICANS organizers, which has allowed the sharing of this wonderful news!) The project is now underway, and we fully expect that the year 2006 will see full utilization of neutron beams from the SNS.

REFERENCES

[1] The NSNS Conceptual Design Report, ORNL / NSNS / CDR, May 1997 <http://www.ornl.gov/~nsns/nsns.html>

[2] "Los Alamos Next-Generation Spallation Source," LA-UR-95-4300, December 1995, Vol 1, Figure 3-12, page 3-20.

[3] Lowell Charlton, ORNL, Private Communication, and NSNS CDR, Section 5 p. 5-97

[4] 'Next Generation Spallation Source Committee Report" BESAC, Feb 1996, Thomas Russell, Chair.

[5] "Neutron Sources for America's Future – Report of the Basic Energy Sciences Advisory Committee Panel on Neutron Sources" January 1993, Walter Kohn, Chair. DOE/ER-0576P

[6] K. Saadatmand, K-N Leung, private communication. The source provided by LBNL for the SSC actually operated at over 100 mA, but for duty factors of the order of 0.1%.

ICANS-XIV
14th Meeting of the International Collaboration on Advanced Neutron Sources
June 14-19, 1998
Starved Rock Lodge, Utica, Illinois, USA

Ring Developments Relevant to Short-Pulse Spallation Neutron Sources

Robert J. Macek

Los Alamos National Laboratory
LANSCE-DO
MS-H848
Los Alamos NM, 87545, USA

ABSTRACT

Recent developments on major design and performance issues in the circular accelerator drivers for short-pulse spallation neutron sources are reviewed.

1. Introduction

The demand for higher intensity short-pulse spallation neutron sources has stimulated work on the intensity limitations of the circular accelerator drivers. It has also lead to a number of proposals for new facilities and upgrades to existing facilities. The two main options for new facilities are the linac plus rapid cycling synchrotron (RCS) option and the linac plus accumulator (compressor) ring option. Both make use of multi-turn injection obtained by stripping H^- beam in the injection region of the ring. Both are subject to many of the same limiting factors - space charge, beam losses and instabilities - but to differing degrees.

Both options are possible contenders for the next generation spallation sources. The RCS has the advantage that injection losses occur at a lower energy and therefore cause less radio-activation per lost proton. It has the disadvantage that the space charge limit at injection is more severe. The linac-accumulator ring has the advantage of a significantly higher space charge limit and of providing all of acceleration and beam power in a rf linac. Its main drawback is that beam losses in the ring all occur at the final energy with the consequence that there is greater induced activation per lost proton. At this time, the major new "green field" projects have tilted towards the linac-accumulator ring option but not for any single reason.

Numerous recent advances in the science and technology of circular accelerators deserve mention. However, it is not the purpose of this paper to provide a complete and exhaustive review. Instead, topics were selected that were judged of particular importance to the new machines and to the ISIS and PSR upgrades. Of prime importance are the advances made in the understanding and amelioration of the factors that limit intensity especially space charge, beam losses and instabilities. Other selected topics include stripper foil heating and foil lifetime considerations, new ideas for injection without foils (laser-aided injection), and inductive inserts for passive compensation of longitudinal space charge.

2. Limitations from Transverse Space Charge

The transverse space charge limit is one of the first constraints to consider in ring design. By now, it is a classic "text book" limit on intensity and is due to the defocusing effect of space charge which depresses the betatron tunes of individual beam particles. The simplest model that can be calculated analytically i.e. a proton oscillating inside a uniform beam distribution of circular cross section, will illustrate the essential features. In this approximation the tune shift or more precisely the incoherent tune shift, $\Delta\nu$, is given by equation (1) below:

$$(1)\quad \Delta\nu = -\frac{r_p N}{2\pi\beta^2\gamma^3\varepsilon B_f}$$

Here N is the number protons in the ring, r_p the classical radius of the proton, β and γ the usual relativistic factors, ε the transverse emittance and B_f the longitudinal bunching factor. From this formula it is apparent that the tune shift is largest at the injection energy because of the $\beta^2\gamma^3$ term in the denominator. The tune shift also depends on beam size through the emittance. A larger beam size results in a larger emittance and, therefore, a smaller tune shift.

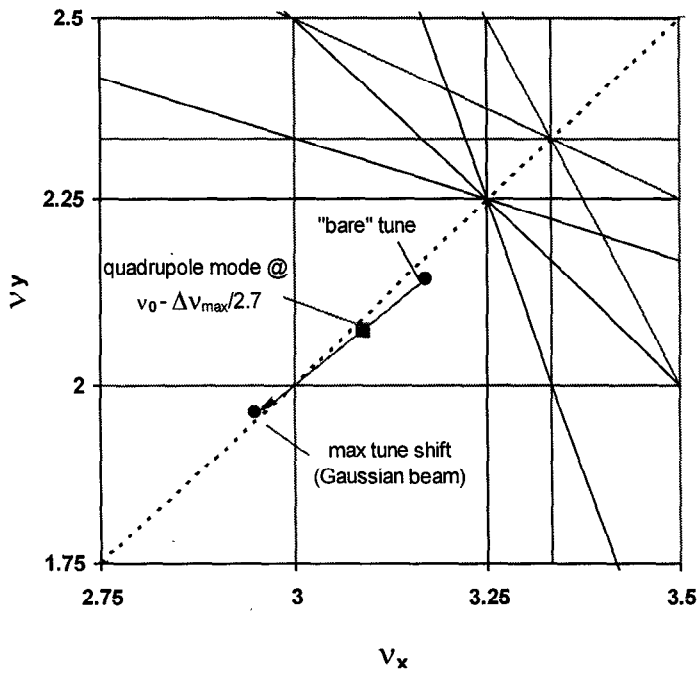

Figure 1. PSR betatron tune space diagram

The standard design criterion has been to avoid incoherent tune shifts that depress the tune over low order betatron resonances especially the integer, 1/2 integer or 1/3 integer lines. Thus, designers strive to keep $-\Delta\nu_{max} \leq \sim 0.25$. This criterion has been exceeded in a number of operating machines as the intensity was pushed up. For example, ISIS operates with a tune shift of ~ -0.4, the AGS ~-0.58 and at PSR the maximum incoherent tune shift moves the tune across the integer resonance (see Figure 1).

The reasons for being able to cross integer and half integer resonances are now better and more widely understood as was made clear by Rick Baartman at the recent Shelter Island Workshop [1]. The standard criterion is too conservative. Beam losses from space charge require consideration of collective modes and envelope oscillations. For example, with a Gaussian beam, the quadrupole mode (a low order collective mode) is not resonant until the maximum incoherent tune shift is 2.7 times that which moves the tune across the integer (see Figure 1). Higher order modes are resonant closer to the maximum tune shift.

Intensity-dependent emittance growth, presumably due to space charge, has been observed at several accelerators. Data from PSR, shown in Figure 2, illustrate the effect. In Figure 2, beam profiles at extraction are plotted for two different injection configurations, the standard injection

set up and one that produces a smaller initial beam size in the ring. For each configuration, profiles for 3 different intensities are shown. Intensity is varied in steps of a factor of 2 by changing the number of injected pulses using the front end beam chopper which can be commanded to let through every nth pulse (given by the countdown parameter, CD). Thus, for CD=1 every pulse gets through, CD =2 every other pulse and CD=4 every 4th pulse.

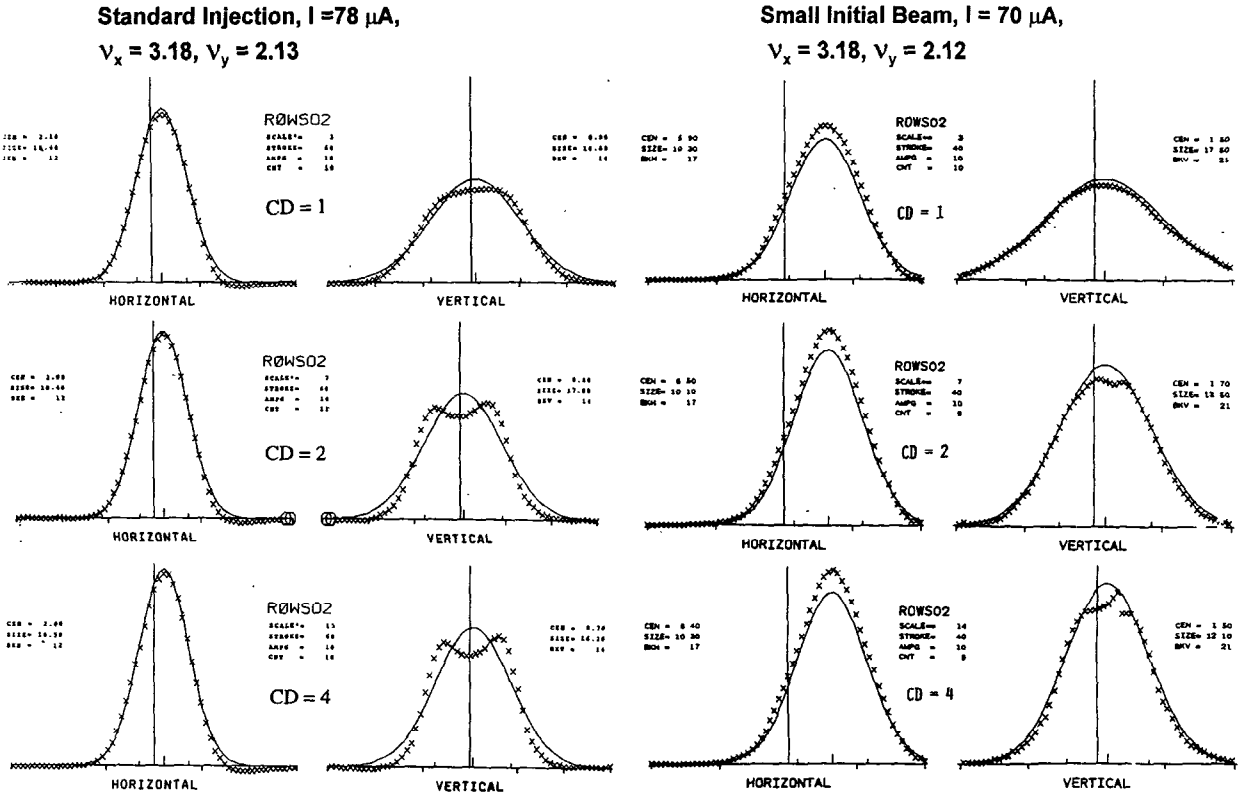

Figure 2. Beam sizes at various intensities in PSR.

The profiles of Figure 2 show that the beam emittance (proportional to the square of the beam size) increases with intensity, particularly in the vertical plane. The effect is more pronounced for the configuration with the smaller initial emittance. Here the vertical emittance increases by a factor of 1.7 for a factor of 2 change in intensity (CD=2 to CD=1).

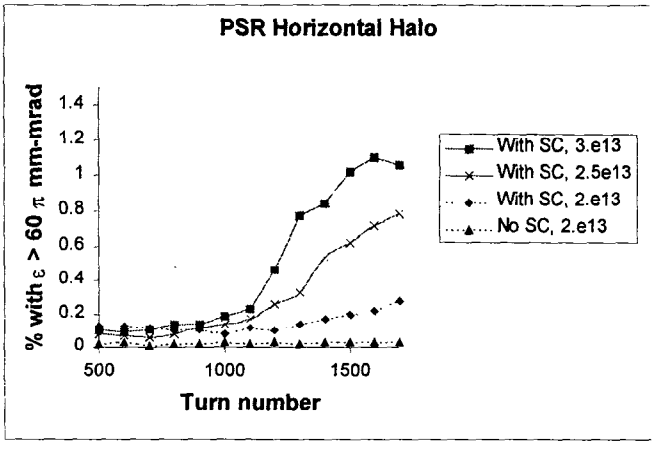

Figure 3. PIC calculations of beam halo with and without space charge.

Computation of emittance growth is a difficult problem since space charge is fundamentally a many body problem that would require enormous computing capability to treat exactly. Nevertheless, considerable progress has been made in numerical simulations as was brought out at the Shelter Island Workshop [2]. For example, the ORNL group has carried out computations of beam halo produced by space charge in the 1998 PSR using a

particle-in-cell (PIC) code [3]. Results of their calculations for PSR are shown Figure 3. These show details of the growth of emittance halo as the accumulation proceeds and as the final intensity increases. This behavior is in qualitative agreement with the experience at PSR. More quantitative comparisons are planned for the future.

With the constant demand to increase intensity, there is great interest in measures to increase the space charge limit. From equation (1) it is apparent that increasing the injection energy, increasing the longitudinal bunching factor and increasing the emittance will decrease the tune shift hence raise the space charge limit. The accumulator rings capitalize on having the highest injection energy for a given final energy. Improving the longitudinal bunching factor by adding dual harmonic rf is a feature of the new machines and a key feature of ISIS and PSR upgrades. The ISIS dual harmonic upgrade is expected to raise the intensity to 300 μA from the present 200 μA while keeping the losses constant. For PSR a second harmonic buncher will improve the bunching factor by 40% (0.5 from 0.35).

The new rings proposed for SNS, ESS, SNF (5 MW spallation neutron facility proposed for JAERI) and JHF are designed to have large transverse acceptance thereby allowing large emittances and thus smaller tune shifts. A comparison of emittance and calculated tune shifts for several rings are given in Table I below.

Table I. Comparison of emittance and maximum tune shift for several facilities.

Ring	ε (π mm-mrad)	$-\Delta\nu_{max}$
PSR 97	27- 39 (95%)	0.22
SNS	120	0.2
ESS	120	0.1
SNF	200	0.1
JHF	214	0.36

3. Beam Losses from Foil Scattering

The stripper foil is a major cause of losses for accumulator rings. Foil scattering and field stripping of excited states of H^0 produced in the foil are leading beam loss mechanisms. Stored beam particles are lost when undergoing nuclear or large angle Coulomb scattering in traversing the stripper foil. The beam loss depends on the number of foil hits, the foil thickness and the probability that the scattered particle is lost from the ring acceptance. Mitigation can be achieved by reducing the foil hits, increasing the acceptance for Coulomb scattered beam, using collimators to control the location of beam losses and by minimizing the foil thickness. The foil thickness is a trade-off with other criteria such as the amount of neutral beam that can be allowed go to the waste beam dump and minimizing the production of excited states of H^0.

The experience with PSR illustrates the problem of beam loss from foil scattering and means to reduce it. The important features of injection for PSR in 1997 operations are depicted in Figure 4 where the transverse phase space at the stripper foil is shown. The foil hits, hence beam losses from scattering, for this configuration are high ~ 300/protron or 35% chance per turn. The foil

hits are high because of certain disadvantages of H^0 injection. First, there is a factor of ~3 in emittance growth of the H^0 beam in the bend plane of the stripper magnet that creates the H^0 from H^-. Second, there is a large mismatch of the H^0 to the acceptance ellipse of the ring that exacerbates the inability to manipulate or tailor a neutral beam for optimum filling ("painting") of transverse phase space for minimum foil hits.

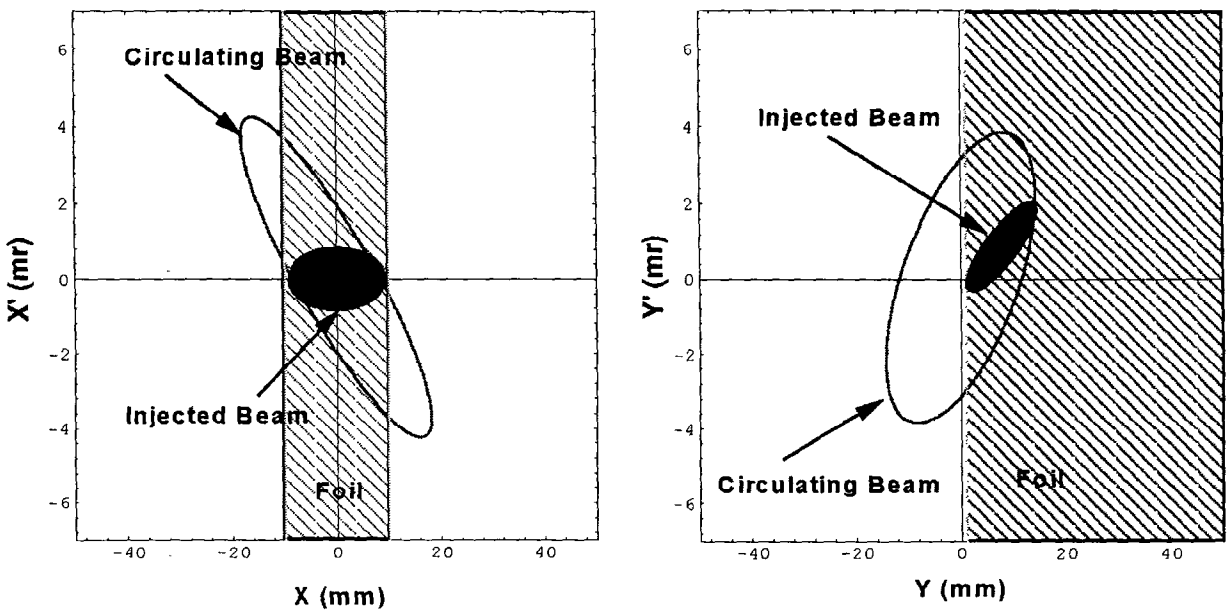

Figure 4. Transverse phase space at the foil for H^0 injection at PSR in 1997.

The upgrade to direct H^- injection depicted in Figure 5 is expected to reduce the foil hits by a factor of 10. This is accomplished by using double offset injection with a programmed closed orbit bump in the vertical plane at the foil.

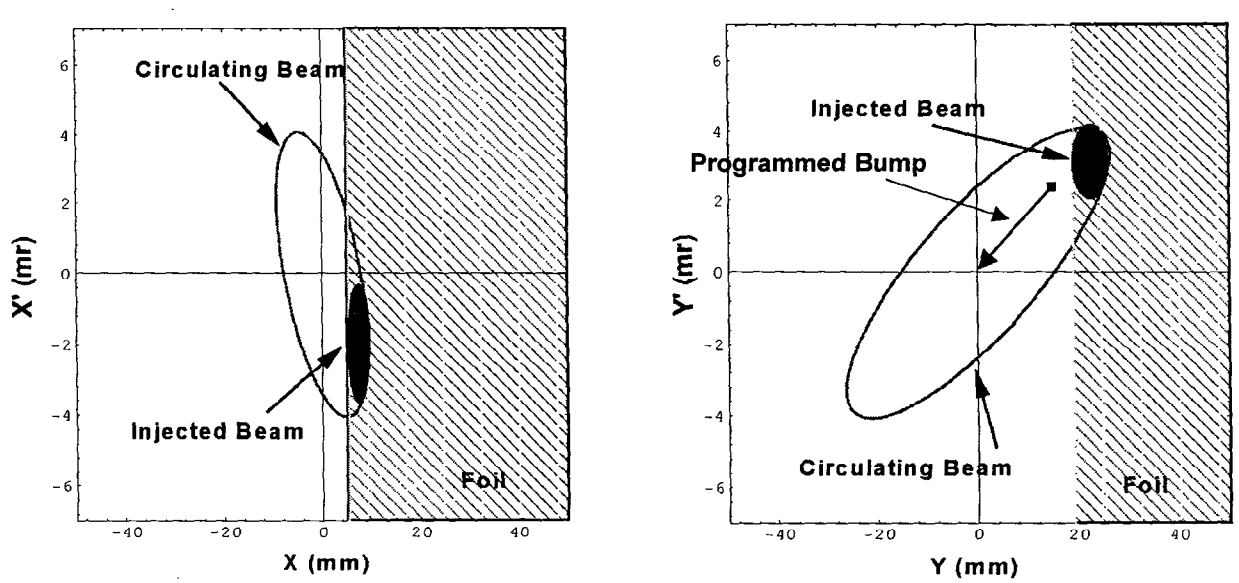

Figure 5. Transverse phase space at the stripper foil for the direct H^- upgrade to PSR.

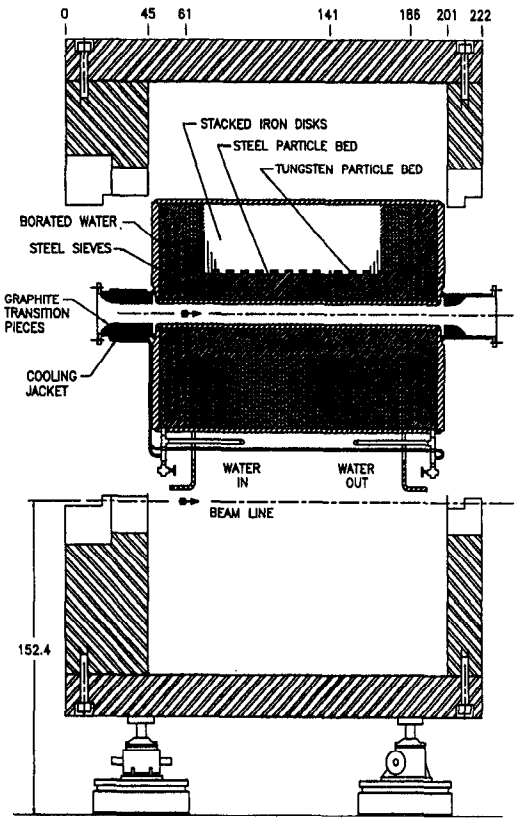

Figure 6. SNS collimator assembly [4].

Collimators can be used in the ring to provide the limiting apertures and thus control the location of beam losses. However, their design is not a simple matter of adding scrappers to an existing lattice. The lattice must be optimized specifically for the use of collimators. In addition, the collimator assemblies must be highly reliable and contain the activation produced by beam lost at the collimator. These features are illustrated in the collimator design for SNS shown in Figure 6 [4]. It has low Z, graphite transition pieces, water-cooling, and considerable absorber material all surrounded by iron shielding.

All of the proposed 1-5 MW spallation sources plan to use collimators. To date, it has not been possible to make effective use of scrappers or collimators at PSR because there is not enough space for them and because the lattice is not well suited to their use.

A comparison of measured (PSR 97) or expected losses from foil scattering for various rings is given in Table II below. Also shown are the parameters that are most important for determining losses from foil scattering. The parameter showing the greatest variation is the number of foil hits per stored proton which ranges from a high of ~300 for PSR in 1997 to 4-7 for the proposed next generation sources. The great improvement in expected losses for the new rings (compared with the 1997 PSR) stems largely from the small number of foil hits expected in the new rings. The larger acceptance and use of collimators also have a significant influence.

Table II. Comparison of foil scattering losses at various rings.

Ring	Foil hits /proton	Foil thickness ($\mu g/cm^2$)	Acceptance (π mm-mrad)	Collimator Acceptance (π mm mrad)	Scattering Losses %
PSR 97	300	200-220	130	NA	0.4
PSR Inj Upgrade	30	400	130	NA	0.08
SNS	4	300	312	~240	0.01
ESS	6-7	345	480	260	0.01
JHP-3GeV	3-4	200	?	312	?
SNF	?	?	530	200	?

4. Beam Losses from Field Stripping of H^0 Excited States

Foil scattering is not the only loss mechanism associated with the stripping foil. Foil stripping also leads to the production of excited states of H^0 that can field strip (via the Stark effect) part way through the magnetic fields that separate H^0, H^+ and H^- after the foil. The trajectory errors of the protons produced by field stripping can be large enough that they fall outside of the ring acceptance and are lost [5]. At PSR (1997) this mechanism accounts for a sizeable fraction (~30%) of the losses.

The yield of excited states (labeled as $H^0(n)$ where n is the principle quantum number) at 800 MeV has been measured [6]. The yield is observed to vary as $n^{-2.8}$. The lifetime of $H^0(n)$ moving in a magnetic field, B, is a strong function of n and B such that low n states are more difficult to strip. For a given B, there is a low value of n for which field stripping is negligible. For PSR at 800 MeV and a peak field of 1.2 T, the n=1 and 2 states do not strip but the higher ones ($n \geq 3$) do. For n sufficiently large, the lifetime is so short that they strip very quickly and the resulting protons stay within the ring acceptance. Thus, at PSR only the n=3,4 and 5 states lead to prompt losses. Stark states from n=5 and 6 can also add to the beam halo.

Losses from this mechanism can be mitigated by using lower magnetic fields to separate the three species emerging from the foil, by use of thicker foils to reduce the yield of $H^0(n)$ and by placing the foil in the field. The proposed rings for SNS, ESS and JHP are being designed to make optimal use of these measures to greatly reduce the expected losses from field stripping of $H^0(n)$. The experience from PSR and the expectations for the upgrade and the new rings are summarized in Table III below.

Table III. Comparison of losses from field stripping of $H^0(n)$.

Ring	Foil ($\mu g/cm^2$)	B (T)	n (loss)	Loss
PSR 1997	220	1.2	3,4,5	2.5×10^{-3}
PSR 1998	400	1.08	3,4,5	0.5×10^{-3}
SNS	300	0.25	4,5	$<10^{-6}$
ESS	345	0.177	4,5	10^{-5}
JHP	200	0.5	>4	$<8 \times 10^{-5}$

5. Stripper Foil Heating

Foil heating and radiation damage to the foil are additional consequences of charge exchange injection using stripper foils. Foil traversals by the stored beam heat the foil, which then cools by radiation primarily. Elevated temperatures are encountered which can greatly limit foil lifetime. For the 5 MW rings of the next generation spallation sources, foil heating is a serious problem. Calculated foil temperatures for various rings are shown in Table IV below.

Foil temperature depends on foil thickness, beam flux density striking the foil, foil emissivity, the number of radiating surfaces, specific heat and to a lesser extent on thermal conductivity. Foil materials in common use are graphite and aluminum oxide (Al_2O_3). Both are refractory materials with high melting or sublimation temperatures. Both are low Z materials with low Coulomb scattering cross-sections. Aluminum oxide suffers from a low emissivity, which may

rule it out for the 5 MW rings. In ESS design studies, the Al_2O_3 foil temperature is calculated to exceed the melting point.

Table IV. Calculate foil temperatures.

Ring	T(graphite) °K	T(Al_2O_3) °K
PSR 97	1780	
PSR 98	1490	
PSR/SPSS	1870	
SNS	3130	
ESS	2320	3083 (melts)

For injection schemes where the foil is placed in a magnetic field (e.g. ESS and SNS), it will be necessary to stop the stripped electrons from returning to the foil and adding to the heat load. An electron-absorbing block is placed to absorb the electrons before they return to the foil. Here it is important that the e-blocker be kept out of the way of the stored proton beam.

At PSR the commercially available foils showed a lifetime of 7-10 days in operation at 70 μA. Since changing foils entailed significant radiation dose and beam downtime, a longer lifetime foil was sought. Development of composite graphite foils by Sugai at Tokyo University has resulted in foils that lasted for ~3 months in PSR operations in 1996 and 1997 [7]. It is not known what the lifetime would be in operation at 3000 °K. This is an important R&D issue for the 5 MW rings.

6. Injection without Foils (laser-aided injection)

Given all the problems associated with the stripper foil, it would be very desirable to inject without foils. Laser stripping comes to mind as a possibility. H^0 can be efficiently produced by field stripping but photo ionization of the H^0 ground state takes a lot of short wavelength laser power and is not considered practical. In the past year, two promising new ideas have been proposed for charge-exchange injection without foils one by Y. Suzuki (JAERI) [8] and the second by I. Yamane (KEK) [9].

The layout for the Suzuki proposal is shown in Figure 7 and the profile of the undulator fields in Figure 8. His scheme makes use of a tapered undulator to strip H^- to the H^0 ground state, a laser system (ring resonator) to pump the H^0 ground state to the 3p state and a 7-period undulator (Figure 8) to ionize the 3p state. Referring to Figure 8, the laser beam pumps the H^0 ground state population to the 3p-state equilibrium population in the field-free regions and then the 3p-state population is field stripped to protons at the peak of the undulator field. This sequence is repeated 14 times in the undulator and results in a low fraction, 10^{-5}, of H^0 ground state at the exit of the undulator. The required laser power at 1062 nm is about 1 kW peak, 300 W average.

Suzuki's injection scheme was proposed for the 5 MW source at JAERI (SNF) and since then the ESS design team picked up on the idea and are developing an alternative lattice for the ESS ring using this concept. A logical next step toward development of this system would be an

experimental test with an H^- beam of around 1 GeV. Such as test is being considered, possibly with the 800 MeV H^- beam at LANSCE.

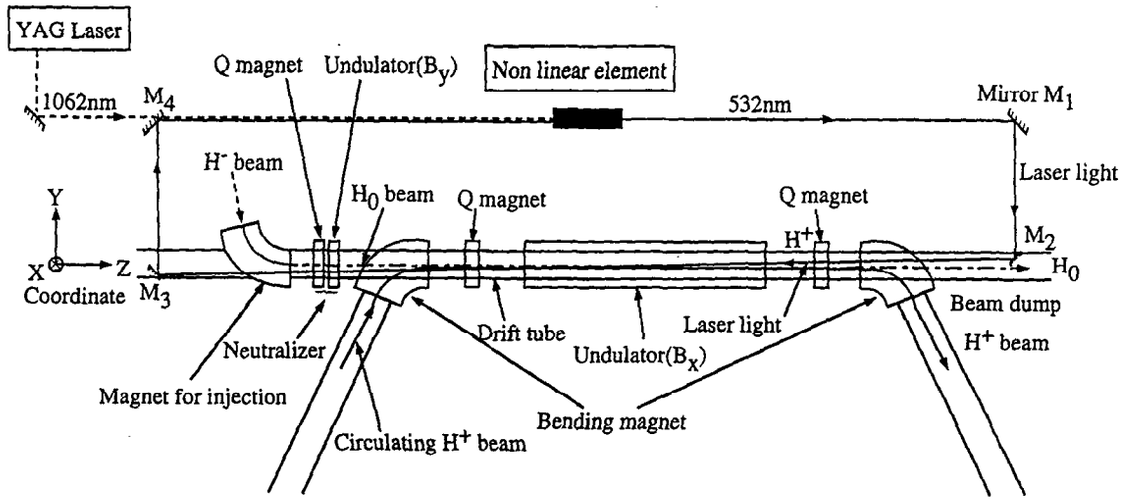

Figure 7. Layout for Suzuki's laser-aided injection system for SNF (JAERI) [8].

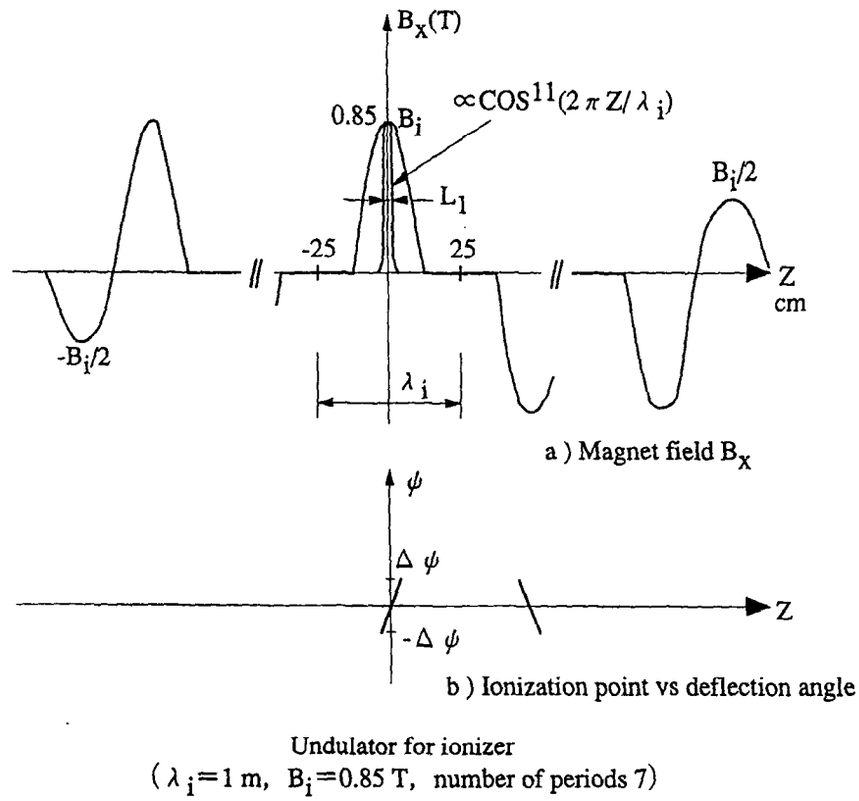

Figure 8. Undulator fields for Suzuki's laser-aided injection system.

The layout for another laser-aided injection system is shown in Figure 9. In Yamnane's concept nearly 100% of H^0 ground state population (obtained from Lorentz stripping H^- in a magnet) is pumped to 3p state by the optical Rabbi oscillation. The length of the collision region is chosen provide a π-phase advance of the oscillation (π pulse). The 3p state is Lorentz-stripped to

protons in another stripping magnet located at the exit of H^0-laser interaction region. There are fewer components in Yamane's concept compared to Suzuki's but the atomic and laser appears to be more delicate. Both ideas are appealing in addressing the goal of charge-exchange injection without foils.

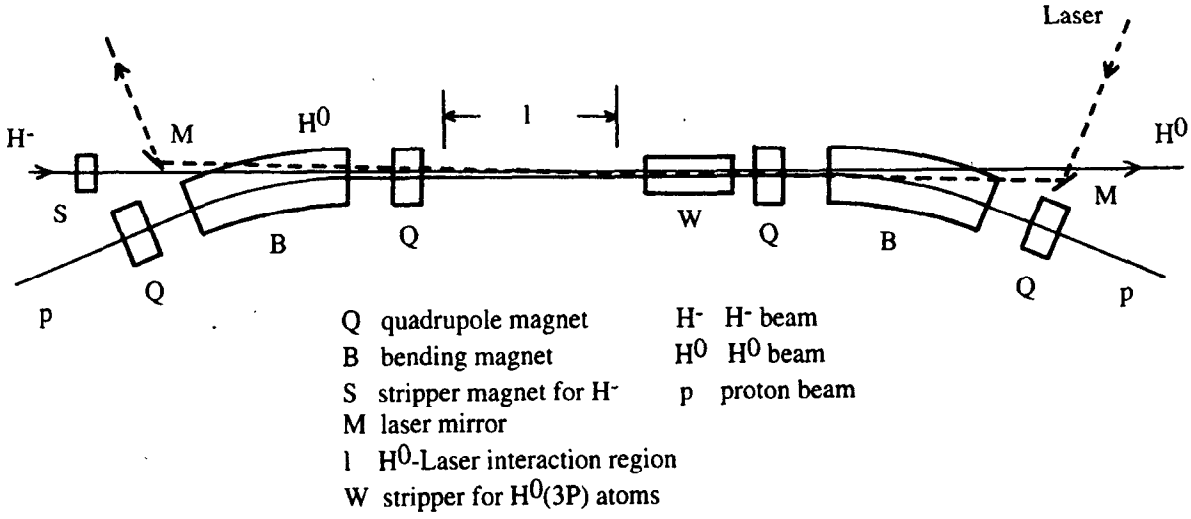

Figure 9. Layout for Yamane's laser-aided injection system [9].

7. Progress on the e-p Instability

Large and rapid beam loss from a fast instability can be a significant risk at high intensity rings. Peak intensity at PSR is limited by a strong instability that all available evidence indicates is the so-called e-p instability, which is a two-stream instability due to coupled oscillations of low energy electrons with the protons of the stored beam. In Neuffer's model, appearance of the e-p instability for a bunched beam requires both a source of electron (there are many at PSR, see Table V below) and a means of trapping some electrons during the passage of the "gap" in the bunched beam [10]. Calculations by Neuffer indicate that trapping which leads to an average beam neutralization, η, of ~1% is sufficient. His calculations also show that a small amount (<1%) of beam leaking into the gap is sufficient to trap electrons.

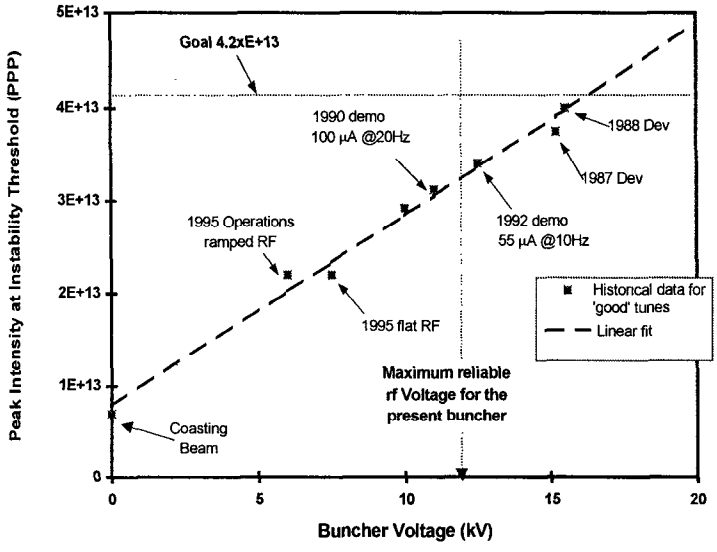

Figure 10. PSR instability threshold curve.

At PSR the stability is controlled primarily by rf voltage and proper tuning of the rf systems. The effect of the rf buncher voltage on the instability threshold intensity is shown in Figure 10. The instability shows up at ~7×10^{12} protons per pulse (PPP) for a coasting beam. The threshold

intensity increases as the buncher voltage is raised. At previous operating currents of 70 μA @ 20 Hz (2.2×10^{13} PPP) the threshold for instability was 6-8 kV (ramped). Various tests and demonstrations have carried the curve to higher intensities.

In 10 years of operating experience at PSR, much evidence has been accumulated supporting the e-p hypothesis [11]. This was discussed extensively at the Santa Fe Workshop [12]. Only the new evidence is presented here. Several experimental studies were carried out in 1997 with the goal of ensuring that the instability could be controlled to the level needed for 200 μA @ 30 Hz. The new studies included a systematic search for all the important control variables that affect the instability, further tests of the e-p hypothesis and a test of an inductive insert to passively compensate longitudinal space charge.

One of the most unambiguous predictions of Neuffer's model is the dependence of the frequency of the unstable motion on the threshold intensity, N, as shown in the following equation:

$$(2) \quad f = \frac{1}{2\pi}\sqrt{\frac{2Nr_e c^2(1-\eta_e)}{\pi b(a+b)R}}$$

Here N is the number of protons in the ring, r_e the classical radius of the electron, η_e, the average beam neutralization fraction, R, the radius of the ring , a, the vertical half size of the beam and b, the horizontal half size. The data plotted in Figure 11 show that the central frequency increases by a factor 1.4 for a factor of two increase in intensity which is in very good agreement with the expected factor of $\sqrt{2}$.

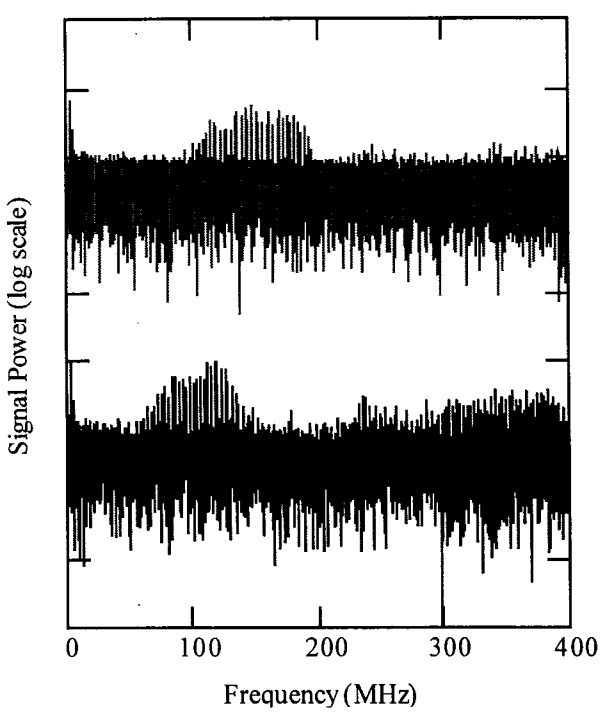

Figure 11. Frequency spectra at two beam intensities differing by a factor of 2.

The top spectrum In Figure 11 was obtained for an unstable beam with twice the intensity used for the bottom spectrum. Beam conditions for the two spectra are the same except for the beam intensity and buncher voltage. Both were taken for beams at the onset of instability.

Another expectation of the e-p model is an increase in threshold intensity as the beam size is increased. Recent measurements show that the threshold intensity increases with increasing vertical beam size.

In Neuffer's picture, a small amount of beam in the gap causes electron trapping. As a test of this idea, small but controlled amounts of beam were introduced into the gap by inhibiting chopping for a few turns of injection. As expected, the threshold was lowered as more protons were placed in the gap.

One question that is often raised is why this instability is not seen at other present day accelerators. In the past year or two there have been observations of fast instabilities at the KEK booster [13] and the CERN PS booster. It is not known if these are e-p, but it is possible.

The knowledge of the e-p instability gained at PSR has been put to good use in the design of the new machines as evidenced in the comparisons shown in Table V. The new machines, SNS and ESS, have introduced measures to greatly reduce the number of low energy electrons generated from a variety of mechanisms. In addition, the new machines will have higher rf voltage and a longer beam free gap, measures that will reduce the trapping of electrons during passage of the gap. One note of caution concerns electrons produced by beam-induced multipactor. At PSR, large numbers of electrons are suspected (but not proven) to come from beam induced multipactor. This source of electrons is not addressed in the design of the new machines.

Table V. Parameters that control the e-p instability.

Source	PSR 97	PSR 98	SNS	ESS
"Convoy" e's from H^-/H^0 stripping	1	2	blocked	blocked
Secondaries from foil	7	0.7	blocked	blocked
Secondaries from beam losses (0.1-100/lost proton	0.0006-0.6	0.00015-0.15	0.00001-0.01	0.00001-0.01
Residual gas ionization	<0.01	<0.01	<0.001	<0.0001
Beam-induced multipactor	?	?	?	?
Total	~8+?	~2.7+?	10^{-5} - 10^{-2}+?	10^{-5} - 10^{-2}+?
Length of Beam Gap (ns)	100	100	250	200
Max rf voltage/turn (kV)	12	18	40	27

8. Inductive Inserts

One of the functions of the rf system in a ring is to overcome the longitudinal space charge force which tends to push beam into the gap and thereby lowers the e-p instability threshold. The net voltage per turn, V_s, from space charge self-voltage and inductive wall impedance (below transition) is given by:

$$(3)\quad V_s = \frac{\partial\lambda(s)}{\partial s}\left[\frac{g_0 Z_0}{2\beta\gamma^2} - \Omega_0 L\right] e\beta c R$$

Here $\lambda(s)$ is the line density of charge, $g_0 = 1 + 2\ln(b/a)$, b the vacuum pipe radius, a the beam radius, $Z_0 = 377$ ohms, Ω_0 the angular frequency of revolution, L the wall inductance and R the mean radius of the ring. The idea of the inductive insert is to add sufficient ferrite to increase L until V_s vanishes.

Inductor tests at PSR carried out by a LANL and FNAL collaboration [14] had three main goals:

- provide a check on space charge compensation;
- measure the effect of the inductor on the PSR instability threshold and
- check that the inductor has no unexpected, deleterious effects on the ring operation.

During the 3-day test with the inductor in place, no unusual problems arose in the operation of the ring that could be attributed to the inductor. A check on space charge compensation was made by measuring the bunch broadening for a narrow (50 ns) pulse and comparing to simulations. The effect was not large but it was reproducible and agreed with the ACCSIM simulations.

The effect of the inductive insert on the e-p instability was studied by measuring the threshold intensity as a function of buncher rf voltage. The results are plotted in Figure 12 along with historical data and other 1997 data. The highest intensity point of the inductor data (triangle symbols) lies to the left of the historical trend line and indicates that less rf voltage was needed to keep the beam stable. However, it is not possible to draw a strong conclusion since other points, not involving the inductor, also lie to the left of the trend line. It is perhaps fair to say that the highest intensity point shows a two-standard deviation effect, which is encouraging but not conclusive or definitive. The effect would be more convincing if contemporaneous measurements of the threshold curve were made with the inductor at full its maximum value and another at a low value. Time ran out before this could be done.

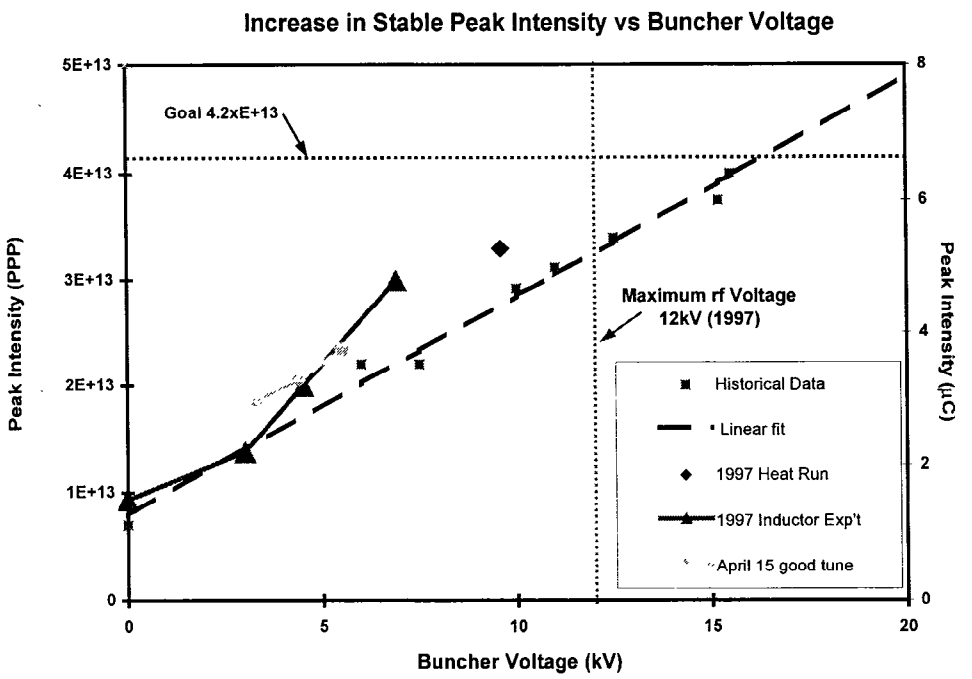

Figure 12. Effect of an inductor on the PSR instability threshold curve.

9. Conclusions

The advent of the new projects for 1-5 MW short pulse sources and other high intensity proton rings has prompted new work on intensity limitations in proton rings and new work on the technologies needed for high intensity. Good, incremental progress has been made in some areas and good beginnings in others. From today's perspective the major issues for the immediate future are the peak intensity from the ion-source and linac (not discussed here), beam losses in the ring, the e-p instability and stripper foil technology.

The PSR has proven to be a good test bed for the linac-accumulator ring option. Its operation has identified important problems that need to be solved for the next generation rings. It is important for future accumulators to fully understand the PSR instability and means to control it.

The recent ideas for laser injection that eliminate the need for stripper foils are quite appealing. However, it is too early in their development to predict the final outcome

10. References

[1] R. Baartman, "Betatron Resonances with Space Charge Due to Self-Fields", Proceedings of Workshop on Space Charge Physics in High Intensity Hadron Rings, May 4-7, 1998, Pridwin Hotel, Shelter Island, Long Island, to be published.

[2] Sessions on simulations, Proceedings of Workshop on Space Charge Physics in High Intensity Hadron Rings, May 4-7, 1998, Pridwin Hotel, Shelter Island, Long Island, to be published.

[3] J Galombus, private communication.

[4] SNS Design manual, June 1998, p 5-98.

[5] R. Hutson and R. Macek, "First Turn Losses in the LANSCE Proton Storage Ring", Proceedings of the 1993 Particle Accelerator Conference, p. 363, 1993.

[6] M. Gulley et al, "Measurement of H^-, H^0 and H^+ yields produced by foil stripping of 800-MeV H^- ions", Phys. Rev. A53 (1996), p 3201-10.

[7] I. Sugai et al, "Development of thick, long-lived carbon stripper foils for PSR of LANL", NIM A 363 (1995) p 70-76.

[8] Y. Suzuki, private communication.

[9] I. Yamane, "A new scheme for H^- charge exchange injection without hazardous stripping foils", KEK Prepring 98-42, May 1998, to be published in Physical Review Special Topics: Accelerators and Beams.

[10] D. Neuffer et al, "Observations of a fast transverse instability in the PSR", NIM A321 (1992), p 1-12.

[11] M. A. Plum et al, "Recent Experimental Evidence for the Los Alamos Proton Storage Ring Instability", Proceedings of the 1997 Particle Accelerator Conference, 12-16 May 1997, Vancouver, BC, Canada, to be published.

[12] Proceedings of the Santa Fe Workshop on Electron Effects, March 5-7, 1997, LANL report, LA-UR-98-1601.

[13] Y. Irie et al, "Electron-Proton or Ion-Oscillation-Like Instabilities in the KEK Booster Synchrotron", Proceedings of the International Workshop on Multibunch Instabilities in Future Electron and Positron Accelerators, July 15-18, 1997 KEK, Tsukuba, Japan, p 247-255.

[14] M. A. Plum et al, "Experimental Study of Passive Compensation of Space Charge Potential Well Distortion at the LANL Proton Storage Ring", PSR Tech note 98-013, April 1998.

ICANS-XIV
14th Meeting of the International Collaboration on
Advanced Neutron Sources
June 14-19, 1998
Starved Rock Lodge, Utica, Illinois, USA

Report on the International Workshop on Cold Moderators for Pulsed Neutron Sources

J. M. Carpenter
Intense Pulsed Neutron Source
Argonne National Laboratory
Argonne, IL 60439

The International Workshop on Cold Moderators for Pulsed Neutron Sources resulted from the coincidence of two forces. Our sponsors in the Materials Sciences Branch of DOE's Office of Energy Research and the community of moderator and neutron facility developers both realized that it was time. The Neutron Sources Working Group of the Megascience Forum of the Organization for Economic Cooperation and Development offered to contribute its support by publishing the proceedings, which with DOE and Argonne sponsorship cemented the initiative.

This workshop was the second of its kind. The earlier one, the International Workshop on Cold Neutron Sources, took place at Los Alamos National Laboratory March 5–8, 1990 [1].

Although originally our idea was to convene the meeting on the windswept shore of Lake Michigan in February, this and other notions for venues and dates did not work out. Finally we took the waning opportunity to use Argonne's *gemütlich* old Freund Lodge. The workshop took place September 28–October 2, 1997, with meals served in the Lodge and meetings held in the IPNS office area. Participation was by invitation, which, as workshop organizer, I arranged after consulting with my colleagues who are prominent in the field. Thirty-two scientists took part, representing sixteen institutions from eight countries, on four continents in two hemispheres. This demonstrates the 2^n rule of conference organization (an unplanned outcome) and the unity of one world in science. Laura J. Miller served as our super-effective workshop secretary during all phases of workshop planning and execution.

The purposes of the workshop were:

- to recall and improve the theoretical groundwork of time-dependent neutron thermalization
- to pose and examine the needs for and benefits of cold moderators for neutron scattering and other applications of pulsed neutron sources
- to summarize experience with pulsed source cold moderators, their performance, effectiveness, successes, problems and solutions, and the needs for operational data
- to compile and evaluate new ideas for cold moderator materials and geometries
- to review methods of measuring and characterizing pulsed source cold moderator performance
- to appraise methods of calculating needed source characteristics and to evaluate the needs and prospects for improvements
- to assess the state of knowledge of data needed for calculating the neutronic and engineering performance of cold moderators, and
- to outline the needs for facilities for testing various aspects of pulsed source cold moderator performance.

A reception followed by dinner on Sunday evening at the Freund Lodge prepared the participants for the workshop. Plenary sessions consumed the first day and a half, following

which participants met in Working Groups designated to undertake discussions in six topical areas. Some participants offered their presentations as posters.

Bruce Brown, IPNS director, set the workshop in motion at an early hour Monday with his welcoming remarks. After an explanation of the organization of the workshop, Jack Carpenter provided some background information on the development of cold sources and on some fundamentals. Five sessions with twenty-minute talks and ten-minute discussions followed, with overviews given by Kent Crawford on an instrument designer's point of view, and Günter Bauer on pulsed moderator concepts. The second session, on existing pulsed source cold moderators, included presentations by Tim Broome (ISIS), Michi Furusaka (KENS, also describing plans for moderators at the N-arena at the planned JHP), Phil Ferguson (MLNSC), and Alexandre Beliakov (IBR-2). A third session, on existing steady source moderators, comprised talks on the sources at NIST (Bob Williams), Kurchatov (Mikhail Zemlyanov), and SINQ (Harald Spitzer). The subject of the fourth session was new pulsed sources, in which Noboru Watanabe described the plans at JAERI, and Tony Gabriel those at ORNL, while Lowell Charlton reported his recent Monte Carlo results and Trevor Lucas the designs for L-H_2 cold sources for HFIR and SNS.

The fifth session addressed calculations and measurements and included talks by Gary Russell on MLNSC L-H_2 spectral data and calculations, Torben Brun on pulse shapes of the MLNSC L-H_2 moderators and the ortho-para question, Luke Daemen on calculations of the same things, and David Picton on his calculations of the ISIS L-H_2 cold source. Erik Iverson reported on recent measurements and calculations on the IPNS solid and liquid methane moderators. Dinner at the Freund Lodge ended the last session of the day nearly twelve hours after the start.

During breaks for coffee and lunch, participants viewed posters on display. There were five: Erik Iverson's on absolute spectrum measurements of IPNS moderators, Karsten Stendal's on L-H_2 cold moderator systems at GKSS, HMI and Risø, Harry Jones's on the ISIS cold moderators, Hans Ludewig's on the HFBR L-H_2 moderator, and Terry Scott's and Martha Miller's on the IPNS solid methane moderators.

In a laboratory near the break rooms was a moderator zoo, which contained cutaway examples of ISIS L-H_2 and L-CH_4 moderators, an assembled grooved IPNS S-CH_4 moderator, a flat, yet-to-be-assembled, IPNS S-CH_4 moderator and a set of IPNS graphite inner reflector blocks.

The sixth session, on the subject of scattering kernels for cold moderator materials, again began early with a talk by Rolando Granada about his technique for constructing synthetic kernels, and one by Bob MacFarlane on the kernels that he has produced for cold moderator materials. In the seventh session, devoted to new materials, testing, and applications, Yoshiaki Kiyanagi described the facility at the Hokkaido electron linac and recent measurements on mixed polyethylene-L-H_2 moderators, and László Cser brought forward his suggestions for methylated benzene moderators. Genya Shabalin related his results of measurements and theoretical analysis of the burping phenomenon in the cold solid CH_4 moderator at IBR-2. Jack Carpenter stood in for Paul Sokol for his talk on the Cold Neutron Irradiation Facility at the Penn State Reactor, and Dick Lanza surveyed the prospects for small accelerator-based pulsed neutron sources, emphasizing recently developed compact systems.

After lunch, the final talk was by Jack Dorning, who reviewed alternative (to Monte Carlo) methods of calculation, general features of the time-dependent neutron thermalization problem, approaches to moderator characterization that we should but don't now use, and who appraised the general non-linear dynamical problem we call burping.

Participants split up for tours of IPNS for an hour before boarding the bus for an excursion to Chicago. We enjoyed a guided tour of Chicago's new Museum of Contemporary Art and relaxed in the sculpture garden in the shadow of the Hancock Building. Dinner at the Blackhawk Lodge nearby capped the day.

All day Wednesday and Thursday morning, participants broke into working groups for discussions on seven topics. Gary Russell chaired discussions on scattering kernels and

cross sections, Tim Broome chaired a group on the creation of a moderator performance database (to be set up on the Web), Dick Lanza led a group on applications of cold sources, large and small, and Günter Bauer chaired discussions of needs and opportunities for testing facilities. Tony Gabriel led a working group on calculational methods and Noboru Watanabe led the group that worked to define a "round robin" set of standard measurements and methods for characterizing pulsed cold moderators. After dinner on Wednesday, everyone convened for a brainstorming session which Kent Crawford led, listing ideas for new materials and new concepts. It, as well as the scientists' endurance, lasted for two hours.

Everyone willingly worked long, thought hard, and brought a trove of new information and ideas. The full difficulties of some of the tough problems came to light. The difficulties of modeling, characterizing, understanding, measuring, representing the spectra and pulse width characteristics of the mixed ortho- and para- liquid hydrogens were recurring themes. People left with new determination to perform careful measurements and calculations, not least among these, to devise means to determine the ortho/para ratio in situ. Its attractiveness as a moderator and the resistance of cold solid methane to understanding of its unstable behavior continue to absorb those concerned with cold moderator systems. More measurements are needed, and more analytical work. The admittedly small library of cross section data does not stand the tests of measurements. Working groups identified certain changes that will be made in short order and agreed that the workers present represent an eligible testing group who can evaluate new cross section data before widespread dissemination. Another group set in motion the processes of compiling a moderator performance data base and of measuring and inter-comparing pulsed source moderator data worldwide. Some new, hopeful results came to light, namely very likely-looking prospects for a "100 K" (liquid methane-like) moderator; liquid propane, long in successful service at the Kurchatov reactor, and composite systems such as $L\text{-}H_2$+$L\text{-}H_2O$ and mixed $L\text{-}H_2$+$(CH_2)_n$, which may offer prospects for tailoring of performance.

After lunch on the last day, Thursday, the workshop reconvened to hear reports of the Working Groups, delivered by their chairs, then adjourned in mid-afternoon.

We re-formatted most of the submitted manuscripts and carried out a gentle edit, consulting with the authors on what we thought were significant points. Erik B. Iverson served as co-editor with me. The Proceedings will soon be available as a Megascience Forum publication, and in electronic form on the World Wide Web through the IPNS home page.

At the beginning, as Organizer, I charged the participants, "Only rarely has a community such an opportunity as this. We have that opportunity and therefore the obligation TO DEFINE THE STATE OF THE ART OF PULSED SOURCE COLD MODERATOR DESIGN and TO SEND THE FIELD IN A NEW DIRECTION. LET'S DO IT!" They accomplished much toward fulfilling the purposes of the workshop and responding to the charge. I believe that much further will result from the initiatives that were launched and the spirit of collaboration and communication that began there.

REFERENCE

[1.] "International Workshop on Cold Neutron Sources," Los Alamos National Laboratory, March 5-8, 1990, editors G. J. Russell and C. D. West, Los Alamos report LA-12146-C/ UC-413, August, 1991.

ICANS-XIV
14th Meeting of the International Collaboration on Advanced Neutron Sources
Starved Rock Lodge, Utica Ill., USA
June 14-19, 1998

The ACoM Collaboration
An International Effort to Develop Advanced Cold Moderators

G.S. Bauer

Paul Scherrer Institut, Ch-5232 Villigen-PSI, Switzerland

Abstract

Several laboratories world wide have decided to join forces in developing a cryogenic moderator system that would come close to what one can obtain from solid methane but would solve the problems associated with the use of solid methane in high radiation fields. The concept is based on a heterogeneously cooled pellet bed from which the pellets would be periodically removed to release the stored energy with minimum perturbation of the source operation. In addition to methane other potential moderator materials are examined.

1. Introduction

With new, high power spallation sources currently being proposed and designed in several locations world-wide [1], [2], [3], [4], [5], the need for efficient cold moderators that can operate at source beam power levels of 1 MW and above becomes pressing. Users requests to the moderator characteristics [6], [7], that resulted from extensive consultations are summarized in Table 1.

Table 1:. *Users' requests to moderator characteristics for ESS and SNS to meet the requirements of the next generation pulsed source instruments and science Numbers before and behind the / refer to the high repetition and low repetition rate target stations respectively. ESS planners were not offered an intermediate temperature option*

	Ambient temperature	Intermediate temp. (100 K)	Cryogenic (25 K)
	ESS: 50 Hz / 10 Hz		
High intensity	0 / 0		0 / 8
High resolution	9 / 0		15 / 12
	SNS: 60 Hz / ≤20 Hz		
High intensity	0 / 0	0 / 0	0 / 9
High resolution	4 / 0	11 / 6	1 / 6

Keywords: Cryogenic moderators; methane; methane hydrate, radiation effects; density of states

This table clearly demonstrates the trend to take advantage of two possibilities in the next generation neutron sources

1. to exploit the high phase space density of neutrons at low energies offered by cryogenic moderators and

2. to use the extra neutron flux on these sources to improve the resolution of the instruments by working with narrow pulses of good shape.

In a workshop sponsored by the OECD and held at Argonne, Ill., in September 1997, possibilities of improving cryogenic moderators for pulsed sources were scrutinized in detail [8] and several opportunities for improved understanding of cold moderators and for novel developments were identified. One outcome of this conference is that the ESS-task group on cold Moderator development that had existed previously was expanded into a world wide collaboration to which representatives of the following institutions have, so far, agreed to subscribe:

Forschungszentrum Juelich (FZJ), Germany) *
Paul Scherrer Institut (PSI), Switzerland *
Risø National Laboratory, (RNL) Denmark *
Rutherford Appleton Laboratory (RAL), UK *
Argonne National Laboratory (ANL), USA
Brookhaven National Laboratory (BNL), USA
Centro Atomico Bariloche (CAB), Argentina
High Energy Accelerator Research Organisation (KEK) Japan
Japan Atomic Energy Research Institute (JAERI) Japan
Joint Institute for Nuclear Research (JINR), Russia
Oak Ridge National Laboratory (ORNL), USA
University of Hokkaido (UH) Japan

* Member of the original ESS-task group

The charter meeting of the expanded collaboration (ACoM-2) was held on Feb. 24 and 25, 1998 at Paul Scherrer Institut, Switzerland. At that meeting the author of this paper was charged to act as spokesman of the collaboration. A Memorandum of Understanding was drafted that was subsequently sent out to the interested laboratories for comments and completion. A follow-up meeting was hosted by Oak Ridge National Laboratory on June 11 and 12, 1998, in which details of the responsibility to be taken on by the participating institutions were worked out. The present paper describes the scientific and technical ideas underlying this collaboration and the working plan the group agreed upon.

2. The potential and characteristics of cryogenic moderators

Cryogenic moderators have become an essential asset in the utilization of research neutron sources over the past decades. This is true for continuous sources such as SINQ and research reactors as well as for pulsed sources. While both types of sources have the common goal of providing the highest possible flux of cold neutrons, pulsed sources have the additional

requirement of a short pulse duration. This makes the route chosen for some continuous sources, namely a relatively large volume of 20 to 30 liters of liquid deuterium at 25 K embedded in a thermal moderator vessel impractical. Such cold moderators are of the "re-thermalizing" type, i.e. they accept neutrons in thermal equilibrium at ambient temperature from their surroundings and establish (more or less) a new equilibrium at their low temperature. By contrast, pulsed source cryogenic moderators should slow down the source neutrons as fast as possible and in as small a volume as possible all the way from their original energy of around 1-2 MeV through almost nine orders of magnitude in energy. Design criteria and engineering aspects for cold moderators have been reviewed recently [9] and only a brief summary will be given here:

Clearly, Hydrogen, being of the same atomic mass as a neutron, is most efficient in picking up a large fraction of the neutron's energy in a single collision and is, therefore, the most desirable moderator substance. The cross section of hydrogen and hence the mean free path between two collisions being nearly constant in the whole slowing down regime, the time a neutron lives in a given energy interval is inversely proportional to its velocity. Consequently the product of the neutron velocity and pulse width is a constant whose magnitude is inversely proportional to the number of hydrogen atoms per unit volume. Another important requirement to a good cryogenic moderator material is that it should have sufficiently low-lying modes in its energy spectrum to which slow neutrons can couple. While liquid hydrogen has a rather low density, a material with very good properties in this respect is solid or liquid methane which has nearly free rotational modes at 1 meV. It is for this reason that early, low power pulsed spallation sources used solid methane at low temperatures (around 15 K) with great success. Gains of a factor of 3.5 in cold neutron intensities for wavelengths above 0.4 nm for solid methane relative to liquid hydrogen have been measured for an identical geometry for the time average flux [10], with even better performance in the pulse. Gains may be somewhat lower if the moderator geometries are optimized individually, but will still be more than a factor of 2.5, which certainly makes a solid methane moderator a highly desirable feature on any pulsed neutron source. However, even at a few kW of beam power (ESS is planned to run at 5 MW !), a phenomenon called "burping" has been observed, which manifested itself in a sudden energy and gas release after a certain irradiation dose and which can lead to the destruction of the container. This phenomenon now is largely understood and solid methane moderators are still in use at low power sources but must be warmed up at regular intervals to release the stored energy. In view of these difficulties, intermediate power sources (ISIS, 160 kW) use liquid hydrogen as their cryogenic moderator and liquid methane at 100 K. However, even liquid methane suffers from radiation damage and the radicals form higher polymers that cling to the walls of the moderator vessel and tubes and eventually lead to complete blockage of the system. Currently ISIS has developed a system that allows online replacement of the liquid methane every two days (i.e. after 0.3 MWd), but still the moderator vessel is replaced twice a year (i.e. after 300 mAh or 10 MWd) because the polymerization products continue to build up [11].

3. The general concept of an advanced cryogenic moderator

Since solid, hydrogen rich materials with low-lying energy modes clearly offer the best chance to accomplish the goal of an improved moderator system, ways should be sought to use a good solid moderator. While the need for heat removal, together with the low thermal conductivity at low temperatures, requires the use of relatively finely dispersed material, the desire to achieve a fairly high average hydrogen density let the collaboration choose a concept, in which pellets - preferably spherical ones- would be cooled by liquid or supercritical hydrogen and would be removed from the moderator vessel after as short enough residence time to avoid spontaneous release of stored energy. According to first estimates this would have to happen every 20 minutes, or so [12]. One possibility to accomplish this was presented at the ICANS XIII-meeting [13]. It involves the use of a continuously operating mechanical device (e.g. a helical screw bar) to remove the moderator pellets from the vessel. In contrast to the original concept which foresaw melting of the pellets after each passage, the preferred solution now is periodic heating to a temperature where the stored energy is released (Fig. 1). This makes the overall process technology somewhat easier. Batch disposal of the pellets would become necessary when the performance of the moderator starts to degrade due to non-annealable radiation effects.

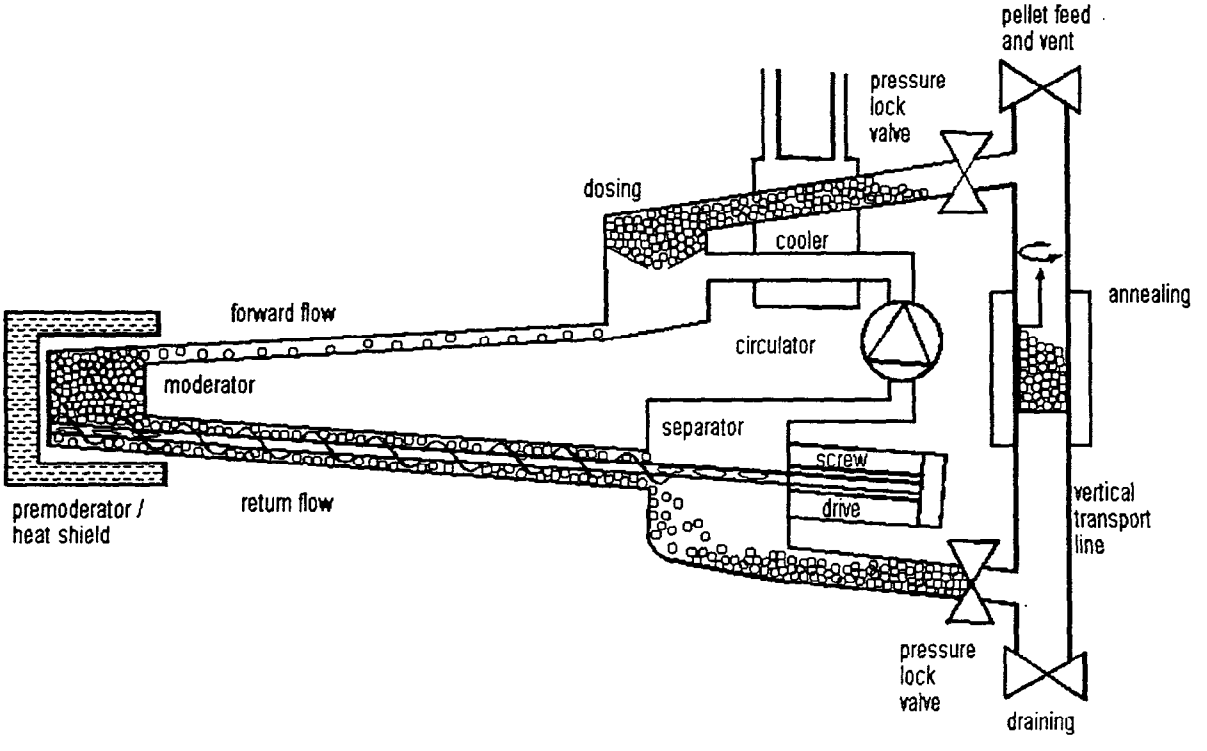

Figure 1: Scheme of a pelletized moderator system with mechanical removal of the pellets from the moderator vessel and recirculation after heating for stored energy release.

A second possibility to transport pellets into and out of the moderator vessel that is more in line with current concepts of moderators that are supplied from and removed to the top of the target block is also considered [14]. This involves fluidizing the pebble bed prior to emptying and "blowing" the pebbles out pneumatically by reversing and increasing the flow of hydrogen. This concept requires some extra volume in the moderator vessel to enable fluidization. The consequences of this "void" and other technical requirements on neutronic performance will have to be studied in detail.

Other options, such as in situ melting of the pellets are also considered, but it will have to be shown that this does not defeat the idea of removing the polymerization products without giving them a chance to cling to the walls and build up a solid or tar-like layer there. This option also depends strongly on the type of moderator material chosen.

4. Some candidate moderator materials

The most popular material for cryogenic solid moderators is clearly methane, which is known to have worked well in low power applications due to the nearly free rotational states of the CH_4-molecule at low temperatures, which gives rise to energy levels at 1 meV and above. Although a wealth of studies on the lattice and molecular dynamics of methane have been performed, little is known on its physical and mechanical properties. Collecting such information is important if transport by mechanical or pneumatic means is foreseen, because excessive deformation, abrasion or breaking of pellets would certainly be difficult to cope with.

Another opportunity to take advantage of the nearly free rotation of methane in a cage is the use of methane hydrate (clathrate). Under certain conditions significant amounts of methane can be stored in the cage-structure of ice. Ice is known to exist in a large number of different modifications, depending on the environmental conditions. The structure that can store methane (and other "small" molecules) is shown in Fig. 2. The degree of filling of the cages depends on pressure and temperature (Fig. 3) but, when all possible cages are occupied, up to 0.17 CH_4-molecules per H_2O-molecule (y=1) can be stored, increasing the hydrogen density by as much as 34 %. From the phase diagram of the CH_4-H_2O system, shown in Fig. 4, it can be seen that making clathrate, while not excessively difficult, is not as straight forward a process as making ice. Suitable methods to fabricate clathrate pellets will have to be developed by the collaboration, if this system is to be used. Fortunately, once trapped, the methane escapes from the ice only very slowly when kept at atmospheric pressure around -20°C.

Experimental data on the frequency spectrum of methane-hydrate are shown in Fig. 5. It can be seen that, compared to the frequency spectrum of water (which is well reproduced in the top frame, cf. Fig 6), the low energy modes are very intense. Note the change in scale between the frames.

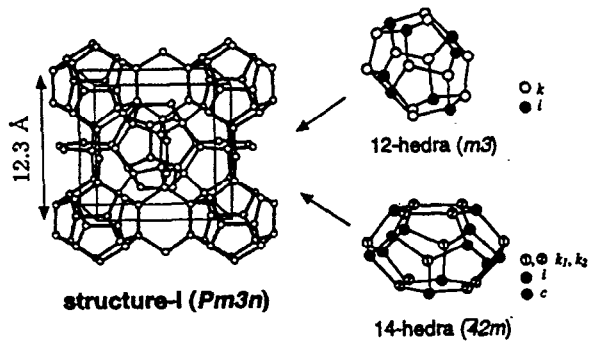

Figure 2: Structure of Hydrates (Structure 1), composed of 12-hedral and 14-hedral "cages" in which methane molecules can be "trapped".

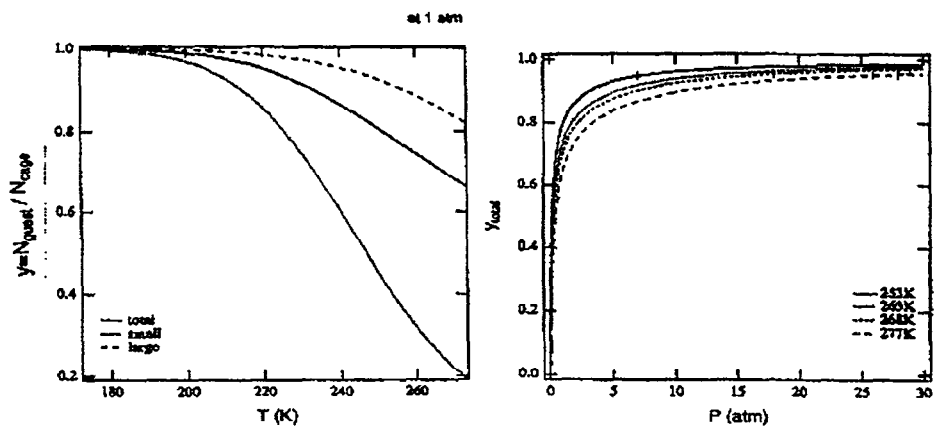

Figure 3: Degree of occupancy of the ice cages by methane as a function of pressure and temperature; y=1 corresponds to ~0.17 CH_4-molecules per H_2O-molecule

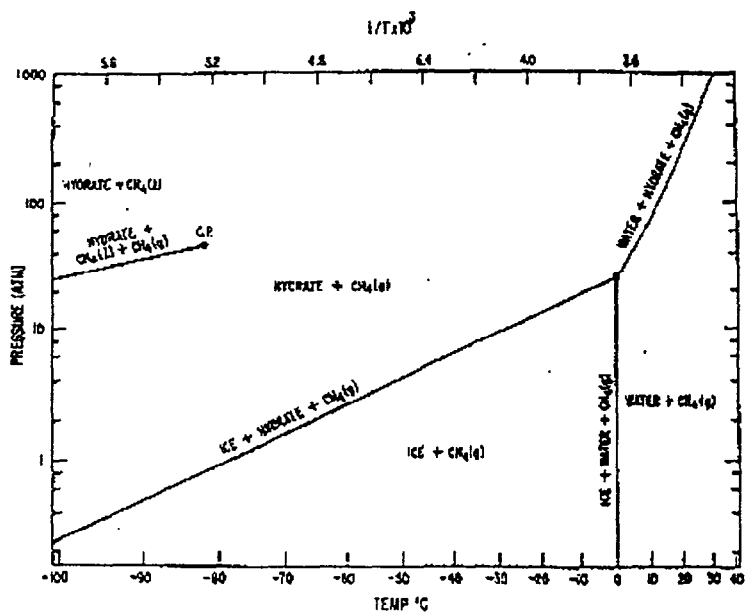

Figure 4: Phase diagram of methane-water

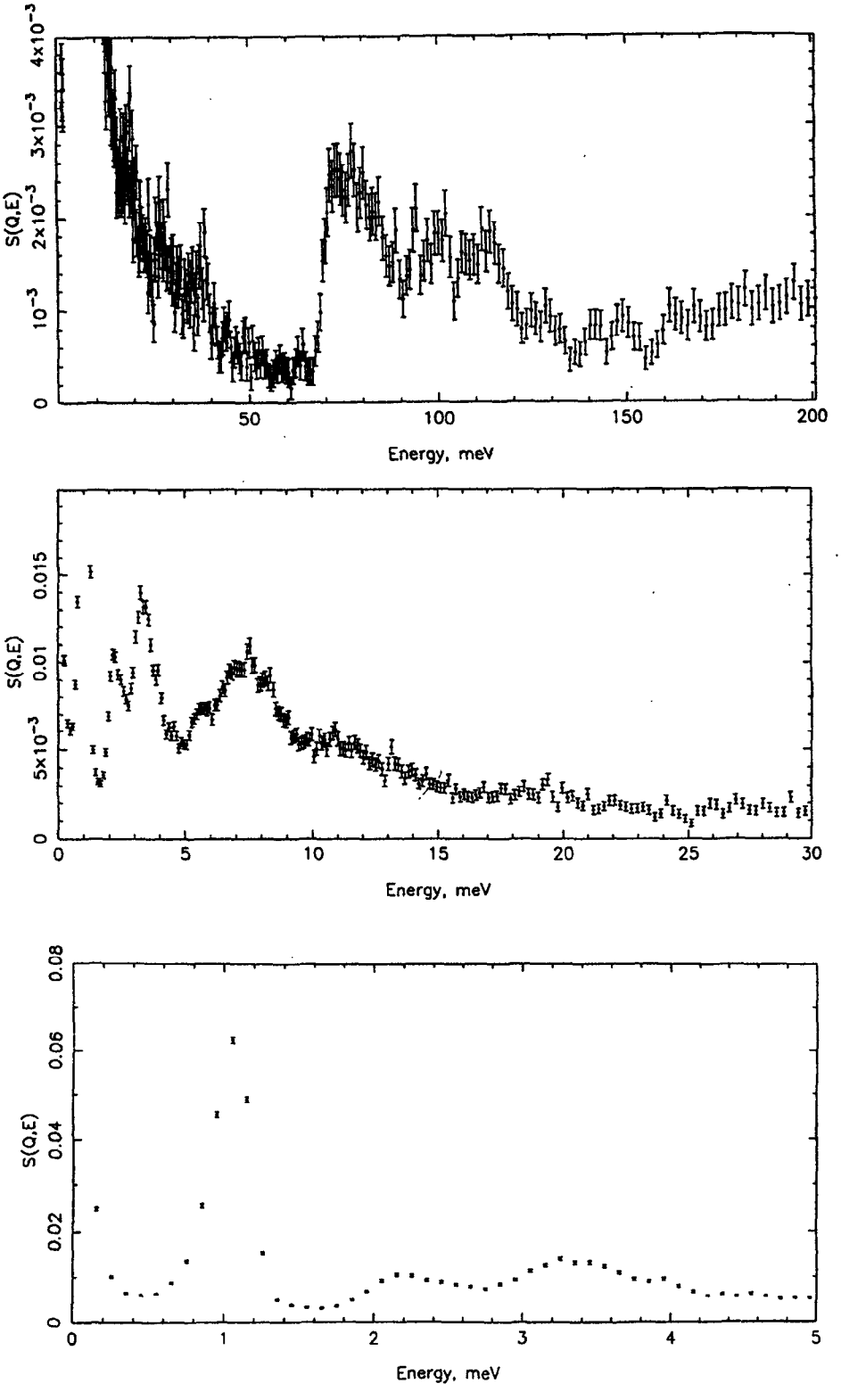

Figure 5: Frequency spectrum of methane hydrate [15]. The three frames show consecutively enlarged sections of the low energy spectrum. Note the change in scale from top to bottom.

The respective spectrum of pure water ice is shown in Fig. 6. In contrast to methane hydrate, pure water ice has no significant density of states below 7 meV and most of the spectrum is concentrated above 65 meV. (This part is also clearly seen in the top frame of Fig. 5).

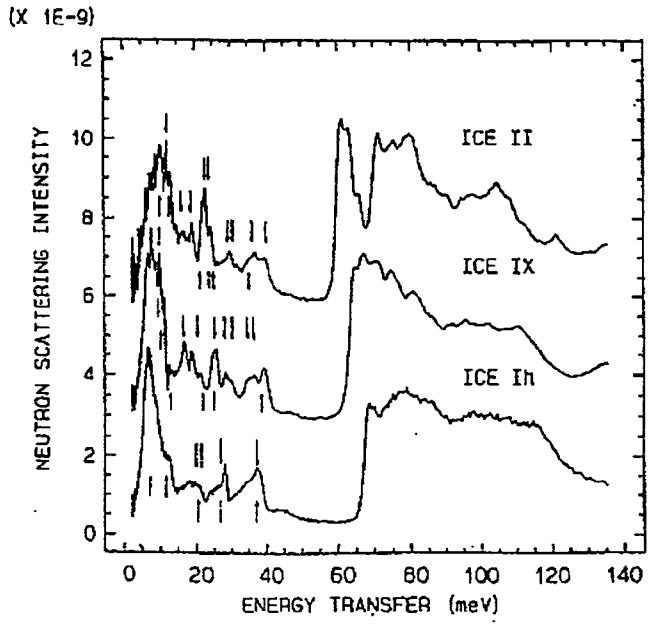

Figure 6: Frequency spectrum of H_2O ice, measured by incoherent inelastic neutron scattering (from [16]). The arrows above the spectra refer to peaks seen in the Raman and those below to peaks seen in the IR.

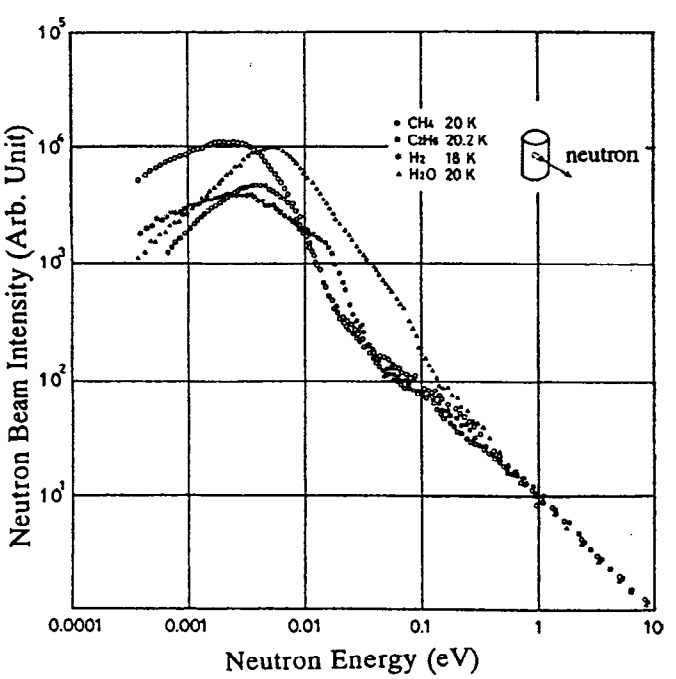

Figure 7: Measured neutron spectra from different moderator materials at 20 K [17]

From measured neutron energy spectra for different kinds of moderators, shown in Fig. 7, it is obvious that H_2O-ice is an excellent moderator down to its lowest frequency mode of about 7 meV. Below 5 meV CH_4 is clearly superior. The hope associated to the use of liquid hydrogen cooled methane hydrate clearly is that the favorable properties of the three materials could be combined to generate a moderator of high performance in the whole energy regime of interest.

Although numerous questions relating to this system, such as radiation damage, mechanical properties at 20 K etc. must still be investigated and several technical problems must be solved, the prospect of improving the performance of cold sources in this way make this a worthwhile effort.

Although methane hydrate, next to methane, is currently the main focus of R+D activities in the collaboration, other opportunities of finding suitable moderator materials are explored as well. This includes examination of different substances, such as propane, and ways to store them in solid materials, in particular different kinds of zeolites or other cage structures.

5. The ACoM working plan

In its charter meeting on Feb. 24 and 25 at Paul Scherrer Institut, Switzerland, the collaboration agreed to set a goal for the decision on the final system to be pursued, which is the end of the first quarter of the year 2000. Until then the following milestones have been agreed upon:

01/1999 Working model(s) for pellet transport at room temperature ready

06/1999 Moderator materials: neutronic performance examined in low power facilities; scattering kernels developed and integrated in NJOY

03/2000 Moderator materials: radiation effects assessed
pellet production: method demonstrated
decision on proceeding with full scale low temperature test rig (outside radiation field)

If funding for the final test rig can be found, the goal would be to have a facility working outside a radiation field by the end of the year 2002. This facility would then be used to gain "hands on" experience with such a system and to study its behavior under various conditions before a final cryogenic moderator for use on a spallation source could be designed.

As a more short term solution to the problem of increasing the moderator performance in the intermediate energy range, the ORNL group is following up on the concept of placing a thin ("semi-transparent") liquid H_2 moderator in front of an ambient temperature water moderator in order to profit from the high phase space density regions of both types. While this is not expected to match an optimized pellet system in the whole spectral region, calculations have yielded promising results and the system would certainly be much simpler and is based exclusively on existing technology. The collaboration as a whole supports this effort.

6. References

[1] "ESS, A Next Generation Neutron Source for Europe"; Vol. III, The ESS Technical Study; G.S. Bauer, T.A. Broome, D. Filges, H. Jones, H. Lengeler, A. Letchford, G. Rees, H. Stechemesser, G. Thomas, eds. The ESS Council, ESS-96-53-M; ISBN 090 237 6659 (1997)

[2] B. Appleton, SNS status report, this conference

[3] M. Furusaka, JHF status report, this conference

[4] T. Mukaiyama, Y. Oyama, M. Mizumoto, T. Takizuka, R. Hino "Neutron Science Project at JAERI" Proc. Top. Meeting on Nuclear Applications of Accelerator Technology, Albuquerque, ANS Order No. 700249 (1997) pp 398-404

[5] G.J. Russell, E.J. Pitcher, P.D. Ferguson, B.W. Patton "Long Pulse Spallation Source Neutronic Performance" J. Neutron Research, **6,** (1997) pp. 33-62

[6] "ESS A Next Generation Neutron Source for Europe", Vol.2, The Scientific Case; ESS Council, (March 1997), ISBN 090 237 6 608

[7] Instrumentation for a High-Power Pulsed Spallation Neutron Source" Proc. of an NSNS workshop held at Oak Ridge, Ten Oct 31 - Nov 1, 1996, ORNL (May 1997)

[8] Proc. International Workshop on Cold Modeators for Pulsed Neutron Sources Argonne, Ill. Sept 28 -Oct 2, 1997

[9] G.S. Bauer "Pulsed Neutron Source Moderator Design and Engineering" in [8]

[10] R.K. Crawford, P. Thiyagarajan, J.E. Eppreson, F. Trouw, R. Kleb, D. Wozinak, D. Leach " The New Small Angle Diffractometer SAND at IPNS" Proc. ICANS XIII; PSI-Proceedings 95-2 (1995) pp 99-117

[11] T.A. Broome, "ISIS Target and Moderator Materials" Proc 2nd Int. Workshop on Spallation Target Materials Technology, Ancona, I; report Jül 3450 (1997) pp55-69

[12] E. Shabalin, this conference

[13] T. Lucas, G.S. Bauer, C.D. Sulfredge "A Pelletized Solid Methane Moderator for a Medium-to-High Power Neutron Source" Proc. ICANS XIII PSI-Proceedings 95-2 (1995) pp 644-653

[14] H. Barnert-Wiemer, this conference

[15] F. Trouw, Argonne National Laboratory; private communication

[16] J.-C. Li, J.D. Londono, K.D. Ross, J.L. Finney, J. Tomkinson, W.F.Sherman, "An inelastic incoherent neutron scattering study of ice II, IX, V and VI in the range frim 2 to 140 meV" J. Chem.Phys. **94** (10) 1991,p 6770

[17] K. Inoeu, H. Iwasa ,Y. Kiyanagi, J. At. Energy Soc. Japan, **21** (1979) 865

Neutron Scattering Instruments

INSTRUMENTATION AND TECHNIQUES

ICANS-XIV
14th meeting of the International Collaboration on Advanced Neutron Sources
June 14-19, 1998
Starved Rock Lodge and Conference Center
Utica, IL, USA

BACKSCATTERING SPECTROSCOPY WITH 2 μeV RESOLUTION AT PULSED SPALLATION SOURCES

F. Mezei and G. Zsigmond
Los Alamos National Laboratory, MS H805, NM 87545, USA, and
Hahn-Meitner-Institut Berlin, D-14109 Berlin, Germany

The energy resolution of standard, established IRIS type inverted geometry time-of-flight backscattering (TOF-BS) spectrometers at pulsed spallation sources amounts to about 15 μeV using graphite analyzer at 6.7 Å wavelength in contrast to typical continuos source instruments, which provide 1-2 μeV resolution Si(111) crystal analyzer at 6.27 Å. By the IRIS type technique this kind of high resolution can only be achieved by mica analyzers at about 19 Å wavelength at the expense of a large losses in beam intensity and available momentum transfer range. It is shown in this work that by adding an optional fast chopper at some 5 m from the moderator and using Si analyzer crystals on an IRIS type instrument, a resolution close to that of the continuous sources machines can be attained at very competitive intensities and without the above drawbacks of going to 19 Å wavelength. The performance of an apparatus with the basic dimensions of IRIS and operating on a partially coupled cold moderator with 150 μs FWHM pulse length at the upgraded LANSCE source was quantitatively evaluated using detailed Monte Carlo simulation.

1. Introduction

In high resolution neutron spectroscopy one crucial requirement is to be able to tune the resolution. This implies, that depending on the behavior of the sample studied one has to have the freedom of trading resolution for intensity and vice versa. This flexibility is one of the keys of the historic success of triple axis spectroscopy (TAS). Continuous source (CW) TOF spectrometers are also easily tunable in resolution by changing the chopper speed or, more recently, by choosing the width of the chopper window. With the pulse width determined by the source moderator, spallation source instruments of the by now established design lack this flexibility, which is a substantial drawback. The resolution of backscattering spectrometers, CW or pulsed, is not easy to tune anyway, since it requires changing the whole set of analyzer crystals. It is nevertheless a standard approach to share the covered solid angle between two sets of different analyzers of different resolutions. Both from economical point of view and from that of reliable data collection it is preferable to have the flexibility of adapting the resolution to the requirement of the experiment on the same instrument, as opposed to operating several similar

instruments with different resolutions. On pulsed sources the latter, less favorable solution appears most often to be the only option, in view of the handicap of not being able to change the pulse length and intensity of the moderator chosen once for ever (or at least for many years).

This sizable drawback of pulsed spallation sources can be overcome by a simple, but by now never implemented technique of using an optional chopper upstream in the beam in order to shorten, if needed, the pulse length of the moderator chosen to be optimized for highest intensity. Without this (and a number of other innovative techniques, a good number of them already proposed, but not yet tested) pulsed spallation sources will continue to remain inferior to CW reactor sources (also in terms of cost/performance ratio) in those applications which currently are best performed at the leading CW sources. These applications notably include most of thermal neutron and virtually all of cold neutron diffraction and spectroscopy. For the first time in spallation history, maximized intensity coupled moderators have been installed at LANSCE, and this opens up opportunities for achieving by now unprecedented instrument performances at spallation sources, in particular in cold neutron spectroscopy, such TOF-BS.

2. TOF-Backscattering with an optional pulse-shaping chopper.

The aim of our proposed improvement of the standard TOf-BS technique (IRIS) is to provide better and easily tunable resolution at best possible intensity conditions and unrestricted q range. This flexibility will largely enhance the instrumental capability in many respects. For example a weak very sharp structure in the spectrum can be lost in the instrumental background if looked at with insufficient resolution.

Compared to CW backscattering instruments existing TOF-BS spectrometers like IRIS at ISIS [1] are characterized by a large dynamic range due to the inverted geometry (e.g. from -0.2 to 3.5 meV) and a moderate energy resolution of 15 μeV. For example IN10 (ILL) offers ~ 1μeV energy resolution at a dynamic scan width of not more than ± 30 μeV, although it has been proposed to enhance dynamic range to 500 μeV by scanning the temperature of the monochromator crystal [2]. Using bent crystal elements also allows adjusting somewhat the resolution [3]. Let us note that the large dynamic scan range of the pulsed source instruments is not always a real advantage. On the one hand side, it allows one to investigate large energy transfers with the basic good resolution (which on CW sources can only be achieved by scanning the temperature of the monochromator or by the rather cumbersome way using a monochromator crystal different from the analyzer.) On the other hand, often there are no sharp structures requiring high resolution distributed over a broad energy range, so much of the, at pulsed sources little adjustable, broad scan delivers no useful information.

The scheme of a TOF-BS spectrometer with an optional fast pulse-shaping chopper is shown in Fig. 1. The Si analyzer crystals are assumed to cover part of the analyzer solid angle and another part is covered by graphite crystals, quite similarly to the manner mica and graphite are disposed in IRIS on two opposite sides of the scattering chamber.

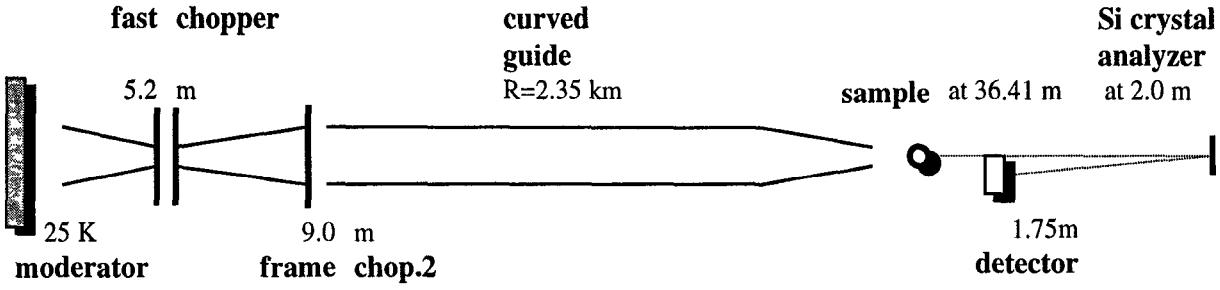

Figure 1. Layout of a pulsed source backscattering instrument with an optional fast chopper at 5.2 m from the moderator. The other distances essentially correspond to that of IRIS.

3. Instrument performance evaluated by Monte Carlo simulation

The Monte-Carlo simulation technique we have developed for evaluating experiments at IRIS has been described elsewhere in detail. Compared to IRIS, the basic difference in the high-resolution operation mode is that the incoming neutron pulse length is determined by the fast chopper. We have assumed a 250 Hz revolution disc chopper device with two counter-rotating discs producing 23.5 μs pulses. An 'eye-of-the needle' convergent + divergent $3\theta_{Ni}$ supermirror guide combination [5] was assumed to focus the neutrons from the moderator on the fast chopper window, in order to reduce the beam width at the chopper, i.e. to achieve a shorter pulse length. Note that a Fermi type chopper could also be envisaged instead of the disc chopper, since only a narrow wavelength band is to be transmitted simultaneously. The moderator pulse was assumed to display the 150 μs FWHM pulse shape corresponding to what is expected at LANSCE for a partially coupled liquid H_2 moderator. (Fig.2). The disc chopper at 9 m serves to eliminate frame overlap from consecutive pulses. It is a standard feature of the IRIS type design. In order to improve the angular resolution for the scattered beam the spherically focussing Si(111) analyzer crystal arrangement was assumed to be at 2 m from the sample. This extension of the total flight path has little effect either on the TOF resolution or on the analyzer energy resolution.

The cylindrical sample size (r = 1 cm, h = 3 cm) considered is small enough to avoid reduction of resolution due to TOF path differences. The analyzer was assumed to consist of 0.5×0.5 cm flat elements, in order to achieve perfect focussing to the detector. The spot size on the detector determines the angular resolution. In the current simulation we have only concentrated on the energy resolution, which is fairly well decoupled from the angular or q resolution. The sample scattering function used in the calculations was independent of momentum transfers. A single scattering angle, 140° was evaluated, at which angle the path differences in the sample is close to the worse case maximum. The sample absorption was set to a negligible level.

Some results of the simulation calculations are shown in the next two figures. In Fig 3 the instrumental resolution is illustrated by the calculated instrumental response for a model quasielastic Lorentzian line with 1μeV FWHM. The "measured" line can be fitted by a Lorentzian with 2.9 μeV FWHM, thus the instrumental energy resolution amounts to about 2 μeV FWHM.

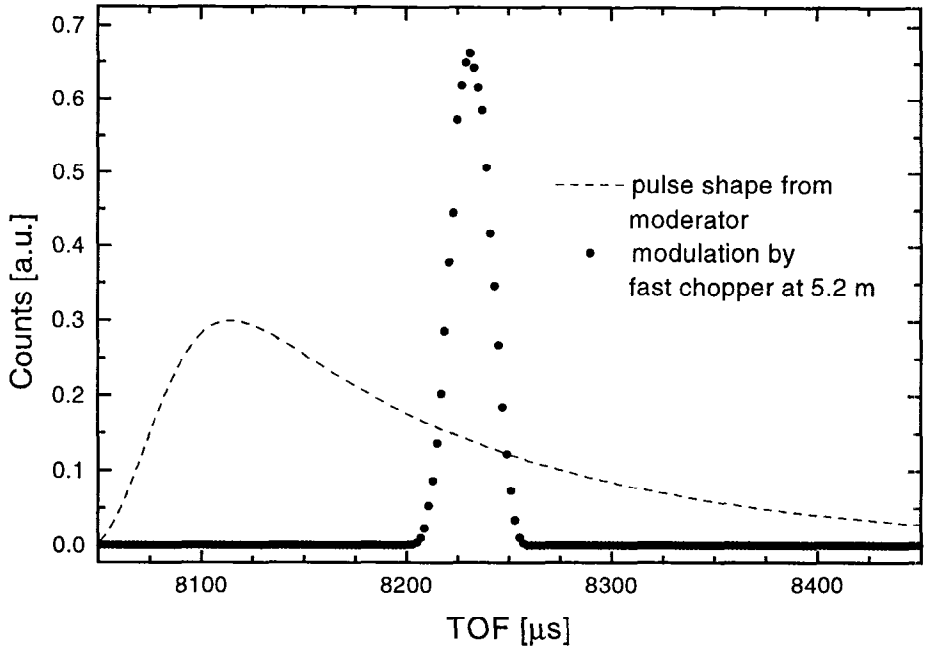

Figure 2. Comparison of the partially coupled moderator pulse shape (expected at LANSCE, analytic approximation) and the fast double disc chopper pulse shape (simulation).

Due to the finite distance, determined by the thickness of the bulk shielding, between the moderator and the fast pulse-shaping chopper, the moderator – chopper system also act as a monochromator, i.e. only neutrons in a narrow neutron energy band width pass the chopper. This band determines the scan width in the chopper mode of operation, which turns out to be rather close to the those achieved on CW source high resolution instruments, as discussed above. In order to explore this scan width we have calculated the instrumental response to a series of inelastic lines separated by 10 μeV. The results in Fig. 4 show indeed that we can efficiently simultaneously explore an energy interval of about 90 μeV, which is very small compared with scan width of the instrument in the low resolution (15 μeV) conventional IRIS type configuration with the fast chopper removed (or stopped in the open position, a standard feature of state of the art disc choppers). Here again, as discussed above in connection with the similarly narrow scan width of the CW source backscattering instruments, this simultaneously explorable narrow energy window will rarely mean a particular handicap. Typically one will be interested in zooming in with high resolution to a particular structure in the spectrum only. By adjusting the phasing of the fast chopper, one can easily position the high resolution scan window to any part of the broad energy range normally accessible in the low resolution configuration, a clear advantage compared to CW instruments.

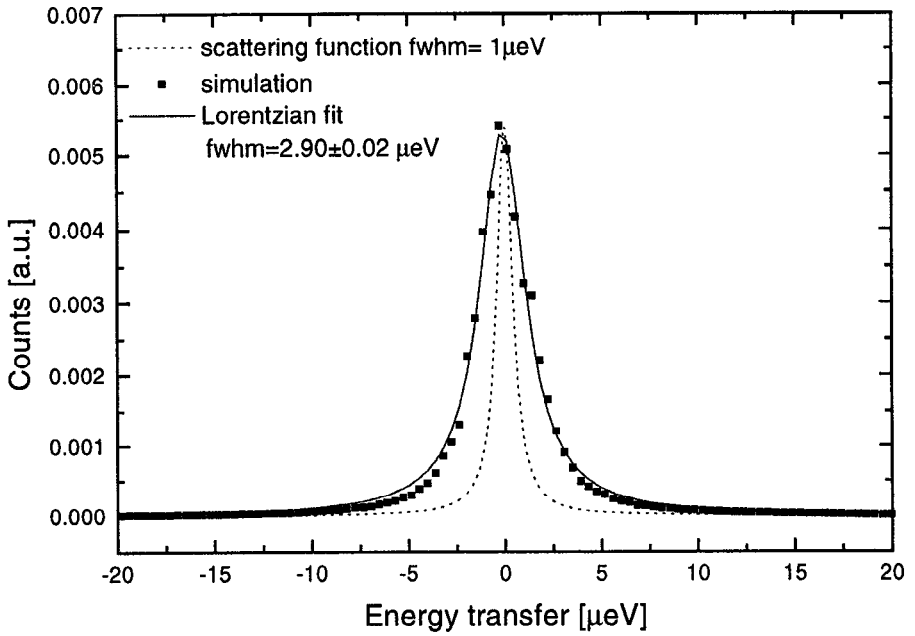

Figure 3. Evaluation of the instrumental resolution: simulated data points for a Lorentzian quasielastic line of 1 μeV full width (dotted line). The solid line is a Lorentzian fir to the simulated data.

The scattered beam intensity relative to the best similar resolution CW source instruments has not been evaluated in this simulation. A rough analytic estimate shows that assuming the planned flux at LANSCE after the upgrade the high resolution mode of operation considered here would offer comparable counting rates for equal analyzer solid angle and 2 times less resolution than the recently built IN16 at ILL. The narrow scan width (Fig. 4.) means an effective data collection duty factor of about 3 %, compared to the 50 % duty factor of the CW spectrometers (background chopper). This is partially compensated by the about 4 times higher peak flux and by the fact that the resolution cannot be traded for intensity on IN16 beyond 1 μeV.

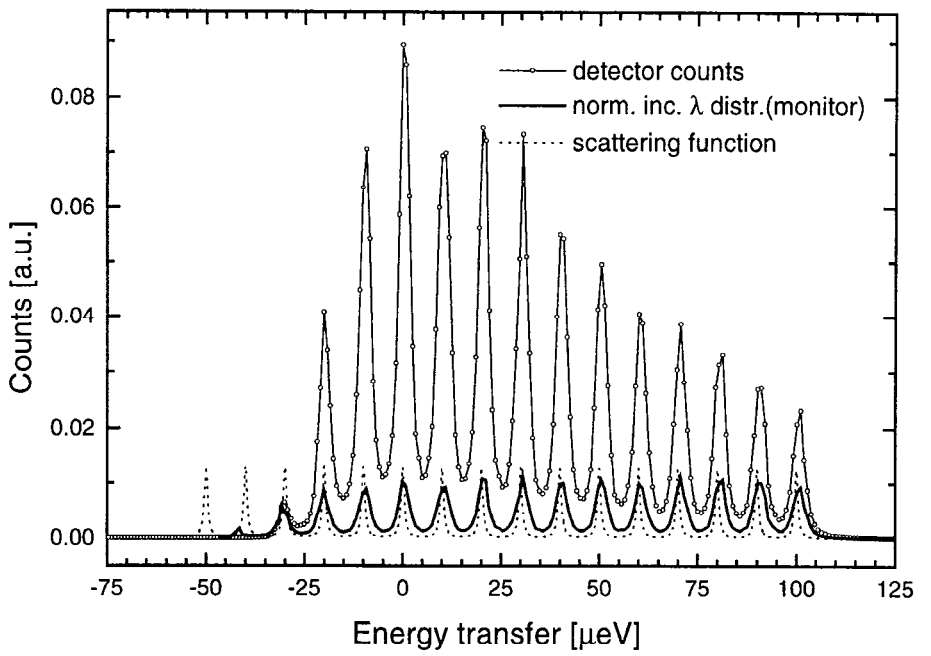

Figure 4. Evaluation of the simultaneously explored energy window: the instrumental response to a series of inelastic lines separated by 10 μeV. The dashed line shows is the model scattering function, the points are the simulated data and the lower solid curve is the "measured" spectrum normalized to the moderator pulse shape in Fig. 2.

4. Conclusion

The pulse-shaping fast chopper and Si crystal analyzer option can very efficiently enhance the global performance of a standard IRIS type pulsed source backscattering spectrometer by offering the possibility to zoom in to parts of the studied spectra with an about 7 times better resolution. In this high-resolution mode of operation a spectrometer at a source like LANSCE will provide comparable intensities to the best existing μeV resolution reactor source instruments.

References

1. C. J. Carlile and M. A. Adams, Physica B 182, 1992, 431
2. J. C. Cook, W. Petry, A. Heidemann and J-F. Barthelemy, Nucl. Instr. and Meth in Phys. Res. A **312,** 1992, 553
3. B. Frick, A. Magerl, Y. Blanc and R. Rebesco, Physica B **234-236**, 1997, 1177
4. G. Zsigmond, PhD Thesis, Technische Universität Berlin - Germany D83, 1998
5. F. Mezei in Proc. ICANS XII, 1993, I-377

ICANS-XIV
14th meeting of the International Collaboration on Advanced Neutron Sources
June 14-19, 1998
Starved Rock Lodge and Conference Center
Utica, IL, USA

EXPERIMENTAL TEST OF CONSTANT **q** SINGLE CRYSTAL SPECTROSCOPY ON A TIME-OF-FLIGHT SPECTROMETER.

S. Schorr and F. Mezei
Hahn-Meitner-Institut Berlin, Glienicker Str. 100, D-14109 Berlin, Germany, and
Los Alamos National Laboratory, LANSCE, Los Alamos, NM 87544, USA

Triple-axis spectroscopy (TAS) is the method of predilection for constant **q** single crystal spectroscopy on continuous sources. This method is not naturally adapted for pulsed sources and actually it has actually never been implemented on such a source. It has been argued that time-of-flight (TOF) spectroscopy can take over the role of TAS on pulsed facilities. TOF is actually well adapted for both pulsed and continuous neutron beams, but it is not an established method for constant **q** spectroscopy. In order to compare the data collection efficiency of both techniques, we have performed the same experiment on the same sample with the same resolution on instruments of both types at the same continuous reactor source at Hahn-Meitner-Institut, Berlin. The results show that, even on a continuous source, the TOF method is comparable to TAS if at least a few (<10) constant **q** points are to be explored in a single symmetry direction. It becomes superior or vastly superior if the fraction of **q** space expected to be explored contains more than the above small number of resolution elements, i.e. in the case of exploring isotropic phenomena. This observation implies, that on for TOF more favorable pulsed sources single crystal spectroscopy, including most demanding constant **q** scans, can be advantageously performed by this technique, and there is no need to adapt the TAS for pulsed sources.

1. Introduction

Constant **q** spectroscopy is a crucial tool in neutron scattering study of single crystals. Traditionally triple axis spectrometers (TAS) are used with great success for this purpose on continuous (CW) neutron sources. TAS spectroscopy, however, cannot take primary advantage of the time structure of pulsed sources and in actual fact it also has substantial drawbacks on CW sources, such as higher order contamination, "spurions" (e.g. diffuse scattering on the analyzer crystal) or the notorious complexity and limited reliability of determining absolute cross sections.

Time-of-flight (TOF) inelastic spectroscopy, a method practically never used for constant **q** spectroscopy by now, can be easily and – under the condition of making use of the recently

introduced repetition rate multiplication technique [1] – also efficiently transferred from CW sources to pulsed spallation sources. In addition, the TOF method does not suffer from the above mentioned drawbacks of TAS and in cases where its large solid angle capability can be made use of, e.g. with polycrystalline or amorphous samples it provides vastly superior data collection rates compared to TAS. Recently we have investigated with encouraging results the feasibility of constant **q** spectroscopy by TOF techniques using Monte-Carlo simulation [2, 3].

Our goal in the present study was to establish a real life experimental comparison of the data collection efficiency of the TAS and TOF approach in single crystal spectroscopy at the same CW source, on the same sample and with the same resolution. For this purpose we have used two up to date instruments, built at the same period of time (early 90's) following to the same high standards, and facing the same cold source at the BER-II research reactor at HMI, Berlin, namely FLEX and NEAT, respectively. In terms of counting rate vs. source flux both of these instruments substantially outperform their competitors worldwide, for the same sample and resolution the counting rate on FLEX is only 3 times less than on the best comparable ILL instrument, IN14, and on NEAT only 1.2 times less than on IN5, in spite of more than a factor of 10 difference in the cold source flux between the two sources.

2. Comparison for isotropic magnetic excitations.

For the purpose of this comparison we have measured a few spectra on the TOF instrument NEAT comparable to those taken previously on FLEX as part of an investigation of magnon renormalization near the Curie point T_c in EuO. The sample is not an easy one to work with, it absorbs about 90 % of the incoming beam. We have worked around the (000) reciprocal lattice point, at small scattering angles in the range of 5 – 15°. Fig. 1 shows typical spectra obtained at the same temperature below T_c. The experiment on NEAT only used beam time over a weekend which could not be filled in otherwise after a user no-show, so we had to live with the detector settings of the previous experiment, i.e. the lowest scattering angle was just above the highest on FLEX. This was, however, perfectly sufficient to establish the intensity ratio of the magnon signal on both instruments. Note that at $q = 0.3$ Å^{-1} the magnon signal is already nearly lost in the background on FLEX (in contrast to NEAT), so its intensity was actually determined by fitting the expected q dependence over the whole q range of the TAS experiment. The TOF scans in Fig.1 are at constant angle, not at constant q. We have also verified that the elastic energy resolutions are indeed the same in both cases. We have only considered TOF detector tubes centered around the horizontal scattering plane, which implies 5.5° vertical collimation, about 1.5 times larger than on FLEX.

If we can assume that the scattering features, e.g. magnon dispersion relation is isotropic enough for the purpose of the experiment, it is sufficient to take TOF spectra with a single sample orientation, and it is a standard procedure in TOF spectroscopy to convert the directly observed constant scattering angle data into constant $q = |\mathbf{q}|$ spectra. For the comparison of the two methods we have required that for the lowest intensity magnon group in the TAS study ($q = 0.3$ Å^{-1}) the same number of neutron counts are registered in both cases. (This requirement actually favors TAS, in view of its worse signal to noise ratio equal counts in the signal in reality mean lesser amount of information.) With TOF all q's will then be measured simultaneously for the same length of time (assuming that there are indeed detectors placed at the smaller angles required here, of course). In the actual TAS experiment 7 q values were studied, namely the

higher intensity signals for shorter time (see Fig. 3) and the total measuring time for the 7 points was 8500 min. In comparison, in the TOF experiment 700 min was found to be sufficient to provide equal signal around q = 0.3 Å^{-1}, and superior ones at smaller q's.

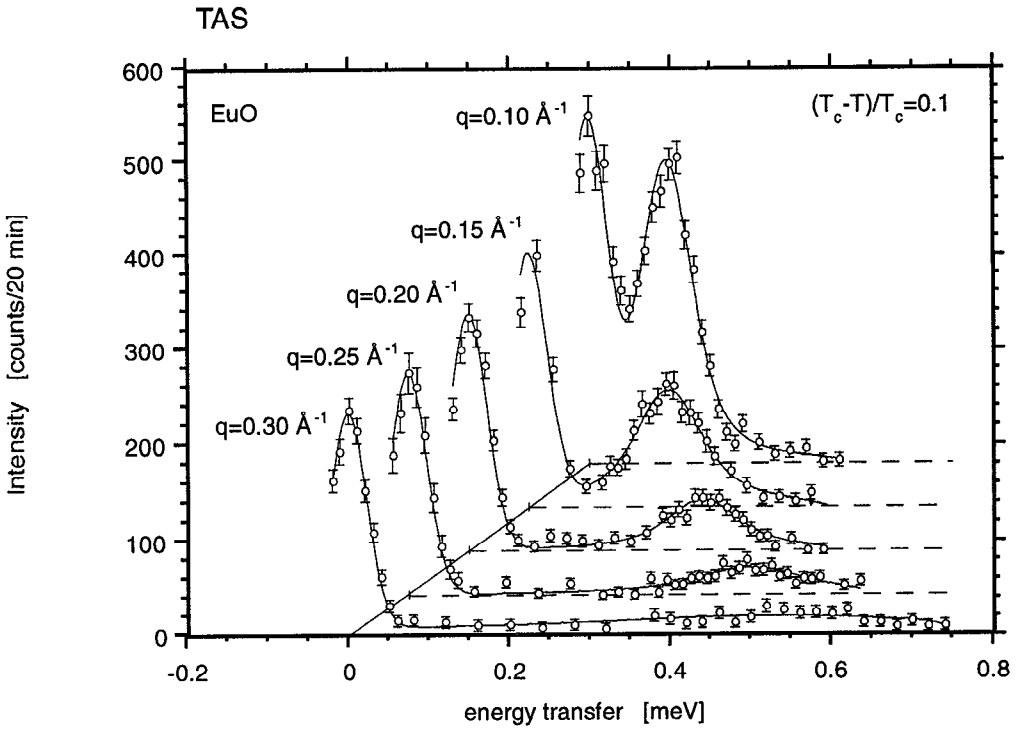

Figure 1. TAS constant **q** scans measured on FLEX for exploring the magnon in the q range of 0.1 – 0.3 Å^{-1}.

The conclusion from this comparison is therefore, that if an experiment is aimed at collecting information at least at 5 - 10 different q's (e.g. determining a fraction of an excitation dispersion relation) and it is acceptable to observe the scattering function S(**q**,ω) along a set of **q** trajectories in the scattering plane determined by neutron kinematics rather than by the symmetry of the sample crystal, TOF as represented by NEAT is more than an order of magnitude more efficient than TAS as represented by FLEX. This situation applies to all isotropic samples and phenomena, but it can also be the case for single crystals if the theoretical models used for the interpretation of the data can be evaluated for any **q**, not only for those in symmetry directions.

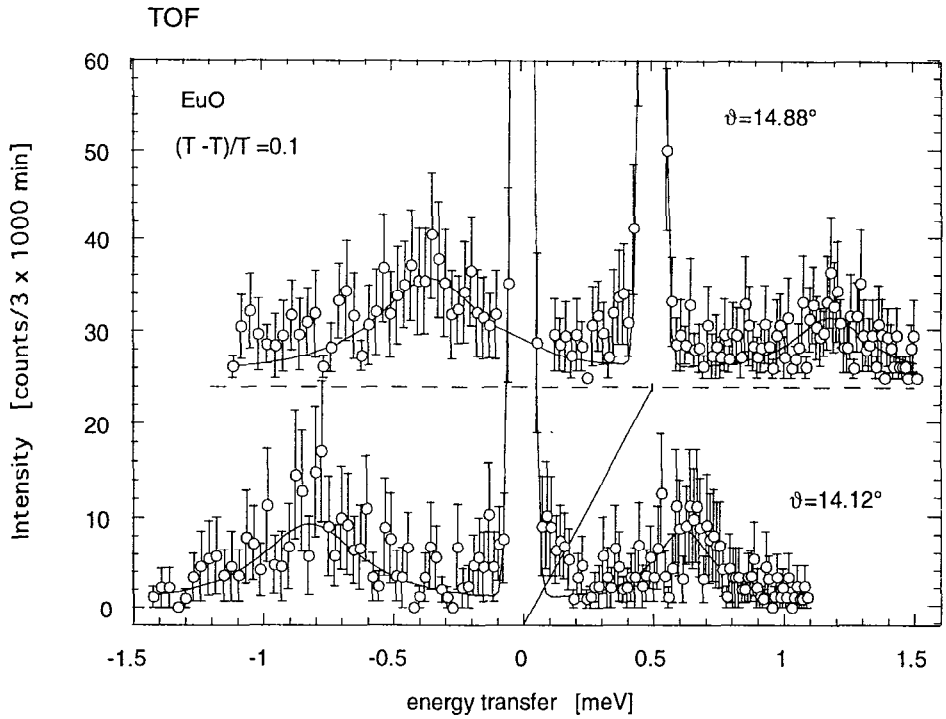

Figure 2: TOF scans measured on NEAT on the same EuO single crystal sample. The constant scattering angle ϑ spectra measured at a fixed sample orientation correspond to q values between 0.32 and 0.35 $Å^{-1}$

3. Comparison in exact constant q spectroscopy in a single symmetry direction.

The worst case for the TOF approach is exact constant **q** (vector) data collection in a single prescribed crystal symmetry direction. At a given sample orientation from the vast 2 dimensional data set (angle and time-of-flight) collected by TOF we only can at best only use infinitesimal 1 dimensional locus. This is illustrated in Fig.4. For example, the set of points at the upper boundary of the area covered by dots shows for each of the 18 detector tubes placed between about 2.5 and 15.5° scattering angle the energy value of the single bin in the collected histogram, which belongs to a **q** vector pointing in the given symmetry direction of the crystal. The area covered by points in the figure shows the (**q**,ω) domain (**q** in the [110] symmetry direction) which can be covered by rotating the sample over a 65° range. In order to explore this range with a similar density as in the TAS experiment, we would need to take data at 34 different rotational position of the single crystal sample. Under the requirement of collecting equal number of signal counts in the lowest intensity group considered, we find that the TOF instrument would need about 11000 min time, quite similar to the 8500 min actually used on FLEX.

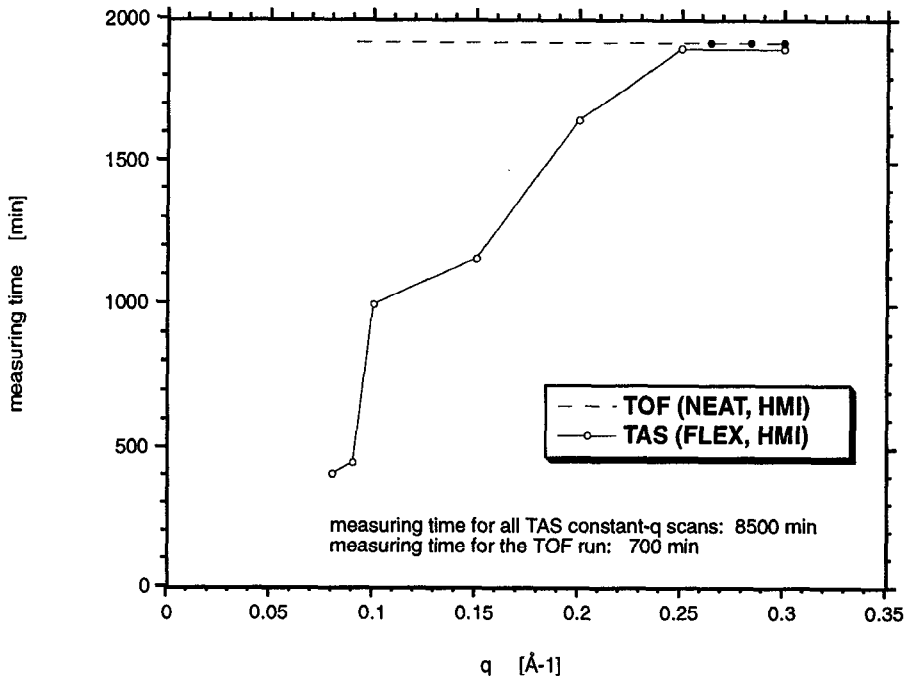

Figure 3: The measuring times needed for the various TAS constant-**q** scans shown in Fig. 1. In comparison, the dashed line indicates the relative intensity of the collected signal in a 700 min TOF run (not constant-**q**) expressed as equivalent TAS data collection time at each q.

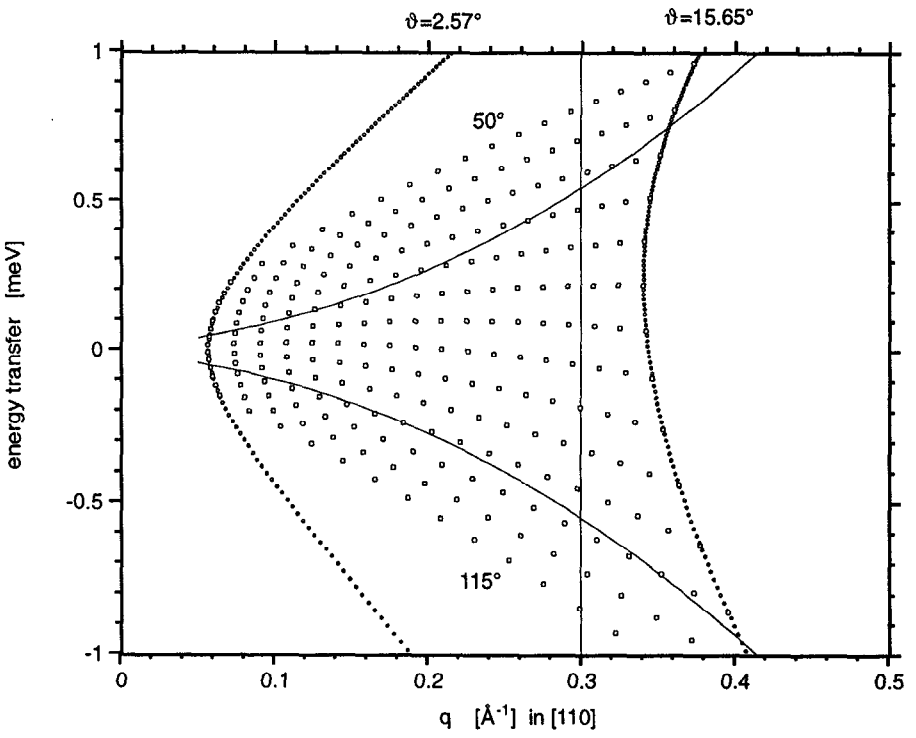

Figure 4: Mapping a symmetry direction cut of the (**q**,ω) variable space by the TOF technique. One dot represents one of 18 detector tubes between and one of 14 sample orientations shown. The continuous lines show magnon the dispersion relation in EuO at the chosen temperature.

4. Conclusion

The real life comparison between data collection times on two instruments of the same generation at the same CW source at HMI, Berlin shows, that the TOF approach is about equally efficient compared to the conventional TAS technique in constant **q** spectroscopy in single crystal samples, assuming that at least some 5-10 different points in the reciprocal space are of interest. Our comparison was very conservative, in favor of the conventional TAS approach, e.g. we did not take into account the possibility of detecting neutrons by TOF on both sides of the incoming beam and that the TOF technique usually provides data in more than one symmetry directions simultaneously. In experiments in which information corresponding to **q**'s outside the symmetry directions is also of value, the TOF technique becomes superior, by up to more than an order of magnitude. This means that, even on a CW source, TOF spectrometers (adapted to the requirement of being able to align a single crystal sample in any direction) are comparable or superior in efficiency to TAS in typical inelastic experiments in single crystals. The TOF technique can obviously take more advantage of the time structure of pulsed beams on a pulsed spallation source than TAS. Therefore we can conclude that there is no need to trying to implement TAS on pulsed sources: the job can be better done by TOF spectroscopy. Actually we believe, that we might end up with virtually the same situation on CW sources too, once TOF spectrometers are built with keeping single crystal spectroscopy in mind.

References

[1] F. Mezei, Proc. ICANSXIII (PSI 1995) 400.
[2] S. Schorr, F. Mezei, J. Stride and C. Guy, J. Neutron Research 6 (1997) 113.
[3] S. Schorr and F. Mezei, Physica B, **241-243** (1998) 166

ICANS-XIV
The 14th Meeting of the International Collaboration on Advanced Neutron Sources
June 14-19,1998
Starved Rock Lodge, Utica, Illinois

Experimental studies on cold neutron beam focusing by magnetic field

Y.Kiyanagi, Y. Suda, H. Nakagawa, T. Kamiyama, Y. Ogawa, H. Iwasa
H. M. Shimizu*, H. Kato*, T. Oku* and T. Wakabayashi**

Graduate School of Engineering, Hokkaido University, Sapporo 060-8628, Japan
*The Institute of Physical and Chemical Research, Wako, Saitama 351-0198, Japan
**Power Reactor and Nuclear Fuel Development Corporation, Ibaraki 305-0801, Japan

Abstract

A wavelength spectrum which clearly indicated the neutron beam focusing around 14 Å by a magnetic field was observed. The intensity of neutrons at the focusing wavelength increases by about 40 times compared with the case without the field. The spatial dependence of the intensity of the focusing neutrons and the wavelength distributions were also measured. The distribution changed drastically width position around the wavelength of focusing region.

I. Introduction

An efficient target-moderator-reflector assembly and spectrometers with good performance are indispensable to improve the total performance of the neutron scattering facility. Furthermore, devices to improve the transmittance of neutrons between the moderator and the spectrometers are very important necessarily for the existing facilities and also for the new spallation sources planed in the world, in which the performances of the spectrometers should be optimized totally by taking into account all performances, namely, performances of; the moderator system, the beam transport lines and the spectrometers.

Keywords: focusing, magnetic field, gain, wavelength dependence, spatial distribution

So far, neutron guide tube has been mainly used.

New device to transport or focus the neutron beams, multi-capillary fibers, has been proposed and used. Neutron beam control by using a magnetic field is a new candidate. Principle of focusing of the neutrons by using magnetic fields is well known[1]. Neutron beam profiles focused by a magnetic field were reported as an accompanying results of ^{3}He focusing, in which intensity gain by focusing and the energy dependence are not presented[2].

We were trying the observe the neutron focusing in order to know the fundamental features of the focusing effects and during almost the same period the neutron focusing by using sextuple magnets was observed independently[3] by using the Hokkaido linac as a neutron generator. We could get an intensity gain of about 30 times around 14 Å neutrons when using 2mm diameter entrance and exit collimators.

After then, we have performed the focusing experiments to obtain information such as spatial distributions and spatial dependent wavelength spectra. Here, we report the results of the focusing by using a sextuple magnet neutron lens.

II. Principal of neutron focusing by a magnetic field

A trajectory of neutron can be controlled by using an inhomogeneous magnetic field due to an interaction between the neutron magnetic moment and the magnetic field[1]. A motion in a magnetic field is described by

$$\left(\frac{d^2\mathbf{r}}{dt^2}\right) = \mp\left|\frac{\mu}{m}\right|\nabla|\mathbf{B}|,$$

μ : magnetic moment of neutron

m: mass of neutron

-:corresponding to neutron spin parallel to field

+: corresponding to neutron spin anti-parallel to field

In the case of sextuple magnet the field is defined as $|B|=c(x^2+y^2)/2$. Here, c is constant.

We chose the z axis along the neutron beam line, and the x (horizontal) and y(vertical) axes are perpendicular to the beam line.

The solution for parallel case is for focusing one, and the other for the dispensing one. The solution for the focusing neutrons is as follows[3];

$$(x,y) = (x,y)\big|_{z=0}\cos(zm\lambda\omega/h) + (V_x,V_y)\big|_{z=0}\sin(zm\lambda\omega/h),$$

where $\omega^2=|c\,\mu/m|$, λ is the neutron wavelength, and z is the distance from the entrance of the neutron lens. When $z=(h\,\pi/m\,\lambda\,\omega)$, the neutrons with a wavelength λ are focused.

III. Experimental

Magnets used in this measurement are a permanent magnet, NEOMAX-48[4], which is a sintered anisotropic magnet ($Nd_2Fe_{14}B$). Flux density reported is 1.39T. The size of the magnet is 5mm×5mm×50mm. We composed a sextuple magnet unit by using this magnet as shown in Fig.1. The magnet unit is made of aluminum block with a size of 24mm×24mm×50mm and a neutron beam hole of 10mm diameter is opened along the center of the unit. In this case c is estimated to 3.9×10^4 T/m^2. A 2m tube consisting of 40 magnet units, we call this system as "neutron lens" in this paper, is shown in Fig.2. Cd pipes are placed inside the neutron beam hole to suppress neutron reflections from the surfaces of the magnet units. We put Cd slits at entrance and exit of the lens to collimate the neutron beam. We chose 2mm in diameter from the neutron intensity point of view. However, the intensity gain by focusing and the region of the focusing wavelength are dependent on the size of the holes. The wavelength of neutrons focused by this lens is expected to be around 13 Å.

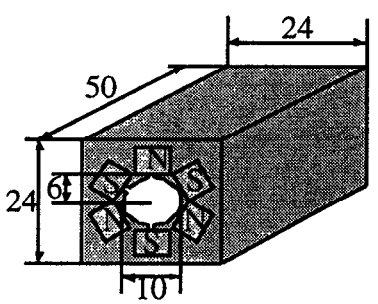

Fig.1 Sextuple magnet unit composed of NEOMAX-48.

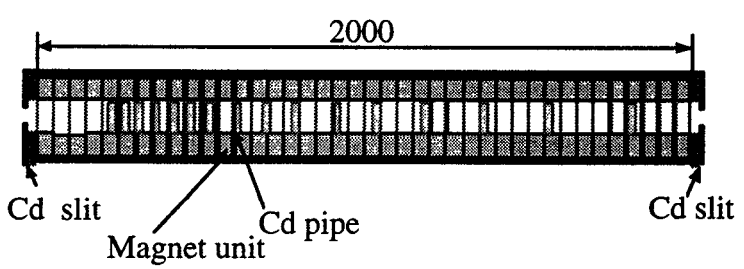

Fig.2 Schematic view of the neutron lens tube consists of 40 magnet units.

Experiments were performed by using a cold neutron source equipped in Hokkaido linac since linac parameters such as pulse width and repetition rate can be adjust according to experimental demands, and a flight path with no disturbance is available; to use dedicate beam line is not so easy in the existing large facilities used for the

scattering experiments. These can allow us to measure spectra without distortion and also to estimate easily a gain of neutron intensity. From these reason the Hokkaido linac facility is very convenient for the experiments to study the fundamental processes of neutron devices.

A schematic view of the experimental set-up for the neutron beam focusing is indicated in Fig.3. The flight path length from the center of the moderator to the detector is about 5.1m. A 2m flight tube, which was evacuated, was used to make short the flight path as short as possible within allowance of wavelength resolution, since it allows us to operate the linac at higher repetition rate, namely, higher neutron intensity. The neutron lens tube is placed just after the flight tube. Neutron collimaters with a hole of 2mm diameter are set at entrance and exit of the lens. The orientation of the neutron lens to the neutron beam line was adjusted by using two goniometers.

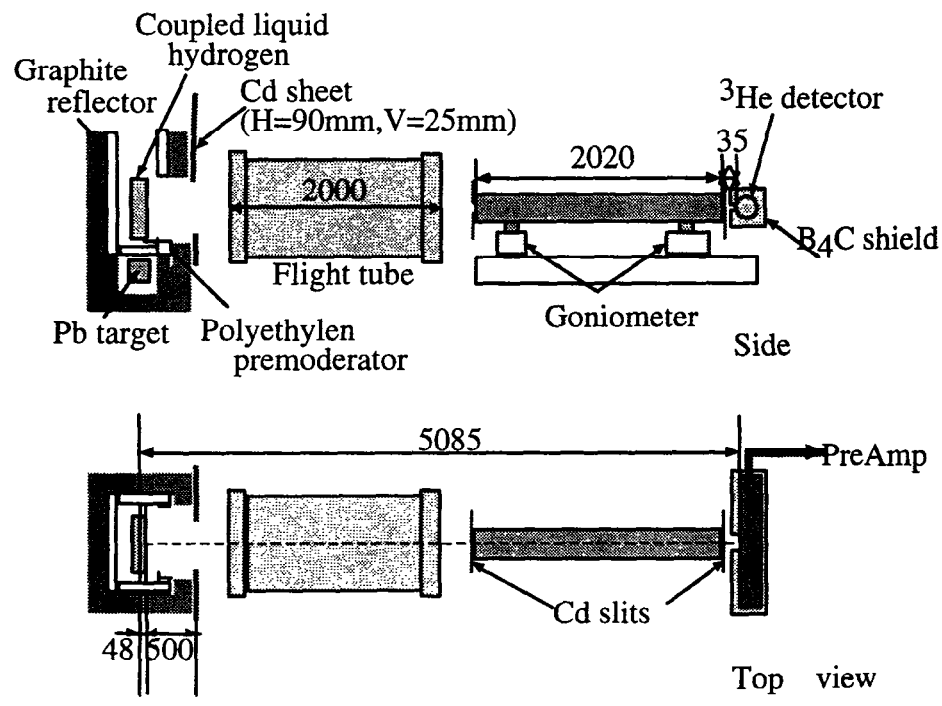

Fig.3 Schematic view of the experimental set-up for the measurements of neutron beam focusing.

The operational conditions of the linac was as follows; electron pulse width = 3 μ s, reparation rate = 40Hz, average current=20 μ A, and electron energy 35MeV.

IV. Results and Discussion

First we measured wavelength spectra through the neutron lens without Cd pipes, which are shown in Fig.4. The direct spectrum from the moderator (without magnet units) is also shown. The measurement of "magnetic field off" means the one using the same material as the magnet but not magnetized. We observed a large hump around 14 Å when compared the spectrum in the case of field-on with that in field-off and we considered that it was due to the neutron focusing. However, a hump around 6 Å also appeared in the spectra through the neutron lens compared with the direct spectrum. We thought that this was attributed to the neutron reflections from the surfaces of the magnet units. This effect causes a large error in the estimation of the neutron intensity gain obtained by the focusing. Then, we decided to put Cd pipes with a thickness of 0.5mm in the neutron beam hole to suppress the reflection, which were already indicated in Fig.2.

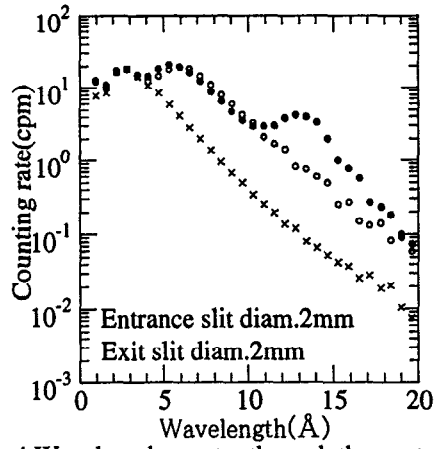

Fig.4.Wavelength spectra through the neutron lens tube without Cd pipes as well as a direct one without magnet units.

× : Without magnet units,
● : Magnet field ON,
○ : Magnet field OFF

Figure5 shows the wavelength spectra from both cases, field on and off, where the hump around 6 Å disappeared. The enhancement around 14 Å is huge. We have defined the intensity gain by dividing intensity (field on) by intensity (field off). The gain

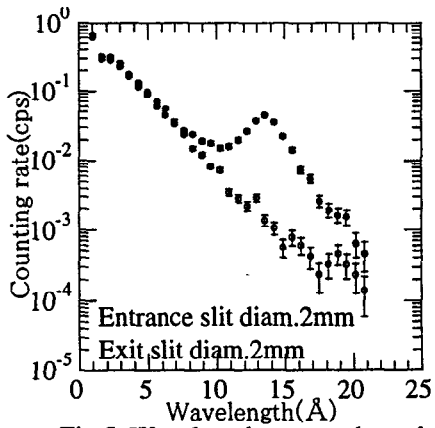

Fig.5 Wavelength spectra through the neutronlens tube with Cd pipes.

● : Magnet field ON,
○ : Magnet field OFF

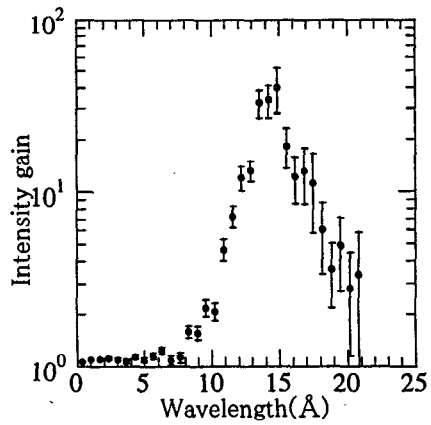

Fig.6 Intensity gain factor as a function of wavelength.

factor is shown in Fig.6 as a function of wavelength. The gain starts to increase around 8Å, make a peak around 13~15Å and decrease at longer wavelength. We can get a gain factor of about 40, which is very large.

We also examined the spatial dependence of the intensity of the focused neutrons and the wavelength spectra. We measured the spectra by moving the Cd slit attached to the detector along X and Y axes. Figure7 shows the spatial distributions along (a) X axis (horizontal direction) and (b) Y axis (vertical direction) at the exit of the neutron lens. The origins do not correspond to the exact geometrical centers of both axes, which were only for convenience for experiments. Both distributions have very similar shapes with a full width at half maximum of about 2mm.

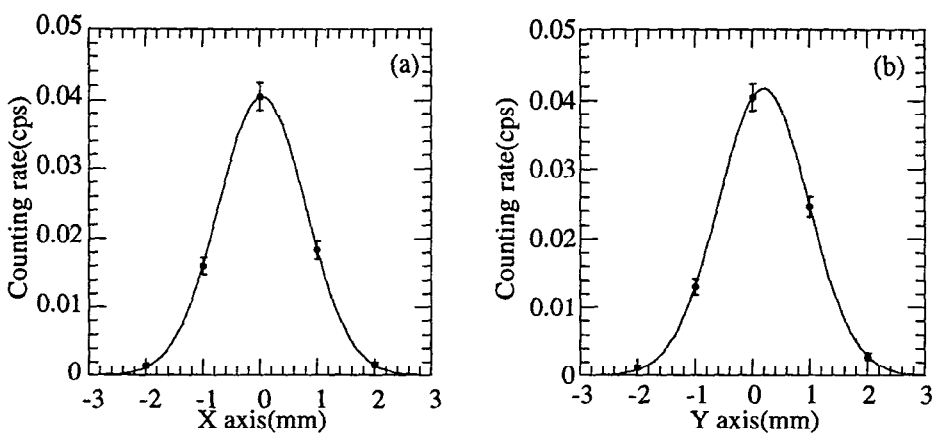

Fig.7 Spantial distributions of neutrons around 14Å.
(a)X axis: horizontal, (b) Y axis: vertial

The change of the wavelength distributions along X axis is indicated in Fig.8, which are only for comparison of the spectral shape, not for intensity comparison. Almost the same distributions were obtained for Y axis. We can recognize the drastic intensity change around 14Å. The distributions are depressed around 14Å at ±2mm. These data clearly demonstrate the feature of the focusing.

V. Conclusion

Neutron beam focusing by magnetic field has beam clearly observed. The gain factor is about 40 . However, the gain factor suggested by our preliminary simulation is about twice as large as that of the experiments. The discrepancy may be due to the reflections from Cd pipes. This effect should be estimated by calculation.

Here, we examined the focusing phenomena, where the focused neutrons are polarized ones but after focusing the neutrons disperse. However, if we put a spin-flipper between a convex and a concave lens, first we can focus the neutron beam and after then align the orientations of the neutrons. This system necessarily produces polarized neutrons.

We are now planning to make a such a system and to use in the neutron scattering experiments.

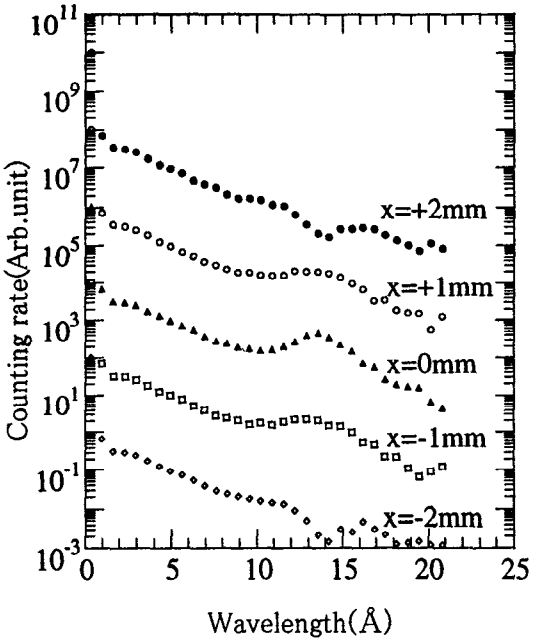

Fig.8 Spantial dependence of wavelength spectra along X (horizontal) axis.

References

[1] P. S. Farago, Nucl. Inst. Meth., 30(1964)271.

[2] A. Steinhof, Nucl. Inst. Meth., A397(1997)371.

[3] H. M. Shimizu et al., Physica B, 241-243(1998)172.

[4] Nd-Fe-B sintered magnet produced by Sumitomo Special Metals Co. Ltd.

[5] Y. Kiyanagi et al., Nucl. Inst. Meth., A312(1992)561.

Enhancement of Reflectivity of Short D-Spacing Multilayer Mirrors by Ion Polishing in Combination with Ion Beam Sputtering Deposition

Kazuhiko SOYAMA
Japan Atomic Energy Research Institute
Tokai, Naka, Ibaraki, 319-11 JAPAN

Wakana ISHIYAMA and Katsuhiko MURAKAMI
Nikon Corporation
Nishi-ohi, Shinagawa, Tokyo 140 JAPAN

ABSTRACT

The reflectivity of multilayer mirrors depend on the interface roughness created during deposition of the layers. We have investigated the influence of argon ion bombardment after deposition by ion beam sputtering of nickel or titanium on the interface roughness of an Ni/Ti multilayer. Roughness changes have been measured by X-ray and neutron reflection. The process is applied to Ni/Ti multilayers with a d-spacing of 26.6 Å and 50 bilayers, and the interfacial roughness of 3.0 Årms has been evaluated.

1. Introduction

Multilayer neutron monochromators(1) and supermirrors(2) are now widely used at many neutron sources for neutron optical devices. A decrease of the d-spacing of multilayer is desirable to lead grater angles of reflection for most applications such as neutron guide with higher transportation efficiency.

One of the most important problem in the case of producing the small d-spacing multilayers is the interface roughness which becomes large with an increase in the number of bilayers deposited. If the interface roughness can be kept small compared to the bilayer spacing for a number of bilayers, a large reflectivity can be achieved by making a sufficient number of layers.

When Ni/Ti multilayers, which are widely used for these neutron optical devices, are fabricated, the above mention problem is also pointed out. The Ni layers are very highly oriented with the (111) planes parallel to the substrate plane, and the large grained Ni layers with a structure of columnar growth lead to rough interfaces and a

gradual degradation in layer structure with an increase in the number of layers[3]. The decrease of crystallization of Ni has been carried out successfully by Ni-C alloying and it also increases the scattering length density[4],[5]. Nowadays NiC/Ti multilayers are used most commonly, and have been fabricated with d=40Å and a roughness $\sigma \sim 6$Å.

If we are getting toward the coating of multilayer with less surface roughness and toward coating of the smaller d-spacing multilayer with d= ~ 20Å, which would be utilized for a multilayer ultracold neutron turbine source[6] and focusing system[7], a new technique to control the surface roughness with few atoms layer is required.

Recently ion polishing (also called as ion bombardment) in combination with electron beam deposition has been shown to be a promising tool in the production of X-ray reflecting multilayer structures[8]-[9]. The concept of ion polishing is mainly explained as follows, particles with the lowest binding energy, which are in a valley of the surface, will be removed first by recoil effects after ion bombardment. But the roughening and intermixing of interface might take place in the case of higher energy ion bombardment. In this study, we have applied ion polishing with a combination with ion beam sputtering deposition for the fabrication of Ni/Ti multilayers. Because of an advantage of sputtering that the sputtered atoms arrive with higher energy (10~30 eV) than vacuum evaporation (~0.1eV), it can produce good quality layers with higher density and small grain size. In this paper we have investigated that the influence of argon ion polishing in the interface roughness of the ion beam sputtered Ni/Ti system over a wide range in order to optimize the Ar^+ ion beam parameters.

2. Experimental and characterization

Ni/Ti multilayers were deposited and ion-polished using the ion beam sputtering system which is shown in Fig.1[10]. The system is equipped with dual bucket sources which are used to generate Ar^+ ions. One is used for sputtering deposition of Ni/Ti multilayers. The other is used for ion polishing. The base pressure during the operation was 1×10^{-7} mbar. Multilayers were deposited on Si(111) substrates of 75mmϕ with each surface roughness less than 3 Årms. The ion treatment was applied immediately after deposition of each of the nickel or titanium layers to smoothen the layers.

The d-spacing and effect of interfacial roughness of multilayers were measured with X-ray grazing angle reflectivity measurements, which were performed in a θ-2θ mode between 0° and 10° using Cu K_α radiation (λ=1.54Å). Neutron reflectivity measurements were conducted on the C3-1-2 reflectometer of the JRR-3M reactor at

JAERI[11]. A well collimated ($\Delta\theta=1.5\times10^{-4}$ rad) beam with a wavelength of 12.6Å ($\Delta\lambda/\lambda=3.2\%$) was used in θ-2θ mode experiments.

In this study, the time dependence of ion bombardment as well as the energy and incidence angle, was studied within the energy range 100eV - 600eV, an angular range of 10° and 45° to optimize the parameters of Ar^+ ion bombardment. Ni/Ti multilayers (d=100 Å) were mainly deposited and characterized to optimize the ion parameters. Ni/Ti multilayer with a very small period (d=20Å, N=50bilayers) has been fabricated and characterized after obtainment of the optimum smoothening parameters.

3. Results and discussion

3.1 Polishing time

In order to apply ion polishing to each layer in a Ni/Ti multilayer, the optimum polishing time of nickel or titanium layer has been investigated. Ni/Ti multilayers (d= 120Å, N=10bilayer) with all Ni layers or all Ti layers ion-polished were coated as a function of Ar^+ ion polishing time. The multilayers were characterized by X-ray reflectivity measurements which is sensitive to the properties of the interfaces and multilayer structure. The ion energy and incidence angles were constant at 100eV and 10° during this experiment.

Figure 2 shows the results of Cu Kα measurements of multilayers with all Ni layers ion-polished for various ion polishing times. The diffraction patterns show Bragg peaks indicating a well defined composition modulation in the growing direction of the multilayers. It is obvious that Bragg peaks up to the 10th order are observed at an ion polishing time of 69 sec from Fig.2. The optimal ion polishing time seems to be in this time range.

Figure 3 shows the results of Cu Kα measurements of multilayers with all Ti layers ion-polished for various polishing times. Bragg peaks up to the 7th order are observed at the sample without ion polishing. On the other hand, Bragg peaks up to the 9th order are observed at polishing time of 127sec and 1310sec from Fig.3. The optimal polishing time seems to be in the time range of 127sec, since a maximum number of Bragg peaks up to a maximum scattering angle is observed in this case.

It is concluded that the quality of multilayers are obviously improved using ion polishing by reducing the interface roughness.

Table 1 shows the measured multilayer periods of these samples as a function of ion polish time. For the samples with all Ni layers ion-polished, the periods are almost constant with an increase in the ion polishing time. On the other hand, as for the

samples with all Ti layers ion-polished, they increase with an increase in the ion polishing time. It may be caused by the density reduction of Ti layers or the limitation of inter-diffusions between Ni and Ti layers.

3.2 Ar^+ ion energy

The optimum Ar^+ ion energy has been investigated. Ni/Ti multilayers (d=100Å, N=10bilayer) with all Ni layers ion-polished or all Ti layers ion-polished were coated as a function of ion energy (100eV, 300eV and 600eV). The incidence angle was constant at 10° and each ion polishing time was constant at 69sec for Ni layers and 127sec for Ti layers during these experiments. Figure 4 shows the results of Cu Kα measurements of multilayers with all Ni layers ion-polished for various ion energies. It is obvious that Bragg peaks up to the 8th order are observed at each case, so the clear ion energy dependence is not confirmed in this range. The results of multilayers with all Ti layers ion-polished are shown in Fig.5, and the clear ion energy dependence is not also observed in this range.

3.3 Incidence angle

The optimum incidence angle of Ar^+ ion energy has been investigated. Ni/Ti multilayers (d=100Å, N=10bilayer) with all Ni layers ion-polished or all Ti layers ion-polished were coated as a function of incidence angles (10° and 45°). The ion energy was constant at 100eV and each ion polishing time was constant at 69sec for Ni layers and 127sec for Ti layers during these experiments. Figure 6 shows the results of Cu Kα measurements of multilayers with all Ni layers ion-polished for two incidence angles. Bragg peaks up to the 8th order are observed at the sample with an incidence angle of 10°, on the other hand, it is reduced to the 6th order at the sample with an incidence angle of 45°. From Fig.7, same tendency is observed at the sample with all Ti layers ion-polished. Bragg peaks up to the 8th order are observed at the sample with an incidence angle of 10°, on the other hand, it is reduced to the 7th order at the sample with an incidence angle of 45°.

3.4 Performance of very small d-spacing multilayer

We have prepared two Ni/Ti multilayers with a period of about 20Å and 50 bilayers. One has been fabricated with all Ni layers ion-polished based on the optimized polishing condition with an ion polishing time of 69sec, ion energy of 100eV, and incidence angle of 10°. The other has been fabricated without ion polishing. They were coated on Si(111) substrates of 75mmϕ with each surface roughness less than 3

Ârms.

X-ray reflectivity measurements were performed with Cu Kα radiation using a low angle diffractometer. It was observed that a maximum of reflectivity of the first order peak was 11.6% and a d-spacing was 26.5Å at the sample having ion-polished Ni layers, while they were 0.37% and 22.5Å at the sample without ion polishing. On the other hand, calculated reflectivity using the optical constants of the bulk was 24.4% at the sample with a d-spacing of 26.5Å and 50 bilayers, while that of the sample with a d-spacing of 22.5Å and 50 bilayers was 15.0%. Then it is derived that the Debye-Waller factor which define the interfacial roughness is 3.0 Ârms at the sample having ion-polished Ni layers and that of non ion-polished sample is 7.5 Ârms.

Neutron reflectivity measurements for the same samples were performed using the neutron reflectometer at fixed wavelength (λ=12.6Å). From Fig.8, it is observed that a maximum of reflectivity is 0.48% and a d-spacing is 26.6Å at the sample with ion-polished Ni layers, while they are 0.11% and 22.7Å at the sample without ion polishing. On the other hand, calculated reflectivity based on the dynamical theory[12] assuming stoichiometric nickel and titanium at theoretical density is 6.24% for the sample with a d-spacing of 26.6Å and 50 bilayers, and that of the sample with a d-spacing of 22.7Å and 50 bilayers is 3.38%. In consideration of the difference of periods, the reflectivity of ion-polished sample is increased by a factor of 2.4 in comparison with the sample without ion-polishing. For the reliable evaluation of the interfacial roughness, the wavelength resolution of 3.2% of this machine may be not adequate, so the higher resolution experiment is being planned. Measured multilayer period agrees with that was measured by x-ray reflectivity measurement very well.

From above results, we can also concluded that the quality of multilayer is obviously improved using ion polishing by reducing the interface roughness even a very small d-spacing multilayer with a period of 20 Å.

4. Conclusion

In this paper, in order to apply ion polishing technique to producing of Ni/Ti multilayer in combination with ion beam sputtering deposition, the optimum ion beam parameters of ion polishing time, ion energy and incident angle have been investigated. The process is applied to Ni/Ti multilayer with a very short period of 26.6 Å and N=50bilayers, based on the optimized polishing condition with an ion polishing time of 69sec, ion energy of 100eV, and incident angle of 10°. The interfacial roughness of 3.0 Å rms has been evaluated.

Acknowledgements

The authors wish to express their thanks to Dr. T. Ebisawa, for his technical supports in the neutron reflectivity experiment.

References

(1) B. P. Schoenborn, D. L. D. Caspar and O. F. Kammerer, J. Appl. Cryst. 7 (1974) 508-510

(2) F. Mezei, Commun. Phys. 1 (1976) 81-85

(3) J. E. Keem, J. Wood, N. Grupido, K. Hart, S. Nutt, D. G. Reichel and W. B. Yelon, SPIE Vol. 983 (1988) 38-52

(4) J. L. Wood, SPIE Vol.1738 (1992) 22-29

(5) B. Vidal, Z. Jiang, F. Samuel, SPIE Vol.1738 (1992) 30-31

(6) M. L. Crow, L. Esibov, A. Steyerl, Nucl. Instr. and Meth. in Phys. Res. A 386 (1997) 474-482

(7) F. Mezei, SPIE Vol.983 (1988) 10-17

(8) E. J. Puik, M. J. van der Wiel, J. Verhoeven, H. Zeijlemaker, Thin Soild Films, 193/194 (1990) 782-787

(9) E. Spiller, SPIE Vol. 1160 (1989) 271-279

(10) K. Murakami, H. Nakamura, T. Oshino and H. Nikaido, OSA Proceedings on Soft-X-Ray Projection Lithography, Vol 12 (1991) 101-105

(11) T. Ebisawa, S. Tasaki, Y. Otake, H. Funahashi, K. Soyama, N. Torikai, Y. Matsushita, Physica B 213&214 (1995) 901-903

(12) V. F. Sears, Acta Crys., A39, 601 (1983)

Table 1 Multilayer d-spacings as a function of ion polish time

Ion polished material	Ion polish time	d [Å]	Δd [Å]
Ni layers	0	117.3	0.0
〃	9	117.4	0.1
〃	69	117.0	- 0.3
〃	320	117.6	0.3
〃	714	116.5	- 0.8
Ti layers	0	117.3	0.0
〃	127	124.8	7.5
〃	420	127.8	10.5
〃	1310	131.7	14.4

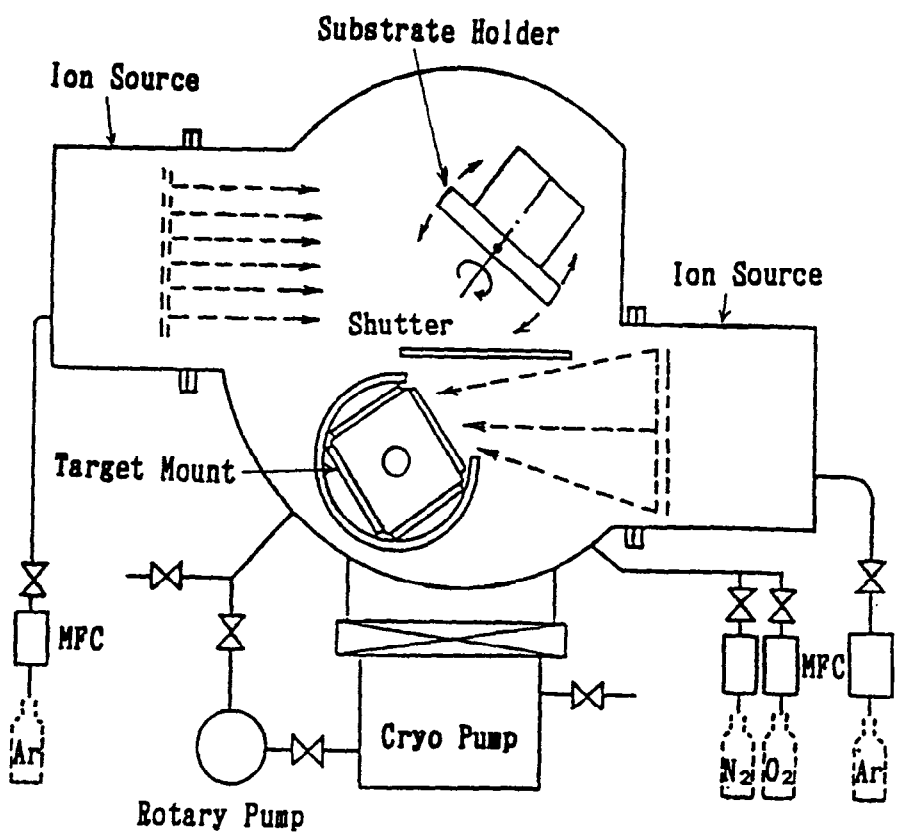

Fig.1 Schematic diagram of the ion beam sputtering deposition system

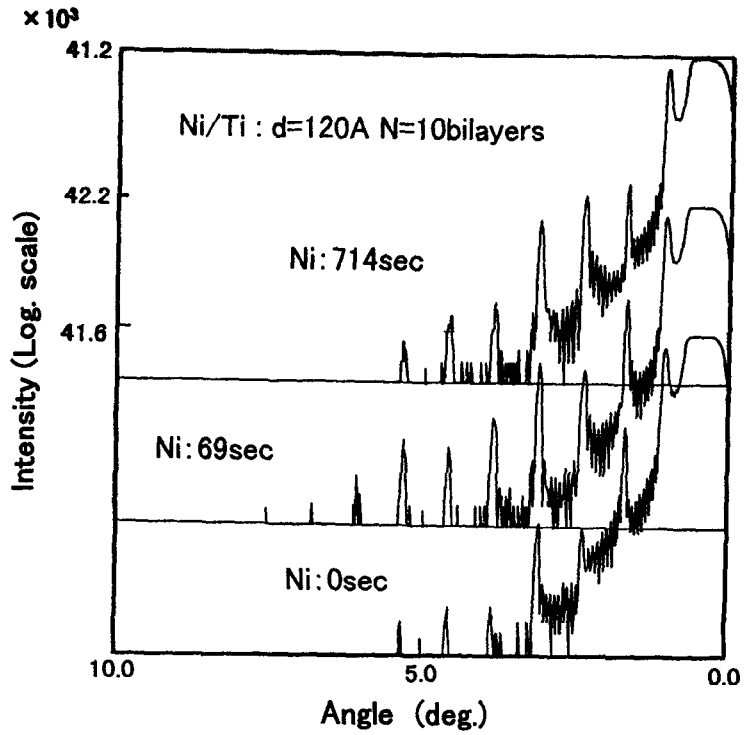

Fig.2 Cu Kα reflection profiles of Ni/Ti multilayers having ion polished Ni layers with variable ion polishing times

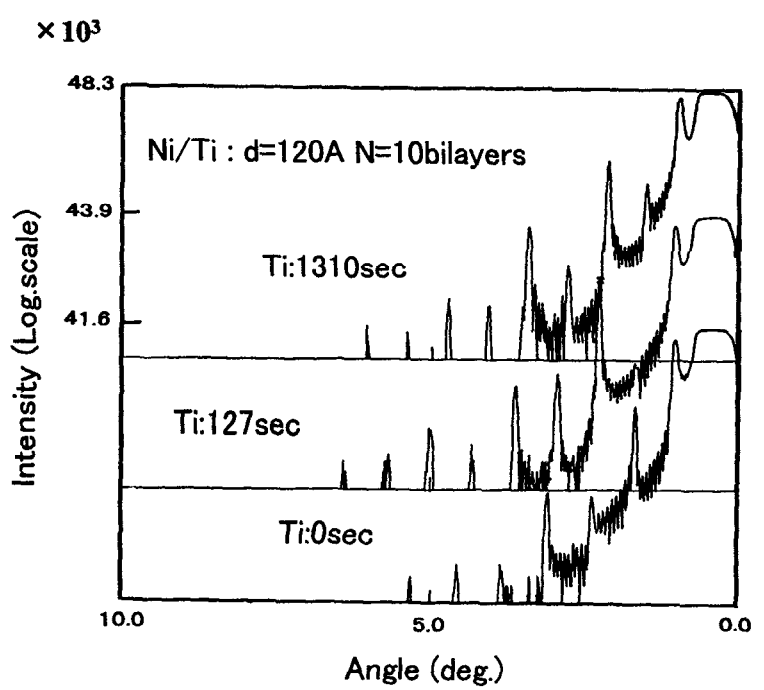

Fig.3 Cu Kα reflection profiles of Ni/Ti multilayers having Ti layers ion polished with variable polishing times

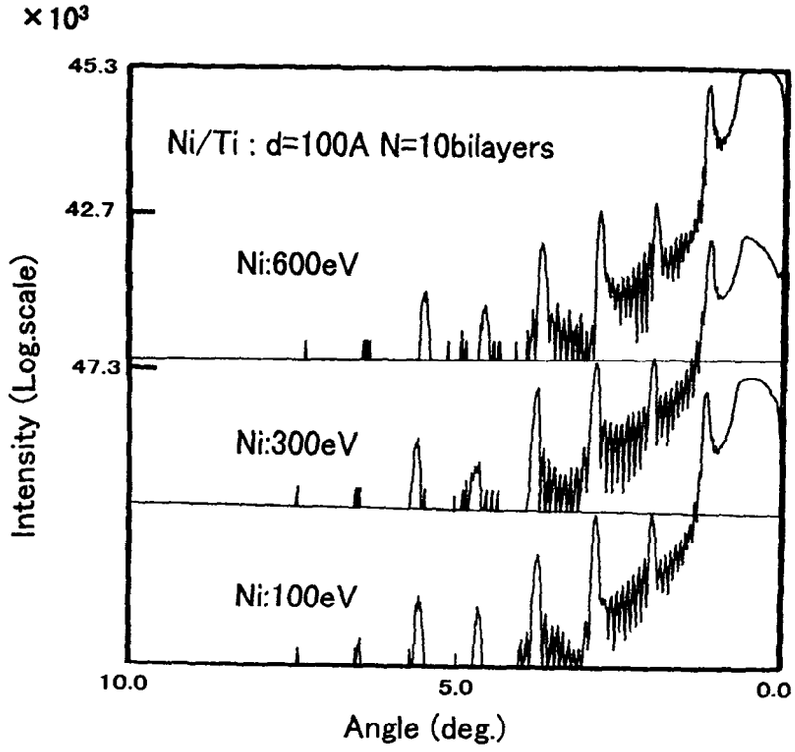

Fig.4 Cu Kα reflection profiles of Ni/Ti multilayers having Ni layers ion polished with variable ion energies

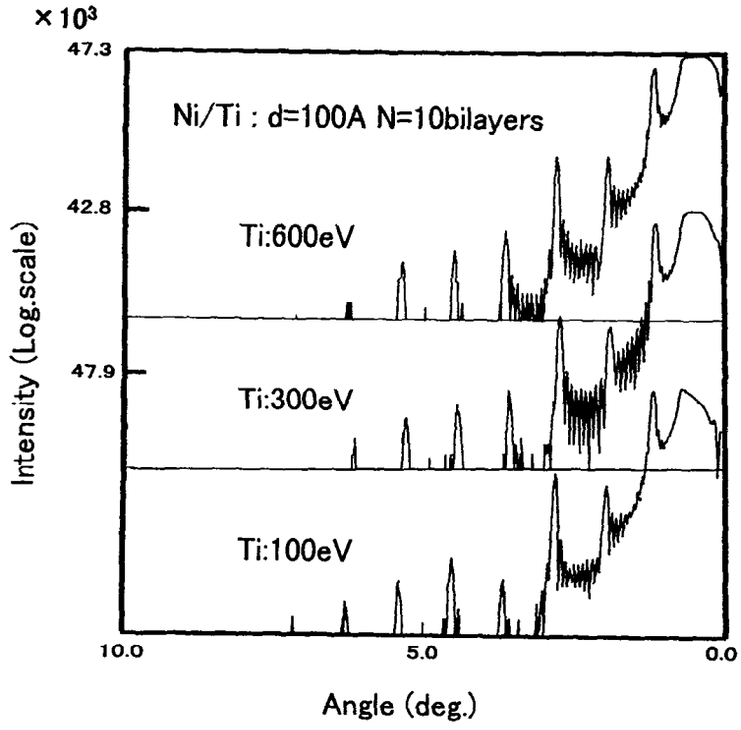

Fig.5 Cu Kα reflection profiles of Ni/Ti multilayers having Ti layers ion polished with variable ion energies

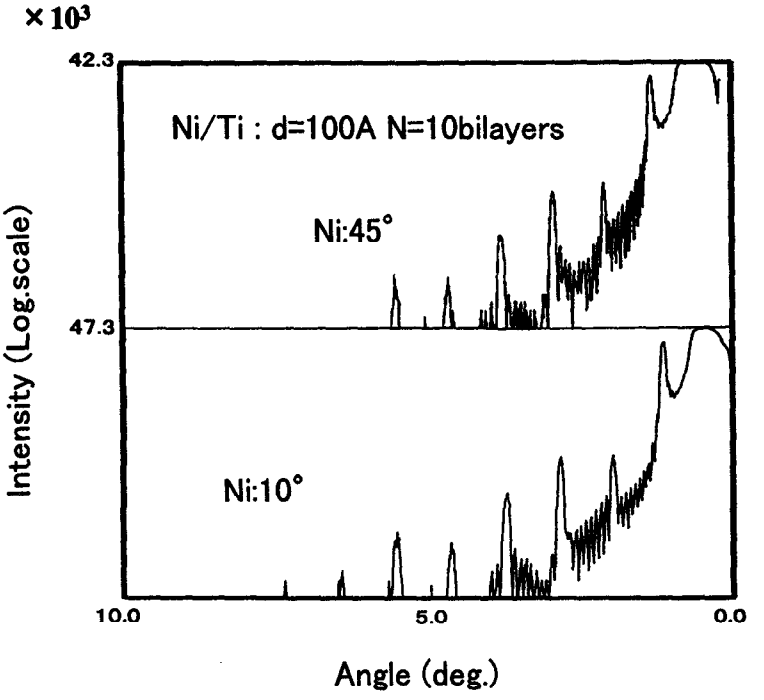

Fig.6 Cu Kα reflection profiles of Ni/Ti multilayers
having Ni layers ion polished with variable incident angles

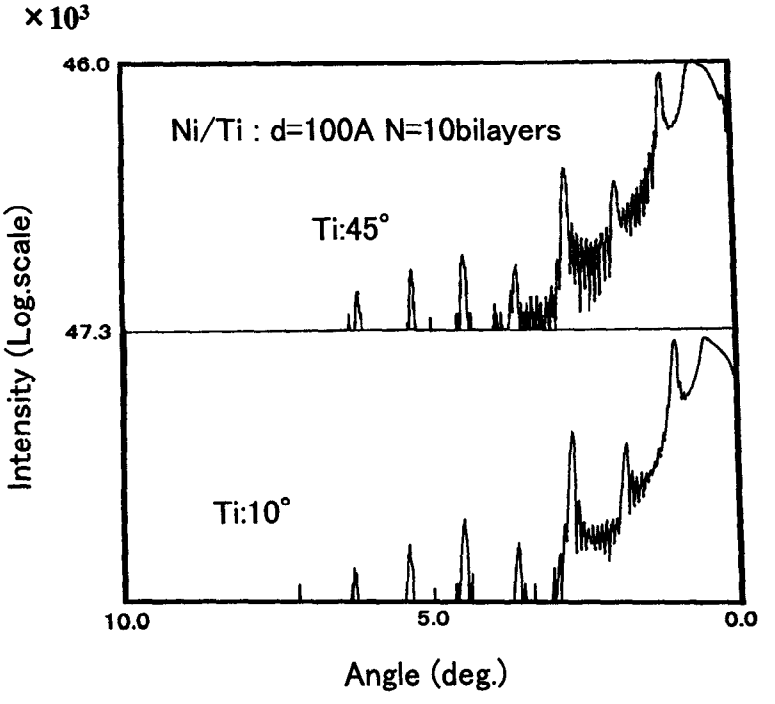

Fig.7 Cu Kα reflection profiles of Ni/Ti multilayers
having Ti layers ion polished with variable incident angles

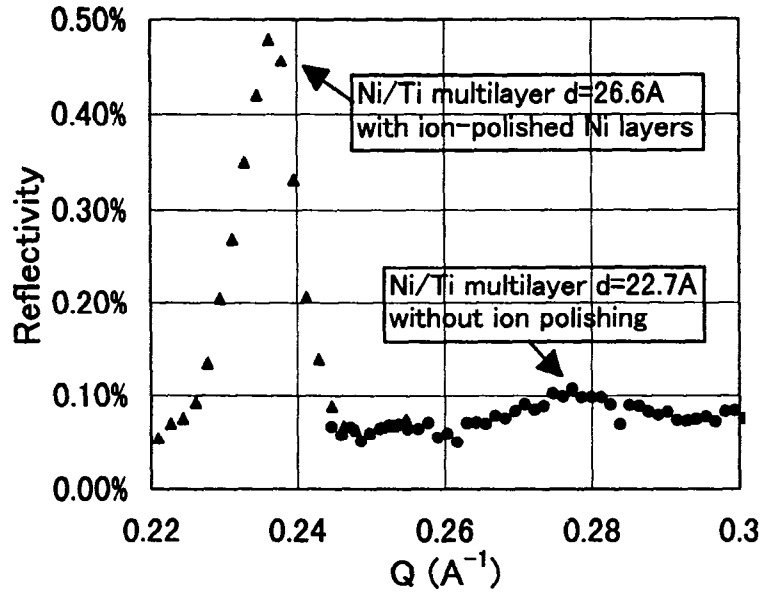

Fig.8 Neutron reflectivity profiles of Ni/Ti multilayers,
▲ with ion-polished Ni layers, ● without ion polishing

This page has intentionally been left blank.

ICANS-XIV
14th Meeting of the International Collaboration on
Advanced Neutron Sources
June 14-19, 1998
Starved Rock Lodge, Utica, Illinois, USA

General Time-Focusing of the Pulsed-Source Crystal Analyzer Spectrometer*

J. M. Carpenter
Intense Pulsed Neutron Source
Argonne National Laboratory

ABSTRACT

This paper outlines the derivation of an expression for the resolution of a crystal analyzer spectrometer and gives explicit conditions for geometric focusing. The development preserves full 3-dimensional generality so as to guide the choice of geometric parameters in the design of instruments. Historically, the high-resolution crystal analyzers are "backscattering" instruments, for which the Bragg angle is close to 90 degrees. The present results indicate that comparable high resolution can be attained using more general analyzer angles, which may provide some advantageous options for design. The focusing relationships define continuous, focused surfaces, and the results also provide a way to assess the resolution of a spectrometer built up of small, focused planar elements.

1. PRELIMINARY ANALYSIS

Figure 1 shows the conceptual layout of a crystal analyzer spectrometer. Pulses of neutrons emerge from the moderator surface "m" having wavelength λ'. Neutrons strike a sample "s" where they are scattered inelastically with energy gain ε to wavelength λ. Scattered neutrons impinge on the analyzer crystal "x" where, if their wavelength and incident angle are appropriate, they scatter, and if scattered in the appropriate direction, register in the detector "d".

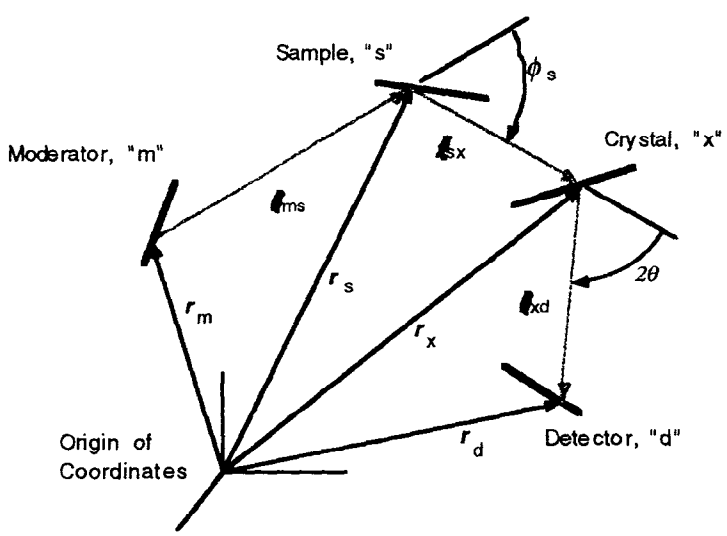

Figure 1. Schematic diagram of a crystal analyzer spectrometer. The figure shows a general neutron trajectory through the instrument (red). The elements m, s, x, and d (blue) are two-dimensional surfaces in a general, three-dimensional, non-planar arrangement.

* This work was performed under U. S. Government contract No. W-31-109-ENG-38.

We treat the instrument as having a thin sample, a thin analyzer crystal, and a thin detector, all planar. The angular distribution of neutrons from the source is isotropic and we ignore angular variation of the scattering and detection probabilities. There are no collimators.

The time to fly from the moderator surface to the detector is

$$t = \ell_1/v' + (\ell_2 + \ell_3)/v \,, \tag{1}$$

where v' and v are the neutron speeds before and after scattering, and ℓ_1, ℓ_2 and ℓ_3 are the distances between general points $\boldsymbol{r}_m$, $\boldsymbol{r}_s$, $\boldsymbol{r}_x$ and $\boldsymbol{r}_d$ on the moderator, sample, analyzer crystal, and detector surfaces, respectively. We seek to describe the instrument response when the scattering energy gain ε is unique,

$$\varepsilon = \frac{h^2}{2m}\left(1/\lambda'^2 - 1/\lambda^2\right) . \tag{2}$$

Then the flight time is

$$t = \frac{m}{h}(\ell_1\lambda' + (\ell_2 + \ell_3)\lambda) \,, \tag{3}$$

where

$$\lambda = \frac{h}{mv} \,. \tag{4}$$

2. FLIGHT PATH LENGTHS AND TIME OF FLIGHT

We pursue an analysis linearized in the small deviations of quantities from their mean values. While there are a number of equivalent ways to go about it, we develop an expression for the flight time, term by term and factor by factor, using expansions to first order in the deviations to arrive finally at a result which is linear in the deviations. This approach has the advantage of transparency, albeit at the expense of length.

We express the lengths of flight paths in terms of mean values and deviations from the mean values,

$$\ell_1 = \ell_1(\boldsymbol{r}_m,\boldsymbol{r}_s) = L_1 + \delta\,\ell_1(\boldsymbol{r}_m,\boldsymbol{r}_s) \tag{5}$$

$$\ell_2 = \ell_2(\boldsymbol{r}_s,\boldsymbol{r}_x) = L_2 + \delta\,\ell_2(\boldsymbol{r}_s,\boldsymbol{r}_x) \tag{6}$$

$$\ell_3 = \ell_3(\boldsymbol{r}_x,\boldsymbol{r}_d) = L_3 + \delta\,\ell_3(\boldsymbol{r}_x,\boldsymbol{r}_d) \tag{7}$$

where the mean values are

$$L_1 = \left\langle \ell_1(\boldsymbol{r}_m,\boldsymbol{r}_s) \right\rangle \,, \text{ etc.} \tag{8}$$

The averages are taken over the allowed positions on m, s, x and d. Throughout, boldface characters denote vector quantities; the circumflex designates a unit vector.

For a given path ($\boldsymbol{r}_m$, $\boldsymbol{r}_s$, $\boldsymbol{r}_x$, $\boldsymbol{r}_d$) through the instrument the analyzer scattering angle 2θ is unique, the Bragg angle is

$$\theta = \theta(\boldsymbol{r}_s,\boldsymbol{r}_x,\boldsymbol{r}_d) = \theta_o + \delta\,\theta(\boldsymbol{r}_s,\boldsymbol{r}_x,\boldsymbol{r}_d) \tag{9}$$

and only one wavelength λ is reflected,

$$\lambda = \lambda(r_s, r_x, r_d) = 2d \sin\left(\theta(r_s, r_x, r_d)\right), \tag{10}$$

$$\lambda = 2d \sin \theta_o(1 + \cot \theta_o \delta\, \theta(r_s, r_x, r_d)) = \lambda_o + \delta\, \lambda(r_s, r_x, r_d)\,. \tag{11}$$

For scattering with unique energy gain ε [equation (2)] if the mean wavelength after scattering is λ_o, the mean incident wavelength is λ'_o

$$\lambda'^{\,2}_o = 1/(1/\lambda_o^2 + 2m\varepsilon/h^2) \tag{12}$$

so the ratio of pre- and post-scattering wavelengths is

$$\lambda'_o / \lambda_o = 1/\sqrt{1 + 2m\varepsilon\lambda_o^2/h^2}\,. \tag{13}$$

Meanwhile, with ε fixed, when λ differs from λ_o then λ' differs from λ_o' by an amount found by differentiating the relationship (2), expressed in homogeneous form,

$$F(\lambda, \lambda'; \varepsilon) = 1/\lambda'^2 - 1/\lambda^2 - 2m\varepsilon/h^2 = 0\,, \tag{2'}$$

$$\left.\frac{\partial F}{\partial \lambda}\right|_{\lambda_o} \delta\lambda + \left.\frac{\partial F}{\partial \lambda'}\right|_{\lambda'_o} \delta\lambda' = 2/\lambda_o^3 \delta\lambda - 2/\lambda'^{\,3}_o \delta\lambda' = 0 \tag{14}$$

so that

$$\delta\lambda' = (\lambda'_o/\lambda_o)^3 \delta\lambda\,. \tag{15}$$

Then the flight time for a general neutron trajectory is

$$t = t(r_m, r_s, r_x, r_d) = \frac{m}{h}\{(L_1 + \delta\ell_1(r_m, r_s))(\lambda'_o + \delta\lambda') +$$

$$+ (L_2 + \delta\ell_2(r_s, r_x) + L_3 + \delta\ell_3(r_x, r_d))(\lambda_o + \delta\lambda)\} \tag{16}$$

which to first order in the deviations of the flight paths and wavelengths from the means is

$$t = \frac{m}{h}\{\lambda'_o L_1 + \lambda_o(L_2 + L_3) + \lambda'_o \delta\ell_1 + \lambda_o(\delta\ell_2 + \delta\ell_3) + L_1 \delta\lambda' + (L_2 + L_3)\delta\lambda\}\,. \tag{17}$$

We have defined the mean values so that the deviations average to zero. The first term is the dominant term t_o,

$$t_o = \frac{m}{h}(\lambda'_o L_1 + \lambda_o(L_2 + L_3))\,, \tag{18}$$

which is independent of the deviations. Thus, after a few steps of algebra, in view of (11), we can express the time of flight in terms of the deviations (which depend on the path through the instrument)

$$t = t_o + \frac{1}{v_o}[(\lambda'_o/\lambda_o)\delta\ell_1 + (\delta\ell_2 + \delta\ell_3)] + \frac{1}{v_o}[(\lambda'_o/\lambda_o)^3 L_1 + (L_2 + L_3)] \cot \theta_o \delta\theta\,. \tag{19}$$

It turns out to be more convenient to express the wavelength deviation

$$\delta\lambda = \lambda_o \cot\theta_o \delta\theta \tag{20}$$

in terms of the deviation of $\cos 2\theta$ from its nominal value,

$$\delta\lambda = 2d\,\delta(\sin\theta) = 2d\frac{\partial(\sin\theta)}{\partial(\cos 2\theta)}\delta(\cos 2\theta)\,. \tag{21}$$

Since

$$\sin\theta = \sqrt{(1-\cos 2\theta)/2}\,, \tag{22}$$

$$\frac{\partial(\sin\theta)}{\partial(\cos 2\theta)} = -\frac{1}{4}\frac{1}{\sqrt{(1-\cos 2\theta)/2}} = -\frac{1}{4\sin\theta} \tag{23}$$

so that

$$\delta\lambda = -2d\left(\frac{1}{4\sin\theta_o}\right)\delta(\cos 2\theta) = -\lambda_o\delta(\cos 2\theta)/4\sin^2\theta_o\,. \tag{24}$$

Therefore the flight time for a general neutron trajectory is

$$t = t_o + \frac{1}{v_o}[(\lambda'_o/\lambda_o)\delta\ell_1 + (\delta\ell_2 + \delta\ell_3)] - \frac{1}{4v_o}[(\lambda'_o/\lambda_o)^3 L_1 + (L_2 + L_3)]\frac{1}{\sin^2\theta_o}\delta(\cos 2\theta)\,. \tag{25}$$

3. THE COUNTING RATE DISTRIBUTION

The observed counting rate distribution $C(T)$ at time T is the weighted sum of the rates for all the allowed paths through the instrument,

$$C(T) = \int i(\lambda',t')F_m(\mathbf{r}_m)F_s(\mathbf{r}_s)P_x(\mathbf{r}_x,\lambda,\hat{q})P_d(\mathbf{r}_d,\lambda)\delta(T - t' - t(\mathbf{r}_m,\mathbf{r}_s,\mathbf{r}_x,\mathbf{r}_d))\,d^2\mathbf{r}_m\,d^2\mathbf{r}_s\,d^2\mathbf{r}_x\,d^2\mathbf{r}_d\,dt' \tag{26}$$

where the wavelengths λ and λ' depend uniquely on the path through the instrument. Here, $F_m(\mathbf{r}_m)$ represents the distribution of intensity on the moderator surface and $F_s(\mathbf{r}_s)$ represents the distribution of the allowed points on the sample. We assume that the wavelength-time distribution $i(\lambda',t')$ is independent of position on the moderator surface and slowly varying with respect to wavelength, though sharply varying with time,

$$i(\lambda',t') \approx i(\lambda'_o,t')\,. \tag{27}$$

Considering that the detection probability is independent of the position of the incident neutron and (already assumed in the treatment outlined above) independent of the direction of incidence, and moreover, is slowly varying with respect to wavelength,

$$P_d(\mathbf{r}_d,\lambda) = \eta(\lambda)F_d(\mathbf{r}_d) \approx \eta(\lambda_o)F_d(\mathbf{r}_d)\,. \tag{28}$$

Equation (26) does not include an overall normalization factor accounting for, for example, the $1/r^2$ variation of the intensity or for the scattering power of the sample. Thus (26) as written (for simplicity) gives only a relative intensity, while it provides for a valid calculation of the resolution.

The probability of reflection from the crystal decomposes similarly into a product

$$P_x(\boldsymbol{r}_x,\lambda,\hat{q}) = F_x(\boldsymbol{r}_x)p_x(\lambda,\hat{q}) \approx F_x(\boldsymbol{r}_x)p_x(\lambda_o,\hat{q}) \tag{29}$$

in which $F_x(\boldsymbol{r}_x)$ represents the distribution of allowed points on the crystal, and $p_x(\lambda,\boldsymbol{q})$ is the angle-dependent reflection probability, which depends strongly on $\boldsymbol{q}$, the direction of momentum transfer of the neutron, and weakly on the wavelength, since we have already built in the Bragg condition. Figure 2 illustrates the analyzer geometry, which could be either a reflection (shown) or a transmission arrangement.

The reflection probability must account for a mosaic distribution of finite width and for secondary extinction, which flattens the reflectivity distribution. We ignore the shift in reflecting position due to propagation of neutrons in the crystal and incorporate everything else in the function $p_x(\lambda,\boldsymbol{q})$ which depends parametrically on the nominal reflecting vector τ_o , the unit vector perpendicular to the nominal reflecting planes. The 2-dimensional distribution $p_x(\lambda,\boldsymbol{q})$ (a scalar function) depends on individual crystal properties, and is sharply peaked for values of $\boldsymbol{q}$ near τ_o .

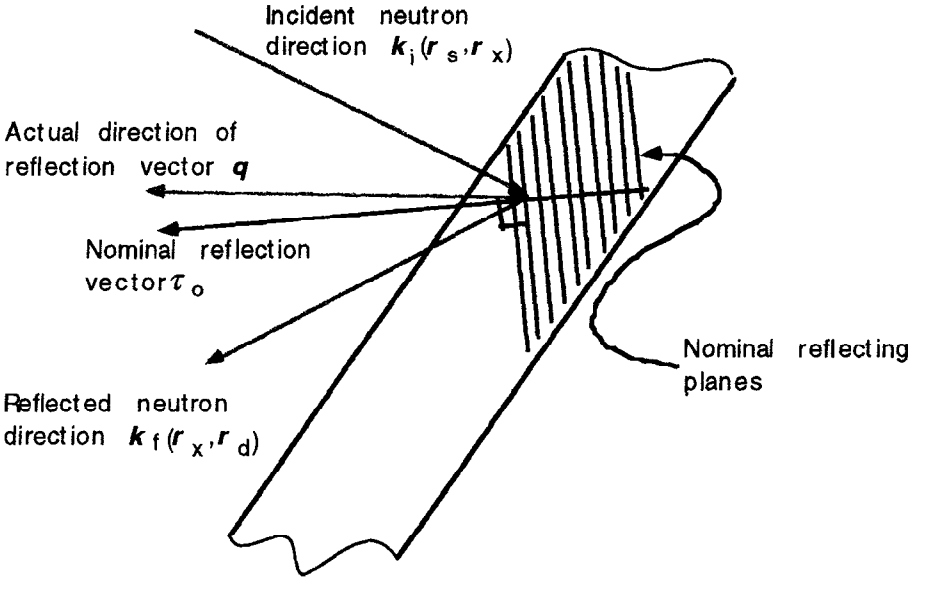

Figure 2. Diagram of crystal reflection, intentionally general in that the reflecting planes are not parallel to the cut plane of the crystal.

For the moment we denote the reflection probability as a function of the vector $\boldsymbol{q}\times\tau_o$, a measure of the deviation of $\boldsymbol{q}$ from τ_o

$$p_x(\lambda_o,\hat{q}) = f_x(\lambda_o,\hat{q}\times\hat{\tau}_o)\,, \tag{30}$$

which is a function similar to that shown in Figure 3.

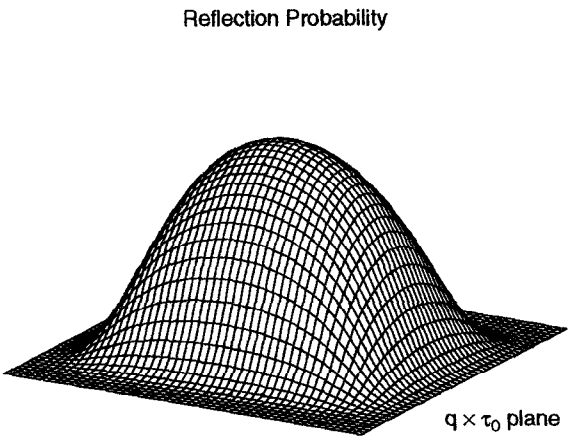

Figure 3. Schematic illustration of the reflection probability function.

The angular distribution of neutrons reflected by the analyzer crystal, and thus the spectrometer resolution in the absence of focusing, is doubly determined: by the strictly geometric effects of the finite sample, analyzer crystal, and detector; and by the effect of the mosaicity and orientation of the reflecting planes of the crystal.

4. OUTLINE OF THE FOCUSING CALCULATION

Now we clarify the intent of our effort. We compute the counting rate function C(T) (which applies for the given, fixed energy transfer ε),

$$C = \int C(T)dT \tag{31}$$

$$\bar{T} = \frac{1}{C}\int T\, C(T)dT \tag{32}$$

$$\sigma_T^2 = \frac{1}{C}\int (T-\bar{T})^2 C(T)dT \tag{33}$$

Focusing implies that σ_T^2 is a minimum with respect to instrument parameters.

It is of central importance to treat the expression for the counting rate function C(T) in terms of distributions of independently distributed variables; these appear in the overall distribution as products of distributions of individual variables. Thus it would be incorrect to compute σ_T^2 using expression (19) assuming, for example, that $\delta\ell_1$ is independent of $\delta\ell_2$ and $\delta\theta$; the independently distributed variables are r_m, r_s, r_x, r_d. Both $\delta\ell_1$ and $\delta\ell_2$ depend, for example, on r_s, so variations in $\delta\ell_2$ are not independent of variations in $\delta\ell_1$. Therefore we must eventually reduce our expression for the time of flight, t, to one that depends explicitly on the independently distributed variables.

First, however, we note a simplifying feature of the problem, namely that the emission time distribution, at least within our approximation, only broadens the overall result and does not require separate analysis. Writing (26) as

$$C(T) = \int i(\lambda'_o, t')\delta\,(T - t' - \tau)c(\tau)dt'd\tau \tag{34}$$

where

$$c(\tau) = \int F_m(\boldsymbol{r}_m) F_s(\boldsymbol{r}_s) F_x(\boldsymbol{r}_x) p_x(\tilde{q}(\boldsymbol{r}_s, \boldsymbol{r}_x, \boldsymbol{r}_d)) F_d(\boldsymbol{r}_d) \eta(\lambda_o) \times$$

$$\times \delta\left(\tau - t(\boldsymbol{r}_m, \boldsymbol{r}_s, \boldsymbol{r}_x, \boldsymbol{r}_d)\right) d^2\boldsymbol{r}_m \, d^2\boldsymbol{r}_s \, d^2\boldsymbol{r}_x \, d^2\boldsymbol{r}_d \tag{35}$$

we find that the mean time of the counting rate distribution is

$$\bar{T} = \bar{T}_i(\lambda'_o) + t_o \tag{36}$$

in which $\bar{T}_i(\lambda'_o)$ is the mean of the pulse emission time distribution for neutrons of wavelength λ'_o, and the variance of the counting time distribution is

$$\sigma_T^2 = \sigma_i^2(\lambda'_o) + \sigma_g^2(\lambda_o) . \tag{37}$$

Here t_o is the mean flight time through the instrument. σ_g^2 is the time variance due to the instrument geometry alone, which is the object of our consideration and is to be minimized while the counting rate C is made maximum. $\sigma_i^2(\lambda'_o)$ is the variance of the emission time distribution which is a quantity determined by the moderator properties. We will ignore effects of the source pulse emission time distribution in the work immediately to follow. However, the width of the emission time distribution imposes an irreducible lower limit on the resolution of the instrument and sets the scale for the geometric resolution.

5. EXPRESSIONS FOR DISTANCES AND ANGLES

Now we must obtain explicit expressions for the distances, angles, etc., and the deviations of these from their mean values, in terms of the independently distributed variables, the positions $\boldsymbol{r}_m$, $\boldsymbol{r}_s$, $\boldsymbol{r}_x$, $\boldsymbol{r}_d$ of vertices of the neutron path on the spectrometer surfaces. We will carry as much generality as possible.

The vector distances between vertices in the neutron path through the instrument are

$$\begin{aligned} \boldsymbol{\ell}_{ms} &= \boldsymbol{r}_s - \boldsymbol{r}_m \\ \boldsymbol{\ell}_{sx} &= \boldsymbol{r}_x - \boldsymbol{r}_s \\ \boldsymbol{\ell}_{xd} &= \boldsymbol{r}_d - \boldsymbol{r}_x . \end{aligned} \tag{38}$$

We define the mean positions of the elements of the instrument as

$$\begin{aligned} \boldsymbol{R}_m &= \langle \boldsymbol{r}_m \rangle = \frac{1}{A_m} \int_{A_m} \boldsymbol{r}_m \, d^2\boldsymbol{r}_m \\ \boldsymbol{R}_s &= \langle \boldsymbol{r}_s \rangle = \frac{1}{A_s} \int_{A_s} \boldsymbol{r}_s \, d^2\boldsymbol{r}_s \\ \boldsymbol{R}_x &= \langle \boldsymbol{r}_x \rangle = \frac{1}{A_x} \int_{A_x} \boldsymbol{r}_x \, d^2\boldsymbol{r}_x \\ \boldsymbol{R}_d &= \langle \boldsymbol{r}_d \rangle = \frac{1}{A_d} \int_{A_d} \boldsymbol{r}_d \, d^2\boldsymbol{r}_d , \end{aligned} \tag{39}$$

where the A s are areas of the relevant surfaces. The mean distances vectors between elements of the instrument are

$$\begin{aligned} \boldsymbol{L}_{ms} &= \boldsymbol{R}_s - \boldsymbol{R}_m \\ \boldsymbol{L}_{sx} &= \boldsymbol{R}_x - \boldsymbol{R}_s \\ \boldsymbol{L}_{xd} &= \boldsymbol{R}_d - \boldsymbol{R}_x . \end{aligned} \tag{40}$$

Nominal scattering angles follow from their cosines: the cosine of the nominal scattering angle at the sample is

$$\cos \varphi_{so} = \hat{L}_{ms} \cdot \hat{L}_{sx} = \frac{L_{ms} \cdot L_{sx}}{|L_{ms}||L_{sx}|} \tag{41}$$

and the cosine of the scattering angle at the analyzer (twice the nominal Bragg angle) is

$$\cos 2\theta_o = \hat{L}_{sx} \cdot \hat{L}_{xd} = \frac{L_{sx} \cdot L_{xd}}{|L_{sx}||L_{xd}|} . \tag{42}$$

Deviations of points on the vertices of the path through the instrument from the mean points are

$$\begin{aligned} \delta_m &= r_m - R_m \\ \delta_s &= r_s - R_s \\ \delta_x &= r_x - R_x \\ \delta_d &= r_d - R_d , \end{aligned} \tag{43}$$

as illustrated in Figure 4. Vector distances between points on the neutron trajectory are

$$\begin{aligned} \ell_{ms} &= R_s - R_m + \delta_s - \delta_m = L_{ms} + \delta_s - \delta_m \\ \ell_{sx} &= R_x - R_s + \delta_x - \delta_s = L_{sx} + \delta_x - \delta_s \\ \ell_{xd} &= R_d - R_x + \delta_d - \delta_x = L_{xd} + \delta_d - \delta_x \end{aligned} \tag{44}$$

and detailed scattering angles on the neutron path are

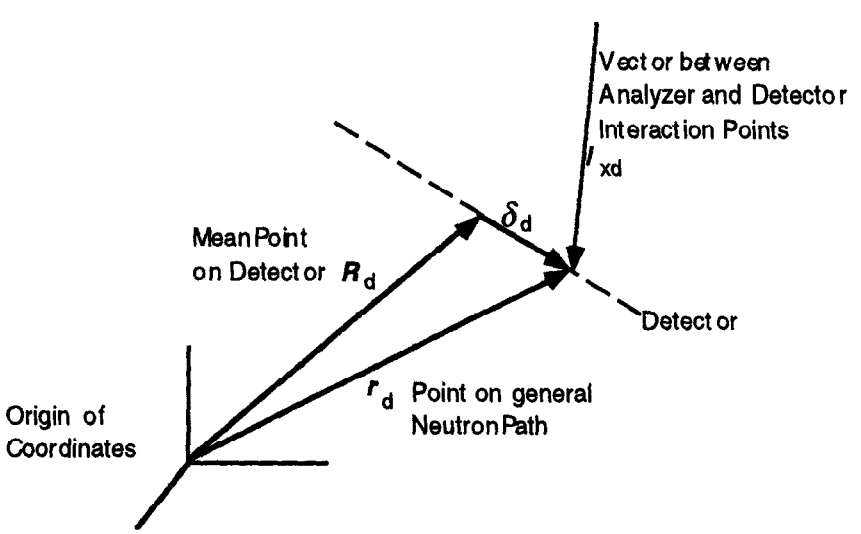

Figure 4. Illustration of the definition of position deviations on (for example) the detector surface.

$$\cos \varphi_s = \hat{\ell}_{ms} \cdot \hat{\ell}_{sx} = \frac{\ell_{ms} \cdot \ell_{sx}}{|\ell_{ms}||\ell_{sx}|} \tag{45}$$

and

$$\cos 2\theta = \hat{\ell}_{sx} \cdot \hat{\ell}_{xd} = \frac{\ell_{sx} \cdot \ell_{xd}}{|\ell_{sx}||\ell_{xd}|}, \tag{46}$$

in which the angles depend on the path through the instrument, that is, on $\boldsymbol{r}_m$, $\boldsymbol{r}_s$, $\boldsymbol{r}_x$, $\boldsymbol{r}_d$ or, equivalently, on the deviations of the positions of the vertices from those of the nominal path through the instrument, δ_m, δ_s, δ_x, δ_d.

Now we work out expressions for various needed quantities as first-order approximations in the position deviations. The (scalar) length of the path between the emission point on the moderator to the scattering point on the sample is, for example,

$$\ell_{ms} = |\ell_{ms}| = (\ell_{ms} \cdot \ell_{ms})^{1/2} \tag{47}$$

so that

$$\ell_{ms} = [L_{ms}^2 + 2L_{ms} \cdot (\boldsymbol{\delta}_s - \boldsymbol{\delta}_m) + (\boldsymbol{\delta}_s - \boldsymbol{\delta}_m)^2]^{1/2}, \tag{48}$$

which to first order in the deviations is

$$\ell_{ms} \approx L_{ms}[1 + \hat{L}_{ms} \cdot (\boldsymbol{\delta}_s - \boldsymbol{\delta}_m) / L_{ms}],$$

thus also

$$\ell_{sx} \approx L_{sx}[1 + \hat{L}_{sx} \cdot (\boldsymbol{\delta}_x - \boldsymbol{\delta}_s) / L_{sx}]$$

and

$$\ell_{xd} \approx L_{xd}[1 + \hat{L}_{xd} \cdot (\boldsymbol{\delta}_d - \boldsymbol{\delta}_x) / L_{xd}]. \tag{49}$$

Similarly, the inverse flight path lengths, to first order, are

$$\frac{1}{\ell_{ms}} \approx \frac{1}{L_{ms}}[1 - \hat{L}_{ms} \cdot (\boldsymbol{\delta}_s - \boldsymbol{\delta}_m) / L_{ms}],$$

$$\frac{1}{\ell_{sx}} \approx \frac{1}{L_{sx}}[1 - \hat{L}_{sx} \cdot (\boldsymbol{\delta}_x - \boldsymbol{\delta}_s) / L_{sx}]$$

and

$$\frac{1}{\ell_{xd}} \approx \frac{1}{L_{xd}}[1 - \hat{L}_{xd} \cdot (\boldsymbol{\delta}_d - \boldsymbol{\delta}_x) / L_{xd}]. \tag{50}$$

The cosine of the scattering angle at the analyzer crystal is

$$\cos 2\theta = \hat{\ell}_{sx} \cdot \hat{\ell}_{xd} = \frac{\ell_{sx} \cdot \ell_{xd}}{\ell_{sx}\ell_{xd}} =$$

$$= \frac{1}{L_{sx}L_{xd}}[1 - \hat{L}_{sx} \cdot (\boldsymbol{\delta}_x - \boldsymbol{\delta}_s) / L_{sx}][1 - \hat{L}_{xd} \cdot (\boldsymbol{\delta}_d - \boldsymbol{\delta}_x) / L_{xd}](L_{sx} + \boldsymbol{\delta}_x - \boldsymbol{\delta}_s) \cdot (L_{xd} + \boldsymbol{\delta}_d - \boldsymbol{\delta}_x), \tag{51}$$

which to first order in the deviations is

$$\cos 2\theta = (\hat{L}_{sx} \cdot \hat{L}_{xd}) - (\hat{L}_{sx} \cdot \hat{L}_{xd})[\hat{L}_{sx} \cdot (\boldsymbol{\delta}_x - \boldsymbol{\delta}_s) / L_{sx} + \hat{L}_{xd} \cdot (\boldsymbol{\delta}_d - \boldsymbol{\delta}_x) / L_{xd}] +$$

$$+ \hat{L}_{sx} \cdot (\boldsymbol{\delta}_d - \boldsymbol{\delta}_x) / L_{xd} + \hat{L}_{xd} \cdot (\boldsymbol{\delta}_x - \boldsymbol{\delta}_s) / L_{sx}. \tag{52}$$

In (52), we recognize the leading term as the cosine of the nominal scattering angle at the analyzer,

$$\cos 2\theta_o = (\hat{L}_{sx} \cdot \hat{L}_{xd}) , \tag{53}$$

with the deviation of $\cos 2\theta$ from its nominal value

$$\delta(\cos 2\theta) = -\cos 2\theta_o [\hat{L}_{sx} \cdot (\delta_x - \delta_s) / L_{sx} + \hat{L}_{xd} \cdot (\delta_d - \delta_x) / L_{xd}] +$$

$$+ \hat{L}_{sx} \cdot (\delta_d - \delta_x) / L_{xd} + \hat{L}_{xd} \cdot (\delta_x - \delta_s) / L_{sx} . \tag{54}$$

The result for the cosine of the scattering angle at the sample is similar to (51) (replace s with m, replace x with s, replace d with x). With the assumed nondispersive (ε independent of the scattering vector) scattering at the sample, we have no explicit use for this. However, in the case of dispersive scattering, the analysis would require it, and would need to be redone with greater generality. We do not provide the result here.

Several tasks remain before the results become explicitly useful: to combine all these results into a first-order expression for the time-of-flight, to collect separately the coefficients of the deviations δ_m, δ_s, δ_x, δ_d; and to set explicit coordinate systems to represent the distributions F_m, F_s, F_x, and F_d. Focusing conditions will appear after the second of these steps is completed, in that the focusing conditions require that the collected coefficients are zero. The expression for the resolution will be explicit after the third step. Finally, representations for the Fs and for the reflectivity function $p_x(\lambda,q)$ are required to complete the calculation for the resolution width σ_g^2.

6. FOCUSING

We recall the expression for the time of arrival in terms of the deviations of the flight path lengths from their mean values and of the cosine of the analyzer scattering angle from its mean value

$$t = t_o + \frac{1}{v_o}[(\lambda'_o/\lambda_o)\delta\ell_1 + (\delta\ell_2 + \delta\ell_3)] - \frac{1}{4v_o}[(\lambda'_o/\lambda_o)^3 L_1 + (L_2 + L_3)] \frac{1}{\sin^2\theta_o}\delta(\cos 2\theta) \tag{25}$$

and introduce the somewhat simplified notation

$$L_1 = L_{ms} , \ \ell_1 = \ell_{ms} , \ \delta\ell_1 = \hat{L}_{ms} \cdot (\delta_s - \delta_m) , \tag{55}$$

$$L_2 = L_{sx} , \ \ell_2 = \ell_{sx} , \ \delta\ell_2 = \hat{L}_{sx} \cdot (\delta_x - \delta_s) , \tag{56}$$

$$L_3 = L_{xd} , \ \ell_3 = \ell_{xd} , \ \delta\ell_3 = \hat{L}_{xd} \cdot (\delta_d - \delta_x) . \tag{57}$$

We now collect terms that represent independently distributed contributions to the distribution of times of arrival:

$$t = t_o + (\delta_m \, term) + (\delta_s \, term) + (\delta_x \, term) + (\delta_d \, term) . \tag{58}$$

When these terms are made to vanish by choice of geometric parameters of the instrument, the corresponding contributions to the resolution width vanish.

The expression (25), correct though it is to first order in the deviations, does not imply that the variance of the time distribution, as, for example, in (37), is the sum of variances of those terms

separately. This is because the crystal reflection probability correlates the δ_s, δ_x, and δ_d distributions. Similar correlations would enter if collimators were included between elements of the instrument and treated in the analysis, which have not been included but could be. Nevertheless, if the terms in (58) are made to vanish by choice of geometric parameters, the corresponding contributions to the resolution vanishes and focusing is accomplished.

The δ_m term is

$$(\boldsymbol{\delta}_m \, term) = -\frac{1}{v_o}(\lambda'_o/\lambda_o)\hat{L}_1 \cdot \boldsymbol{\delta}_m \, . \tag{59}$$

Since δ_m is a vector that lies in the moderator surface, focusing clearly requires that the incident beam emerge perpendicularly from the moderator face; then the δ_m term is zero, independent of the extent of the moderator surface. This result may be intuitively obvious, but it is reassuring that it emerges from the present analysis.

The δ_s term is

$$(\boldsymbol{\delta}_s \, term) = \frac{1}{v_o}\{[(\lambda'_o/\lambda_o)\,\hat{L}_1 - \hat{L}_2] - \frac{1}{4\sin^2\theta_o}[(\lambda'_o/\lambda_o)^3 L_1 + L_2 + L_3]\times$$

$$\times[\cos 2\theta_o \hat{L}_2/L_2 - \hat{L}_3/L_2]\} \cdot \boldsymbol{\delta}_s \tag{60}$$

The geometric implications of this term are not clear at this point; we leave it for further interpretation at a later stage of the analysis.

The δ_x term is

$$(\boldsymbol{\delta}_x \, term) = \frac{1}{v_o}\{(\hat{L}_2 - \hat{L}_3) - \frac{1}{4\sin^2\theta_o}[(\lambda'_o/\lambda_o)^3 L_1 + L_2 + L_3]\times$$

$$\times[-\cos 2\theta_o(\hat{L}_2/L_2 - \hat{L}_3/L_3) - \hat{L}_2/L_3 + \hat{L}_3/L_2]\} \cdot \boldsymbol{\delta}_x \tag{61}$$

and the δ_d term is

$$(\boldsymbol{\delta}_d \, term) = \frac{1}{v_o}\{\hat{L}_3 - \frac{1}{4\sin^2\theta_o}[(\lambda'_o/\lambda_o)^3 L_1 + L_2 + L_3]\times$$

$$\times[-\cos 2\theta_o \hat{L}_3/L_3 + \hat{L}_2/L_3]\} \cdot \boldsymbol{\delta}_d \, , \tag{62}$$

both of which we also leave for interpretation at a later stage of the analysis. Already, however, we can provide a preliminary interpretation. The focusing conditions (59-62) are vector inner products. The expressions can be made zero either if the bracketed quantity, a three-dimensional vector, is perpendicular to the corresponding vector deviation δ (that is, collinear with the vector normal to the surface) or if the vector itself is one of zero length. It may be possible, in view of the presence of the factor (λ_o'/λ_o), to provide exact focusing independently of the value of the energy transfer ε, by separately zeroing and/or orthogonalizing the ε-dependent and ε-independent terms in (60-62). Otherwise, if exact focusing is impossible or inconvenient, adequate reduction of the resolution width may be accomplishable for a finite range of energy transfers by keeping the terms (60-62) small. We note that the length of the initial flight path, L_1, appears explicitly in (60-62) so that focusing and resolution considerations cannot be based solely on the geometry of the secondary spectrometer.

In application, it may be useful to recall that the detector elements can be made small using an area sensitive detector comprising small, independently-operating flat elements, and that the analyzer properties can be varied as a function of position on the analyzer, as in a curved array of flat crystals in which the crystal cut and orientation may vary from one position to another. In addition, there may be cases where the sample is small and the corresponding contribution to the resolution, equation (60), is negligible. Then zeroing equation (60) may be superfluous and the remaining conditions for "partial focusing" may be easier to implement.

Equations (59-62) define elements of surfaces, "focused loci", in general curved, such that variations of position on those surfaces do not affect the time of arrival. They are the first order terms in a vector Taylor expansion of the time of arrival in terms of the local (planar) deviations of the positions from the mean positions of the elements of the spectrometer, equivalent respectively to

$$(\boldsymbol{r}_m - \boldsymbol{R}_m) \cdot \nabla_{\boldsymbol{r}_m} t(\boldsymbol{r}_m, \boldsymbol{r}_s, \boldsymbol{r}_x, \boldsymbol{r}_d)\Big|_{\boldsymbol{R}_m, \boldsymbol{R}_s, \boldsymbol{R}_x, \boldsymbol{R}_d} \tag{63}$$

$$(\boldsymbol{r}_s - \boldsymbol{R}_s) \cdot \nabla_{\boldsymbol{r}_s} t(\boldsymbol{r}_m, \boldsymbol{r}_s, \boldsymbol{r}_x, \boldsymbol{r}_d)\Big|_{\boldsymbol{R}_m, \boldsymbol{R}_s, \boldsymbol{R}_x, \boldsymbol{R}_d} \tag{64}$$

$$(\boldsymbol{r}_x - \boldsymbol{R}_x) \cdot \nabla_{\boldsymbol{r}_x} t(\boldsymbol{r}_m, \boldsymbol{r}_s, \boldsymbol{r}_x, \boldsymbol{r}_d)\Big|_{\boldsymbol{R}_m, \boldsymbol{R}_s, \boldsymbol{R}_x, \boldsymbol{R}_d} \tag{65}$$

$$(\boldsymbol{r}_d - \boldsymbol{R}_d) \cdot \nabla_{\boldsymbol{r}_d} t(\boldsymbol{r}_m, \boldsymbol{r}_s, \boldsymbol{r}_x, \boldsymbol{r}_d)\Big|_{\boldsymbol{R}_m, \boldsymbol{R}_s, \boldsymbol{R}_x, \boldsymbol{R}_d}, \tag{66}$$

although we have derived them by developing first order expansions rather than by calculating gradients. The general curved focused surfaces are defined by the exact equation

$$t\,(\boldsymbol{r}_m, \boldsymbol{r}_s, \boldsymbol{r}_x, \boldsymbol{r}_d) = \text{constant} = t\,(\boldsymbol{R}_m, \boldsymbol{R}_s, \boldsymbol{R}_x, \boldsymbol{R}_d), \tag{67}$$

to which the Taylor expansion is an approximation. Designs based on this linearized focusing analysis, whereby high resolution instrument configurations can be recognized in the analytical forms, need to be checked out, for example, by numerical integration of equation (35) or by Monte Carlo simulation, or by measurements in prototype arrangements.

We have finished our task at a preliminary level at which focusing conditions appear. It remains to introduce explicit geometric representations of the elements of the spectrometer in order to interpret the results and generate estimates of the resolution for non-focused conditions.

7. A NOTE ON THE INSPIRATION FOR THIS ANALYSIS

The inspiration for this analysis is the experience with powder and single-crystal diffraction, wherein it is possible to nullify the geometric instrumental resolution, at least for certain restricted conditions, and in resonance-detector/filter spectrometers. In the first case, the simple algorithm "$L \sin \theta$ = constant" [1] provides conditions on the orientation of source, sample, and detectors that allow use of large apertures and areas and the consequent intensity improvements while preserving q resolution. This focusing also provides data systems simplifications in time-of-flight powder diffraction instruments. Modern powder diffractometers accomplish this electronically. The single-crystal implementation has application in measurements of moderator emission time distributions [2] wherein the requirement is that the instrument contribution to the observed width be negligible within very tight constraints while the intensity is maintained at a useful level. These are "two-leg" instruments. Several crystal analyzer instruments ("three-leg" instruments) employ what might be called "partial focusing," QENS and CHEX at IPNS, TFXA and TOSCA at ISIS, and CAT and the LAM instruments at KENS. However, their designs may not have accounted for the full range of

effects treated here. Meanwhile, the high-resolution crystal analyzer instruments, LAM 80ET at KENS, and IRIS and OSIRIS at ISIS, employ nearly backscattering geometries that possibly can be made more general. In the case of the resonance spectrometers [3,4] (for deep inelastic, i.e. recoil, scattering) the same general ideas also work to improve the resolution.

ACKNOWLEDGMENT

I express my gratitude for the hospitality of the Rutherford Appleton Laboratory, where the opportunity for concentrated attention to this work made its accomplishment possible. I also thank E. B. Iverson and D. F. R. Mildner for assistance in checking the results.

REFERENCES

[1.] J. M. Carpenter, "Extended Detectors in Neutron Time-of-Flight Experiments," *Nucl. Instr. and Meth.* 47, 179 (1967).
[2.] K. F Graham and J. M. Carpenter, "Pulsed Moderator Studies Using a Time-Focused Crystal Spectrometer," *Nucl. Instr. and Meth.* 85, 163 (1970).
[3.] J. M. Carpenter and N. Watanabe, "Time Focusing and Resolution in Resonance Detector Neutron Spectrometers," *Nucl. Instr. and Meth.* 213, Nos. 2,3, 311 (1983).
[4.] J. M. Carpenter, N. Watanabe, S. Ikeda, Y. Masuda and S. Sato, "A Resonance Detector Spectrometer at KENS," *Physica* 120B, 126 (1983).

Appendix
The Wavevector Change for Scattering at the Analyzer

In order to evaluate the intensity and resolution either numerically or analytically, we require specific forms which represent the distributions of accessible positions on the moderator, sample, analyzer, and detector, and an explicit form for the reflection probability. In addition, for the same purposes, we need the expression for the unit reflection vector $\hat{q}$, which we have not worked out above. For convenience in some of the envisioned uses, we represent this in terms of an expansion to first order in the flight path length deviations.

First, we develop a linearized expression for the unit vector $\hat{b}$ that corresponds to a vector b which is itself the sum of two vectors, one large, B, and one small, δ,

$$b = B + \delta \ . \tag{A1}$$

The unit vector is

$$\hat{b} = (B + \delta)/\left|B + \delta\right| \ . \tag{A2}$$

The inverse magnitude of the vector, to first order in the small quantity, is

$$1/\left|B + \delta\right| \approx [B^2 + 2B \cdot \delta]^{-1/2} \approx B^{-1}[1 - \hat{B} \cdot \delta / B] \tag{A3}$$

where $\hat{B}$ is the unit vector and B the magnitude of B,

$$\hat{B} = B / B \tag{A4}$$

and

$$B = \left|B\right| . \tag{A5}$$

Thus, to first order in δ,

$$\hat{b} \approx \frac{1}{B}(B + \delta)[1 - \hat{B} \cdot \delta / B] \approx \hat{B} + \delta / B - \hat{B}(\hat{B} \cdot \delta / B) \ , \tag{A6}$$

which, to first order in δ, is manifestly a unit vector.

Because the scattering is elastic and the incident and scattered wavevectors are parallel to the vectors representing the incident and scattered paths to and from the analyzer, the direction of the wavevector change upon scattering at the analyzer is the same as the direction of the vector q

$$q = \hat{\ell}_3 - \hat{\ell}_2 \ , \tag{A7}$$

where the $\hat{\ell}$ s are <u>unit</u> vectors in the directions of incidence and emergence from the analyzer. In terms of deviations from the means, the connecting <u>distance</u> vectors (44) are of the form

$$\ell = L + \delta\ell \tag{A8}$$

so that for each, according to (A6), the unit vector $\hat{\ell}$ is

$$\hat{\ell} = \hat{L} + \delta\ell / L - \hat{L}(\hat{L} \cdot \delta\ell / L) \ . \tag{A9}$$

Now we express the wavevector $\boldsymbol{q}$ in the form

$$\boldsymbol{q} = \boldsymbol{q}_o + \delta\boldsymbol{q} \ , \tag{A10}$$

where

$$\boldsymbol{q}_o = (\hat{L}_3 - \hat{L}_2) \tag{A11}$$

and

$$\delta\boldsymbol{q} = \frac{\delta\ell_3}{L_3} - \frac{\delta\ell_2}{L_2} - \hat{L}_3(\hat{L}_3 \cdot \frac{\delta\ell_3}{L_3}) + \hat{L}_2(\hat{L}_2 \cdot \frac{\delta\ell_2}{L_2}) \ . \tag{A12}$$

By (A6) we find

$$\hat{\boldsymbol{q}} = \hat{\boldsymbol{q}}_o + \frac{\delta\boldsymbol{q}}{\left|\hat{L}_3 - \hat{L}_2\right|} - \hat{\boldsymbol{q}}_o \frac{\hat{\boldsymbol{q}}_o \cdot \delta\boldsymbol{q}}{\left|\hat{L}_3 - \hat{L}_2\right|} \ . \tag{A13}$$

The leading term in (A13) is the unit vector corresponding to the geometrically definednominal scattering vector at the analyzer, $\hat{\boldsymbol{q}}_o$,

$$\hat{\boldsymbol{q}}_o = \frac{(\hat{L}_3 - \hat{L}_2)}{\left|\hat{L}_3 - \hat{L}_2\right|} \ . \tag{A14}$$

Here,

$$\left|\hat{L}_3 - \hat{L}_2\right|^2 = 2\,(1 - \hat{L}_3 \cdot \hat{L}_2) = 2(\,1 - \cos 2\theta_o\,) = 4\sin^2\theta_o \ , \tag{A15}$$

so that

$$\left|\hat{L}_3 - \hat{L}_2\right| = 2\sin\theta_o \ . \tag{A16}$$

Now writing

$$\hat{\boldsymbol{q}} = \hat{\boldsymbol{q}}_o + \delta\hat{\boldsymbol{q}} \ , \tag{A17}$$

we find from (A13), after some arithmetic, that $\delta\hat{\boldsymbol{q}}$ is

$$\delta\hat{\boldsymbol{q}} = \frac{1}{2\sin\theta_o}\left\{\begin{array}{l} \frac{\delta\ell_3}{L_3} - \frac{\delta\ell_2}{L_2} + \frac{1}{2}(\hat{L}_2 + \hat{L}_3)(\hat{L}_2 \cdot \frac{\delta\ell_2}{L_2} - \hat{L}_3 \cdot \frac{\delta\ell_3}{L_3}) - \\ \qquad - \frac{1}{4\sin^2\theta_o}(\hat{L}_2 - \hat{L}_3)(\hat{L}_2 - \hat{L}_3) \cdot (\frac{\delta\ell_3}{L_3} - \frac{\delta\ell_2}{L_2}) \end{array}\right\} , \tag{A18}$$

in which

$$\delta\ell_2 = \delta_x - \delta_s \tag{A19}$$

and

$$\delta\ell_3 = \delta_d - \delta_x \ . \tag{A20}$$

It is probably as well in practice to use (A14) and (A16) with $\delta\boldsymbol{q}$ from (A12) recursively to compute $\hat{\boldsymbol{q}}$ and $\delta\hat{\boldsymbol{q}}$ in (A13).

ICANS XIV
14th Meeting of the International Collaboration on Advanced Neutron Sources
June 14-19, 1998
Starved Rock Lodge, Utica, IL

Extending the Domain of Time-of-Flight Powder Diffraction Techniques.

Paolo G. Radaelli
ISIS Facility, Rutherford Appleton Laboratory, Chilton Didcot, Oxfordshire, OX11 0QX, UK

ABSTRACT

One of the most significant drawbacks traditionally attributed to the time-of-flight method is its intrinsically limited q-range at low q. For this reason, a significant number of scientific application of neutron powder diffraction have remained almost exclusive domain of constant-wavelength techniques. In this paper, we will discuss a number of possible routes to extend the q-domain of the time-of-flight technique. Some of these methods can be applied to the new instruments which are currently being constructed, with only minor modifications to the detector and software design. We will also discuss an "angular focusing" technique, which would require an altogether different detector concept, but would produce significant advantages both in terms of instrument performances and of q-range.

I. INTRODUCTION

Up to now, the field of neutron powder diffraction has enormously benefited from the complementary nature of time-of-flight (TOF) and constant-wavelength (CW) techniques. Broadly speaking, TOF powder diffraction has concentrated on producing histograms where constant resolution is obtained over relatively narrow d-spacing ranges (Δd = 2-4 Å), possibly extending to very high $q=2\pi/d$ (q is the so-called elastic momentum transfer), whereas CW powder diffraction allows a very large d-spacing range to be accessed on a single histogram (Δd = 20-40 Å), albeit with variable resolution and relatively low q_{Max}. Clearly, there is a significant overlap between the two techniques, but a non-negligible subset of the powder diffraction applications requires either high q_{Max} (e.g., Fourier transform-based methods like pair distribution function analysis, or PDF) or extended d-spacing ranges (e.g., magneto-structural determinations, host/guest problems etc.). However, since in the future the most intense advanced neutron scattering facilities will be pulsed sources, an increasingly large fraction of the available beam time for neutron powder diffraction will be at TOF instrument. If the quality of the demand from the scientific community does not change, this requires the domain of TOF powder diffraction to be progressively extended towards areas which have up to now been regarded as almost exclusive to CW instruments. To this effect, three approaches could be envisaged: 1) Promoting a more effective use of the available solid angle at low 2θ, by making multi-bank indexing and refinements a routine practice for the average user. 2) Extending the q-range of single histograms on individual banks. 3) Combining all the available solid angle in a *single* histogram with *variable* resolution, as it is done on CW diffractometers. The first two approaches can be implemented on thermal-neutron diffractometers using current technology, and are presently guiding the development of new machines like the General Material Diffractometer GEM at ISIS. The feasibility of the third approach, namely for cold-neutron diffractometers, will also be discussed in the present paper.

II. THE MULTI-BANK APPROACH

Most TOF powder diffractometers are equipped with more than one detector bank, and typically have banks at back-scattering, 90 degrees and "low angle" (60-30 degrees), the first two being the most frequently used for high-resolution and special-environment applications, respectively. Although each of these banks is used for particular applications, the *simultaneous* use of all banks is not routine practice. In fact, setting up and successfully completing a multi-histogram Rietveld refinement is a rather complex task, which is undertaken only when the potential benefit of the additional information is clearly perceived. For this reason, simultaneous x-ray and neutron (X&N) refinements are more common than multi-bank refinements, due to the enhanced elemental sensitivity of the X&N technique. Furthermore, the benefit of the additional information at low q is not infrequently offset by the overall increase of χ^2, since the quality of the multi-bank fits is lower than that of single-banks ones. This situation can only be reversed if the bank structure is made *transparent* to the user, in the sense that the TOF-to-d-spacing conversion parameters (e.g., DIFA and DIFC in the GSAS notation[1]) and the instrumental profile parameters are determined once and for all by the instrument scientist and not refined every time. An even more stringent requirement concerns

multi-bank *indexing:* it should be possible to feed the extracted Bragg peak positions to an auto-indexing code and

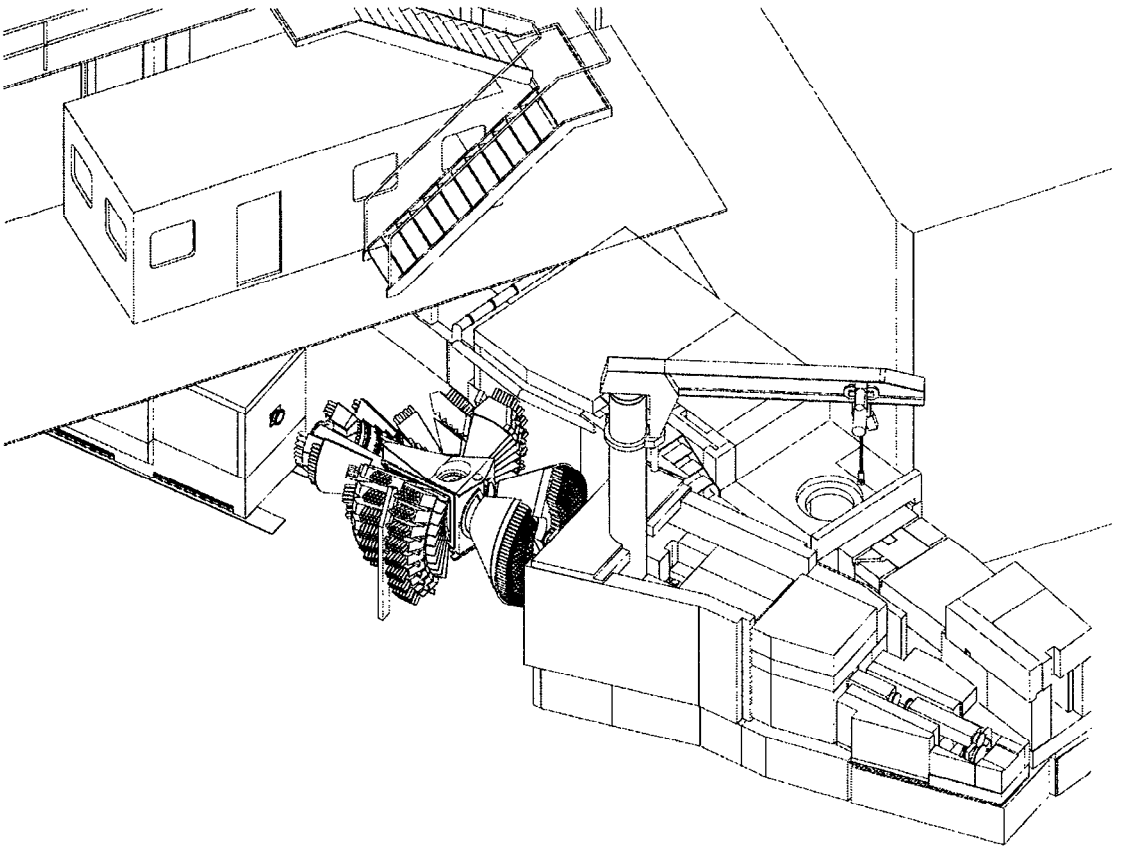

Figure 1: An artist's view of the new high-intensity General Materials Diffractometer GEM, which is presently under construction at ISIS.

obtain good quality factors for the correct solution. Such ambitious goals present major challenges for both the instrument designer and the software developer, and require a different approach to the measurement itself.

Instrument Requirements: Understanding in detail the pulse-shape profile is in itself a major challenge, which is presently best accomplished through analytical expressions like the Ikeda-Carpenter function[2]. However, is unlikely that a profile resulting from the convolution of the Ikeda-Carpenter function with another asymmetric function could be properly modelled. Therefore, all other contribution to the instrumental peak profiles should be well understood, "simple" and symmetric for all banks. The sample size and shape should be accounted for by simple functions. This amounts to constructing instruments with *intrinsic rotational symmetry* around the incident beam. In fact, in addition to the pulse-shape function, the other major source of asymmetry in the peak profiles is the so-called *axial divergence*, which occurs whenever the Debye-Scherrer cones are not geometrically matched with the detector receiving surfaces. The only solution to this problem is to avoid axial asymmetry altogether, by matching the detector elements as close as possible to the Debye-Scherrer rings. This approach has already been implemented in back-scattering (HRPD, POLARIS, OSIRIS), but should become commonplace also for the other detector banks, if a truly user-friendly multi-bank analysis is envisaged. In the development of the new, high-flux General Materials Diffractometer GEM at ISIS, we have been paying close attention to this aspect. The aim of GEM (an artist view of the instrument is shown in Figure 1) is to achieve extremely fast data collection rates with a very wide solid angle coverage at all values of 2θ (see Table I), while still maintaining a sufficiently good resolution in back-scattering (2-3×10^{-3}). Once fully commissioned, GEM will be able to produce data suitable for refinements of complex nuclear and magnetic structures as a function of a rapidly changing variable (temperature, time, etc.). Also, the exceptional stability achieved on the GEM scintillator prototypes ($\sim1\times10^{-4}$) will allow GEM to excel also in the liquid/amorphous material arena, as well as for measurements of total scattering. Figure 2 shows the calculated peak

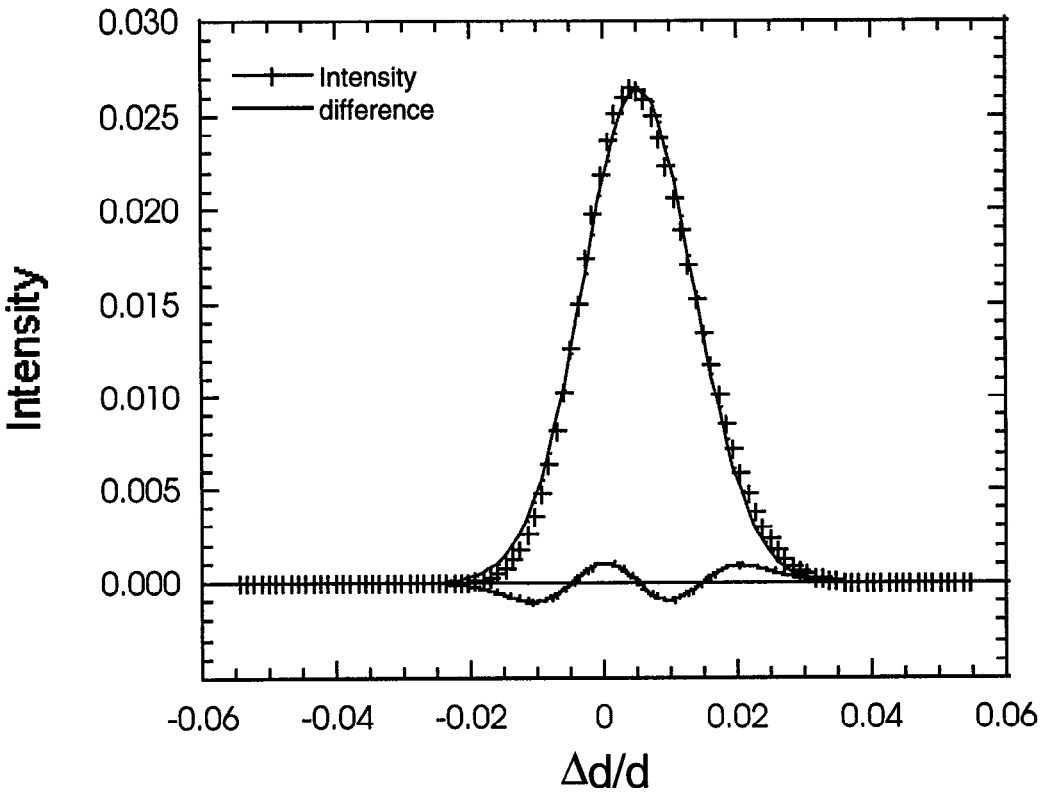

Figure 2: Calculated profile (crosses) and Gaussian fit (continuous line) for a typical setting of GEM-Bank2. Note the asymmetric profile and the shift from the ideal "Bragg" position, due to axial divergence..

profile for the 20-degree bank (GEM-Bank2) assuming that the receiving detector element is a vertical 200mm × 5mm × 5mm parallelepiped. Also shown is the best Gaussian fit to the data. The poor matching between the two curves is clearly evidenced by the difference curve. Note that neither of the two curves peaks at 0 (which is the ideal Bragg value), because the axial divergence not only affects peak *shapes*, but also peak *positions*. The calculation does not include the pulse-shape function, the effect of which is minute at 20 degrees. However, it should be kept in mind that, for higher angle banks, the total profile results from the convolution of these two asymmetric profiles. A quantitative description of the profiles resulting from axial divergence has been developed by Van Laar and Yelon for the case of constant-wavelength diffractometers [3], and has recently been implemented in the Rietveld code GSAS in a slightly modified form [4]. However, a convolution of the Van Laar-Yelon function with the Ikeda-Carpenter function is not currently implemented in any Rietveld code, and would presumably be very difficult to model and calibrated (note that the Van Laar-Yelon profile depends on sample *height*). A simplified description in terms of split functions could be envisaged, but such an approach would prevent absolute cross-bank calibration, because the position of the peak *maximum* (related to the DIFA parameter) depends on the width of the convoluting Gaussian, i.e., on parameters such as sample diameter, strain etc. Figure 3 shows a schematic layout of GEM-Bank2, as it is presently been detailed after performing the aforementioned analysis. The length of the detector elements (80 mm) is such that the width of the Debye-Scherrer rings across the element does not exceed the width of the detector.

Software Requirements.: Making the bank structure transparent to the user requires a change in the traditional layout of the Rietveld input files. The sample contribution to the peak profiles (to be routinely refined) should be kept separate from the instrument contribution. Also, geometric effects such as "effective" sample position (including transparency effects) should be properly taken into account.

Experimental Requirements. Carried to the extreme, the multi-bank approach implies that a *single* scale factor should be refined for all banks. In fact, one may argue that one should refine *no scale factor at all*, since the scale

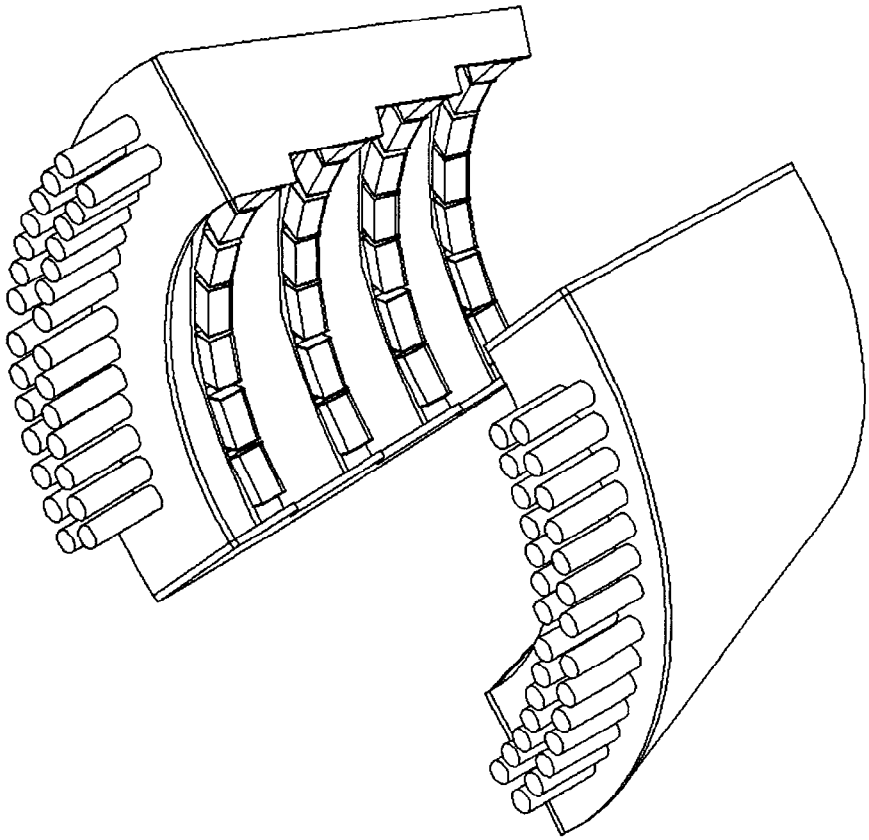

Figure 3: The layout of the 20-degree Bank 2 for GEM. Note the Debye-Scherrer binning over the large elevation angle range.

factor is nothing but a measure of the sample weight, which can obviously be obtained very precisely by other means. Such an approach, if implemented with sufficient accuracy, could have a non-negligible scientific value, especially in problems involving multiple site substitutions. Clearly, this is only possible if absorption, multiple-scattering and vanadium corrections (the latter for efficiency and incident flux) are performed consistently for every measurement. In other words, each measurement should yield *absolute cross sections* (Barns/Sterad/f.u.). This would have the additional benefit of making possible quantitative comparisons between coherent and incoherent scattering. It is noteworthy that absolute cross section measurements are routinely performed on liquid and amorphous materials.

III. THE SINGLE-BANK, NARROW BANDWIDTH APPROACH

Angle-dispersive and wavelength-dispersive techniques significantly differ in the way reciprocal space coverage is achieved. For CW instruments,

$$\Delta q = \frac{4\pi}{\lambda} \cdot \Delta(\sin\theta) \leq \frac{4\pi}{\lambda} = q_{MAX} \quad ; \quad q_{\min} = \frac{4\pi}{\lambda} \cdot \sin\theta_{\min} \tag{1}$$

In other words, for a given wavelength (histogram) there is an intrinsic limit to q_{MAX}, but the value of q_{min} is only dictated by the minimum measured value of the scattering angle. For instance, with a wavelength $\lambda = 2.4$ Å (near-optimum on thermal beams), values of $q_{min} \sim 0.2$ Å^{-1} (d~30 Å) can routinely be achieved Å, while keeping respectably high values of $q_{MAX} \sim 5$ Å^{-1}. The situation is completely different for the TOF technique: for a single bank focused at $2\theta_B$. In fact, for a given time frame,

$$\Delta q = (\hat{q})^2 \cdot \Delta\frac{1}{q} = (\hat{q})^2 \cdot \frac{1}{4\pi \sin\theta_B} \cdot \Delta\lambda \quad = \frac{3957\left[m \cdot \sec^{-1} \cdot \text{Å}\right]}{4\pi \sin\theta_B \cdot L[m]} \times \frac{(\hat{q})^2}{\nu\left[\sec^{-1}\right]} \qquad (2)$$

where $\hat{q} = \sqrt{q_{\min} \cdot q_{MAX}}$, L is the flight-path and ν is the repetition rate. In other words, Δq is proportional to the *square* of $\hat{q}$ (logarithmic average of the reciprocal space vector modulus) and *inversely proportional to the repetition rate*, all other parameters being fixed by the instrument geometry. This means, first of all, that it is much easier to cover the reciprocal space efficiently at high q than for CW instruments, which explains the extraordinary success of TOF instruments for applications where a high value of q_{MAX} is required. However, the implication is that low-q coverage is an exercise of diminishing returns, particularly for high-resolution instruments. For instance, for HRPD in back-scattering (L ~100 m; ν 10 Hz; ΔT~100 msec) the typical frame setting (30 msec < T < 130 msec) covers a q-range 2.4 Å^{-1}< q < 10.42 Å^{-1}; Δq = 8.02 Å^{-1}. The next frame setting (130 msec < T < 230 msec) covers 1.36 Å^{-1}< q < 2.40 Å^{-1}, with Δq = 1.04 Å^{-1}.

To a certain extent, these constraints are imposed by the nature of the wavelength-dispersive technique. However, it is possible to obtain extended q-space histograms by carefully choosing the data acquisition strategy. Traditionally, in high-resolution TOF, extended q-data sets are obtained by reducing the repetition rate (see equation (2)). This approach has the disadvantage that the integrated flux, and, as a consequence, the statistical quality of the data, widely vary across the histogram. A better choice is to run the instrument at *high repetition rate* (narrow bandwidth), and accumulate data across the desired q-range by varying $\overline{\lambda}$. This narrow bandwidth (NBW) method is currently employed for cold neutron diffractometers, like OSIRIS, where the typical required d-spacing range (>10 Å) is much bigger than the typical d-spacing window (~2 Å). As an example, Figure 4 shows two low-temperature powder diffraction patterns for the antiferromagnetic compound $La_{0.5}Ca_{0.5}MnO_3$, as obtained on a CW instrument (D2B at the ILL) and on a TOF instrument (OSIRIS at ISIS). For OSIRIS, the complete powder pattern was reconstructed by adding up a series of 8 individual histogram, each with a d-spacing range of 2 Å. In order to estimate the required acquisition times to obtain uniform statistics, we recall that, in the TOF method, the integrated intensity of a Bragg peak is given by the formula:

$$I_{hkl} = N \cdot i(\lambda) \frac{\lambda^4}{32\pi v_0} m_{hkl} \left|F_{hkl}\right|^2 \frac{\Omega}{\sin^3\theta} \qquad (3)$$

where the following symbols are used:

N Number of Unit Cells
$i(\lambda)$ Incident Flux
v_0 Unit Cell Volume
m_{hkl} Reflection Multipliciy
$\left|F_{hkl}\right|^2$ Structure Factor
Ω Detector Solid Angle
θ Bragg angle

Therefore, uniform statistics would be obtained by setting an acquisition time T such that the function $T \cdot i(\lambda) \cdot \lambda^4$ is constant . Note that CW data *do not have uniform statistics*, but are biased at low q due to the Lorentz factor $\frac{1}{\sin 2\theta \cdot \sin\theta}$, which is roughly proportional to $\frac{1}{q^2}$ (the exact q-dependence of the Lorentz factor depends on the wavelength). In order to have the same bias in the TOF method, one would need to operate at constant $T \cdot i(\lambda) \cdot \lambda^2$. Clearly, the details of the scientific case for each experiment may require a different bias, which may

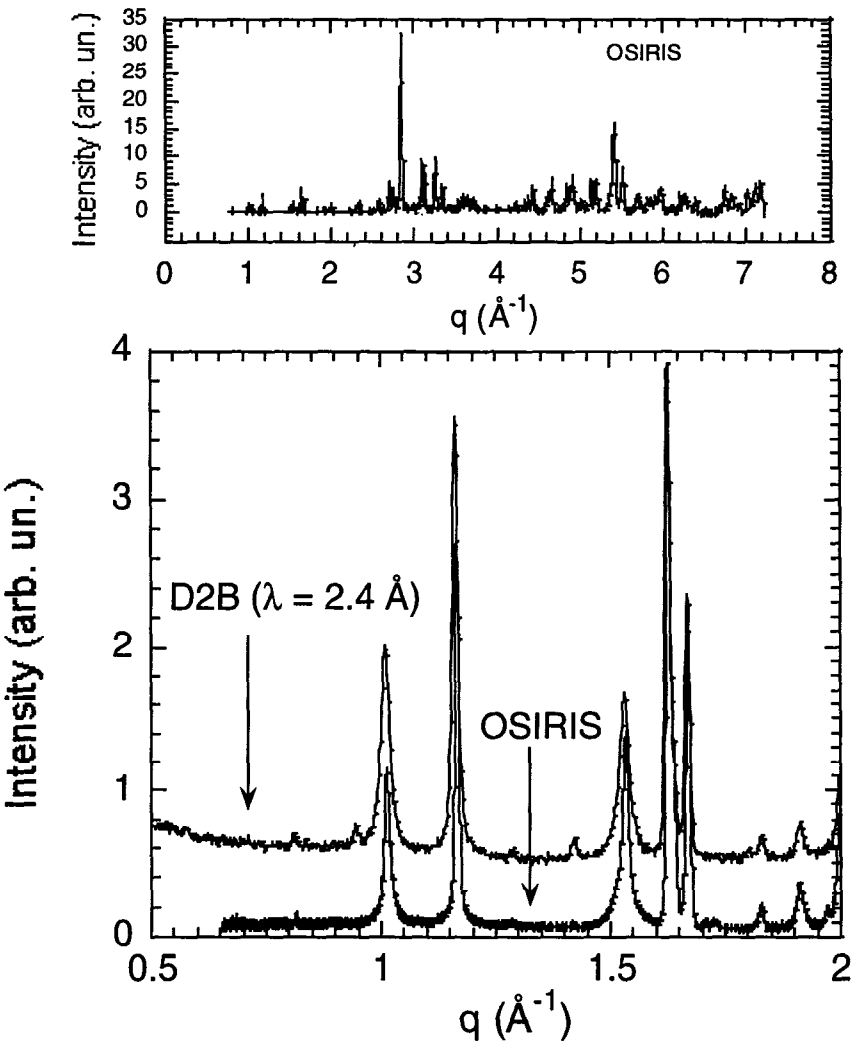

Figure 4: **Top:** Extended q-range histogram for $La_{0.5}Ca_{0.5}MnO_3$ as measured on OSIRIS, by combining data from 8 chopper phase settings. With the $\lambda = 2.4$ Å wavelength, D2B has a q-range of ~ 5 Å^{-1}. **Bottom:** Comparison between OSIRIS and D2B ($\lambda = 2.4$ Å) in the low-q range for the same compound. Note the better resolution and the absence of contamination in the OSIRIS data.

be achieved with an appropriate acquisition scheme. Figure 5 shows the functions $i(\lambda) \cdot \lambda^4$ and $i(\lambda) \cdot \lambda^2$, for the instrument HRPD at ISIS. It is clear by inspection that, by using a single large bandwidth window, the high-q data are enormously under-sampled, also due to the guide cut-off for epithermal neutrons, and there is potentially a very

significant high-q statistical gain to be obtained by operating the instrument at 50 Hz with variable acquisition times. There is also some under-sampling at long wavelengths for the "CW" bias.

It should be noted that the NBW optimisation is more efficient if a narrow wavelength window is selected. In other words, the NBW method yields the maximum gain in statistics if the instrument is operated at the *source frequency*. However, the efficiency of this mode of operation is reduced by the opening and closing time of the bandwidth-selecting chopper, which normally operates at constant frequency and with a variable aperture. Therefore, the use of the NBW method would be favoured by the development of high-speed choppers.

A distinct *disadvantage* of the NBW method is the fact that not all the final q-range is collected at the same time. Therefore, one would have to wait until the end of the measurement in order to see the low-q data, which significantly hampers the ability of the user to plan ahead in the experiment. A possible solution would be represented by the development of variable-speed choppers, which would "sweep" the required wavelength range many times during the measurements, according to a pre-established distribution. A similar method is employed in the Fourier Diffraction technique (Reference 5). It is noteworthy that the control over the phase of the chopper does not need to be very accurate, since all the data (including the incident spectrum) would be accumulated into an extended time frame, and treated as a single histogram.

IV. ANGLE-DISPERSIVE DATA BY THE TOF TECHNIQUE

The NBW method is a first step to bridge the gap between CW and traditional TOF instruments, since, at least at the low-q end of the spectrum, the bandwidth would only be a fraction of the average wavelength. One may think to go all the way along this line, and investigate the instrument requirements to obtain *angle-dispersive* data with the TOF

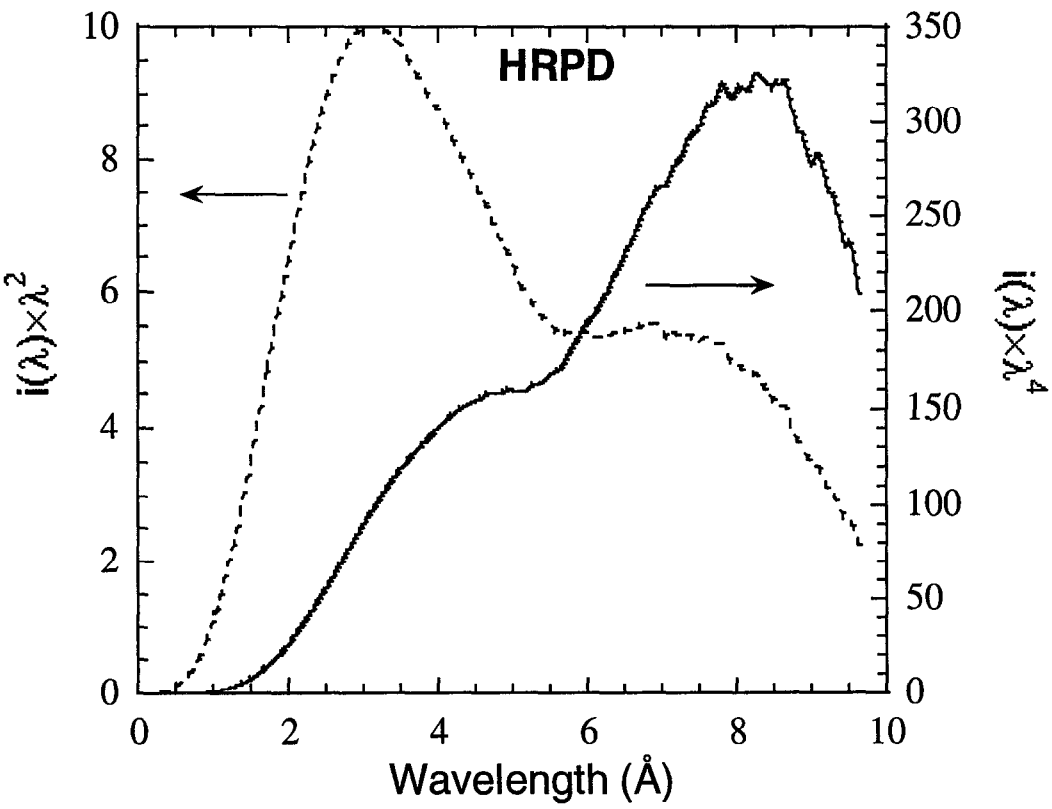

Figure 5: The two functions $i(\lambda)\cdot\lambda^4$ (right) and $i(\lambda)\cdot\lambda^2$ (left) for the instrument HRPD. The reciprocal of these functions is proportional to the data acquisition time for uniform statistics and "CW" statistics, respectively (see text).

method. This is only apparently a contradiction in terms. In fact, as long as the bandwidth is sufficiently small, it is possible to reconstruct a single, angle dispersive data set from TOF data by assigning to each TOF an angular correction (*angular focusing*). Table I shows that angular focusing is the "mirror image" of time focusing with respect to resolution focusing.

Table I: Relationship between different focusing techniques in TOF diffraction.

Technique	Time Focusing (TF)	Resolution Focus. (RF)	Angular Focusing (AF)
Focusing	$\tau \rightarrow \tau \pm \Delta\tau(2\theta)$	$q = q(\tau, 2\theta)$	$2\theta \rightarrow 2\theta \pm \Delta 2\theta(\tau)$
Angular Range	Narrow	Broad (in principle)	Broad
Wavelength Range	Broad	Broad	Narrow
Resolution	Fixed	Fixed	Variable
Histograms Types	Multiple angles	Single/Multiple angles	Multiple Wavelengths

In other words, in the TF technique, the angular range is limited by the need to limit resolution variations across the banks. Likewise, in the AF method, it is the *wavelength* range to be limited by the same requirement. If the "natural" bandwidth of the instrument (given by the source repetition rate through equation (2)) is *broader* than the required bandwidth, multiple wavelength-histograms can be obtained (each with a narrow BW), exactly as for the TF case, where multiple angle-histograms are measured. In principle, the RF focusing method is the best of both worlds, since it could be applied to large detector banks and broad BW. However, in practice, it is impossible to build resolution-focused detectors with very large 2θ ranges, and the RF technique remains confined to individual banks.

In order to assess the viability of the AF method, we need to calculate the fluctuation in resolution across the wavelength band that is focused to a given Bragg angle. To simplify the problem, we use the following expression for the resolution R (Reference 6):

$$R = \left[c^2 + (\delta \cdot \cot\theta)^2\right]^{1/2}, \tag{4}$$

where δ is the angular detector resolution, which includes contributions from the source divergence, sample size and detector element width, and c is the flight-path/pulse width uncertainty, which is, to first approximation, wavelength-independent. In this example, the parameter δ is assumed to be constant, as it would be the case for an instrument with constant secondary flight-path. It is important to stress, however, that this is not a requirement for the applicability of the AF method. The only true requirement is that *δ varies smoothly as a function of 2θ.* In fact, it may be convenient to have a variable secondary flight-path, to approach as much as possible the RF case. This would entail a slowly-varying resolution function, and would allow an even wider band-width to be accepted. In the simple case of δ constant, from equation (4) follows:

$$\frac{\Delta R}{R} = \frac{\delta^2 \cdot \cot\theta \cdot \dfrac{1}{\sin^2\theta}}{c^2 + (\delta \cdot \cot\theta)^2} \cdot \Delta\theta, \tag{5}$$

where $\Delta\theta$ is the angular spread associated to the wavelength band that is re-focused to a single value of θ, and is given by:

$$\Delta\theta = \frac{\Delta\lambda}{\lambda} \cdot \tan\theta \tag{6}$$

By combining equations (5) and (6) we obtain

$$\frac{\Delta R}{R} = \frac{1}{f^2 \cdot \sin^2\theta + \cos^2\theta} \cdot \frac{\Delta\lambda}{\lambda}, \text{ where } f^2 = \frac{c^2}{\delta^2} \tag{7}$$

We note that in the special case $c = \delta$ we get $\frac{\Delta R}{R} = \frac{\Delta \lambda}{\lambda}$. Therefore, the resolution fluctuation is comparable to the bandwidth. Clearly, in order to contain the resolution fluctuations, the data may need to be broken up into histograms, each one associated with a narrow BW.

Table II lists the relevant parameters of hypothetical cold-neutron AF instrument with a peak resolution of the order of 0.2%. The geometrical parameters are similar those of OSIRIS at ISIS, but, in our hypothesis, the present back-scattering bank is replaced with a continuous bank (from low- to high-angle) at fixed distance from the sample. The detector elevation angle is assumed to vary from -20° to 20°.

The advantages of this approach are significant: even with a rather conservative elevation angle range, this instrument would have 6.5 times the present OSIRIS solid angle. Also, since OSIRIS currently operates at 25 Hz, the incident flux will be the same, in spite of the narrower bandwidth. In addition, with our resolution fluctuation tolerance, a *single* histogram will be generated for $\lambda \geq 8$ Å. Furthermore, this instrument would have an enormous d-spacing range, whilst still retaining the same *maximum* resolution. The price to pay is that the resolution of this detector will *vary* as a function of 2θ, exactly as for CW instruments. However, this detector can very well coexist with a large-solid angle back-scattering detector, which could be operated either in the usual mode or in the NBW mode, providing constant-resolution data, when needed.

Table II: Geometrical parameters of a hypothetical instrument employing the angular focusing method.

PARAMETER	VALUE
Total Flightpath (m)	40.0
Flightpath/pulse width uncertainty (c)	0.00177
Secondary flightpath (mm)	2000.0
Detector element width (mm)	5.0
Source divergence (rad)	0.00125
Parameter δ	0.00177
Parameter f	1.0
Detector solid angle w. $-20° \leq \phi \leq 20°$ (Sterad)	4.3
"Natural" bandwidth $\Delta\lambda$ @ 50 Hz (Å)	2.0
# of histograms for $\frac{\Delta R}{R} = \pm 10\%$:	
$\lambda = 2$ Å	5
$\lambda = 4$ Å	3
$\lambda = 6$ Å	2
$8 \text{ Å} \leq \lambda \leq 30$ Å	1

V. CONCLUSIONS

As we have shown in this brief discussion, extending the domain of TOF powder diffraction represents a major challenge for future instruments. Some of the possible routes toward the solution of this problem have been outlined. Clearly, with the generation of diffractometers that are presently being built, a major effort should be put into making multi-bank analysis a routine technique. This involves a development both of the instrument design and of the data analysis software. Future instruments may benefit from the narrow-bandwidth and angular-focusing techniques, which will allow them to combine the benefits of the CW and TOF methods. With these instruments, in addition to the normal mode of operation and/or the NBW technique, it should be possible to acquire data with a *single* detector bank, having a very large solid angle and an extended 2θ range One of the major qualities of these instruments is that, similar to the CW instruments, they will produce data across extended q ranges with slowly-varying-resolution. This would make them appealing for a significant segment of the neutron diffraction community, which has so far employed exclusively the CW techniques.

VI. REFERENCES

1 R. B. von Dreele, J. D. Jorgensen, and C. J. Windsor, J.Appl.Cryst. **15**, 581 (1982).

2 S. Ikeda and J. M. Carpenter, Nuc. Instr. and Meth. **A239**, 536 (1985).

3 B. Van Laar and W. B. Yelon, J. Appl. Cryst. **17**, 47 (1984).

4 L. W. Finger, D. E. Cox, and A. P. Jephcoat, J. Appl. Cryst. **27**, 892 (1994).

5 V. L. Aksenov and A. M. Balagurov, Usp. Fizi. Nauk **166**, 955 (1996).

6 J. D. Jorgensen, J. Faber Jr, J. M. Carpenter, *et al.*, J.of Appl. Cryst. **22**, 321 (1989).

ICANS XIV
14th Meeting of the International Collaboration on
Advanced Neutron Sources
June 14-19, 1998
Starved Rock Lodge, Utica, IL

Polarisation Modulated Crosscorrelation Neutron Spectroscopy using ^{3}He Polarising Filters on a Pulsed Source

W. G. Williams

ISIS Facility, Rutherford Appleton Laboratory,
Chilton, Didcot, Oxon OX11 0QX, UK.

Abstract

A polarisation modulated crosscorrelation spectrometer using polarised ^{3}He spin filters is outlined. Current developments in polarised ^{3}He technology indicate that this spectrometer will be viable on the third generation pulsed neutron sources now being planned, providing a novel spectroscopic tool for magnetic studies. This paper focusses on discussing the optimisation of the performance of the ^{3}He polarising filters.

1. Introduction

The concept of extending the crosscorrelation neutron time-of-flight (TOF) technique from reactor to pulsed sources was first explored experimentally by Kroo et al. [1], and theoretically by Matthes [2]. The method relies on the use of a pseudorandom modulation device placed before the scatterer which allows the scattered neutron flight time to be measured; this together with the total TOF measurement enables the incident and scattered neutron wavevectors (and energies) to be determined. The first modulating devices were disc choppers on which a pseudorandom sequence was etched in the neutron absorbing material.

Cywinski and Williams [3] proposed an alternative cross-correlation method, polarisation (or spin) modulated crosscorrelation spectroscopy, based on a pulsed source total scattering polarisation analysis instrument with ^{149}Sm filters as the polariser and spin analyser. A limiting feature of ^{149}Sm polarising filters is that they are only effective over a modest neutron energy band, ~ 1 - 100 meV. Instead of modulating intensity (as with choppers) the polarisation state of the incident neutrons is modulated pseudorandomly using a pulsed spin flipper placed in front of the scatterer. Subsequent crosscorrelation of the measured intensity with the modulating sequence provides a TOF spectrum which is the difference between the TOF spectra of neutrons with the two spin polarisations. The technically demanding components of the instrument are the broad-band polarising filters.

It is now opportune, following the spectacular advances achieved in developing ^{3}He polarising filters [4], to review the potential of spin correlation spectroscopy, particularly in relation to instruments for third generation (Power > 1Mw) spallation neutron sources. This paper focusses on examining the ^{3}He polariser properties required for a spin crosscorrelation spectrometer.

2. Spin Crosscorrelation Spectroscopy - Basic Principles

A schematic diagram of the basic components in a pulsed source spin crosscorrelation spectrometer is shown in Figure 1. A background chopper is recommended to minimise fast neutron moderation and scattering in the bulky environment surrounding the scatterer. It is important to maximise the solid angle covered by the spin analysers, and the feasibility of building banana-shaped ^{3}He cells which analyse over ± 90° in the equatorial plane has already been demonstrated [5]. Spin flipper efficiencies approaching 100% over broad neutron energy bands are now commonplace, see ref. [6], and Badurek [7] has built very

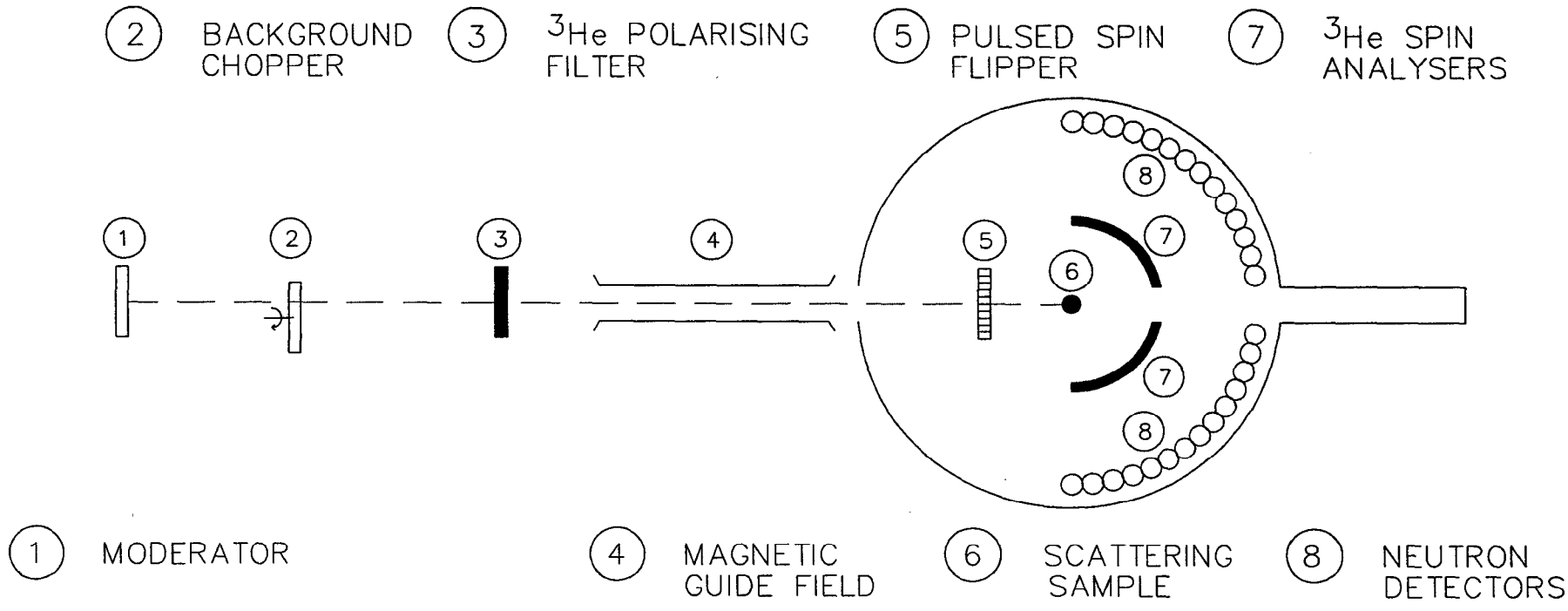

Figure 1: Schematic layout of a pulsed source spin crosscorrelation spectrometer.

compact pulsed spin flippers with switching times ~ 1μs which would be ideal for this application. Modulating sequences can be readily changed electronically and it is straightforward to provide the flipper with a pseudorandomly varied phase with respect to the source pulse.

Expressions for the momentum transfer ($\hbar Q$) and energy transfer ($\hbar\omega$) ranges, as well as their resolutions for this type of spectrometer were derived by Cywinski and Williams [3]. The larger neutron energy range and analysed solid angle range of ^{3}He filters compared with ^{149}Sm filters means that the accessible dynamic range (**Q**, ω) of this spectrometer is much larger than that indicated in the original publication. Major contributions to the $\hbar\omega$ and Q resolutions derive from terms which are proportional to $1/L_2^2$, where L_2 is the scatterer/detector distance. There are similar terms containing $1/L_1^2$, where L_1 is the primary flightpath, and we suggest that L_1 and L_2 should be made as equal as possible. L_1 ~ 10m, L_2 ~ 4m is a more optimum geometry than L_1 = 12m, L_2 = 2m as given in reference [3].

Figure 2 shows the distance-time diagram for the spectrometer and indicates the method of time-labelling; the detected events illustrated represent (1) energy loss, non-spinflip, (2) elastic, spin flip and (3) energy gain, non-spinflip scattering (for the same type of polariser and analyser). A neutron arriving at the detector at time τ can be characterised by two time labels (τ, t_2). τ is the total TOF from moderator to detector , and t_2 is provided by the bit of the spinflipper pseudorandom modulating sequence which is current at the time of arrival of the neutron at the detector. t_2 is an intermediate time label through which the sample to detector TOF τ_2 is recovered by the crosscorrelation procedure; the incident neutron TOF is therefore $\tau_1 = \tau - \tau_2$.

Cywinski and Williams [3] showed that, in essence, the spin crosscorrelation method is a switching between two transfer functions:

the spinflipper 'off' transfer function, representing mainly non-spinflip scattering,

$$N_{\tau,\tau_2} \propto \tfrac{1}{2} T_1(\tau_1) T_2(\tau_2) \left\{ \left(\frac{d\sigma}{d\Omega}\right)^{TOT}_{\tau,\tau_2} + P_1(\tau_1) P_2(\tau_2) \left[\left(\frac{d\sigma}{d\Omega}\right)^{NSF}_{\tau,\tau_2} - \left(\frac{d\sigma}{d\Omega}\right)^{SF}_{\tau,\tau_2} \right] \right\} \qquad (2.1)$$

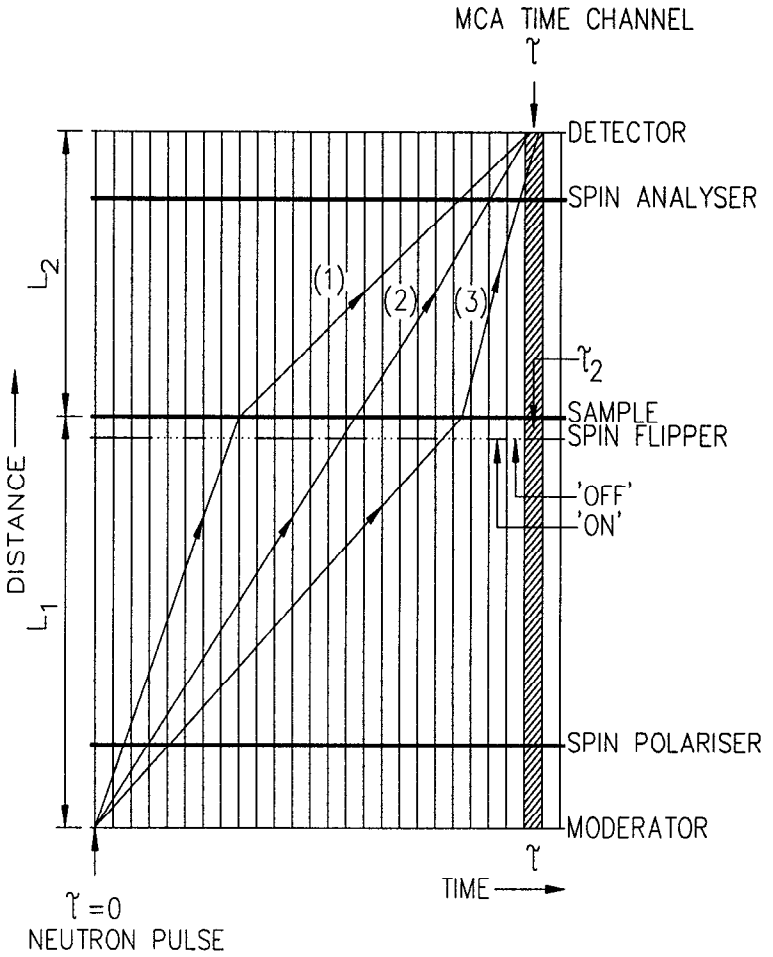

Figure 2: Distance-time diagram for a pulsed source polarisation modulated crosscorrelation spectrometer.

where NSF, SF and TOT refer to the non-spinflip, spinflip and total differential cross-sections, P and T are the polarising efficiencies and unpolarised beam transmittances of the filters (see section 3.2) with subscripts 1 and 2 denoting the values of these parameters in the incident and scattering beams respectively, and

the spinflipper 'on' transfer function, representing mainly spinflip scattering,

$$S_{\tau,\tau_2} \propto \tfrac{1}{2}T_1(\tau_1)T_2(\tau_2)\left\{\left(\frac{d\sigma}{d\Omega}\right)^{TOT}_{\tau,\tau_2} + P_1(\tau_1)P_2(\tau_2)\left[1-2f(\tau_1)\right]\left[\left(\frac{d\sigma}{d\Omega}\right)^{NSF}_{\tau,\tau_2} - \left(\frac{d\sigma}{d\Omega}\right)^{SF}_{\tau,\tau_2}\right]\right\} \quad (2.2)$$

where $f(\tau_1)$ is the spin flipper efficiency.

The difference function, which is measured in the crosscorrelation experiment, is

$$D_{\tau,\tau_2} = S_{\tau,\tau_2} - N_{\tau,\tau_2} \propto f_1(\tau_1)P_1(\tau_1)P_2(\tau_2)T_1(\tau_1)T_2(\tau_2)\left[\left(\frac{d\sigma}{d\Omega}\right)^{SF}_{\tau,\tau_2} - \left(\frac{d\sigma}{d\Omega}\right)^{NSF}_{\tau,\tau_2}\right] \tag{2.3}$$

$$\propto G(\tau_1,\tau_2)\left[\left(\frac{d\sigma}{d\Omega}\right)^{SF}_{\tau,\tau_2} - \left(\frac{d\sigma}{d\Omega}\right)^{NSF}_{\tau,\tau_2}\right] \tag{2.4}$$

where $G(\tau_1, \tau_2)$ encapsulates the spectrometer dependent terms. One method for optimising the polarising filter parameters in spin crosscorrelation spectrometers is to maximise this G term. This approach is developed later in section 3.2.

An alternative approach is to maximise the ratio R_{τ,τ_2} of the difference counts in a particular channel to the "background of ignorance" due to the sample scattering. This ratio is given by

$$R_{\tau,\tau_2} = (1-c)D_{\tau,\tau_2} \Big/ \left(c\sum_{\tau_2} S_{\tau,\tau_2} + (1-c)\sum_{\tau_2} N_{\tau,\tau_2}\right) \tag{2.5}$$

where c is the duty cycle of the pseudorandom sequence. For a duty cycle c = 0.5 and a perfectly efficient spinflipper (f=1) this ratio becomes

$$R_{\tau,\tau_2} = \frac{P_1(\tau_1)P_2(\tau_2)T_1(\tau_1)T_2(\tau_2)\left[\left(\frac{d\sigma}{d\Omega}\right)^{SF}_{\tau,\tau_2} - \left(\frac{d\sigma}{d\Omega}\right)^{NSF}_{\tau,\tau_2}\right]}{\sum_{\tau_2} T_1(\tau_1)T_2(\tau_2)\left(\frac{d\sigma}{d\Omega}\right)^{TOT}_{\tau,\tau_2}} \tag{2.6}$$

The maximisation of R_{τ,τ_2} requires a detailed knowledge of all the spinflip and non-spinflip cross-sections and will vary from experiment to experiment. We may conclude that this method for optimising the polarising filter parameters P and T is impractical.

The need to maximise the difference count is such a dominating feature of crosscorrelation spectroscopy that in the polarisation modulated version using filter polarisers we propose that the appropriate filter parameter to be maximised should be the product of the polarising efficiency and transmittance P(E)T(E); see section 3.2. We shall see however that, since the neutron energy dependent filter transmittances are important in determining the background of ignorance, variations in the transmission products $T_1(\tau_1)\ T_2(\tau_2)$ due to ^{3}He nuclear spin relaxation need to be considered carefully in the proposed spectrometer.

The SF and NSF cross-sections are related to the nuclear spin incoherent cross-section, the nuclear coherent and isotopic incoherent cross-section, and the geometry-dependent magnetic cross-section. A unique feature of neutron polarisation analysis is that an unambiguous separation of magnetic and nuclear cross-sections can be effected by manipulation of the polarisation direction with respect to the scattering vector [8].

3. ^{3}He Neutron Polarising Filters

3.1 Practical Aspects

Following a major development programme over the past 5 years, the currently favoured method for polarising gaseous ^{3}He is by direct optically pumping of metastable ^{3}He atoms in a ^{3}He plasma at a pressure ~ 1mbar [4]. Recent advances have followed the introduction of powerful pumping lasers at wavelengths ~ 1083 nm. The polarisation build-up time is fast (1μs) and the main drawback of the technique is that it only functions a low pressures. Fortunately, compression of the gas by a factor ~ 10,000 (which produces atomic densities suitable for the polarising filter application) results in only a modest loss in ^{3}He nuclear polarisation, and polarising filter cells with gas pressures ~ 10 bar can be produced. The cells are readily emptied and refilled with polarised gas after the ^{3}He nuclear polarisation has relaxed to an unacceptably low level.

The current status of the development of ^{3}He polarising filters may be summarised as follows [5]: i) initial ^{3}He polarisation values ~ 60-65% are achievable, ii) compression enables neutron spin filter cells of ~ 300 cm^2 volume with 4 bar pressure and 50 - 55% ^{3}He polarisation to be prepared in about 4 hours, and iii) ^{3}He spin relaxation times in excess of 100 hours can be achieved in caesium-coated cells. In a typical operating cycle the filters are exchanged daily. Improvements in all these performance parameters can be expected over the next 5 years, and the goal of 70% ^{3}He polarisation in the spin filter cells remains a realistic perspective [9]. It is also likely that longer relaxation times will be achieved as further knowledge of the depolarisation mechanisms is gained [10].

3.2 ^{3}He Filter Performance Quality Factors and Optimisation

The principle underlying the operation of ^{3}He filters as neutron polarisation filters is the large spin dependence of capture into the broad (Γ = 270 keV) unbound resonance (J = I - ½=0) of the intermediate ^{4}He* state. The capture cross-section σ_c is large (5327 b atom^{-1} at a neutron energy E =25.3 meV, decreasing inversely with neutron velocity), and the ratio of the cross-section for antiparallel neutron spin capture to the total cross-section has been experimentally determined to be 1-010 ± 0.032 [11]. The neutron spin dependent cross-sections are related to the ^{3}He nuclear polarisation $P_{^3He}$ by

$$\sigma_{\pm} = \sigma_c \, (1 \mp P_{^3He}) \tag{3.1}$$

and the transmittances $T_{\pm}$ of (±) spin neutrons through the filter are given by exp-($\sigma_{\pm}$Nt), where Nt is the ^{3}He atomic thickness (at cm^{-2}). These transmittances have a substantial neutron energy dependence through the energy dependence of σ_c ($\propto E^{-1/2}$).

The performance of a ^{3}He polarising filter may be defined by two parameters: its polarising efficiency P, which is the transmitted beam polarisation for an unpolarised incident beam,

$$P = (T_+ - T_-) / (T_+ + T_-) = \tanh (\sigma_c P_{^3He} Nt) = \tanh \alpha P_{^3He} \tag{3.2}$$

where $\alpha = \sigma_c Nt$ is the opacity of the filter, and its unpolarised beam transmittance,

$$T = (T_+ + T_-) / 2 = \exp(-\alpha) \cosh (\alpha P_{^3He}). \tag{3.3}$$

For given values of $P_{^3He}$ and σ_c (fixed neutron energy) the filter designer is confronted with optimising the product of the gas pressure and filter thickness Nt. Nt can be increased to produce a higher neutron polarisation P, but only at the expense of lowering the transmittance T.

Tasset and Ressouche [12] have published a detailed analysis of the optimisation of α for the classical polarised neutron experiment which measures the ratio of scattered intensities for 'up' and 'down' spin neutrons - this ratio relates straightforwardly to the asymmetry.

These authors deduced that the optimum opacity α_{OPT} depends on the scattering experiment, and needs to be increased where reflections have a greater magnetic component. However, in the regime of low magnetic amplitudes where the classical diffraction experiments are most powerful it was concluded that α_{OPT} corresponds to a maximisation of $P\sqrt{T}$, as proposed earlier by Williams [13]. For asymmetry (or ratio) measurements we therefore define a filter quality factor

$$Q_1 = P\sqrt{T}. \tag{3.4}$$

However in many applications of polarised neutron beams, for example in inelastic scattering experiments, it is sufficient to measure the countrate difference for the two neutron spin states; see Williams [14]. For these the statistical accuracy of the measurements is proportional to product of the polarisation and beam intensity [14]. This also pertains in spin crosscorrelation spectroscopy, see eqn (2.3), where the difference cross-section depends on the PT products for the polariser and analyser individually. We have therefore used the filter quality factor

$$Q_2 = PT \tag{3.5}$$

to optimise the filter opacities α in the spin crosscorrelation spectrometer. Qualitatively, difference experiments place more emphasis on the filter transmittance, hence require lower opacities than experiments which measure asymmetries.

The optimisation of Q_1 has been derived by Surkau et al. [4] who give the optimum opacity $\alpha_{1(OPT)}$ for asymmetry experiments to be:

$$\alpha_{1(OPT)} = P_{^3He}^{-1} \text{ arctanh}\left\{\left[2 + (2P_{^3He})^{-2}\right]^{1/2} - 0.5\, P_{^3He}^{-1}\right\} \tag{3.6}$$

The equivalent optimisation of Q_2 gives the particularly simple expressions:

$$\alpha_{2(OPT)} = P_{^3He}^{-1} \text{ arctanh}\left\{P_{^3He}\right\} \tag{3.7}$$

$$= P^{-1} \text{ arctanh}\{P\} \tag{3.8}$$

where the nuclear polarisation $P_{^3He}$ and transmitted neutron polarisation P are equal.

The calculated values of $\alpha_{1(OPT)}$ and $\alpha_{2(OPT)}$ as a function of $P_{^3He}$ are shown in Figure 3. The variations of both these quantities in the ^3He polarisation range of practical importance ($P_{^3He} < 0.8$) are small; opacity changes have much less influence on the filter parameters than changes in the neutron energy dependent capture cross-section. As expected from our qualitative argument $\alpha_{1(OPT)} > \alpha_{2(OPT)}$ for all $P_{^3He}$ values, though the importance of the present results is that they show quantitatively that the optimum opacities of the ^3He filter can be reduced by a factor ~ x 0.65 in applications such as spin crosscorrelation spectroscopy which measure a difference signal.

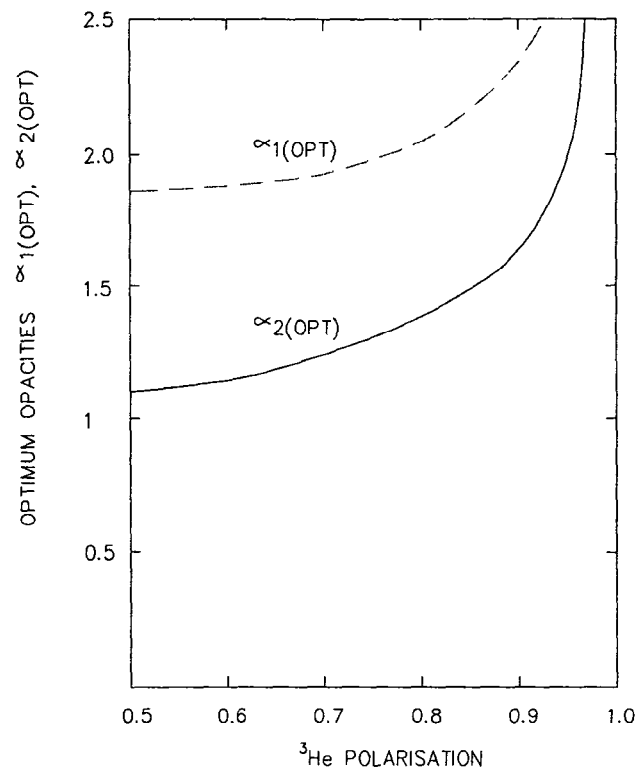

Figure 3: Optimum opacities $\alpha_{1(OPT)}$ and $\alpha_{2(OPT)}$ for ^3He polarising filters obtained by maximising Q_1 and Q_2 for ^3He polarisation values > 0.5.

We now examine the neutron energy dependence of Q_2^2 (or P^2T^2) as a measure of the quality of performance of a two-filter spin crosscorrelation spectrometer when measuring elastic scattering - this is the filter-dependent term in the G term of eqn. (2.4). P^2T^2 is plotted as a function of neutron energy first for a filter with atomic thickness Nt = 4.86 x 10^{20} at cm^{-2} and a range of $P_{^3He}$ values in Figure 4. This atomic thickness corresponds to $\alpha_{2\,(OPT)} = 1.23$ when $P_{^3He} = 0.70$ for neutrons with energy E = 0.1 eV, and, in practical terms, to a 5 cm long filter cell with 4 bar ^3He pressure at 300K. The large $(PT)^2$ variation

with ^{3}He polarisation is evident and illustrates i) the significant gains which result from increasing $P_{^3He}$, and ii) the potentially problematic effect of ^{3}He spin relaxation to the instrument performance - this point will be addressed later. The effect of changing the atomic thickness Nt on all polarising filter parameters (PT, P^2T^2, T^2 etc) at a fixed ^{3}He polarisation value is simply to linearly translate these curves in the direction of the E axis. This is a consequence of the neutron energy dependence of σ_c ($\alpha E^{-1/2}$), and is illustrated for a filter with Nt = 2.19 x 10^{20} at cm^{-2} with $P_{^3He}$ = 0.70 by the dashed curve of Figure 4. The selection of the appropriate atomic thicknesses of the filters (once the limiting ^{3}He polarisations are known) will depend on the neutron energy requirements of the experiment.

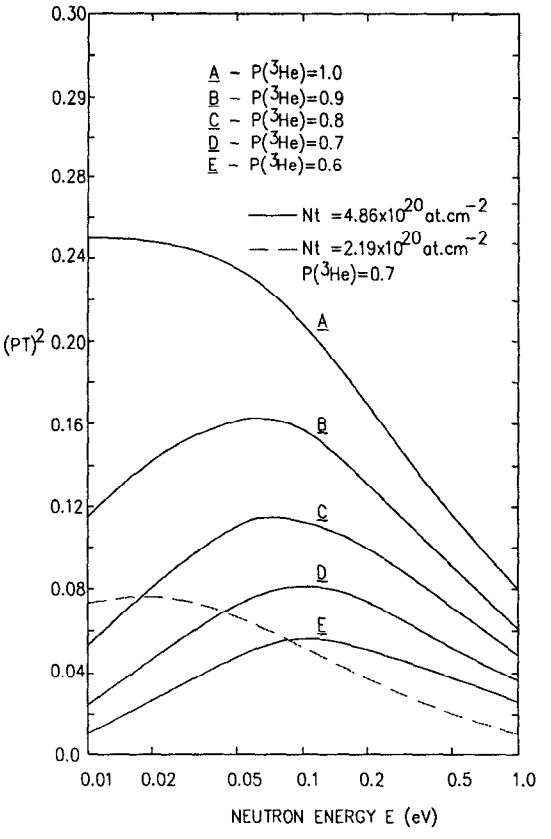

NEUTRON ENERGY E (eV)

Figure 4: Quality factors in elastic spin cross-correlation measurements with He-3 polarising filters of optimum opacity $\alpha = 1.24$ (He-3 polarisation = 0.70) as a function of neutron energy.

The neutron energy dependences of $T(E)^2$ for filters with atomic thicknesses 2.19 x 10^{20} at cm^{-2} and 4.86 x 10^{20} at cm^{-2} and ^{3}He nuclear polarisation values 0.6, 0.7 and 0.8 are shown in Figure 5. We recall that the lower atomic thickness filter was optimised for operation in the thermal neutron energy range with $(PT)^2$ maximum at 20 meV (see Fig. 4). Although this filter gives higher $T(E)^2$ values (and consequently a larger background of ignorance in the spin crosscorrelation experiment), we note that the fractional changes in this parameter

due to changes in $P_{^3He}$ are much smaller than for the denser filter. For example, the fractional reduction $\Delta(T(E))^2/(T(E))^2$ for the Nt = 2.19 x 10^{20} at cm^{-2} filter is ~ 6% over the neutron energy interval 20 meV - 100 meV for a $P_{^3He}$ reduction of 10%. The corresponding reduction is $\Delta(T(E))^2/(T(E))^2$ for the Nt = 4.86 x 10^{20} at cm^{-2} filter is ~ 40%, although this filter produces a background of ignorance of approximately one-third that for the less dense filter.

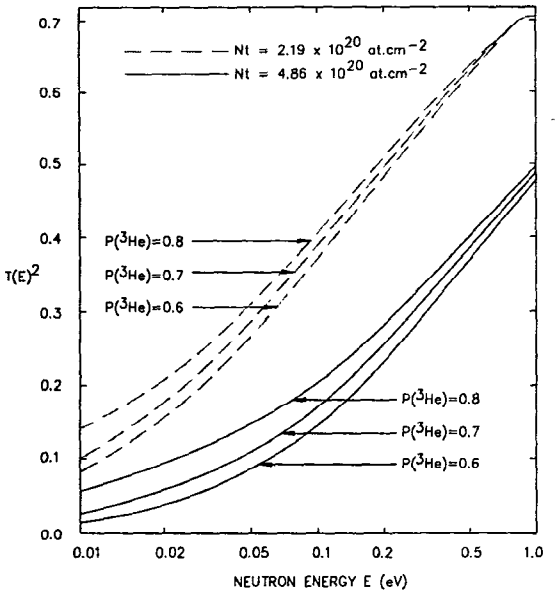

NEUTRON ENERGY E (eV)

Figure 5: Neutron energy dependences of $T(E)^2$ for two ^3He polarising filters with nuclear polarisation values 0.6, 0.7 and 0.8.

Correlation techniques demand that the background of ignorance (which is often substantial) be as constant as possible and, in view of this requirement, we recommend that the lower atomic thickness filter would be preferable for measurements in the thermal neutron energy range. It is worth noting that $P_{^3He}$ reductions of 10% due to spin lattice relaxation would take place in approx. 12 hours in the best "long-life" filters built so far. This loss in ^3He polarisation results in a **reduced** background of ignorance in the spin crosscorrelation method, and the data must be corrected to account for this.

3.3 Effect of ^3He nuclear spin relaxation.

One disadvantage of the currently favoured method for polarising ^3He is that it cannot provide a stable filter performance due to ^3He spin relaxation. Currently, spin relaxation times in excess of 100 hours have been achieved, but even this is potentially problematical in long experiments with filter polarisers and analysers; we anticipate that even on third

generation pulsed sources measuring times up to several tens of hours will be required periodically.

Fig 6 shows the reduction in the quality parameter $(PT)^2$ for a ^3He polarising filter with initial polarisation $P_{^3He}$ = 70% and optimum opacity $\alpha_{2(OPT)}$ = 1.24, where the spin lattice relaxation times τ are 50 hr, 200 hr, and 500 hr. Again we restrict our calculations to the case relevant to elastic scattering processes. It is difficult to prejudge what fractional change in $(PT)^2$ can be tolerated during a single measurement since, in principle, this variation can be allowed for (with some uncertainty) at the data analysis stage. In the optimistic case that τ ~ 500 hr will be achieved over the next 10 years (this will require more R & D effort on wall depolarisation) and that $\Delta(PT)^2/(PT)^2$ = 10% is acceptable, then this would allow measuring times up to ~ 20 hrs in the spin crosscorrelation experiment. Clearly any progress in lengthening the ^3He spin relaxation time will impact strongly on the feasibility of this experimental technique.

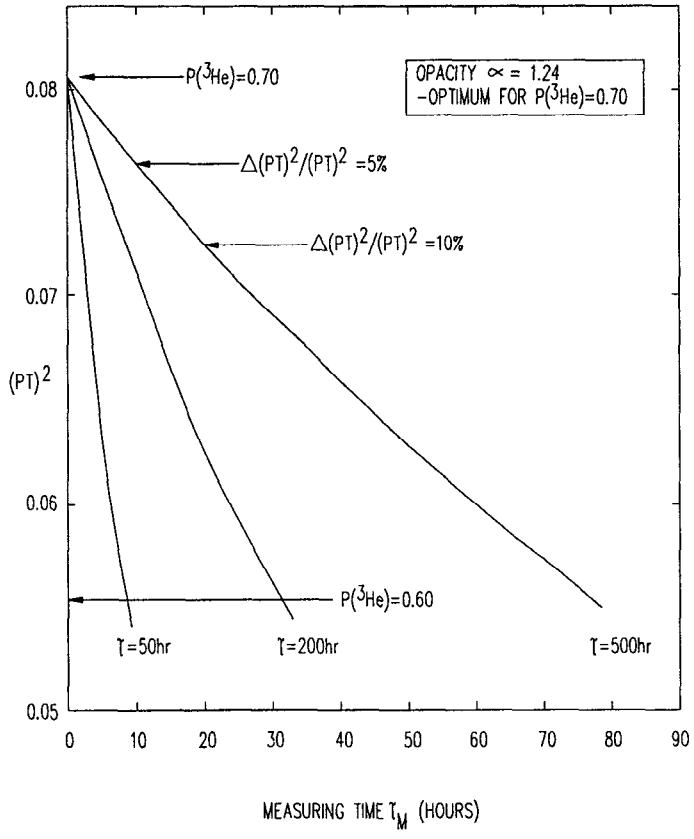

MEASURING TIME t_M (Hours)

Figure 6: Effect of He-3 nuclear spin relaxation on the spin cross-correlation signal for elastic scattering with optimum filter opacity for 70% ^3He polarisation.

The effect of ^3He spin relaxation in the polariser and analyser is not expected to have a significant effect on the signal to background ratio R_{τ,τ_2} in the crosscorrelation

experiment. Note that a reduction in $P_{^3He}$ causes a **reduction** in the filter transmittance T, hence reducing the denominator in eqn (2.6). Since similar transmittance products appear in the numerator, the principal cause of the reduction in $R_{\tau_1\tau_2}$ due to ^{3}He spin relaxation can be attributed to smaller polarisation products P_1P_2 rather than to lower filter transmittances.

4. Summary

A preliminary evaluation of the feasibility of a polarisation modulated crosscorrelation neutron spectrometer, suitable for the third generation pulsed sources, is described. The spectrometer uses the recently developed optically pumped ^{3}He filters as the polarising elements, and the study has focussed on optimising the performance parameters of these filters. Detailed calculations on filters with two atomic thicknesses, $Nt = 2.19 \times 10^{20}$ at cm^{-2} and $Nt = 4.86 \times 10^{20}$ at cm^{-2}, showed that the former was more suitable for spin crosscorrelation experiments in the thermal neutron energy range. The effect of ^{3}He nuclear relaxation has been examined with the conclusion that R & D effort towards producing longer ^{3}He spin relaxation times would be beneficial to this technique. The method is only marginably viable given the current status of the development. ^{3}He polarisations in excess of 80% are needed compared with $P_{^3He}$ ~ 60% now achievable, but there is every prospect that such improvements will take place over the next 10 years.

References

1. N. Kroo, P. Pellionisz, I. Vizi, G. Zsigmund and G. Nagy, I.A.E.A. Symp. On Neutron Inelastic Scattering, IAEA/SM-155/F-6, (1972).

2. W. Matthes, ibid IAEA/SM-155/F-7.

3. R. Cywinski and W. G. Williams, Nucl. Instrum. Meth. **228** 406 (1985).

4. R. Surkau, J. Becker, M. Ebert, T. Grossman, W. Heil, D. Hofmann, H. Himblot, M. Leduc, E. W. Otten, D. Rohe, K. Siemensmeyer, M. Steiner, F. Tasset and N. Trautmann, Nucl. Instrum. Method **A384** 444 (1997).

5. W. Heil, private communication (1998).

6. W. G. Williams, Rutherford Appleton Laboratory Report, RAL-90-052 (1990).

7. G. Badurek, Nucl. Instrum. Meth. **189** 543 (1981).

8. R. M. Moon, T. Riste and W. C. Koehler, Phys. Rev. **181** 920 (1969).

9. K. Andersen, W. Heil, D. Hofmann, H. Humblot, J. Kulda, E. Liévre-Berna, O. Schärpf and F. Tasset. "^{3}He Neutron Spin Filter at ILL: First Experiments", to be published.

10. W. Heil, H. Humblot, E. Otten, M. Schafer, R. Sarkau and M. Ludue, Phys. Lett. **A201** 337 (1995).

11. L. Passell and R. I. Schermer, Phys. Rev. **150** 146 (1966).

12. F. Tasset and E. Ressouche, Nucl. Instrum. Meth. **A359** 537 (1995).

13. W. G. Williams, 'Gaseous Helium-3 Neutron Polarisers' Rutherford Appleton Laboratory Report RAL-90-052 (1990).

14. W. G. Williams, 'Polarized Neutrons', Oxford University Press, (1988).

ICANS XIV
14th Meeting of the International Collaboration on Advanced Neutron Sources
June 14-19, 1998
Starved Rock Lodge, Utica, IL

New Horizons with Position Sensitive ^{3}He Detectors

C.D.Frost[a], R.S.Eccleston[a], J.Norris[b], N.J.Rhodes[a] and D.J.White[b]

[a] ISIS Facilty, CLRC Rutherford Appleton Laboratory, Chilton, Didcot, UK.
[b]Technology Dept., CLRC Rutherford Appleton Laboratory, Chilton, Didcot, UK.

Abstract

We describe the design and performance of position sensitive detectors based on resistive wire ^{3}He detector tubes that have been designed for inelastic single crystal measurements on chopper spectrometers at a pulsed source. An array of 26 of these detectors was installed on HET in May 1997, and approximately 600 of them will be used on the new inelastic single crystal spectrometer, MAPS, currently under construction at ISIS.

Introduction

The use of direct geometry time-of-flight chopper spectrometers for measurements of the magnetic inelastic response of polycrystalline samples is a well established technique. More recently, the availability of high-flux pulsed spallation sources like ISIS have enabled the extension of this technique to single crystal measurements. The chopper spectrometers HET and MARI have been at the forefront of these investigations and have made substantial contributions to many areas in contemporary magnetism. A new instrument, MAPS, is currently under construction at ISIS that aims to build on this success and has been specifically designed for single crystal experiments. A key part of its design is the use of position sensitive detector arrays that are based on resistive-wire ^{3}He detector tube technology. These will enable the experimentalist to construct scans in any direction in reciprocal space and optimise the instrumental resolution for that measurement.

Several position sensitive detector systems already exist on time-of -flight instruments: the GLAD spectrometer at IPNS, Argonne National Laboratory, USA [1] and VEGA and SIRIUS at KENS, National Laboratory for High Energy Physics (KEK), Japan [2]. The detector systems designed for these instruments are, however, optimised for measurements of elastic neutron scattering from polycrystalline, liquid or amorphous samples making them unsuitable for use on the MAPS spectrometer.

A position sensitive detector array for use on an inelastic neutron spectrometer using the time-of-flight technique has to be designed to cope with two characteristics of the neutron response in a typical single crystal experiment. The first is that high intensity Bragg peaks can occur as a result of the orientation of the single crystal sample and choice of incident neutron energy; the second is that the typical cross section for the inelastic response of the sample is often many orders of magnitude lower than these Bragg reflections. The detector system therefore has to have a short dead-time so that the highly intense Bragg reflection does not impede the measurement of the

inelastic response and it has to have a low background count. In addition we required that the detectors had good stability, both temporally and spatially, a linear positional response, a comparable efficiency at all neutron energies with the standard ^{3}He detectors on MARI and HET and a resolution along the detector comparable to its width (of 25.4mm). The MAPS spectrometer will also require of the order of 600 such detectors so that a low maintenance system is highly desirable.

As part of the ongoing instrument upgrade program at ISIS, and as a prerequisite test to enable experimentalists to gain experience in the use of PSDs prior to the construction and commissioning of the MAPS instrument, half of the 4m detector banks on the HET spectrometer at ISIS were replaced with 26 PSDs in May 1997. This array providing an additional 1536 individual detector channels and has now been in successful operation for almost a year. In this paper we aim to describe the PSD system and its implementation on HET.

Section A - The PSD Detector System

A block diagram of the detector system is shown in figure 1. Its operation can be divided into three stages; physical neutron detection, pre-amplification of the detected signal and encoding of the neutron position.

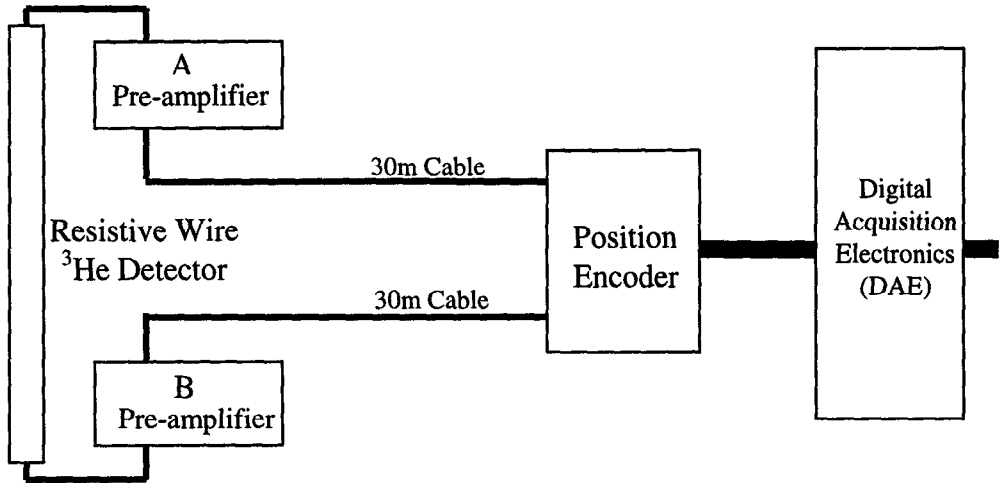

Figure 1: The PSD system

Neutron Detection

The position sensitive detector tubes are cylindrical ^{3}He resistive wire proportional counters each 25.4mm in diameter by 914mm active length filled with ^{3}He at a partial pressure of 6.5 atmospheres and other stopping and quenching gases. These tubes are operated in proportional mode by the application of a bias voltage of 1960V between the central resistive wire and the outer steel gas container.

Detection of a neutron is through the reaction

$$n + {}^{3}He \rightarrow {}^{1}H + {}^{3}H + 765keV$$

followed by ionisation of the stopping-gas by the proton and tritium, and gas amplification from the proportional mode of operation. This results in a charge being deposited on the central anode wire at the position of the incident neutron.

It is the division and measurement of this charge that allows the encoding of the position of the incident neutron to be determined. The accuracy of the determination of the neutron position is highly dependent upon the characteristics of the pre-amplifiers and encoding circuits.

Pre - Amplifier Circuit

The pre-amplifiers are charge amplifiers that convert the charge collected at each end of the tube resulting from a neutron event to two voltage signals that are compared in the position encoding circuit. Distortion of the charge signal by these circuits degrades the resolution of the system and can also lead to systematic errors in the final encoded position of the incident neutron.

The pre-amplifiers developed at ISIS for HET were designed with two criteria in mind. The first was to ensure that the detector and pre-amplifier electrical characteristics should have a minimal effect on the detected signals and the second was that the design should be simple.

To implement the first of these criteria, the design addressed three properties that could adversely affect the encoded position.

The first consideration is that the resistance of the anode wire within the detector is likely to vary from detector to detector. Our design incorporates a pre-amplifier with low impedance, low enough so that the anode resistance tolerance becomes negligible, which means that there is no need to match detectors to electronics. Different length tubes, with different anode resistances, can also be connected to the same electronics.

Secondly, we considered that the pulse shape from a detected event may have fast or slow rise-time, depending on the position and angle of the created triton and proton to the anode wire. The variation in rise-time meant that we used a pre-amplifier with wide bandwidth and flat response.

The third consideration was the potential error that could occur if the gains from pre-amplifiers either side of the detector are mismatched. To overcome this we ensured that the gains of the amplifiers were precisely matched by using precision 0.1% resistors. The amplifiers used in the pre-amplifier circuit were also chosen to have low internal offsets and low noise.

Our second criteria, simplicity, was in response to the fact that MAPS will require approximately 600 PSD detectors. Simplicity of design, with minimal components, increasing reliability and reduced maintenance. In the past the ^{3}He proportional counter pre-amplifiers have been built at ISIS on an individual basis. To vastly reduce the number of interconnections it was decided to

group together the low impedance pre-amplifier stage, a 50Ω cable driver stage, and the filtered HT and pre-amplifier power supplies for several PSD detectors into a single module. For the implementation of PSDs onto HET this module was for thirteen detectors.

The pre-amplifier design also incorporates a method for electronic injection of test pulses into the circuit. This is used to test for cable connectivity and as a crude method of simulating an encoded neutron event. A more accurate electronic method was excluded because it was prohibitive in cost, requiring a test pulse generation and delivery system that would have to be extremely accurate and stable.

Position Encoding Circuit

The position encoding circuit's function is to take the two analogue outputs from the pre-amplifier stages and convert them to a 6-bit digital *word* representation of the position of the incident neutron for use by the standard ISIS digital acquisition electronics (DAE).

The theory of the encoding of the incident neutron's position on the detector is basically the same in all restive wire detector systems. If we label the ends of the detector tube ***a*** and ***b***, and the position at which the neutron is incident x, then the position x can be thought of as also dividing total resistance of the resistive wire into two. Measurement of the charge collected at each end of the resistive wire (A at ***a*** and B at ***b***) which results from the division of the charge created by the incident neutron event by the resistance paths from ***x*** to ***a*** and ***b***, allows the position ***x*** to be calculated. The position along the detector from the B end is given (as a fraction) by

$$x = \frac{A}{A+B}. \qquad [1]$$

In the ISIS HET position encoding electronics (a block diagram is shown in figure 2), the two pre-amplifier outputs are buffered by receiving amplifiers, one of which has an adjustable gain. The adjustment is used to compensate for the slight variations in impedance that are a consequence of tolerance of the 30m interconnecting cables. It should be highlighted that this is the *only* adjustable part of the whole system. The outputs from these amplifiers are then used by three amplifiers to provide outputs representing the charge collected at the A, B ends of the tubes and their sum, A+B. The B signal is not subsequently used but is incorporated to ensure that the A and B inputs are treated symmetrically by the electronics. The A+B signal, which in a single-ended tube represents the dynamic range of the input, is used in the discrimination process.

The discriminator uses the differentiated A+B signal to first cross a threshold value, in a similar way to a normal low level discriminator, and then to provide a switch at the peak of the A+B signal. The peak of A+B is easily determined by detecting when the differentiated A+B signal crosses zero. This method gives a better timing performance than the standard threshold crossing technique, whose timing may depend on the amplitude of the signal.

The peak values of A and A+B are then converted to 8-bit digital words using high speed FLASH architecture analogue-to-digital converters (ADC's). With this type of ADC there is minimal analogue voltage set-up and hold-time before digitisation. These words are then input into a 64Kbyte FLASH lookup table containing the fractional position of the event (c.f. equation [1]) and its output is a 6-bit position word (figure 3). A second FLASH memory device is used to reject any events that are computed as being outside the Lookup table map. The purpose of the second memory is to allow the first memory to be expanded to output an 8-bit word in future configurations.

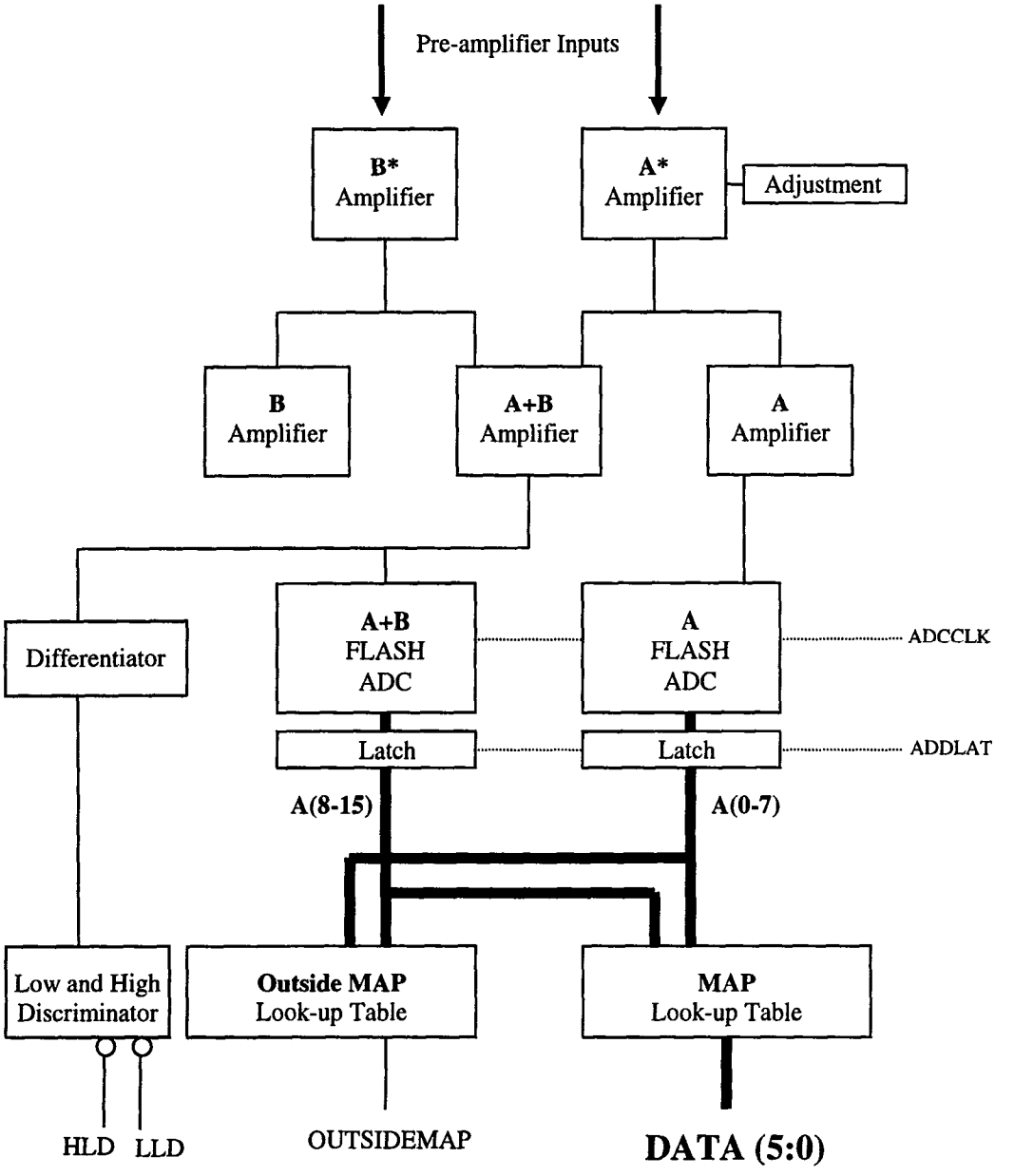

Figure 2: Diagram of the Position Encoding

The timing of the digitisation and encoding process is achieved through a single complex programmable logic device of approx. 5 thousand gates.

The ADC circuit is fabricated on a 6U multi-layer printed circuit board and is able to accommodate two PSD tubes. The 6-bit outputs are multiplexed onto a 7-bit output word plus strobe either as differential ECL or single-ended TTL. With the low detector event rates on HET the board is further multiplexed by multiplexing pairs of ADC cards using the back-plane of the ADC Crate, thus creating an 8-bit output.

We would like to emphasise two things about the system design. The first is its simplicity requiring only one amplifier to be adjusted to match the electronics to any particular detector. This is the result of using low noise, low impedance amplifiers with a wide bandwidth. The second is that the FLASH ADC's do not require long hold times for the analogue voltages, as is the case when the comparison of the A and A+B *analogue* signals is carried out *directly* with a ratiometric ADC. The comparison of the A and A+B signal *after* digitisation is at the heart of the ISIS design and has enabled us to build a high speed device.

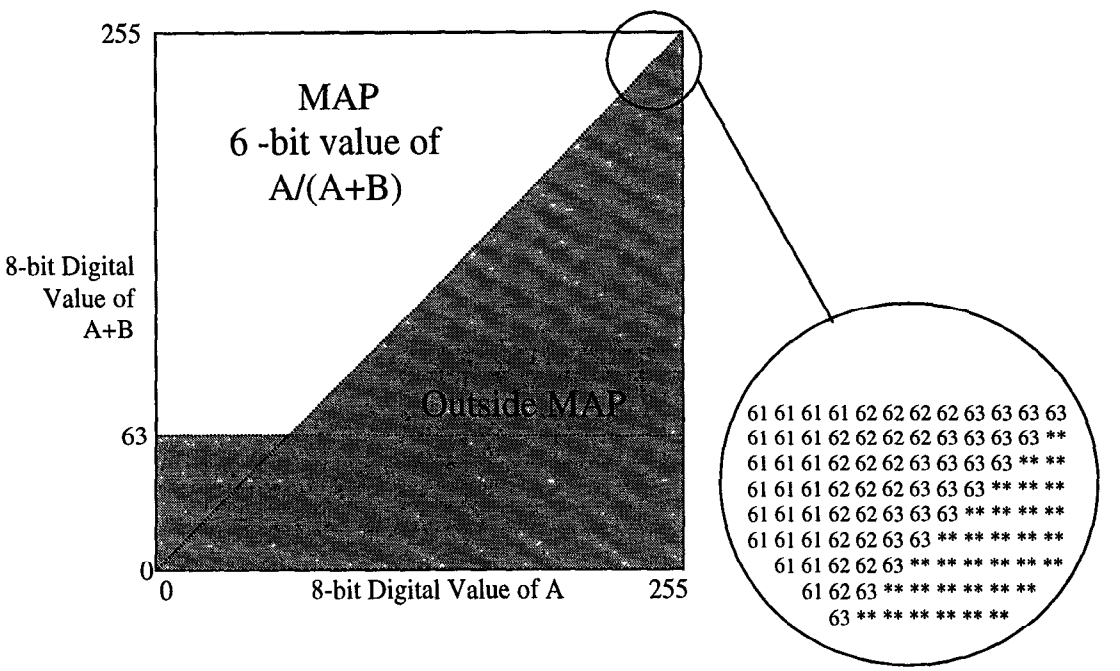

Figure 3: Diagram of the MAP contained in the FLASH 16-bit Memory

Section B - Performance of the PSDs

Characterisation of the performance of the whole detector system has been carried out in two ways; dedicated tests of PSD tubes were carried out on a test experimental set-up followed by the

installation, commissioning and on-going monitoring of an array of 26 PSD tubes installed on the HET spectrometer in May 1997.

The testing facility, installed on the ROTAX beamline at ISIS allowed us to test the tubes using a variety of samples and shielding configurations. In this way many of the operational parameters such as spatial resolution, positional linearity, efficiency when compared to a standard HET or MARI detector tubes could be accurately determined under controlled conditions. Illumination of the tubes with different neutron fluxes including intense Bragg peak reflections also allowed us to measure the tubes performance under near operational conditions.

In addition to these measurements, periodic measurements have been made on the PSD installed on HET. A movable calibration bar, made with neutron absorbing material, that can be placed at any position along the PSD array had been installed for this purpose. With this device the temporal stability of both the position and resolution of the PSD tubes have been monitored since the installation of the system. We have in addition checked the linearity and efficiency of the tubes.

Table 1: Summary of PSD Parameters and Performance

Physical Parameters	
Tube dimensions	25.4mm∅ × 1050mm
Active length	914mm
^{3}He Pressure	6.5 Atmospheres
Pixel Size (64 pixels per tubes)	14.3mm× 25.4mm
Performance	
FWHM	23±4mm
Efficiency (w.r.t. standard HET/MARI detector)	80% E_i>50meV rises to 100% below 30meV
Quiet Count	0.2623 counts/hour/channel
Total circuit deadtime	1μS individual 5μS multiplexed
Pulse Pair Resolution	<4μS
Positional Stability (change in the measured position of the calibration bar)	< ±0.2 channels in 4 months (≈ 3mm)
Resolution Stability (change in the FWHM measured at the same position)	≈0.15 channels in 4 months (≈ 2mm)

The MAPS detectors are longer (having an active length of 1000mm) and contain a higher partial pressure of ^{3}He (at 10 Atms). They have been tested alongside the HET tubes and show almost identical characteristics except that the high ^{3}He content makes them 100% efficient when compared to a standard HET/MARI detector.

Section C - Scientific Experiments with PSDs

The replacement of two of the 4m detector banks on the HET spectrometer at ISIS by 26 PSDs with characteristics given in Table 1 has opened up new scientific opportunities.

On HET the data from the PSD array is collected in the digital acquisition electronics, which bins it according to the time of flight of arrival and into which particular pixel element of the PSD detector array it arrived. Knowledge of the time of flight (~2000 bins) and the position of the pixel elements (1536 elements) allows us to construct, in software, a volume of reciprocal space that is divided into many thousands of small reciprocal space volume elements. Each volume element results from the particular trajectory through reciprocal space of the PSD pixel elements as a function of the time of flight.

Software can then be used to bin these reciprocal space volume elements together and project the results onto planes within reciprocal space to obtain intensity maps of the neutron scattering from the sample under investigation.

Figure 4 is an example of the use of the HET PSD for the investigation of magnetic scattering in a high temperature superconductor. In this experiment the magnetic zone centre around which the magnetic excitations were expected was placed in the centre of the reciprocal space volume measured by the PSD array. The figure shows a slice taken on a high symmetry plane through this volume that reveals the magnetic excitations that surround this magnetic zone centre. This particular cut was taken in an out of plane direction (because of the necessity for l in the reciprocal space co-ordinate (hkl) to be non-zero to give a non-zero structure factor for the excitations). This measurement was not possible before the installation of the PSDs.

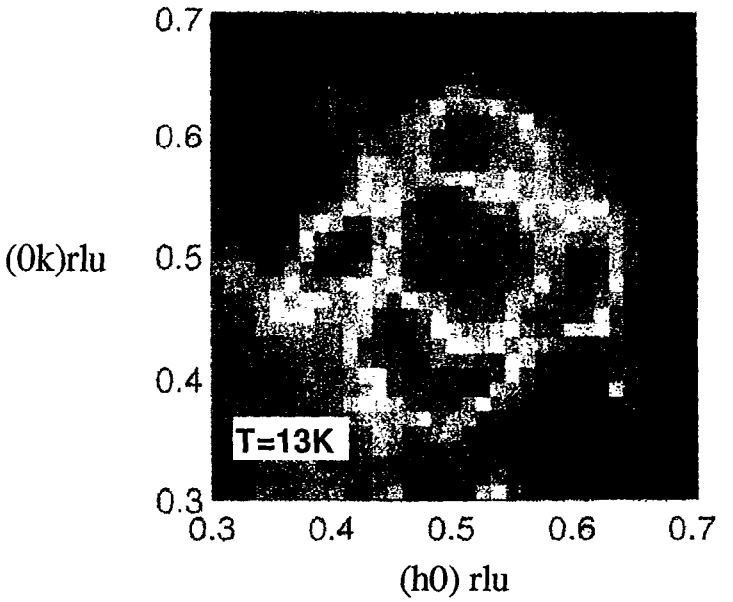

Figure 4: Magnetic Excitations from $YBa_2Cu_3O_{7-\delta}$ measured in PSD array on HET with an incident energy of 34meV from reference [3].

Section D - Concluding Comments

The installation of PSD onto HET has already led to new results in the area of contemporary magnetism. The flexibility that they provide for exploring the inelastic excitations of materials has led to an increasing demand for experimental time on HET at ISIS. The new spectrometer MAPS, due to be commissioned at the end of 1998, will incorporate over 600 such detectors and is expected to provide unique opportunities for scientific experiments and truly represent the next generation of inelastic chopper spectrometer.

References

1. K.Crawford and J.R.Haumann, IEEE Trans. Nucl. Science, vol **37** number 2, pp 72-81, 1990
2. T.Kamiyama *et al*, Physica B, **213**, pp 875-877, 1995
3. H.A.Mook, Pengcheng Dai, S.M.Hayden, G.Aeppli, T.G.Perring and F.Dogan, Private Communication

Neutron Scattering Instruments

COMPUTER SOFTWARE

ICANS XIV
14th Meeting of the International Collaboration on Advanced Neutron Sources
June 14-19, 1998
Starved Rock Lodge, Utica, IL

Remote Data Collection and Analysis

Tom Worlton
Argonne National Laboratory

1. Introduction

Neutron sources are getting more intense and the quantities of data produced for a given experiment are increasing. Some experiments can be done in a few minutes. The number of experiments which can be performed and the number of papers which can be written is limited by speed of analysis. Instrument Scientists at the major facilities spend much of their time helping users, not only with data collection, but also with data analysis. Ideally, the outside users should be able to take a larger share of the responsibility for data collection and analysis. This would allow the Instrument Scientists to work with more users and more papers could be produced.

One of the factors limiting data collection and analysis by outside users is the difficulty in using the software that has been developed. The software generally is written in such a way that the user must type a lot of input. The software needs to become easier and more intuitive to use. The other factor limiting data collection and analysis by outside users is the need to travel to the facility to perform the experiment and analyze the data. Allowing this to be done remotely could greatly expand the number of users of the neutron facilities.

2. Remote Data Collection and Analysis Project

In order to enable scientists to more easily collect and analyze data and to allow them to do experiments remotely, we have begun a project to provide remote user-friendly data access, viewing, and manipulation. We also plan to provide an interface between this data viewing and manipulation software and specialized analysis programs. This project is possible because of recent developments in computer technology such as html and Java.

Steps in data collection and analysis are shown in Table 1. Most steps can be performed locally, but the steps in the shaded areas will still need to be performed locally.

Table 1 Remote data collection and analysis. Most steps of the data analysis procedures can be done remotely, but the shaded steps must still be performed locally.

Data Collection	Data Analysis
Load sample	Archive data
Enable user control	Read data
Set up data collection	View spectra
Start collection	Operate on Spectra
Control Sample Environment	Analyze data or prepare analysis input files
Stop Collection	Collaborate with Instrument Scientist

For remote data collection and analysis, samples will still need to be loaded locally, but a sample changer could allow batch loading of samples. Because more than one user might be using the instrument, it will be necessary for the facility to enable data collection for a specific user. Otherwise, it would be possible for one user to interfere with another or for an arbitrary person to interfere with data collection and instrument operation. Although environmental parameters could be controlled remotely, there would need to be hardware or software limits imposed by the facility.

Archiving of data should be handled by the facility and could be done automatically, by connecting the data transfer to the data collection process. Because CDROM drives are now found on nearly all computers, CD Recordable (CDR) is a very desirable storage and distribution medium. CDR disks will last much longer than tape and it will probably be many years before CDROM drives disappear. By that time, DVD drives will have replaced CDROM drives and they will also be able to read CDR disks. The other advantage of using CDR is that remote users cannot accidentally (or intentionally) overwrite the data once it has been archived. Data can be archived and accessed without operator intervention, if a CD jukebox is used.

We have chosen to write most software in the Java programming language because Java is designed as a network-based, operating system-independent language (see http://www.javasoft.com/). Java is also secure, object-oriented, and easier to write than C++ code. Java is also more suitable for use by non-professional programmers because it manages memory and does not have pointers. This prevents the programmer from creating memory leaks or accessing memory used by other programs. If the software is intended to run only on the server, it can be written in a native language such as C, C++, or Fortran.

Java programs can be compiled either as "applications" or as "applets". An applet runs inside a web browser, while an application can be run independent of a web browser. Java achieves machine and operating system independence by defining a "byte code" which can be run by a Java virtual machine installed on the local computer. In the case of applets, the virtual machine is provided by the browser. The use of an interpreted byte code means Java programs run slower than native language programs such as C and C++ that are compiled for the target machine. However, Java Just In Time compilers can be used to compile byte code into machine code and speed up execution.

One of the attractive features of Java is the ease with which one can write Graphical User Interfaces which can run on different platforms with a native look and feel. The Java GUI routines are in the Active Windowing Toolkit which appeared in Java version 1.1. Another class called SWING, provides even more powerful GUI functions. Swing will become standard in Java version 1.2. Sample menus showing Java menus and the File dialog box provided by Java are shown in Figs. 1 and 2.

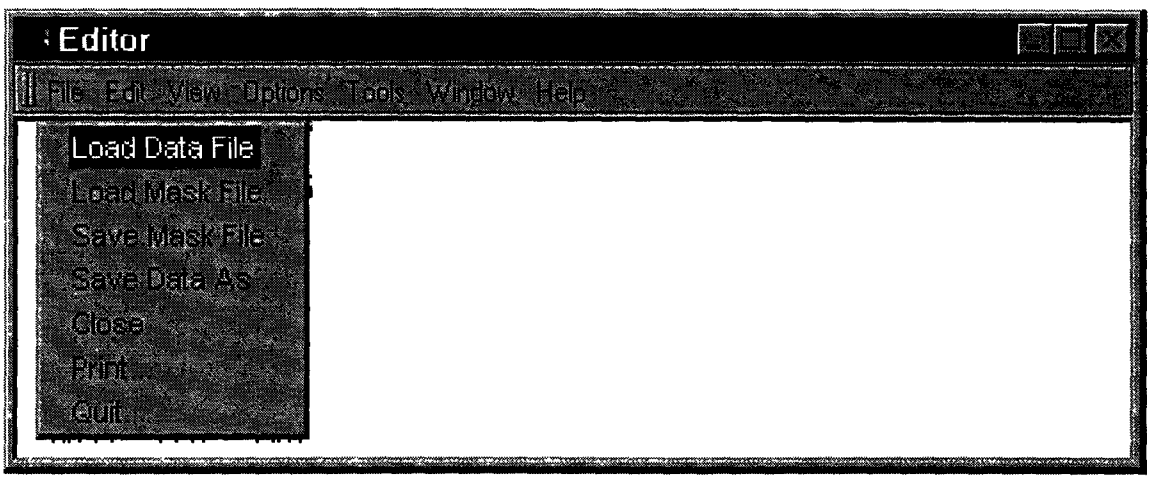

Figure 1 A sample Java menu bar and pull-down File menu.

A sample Java file dialog box is shown in Fig. 2. The built-in classes in the Java AWT and Swing provide a simple method for interactively selecting and reading files.

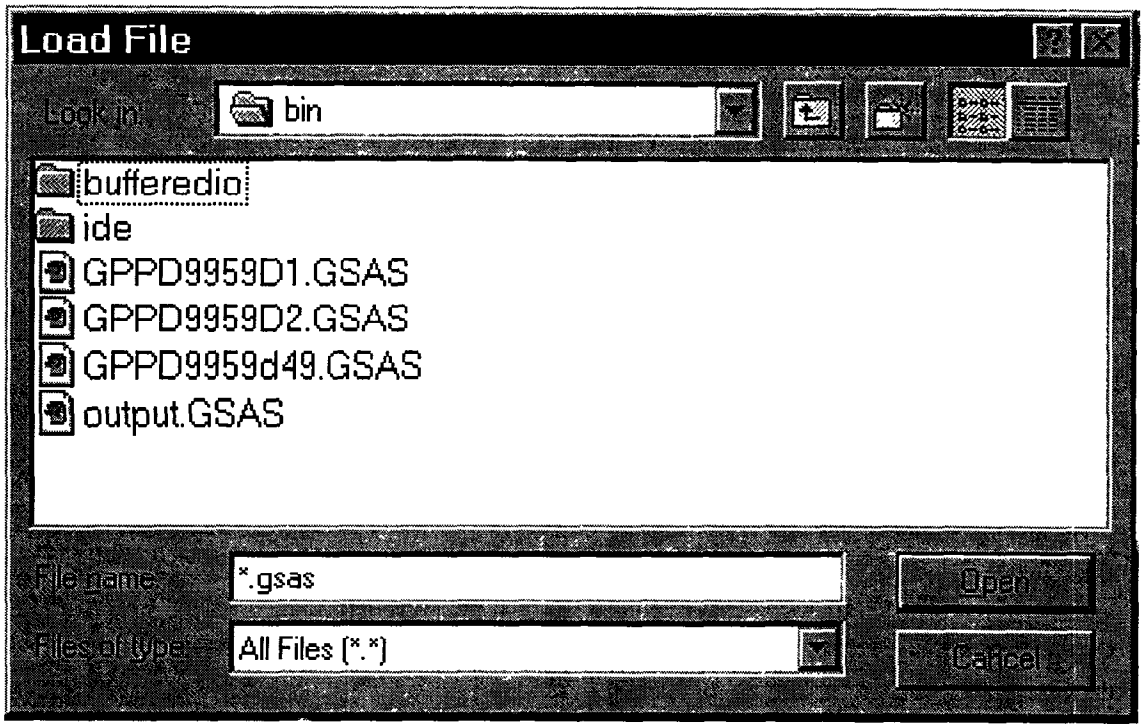

Figure 2 A sample Java File dialog box for selecting and reading files.

Menu bars and pull-down menus are quite familiar to most computer users now because of the ubiquity of Microsoft Windows and the Macintosh as personal computers. One of the goals of new software design is to make the use intuitively obvious so that new or inexperienced users can find their way through the operations provided by the program without assistance from other users and without the use of a user manual. This can be accomplished through the use of a familiar menu structure such as shown in Figs. 1-3.

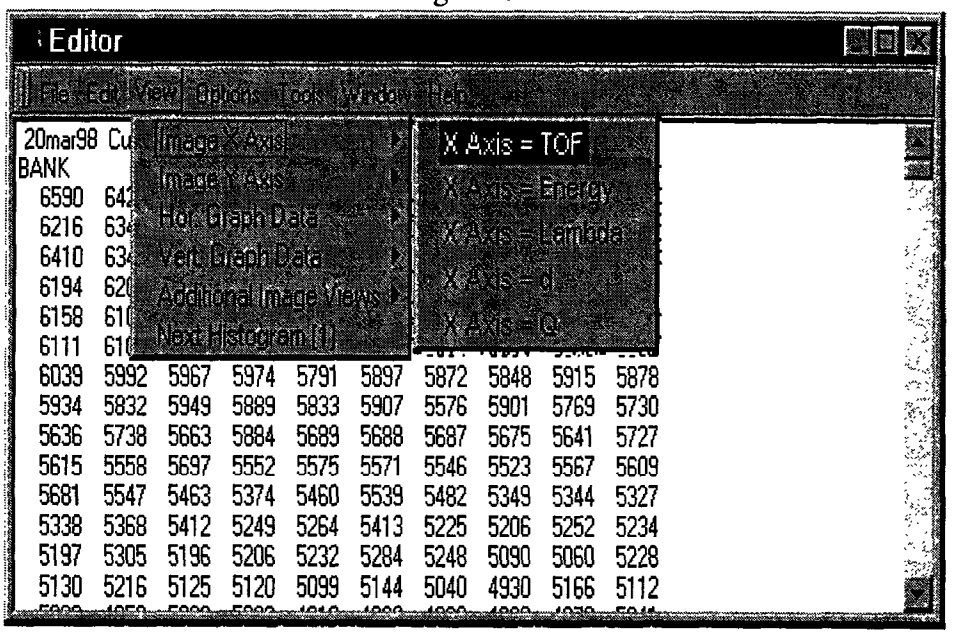

Figure 3 Sample Java menus for selecting viewing options.

Although we are writing our code in Java, we may still execute some functions through the web browser and CGI for simplicity. The web browser can execute CGI scripts written in Perl, TCL, JavaScript, Visual Basic, or some other scripting language native to the machine being used as a web server (See http://www.w3.org/MarkUp/, http://hoohoo.ncsa.uiuc.edu/cgi/, http://www.perl.org/,. http://www.scriptics.com/scripting/)

3. Project Status

Initially we planned to put the data in a database so we could use standard Java DataBase Connectivity (JDBC) tools to access the data. We tested this with the free Postgress database and found it too slow and inefficient. We then switched to Microsoft SQL server and found quite good response and efficiency. This is an acceptable method for instruments with moderate amounts of information, but for instruments with very large data sets, we decided that it is better to read the spectra from the raw data files. The raw data files will be read from the disk drives on the data collection computers or from the CDR data archive. Storing the header information in the database is still preferred for convenience in searching for desired data sets.

The Java routines for searching the database and reading the data from the database are working. Programs to load the data into the database are also working. We used C for writing data to the database since the database is local, and populating the database does not require software to run on a client machine. Java was used for the routines to read from the database since they will typically be run remotely on the client machines.

For highest storage efficiency and speed of access, we have written routines to read the data directly from the raw IPNS Run Files. Since access routines for these files were already available in C, the routines were written in C with a Java interface to the native methods. We may later rewrite these routines in pure Java to allow users to download the raw data and access it using our read routines. We will also write data retrieval routines for other types of data such as NeXUS [P. Klosowski, et al. 1997].

We have designed Data objects to contain a single spectrum and DataSet objects to hold multiple Data objects with common independent variables. The Data object includes an XScale, an array of y-values, and an array of errors. It can also contain Attributes such as temperature or pressure. Attributes are optional and can be any string or float parameter. The Attribute class has a comparison method that allows a program to sort without needing to read and compare the attributes. Methods available for Data objects include add, subtract, multiply, divide, rebin, set attribute, and get attribute. The error array in the Data objects contains the statistical uncertainty for each data value. Raw neutron scattering data has a statistical uncertainty equal to the square root of the total number of counts, so a method has been included to set the errors to those values. As the data is manipulated, the data errors will be combined to properly propagate errors.

Each IPNS run would map to a DataSet with the spectrum from each detector element mapping to a Data object within the DataSet. DataSet objects include methods to add and remove Data objects, to set and get labels, IDs, titles, and axis units, and to get data ranges. The DataSet object includes a log of operations that have been performed on the Data in the DataSet. We will

also have a DataSetContainer that allows handling multiple runs such as a series of measurements at different temperatures.

Programs have been written to display an x-y plot of a selected Data from a DataSet, and to display an image composed of all the data from a DataSet. The intensities of points in the image are represented by the pixel color and each row of the image represents a Data. The image display we have produced is similar to that generated in the TOF_VIS program [Mikkelson and Worlton, 1997].

Currently the rows of the image are sorted by detector element number and the data all comes from one DataSet. We are working on generalizing the selection and sorting of the different Data objects that make up the image so they can be selected from different DataSets in a DataSetContainer. This will allow us to display an image composed of spectra sorted by temperature or other variable.

We initially were uncertain whether Java would work well with cursor interaction, but have been pleasantly surprised. We are able to generate x-y plots and display selected values in real time as the cursor is moved over the image.

4. Conclusion

An increase in the neutron scattering user community is necessary to make full use of neutron sources. Software that is easier to use and that can be run remotely will facilitate involving new users with neutron scattering. World Wide Web browsers and Java make it possible to design software that can run on multiple computing platforms and can run over the Internet. IPNS has begun a project to design software to allow remote data collection and analysis. A database is being used for storing and organizing information about experiments. Java code has been written to search and retrieve information about experiments and Java classes have been written for reading IPNS data. Methods are included to view, manipulate, and save data sets. Work on the project is ongoing.

5. Acknowledgements

The funding for this project came through a grant from the office of the Director of Physical Research at Argonne National Laboratory as result of a proposal submitted by C.-K. Loong, J.P. Hammonds, R. Osborn, T. Morgan, and T. Diesz. Joe Nipko, Dennis Mikkelson, and Dhar Desai have written software most of the software described here.

6. References

P. Klosowski, M. Koennecke, J.Z. Tischler, R. Osborn, NeXus: A common format for the exchange of neutron and synchrotron data, Physica B: Physics Of Condensed Matter (241-243)1-4 (1998) pp. 151-153

D. Mikkelson, T. Worlton, TOF-VIS, software for interactive exploration of time-of-flight data, Physica B: Physics Of Condensed Matter (241-243)1-4 (1998) pp. 142-144

Report on the Workshop on Monte Carlo Simulation of Neutron Scattering Instruments

R. K. Crawford, Argonne National Laboratory, Argonne, IL 60439 USA

A Workshop on Monte Carlo Simulation of Neutron Scattering Instruments was held at Argonne National Laboratory on November 13-14, 1997. This workshop was organized and sponsored by the Spallation Neutron Source (SNS) Project. There were 17 attendees from Argonne National Laboratory (ANL), Brookhaven National Laboratory (BNL), Los Alamos National Laboratory (LANL), National Institute of Standards and Technology (NIST), Oak Ridge National Laboratory (ORNL), Institute Laue Langevin (ILL), Rutherford Appleton Laboratory (RAL), and Risø.

The primary goal of this workshop was to get this broad and diverse international group of developers and users of Monte Carlo software for simulating neutron scattering instruments to agree to pursue development of a common suite of such software in order to minimize duplication of effort. Secondary goals were to acquaint the participants with the Monte Carlo capabilities and efforts at the other laboratories and to establish a preliminary set of functional and operational requirements. All of these goals were achieved.

The most extensive efforts to date at using Monte Carlo simulations to model entire instruments have been those at Los Alamos. Most recently, Los Alamos has been developing a graphical user interface to facilitate the use of their software by non-experts. The current version of this user interface was demonstrated at the workshop, and the participants generally agreed that this interface represented a large improvement.

The participants agreed to develop a set of standards for a Monte Carlo simulation software suite that would meet the needs of the neutron scattering community. These standards will permit software developers at the various laboratories to create modules that work together rather than having each laboratory create and maintain its own complete suite of Monte Carlo codes. The Los Alamos and Oak Ridge groups agreed to take the lead in developing these standards. The participants also agreed to circulate information about this collaborative project to a broader cross-section of the community, and to set up e-mail lists and a web site to facilitate exchange of information among the collaborators. The ISIS representatives agreed to set up a computer site at ISIS that would mirror the current Los Alamos software site.

An International Advisory Committee was established to provide community input into the management of these processes. Members of the International Advisory Committee include Kent Crawford (ANL-chair), Ulrich Wildgruber (BNL), Luke Daemen (LANL), Lee Robertson (ORNL), Ian Anderson (ILL), and Mark Hagen (RAL). Others will be added as broader community involvement is established.

In summary, this was a very successful workshop that met all its goals. A process has been initiated for inter-laboratory collaboration to avoid duplication of effort in this important area of Monte Carlo simulation software. However, a large amount of detailed work needs to be done to make this collaboration a reality. The workshop participants established an International Advisory Committee ensure that this process continues in a timely fashion and that the results meet the needs of a broad community. For a copy of the workshop report, contact Kent Crawford (rkcrawford@anl.gov).

ICANS-XIV
14th Meeting of the International Collaboration on
Advanced Neutron Sources
June 14–19, 1998
Starved Rock Lodge, Utica, Illinois, U.S.A.

THE NEUTRON INSTRUMENT MONTE CARLO LIBRARY MCLIB: RECENT DEVELOPMENTS

Philip A. Seeger, Luke L. Daemen, Rex P. Hjelm, Jr., and Thierry G. Thelliez

Manuel Lujan Jr. Neutron Scattering Center, Los Alamos National Laboratory
Los Alamos, NM 87545, U.S.A.
E-mail: PASeeger@aol.com

ABSTRACT

A brief review is given of the developments since the ICANS-XIII meeting made in the neutron instrument design codes using the Monte Carlo library MCLIB. Much of the effort has been to assure that the library and the executing code MC_RUN connect efficiently with the World Wide Web application MC_Web as part of the Los Alamos Neutron Instrument Simulation Package (NISP). Since one of the most important features of MCLIB is its open structure and capability to incorporate any possible neutron transport or scattering algorithm, this document describes the current procedure that would be used by an outside user to add a feature to MCLIB. Details of the calling sequence of the core subroutine OPERATE are discussed, and questions of style are considered and additional guidelines given. Suggestions for standardization are solicited, as well as code for new algorithms.

1. Introduction

Monte Carlo is a method to integrate over a large number of variables. Random numbers are used to select a value for each variable, and the integrand is evaluated. The process is repeated a large number of times and the resulting values are averaged. For a neutron transport problem, we first select a neutron from the source distribution, and project it through the instrument using either deterministic or probabilistic algorithms to describe its interaction whenever it hits something. If it hits a detector, we tally it in a histogram representing where and when it was detected. This is intended to simulate the process of running an actual experiment (but it is *much* slower). Monte Carlo is a useful supplement to analytical treatment of an instrument, in particular to check and demonstrate "non-intuitive" focusing arrangements, but should never be used as a substitute for thinking. (We are grateful to Jack Carpenter for reminding us of this limitation of Monte Carlo.)

Keywords: MCLIB, Monte Carlo, simulation, instruments

The approach generally used in the MCLIB library routines is to treat the optical properties of neutron transport rather than microscopic nuclear interactions (although microscopic processes may be included in specific algorithms). The philosophy and structure of MCLIB (and of the executing program MC_RUN) were presented at ICANS-XIII [1], and that report, augmented by the proceedings of the 1996 Berkeley Workshop [2], has become the reference document for MCLIB. The current version may be accessed by anonymous ftp from

ftp://azoth.lansce.lanl.gov/pub/mclib/document

in three formats. Note that this document is updated frequently as features are added to the library. The source codes are also available through this ftp site.

The most exciting new features to report are the establishment of a Web application and standardization of the code under the name Neutron Instrument Simulation Package (NISP). That work is reported elsewhere in these proceedings [3], but all users and prospective users of NISP are urged to visit the web site at

http://bayberry.lanl.gov/lansce/Welcome.html

2. New Library Features and MC_RUN Updates

There are two new options for neutron sources. You may specify a file of individual neutron histories generated as a monitor output from a previous execution of MC_RUN, or you may specify a square (uniform) distribution of velocities.

A new region type is type 14, "toroidal mirror." Since the geometry of surfaces and regions is limited to quadratic, a torus can not be defined as a simple surface. This type illustrates how *any* form of geometry may be implemented *within* a region, which is itself bounded by quadratic surfaces.

The definitions of most sample types have been modified to allow the final directions of the neutrons to be limited in solid angle, for the purpose of variance reduction when detectors don't cover 4π. In particular, the isotropic scattering type 32 may have its solid angle defined by bands of direction cosines with respect to each axis. An auxiliary routine dOMEGA is provided to compute the resulting solid angle (if any!) for normalization. Sample types that are not isotropic (30, 34, and 36) can not be randomized in polar angle, but may have the azimuthal angle biased to illuminate specific detector geometries. Note that whenever solid-angle limits are used, multiple scattering is turned off. Another change in type 32 is that you may now specify a spectrum of δ-function energy changes instead of a single energy.

The encoding of two-dimensional detectors (type 43) now includes cylindrical and spherical coordinates as subtypes, as well as rectilinear and plane-polar. This makes the use of detectors with curved surfaces easier.

Many additions have been made to program MC_RUN to assist in debugging and to study "unexpected" events. A monitor (.MON) file may be written to record the passage of neutrons across a given surface (and this file may be used subsequently as a source file, see above). It is now possible to flag a surface preceding the monitor surface for correlation; then any neutron that crosses the correlation surface and subsequently reaches the monitor surface will be recorded in a .COR file. Another option is that the .COR file may record where the neutron was

immediately before reaching the surface being monitored. These files are direct-access binary, so special programs (such as SUPER_KNOW) must be adapted to extract the relevant information.

In response to a request at a recent workshop [4], a backtracking feature has been implemented. First, a neutron may be flagged as "bad" by some procedure during its transport, for example by coming through a chopper opening out of phase. If such a "bad" neutron reaches either the sample or any detector, then the complete history of surface and region crossings of that neutron will be written to a .BAD file in an ASCII format allowing subsequent study.

More variance-reduction features have been incorporated, also in response to the workshop [4]. In addition to the solid-angle biasing described above, up to 32 levels of splitting (or secondary neutron production) may be applied to a neutron. This includes multiple use of histories reaching the sample, or doubling when crossing flagged surfaces. User routines have the capability to split or create neutrons, as will be discussed below.

3. Program MC_RUN

A flow chart of the execution program MC_RUN is given in Fig. 1. There are three nested loops: the outermost loop is over the number of source neutrons (with a branch for stored and repeated neutrons); the next is transport between regions, determination of the subsequent region, and the interaction at the surface; and the innermost loop is what happens within any given region (subroutine OPERATE). All geometric relations between regions are handled in this main code, and all physics and algorithms of elements within regions are accessed through OPERATE, either

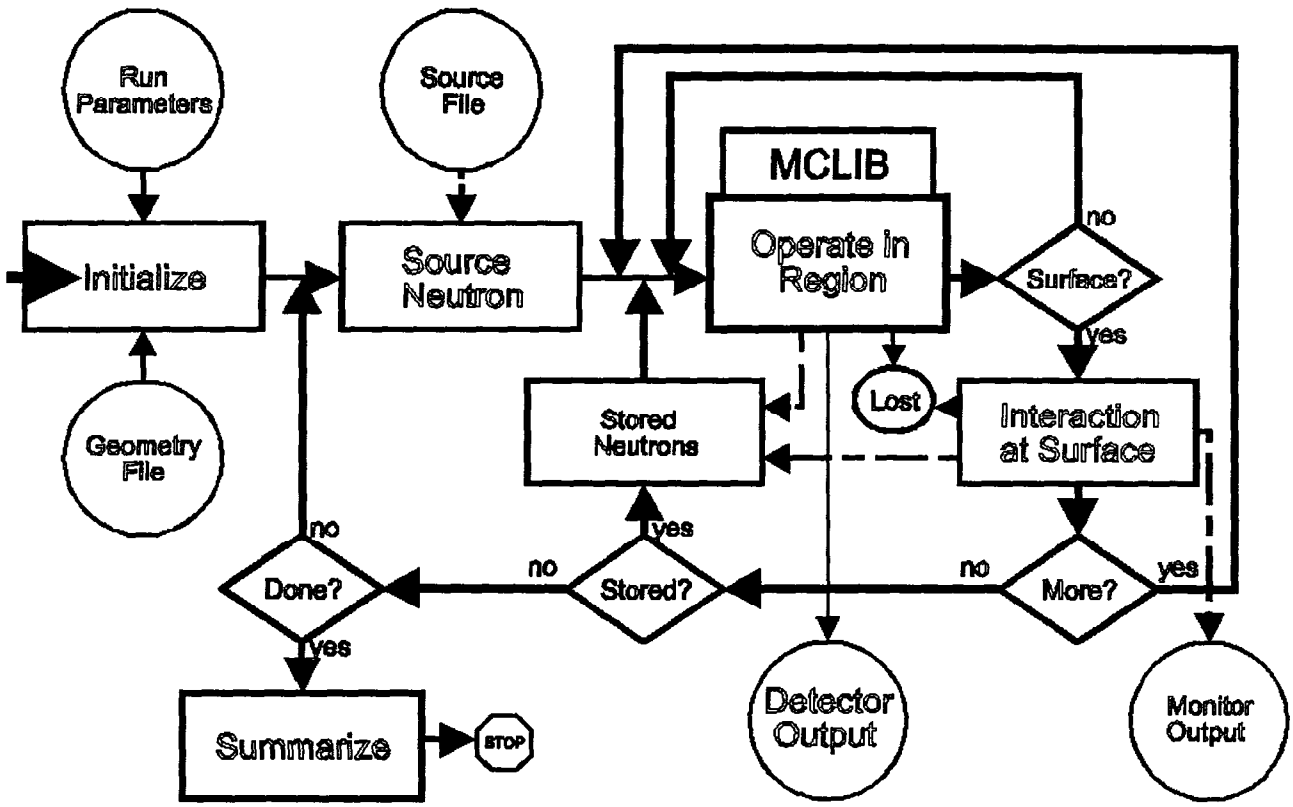

Figure 1. Flow diagram of program MC_RUN

as in-line code or as external procedures. The operation loop continues until the neutron reaches an exit surface of the region (or vanishes). Possible outputs of the operation include storing a created neutron for subsequent tracking, detection of the neutron, or absorption. It is within this loop that the MCLIB library is applied, and it is here that new features and modules may be inserted. This report is intended to assist in the incorporation of such new features.

4. Structures used in MCLIB / MC_RUN

The source codes for the Monte Carlo Library MCLIB and MC_RUN are written in a subset of ANSI-standard Fortran 90 (F90). To improve portability, only F90 features that are also included as "VAX extensions" to F77 are used (F77/VAX). Declaration statements use the F77 format, which is allowed in F90. Two exceptions to the F90 standard are that the character "." is used as the structure delimiter instead of "%", and that structures are defined and declared in STRUCTURE and RECORD statements instead of TYPE; these are again to improve portability to F77/VAX compilers.. F90 is a structured language, but not object oriented. Some concepts of object-oriented programming are used, but the emphasis is placed on execution speed.

The coordinate system used in MCLIB assumes that the beam axis is generally in the z-direction, the x-direction is to the particle's right as it travels in the z-direction, and the y-direction is always vertically upward (because gravity always acts in the negative y-direction). This left-handed coordinate system was chosen to match the X-Y coordinates of a plane detector in small-angle geometry. A module may rotate coordinates in the X-Z plane, but changing the direction

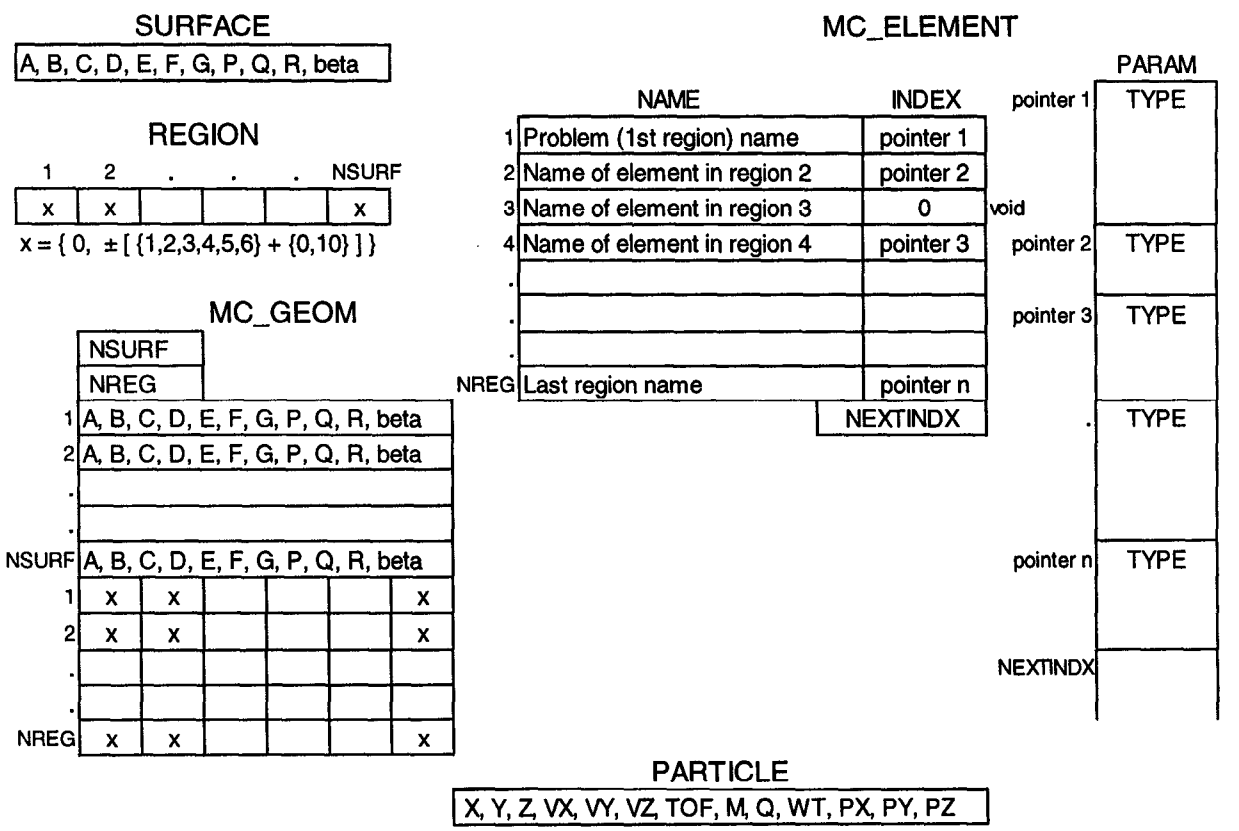

Figure 2. Structures used in MCLIB and MC_RUN

of gravity is strongly discouraged. The fundamental structures are PARTICLE, SURFACE, REGION, and MC_ELEMENT. These are illustrated in Fig. 2, and defined in an include file, MC_GEOM.INC, which is available with the source code at

ftp://azoth.lansce.lanl.gov/pub/mclib/fortran

All elements in PARTICLE and SURFACE structures are REAL*4. Compared to REAL*8, there is a significant reduction of the length of history files containing large numbers of particles, but there are some limitations in defining surfaces, which will be described below.

The elements of a PARTICLE structure are

(X, Y, Z) = position of the particle (m)

(VX, VY, VZ) = particle velocity (m/μs)

TOF = particle time-of-flight (μs)

M = atomic mass number, *e.g.*, 1 for a neutron or 0 for a photon

Q = atomic number of particle, *e.g.*, 0 for a neutron or +1 for a proton

WT = statistical weight of particle. A single tracked history may represent more or less than one neutron. This allows source weighting and the tracking of low-probability events for variance reduction.

(PX, PY, PZ) = average polarization vector of particle beam. The magnitude of the vector represents the degree of polarization.

A module may use and change any of the components of a particle sent to it. For instance, motion is accomplished by updating X, Y, Z, and TOF, or partial absorption by decreasing WT. A particle may be split by making a copy and apportioning the original WT between the two instances.

The elements of a SURFACE structure are the ten coefficients of a general quadratic surface and a parameter describing the surface roughness. The equation of a surface is

$$Ax^2 + Bx + Cy^2 + Dy + Ez^2 + Fz + G + Pxy + Qzy + Rzx = 0 \qquad (1)$$

The use of single-precision real numbers limits the definitions of surfaces with quadratic terms if they are far from the origin. This is not a severe problem if the origin of the coordinate system is placed at the sample location, since the quadratic surfaces used tend to be centered near the sample. The surface roughness parameter BETA is presently defined only for values between 0 and +1 as a long-range waviness. It is the maximum slope error in a cosine distribution, with *rms* ≈ 0.58 BETA for small values of BETA. We are exploring representation of surface irregularities on shorter length scales, which could be represented by using the sign of BETA as a flag, or by using values > 1. A module may use any predefined surfaces, and may create a surface for its internal use, but must not modify any existing surfaces. Any surface more complex than quadratic (*e.g.*, a toroid) can only be defined within a module.

A REGION structure is a vector IGEOM of signed integers (INTEGER*2) which give the relationship of the region to every surface. If IGEOM(JSURF) = 0, the region is not bounded by surface JSURF. If not zero, then the sign of the integer defines which side of the surface is "inside" the region by the sign of eq. (1) when evaluated at a point (x, y, z). That is, in order for a particle to be inside the region, the left side of eq. (1) must have the same sign as IGEOM for the surface. (If eq. (1) evaluates to 0, then 1st and 2nd derivatives will also be considered.) The numeric value of IGEOM is also significant:

1: ordinary surface described by roughness BETA, with possibility of refraction or critical

reflection depending on wavelength and relative index of refraction

2.: totally reflecting surface (from inside the region)

4: totally absorbing surface when hit from inside the region; *i.e.*, no exit

5: special conditions apply before exiting region; for instance, a coordinate transform may be required. Then treat as type 1. An example of this usage is given below.

6: treat as type 1, but split the particle into 2 equal instances after crossing

The value of IGEOM is increased by 10 if the surface is that of a region "embedded" within the region being defined (embedded and reentrant regions are discussed in the MCLIB Document). Modules have access to the region definitions, but should not have to deal with anything but the sign of IGEOM. No changes of region definitions are allowed in modules.

The structure MC_ELEMENT is most relevant when writing a module, because this is the structure used to define the contents of all regions. There is a one-to-one correspondence of elements and regions. An element has a 40-character NAME and an integer pointer INDEX into an array of REAL*4 parameters, PARAM. (A special case is void regions, which have INDEX = 0.) The number in the PARAM block at the location INDEX is the ELMNT_TYPE of the region; the integer part of the value is the type and fractions may be used for subtypes. Any number of parameters may be defined; for each defined type nn, there is also a parameter NUMBER_nn that is one more than the number of parameters defined. The author of a module must obtain or assign a type number (70 through 79 are available for *ad hoc* or development use), and must define variables with global names. (Global names are necessary so that the creator of the geometry file will have exactly the same definitions as the executing program!) Descriptive names are preferred, and a prefix may be used to identify the relevant module; documentation of the meanings of the variables is essential. The names are defined in PARAMETER statements as integer offsets in the PARAM block, counting from 0 at the location referenced by INDEX. The complete list of defined types is given in the include file MC_ELMNT.INC, found at the ftp site. A module may modify an entry in the PARAM block for its own later use, but *not* as a mechanism for returning a value to MC_RUN. Use of static local variables (SAVE statements) is preferred over modifying PARAM entries. The NAME variable may be used to pass a file name to the module. The communication between MC_RUN and the modules is described in the next section. Note that there are rough "classes" of modules, organized by decades of the type number. In particular, samples are in the range 30–39 and detectors in the range 40–49. Such classes share common variable names.

5. Subroutine OPERATE

This subroutine contains the "methods" for every type of element, either in-line or as external subroutine calls. The task of an author of a new module is to incorporate the new type into OPERATE by including a new case. For development, dummy routines for cases 70–79 are pre-linked, so that a user may substitute his own routine for the dummy one without having to modify OPERATE. For examples and to show the case structure, excerpts from the subroutine are listed in Appendix A. All of the routines in the MCLIB library as listed and described in the MCLIB document are available to use in support of new modules. The calling sequence of OPERATE contains arguments to support a variety of classes of elements; for instance, detectors need to return encoding information. The arguments in the calling sequence are listed in order in Table 1. Any of these may also be used as arguments to additional lower-level subroutines. All arguments are passed by reference, so the programmer has the responsibility to use care in changing values.

Table 1. Arguments in Calling Sequence of Subroutine OPERATE

Input	Name	Type	Description	Output
Neutron	PART	Structure	A PARTICLE structure. Position, velocity, statistical weight, & polarization may change depending on the case.	Updated Neutron
Escape Distance	EXDIST	REAL*4	Recompute if velocity changes. Will be 0 if the neutron is moved all the way to an exit surface.	New Escape Distance
Parameters of Region	PARAMS	REAL*4 (0:*)	From the PARAM array. First value is type number of the region, used in CASE structure.	
MC_GEOM Structure	GEOM	Structure	All surface and region geometry definitions.	
Region Number	IREG	INT*4	Modified if region contains subregions, *e.g.*, chopper or Soller-slit package.	Subregion Number
Entrance Surface	JSURF	INT*4	Surface neutron is on initially, or 0 if not on a surface.	
Exit Surface	KSURF	INT*4	Surface toward which the velocity points; updated if direction changes; set to negative if reflection occurs.	New Exit Surface
Name of Region	NAME	CHAR*40	The region name may be an external file name, *e.g.*, an S(α,β) file for inelastic scattering.	
Transmission Flag	TRANSMIT	LOGICAL	Used by sample class to know when to split neutron into scattered and non-scattered histories.	
	FLAG	LOGICAL	Set to .FALSE. if something is peculiar, *e.g.*, neutron in wrong chopper frame.	Bad-Neutron Flag
	PART_2	Structure	Typically used to save the "scattered" neutron independently from "transmitted."	Second Neutron
	DET_WT	REAL*4	Non-zero output identifies region as detector. Includes detector efficiency.	Detected Statistical Weight
	IX	INT*4	First coordinate of position-sensitive detector.	Detector Cell Number, IX
	IY	INT*4	Second coordinate (if 2D detector).	Detector Cell Number, IY
Random-Number Seed	ISEED	INT*4	A single pseudo-random sequence is used throughout the package.	Random-Number Seed

The first argument, PART, is the neutron being tracked. The set of values from the PARAM block that is specific to this element is passed as a vector PARAMS. Values may thus be referenced in the form PARAMS(ParameterName), *e.g.*,

```
NSIG = PARAMS(NSIGMA0) + PARAMS(NSIGMAV)/SQRT(PART.VX**2+PART.VY**2+PART.VZ**2)
```

(this and other examples will be found in context in Appendix A). Note that PARAMS is declared in OPERATE to begin with index 0 (the type number), and this is a useful convention to use in lower-level subroutines as well so that the indexing of locations in the block needs no offset.

When OPERATE is called, MC_RUN has already determined the distance EXDIST to escape from the region along the initial trajectory (including gravity), and this is passed as the second

argument (useful for determining attenuation). If the velocity vector (magnitude or direction) changes within the module, EXDIST must be recomputed by a call to DTOEX. This allows OPERATE to loop internally (instead of returning to MC_RUN at each step) for effects such as multiple scattering, but it means that the entire geometry structure (GEOM) and the region and surface numbers (IREG, JSURF, and KSURF) must also be passed as arguments. For an example of multiple scattering, see type 36 in Appendix A. By default, OPERATE will move the particle by the distance EXDIST and will therefore return with EXDIST = 0; to avoid this for a particular case, end the case with a RETURN statement instead of falling through. IREG and KSURF are also output parameters in special cases. The final example in this section shows the use of subregions, and type 13 (Appendix A) shows negative KSURF used as a flag for reflection. The development cases 70–74 have calling sequences without detector binning or instrument geometry, and cases 75–79 have the complete calling sequence of OPERATE.

The calling sequence includes two logical variables for state information. MC_RUN expects to track neutrons transmitted through a sample as well as scattered neutrons. The flag TRANSMIT is initially .TRUE. and is used to identify the first encounter of a neutron with the sample so that the code will generate a second neutron (PART_2). That neutron will be scattered on a subsequent entry when TRANSMIT = .FALSE. (see type 36 in Appendix A). Any call to OPERATE is allowed to generate a new PART_2. The output variable FLAG is a debugging aide. When a module recognizes that something about the neutron deserves attention, such as passing through a chopper in the wrong frame (see type 20 in Appendix A), FLAG is set to .FALSE.. If such a "bad" neutron subsequently hits a sample or a detector, then MC_RUN will tally it and (if requested) will also write its full history to a file. This feature may also be used in *ad hoc* versions of OPERATE to address rare occurrences.

All histogramming functions are performed by MC_RUN, but detector encoding is a function of a detector-class element. The statistical weight detected and one or two cell numbers are returned through the calling sequence respectively as DET_WT, IX, and IY. (The example in Appendix C, type 43, also shows how all of the arithmetic of a module may be moved to a separate procedure, in this case a call to DET_2D.) Time-of-flight slices, which may be non-linear and different for each detector, are computed in MC_RUN because they involve storing arrays of slice boundaries and (since dynamic memory allocation is not available in F77/VAX) all variable-length memory arrays are reserved for management in the main program. The final argument is ISEED, the seed of the random-number generator, which is propagated through all levels of subroutines in MCLIB so that a single pseudo-random number sequence is used.

An example of a complex region (containing subregions, and also using a coordinate transformation) is a multi-slit collimator, type 11 in Appendix A. This type encompasses Sollers, tapered Sollers, and benders. Instead of defining every surface and region explicitly, the package is defined by its external geometry and by the slit spacing, taper (if any), and bend angle (for a bender consisting of cylindrical slits). The code for type 11 uses the slit spacing to determine which slit number the neutron is entering, and then translates and rotates the coordinate system so that the neutron appears to be in the one slit which is defined. A logical variable identifying that the neutron is in this type of region and the parameters used for the coordinate transformation are stored in static local variables so that they will be available to undo the transform when the neutron exits the region. There may be as many as five subregions to describe one opening: the lumen, the coating materials on each side, and half of the substrate on

each side. (Alternatively if the center of the array is a blade instead of an opening, the subregions could be the substrate, the two coatings, and half of the lumen on each side of the substrate.) The code tests the five regions immediately following the type 11 region in the geometry definitions, sets IREG to the proper value, and executes a RETURN without moving the particle. The entrance and exit surfaces and also the outer longitudinal surfaces of the slit descriptive regions must be tagged in the REGION structure with a value of 5 so that MC_RUN will call EXIT_REG (a second entry point in OPERATE) when a neutron crosses. This entry point is shown at the end of Appendix C, including the code relating to type 11. There are two situations. If the particle is still within the exterior geometry of the slit package (*i.e.*, still within the bounds of the type 11 region), then it must be crossing from one slit to another within the package. The slit number is changed and the coordinates transformed again so that it is once more entering the defined opening. If on the other hand the neutron is leaving the whole package, then the coordinate system is reconverted to match the outside world.
This example also shows how a permanent change of the coordinate system may occur in an element. If the type 11 region was a bender, then the z-axis is rotated. Another example of rotation in the X-Z plane is a crystal monochromator (see type 13 in Appendix A).

6. Style and Guidelines

Appendix A may also be used as a style guide for writing code for inclusion in MCLIB. By nature, questions of "style" are arbitrary, but some level of consistency will assist later generations in maintaining the code package. Upper case is preferred except for variable names that make more sense with mixed or lower case characters. Continuation lines should be written to be compatible with either fixed or floating format Fortran, by placing "&" in column 73 of the line to be continued and another "&" in column 6 of the continuation line. Always use IMPLICIT NONE before the INCLUDE statements or before any declaration statements, and declare every variable. DO and IF blocks should be indented by 3 characters. Numbered statements should be avoided. Lots of comments throughout, and enough spaces in code lines to see where the operators are. Make me jealous by writing code that is easier to read and to understand than mine (as well as being correct, of course).

All lines between the comment lines "C++" and "C—" will be included in the subroutine abstracts in Appendix B of the MCLIB Document. The "required" information includes a brief description of the purpose and methods used in the procedure, the original author and date and any references to publications or other sources of algorithms, the update history, any INCLUDE statements, descriptions and Fortran declarations of all variables in the calling sequence, and a list of any external routines called and declarations for those which are functions. For more examples, see the MCLIB Document. The complete source codes are also available (in 3 file formats) at the anonymous ftp site, *ftp://azoth.lansce.lanl.gov/pub/mclib/fortran.*

Physical and mathematical constants should be defined and placed in PARAMETER statements at the beginning of the procedure, or better yet given global names and included in the file CONSTANT.INC so that everyone will be using the same values. The present quantities in CONSTANT.INC are

GOVER2	= half the acceleration of gravity	= 4.858×10^{-12} m/μs^2
HOVERM	= Plank's constant/neutron mass	= 0.0039560339 m-Å/μs
HSQOV2M	= Plank's constant squared over 2 Mneutron	= 0.0818145347 eV-Å^2

PRECES_N	= neutron magnetic-moment precession rate factor	
	= $2\pi\mu_n M_n/h^2$	= 23160.451 radian/T/m/Å
ROOTM_2	= square root of half the neutron mass	= 72.298 $eV^{0.5}$-μs/m
TWOPI	= 2π	= 6.283185307

The units used throughout MCLIB are distance in m, time in μs, wavelength in Å, and energy in eV.

The examples in the previous section of this report describe operations within a region. It may be desired also to consider refraction and reflection when crossing the surface of a region, and this requires a method to determine the index of refraction (or equivalently the scattering-length density). Presently only two element types (amorphous materials and supermirrors) provide this information, through the complex function GET_RHO. Addition of other types to this function should be straightforward.

7. Conclusion

This report has described the current status of the structure of the MCLIB library, and the procedure by which new features can be added to the low-level code. We propose this as a standard. However, many features are arbitrary accidents of history, and we are requesting input from users to determine what *should* be changed and what *must* be changed before the standard is established. Although we have tried to describe the functionality requirements that led to the present status, it must be expected that improvements will be made both from the point of view of computer science and also run-time efficiency (which we take to be the ultimate test). Please address any questions and suggestions to PASeeger@aol.com.

Acknowledgments

This effort has been supported historically by the Los Alamos National Laboratory and the Manuel Lujan Jr. Neutron Scattering Center, a national user facility funded by the United States Department of Energy, Office of Basic Energy Sciences-Materials Science, under contract number W-7405-ENG-36 with the University of California.

References

[1] P. A. Seeger, "The MCLIB Library: Monte Carlo simulation of neutron scattering instruments," 13th Meeting of the International Collaboration on Advanced Neutron Sources, October 11–14, 1995, Paul Scherrer Institut, Villigen, Switzerland, PSI Proceedings 95-02, pp. 194–212.

[2] P. A. Seeger, "The MCLIB Library: new features," Workshop on Methods of Neutron Scattering Instrument Design," Lawrence Berkeley Laboratory, Berkeley, CA, Sept 23–27, 1996.

[3] T. G. Thelliez, L. L. Daemen, P. A. Seeger, and R. P. Hjelm, Jr., "MC-Web: A WWW-based application for NISP," 14th Meeting of the International Collaboration on Advanced Neutron Sources, June 14–19, 1998, Starved Rock Lodge, IL (these proceedings).

[4] R. K. Crawford, "Report on the Workshop on Monte Carlo Simulation of Neutron Scattering Instruments," Nov. 13–14, 1997, Argonne National Laboratory.

Appendix A. Excerpts from Subroutine OPERATE

```
C++
C**********  O P E R A T E  **********
C********** E X I T _ R E G **********
C
      SUBROUTINE OPERATE(PART, EXDIST, PARAMS, GEOM, IREG, JSURF, KSURF,&
     &                   NAME, TRANSMIT, FLAG, PART_2, DET_WT,          &
     &                   IX, IY, ISEED)
C
C                EXIT_REG(PART, GEOM, IREG, JSURF)
C
C  Routines to operate on a particle within (or exiting from) a region
C    containing material, collimation elements, time-dependent devices,
C    samples, or detectors.  Included region types/actions are
C         1    amorphous unpolarized material: move to exit w/reduced weight
C         2    aluminum: move to exit w/reduced weight
C         5    beryllium: move to exit w/reduced weight
C         6    single-crystal filter: move to exit w/reduced weight
C        11    multi-slit collimator, vertical: selects subregion w/o moving
C        12    multi-slit collimator, horizontal: selects subregion w/o moving
C        13    crystal monochromator: reflect from surface or move to exit, and
C              rotate coordinates
C        14    toroidal mirror: region divided into subregions by toroidal
C              mirror: move to exit w/reduced weight
C        20    blade or disk chopper: move to exit OR select subregion
C        22    gravity focuser: selects subregion without moving
C        23    removable beamstop: set weight=0 if not transmission mode
C        30    fixed-Q or hard-sphere scatterer: transmitted or scattered
C              particle moves to exit with modified weight
C        32    isotropic scatterer with spectrum of energy changes: transmitted
C              or scattered particle is moved to exit with modified weight
C        34    inelastic scatter using S(alpha,beta) from MCNP: transmitted or
C              scattered particle is moved to exit with modified weight
C        35    reflectometry, multilayer: reflect from surface w/o moving,
C              same weight if transmitted or reduced weight if scattered
C        36    general powder scatterer: transmitted or scattered particle moves
C              to exit with modified weight
C        40    single detector: determine detection probability
C        41    linear detector, vertical: determine y-bin and probability
C        42    linear detector, transverse: determine x-bin and probability
C        43    2-dimensional detector: determine x- and y-bins and probability
C        44    linear detector, longitudinal: determine x-bin and probability
C        90    source size and phase space: weight=0 if outside surface
C
C  P. A. Seeger, April 20, 1994
C    . . . (modification history)
C    13 May 1998: subtype 32.2, 30.1, 30.2, 34.1, 36.1 [LLD,PAS]
C
C  Definitions of STRUCTUREs:
      IMPLICIT NONE
      INCLUDE 'mc_geom.inc'
      INCLUDE 'mc_elmnt.inc'
      INCLUDE 'constant.inc'
C
C  Variables in calling sequence:
C    PART = record containing description of particle (input/output)
C    EXDIST = distance to exit surface particle is aimed at (m) (input/output)
```

```
C    PARAMS = array with description of what is in this region (input)
C    GEOM = structure with all surface and region definitions (input)
C    IREG = region number of device, or subregion within device (input/output)
C    JSURF = surface number, if particle is initially on surface (input)
C    KSURF = surface number that particle is pointed toward (input/output)
C    NAME = name of region, used as file name for type 34 (input)
C    TRANSMIT = flag to compute transmission of sample types 30-39 (input)
C    FLAG = flag set to .FALSE. if (e.g.) chopper in wrong frame (output)
C    PART_2 = description of particle created by operation (output)
C    DET_WT = statistical weight of detected particle (output)
C    IX, IY = position bin numbers of detected particle (output)
C    ISEED = random-number generator seed (input/output)
      RECORD    /PARTICLE/ PART, PART_2
      RECORD    /MC_GEOM/  GEOM
      REAL*4    PARAMS(0:*), EXDIST, DET_WT
      INTEGER   IREG, JSURF, KSURF, IX, IY, ISEED
      CHARACTER NAME*40
      LOGICAL   TRANSMIT, FLAG
C
C  Externals:
C    ANGLI     ANGTORUS  ATTEN_Al  ATTEN_Be  ATTEN_X   DET_2D    DISTORUS
C    DTOEX     ELSCAT    GET_RHO   GRAV_FOC  KERNEL    LMONOCRM  LORRAND
C    LREFLCT   MOVEX     NEXTRG    ORRAND    PLEXP     PLNORM    PLQSPHR
C    POWDER    RAN       REFLAYER  RFLN      SNELL     TESTIN    XCHOPPER
      REAL*4    ATTEN_Al, ATTEN_Be, ATTEN_X, DET_2D, DISTORUS, GRAV_FOC,&
     &          PLEXP, PLNORM, PLQSPHR, RAN, REFLAYER, XCHOPPER
      COMPLEX*8 GET_RHO
      INTEGER   NEXTRG
      LOGICAL   LMONOCRM, LORRAND, LREFLCT, TESTIN
C--
C  Local variables:
      REAL*4  NSIG, LAMBDA, XC, YGF, X, Y, D, TRANPROB, ATTEN,          &
     &        ALPHA, SLIT, DELTA, TAPER, ZENTER, SIN_PHI, COS_PHI,      &
     &        COS_TH, SIN_TH, V, AP, BP, CP, REFPROB, F, Q, KZ, EN0,    &
     &        EN1, EN2, TWOSINTH, SIGSCAT, SIGABS, S_MULT, RATIO
      COMPLEX CXRATIO
      INTEGER I, ITYPE, NREG, SUBTYPE, JINDX, JTYPE, KINDX, KTYPE
      LOGICAL LOPENING, LGF, LMULTX, LMULTY, LOPEN, DONE, VERTICAL,     &
     &        INSIDE
C
      SAVE    LGF, LMULTX, LMULTY, YGF, SLIT, DELTA, TAPER,             &
     &        ZENTER, SIN_PHI, COS_PHI, NREG, ATTEN, ALPHA, LAMBDA, Q,  &
     &        EN0, TWOSINTH, TRANPROB
      DATA    LGF,    LMULTX, LMULTY, YGF,SLIT/                         &
     &        .FALSE.,.FALSE.,.FALSE.,0., 0.  /
C
      PART_2.WT = 0.
      DET_WT = 0.
      FLAG = .TRUE.
C
      ITYPE = PARAMS(0)
      IF (ITYPE .EQ. 0) THEN
C        Material is total absorber
         EXDIST = 0.
         PART.WT = 0.
C
      ELSE IF (ITYPE .EQ. 1) THEN
C        Material is amorphous unpolarized
         NSIG = PARAMS(NSIGMA0) + PARAMS(NSIGMAV)/SQRT(PART.VX**2 +     &
```

```
     &                                          PART.VY**2 + PART.VZ**2)
         IF (NSIG .GT. 0.) THEN
            IF (NSIG*EXDIST .LT. 12.) THEN
               PART.WT = PART.WT * EXP(-EXDIST*NSIG)
            ELSE
               PART.WT = 0.
            END IF
         END IF
C
      ELSE IF (ITYPE .EQ. 11) THEN
C        Region contains a multi-slit collimator with vertical blades
         LMULTX = .TRUE.
C        Save parameters to use when exiting region
         NREG    = IREG
         DELTA   = PARAMS(C_DELTA)
         TAPER   = PARAMS(C_TAPER)
         ZENTER  = PARAMS(C_ZENTER)
         SIN_PHI = PARAMS(B_SIN_PHI)
         COS_PHI = PARAMS(B_COS_PHI)
C        Translate particle into central slit
         IF (TAPER.EQ.0. .OR. PART.Z.EQ.ZENTER) THEN
            SLIT = ANINT(PART.X / DELTA)
            PART.X = PART.X - SLIT*DELTA
         ELSE
C           Need to account for taper when determining slit number
            SLIT = ANINT(PART.X / (DELTA-TAPER*(PART.Z-ZENTER)))
            PART.X = PART.X-SLIT*(DELTA-TAPER*(PART.Z-ZENTER))
         END IF
         IF (TAPER .NE. 0.) THEN
C           Tapered slits, also need to rotate particle velocity vector
            COS_TH = 1.-0.5*(SLIT*TAPER)**2
            SIN_TH = SLIT*TAPER*COS_TH
            V = PART.VX
            PART.VX =  COS_TH*V + SIN_TH*PART.VZ
            PART.VZ = -SIN_TH*V + COS_TH*PART.VZ
         END IF
         IF (SIN_PHI .NE. 0.) THEN
C           Element is a bender; rotate velocity vector half the angle
            V = PART.VX
            IF (PART.VZ .GT. 0.) THEN
C              Entering in proper direction, rotate CCW (if phi > 0.)
               PART.VX =  COS_PHI*V - SIN_PHI*PART.VZ
               PART.VZ =  SIN_PHI*V + COS_PHI*PART.VZ
            ELSE
C              Entering backwards, shift CW instead of CCW
               PART.VX =  COS_PHI*V + SIN_PHI*PART.VZ
               PART.VZ = -SIN_PHI*V + COS_PHI*PART.VZ
            END IF
         END IF
C        May be as many a five sub-regions; find which one
         KSURF = JSURF
         DO I=1,5
            IF (TESTIN(PART, GEOM, IREG+I, JSURF)) THEN
               IREG = IREG+I
               RETURN
            END IF
         END DO
         IREG = 0
         RETURN
```

```
C
      ELSE IF (ITYPE .EQ. 13) THEN
C        Region is a crystal monochromator with mosaic spread
         IF (LMONOCRM(PART, PARAMS, GEOM.SURFACE(JSURF),                &
     &                COS_TH, AP, BP, CP, ISEED)) THEN
            CALL RFLN(PART, COS_TH, AP, BP, CP)
            EXDIST = 0.
C           Still on same surface, flag reflection with - sign
            KSURF = - JSURF
         ELSE
C           No reflection; move to exit surface before rotating coordinates
            CALL MOVEX(PART, EXDIST)
         END IF
         IF (PARAMS(M_SIN_2TH) .NE. 0.) THEN
C           Redefine instrument axis; rotate velocity vector
            X = PART.X
            V = PART.VX
            IF (PART.VZ .GT. 0.) THEN
C              Moving in proper direction, rotate CCW (if 2theta > 0.)
               PART.X =  PARAMS(M_COS_2TH)*X                            &
     &                  -PARAMS(M_SIN_2TH)*(PART.Z - PARAMS(M_Z0))
               PART.Z =  PARAMS(M_Z0) + PARAMS(M_SIN_2TH)*X             &
     &                  +PARAMS(M_COS_2TH)*(PART.Z - PARAMS(M_Z0))
               PART.VX = PARAMS(M_COS_2TH)*V-PARAMS(M_SIN_2TH)*PART.VZ
               PART.VZ = PARAMS(M_SIN_2TH)*V+PARAMS(M_COS_2TH)*PART.VZ
            ELSE
C              Moving backwards, shift CW instead of CCW
               PART.X =  PARAMS(M_COS_2TH)*X                            &
     &                  +PARAMS(M_SIN_2TH)*(PART.Z - PARAMS(M_Z0))
               PART.Z =  PARAMS(M_Z0) - PARAMS(M_SIN_2TH)*X             &
     &                  +PARAMS(M_COS_2TH)*(PART.Z - PARAMS(M_Z0))
               PART.VX = PARAMS(M_COS_2TH)*V+PARAMS(M_SIN_2TH)*PART.VZ
               PART.VZ = PARAMS(M_SIN_2TH)*V+PARAMS(M_COS_2TH)*PART.VZ
            END IF
         END IF
C
      ELSE IF (ITYPE .EQ. 20) THEN
C        Region contains a disk or blade chopper; find location of edge
         XC = XCHOPPER(PART.TOF,PARAMS(CHP_OPEN),PARAMS(CHP_CLOSE),     &
     &                 PARAMS(CHP_JITTER), PARAMS(CHP_VEL),             &
     &                 PARAMS(CHP_PERIOD), LOPENING, ISEED)
         SUBTYPE = NINT(10.*(PARAMS(0) - 20.0))
         IF (IAND(SUBTYPE,1) .EQ. 0) THEN
C           Chopper is moving horizontally, compare to PART.X
            X = PART.X
         ELSE
C           Chopper is moving vertically, compare to PART.Y
            X = PART.Y
         END IF
         LOPEN = ((X .LT. XC) .XOR. (PARAMS(CHP_VEL) .GT. 0.))          &
     &             .XOR. LOPENING
C        If counter-rotating chopper, also test absolute values
         IF (SUBTYPE.GE.2 .AND. ABS(X).GT.ABS(XC)) LOPEN = .FALSE.
         IF (LOPEN) THEN
            FLAG = NINT((PART.TOF-.5*(PARAMS(CHP_OPEN) +                &
     &               PARAMS(CHP_CLOSE))) / PARAMS(CHP_PERIOD)) .EQ. 0
         ELSE
C           Didn't make it through this chopper opening
            KSURF = JSURF
```

```
            IF (TESTIN(PART, GEOM, IREG+1, JSURF)) THEN
C              Next region is description of chopper blade material
               IREG = IREG+1
               RETURN
            ELSE
C              Chopper blade is opaque absorber
               EXDIST = 0.
               PART.WT = 0.
            END IF
         END IF
C
      ELSE IF (ITYPE .EQ. 36) THEN
C        Powder sample with Bragg scattering
         IF (TRANSMIT) THEN
C           Save incident particle and wavelength for scattering
            PART_2 = PART
            LAMBDA = HOVERM / SQRT(PART.VX**2 + PART.VY**2 + PART.VZ**2)
C           Transmitted particle has reduced weight, get attenuation terms
            CALL POWDER(PARAMS, LAMBDA, SIN_TH, SIGSCAT, SIGABS, ISEED)
            ALPHA = 100.*(SIGSCAT + SIGABS)
            TRANPROB = EXP(-ALPHA*EXDIST)
            PART.WT = PART.WT * TRANPROB
C           Scattered (or absorbed) particles have the rest of the weight
            PART_2.WT = PART_2.WT * (1. - TRANPROB) *                    &
     &                  SIGSCAT/(SIGSCAT+SIGABS)
         ELSE
C           Prepare for multiple scattering; where was the interaction?
            D = PLEXP(ALPHA, EXDIST, ISEED)
            CALL MOVEX(PART, D)
C           Choose angle from possible Bragg angles
            CALL POWDER(PARAMS, LAMBDA, SIN_TH, SIGSCAT, SIGABS, ISEED)
C           Find new velocity vector
            TWOSINTH = 2.*SIN_TH
            IF (IAND(SUBTYPE,1) .EQ. 0) THEN
C              Random azimuthal angle in 2 pi
               CALL ELSCAT(PART.VX, PART.VY, PART.VZ, TWOSINTH, ISEED)
C              Determine probability of scattering again
               D = PLEXP(ALPHA, 0., ISEED)
            ELSE
C              Limit the azimuthal angle
               CALL ELSCAT2(PART.VX, PART.VY, PART.VZ, TWOSINTH,         &
     &                      PARAMS(PHI_MIN),PARAMS(PHI_MAX),FLAG,ISEED)
               PART.WT = PART.WT * (PARAMS(PHI_MAX) - PARAMS(PHI_MIN))  &
     &                             /TWOPI
C              No multiple scattering in this case
               D = 0.
            END IF
C           Determine probability of scattering again before escaping region
            CALL DTOEX(PART, GEOM, IREG, 0, KSURF, EXDIST)
            DO WHILE (D.LT.EXDIST .AND. D.GT.0.)
               CALL MOVEX(PART, D)
C              Get another Bragg angle (same attenuation length)
               CALL POWDER(PARAMS, LAMBDA, SIN_TH, SIGSCAT, SIGABS,      &
     &                     ISEED)
               IF (RAN(ISEED) .LT. SIGABS/(SIGSCAT+SIGABS)) THEN
C                 Particle has been absorbed
                  PART.WT = 0.
                  D = 0.
               ELSE
```

```
                TWOSINTH = 2.*SIN_TH
                CALL ELSCAT(PART.VX, PART.VY, PART.VZ, TWOSINTH,ISEED)
                CALL DTOEX(PART, GEOM, IREG, 0, KSURF, EXDIST)
                D = PLEXP(ALPHA, 0., ISEED)
             END IF
          END DO
       END IF
C
      ELSE IF (ITYPE .EQ. 43) THEN
C        Detector, 2-dimensional position sensitive
         DET_WT = DET_2D(PART, PARAMS, IX, IY, ISEED)
C
      ELSE IF (ITYPE .EQ. 70) THEN
         CALL TYPE_70(PART, EXDIST, PARAMS, NAME, TRANSMIT, FLAG,       &
     &                PART_2, ISEED)
         RETURN
C
      ELSE IF (ITYPE .EQ. 75) THEN
         CALL TYPE_75(PART, EXDIST, PARAMS, GEOM, IREG, JSURF, KSURF,   &
     &               NAME, TRANSMIT, FLAG, PART_2, DET_WT, IX, IY, ISEED)
C
      END IF
C
C     Move the particle
      IF (EXDIST .GT. 0.) CALL MOVEX(PART, EXDIST)
C
      IF (DET_WT .NE. 0.) THEN
C        Particle was detected, so check detector efficiency
         IF (PARAMS(D_ALPHA_1A) .GT. 0.) THEN
            LAMBDA = HOVERM / SQRT(PART.VX**2 + PART.VY**2 + PART.VZ**2)
            DET_WT = DET_WT*(1. - EXP(-LAMBDA*PARAMS(D_ALPHA_1A)))
         END IF
         PART.WT = PART.WT - DET_WT
      END IF
C
      RETURN
C
C     Need special actions when leaving some regions
C
      ENTRY EXIT_REG(PART, GEOM, IREG, JSURF)
C
      IF (LMULTX) THEN
C        Crossing a surface in a multi-slit (vertical) device
         IF (NEXTRG(PART, GEOM, NREG, JSURF) .EQ. NREG) THEN
C           Still within device, shifting to neighboring slit
            IF (PART.X .GT. 0.) THEN
               D = +1.
            ELSE
               D = -1.
            END IF
            SLIT = SLIT + D
            PART.X = PART.X - D*DELTA
            IF (TAPER .NE. 0.) THEN
               PART.X = PART.X + D*TAPER*(PART.Z - ZENTER)
               COS_TH = 1. - 0.5*TAPER**2
               SIN_TH = D*TAPER*COS_TH
               V = PART.VX
               PART.VX =  COS_TH*V + SIN_TH*PART.VZ
               PART.VZ = -SIN_TH*V + COS_TH*PART.VZ
```

```
            END IF
         ELSE
C           Actually exiting from device, restore X, VX, and VZ
            PART.X = PART.X + SLIT*DELTA
            IF (TAPER .NE. 0.) THEN
C              Tapered slits, exit not at same offset as entrance
               PART.X = PART.X - SLIT*TAPER*(PART.Z - ZENTER)
C              Also need to rotate particle velocity vector
               COS_TH = 1.-0.5*(SLIT*TAPER)**2
               SIN_TH = SLIT*TAPER*COS_TH
               V = PART.VX
               PART.VX = COS_TH*V - SIN_TH*PART.VZ
               PART.VZ = SIN_TH*V + COS_TH*PART.VZ
            END IF
            IF (SIN_PHI .NE. 0.) THEN
C              Element is a bender; rotate by the second half of the angle
               V = PART.VX
               IF (PART.VZ .GT. 0.) THEN
C                 Exiting in proper direction, rotate CCW (if phi > 0.)
                  PART.VX =  COS_PHI*V - SIN_PHI*PART.VZ
                  PART.VZ =  SIN_PHI*V + COS_PHI*PART.VZ
               ELSE
C                 Exiting backwards, rotate CW instead of CCW
                  PART.VX =  COS_PHI*V + SIN_PHI*PART.VZ
                  PART.VZ = -SIN_PHI*V + COS_PHI*PART.VZ
               END IF
            END IF
            LMULTX = .FALSE.
         END IF
C
      END IF
      RETURN
      END
```

Neutron Scattering Instruments

INSTRUMENT SUITES

ICANS XIV
14th Meeting of the International Collaboration on Advanced Neutron Sources
June 14-19, 1998
Starved Rock Lodge, Utica, IL

Neutron Scattering Instruments for the Spallation Neutron Source (SNS)

R. K. Crawford[1], K. W. Herwig[2], and T. Fornek[1]
Argonne, IL 60439 USA
[1]Argonne National Laboratory and the Spallation Neutron Source Project
[2]Oak RidgeNational Laboratory and the Spallation Neutron Source Project

Abstract:

The Spallation Neutron Source (SNS) is a 1 MW pulsed spallation source for neutron scattering planned for construction at Oak Ridge National Laboratory. This facility is being designed as a 5-laboratory collaboration project. This paper addresses the proposed facility layout, the process for selection and construction of neutron scattering instruments at the SNS, the initial planning done on the basis of a reference set of ten instruments, and the plans for research and development (R&D) to support construction of the first ten instruments and to establish the infrastructure to support later development and construction of additional instruments.

Overview of the SNS Facility

The Spallation Neutron Source (SNS) is an accelerator-based facility designed to meet the needs of the neutron scattering community in the United States well into the next century. SNS is a U.S. Department of Energy (DOE) project that is being designed and will be constructed at Oak Ridge National Laboratory by a collaboration including Argonne National Laboratory (ANL), Brookhaven National Laboratory (BNL), Lawrence Berkeley National Laboratory (LBNL), Los Alamos National Laboratory (LANL) and Oak Ridge National Laboratory (ORNL). The functional requirements for the SNS have been set by the scientific community in conjunction with DOE.

In operation, a front-end system and a linac produce and accelerate large currents of H^- ions to 1 GeV. A stripping process is used to inject these ions into a proton accumulator ring, where they are collected and then extracted as very short (<1 μs) intense pulses of protons. These proton pulses bombard a mercury target, producing large quantities of fast neutrons by the spallation process. Two ambient temperature water moderators and two cryogenic liquid hydrogen moderators slow the neutrons from the target to produce beams of thermal and cold neutrons optimized for neutron scattering experiments. This facility is fully described in a Conceptual Design Report.[1] Figure 1 shows the proposed facility configuration. LBNL is responsible for the front end, LANL for the linac, BNL for the accumulator ring, ORNL for the target station, and ANL for the neutron scattering instruments.

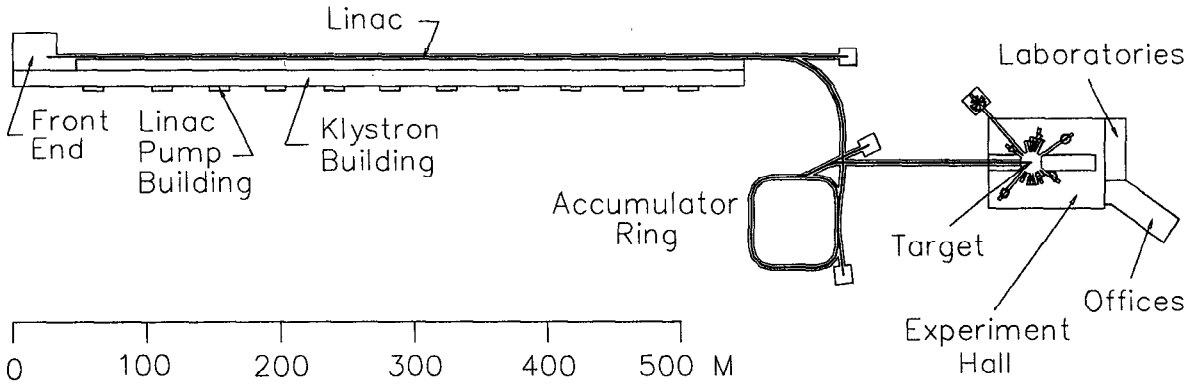

Figure 1. Proposed layout of the SNS facility.

* Work supported in part by the U. S. Department of Energy, BES, contract No. W-31-109-ENG-38.

SNS will initially operate at 1 MW and 60 Hz with one target station having 18 beam ports. The construction project provides funding to design and construct ten instruments for neutron scattering experiments. Upgrade paths have been identified for providing additional instruments, a second target station operating at 10-20 Hz, and substantial increases in power. The eventual configuration with two target stations will provide at least 36 fully-instrumented neutron beams, and ultimate accelerator power of at least 4 MW. This upgrade process is designed to allow SNS to grow as the needs of the scientific community expand.

Construction of the SNS facility will require 7 years, starting in October, 1998. Total project cost is $1,333 M, of which $59 M is for construction of the ten neutron scattering instruments and $24 M is for instrument R&D.

Selection, Design, Construction, and Installation of Instruments

As noted above, the SNS construction project contains funding for design and construction of the first ten neutron scattering instruments. These will be selected on the basis of input from the user community, and will span the types of science anticipated to be most important for this facility. These ten instruments will be installed and ready for commissioning at the time the source turns on late in 2005. It is expected that additional instruments will be installed soon after that.

The broad user community will be involved in the selection, design, construction, and operation of the neutron scattering instruments. Their involvement in this activity has already begun. A workshop held in October 1996 provided user recommendations for more than 30 neutron scattering instruments to support the different types of science. A second user workshop is scheduled for Fall, 1998. This workshop will lead to the formation of Instrument Advisory Teams, made up of scientists with interests in specific types of instruments. These teams will formulate concepts for the different instruments. An Instrument Oversight Committee of external scientists will then advise SNS management about which of these concepts should be selected for design and construction.

Argonne National Laboratory, working with scientists from Oak Ridge National Laboratory, is responsible for the design, construction, and installation of the first ten neutron scattering instruments. The Instrument Advisory Teams will play a major role in this process as well. Each instrument will have an associated ORNL scientist responsible for directing the design and construction effort. These instrument scientists are currently being hired. They will be stationed at ANL and work with experienced ANL scientists during the design and construction phases, and will then move to ORNL to supervise installation of the instruments. When the facility is operational, these scientists will be the "instrument scientists" responsible for the operation of these ten instruments for the user community. This process will ensure that the facility will have a core of trained scientists to enhance its effectiveness as a user facility.

The Reference Set of Instruments

The recommendations of the first User Workshop have been distilled to define a reference set of ten instruments to be used for planning purposes, and reference design concepts have been prepared for this set. Table 1 lists this reference set. Each instrument selected is one of the highest priority instruments specified at the workshop and is capable of effective operation at the 60-Hz target station. Instruments in the reference set span a very wide and representative range of science and a representative range of instrument types and costs.

A layout of this reference set of instruments on the neutron beams was developed to provide a realistic optimization of the configuration of the experiment hall and to define in detail a suitable interface between realistic instruments and the target station, including shielded locations for choppers. Figure 2 shows the optimized layout of this reference set of instruments in the experiment hall based on these reference instrument conceptual designs. In this layout each instrument views its appropriate moderator and the high-resolution powder diffractometers view their respective moderators at normal incidence in order to provide the best time-of-flight resolution. Side access to instruments is preserved wherever possible, with as many as practical of the instruments lying under crane coverage within the experiment hall. These reference instruments have also been subjected to a careful cost and schedule analysis to make sure the planned budget and schedule for the instruments is realistic.

Table 1. Reference Set of Instruments

Label	Description	Resolution (fwhm)	Incident Path (m)
POW3	General purpose powder diffractometer	$\Delta d/d = 0.0013$	30
POW6	High-resolution engineering powder diffractometer	$\Delta d/d = 0.0007$	60
POW7	Glasses/liquids diffractometer	$\Delta Q/Q = 0.007\text{-}0.1$	9
SCD1	General purpose single crystal diffractometer	$\Delta d/d = 0.005$	12
SANS2	General/lower-Q high resolution SANS	$Q_{min} = 0.001$ Å	17
REF1	Horizontal-surface reflectometer	$\Delta q/q = 0.02\text{-}0.1$	12
INEL1	Microvolt spectrometer	$\Delta E = 5$ μeV	31
INEL2	100-microvolt spectrometer	$\Delta E = 70$ μeV	12
INEL4	Wide-angle chopper spectrometer	$\Delta E/E = 0.01$	18
INEL5	Large-solid-angle single-crystal spectrometer	$\Delta E/E = 0.01$	15

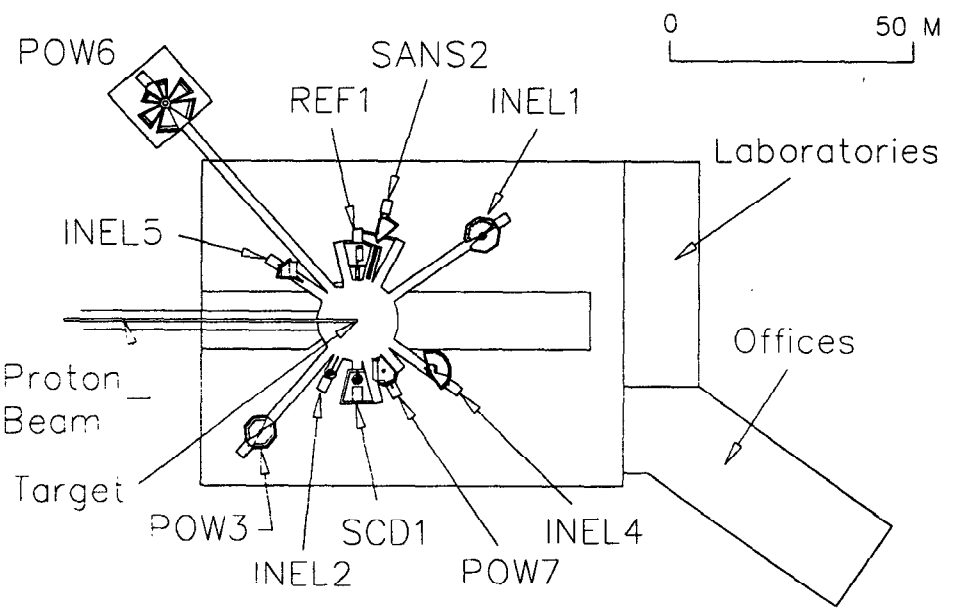

Figure 2. Layout of the reference set of instruments in the SNS experiment hall.

Research and Development

The $24 M earmarked for instrument-related R&D activities is intended not only to support the design and construction of the first ten instruments, but also to enhance the infrastructure for the development of future instruments. This R&D effort is divided into the 9 separate categories described briefly below.

Instrument Specification

This task largely concerns the development of concepts for a variety of neutron scattering instruments. Instrument Advisory Teams will be formed to provide extensive user input into this process. Instruments in use at

existing pulsed neutron facilities, particularly ISIS, will be studied and used as starting points. Other documentation will also be utilized such as the IPNS upgrade study and various European Spallation Source studies. Coordination will also take place with the LANSCE instrument upgrade. Prototyping of some of these instrument concepts will be carried out at IPNS and LANSCE, and possibly at other facilities. This work is intended to provide the basis for selecting the ten instruments to be built as part of the construction project. Some activity in this task will continue to provide the basis for design choices for specific components for the selected instruments.

Design Tool Development

This task involves the development of software tools for design of neutron scattering instruments. Primary emphasis will be placed on the development of Monte Carlo codes for simulating the performance of the different kinds of instruments. These codes will be developed as a set of modules for individual neutron optical components, so that these modules can then be linked together to simulate an entire instrument. In this way a small number of optical component code modules can provide the basis for a large variety of instruments simply by changing the linking of the modules. SNS will work with the international community to set standards for such modules. This will enable modules developed at various other facilities tobe readily used, so that not all of the necessary code need be supplied by SNS. This Monte Carlo software suite will be used in the instrument evaluation process and in the optimization of the instruments. Development of this software will continue to the point where the software is useful in diagnosing problems during the instrument commissioning phase, and in diagnosing problems with specific experiments once the instruments are operational.

Concept Evaluation and Instrument Selection

The Monte Carlo simulation codes and other design tools will be used to model the most promising of the instrument concepts. Full simulations based on these instrument concepts will be used to evaluate the relative performance of the different concepts. This information will serve as input for the process of selecting the ten instruments to be constructed. This process will involve the Instrument Advisory Teams, the Instrument Oversight Committee, and SNS management.

Data Acquisition System Development

The heart of any time-of-flight neutron scattering instrument, such as all of the instruments at SNS, is the system that collects the pulses from the detectors and histograms these pulses in a manner that is meaningful to the instrument user. Data on the SNS instruments will be generated in a multi-parameter form. In all cases the position and the time-of-flight of the detected neutron are important, and in some cases other parameters such as the chopper phase or state of a time-varying field on the sample will also be important. Data rates will be very high on many of the SNS neutron scattering instruments, and all of these instruments will collect and histogram many channels of this multi-parameter data. A new generation of data acquisition system must be developed to meet these requirements. Development of this system will involve construction and testing of prototype systems using realistic conditions on existing pulsed neutron source instruments at IPNS and LANSCE.

Neutron Detector Development

Instruments at pulsed sources can utilize many detectors to simultaneously acquire data at different momentum positions. Standard ^{3}He detectors are generally satisfactory, but are very expensive. In some cases desired data accumulation rates and the need for very high spatial resolution are not possible with existing technology. Scintillation detectors look promising, but still have some problems. Recent work indicates that solid state detectors may also be useful for some applications. Development work will be done to improve the performance of scintillation detectors, to investigate the applicability of solid state detectors, and to produce position sensitive detectors with a high spatial sensitivity and capable of a high count rate. Activities likely to reduce the cost of neutron detectors will also be supported. A SNS Detector Advisory Committee composed of experts external to the project will provide advice concerning choices of technology and vendors for detector R&D. This committee has now been formed, and Table 2 shows the current membership.

Table 2. Current members of the SNS Detector Advisory Committee

Steve Naday	ANL	Chair		
Veljko Radeka	BNL		Nobuo Niimura	JAERI
Jon Kapustinsky	LANL		Carel van Eijk	Delft
Jacques Millaud	LBNL		Jim Schelten	Juelich
Michael Kreisler	LLNL		Peter Geltenbort	ILL
Don Hutchinson	ORNL		Nigel Rhodes	RAL

Neutron Chopper Development

Almost all of the neutron scattering instruments will require neutron choppers of various types. T_0 choppers are used to remove the burst of fast neutrons associated with the prompt pulse, bandwidth choppers restrict the wavelength range of neutrons allowed to reach the detectors, and E_0 choppers are used to select the incident neutron energy in chopper spectrometers. T_0 choppers that can fit within the space in the SNS chopper caves must be developed. T_0 and bandwidth choppers must be developed that can minimize the background in the instruments even when some of the pulses are being eliminated. High-speed E_0 choppers must be developed to provide the best timing resolution for chopper spectrometers. Suitable electronic systems for controlling these choppers must also be developed.

Sample Environment Development

The SNS will make very rapid data collection possible for some experiments. With present equipment it may take longer to change the sample environment (for instance the temperature) than to accumulate the data. In order not to waste neutrons, equipment will have to be developed to make rapid and accurate changes in the sample environment. Additional capabilities for affecting the sample environment will also be developed to enhance the scientific effectiveness of the neutron scattering instruments. These capabilities include specialized cryostats, furnaces, magnets, high pressure cells, etc.

Neutron Optical Component Development

Advances in optics can greatly increase the counting rates for some experiments. Long neutron guides will be required for several of the instruments and development in supermirror technology can reduce their cost and improve their performance. Focusing optics for neutrons, including elliptical mirrors with supermirror or stable isotope coatings and neutron lenses of various types will also be developed to enhance the neutron flux on the samples where practical. Polarized neutrons provide many opportunities to extract additional information from the neutron scattering samples. Polarizers will have to be developed that will polarize a wide energy spectra of neutrons. Transmission polarizers that rely on nuclear orientation would seem to be the best method, but present equipment lacks the desired polarization or transmission. A program will be undertaken to improve present day polarizers. Since good polarizers are needed at all pulsed sources joint programs with other Laboratories will established. Other equipment for manipulating the polarized neutrons will be developed as needed. A SNS Optical Component Advisory Committee composed of experts external to the project will provide advice concerning choices of technology and vendors for optical component R&D. This committee will be formed in Summer, 1998.

Data Analysis and Visualization Software

The SNS instrumentation will acquire data simultaneously at many different momentum and/or energy transfers. In order to proceed optimally with an experiment, data will have to be examined as the experiment is in progress. Some of the spectrometers will acquire more than 10^6 data points each run and the run times could be fairly short (minutes or hours). Data from the runs have to be visualized in an effective way to use the beam time properly. In some cases the data will have to be converted to the parameters of interest such as a bond length or an energy transfer along a given crystal direction. Computer programs will be developed to enable rapid visualization of raw or partially reduced data. Programs will also be required for full reduction and analysis of the data after it is collected. In some cases totally new approaches will have to be developed to make efficient use of all the information in the data sets.

Status and Schedule

The President's budget for FY99 includes funding for a line item construction start for the SNS project. This budget is now proceeding through Congress, and if this item is approved, the construction project will start in October, 1998. The Instrument Advisory Teams and the Instrument Oversight Committee will be formed in late 1998. Plans then call for all ten of the instruments funded by the project to be selected by October, 2000, with some instruments being selected prior to that time. Instrument construction and installation at the SNS facility in Oak Ridge will be complete by October, 2005, which marks the end of the construction project and the beginning of facility operation and instrument commissioning.

Summary

In summary, the SNS short-pulse spallation source will provide a significant increase in the neutron scattering capabilities in the U.S. This facility is planned to be available late in 2005, and the user community is encouraged to begin thinking now about the types of instrumentation desired for this facility. A substantial R&D program is planned to complement the instrument construction effort and to enhance the infrastructure for the development of future instruments. This R&D activity should also benefit other neutron scattering facilities worldwide.

References:

[1] The SNS Collaboration, Spallation Neutron Source Conceptual Design Report, Oak Ridge National Laboratory report SNS/CDR-2 (Oak Ridge National Laboratory, Oak Ridge, Tennessee, 1997).

Neutron Scattering Instruments

LIQUID TARGET SYSTEMS

ICANS XIV
14th Meeting of the International Collaboration on Advanced Neutron Sources,
Starved Rock Lodge, Utica, Ill, USA
June 14-19, 1998

Heat Deposition in Mercury by 24 GeV Protons

G S. Bauer, H. Spitzer, G. von Holzen and L. Ni and J. Hastings*

Paul Scherrer Institut
CH-5232 Villigen-PSI, Switzerland

* Brookhaven National Laboratory
Upton, N. Y. 11973, USA

Abstract

The spatial distribution of the power deposited in a Mercury target by 24 GeV protons was measured in order to be able to validate computer codes used in liquid metal target design by comparing computed stress levels on a liquid metal target container to experimental data. After correcting for the measured deviation of the beam position from the target axis, the measured integral power deposition was found to be 57% of the total beam power, in good agreement with theoretical expectations. This gives confidence in the measured spatial distribution which was found to be rather narrower in axial direction than originally anticipated. The results of this experiment are an important input information for the prediction of pressure waves that arise as a consequence of pulsed power input at high power density.

1. Introduction

One important goal of the ASTE (AGS Spallation Target Experiment) Collaboration [1] is to verify experimentally the predictions with respect to power deposition and pressure wave buildup resulting from a short pulse of high energy content (see e.g. [2], [3]). The present report is on the first experimental run in this collaboration, carried out at the Alternating Gradient Synchrotorn (AGS) in Brookhaven National Laboratory in June 1997. Its purpose is to show the viability of the technique selected and to provide a basis for further theoretical and experimental investigations.

2. Parameterization of the Power Distribution in a Spallation Target

The axial distribution of the power deposition by energetic particles in condensed matter (and hence the temperature distribution after a short pulse) has been found to be described rather well by a parameterization of the form [4]:

$$P(z) = P_0 (1-\exp(-(z-z_0)/\lambda_b))*\exp(-z/\lambda_a). \quad (1)$$

Keywords: Mercury, Power deposition, temperature distribution, pressure waves

The following meaning can be attributed to the individual parameters:
λ_a - attenuation mean free path, λ_b - buildup mean free path, z_0 - extrapolation length (giving the distance in front of the target where the analytic curve crosses zero), P_0 - scaling parameter which must be chosen in the right magnitude and units to give the correct integral of the curve.

Eq. (1) can be used to describe the lateral integral or the maximum of the power deposition along the axis, with properly selected parameters. In order to take into account the radial distribution, equ. (1) must be multiplied with the normalized radial distribution function W(r). The most commonly used analytical expressions for the beam profile are a parabolic distribution or a Gaussian. In this case:

$$W(r) = 2/(\pi r_s^2)*(1-(r/r_s)^2) \quad (2a)$$

for a parabolic distribution of base width r_s or

$$W(r) = 1/(2\pi\sigma^2)*\exp(-r^2/2\sigma^2) \quad (2b)$$

for a Gaussian with standard deviation σ.

(If the beam profile has elliptic rather than axial symmetry, eqs. (2a) and (2b) must be modified accordingly.) Most of the theoretical calculations have been performed [2], [3] for these distributions. In view of the situation found with the present experiments, a triangular distribution is also considered which, in the general case, is described by an elliptical cone. The normalized radial distribution function W(x,y) in the target geometry coordinate system (x,y) then reads:

$$W(x,y) = 1-\{ [(x-x_0)/A]^2 + [(y-y_0)/B]^2 \}^{0.5} \quad (2c)$$

where (x_0,y_0) is the center point of the elliptic cross-section of the proton beam with a semi-major axis A and a semi-minor axis B.

In practice the beam will widen as it penetrates into the material. This can be taken into account by allowing r_s, σ, or A and B to become functions of z:

$r_s = r_s(z)$ (3a) $\sigma = \sigma(z)$ (3b) $A = A(z), B = B(z)$ (3c)

3. Experiment

A 20 cm diameter, 1.2 m long cylindrical stainless steel container with a hemispherical front cap filled with Mercury [5] was used as a spallation target in the experiment. In order to measure the spatial power distribution in the target, an array of 32 thermocouples was placed in the lower half-midplane of the cylinder. The 1.5 mm thick encapsulated Chromel - Alumel thermocouples (type K) were thinned down to 0.5 mm over the last 15 mm in order to improve their time response. The positions of the thermocouple tips inside the target are shown in Fig. 1. They were chosen on the basis of an assumed parabolic radial power distribution with a base width of r_s = 5 cm.

A 32 channel Hewlett Packard fast data logging system was used to scan the thermocouple readings every 15 ms over a period of 30 sec and to record the readings on disk. The length of the cables between the thermocouples and the data logger was 50 m. The noise corresponded to

roughly 0.5 K, in agreement with the specifications given by the manufacturer. Data recording was triggered from a pulse derived from a beam monitor.

For the beam intensity and profile measurement, an Al foil, 20x20 cm^2, 25 μm thick was placed on the beam axis in front of the target near the exit of the beam pipe by the JAERI group[6].

4. Experimental results

4.1 Proton beam profile

The distribution of the proton induced ^{22}Na and ^{7}Be activity was determined by placing the foil on an image plate and integrating the measured radioactivity over pixel sizes of 2x2 mm^2. Fig. 2 shows the resulting intensity distribution for the Al foil. The coordinate system chosen is a right handed system with z along the direction of the proton beam and y in the vertical direction. It can be seen that the beam cross section is roughly elliptic. The beam center is not located in the target coordinate center. The coordinates of the beam axis are $x=x_0$, $y=y_0$. A beam profile with fitted parameters is schematically shown in Fig. 3. The parameters used are (cf section 3.4)

$$(x_0, y_0) = (-0.5\ \text{cm}, -1.0\ \text{cm}) \qquad A = 8.5\ \text{cm} \qquad B = 6\ \text{cm} \tag{4}$$

4.2 Temperature data evaluation procedure

Useful thermal data could only be collected during run 22 in which, according to the information obtained from the AGS control room, two bunches of 24 GeV protons with $4*10^{12}$ particles per bunch were injected into the target. All other runs were of significantly lower power and did not produce useful signals on the thermocouples.

Examples of the thermocouple recordings over the full period of 30 seconds are shown in Fig. 4 for the thermocouples 1 and 2 (located at distances z of 30 and 80 mm from the apex of the hemispherical cap on the axis of the target). Polynomial trend lines were fitted to the measured data using the corresponding feature of EXCEL. Such trend lines (without the original data, for clarity) are also shown for the thermocouples Nr. 7, 20 and 28 for illustration. The initial rise of these trend lines is an artifact resulting from the first (low) data points and should not be taken seriously.

A few striking features are immediately obvious from Fig. 4: The rapid power dissipation over only 10 seconds and a bump for thermocouple Nr.1 after 15 seconds. These will be discussed below in section 3.3.

For the quantitative evaluation of the temperature distribution in the whole target, polynomial fits were applied to the readings of all thermocouples for the first 5 seconds after the pulse. Examples are shown in Fig. 5. The values of the fitted curves at t = 500 ms were taken as representing the maximum temperatures reached and were plotted as a function of position of the thermocouples in Fig.6. The lines are guides to the eye only.

4.3 Temperature dissipation in the target

After the proton pulse the temperature appears to stay more or less constant for almost 1 sec and then starts to drop rapidly. This drop must be attributed to the onset of convection because it cannot be explained in terms of the thermal conductivity of Hg. Calculations of the heat dissipation by conduction alone give a much slower temperature decrease (Fig 7), indicating that it would take minutes for the temperature to return to the original value. By contrast, the measured temperatures are back to their equilibrium values (22.4 °C in Figs. 4 and 5) within less than 25 seconds. This clearly indicates the importance of convection in the system.

The other prominent feature in Fig. 4 is the temperature rise for TC Nr. 1 that starts some 13 seconds after the pulse. Although this still needs to be checked in detail, one possible explanation might be that this is a consequence of the convective motion in combination with the hemispherical shape of the target front cap: Warm liquid rising to the top might have been circulating along the wall of the front cap to replace the liquid moving up from the hot region and might have reached the front most thermocouple before fully cooling down. If this effect is reproduced in future measurements, we will perform suitably detailed calculations to investigate it more closely.

4.4 Lateral distribution of the power deposition

Since the beam maximum was not on the target axis, the maximum of the temperature distribution was not sensed by the thermocouples. The following procedure was adopted to determine the fraction of the total power sensed by the thermocouples from the measured beam distribution:

An indication to the direction of the displacement can be obtained from the neutron leakage distribution measured on four positions of the target periphery [7], albeit on a different 24 GeV run, as shown in Fig. 8. Since the top left detectors recorded the highest intensity, it seems likely that this was the direction of the displacement of the beam axis relative to the target axis. In order to verify this, the measured beam intensity distributions along $x = 0$ and $y = 0$ were plotted in Figs 9a and 9b as a function of position (top scales) and were compared to the temperatures recorded for the thermocouples of the first row (at $z = 80$ mm). Since no thermocouples closer to the beam monitor foil were available, the readings at $z = 80$ mm were taken as representing the temperature measurement for $x = 0$, $y > 0$, $z = 0$. The same thermocouple readings are plotted in all four symmetry planes in order to facilitate the comparison with the beam profile data. Clearly, there is good correspondence of the temperature readings <u>only</u> with one curve, which must, therefore, represent the lower half plane ($x = 0$, $y > 0$). This confirms that the beam profile was displaced to the top left as shown in Fig. 3, where the projection of the plane of the thermocouples is also indicated. From this the assignment of the positive and negative signs to the half axes in x and y follows unambiguously as shown in the bottom scales of Figs. 9a and b. This assignment is also in agreement with the measured neutron distribution (Fig. 3)

The beam profile can be approximated fairly well by an elliptical cone with its peak at (x_0,y_0). This cone was used to fix the parameters given in section 3.1 for an analytical approximation to the beam profile. The triangle shaped intersection curves with the planes $\{x=x_0, y\}$ respectively

$\{x, y=y_0\}$ (symmetry planes of the beam coordinate system) are shown in Figs. 9a and 9b by the symbols. The intersections of the cones with the respective symmetry planes of the target coordinate system (hyperbolae) are shown by the solid lines. These curves are to be compared to the measured beam intensities along the axes $x = 0$ and $y = 0$. Although, in this representation, the fit curves seem to more or less envelope the measured data, the beam integrals under the measured values and the cone used for the fit agree to within 0.13%.

4.5 Axial distribution of the temperature rise

In Fig. 10 the squares show the axial distribution obtained from collecting the maximum thermocouple readings along the axis of the target, together with a fit according to equ.1 for T instead of P (solid line)

The parameters of the fit for $x = 0$, $y = 0$ are:

Parameter	λ_a	λ_b	z_0	T_0	
Fit to experiment	18 cm	8.5 cm	-1.2 cm	7.9 °C	(5)

Since the measured distribution was not along the beam axis but along $x = 0$, $y = 0$ (projection plane in Fig. 3), the temperatures on the beam axis were obtained by extrapolation of the measured values to $x = x_0$, $y = y_0$: The dashed line represents this extrapolation to the beam axis, as discussed below.

4.6 Axial distribution of the lateral power integral.

In order to estimate the total power dissipation in the target, a spatial distribution of the temperature field had to be constructed from the measured values. This requires extrapolation to regions downstream of the volume in which thermocouples were located, using the values of the measured minor semi axes at the positions available. The latter are plotted in Fig. 11. The uncertainty in these data rises with increasing z due to the low temperature rise measured. In particular, the value at $z = 48$ cm should not be taken seriously and has been left out of Fig 11. The values up to $z = 38$ cm do not warrant anything but a linear fit, although, from a physics point of view, a higher order polynomial would be more appropriate. Therefore, as a lower limit to the actual beam spreading in the target, a linear relation can be used to describe the increase of B(z) as a function of z. The relation

$$B_{l,m} = B + y_0 = 4.512+0.061*z \text{ [cm]} \tag{6a}$$

shown by the thin line in Fig. 11 was fit to the experimental data.

As a probably more realistic description, it is also possible to match the second order relation

$$B_{p,m} = B + y_0 = 4.9+0.0015*z^2 [\text{ cm }] \quad (6b)$$

to the experimental points, as shown by the heavy solid line in Fig. 11.

Inserting the value of -1 cm found for y_0 yields:

$$B_l(z) = 5.512 + 0.061*z \text{ [cm]} \quad (7a) \qquad \text{or } B_p(z) = 5.9 + 0.0015\, z^2 \text{ [cm]} \quad (7b)$$

Since no experimental data were available for the horizontal mid-plane, the corresponding relations for the semi-major axis were derived, assuming the ratio A(z)/B(z) to remain the same as for z = 0 cm, i.e. in the proton beam, throughout the target. This yields:

$$A_l(z) = 7.80867 + 0.08642*z \text{ [cm]} \quad (8a) \qquad \text{or } A_p(z) = 8.3583 + 0.002125*z^2 \text{ [cm]} \quad (8b)$$

Using the parabolic extrapolation, the full representation of the temperature distribution becomes

$$T(x,y,z) = 9.6*\exp(-z/18)*[1-\exp(-(z+1.2)/8.5)]*(1-\text{sqrt}\{[(x-x_0)/A(z)]^2 + [(y-y_0)/B(z)]^2\}) \quad (9)$$

with

$A(z) = 8{,}36+0.0021*z^2$ $\qquad B(z) = 5.9+0.0015*z^2$ $\qquad x_0 = -1.0,$ $\qquad y_0 = -0.5$

which, for x = 0, y = 0 represents the measured data (solid line) and for $x = x_0$, $y = y_0$ yields the dashed curve in Fig. 10.

From this it follows that the maximum temperature rise in the target was 4.08°C, corresponding to a peak power density of 7.66 J/cm^3 (using a value of 0.139 J/gK for the specific heat capacity and 13.52 g/cm^3 for the density of mercury)

The corresponding power density distributions around the beam axis at ($x = x_0$, $y = y_0$) in the y,z and x,z planes respectively are plotted in Figs. 12a and b.

Numeric integration over the whole target volume of the power distribution determined in this way yields the total power deposition as listed in Table 1. The values per proton are based on $8*10^{12}$ p/pulse.

Table 1 *Results for the energy deposition in the Mercury target for 24 GeV protons*

Radial extrapolation	Total energy per pulse	Total energy per proton	% of beam power
linear	16.7 kJ	13 GeV	54.4
parabolic	18.7kJ	14.6 GeV	60.9

5. Discussion and Conclusions

In summary, the overall spatial dependence of the power density (J/cm^3) was found to be reasonably well described by the relations

$$p(x,y,z) = P(z)*(1-\{ [(x-x_0)/A]^2 + [(y-y_0)/B]^2 \}^{0.5}) \quad (10a)$$

with P(z) being the power deposited along the center line perpendicular to the elliptic beam at (x_0, y_0):

$$P(z) = P_0 \{1-\exp(-(z+1,2)/8,5)\}*\exp(-z/18) \quad (10b)$$

and with

$$A_p(z) = 8.3583 + 0.002125*z^2 \text{ [cm]} \quad (10c)$$

and

$$B_p(z) = 5.9 + 0.0015*z^2 \text{ [cm]} \quad (10d)$$

The parameter P_0 was determined as 18.05 for 24 GeV protons on Mercury.

The fact that, while the analytical expression for the beam profile used matches the measured integral to within 0.13% (section 3.4), but more or less envelopes the measured data in the main peak area means that the total power deposition is probably represented correctly, but the peak power density is somewhat overestimated. In terms of using this distribution for the stress wave calculations this means that the results will be on the high, i.e, conservative side.

The power integral for the parabolic extrapolation of A(z) and B(z) yields a total of 18.7 kJ, or 60.9% of the total beam energy which is in the same range as those usually found at lower beam energies.
In view of the large uncertainty associated with several of the input data, no attempt was made to establish the confidence level of the results obtained. Nevertheless, it is comforting to see that the data lie well within what is also found at lower proton energies. Since the neutron source distribution is intimately connected with the power density distribution, this shows that, if available, even 24 GeV protons are likely to make a decent spallation neutron source.

In any case, this preliminary experiment clearly showed that a set of thermocouples can be used to determine the power deposition in the Mercury target at the pulse levels available at the AGS. It also became obvious, how important information on the beam profile and position is, in order to be able to evaluate the data properly. Although the Al-foil technique seems to have worked well in the present situation, a second method (wire scanner, giving digital readings directly) as foreseen for future runs will be of great value. Also, the possibility of steering the beam on the target and of measuring with more precision the total number of protons actually hitting the target will be indispensable in determining the confidence level of the experimental results.

While calculations on the stress levels expected on the basis of the current power deposition are in progress, it can be anticipated that the data obtained from future measurements will form a better

basis to compare measured strain data with calculated stress levels and to provide valuable input for the nuclear and CFD-design of the targets and heat removal systems of future spallation neutron sources. Measurements at lower beam energies and more than two bunches per pulse seem, therefore, highly desirable.

6. Acknowledgment

This work was carried out within the ASTE collaboration. The authors are grateful to the operations team of the AGS accelerator for their efforts and cooperation in providing the required proton beam in the experimental line used and also to their colleagues within the collaboration for their help and for sharing information needed to carry out the evaluation of the measured data. The work at Brookhaven National Laboratory was supported by the U. S., Department of Energy under Contract DE-AC02-98-CH10886 with Brookhaven Science Associates.

7. References

[1]G.S. Bauer, J. Hastings and N. Watanabe " Opportunities and Goals of a Spallation Target Test Experiment at the AGS in Brookhaven -The ASTE-Collaboration " in preparation.

[2]K. Skala and G.S. Bauer, "On the Pressure Wave Problem in Liquid Metal Targets for Pulsed Spallation Neutron Sources" Proc. ICANS XIII, PSI-Proceedings 95-02 (1995) pp 559-576

[3]L. Ni and G.S. Bauer "Dynamic Stress of a Liquid Metal Target Container Under Pulsed Heating", submitted for publication to ASME Journal of Pressure Vessel Technology.

[4]G.S. Bauer, H. Sebening, J.-E. Vetter and H. Willax (eds) "Realisierungsstudie zur Spallations-Neutronenquelle" Vol. 1, Report Jül-Spez-113 and KfK 3175 p.75

[5]G:S: Bauer, H. Conrad, P. Martinez and H. Stechemesser, " A Target-Moderaror -Reflcetor System for Spallation Target Test Experiments with Liquid Mercury at the AGS in Brookhaven " in preparation

[6]The JAERI Team, "Measurement of Proton Beam Profile for AGS Target Experiment", Report presented by H. Nakashima, 2nd General ASTE Planning Meeting, Paris, Sept. 25 and 26,1997

[7] The JAERI Neutronics Measurement Group, "Measurement of Reaction Rate Distribution of Activation Detectors on Mercury Target Bombarded with Protons of 1.5, 7 and 24 GeV" Report presented by H. Takada, 2nd General ASTE Planning Meeting, Paris, Sept. 25 and 26,1997

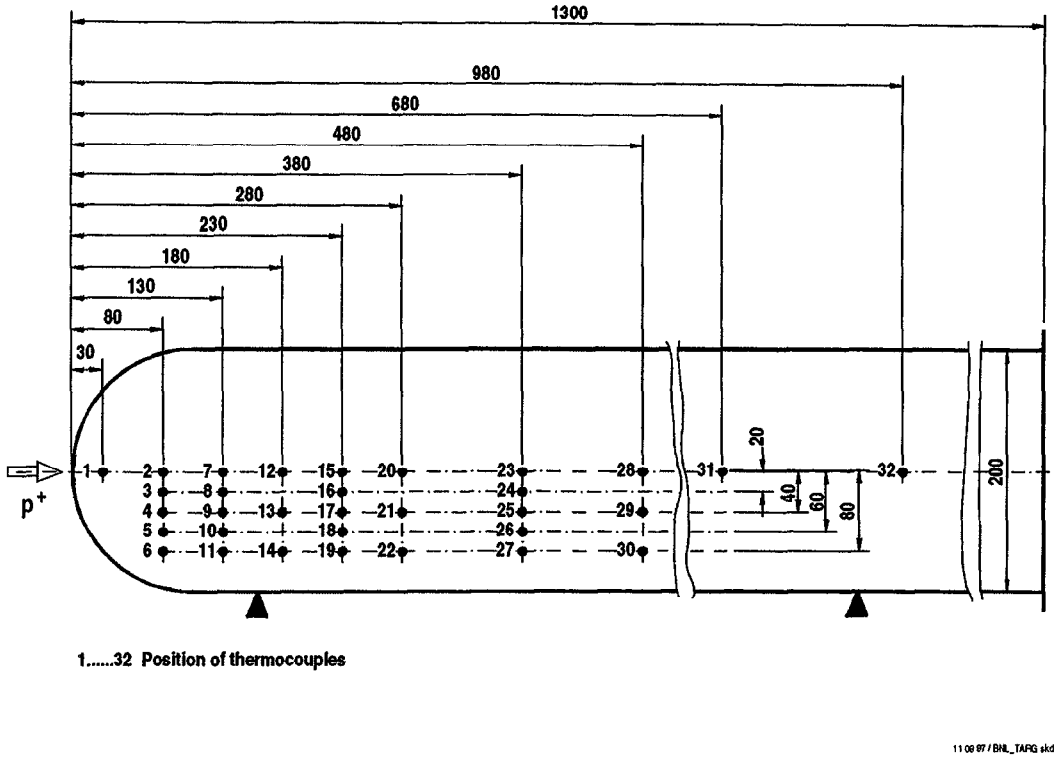

Fig. 1 Positions of the 32 thermocouples in the lower half of the mid-plane inside the target

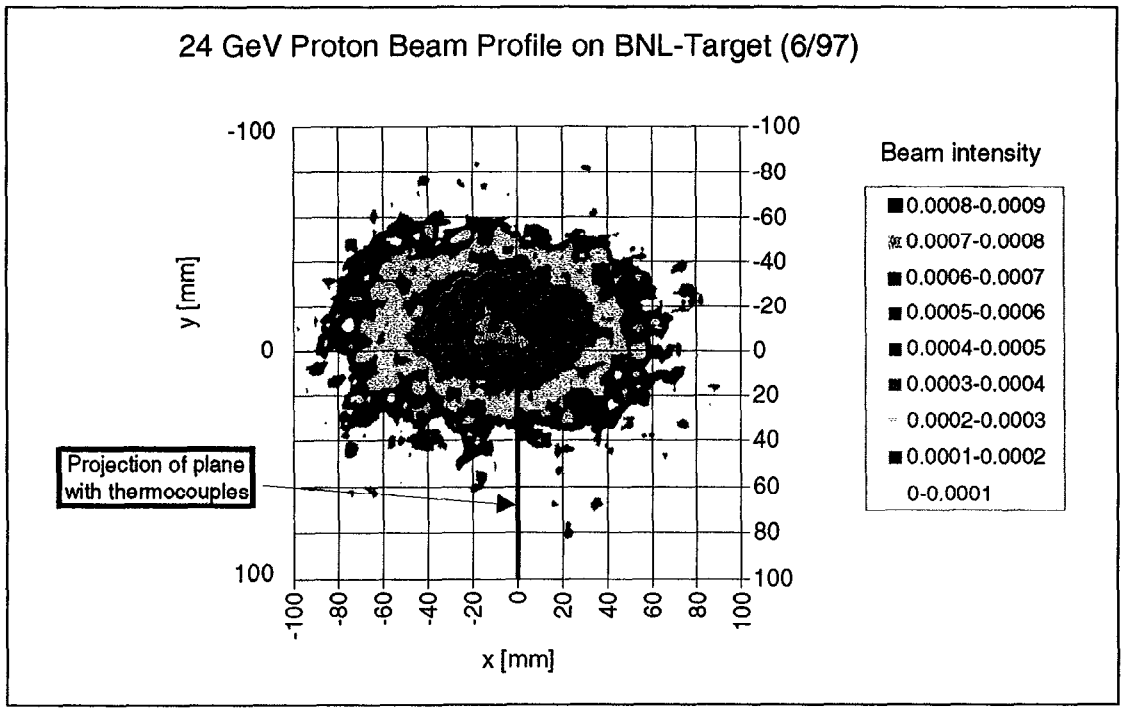

Fig. 2 Measured proton beam profile on the Al foil

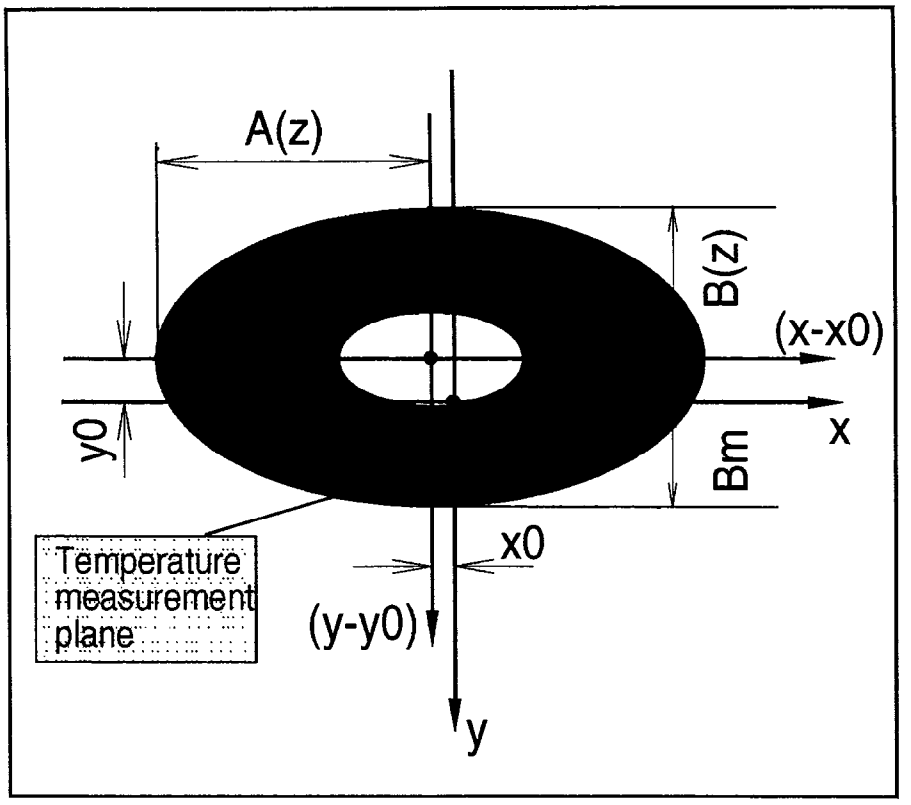

Fig. 3 Nomenclature used for the beam profile

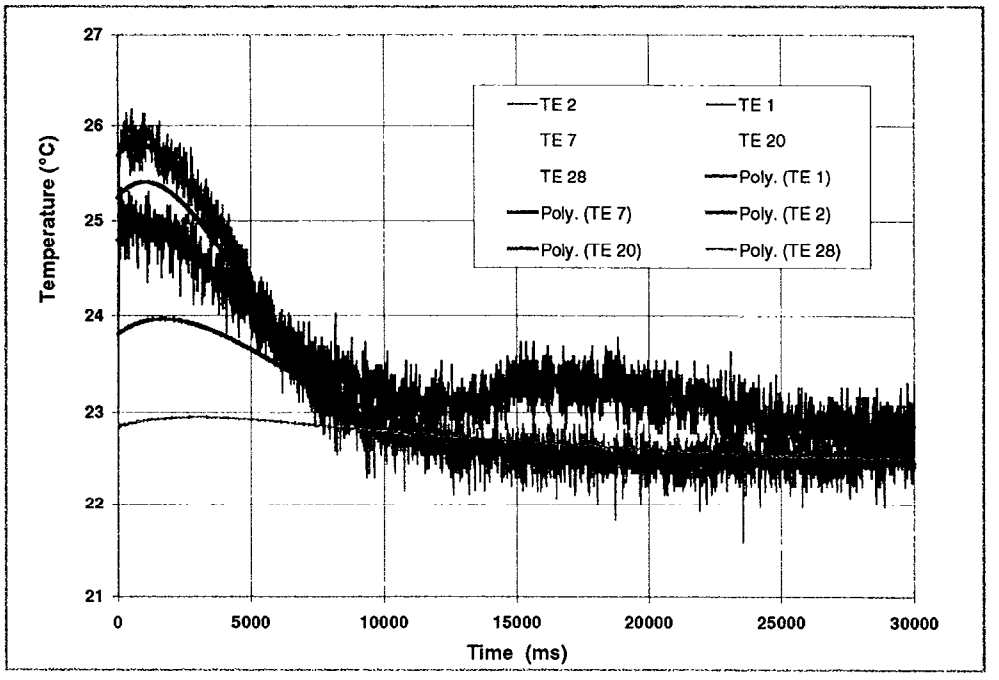

Fig. 4 30 sec temperature evolution for selected on-axis thermocouples

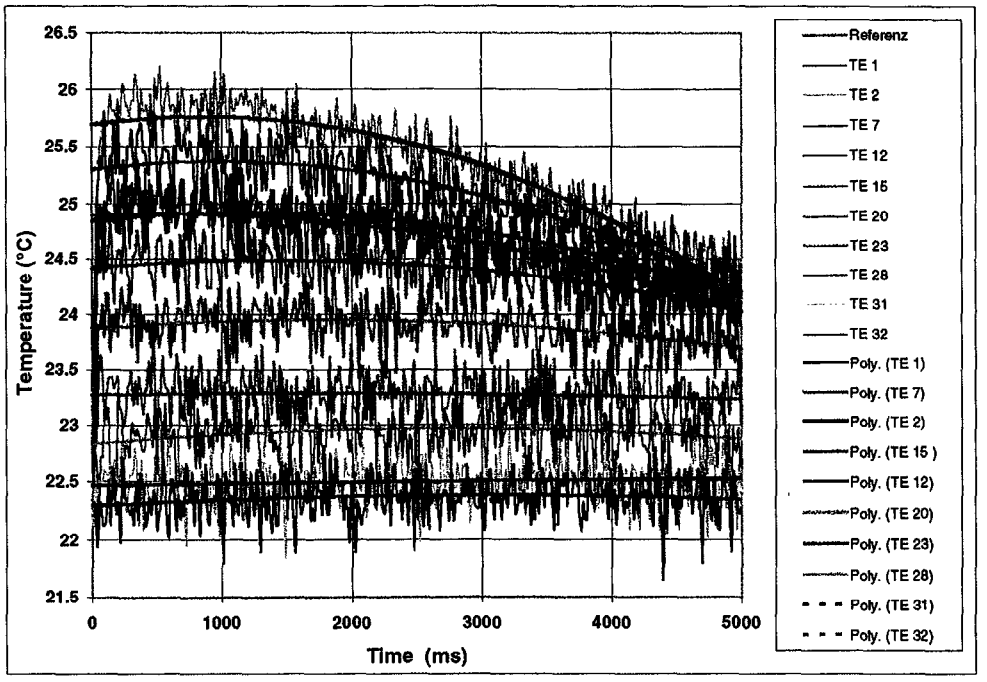

Fig. 5 Temperature histories of the thermocouples for the first 5 seconds

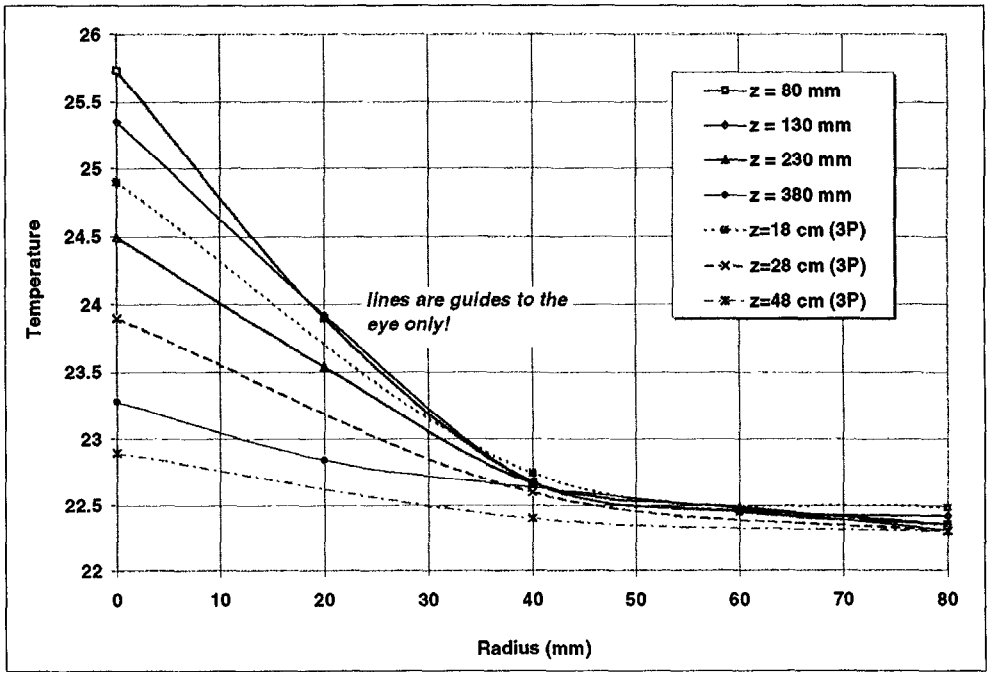

Fig. 6 Radial temperature distribution at various distances z into the target

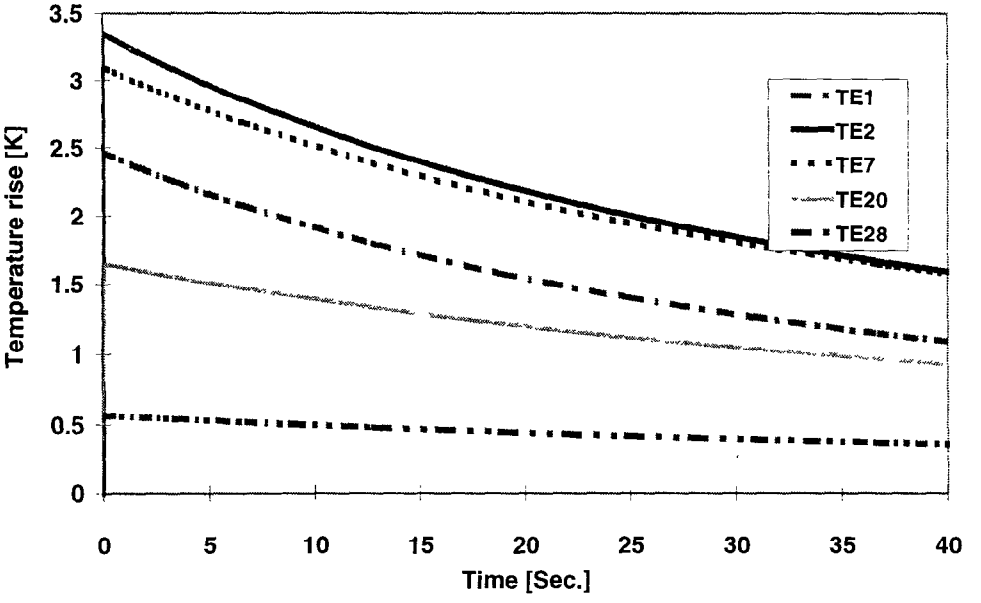

Fig. 7 Calculated temperature evolution for heat dissipation by conduction only

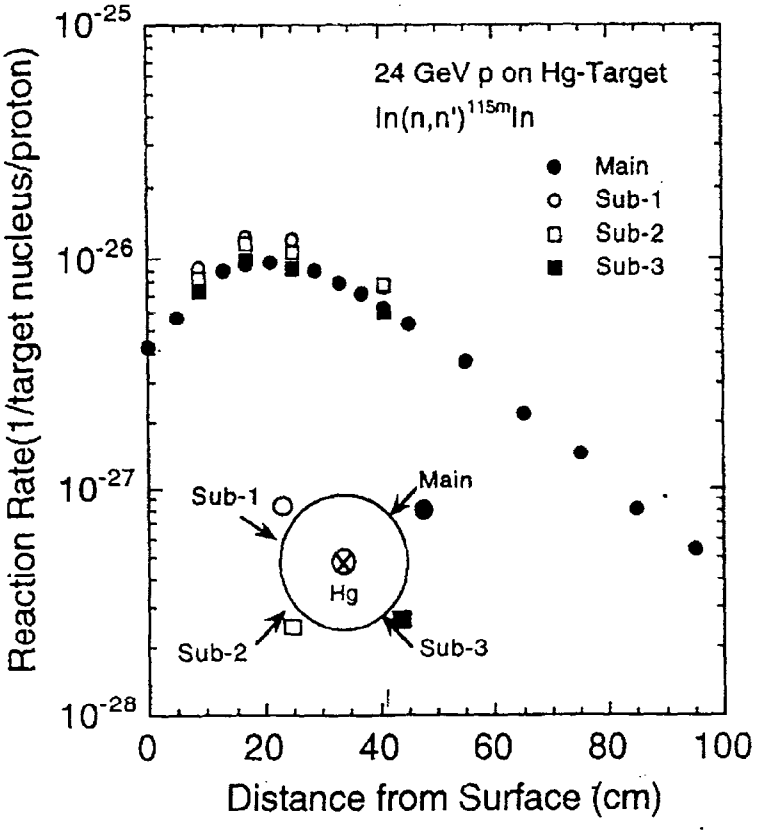

Fig. 8 Reaction rate distribution of $In(n,n)^{115m}$ measured on the cylindrical surface of thick mercury target bombarded with 24GeV protons

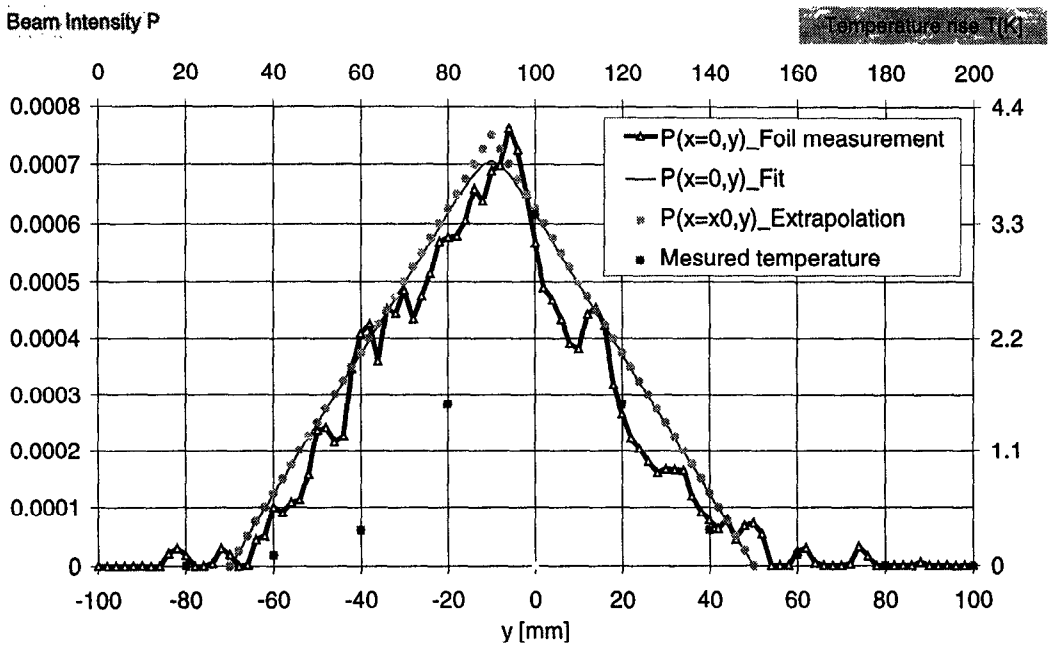

Fig. 9a: Measured and fitted beam distribution along the axes x=0 and $x=x_0$

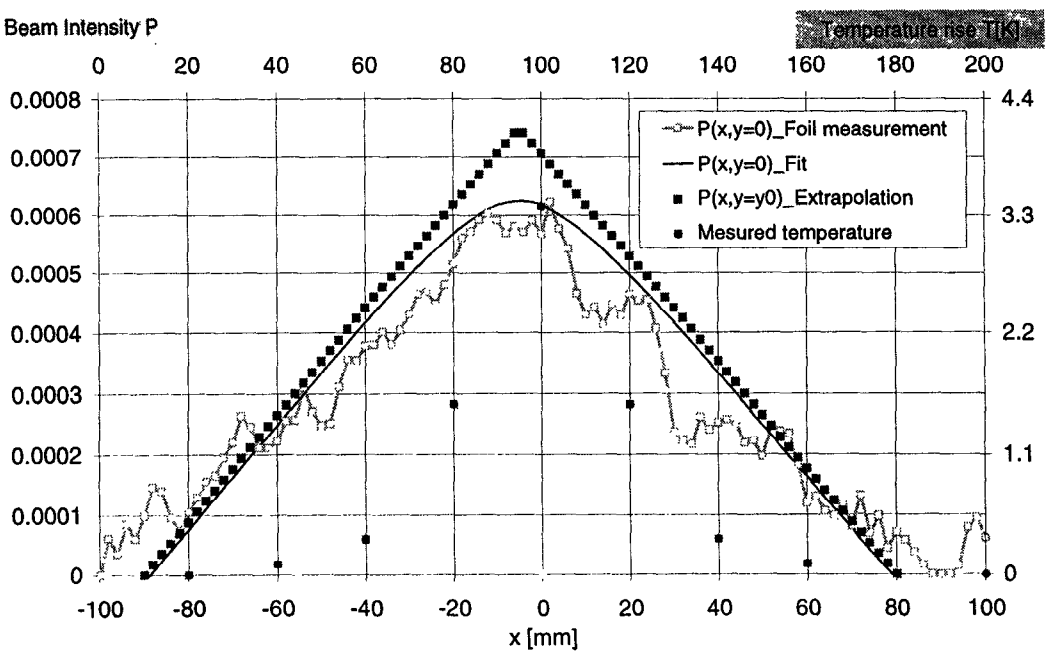

Fig. 9b: Measured and fitted beam distribution along the axes y=0 and $y=y_0$

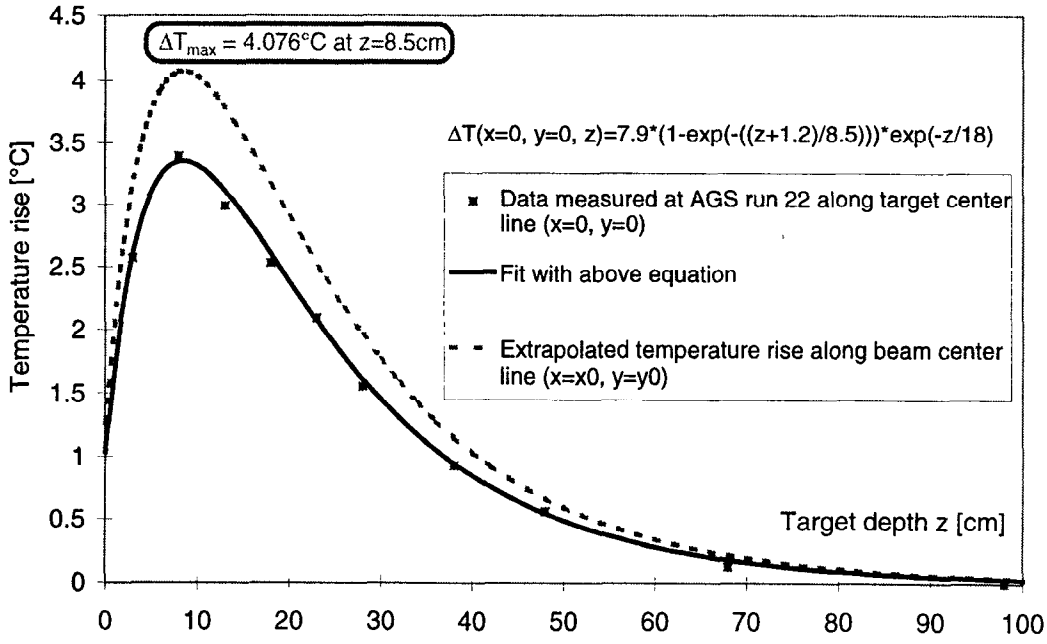

Fig. 10 Measured axial temperature distribution

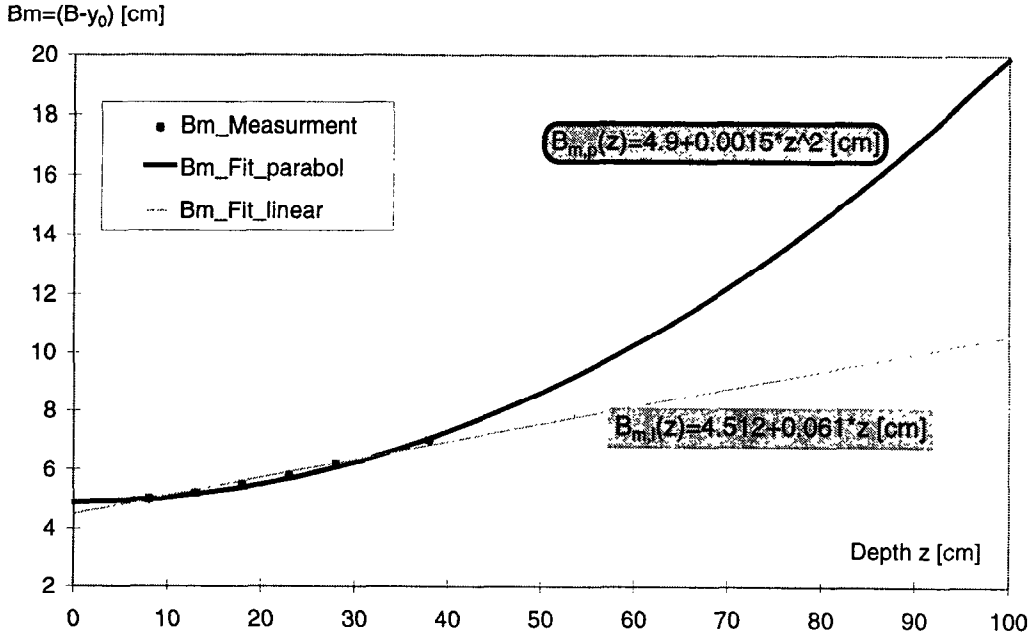

Fig. 11: Fitted semi-minor axes of the elliptic beam

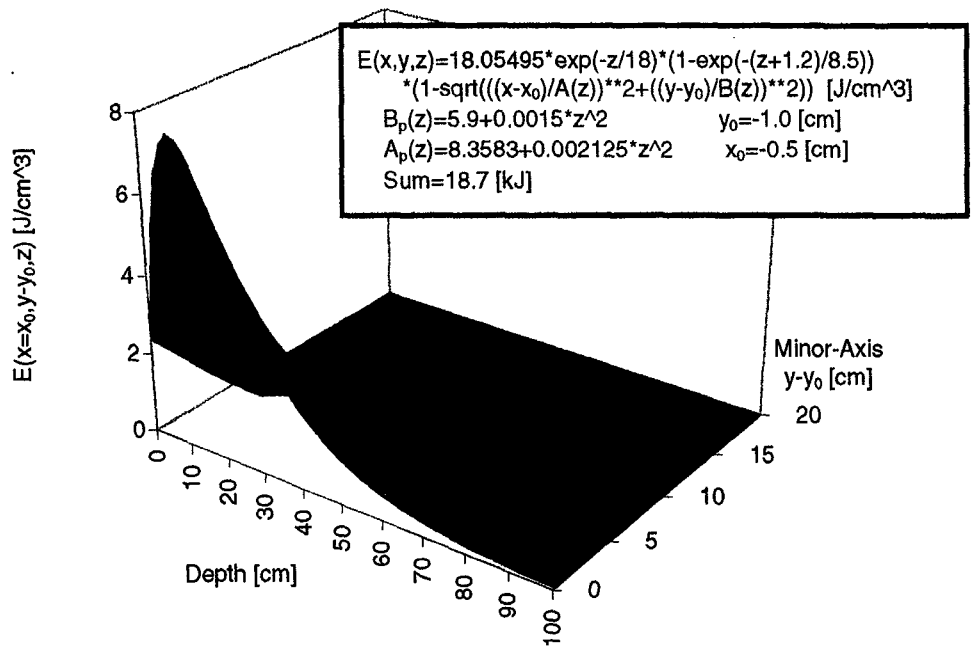

Fig. 12a: Power density distribution along axes $x=x_0$ and z with parabolic fitting

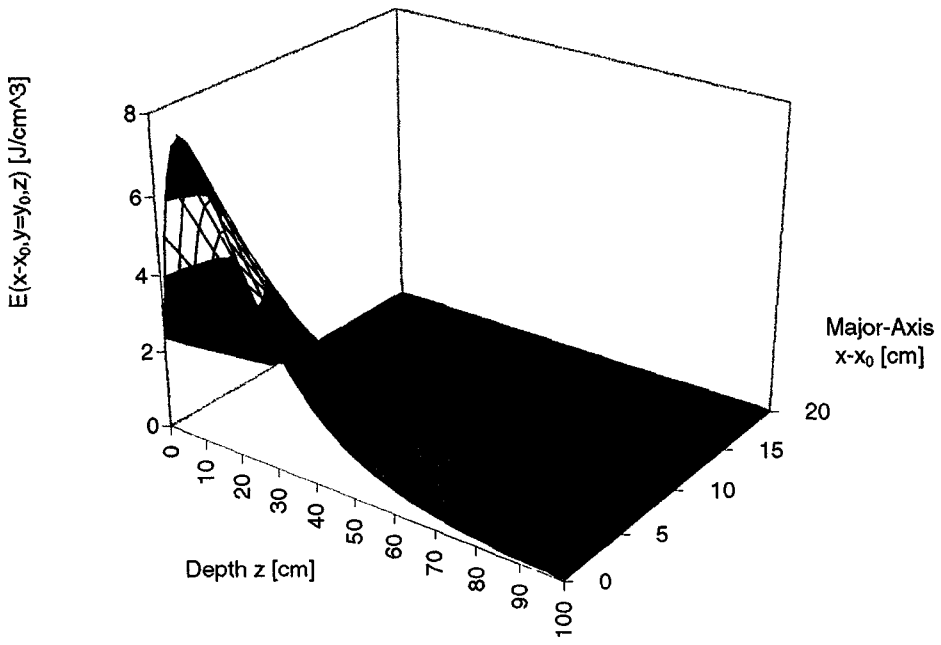

Fig. 12b: Power density distribution along axes $y=y_0$ and z with parabolic fitting

ICANS-XIV
14th Meeting of the International Collaboration
on Advanced Neutron Sources
June 14-19, 1998
Starved Rock Lodge, Utica, Illinois, USA

Measurement of Pressure Wave in Mercury Target

M. Futakawa[1], K. Kikuchi[1], H. Conrad[2], H.Stechemesser[2],
and ASTE collaboration

1) Japan Atomic Energy Research Institute
Tokai-mura, Naka-gun, Ibaraki-ken, 319-1195, Japan
2) Forschungszentrum Jülich GmbH,D-52425 Jülich Germany

ABSTRACT

The international ASTE (AGS Spallation Target Experiment) collaboration has performed a first series of measurements on a spallation neutron source target at the AGS (Alternating Gradient Synchrotron) in Brookhaven. The dynamic response of a liquid mercury target hit by high power proton pulses of about 40 ns duration has been measured by a laser Doppler technique and compared with finite elements calculations using the ABAQUS code. It is shown that the calculation can describe the experimental results for at least the time up to 100 μs after the pulse injection.

1. INTRODUCTION

Recently, worldwide efforts have done into planning and designing third generation spallation neutron sources. Mainly neutronics considerations have indicated that multi-MW sources may essentially benefit from using a liquid metal target and have led the ESS (European Spallation Source) project staff to propose mercury as the preferred target material. Both the US and the Japanese spallation source projects have come to the same conclusion and are pursuing the mercury target option, too.

On the other hand, one of the major problems with liquid targets is the pressure waves generated by the rapid energy deposition during the microsecond proton pulses. When the co investigate ntainer wall is struck, these waves may induce stresses over permissible limit. In order to investigate experimentally this phenomenon and also several other relevant topics under realistic conditions, an international collaboration has been established comprising institutions from Europe, Japan and the US (in alphabetic order). The collaboration has planned, installed and started to operate in 1997 with a scale mercury target at the AGS (Alternating Gradient Synchrotron) in Brookhaven. Being a versatile and powerful proton accelerator the AGS can be operated over a wide range of particle energies from 1.5 to 24 GeV.

The stress wave propagation on the container wall has been caught by measuring the time dependent strains employing two different methods, one of which (a Laser Doppler technique) is presented in this paper. The other (a fiber optic strain gauge method) will be published elsewhere. In this paper we report on the first stress and pressure measurements during the 1997 series of experiments of the ASTE collaboration and compare the experimental results with finite element calculations using the ABAQUS code[1].

2. EXPERIMENT

2.1 Stress wave measurement

(1) Laser Doppler technique

The laser Doppler meters were made to measure the associated in-plane displacement to

the preferable direction. A velocity at a point on the moving object is obtained by a frequency change of the echoed laser signal. A laser beam emitted from a laser beam source is split into two beams: one shots the particular point A on the moving object and the other beam also shots the same point but after passing through a frequency shifter that changes the frequency from f_1 to f_2 where $f_2=f_1+\Delta f$. When the moving object goes to the top direction, the frequency reflected from the point will be signed by the Doppler effect (Fig.1). The frequency of the reflected beam will be shifted by f_d defined by the next equation,

$$f_d = \frac{2V_A}{\Lambda}\sin\frac{\Psi}{2} \qquad \ldots 1$$

where V_A: the velocity of the moving object at the point A, Λ: a wave length of the laser beam, $\psi/2$: an angle of the beam against the moving object as shown in Fig.1. Finally the velocity V_A at the point A, proportional to the voltage converted from the frequency could be found by the next equation.

$$V_A = \frac{f_d \Lambda}{2\sin(\Psi/2)} \qquad \ldots 2$$

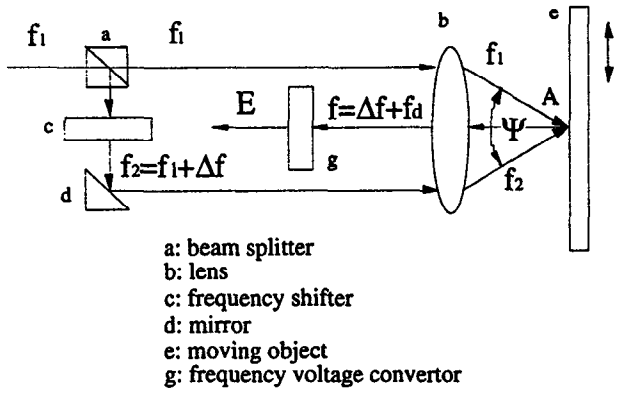

Fig. 1 A beam path in the laser probe.

A displacement X_A at the point A will be given by integrating the velocity as follows:

$$X_A = \int_0^t V_A dt \cdot \qquad \ldots 3$$

(2) Non-contact dynamic strain measuring system

A non-contact dynamic strain probe using the laser Doppler technique was developed by JAERI and ONOSOKKI Co. Ltd.. We used a He-Ne laser at 632.8nm of the wavelength. The performance of frequency response is up to 1MHz. The laser strain probe consists of two laser probe heading in the same direction as shown in Fig.2. The strain ε in defined by a relative displacement between two points and gauge length L.

$$\varepsilon = \frac{X_A - X_B}{L} \qquad \ldots 4$$

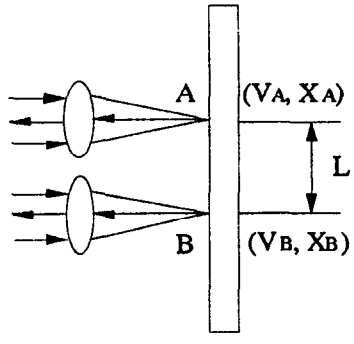

Fig.2 Laser strain probe.

Signals were transmitted to a wave memory, type AR4400 YOKOGAWA Co. Ltd., through a 50-meter optical fibre, FUJIKURA Co. Ltd., type GI, 50 μm in core diameter. The sampling rate is 1/μs for 4 channels. A piezo type accelerometer, Endevco Co. Ltd., type 7259A, was attached to the sensor box mounted to the rod for monitoring a swing induced by a vibration of the target container (Fig.3). All electric circuits were apart from the target container outside the U-line of the AGS and laser beams pass through an optical fibre in the area of proton field.

In this experiment, the intensity in one of two beams was not sufficient by an unsuitable alignment of the sensor head suffered from perturbation after final adjustment. We concentrated to get focusing of just one laser beam line. This means that only a velocity or a displacement at a point will be measured hopefully.

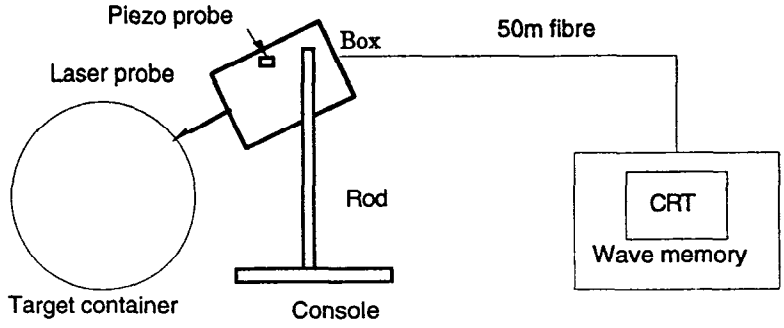

Fig.3 Measuring system.

2.2 Target container

A cylindrical target container with a hemispherical proton beam window has been manufactured at Forschungszentrum Juelich. The material used is the Chromium-Nickel steel X10CrNiMoTi18 10 (German norm DIN 1.4571). The proton beam window has been machined from a solid piece and welded to the cylindrical part, which both have a thickness of 2.5 mm. The hemispherical part including the welding has been polished and super-finished to yield the optimum surface quality. The downstream end of the 1.3 m long container with an inner diameter of 20 cm is closed by a 2.5 cm thick flange designed so as to withstand even a stationary internal pressure of 1.2 MPa without weakening the gas-tight seal.

The laser probe was mounted on the console plate attached on the secondary container using by M6 screw holes on a 40 x 80mm pitch. The plate was set over distance of 400 mm starting from the apex of the hemispherical cap. Although the probe was scheduled to shot some of hemispherical surface, a measuring point was changed to the cylindrical part on the target because there was not enough space for adjusting a focus of the beam. A suitable position for the strain measurement was found 300 mm behind the apex at an angel of 30 degree from the top, 200 mm downstream from a transition part of hemispherical part, after sharing a position with neutron sampling rod (Fig.4).

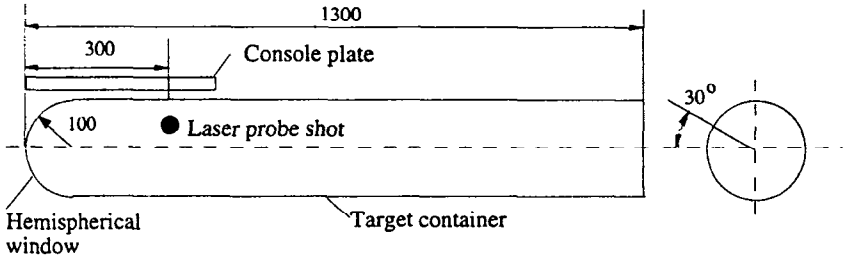

Fig. 4 Top view of the target container: all unit: mm.

3. Calculation for pressure and stress waves propagation in the container

3.1 Calculation model

Number of protons delivered from the AGS accelerator enter into the mercury target. In the target the particles produced in the course of spallation reaction generate an intense nuclear heat that causes pressure waves in the target material and stress waves in the target container.

The equation of motion for an elastic body is described by Eqs.5 and 6 in the polar system if the body force doesn't work

$$\frac{\partial^2 \bar{u}}{\partial t^2} = \frac{\eta + 2G}{\rho} \nabla^2 \bar{u} \qquad ...5$$

$$\nabla = \frac{1}{r}\frac{\partial}{\partial r}\left(r\frac{\partial}{\partial r}\right) + \frac{1}{r^2}\frac{\partial^2}{\partial \theta^2} \qquad ...6$$

where $\bar{u}$: displacement vector, η: elastic constant(=G(2G-E)/(E-3G)), G: modulus of rigidity, ρ: density, (r, θ): polar coordinates. The stress will propagate at the speed of sound in the material as follows:

$$\left(\frac{\lambda + 2G}{\rho}\right)^{1/2} = \left(\frac{3K + 4G}{3\rho}\right)^{1/2} \qquad ...7$$

where K: the bulk modulus, λ: a material constant.

There are two driving forces for the stress occurred in the container: one is the instantaneous thermal expansion of the target material and the other is the pressure wave of the target material that expands the container. The target material is modeled by using CAX4R, axi-symmetric 4-point solid element, from the element library of ABAQUS[1] in the computer simulation. That is, the liquid behavior of mercury is represented by the solid element which has an apparent Young's modulus E to be coincident with the bulk modulus K of the target materials described by K=E/3(1-2ν) and G=E/2(1+ν). Poisson's ratio ν is nearly 0.5, meaning that a shear force might be negligible[2]. Consequently the equation of motion is given by the pressure of mercury p for the target coolant material,

$$\frac{\partial^2 p}{\partial t^2} = \frac{K}{\rho} \nabla^2 p. \qquad ...8$$

The container is modeled by using SAX1, axi-symmetric shell element. In the axi-symmetric shell structure both bending and membrane forces will occur. The basic equations of motion are given by the displacement u, for example,

$$\frac{\partial^2 \bar{u}}{\partial t^2} = \frac{E}{\rho} \nabla^2 \bar{u} \qquad ...9$$

The contacting boundary condition between the mercury and the container wall is allowed the force to convey discountinuously between them.

3.2 Deposited energy

The magnitude of stress and pressure waves generated in the container is very strongly dependent on the total deposited energy into the mercury target and its distribution. There is, however, not an exact information of the beam profile measured by the imaging plate(IP) at 24GeV run when the pressure wave was successfully measured but the beam profile for integrated multi-shots[3]. In fact the maximum intensity of the proton projection normal to the beam line located 1 cm apart from the centre of the target window. It is announced that two bunches were delivered at 24GeV and the number of protons for two bunch was about 8×10^{12}. The total energy deposition in the mercury target is found to be 18.7 kJ for two bunches, as a result of the temperature measurement(PSI)[5]. There are two ways to know the energy deposition over the target space. The direct ways to describe the energy deposition in the target is produced by the temperature measurement(PSI)[5]. The distributed function shapes an ellipse,

$$q(r,z) = \eta\left[1-\exp\left(-\frac{z+1.2}{8.5}\right)\right]\exp\left(-\frac{z}{18}\right)\left[1-\sqrt{\left(\frac{x-x_o}{A(z)}\right)^2+\left(\frac{y-y_o}{B(z)}\right)^2}\right] \quad ...10$$

where $A(z)=8.3583+0.002125z^2$, $B(z)=5.9+0.0015z^2$, $x_o=-0.5$ (cm), $y_o=-1.0$ cm. This is modified to circle for easy calculation under the condition of the same deposition energy.

The indirect ways is to use the IP profile measured by JAERI with a help of the HERMES[4] code calculation. Equation 11 shows a distribution function of the energy deposition in the mercury target in this way,

$$q(r,z) = \xi\left[1-\exp\left(-\frac{z+3.09}{13.7}\right)\right]\exp\left(-\frac{z}{13.7}\right)\exp\left[-\frac{r^2}{2(2.88+0.00476z^2)}\right] \quad ...11$$

where z: a distance along the centre axis from the top of the mercury target, r: a radial distance.: A fitting parameter ξ to the total energy deposition is decided by integrating the temperature distribution measured by PSI.

Figure 6 shows the distribution of energy deposition in the target to z direction(left) and to radial direction(right).

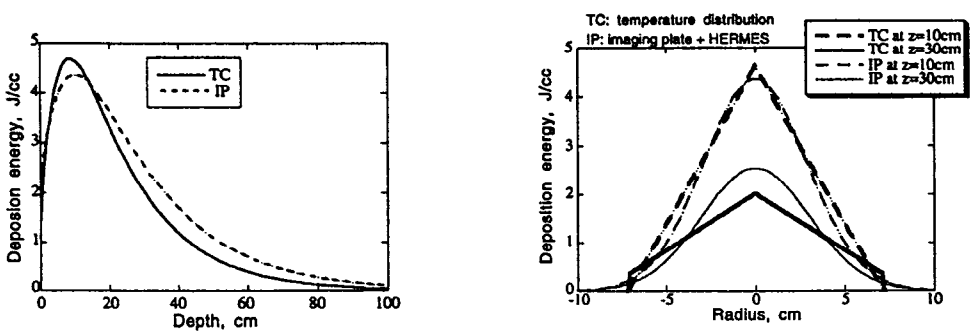

Fig.6 Energy deposition in the target.
q(r,z)=11.0*(1-Exp[-(z+1.2)/8.5])*Exp[-z/18.0]*(1-r/(7.0+0.00181*z^2))*(1/(1+(r/(7.0+0.00181*r^2))^1000)) for TC equation.

4. Results

4.1 Signals obtained from the laser strain prove

A stress wave propagation on the container wall was successfully measured at 24 GeV with the highest proton intensity about 4×10^{12}, AGS announced. In the other energy levels as 1.5 and 7 GeV, no signal was observed by the laser Doppler probe. Next two CRT images copied in the AGS site showed signs of pressure waves at the first and the second bunches at 24GeV energy.

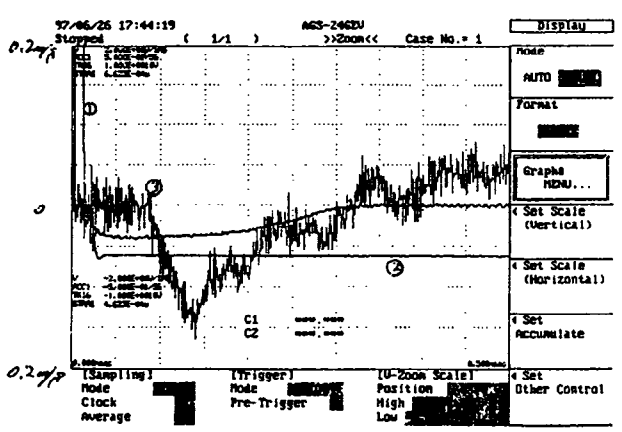

Fig.7 CRT image of the first bunch.

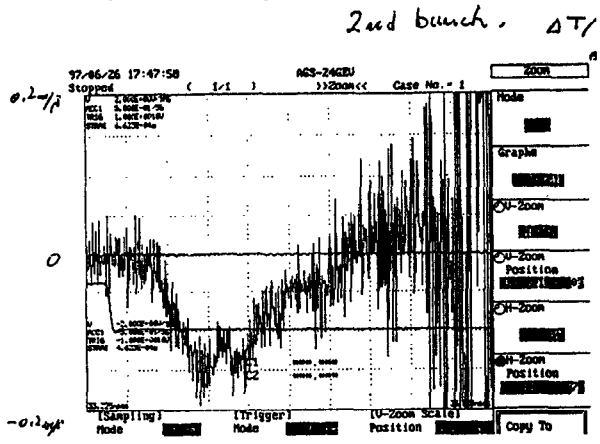

Fig.8 CRT image of the second bunch.

The accelerometer signal, signal "2" in Fig.7, dropped immediately just after a proton beam was injected into a target because over currency was caused by the injected protons. The drop was decided to the time when protons injected into the target. Signal "3" indicates a velocity of the deformation for the target. Signal "1" is a trigger from AGS. It must be stressed on the reproducible for pressure wave in the first and the second bunches (Fig.8).

Figure 9 shows whole history of pressure wave stored in the wave memory for the first bunch. Around 15 ms after the proton injection the vibration of about 5 ms period was observed. It seems to be caused by the natural vibration of the sensor rod, ϕ 30 mm x L300 mm(see Fig.4).

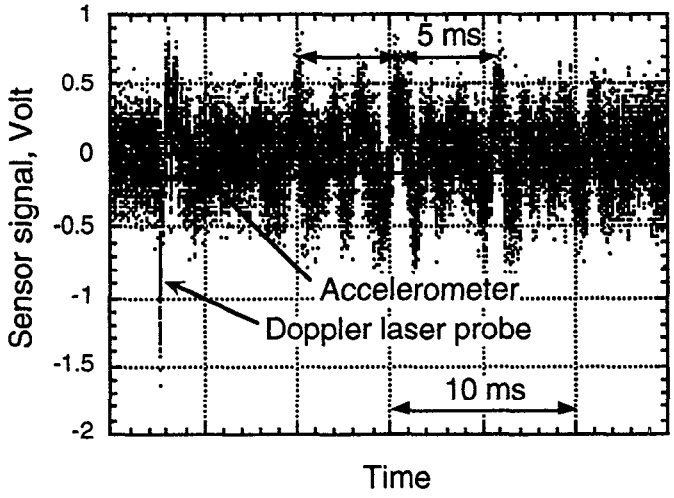

Fig.9 Time response of velocity during 25 ms after first bunch of proton.

4.2 Comparison between experiment and calculated results

Figure 10 shows a comparison between the experimental result for the first bunch and the calculation results. Fig.11 is a replotting of Fig.10 on the short range mat. The target container started to response against the pressure wave at a time of 60 μs and showed the maximum velocity after a couple of tens micron seconds. Calculations followed the decent of velocity before a change of movement. Two calculation results were shown by the different deposition energy distribution in the target. The energy deposition function affected the level of peak values but not the frequency composition of stress waves. Large pressure waves at

a period of 500 μs resulted in a superimpose with reflected waves from a bottom of the target container. This phenomena is also plotted by the calculations.

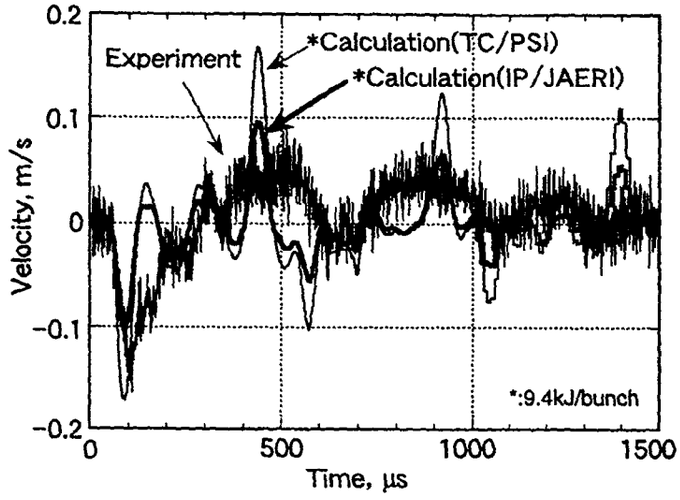

Fig.10 Comparison between experiment and calculation results

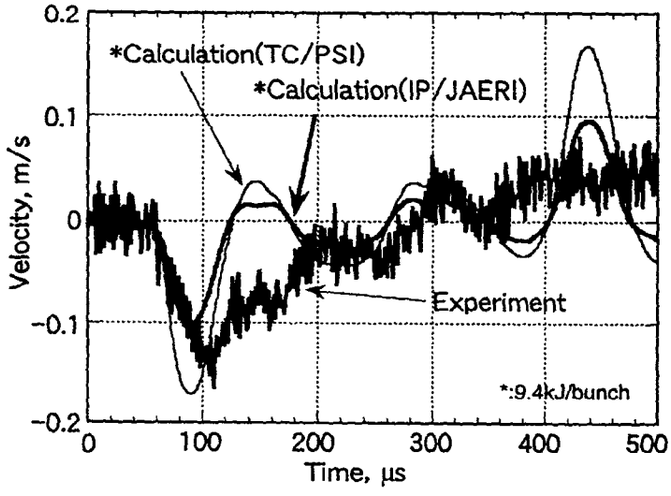

Fig.11 Comparison between experiment and calculation results in the short range of Fig.10.

5. Conclusion

Although the dynamic response of the liquid mercury target container was successfully caught by the non-contact dynamic strain prove using the laser Doppler technique under the present harsh radiation conditions, we don't have a good coincidence on velocity waves between experiment and calculation except for the first 100 μs. For the pressure wave measurement an exact temperature distribution in the target will be necessary for the calculation works of the first response in the target container. A success of the measurement on mercury pressure in the container scheduled in the 1998 test run will decide the state of the mercury, fluid or cavity ?, and the interactive motion between the solid container and the mercury target.

References

(1) Hibbitt, Karlsson & Sorensen, ABAQUS/Explicit Version 5-6.
(2) S Ishikura, K Kikuchi, M Futakawa, R Hino, Transient Stress Wave in a Heavy Liquid-Metal System at High Intensity Proton-Accelerator, ICM&M'97, pp.89-94,(1997).
(3) H Nakashima, et al., Beam profile measurement in AGS experiment.
(4) P Cloth, D Filges, R D Neef, G Sterzenbach, Ch Reul, T W Armstrong, B L Colborn, B Anders and H Bruckmann, KFA Jul-2203, (1988).
(5) G S Bauer, et al., Temperature measurement in AGS experiment.

ICANS-XIV
14th Meeting of the International Collaboration
on Advanced Neutron Sources
June 14-19, 1998
Starved Rock Lodge, Utica, Illinois, USA

Spallation Target Development at JAERI

- R&Ds on thermo-mechanical design -

Ryutaro HINO, Masanori KAMINAGA, Tomokazu ASO, Hiroyuki KOGAWA
Shuichi ISHIKURA, Akira SUSUKI, Atsuhiko TERADA,
Hidetaka KINOSHITA and Katuhiro HAGA

Spallation Target Laboratory
Center for Neutron Science (CENS)
Japan Atomic Energy Research Institute (JAERI)
Tokai, Ibaraki, 319-1195, Japan

ABSTRACT

Rib-roughened plates for a solid target, a cross-flow and a return-flow type containers for a mercury target are proposed as design concepts through a preliminary conceptual design. To realize these concepts, analysis and experimental works are being carried out. This paper describes an outline of the present status of R&D for the target at JAERI such as heat transfer augmentation experiments for the solid target, mercury flow tests with a loop of maximum flow rate of 15 L/min, flow pattern measurements for a cold source moderator etc., as well as preliminary conceptual design works.

1. INTRODUCTION

The Japan Atomic Energy Research Institute (JAERI) has started the Neutron Science Project for utilizing high intensity neutrons relating to fundamental science and nuclear engineering by using a proton accelerator generating a high energy proton beam of 1.5 GeV with a high current of 3.3 mA to produce 5 MW. In the project, a neutron scattering facility is planed to be constructed first, where high intensity neutrons are generated at a target by spallation reaction between target materials and the proton beam. Since technology of a MW-scale target has not been established yet, development of a 5 MW spallation neutron source is one of the most difficult technical challenges in this project.

In the world, the European Spallation Source (ESS) Project in Europe [1] and the

Spallation Neutron Source (SNS) Project in the USA [2] are progressing with the construction of MW-scale target neutron scattering facilities, which are focused on mercury as the target material. Target concepts would be limited to those two types: a solid metal target like the ISIS at the Rutherford Appleton Laboratory in the UK, and the mercury target under conceptual design in the ESS and the SNS projects. While technology of the solid target, especially of KW-scale, has been established and could extend to MW-scale with minimum efforts, there is almost no technology base on the mercury target.

JAERI is going to develop two types of target, the mercury target as the main and the solid target as the backup. In the first step, targets will be operated under 1.5 MW proton beam power to adjust the accelerator system including the proton beam lines. In the 1.5 MW operation, the solid and the mercury targets will be installed in order to establish 5 MW-target technology and to accumulate technical data to improve their structures and performances. In the 5 MW operation following the 1.5 MW operation, the improved targets will be installed in the system. This two-step plan of target R&D was started in April 1997, when the Spallation Target Laboratory was organized at JAERI. This paper presents an outline of one-year activities on target R&D.

2. FRAMEWORK OF TARGET DEVELOPMENT

Figure 1 shows a concept of a mercury target system except moderators and reflectors. The proton beam is led into the target horizontally. The mercury target system consists of circulation pumps, heat exchangers, a surge tank, drain tanks and connecting pipes. Whole components are fixed on a trolley, and are covered by stainless steel plates in order to avoid the leakage of mercury to the environment surrounding the trolley. The trolley can be moved into a maintenance area during a maintenance period, and all components can be handled with remote handling devices.

To construct the target system, a framework as shown in Fig.2 was determined from an engineering viewpoint. The preliminary conceptual design prior to the conceptual design has been carried out with a close connection with both numerical analyses and experiments. After completion of the detailed engineering design based on the conceptual design results, demonstration tests using full-scale mock-up models, including remote handling devices, will be conducted to ensure the structural integrity and the safety aspects of the target system.

To promote conceptual design and analytical works effectively, a basic system of CAE - the computer aided engineering system- has been introduced. Hardware of CAE consists of three groups, analysis servers, personal computers and data servers. Drawings made by using Auto-CAD with the data server are entered into thermal-hydraulic and structural-strength analysis codes installed in the analysis server to

analyze target performances. Using the CAE system, a preliminary conceptual design was carried out to define the specifications of the 1.5 MW / 5 MW target system with more than 30 neutron-beam ports. As a result, the system layout and solid/mercury target concepts were made clear. In the following chapter, an outline of the solid/mercury target concepts as well as R&D activities will be introduced.

3. SOLID TARGET

Figure 3 shows the solid target structure which is being designed on the basis of the existing target structure such as the ISIS. The solid target consists of heavy metal plates made of tungsten or tantalum, whose dimension is 140 x 100 mm, and these plates are cooled by heavy water. Cooling channels between plates are very narrow so as to decrease water volume ratio affecting the neutron yield. In the solid target design, channel height (water gap) is only 1.2 mm, and the water volume ratio to the target metal volume is kept less than 20%.

Figure 4 shows a heat density distribution generated in the tungsten target under 1.5 MW operation, which was calculated with a neutronic code systems NMTC/JAERI [3]. In the thermal-hydraulic and structural design, 20% higher values than the calculated results are used for keeping a wide margin on heat removal; it is necessary to verify this margin by estimating measurement and analytical evaluation errors. Figure 5 illustrates a relationship between plate thickness and heat flux estimated by the heat density distribution shown in Fig.4. Thickness of the target plate increases from 6 mm to 75 mm with an axial length. Then maximum heat flux is 2.9 MW/m^2, which is around 1/8 of the critical heat flux calculated with the Sudo correlation[4].

Using these results, plate temperatures were estimated under 10 m/s of water velocity. Then, heat transfer rates were calculated with the Dittus-Boelter correlation[5] which is available for smooth channels. As seen in Fig.6, surface temperature can be kept below 120℃, which is much lower than the saturation temperature of 1MPa, 180℃; the inlet pressure of the cooling channel is 2MPa and the pressure loss is estimated to 1MPa at maximum. From this result, it can be deducted that the target plates would be cooled down without the flow boiling. But, 10 m/s of water velocity is very high from an engineering viewpoint on flow induced vibration, erosion and flow distribution.

The heat transfer enhancement technique with micro ribs was focused on to decrease water velocity while keeping high heat transfer rates. This is because there is almost no heat transfer data and correlations available for the narrow channel like the target cooling channel. In order to deduce correlations for the target design, a simulated target cooling channel with micro ribs was fabricated as shown in Photo 1. Micro ribs of 0.2 mm in height (k) and width were formed on the surface in pitch (p) of

2 or 4 mm by using a NC machine tool. Water is able to flow in the test section at a maximum velocity of 20 m/s.

Figure 7 shows the relationship between the Nusselt number - dimensionless heat transfer rate - and the Reynolds number - dimensionless velocity - in the channel height of 1.2 mm. The Nusselt number of rib-roughened channel of p/k=10 is more than two times higher than that of the smooth channel when the Reynolds number is less than 20,000 which assumes the operational Reynolds number of the solid target. From this result, it can be expected to decrease water velocity down to 5 m/s while keeping the same plate temperatures as those in the smooth channel under 10 m/s of water velocity.

4. MERCURY TARGET

Figure 8 shows one of JAERI's concepts of the mercury target : a cross-flow type target using baffle plates. Mercury flows across the proton beam through baffle plates so as not to generate a recirculation flow which would make the mercury temperature rise excessively under high heat generation density. The target container will be made of SUS316 and its size presently under design is 590 mm in width, 120 mm in height and 1000 mm in length. Figure 9 shows thermal-hydraulic analysis results of the cross-flow type target using the baffle plates under a 5 MW (1.5 GeV, 3.3 mA) operation. A heat generation density distribution in the mercury target was calculated with the NMTC/JAERI code system[3] as well as the solid target. An inlet temperature of 323 K and a mercury flow rate of 50 m^3/h were assumed in the analysis. As shown in Fig.9, the recirculation flow was hardly observed as we expected. A maximum mercury velocity of 1.5 m/s and a maximum mercury temperature of 494 K were obtained in this case. Further analysis will be carried out to optimize flow patterns in the target vessel by changing configurations of baffle plates or other configuration such as bladed-frames to reduce the maximum temperature of mercury. .

In JAERI, the other type of target concept called "return-flow type", just like ESS or SNS, has also been proposed in the preliminary conceptual design as shown in Fig.10. The target container will be made of SUS316 and its size presently under design is 360 mm in width, 120 mm in height, 650 mm in target region length and 1550 mm in total length. The mercury flow rate of the return-flow type target should be smaller than that of the cross-flow type target to reduce the maximum velocity of mercury in the target. This is because, the cross-sectional area of the return-type target is less than that of the cross-flow type target. But it can not be reduced too much, because of the mercury temperature rise. As a results, 40 m^3/h was selected as the design flow rate for the return-flow type target.

All of the above target containers have an inner and an outer vessel. Almost all

heat generated in the beam windows are expected to be removed by heavy water flowing through a narrow channel between the inner and the outer vessels. Table 1 summarized the merits and demerits of both cross-flow type and return-flow type target concepts. The cross-flow type target container has an advantage from the viewpoint of temperature and velocity. On the other hand, the return-flow type has an advantage from the viewpoint of container size and flow distribution. During the conceptual design period, both types of target containers will be investigated together in relation with the neutron yield and then will be integrated into one concept making use of each advantages.

A pressure wave which is one of the most critical issues for the mercury target design has also been analyzed during the preliminary conceptual design period. Figure 11 shows one of two dimensional analysis results using a simple cylindrical container under 5 MW operation. A rectangular beam profile with uniform power distribution was assumed in the analysis. The target consists of a dome-shaped window and a cylinder of 200 mm in diameter, 1100 mm in length and 2.5 mm in wall thickness. SUS316 was used as a container material. Figure 13 shows pressure distribution in the target 26μs after a proton beam injection. At 26μs , the highest pressure of 93 MPa can be seen near the beam window. In the analysis, a maximum pressure of 97 MPa was generated at the beam window 10 μs after the proton beam injection.

To effectively realize the above target concepts, as a first step, pressure loss and erosion characteristics will be measured using a mercury test loop. Figure 12 shows the flow sheet and an outer view of the mercury test loop. The maximum design flow rate of the mercury is 15 L/min. A test section of annular channel, 25 mm of an outer tube diameter, and 20 mm of an inner tube diameter, is used so as to measure the pressure loss and erosion rate under the velocity up to 1.5 m/s. Mercury is circulated by an electromagnetic pump (EMP), and flow-rate is measured with an electromagnetic flow meter (EMF). These components were fabricated on the basis of existing techniques developed for a fast breeder reactor cooled by liquid sodium. The loop was installed in a movable box enclosed tightly with acrylic plates and a steal tray. 20 liters of mercury were poured into the loop this April, and preliminary tests were carried out to check whether all the components were working properly. Figure 13 shows typical trend graphs of the loop operation and preliminary pressure loss measurement results. Flow rate oscillation shown in Fig.14(a) was caused by argon bubbles flowing through the loop. At this moment, EMF has not been calibrated yet. Therefore, the flow rates shown in Fig.14(a) and (b) are not correct. But as shown in Fig.14(b), pressure loss characteristics of the test section are consistent with those calculated by the Blasius' resistance formula. EMF will be calibrated soon by using an ultra sonic flow meter. This loop will be used efficiently for thermal-hydraulic and

erosion experiments, safety experiments simulating transients and accident conditions, component development tests such as pumps, flow-meters, compact heat exchangers and so on.

5. COLD SOURCE MODERATOR AND TARGET MATERIAL

An other important component consisting included in the target system is a cold source moderator using supercritical hydrogen (1.5 MPa, 20 K). One of the major technical issues in the design is to keep structural strength of a moderator vessel made of aluminum alloy under 1.5 MPa and to prevent temperature rises more than 3 K for keeping a high neutron yield. Figure 14 shows a concept of JAERI's cold source moderator vessel - a supercritical hydrogen container. The vessel is a thin-walled structure supported with thin frames and inner plates. A twisted tape is installed inside the inlet pipe to obtain better heat removal performance on the bottom surface of the vessel. Most of supercritical liquid hydrogen flows through the inlet pipe towards the bottom of the vessel, but small amounts of flow bypass through small holes located at the bottom half of the inlet pipe to suppress recirculation flow in the vessel. To obtain optimum performance of the cold source moderator vessel, structural strength analyses coupled with neutronic analyses will be carried out soon to determine wall thicknesses in cases using forging aluminum alloy, such as A2014. Thermal-hydraulic analysis to determine flow patterns in the vessel will also be performed. While designing the moderator vessel with CAE, a test apparatus was fabricated to visualize flow patterns under water flow conditions in order to obtain design information on the occurrence of the recirculation flow affecting temperature rise. Figure 15 shows a flow diagram and an outer view of the test apparatus. The moderator is simulated with acrylic cylinders in order to visualize the recirculation flow behaviors generated by the jet flow from the inlet pipe using a laser imaging method (PIV system).

On the other hand, thermal shock caused by the pulsed proton beam has the potential to damage the structural integrity of the target and the moderator. Since there is almost no data to verify analysis codes, a pulsed heating apparatus was fabricated to obtain verification data as well as to clarify the thermal shock behavior. Figure 16 shows the pulsed heating apparatus for the target material test. Thermal shock is generated in a disk specimen of 30 mm in diameter and of 1 to 5 mm in thickness which are made of tungsten, SUS316 etc. by using a 0.1 μs-pulsed ruby laser beam. The thermal shock tests will be carried out soon.

6. CONCLUDING REMARKS

In this paper, solid/mercury target concepts and several topics on target R&D were introduced. The solid target consisting of rib-roughened tungsten or tantalum

plates could be adopted to a 1.5 MW proton beam by heavy water cooling. A cross-flow type and a return-flow type containers proposed for the mercury target are identified their advantages and disadvantages, and will be improved through experimental works using a mercury test loop, pulsed heating tests etc. as well as structural and thermal-hydraulic analyses. On the other hand, a cold source moderator vessel of a thin-walled structure with a twisted tape is needed to optimize its design through further R&Ds on mechanical structure, thermal-hydraulics and neutronics.

Acknowledgement

We are grateful to G. Bauer (PSI), Y. Takeda (PSI) , T. A. Broome (ISIS) and all the member of JAERI Neutron Science Project for helpful discussions of the target development.

References

[1] The European Spallation Source Study – Volume III. The ESS Technical Study, ESS-96-53-M(1996).

[2] National Spallation Neutron Source Conceptual Design Report, Volume I. The NSNS Collaboration, NSNS/CDR-2/V1(1997).

[3] Y. Nakahara and T. Tsutsui, JAERI-M 82-198(1982) (in Japanese).

[4] Y. Sudo, Trans. Japan Soc. Mech. Engrs., Ser.B63(608), 1305-1311(1997).

[5] Handbook of Heat Transfer, edited by W.M. Rohsenow and J.P. Hartnett, McGraw Hill, 7-32(1973).

Table 1 Comparison of mercury target between cross flow type and return flow type

Flow Type	Cross Flow Type Proton Beam 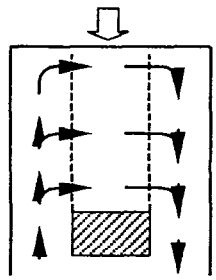	Return Flow Type Proton Beam 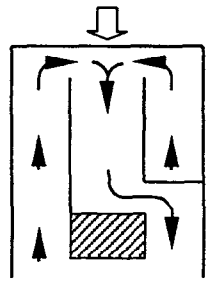
Max. Temperature	Low ○	High
Mercury Velocity	Low ○	High
Container Size	Large	Small ○
Flow Distribution	Complicated	Simple ○

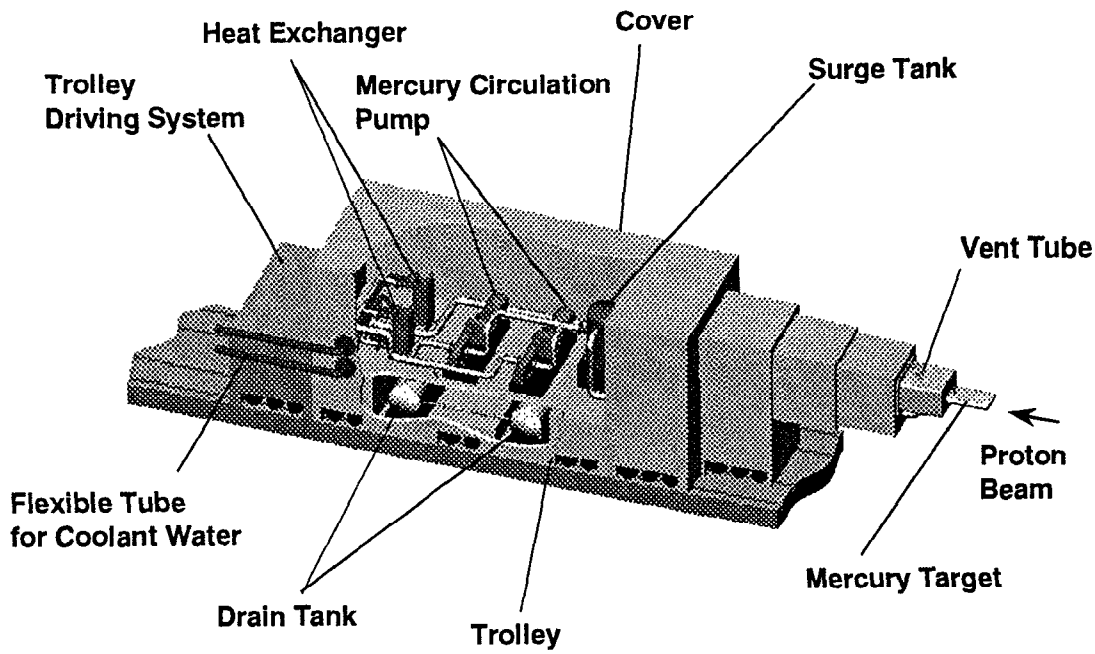

Fig.1 Conceptual design of spallation target system - Mercury target trolley -

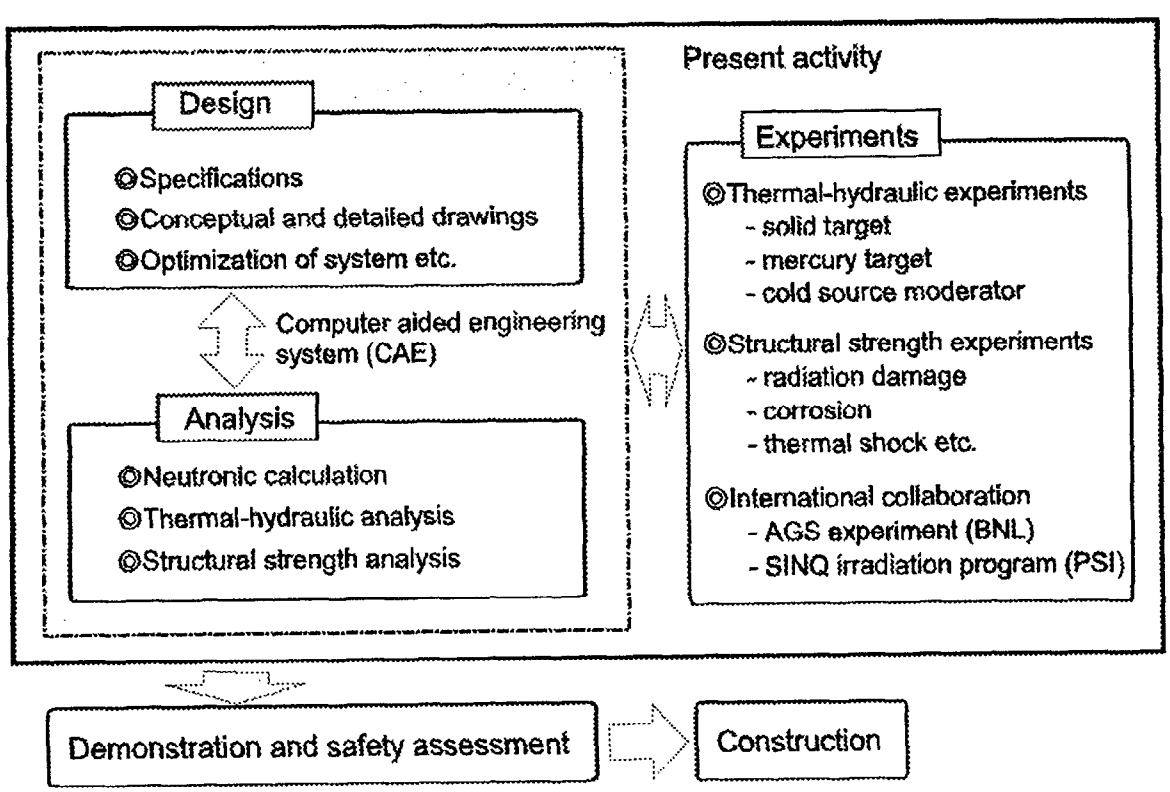

Fig.2 Framework of target development

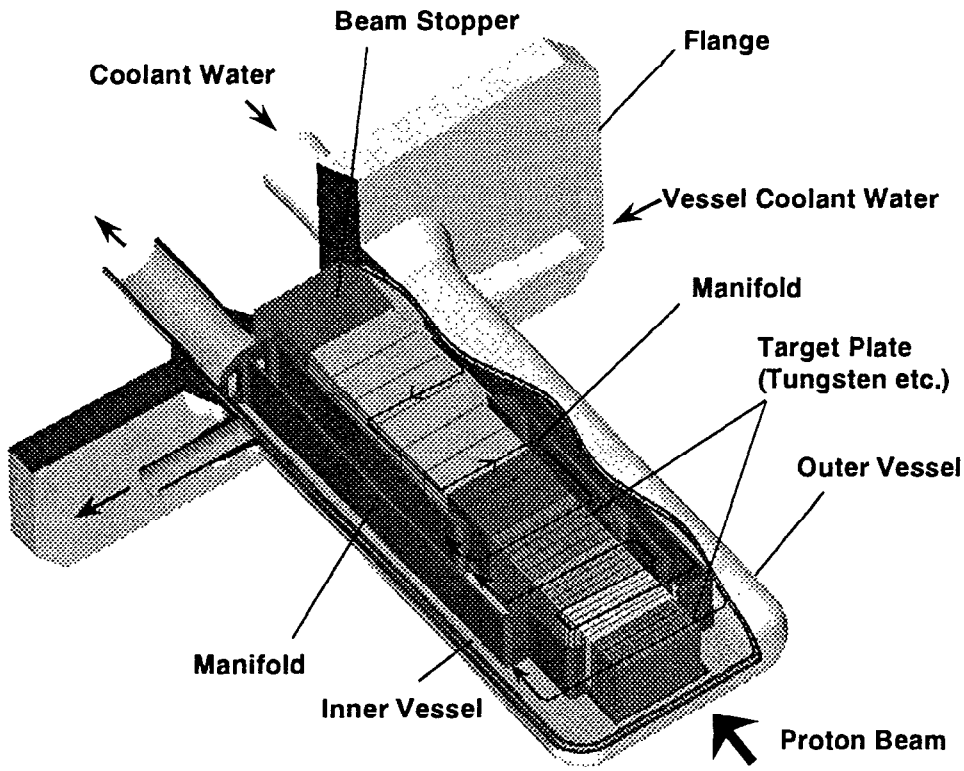

Fig.3 Cutaway view of solid target

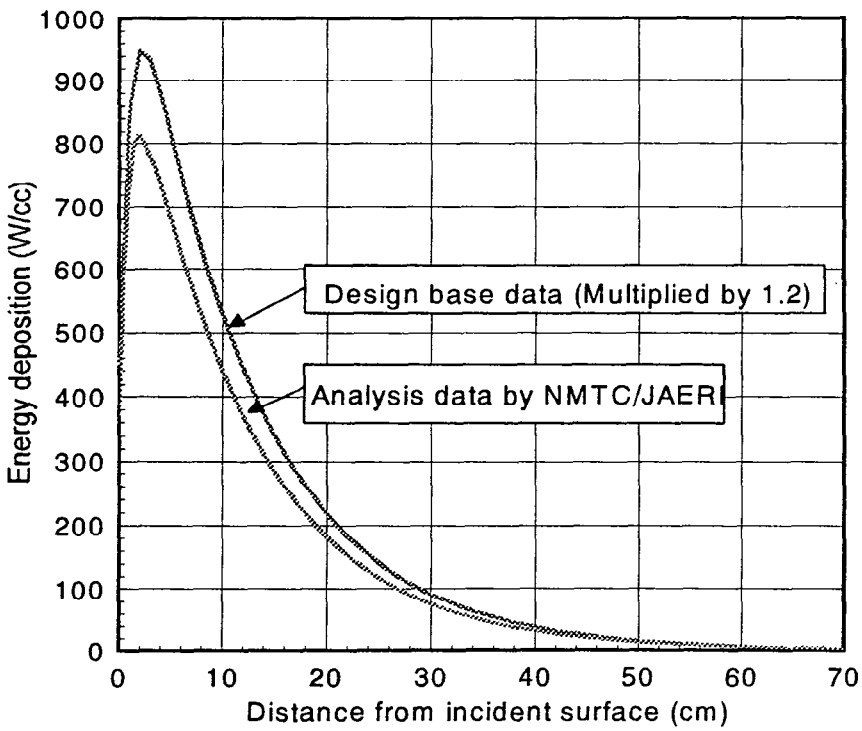

Axial energy deposition in 1.5MW tungsten target

Fig.4 Axial energy deposition in tungsten target under 1.5 MW proton beam incidence

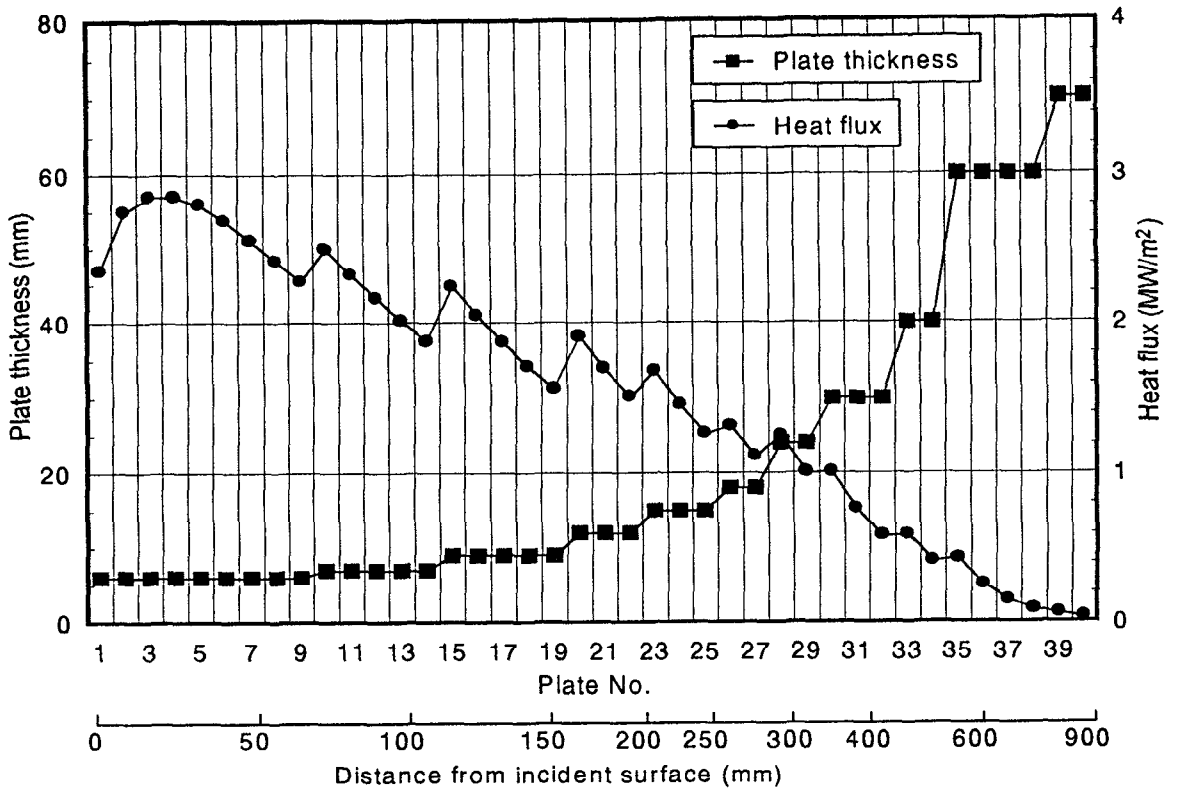

Relation between plate thickness and heat flux
(Tungsten , fromt plate thickness:6mm, coolant gap:1.2mm)

Fig.5 Relationship between plate thickness and heat flux (Tungsten target)

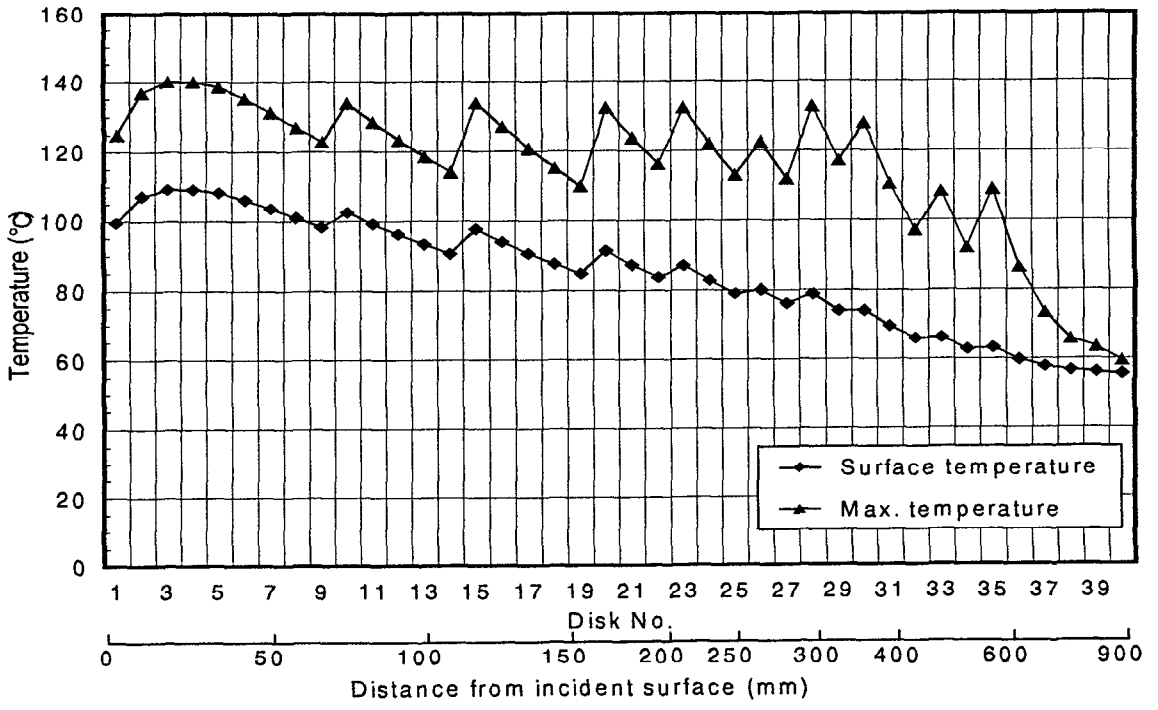

Surface and maximum temperatures of target disk
(tungsten , fromt disk thickness:6mm , coolant gap : 1.2mm)

Fig.6 Surface and maximum temperatures of target plates (Tungsten target)

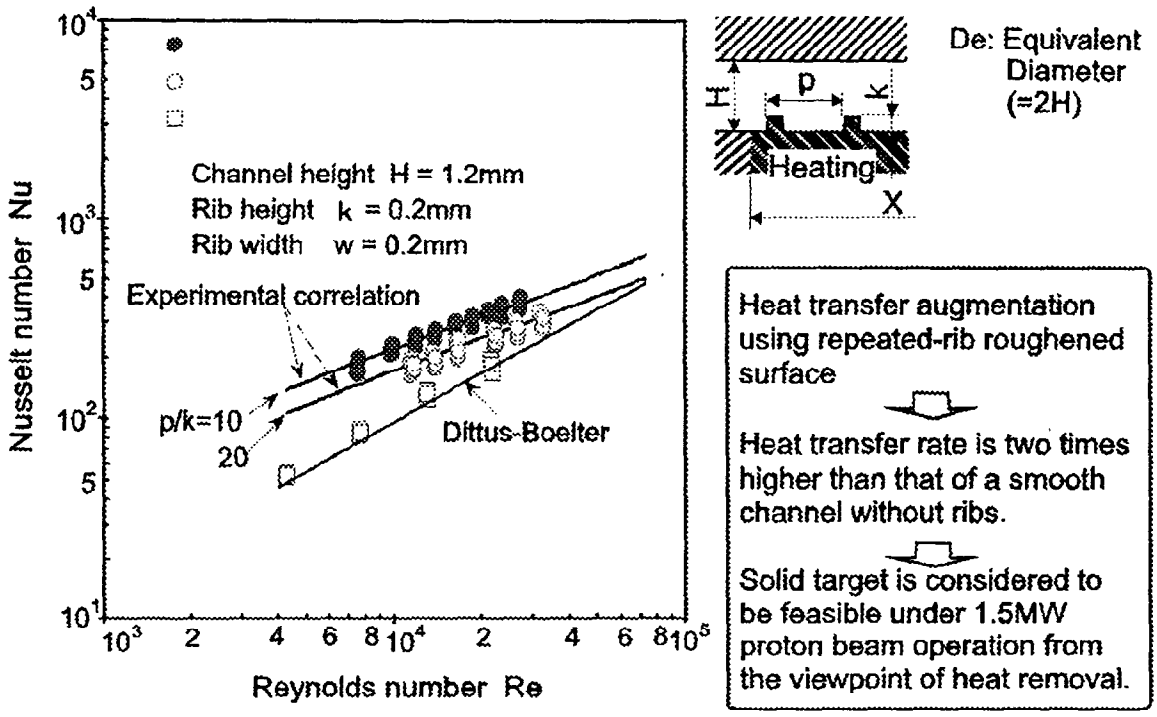

Fig.7 Relationship between Nusselt number and Reynolds number - Experimental results of heat transfer augmentation with micro ribs-

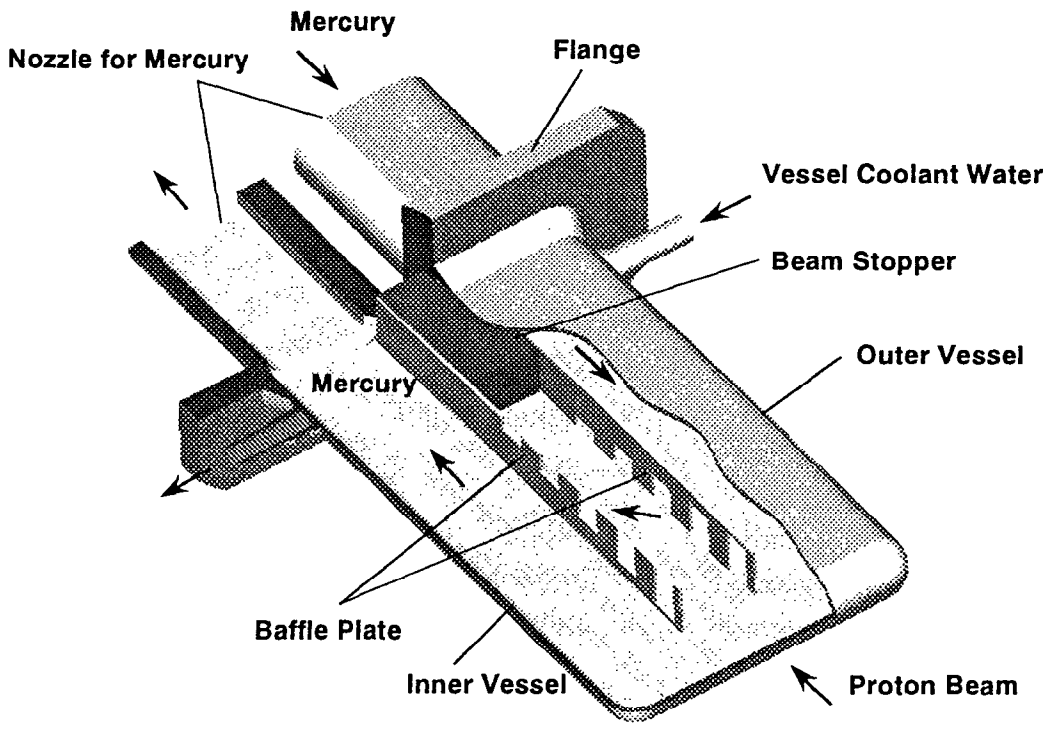

Fig.8 Cutaway view of mercury target -Cross flow type using baffle plates -

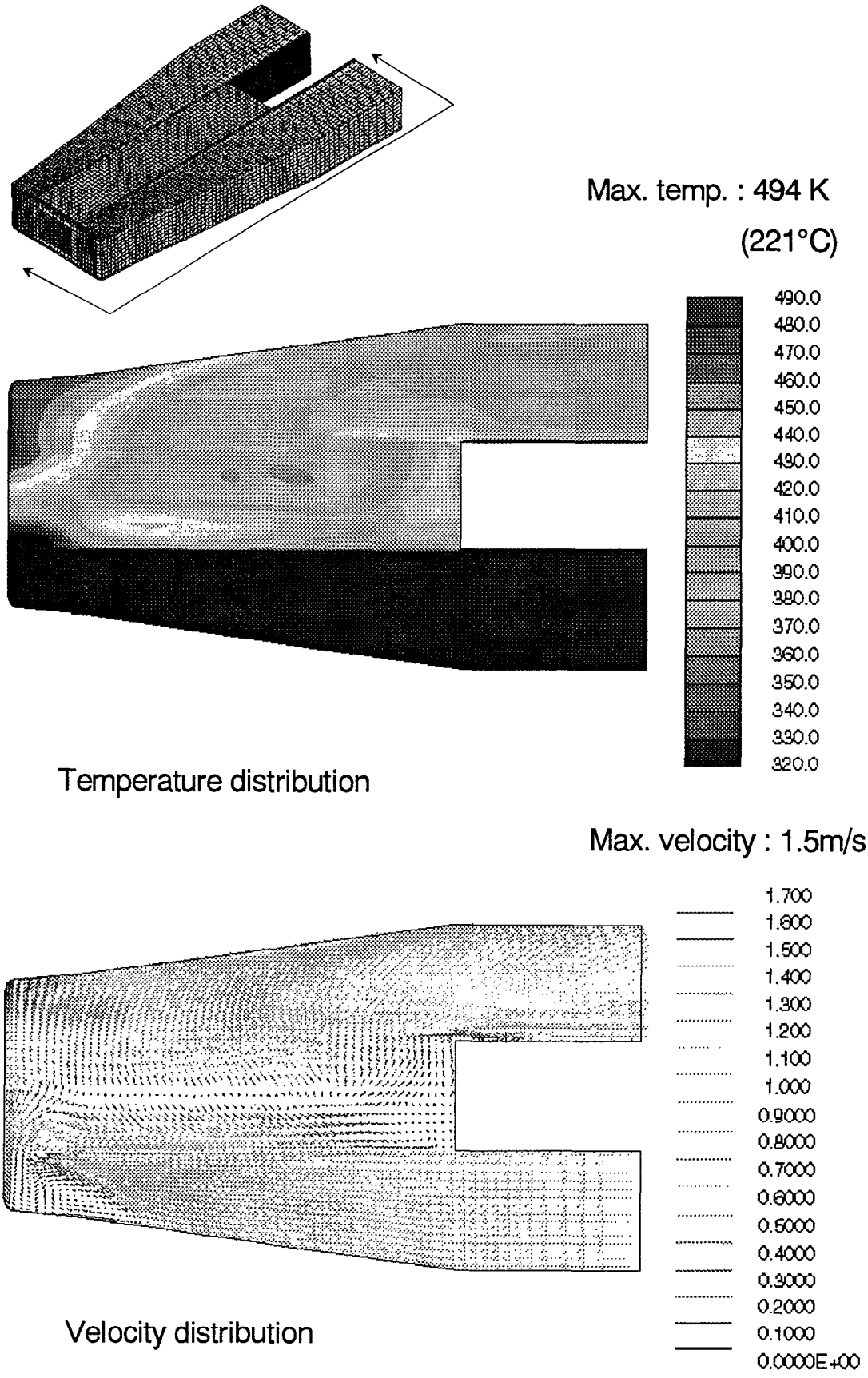

Fig.9 Thermal-hydraulic analysis results of cross flow type mercury target

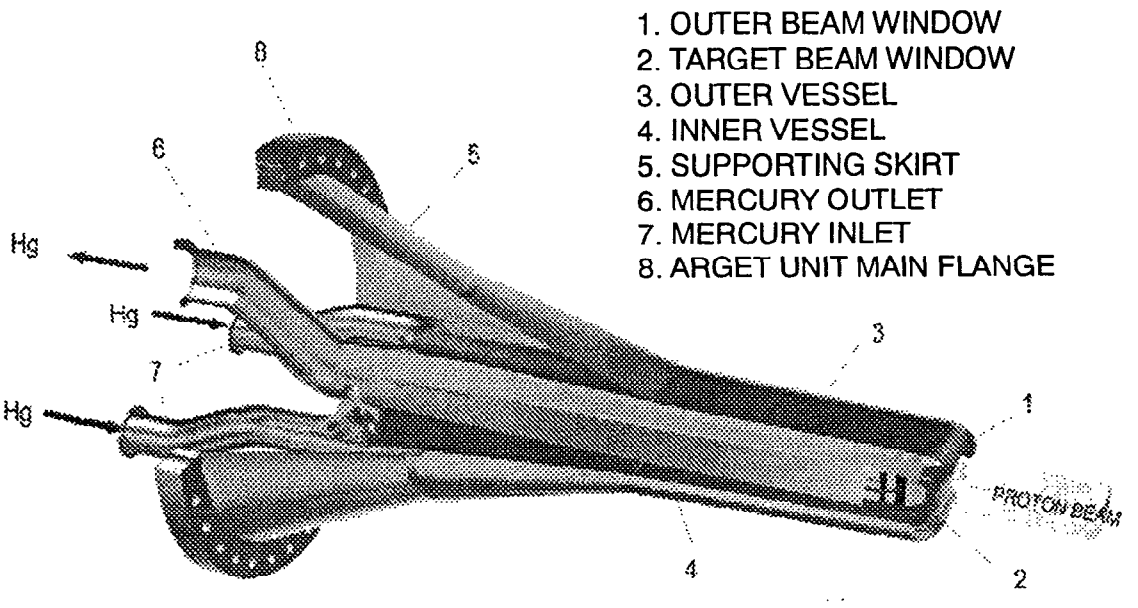

Fig.10 Cutaway view of mercury target - Return flow type

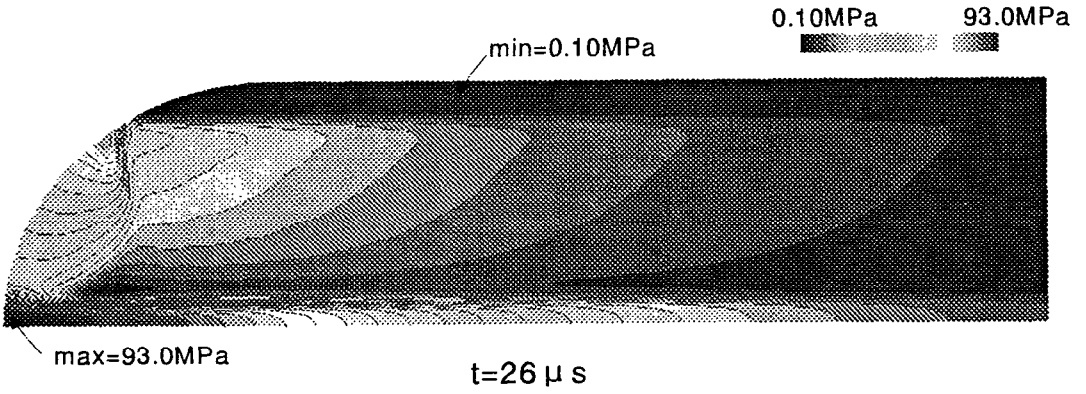

Fig.11 Pressure distribution in the 5MW mercury target
- Pressure contour after 26 μs from proton beam incident -

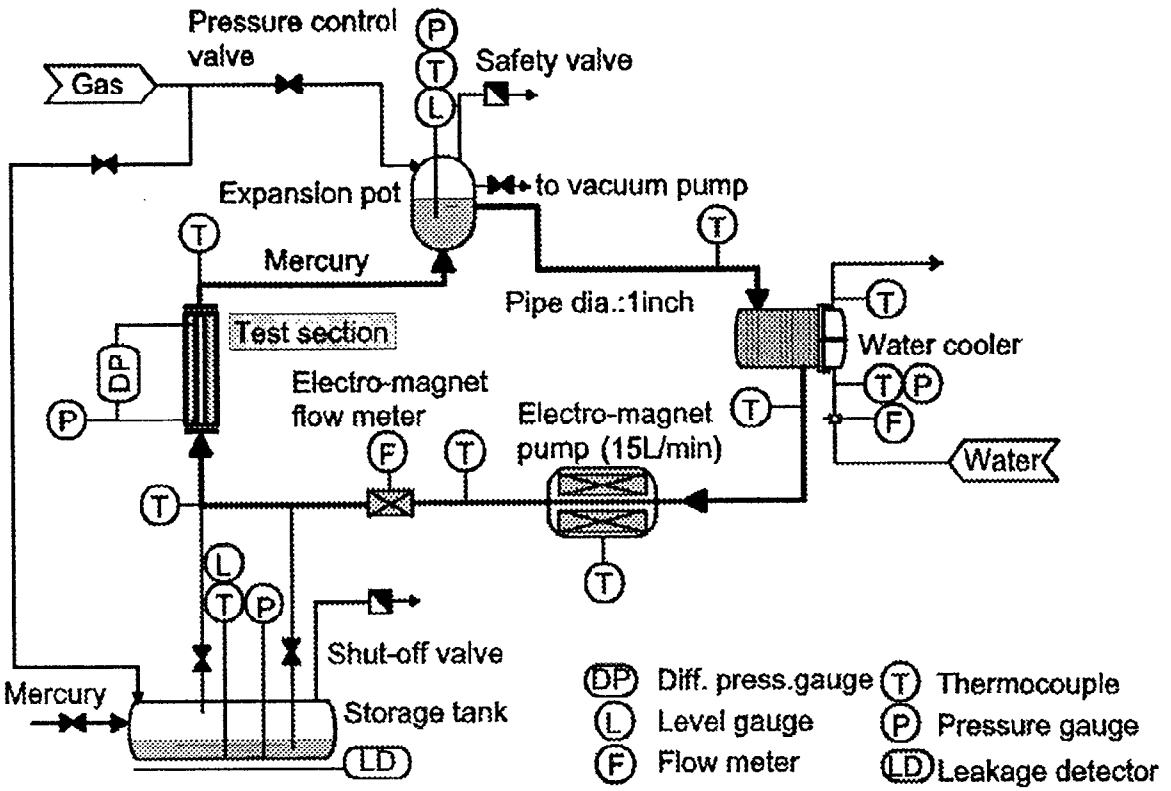

(a) Schematic flow diagram of mercury test loop

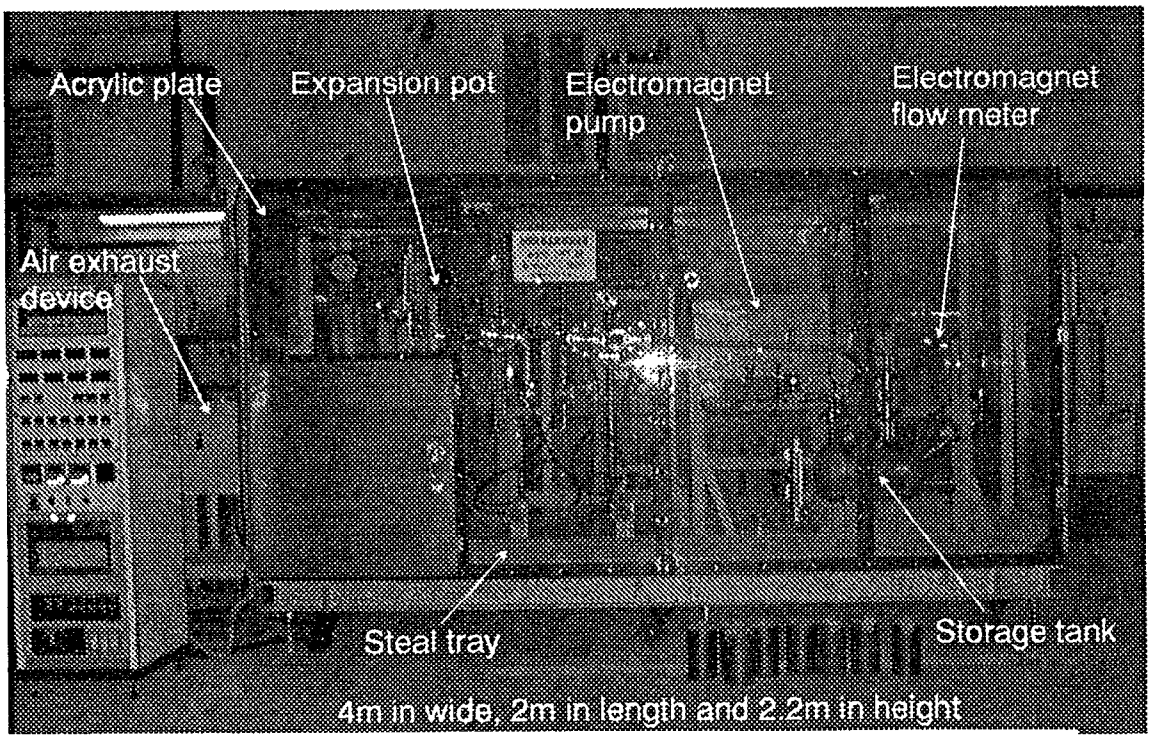

(b) Outer view

Fig.12 Schematic flow diagram and outer view of mercury test loop
Maximum flow rate: 15L/min , Maximum inventory : 400kg

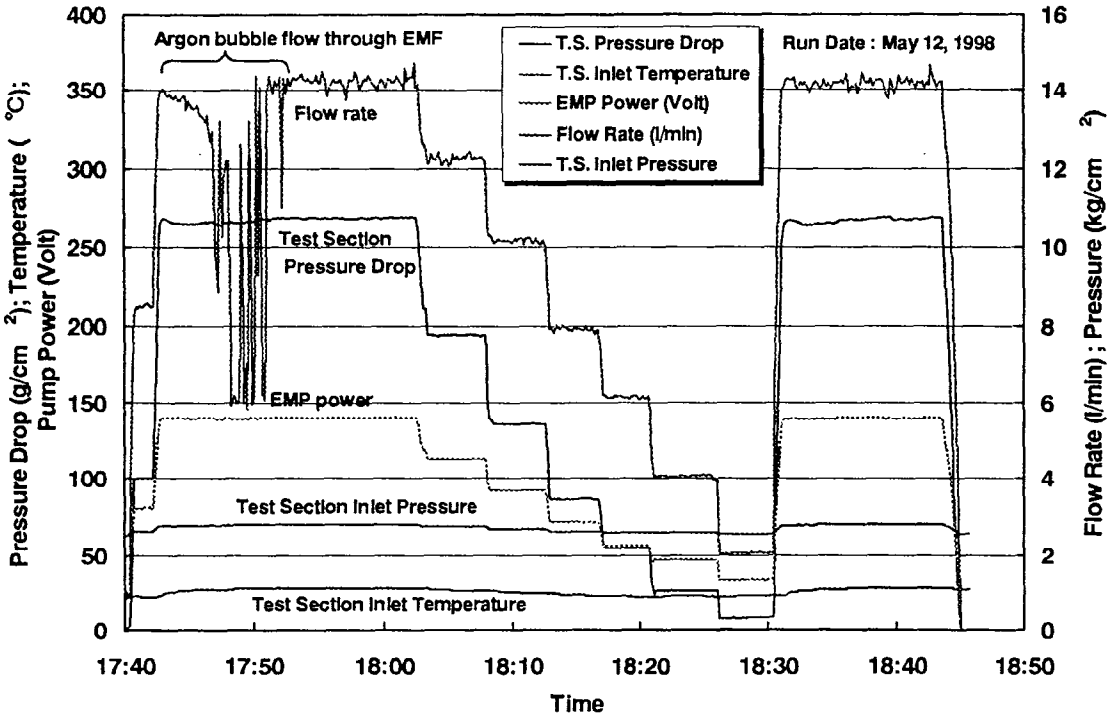

(a) Typical trend graph during loop operation

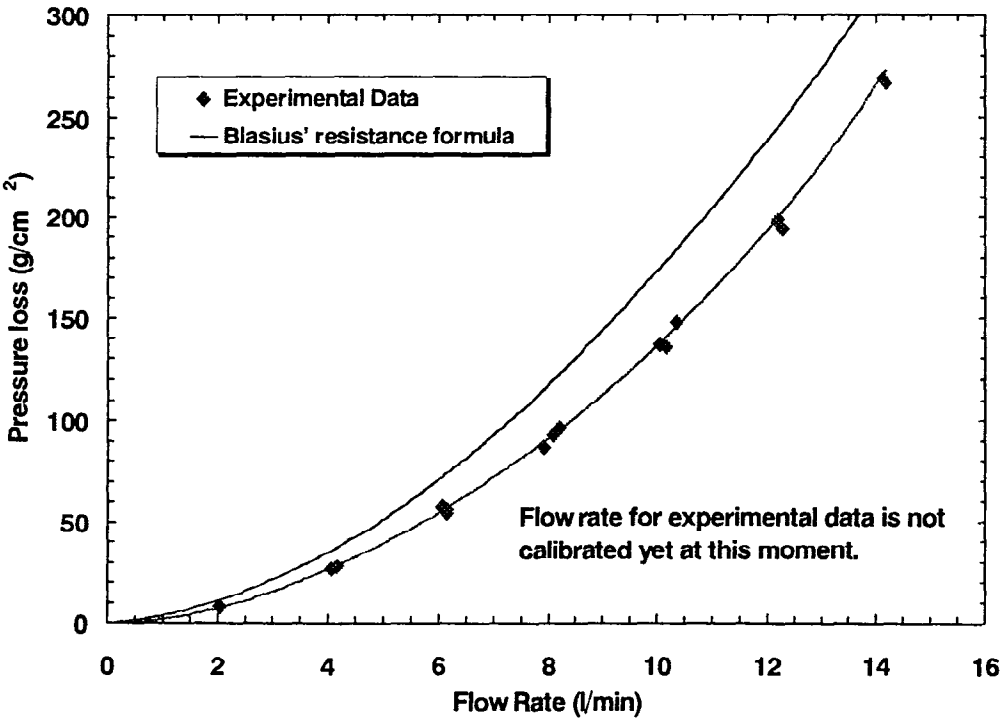

(b) Pressure loss characteristics of a test section

Fig.13 Test results obtained by using a compact-sized mercury loop

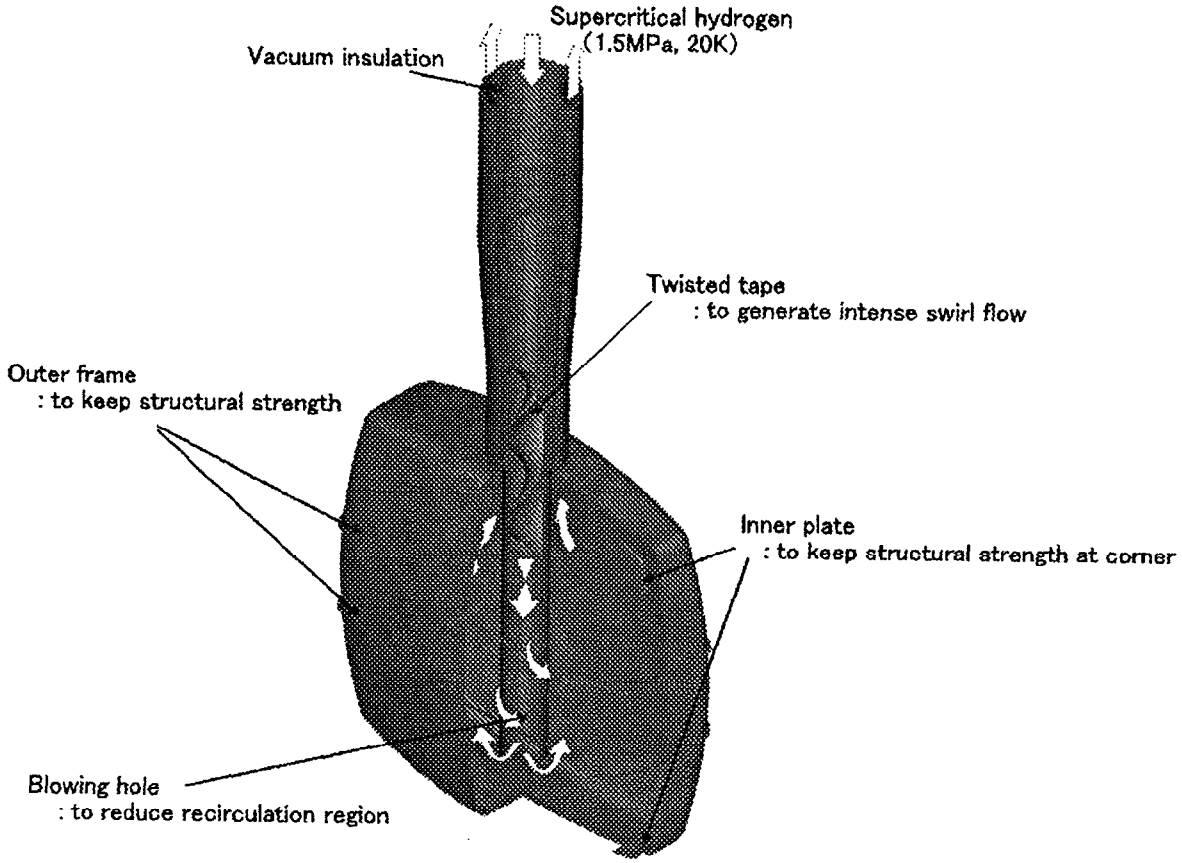

Fig.14 Concept of cold source moderator vessel

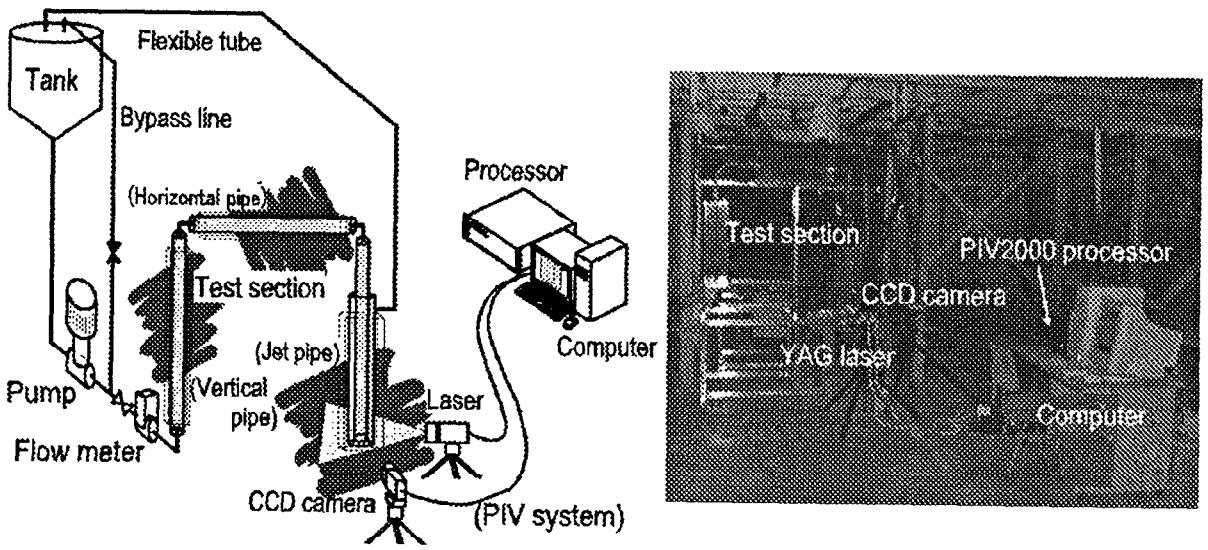

Fig.15 Experimental apparatus for flow pattern measurement

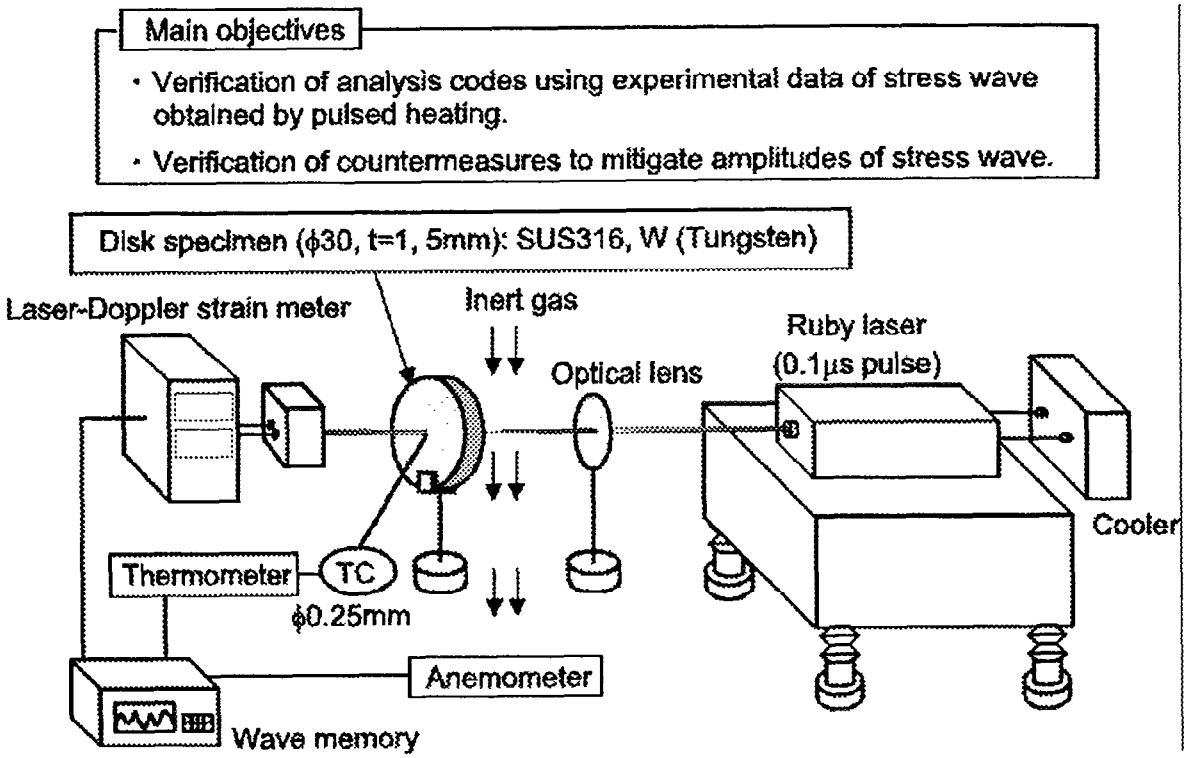

Fig.16 Pulsed heating test apparatus for target materials

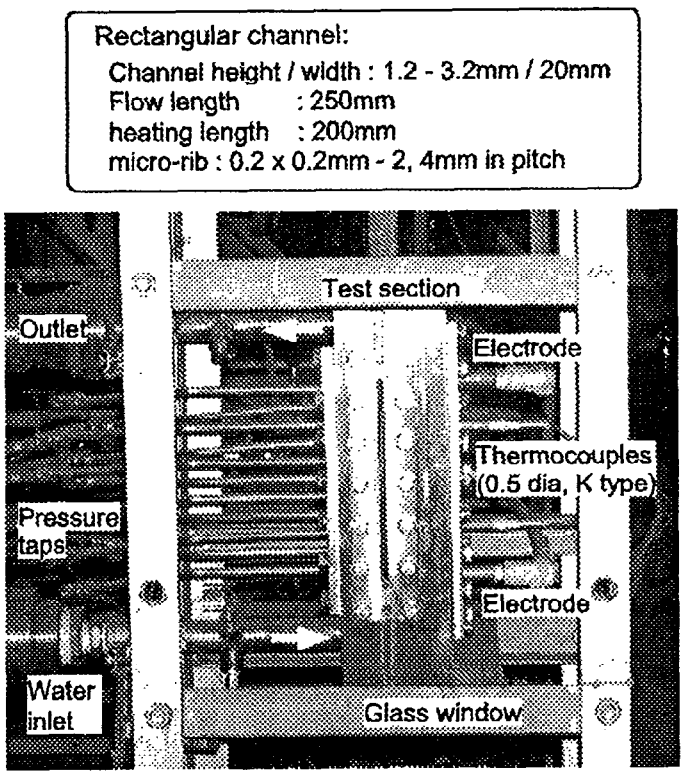

Photo 1 Test section for high heat flux removal transfer
- Simulated solid target cooling channel -

ICANS-XIV
14th Meeting of the International Collaboration on
Advanced Neutron Sources
June 14-19,1998
Starved Rock Lodge Utica, Illinois, USA

Thermal and Hydraulic Design of Mercury Target - Cross Flow Type -

Masanori KAMINAGA, Ryutaro HINO and Akira SUSUKI
Japan Atomic Energy Research Institute (JAERI), JAPAN
Motoaki SAKASHITA
Hitachi Engineering Co., Ltd., JAPAN
Fumito NAKAMURA and Hisato TAGAWA
Hitachi, Ltd., JAPAN

ABSTRACT

For the design of the 5MW mercury target system at JAERI, sufficient heat removal with a slow mercury flow is necessary to prevent corrosion and erosion. In this paper, the conceptual design for the target container of the Cross Flow Type was performed and thermo-hydraulics in the target was numerically investigated with the STAR-CD Code.

It was effective that distribution plates were positioned near the inlet and the outlet in the container and the openings on the distribution plates were made larger near the beam window. As a result, the maximum temperature of mercury was less than 220 C and the maximum flow velocity was less than 1.5 m/s. Simulations with some parameter changes showed that maximum temperature could be reduced further.

1. Introduction

For a target system using a high power proton beam, mercury is the most promising material as spallation target. However, mercury has two undesirable properties: first, it is corrosive at high temperature, and second, it causes erosion when it flows fast. Mercury in the target container can be kept at low temperature if the mercury flow rate is increased, but the mercury flow rate is also restricted by the size of the mercury cooling system and the target container. The size of the target container especially requires the mercury flow rate to be small, because the efficiency of neutron utilization will drop if the target container becomes larger. Therefore, the design of the target container must meet these requirements, that is, it must realize a slow and effective mercury flow that can remove the nuclear heat and keep mercury at low temperature.

Target container can be categorized into the Return Flow Type and the Cross Flow Type according to the mercury flow patterns. In the Return Flow Type target, mercury flows along the proton beam, while in the Cross Flow Type target, mercury flows across the proton beam. Comparing these types, the Cross Flow Type target has more possibility of achieving low temperature with a slow mercury flow, while the appropriate distribution of the mercury flow rate in the target is a difficult problem.

For the development of the 5MW mercury target project at JAERI, in this paper, the conceptual design and elemental specifications of the mercury cooling system was investigated and a prototype model of the Cross Flow Type target was presented. The mercury flow distribution in the target container and its improvements was investigated with the STAR-CD Code.

2. The Conceptual Design of a Mercury Cooling System

Fig. 1 illustrates the conceptual design of a mercury cooling system. As shown in Fig. 1, the mercury cooling system consists of two mercury circulating pumps, two heat exchangers, a surge tank, and two drain tanks, etc. Mercury is driven by the mercury circulating pumps and circulates through the target system. Hot mercury heated in the target is transferred into the surge tank and moved into the heat exchangers. Mercury is cooled below 50 C in the heat exchangers and returns to the target again. The mercury flow rate is set at 50 m^3/h to suppress the temperature rise in the target below 100 C on average. As shown in Fig. 2, the mercury cooling system is installed on a target train. A protective cover encloses all equipment to seal mercury vapor for the accident of mercury leakage from the equipment.

3. The Conceptual Design of a Target Container

3.1 Comparison of Target container type

Target container can be categorized into the Return Flow Type and the Cross Flow Type according to the mercury flow patterns. Table 1 shows the comparison of these two types.

The mercury temperature rise in a target depends on the total heat generated along the mercury flow path. That is, in the Cross Flow Type target, the temperature rise is determined by the total heat integrated along the direction perpendicular to proton beam, while in the Return Flow Type target, the temperature rise is determined by the total heat integrated along the same direction as proton beam. In the case of our beam profile, the total heat generated along the direction perpendicular to proton beam is smaller than that generated along proton beam direction. Therefore, the temperature rise is smaller in the Cross Flow Type target than in the Return Flow Type for the same mercury flow velocity.

The mercury flow velocity in a target depends on the cross sectional area of the channel in the target container. The channel area in the Cross Flow Type target is larger than that in the Return Flow Type target, because the length of the target in the proton beam direction is generally longer than the length across the beam line. Therefore, the mercury flow velocity is

smaller in the Cross Flow Type target than in the Return Flow Type target for the same mercury flow rate.

The size of the Cross Flow Type target is generally larger than the size of the Return Flow Type target, because both an inlet channel and an outlet channel are necessary for the Cross Flow Type target, while the outlet channel is not necessary for the Return Flow Type target.

The technical issue with the Cross Flow Type target is the method of realizing the necessary mercury flow distribution, because the appropriate mercury flow distribution can remove the intense heat and suppresses the temperature rise. In the case of the Return Flow Type target, it is only required for mercury to flow smoothly near the beam window, therefore the flow pattern is simple and the flow distribution is not important.

3.2 The Conceptual Design of a Target Container

Considering advantages and disadvantages discussed above, we selected the Cross Flow Type target and investigated the method to realize the appropriate mercury flow distribution. Fig. 3 shows the illustration of the conceptual design of a mercury target container. The target container is cooled by coolant that flows between the outer and inner containers. Helium gas, light water and heavy water were considered as a candidate. We selected heavy water as a coolant material by following reasons.

(1) In order to remove the generated heat, water coolant is more preferable than helium gas.

(2) Water was not recommended because of vapor explosion possibility in case of inner container failure. This was the reason why helium gas was normally used. However, this possibility is avoidable by keeping mercury at low temperature.

(3) Neutron absorption cross section of heavy water is lower than light water. Therefore, heavy water is better material from the view point of neutron utilization.

The mercury flow crosses the central part of the target, where the pulsed proton beam is injected across the mercury flow and causes heat generation. In order to remove the intense heat near the beam window, the openings on distribution plates near the beam window are designed to be larger than other position. Moreover, the openings on the inlet plate are aligned in the lower part and openings on the outlet plate are aligned in the upper part, so that the heated mercury can flow smoothly with the natural convection.

4. Thermo-Hydraulic Analysis

4.1 Model for Thermo-Hydraulic Analysis

Thermo-hydraulic analysis was carried out with the STAR-CD Code. Computational region was divided into 39,960 cells (X=74, Y=45, Z=12) as shown in Fig. 4. The axial distribution of power density is given in Fig. 5, which is obtained by the averaging the power density calculated by the NMTC/JAERI Code. The mercury flow rate was set at 50 m^3/h and the cross sectional areas of the inlet and the outlet were determined to suppress the mercury flow velocity under 1 m/s. In order to remove the intense heat near the beam window, the openings on distribution plates near the beam window are designed to be larger than other position. The

openings on the inlet plate are aligned in the lower part, while the openings on the outlet plate are aligned in the upper part.

4.2 Results of Thermo-Hydraulic Analysis

Fig. 6 shows the temperature and the velocity distributions of mercury on the middle surface of the target. The maximum temperature of 220 C was observed near the beam window, where the heat generation was relatively large and the mercury flow rate was also relatively small. The maximum flow velocity of 1.5 m/s was observed near the outlet distribution plate. The following two methods for improvement were expected to reduce the maximum temperature:

1st Method Enlarging the cross sectional area of the front part of the target compared to that of the rear part of the target.

2nd Method Increasing the radius of side corner roundness at the front end of the target.

4.3 Effect of Improvements

Simulations with the target containers shown in Fig. 7 were also carried out to prove the effects of 1st & 2nd method on the reduction of temperature. The results are listed in Table 2.

By the 1st method, the maximum temperature could be reduced to about 213 C. On the other hand, the maximum flow velocity increased to about 2.2 m/s, because the cross sectional areas of the inlet and the outlet were decreased. However, the ratio of the maximum velocity relative to the inflow velocity was the same as the base case. Therefore, enlargement of the cross sectional area of the front part in the target container can reduce the mercury temperature without increasing flow velocity. By the 2nd method, the maximum temperature could be reduced to about 211 C, and the maximum velocity was the same as the base case.

These results showed the fact that the maximum temperature could be reduced further by optimizing the shape of the target container.

5. Summary

For the design of the 5MW mercury target system at JAERI, sufficient heat removal with a slow mercury flow is necessary to prevent corrosion and erosion. In this paper, the conceptual design for the target container of the Cross Flow Type was performed and thermo-hydraulics in the target was numerically investigated with the STAR-CD Code.

It was effective that distribution plates were positioned near the inlet and the outlet in the container and the openings on the distribution plates were made larger near the beam window. As a result, the maximum temperature of mercury was less than 220 C and the maximum flow velocity was less than 1.5 m/s. Simulations with some parameter changes showed that maximum temperature could be reduced further.

References

(1) H.TAKADA, N.YOSHIZAWA, K.KOSAKA, K.ISHIBASHI, "An Upgraded Version of Nucleon Meson Transport Code : NMTC/JAERI97", JAERI-Date/Code 98-005, February 1998.

(2) R.HINO, M.KAMINAGA, T.ASO, H.KOGAWA, S.ISHIKURA, A.SUSUKI, A.TERADA, H.KINOSHITA and K.HAGA, "Spallation Target Development at JAERI", June,1998,

(3) R.HINO, K.KAMINAGA, S.ISHIKURA, I.YANAGISAWA, M.UZAWA, K.KUROSAWA, K.IKEDA and S.UCHIDA, "Preliminary Design of Mercury Target -Return Flow Type-", June, 1998.

Table 1 Comparison of Mercury Flow Type between Cross Flow Type and Return Flow Type

Flow Type	Cross Flow Type Proton Beam 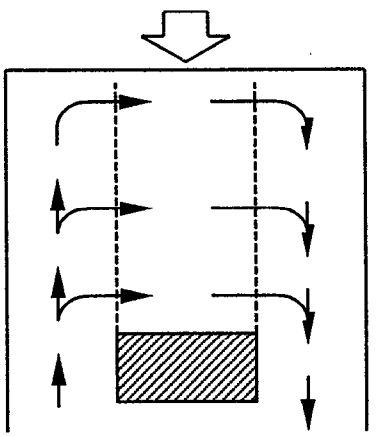	Return Flow Type Proton Beam 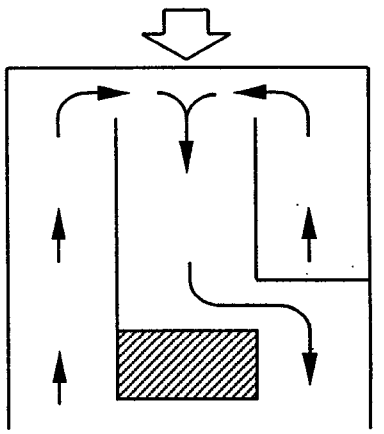
Max. Temperature	Low O	High
Mercury Velocity	Low O	High
Container Size	Large	Small O
Flow Distribution	Complicated	Simple O

Table 2 Result of Parameter Survey Analysis

Item	Inlet & Outlet Channel Size (mm)	Max. Temp. (C)	Max. Velocity (m/s)	$\left[\frac{\text{Max. Vel.}}{\text{Inflow Vel.}}\right]$ (%)
Base case	W145×H98	220	1.5	149
1st method	W 98×H98	213	2.2	148
2nd method	W145×H98	211	1.5	149

Note : Mercury flow rate : $50m^3/h$

Mercury inlet temperature : 50C

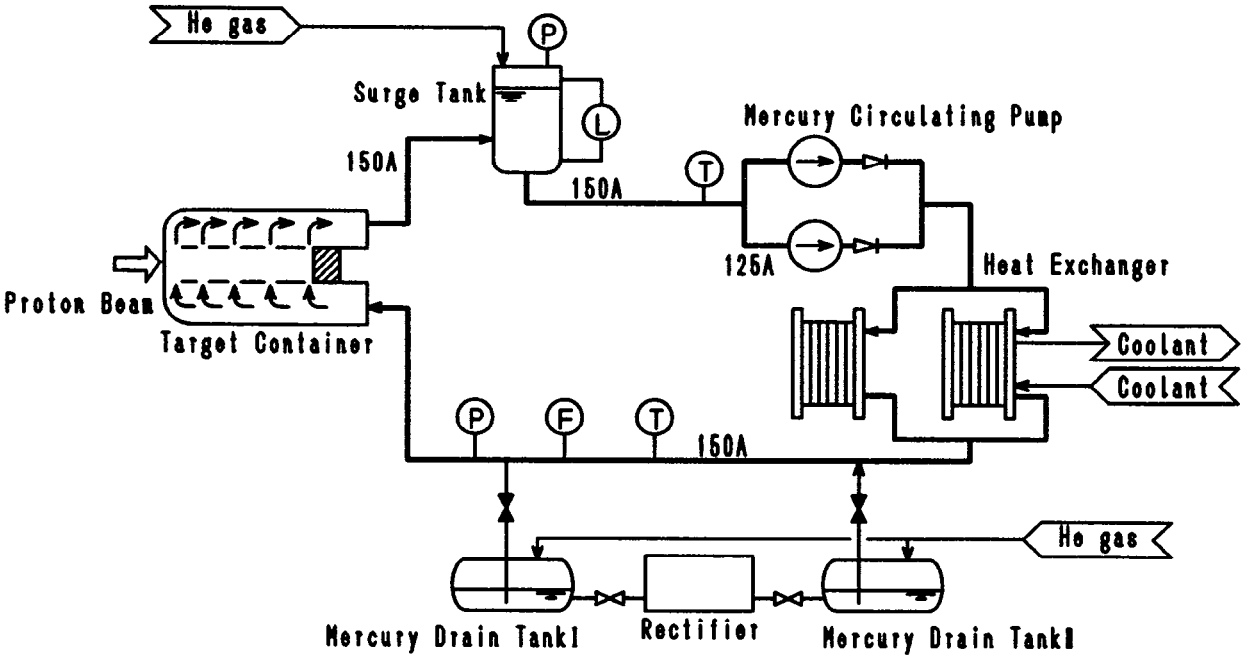

Fig. 1 Conceptual Diagram of Mercury Cooling System

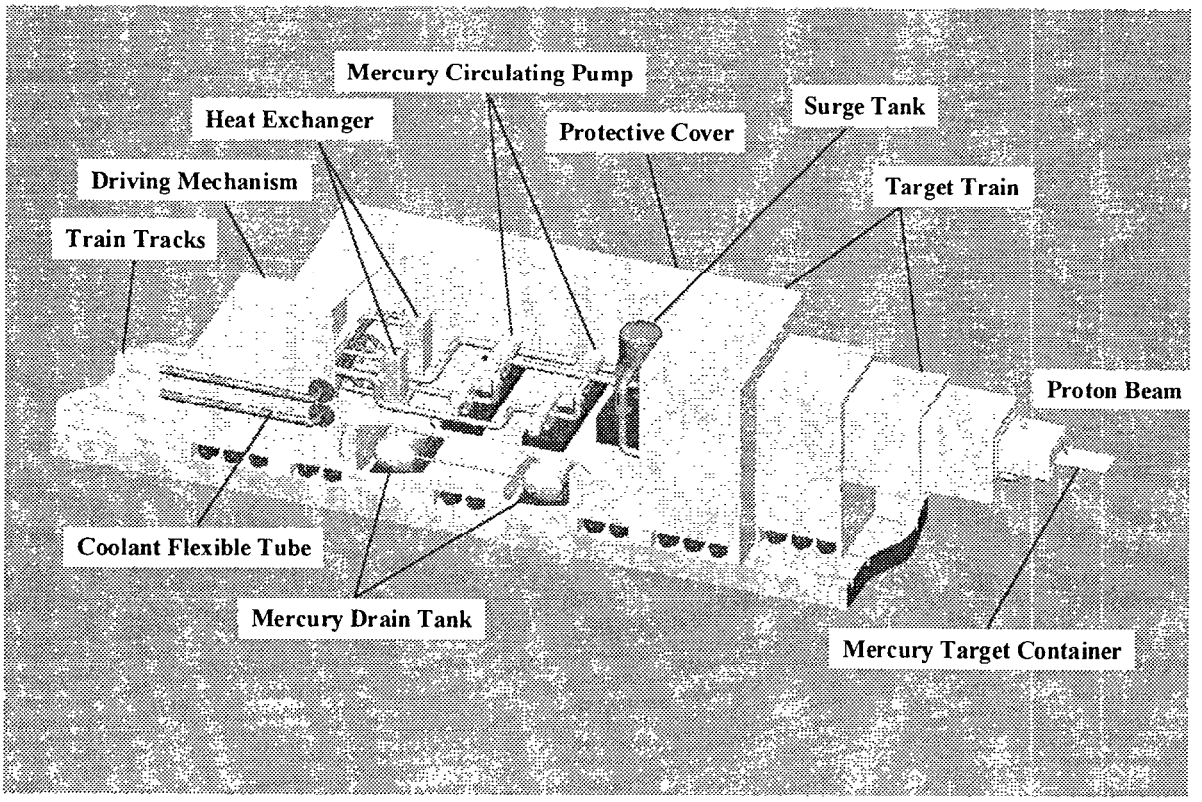

Fig. 2 Bird-eye View of Mercury Cooling System

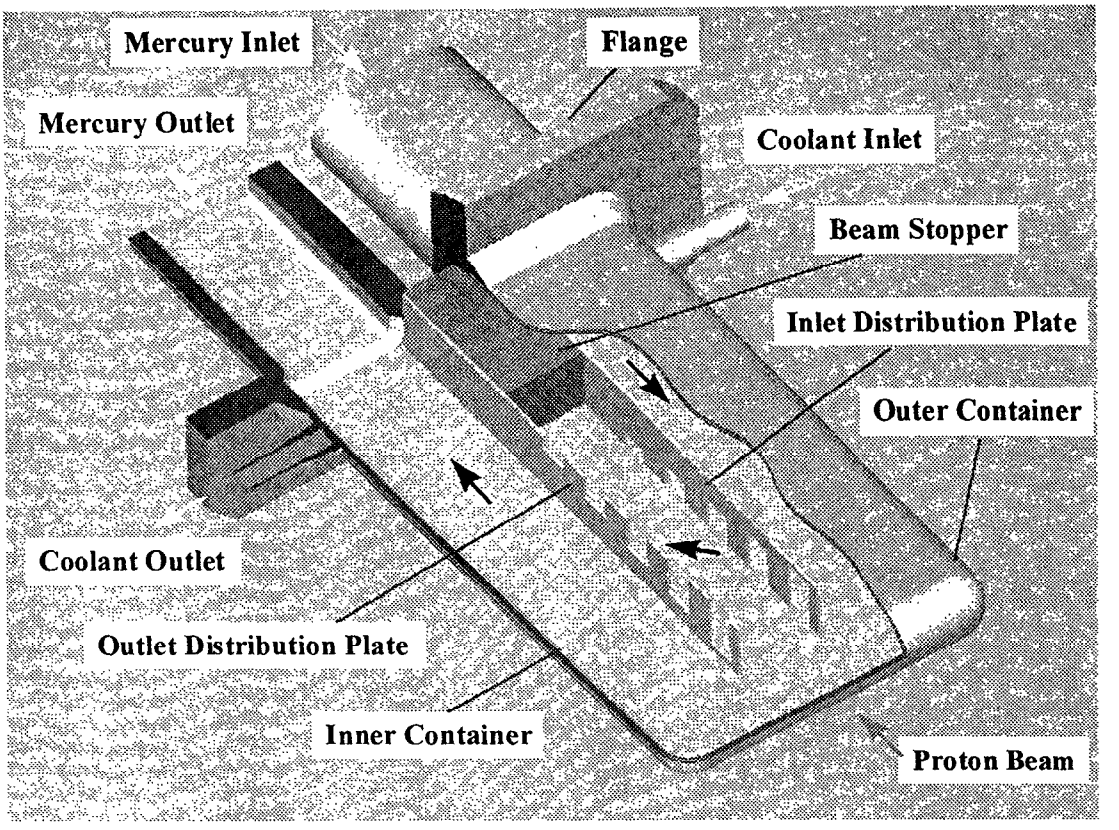

Fig. 3 Illustration of Mercury Target Container of Cross Flow Type

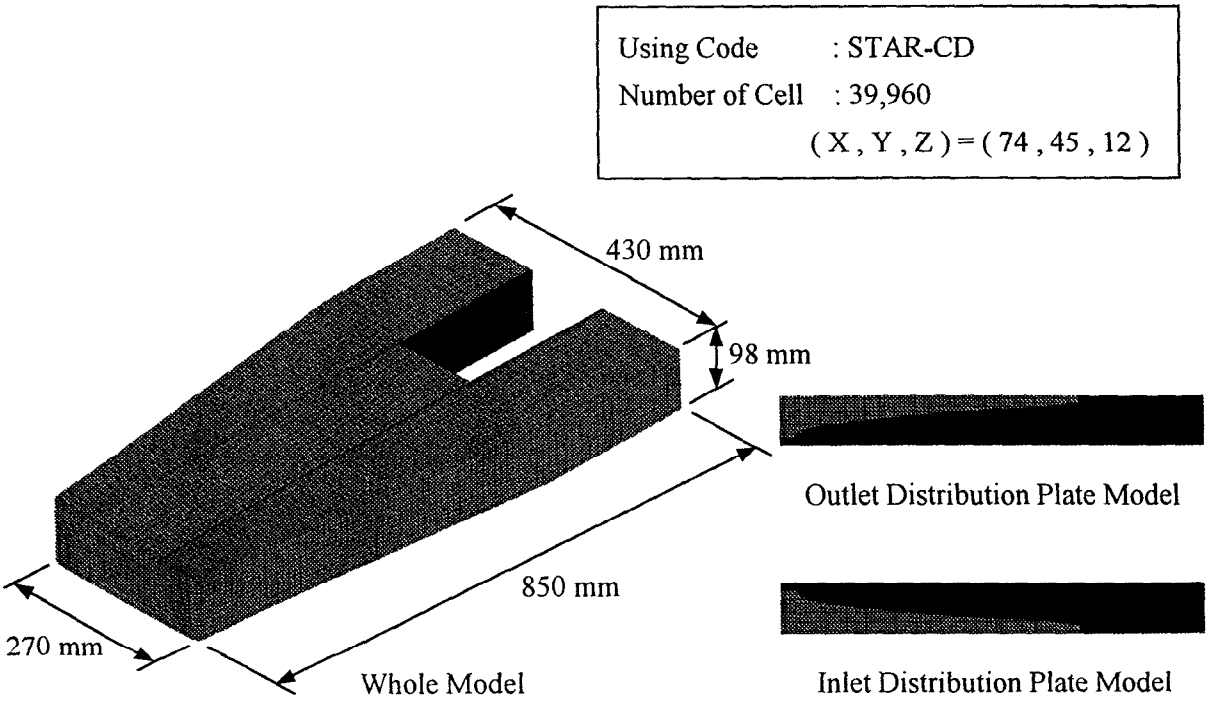

Fig. 4 Model for Thermo-Hydraulic analysis

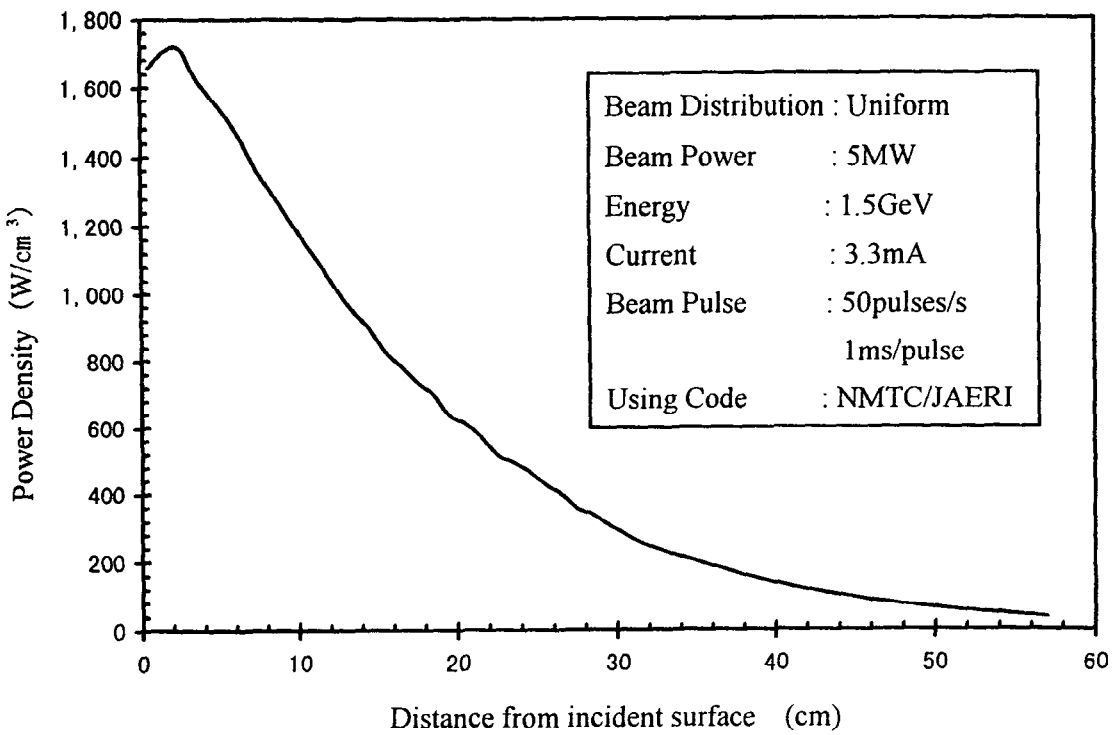

Fig. 5 Axial Distribution of Power Density in Mercury Target

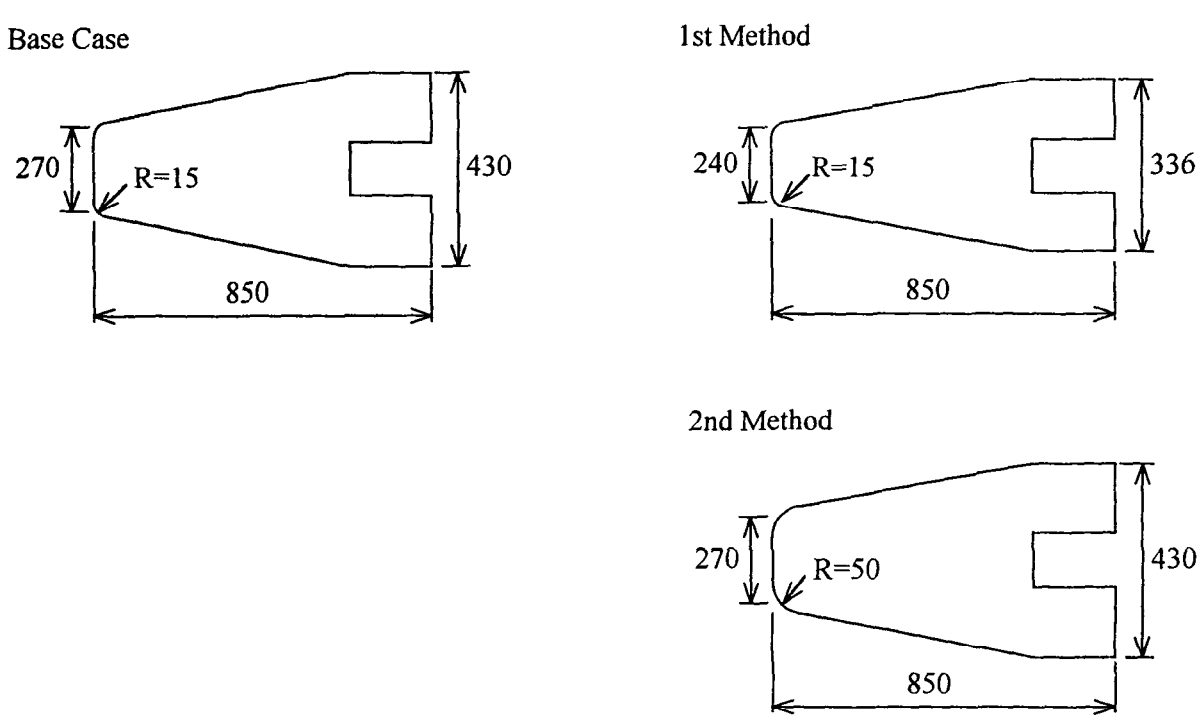

Fig. 7 Mercury Container Shape for Parameter Survey Analysis

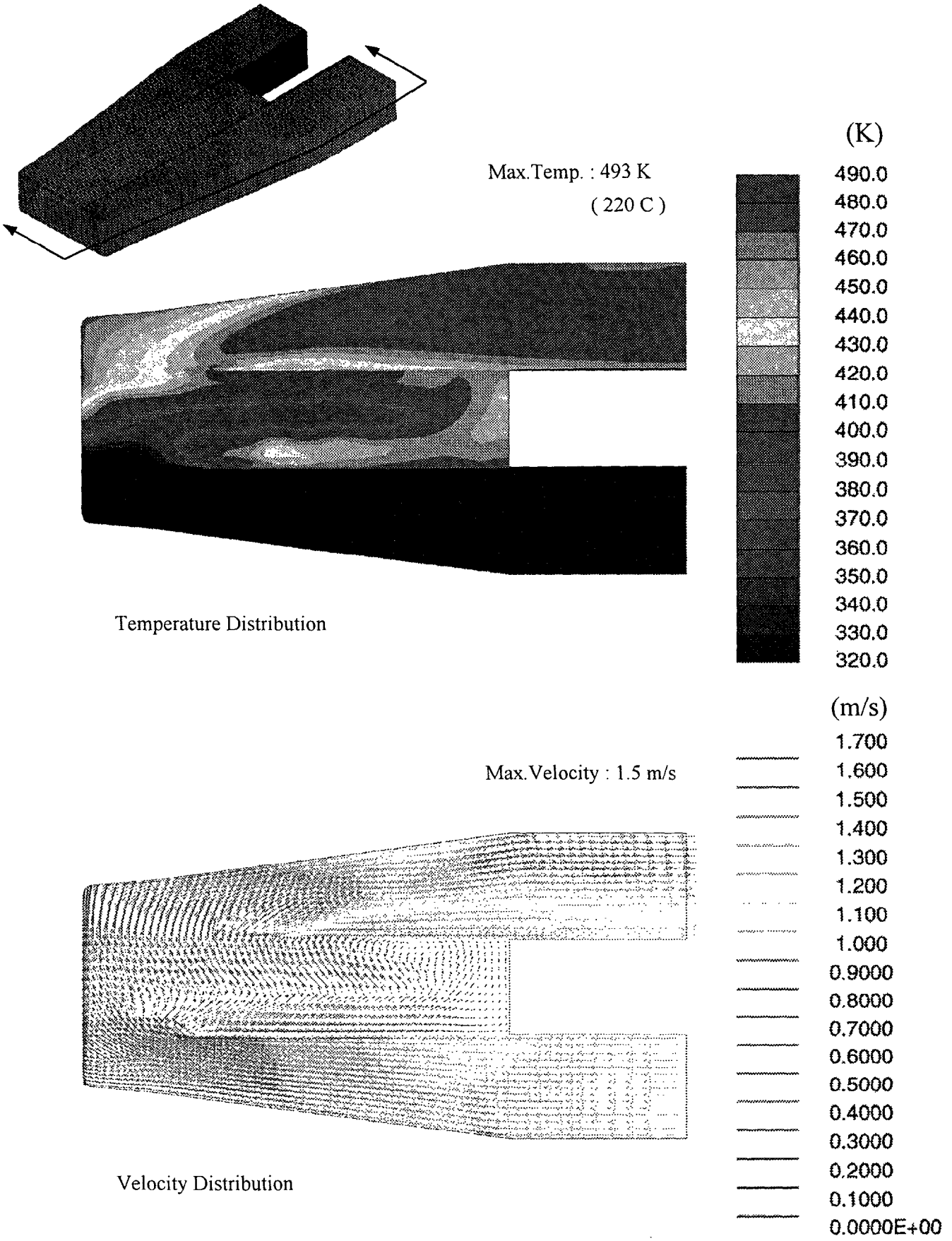

Fig. 6 Result of Thermo-Hydraulic Analysis in Mercury Target of Cross Flow Type

ICANS-XIV
14th Meeting of the International Collaboration on
Advanced Neutron Sources
June 14-19,1998
Starved Rock Lodge, Uthica, Illinois, USA

Preliminary Design of Mercury Target - Return Flow Type -

Ryutaro Hino [*1], Masanori Kaminaga [*1], Shuichi Ishikura [*1], Ichiro Yanagisawa [*2], Masayuki Uzawa [*2], Katsutoshi Kurosawa [*3], Kazumi Ikeda [*3], Shouji Uchida [*4]

ABSTRACT

A preliminary design of 5MW RFT (Return Flow Type) mercury target for JAERI neutron source project has been carried out. Major design parameters and the target geometry were determined based on thermal and structural analyses. Structural and thermal-hydraulic analyses show that the RFT target design is a feasible candidate for JAERI's 5MW mercury target.

1. Introduction

In the development of 5MW mercury target for Japan Atomic Energy Research Institute (JAERI) Spallation Neutron Source project, two types of mercury target concepts, Cross Flow Type (CFT) target and Return Flow Type (RFT) target, have been investigated [1].

In CFT target concept [2], mercury flows crossing (perpendicular to) the proton beam in the beam reaction zone. On the contrary, in RFT target concept, mercury enters the beam reaction zone from both sides of the inlet channel, returning at the beam window. Proton beam bombards parallel flowing mercury in the outlet channel. The potential merits of the RFT target are summarized as follows:

(1) Smaller Target Size
For CFT target, inlet cold plenum region to produce the crossing flow and outlet hot plenum one to accept the flow will be necessary for each side respectively, therefore the CFT target size will be increased compared with the RFT target with entry flow from both sides.

(2) Simple Flow Pattern
The flow pattern of the basic RFT is very simple compared with CFT design where complex flow distribution from the inlet plenum region to the outlet plenum must be designed.

In this paper, we will describe the result of the preliminary design of the RFT mercury target, especially attention to the structural and thermal-hydraulic analyses performed to confirm the feasibility as a candidate for JAERI 's 5MW target.

2. RFT Target Design Description

2.1 Design Condition

*1 Japan Atomic Energy Research Institute
*2 Mitsubishi Heavy Industries, Ltd. Kobe Shipyard & Machinery Works
*3 Mitsubishi Heavy Industries, Ltd. Nuclear Energy Systems Engineering Center
*4 ADVANCED REACTOR TECHNOLOGY Co., Ltd.

Table 1 summarizes the system parameters of the incident proton beam on the mercury target.

Proton beam with uniform profile and rectangular shape is assumed in this study. Assuming that the maximum acceptable current density of the proton beam at the beam window is 48 microA/cm^2, the proton beam size is determined to be 6.88cm in height and 10.0cm.

2.2 RFT Target Design Concept and Geometry

The energy deposition in the target was calculated by using a high-energy hadron transport code system LCS (LAHET code system). The total energy deposition is 744 kW/mA, which is about 50% of the beam power. This result is consistent with that of NMTC-JAERI code. Therefore we use the result of LCS in this study.

Figure 1 shows a schema of the RFT target concept. The following coolant design conditions were adopted:

Volumetric Flow Rate:	40m^3/h
Velocity:	< 1m/s
Pressure:	0.5MPa
Inlet Temperature:	70 deg.C
Outlet Temperature:	200 deg.C (mixed mean)

The mercury velocity was restricted below about 1 m/s in order to mitigate the effect of mercury erosion damage on the structural material surface.

Figure 2 shows the geometry of the RFT target design. The target consists of the followings:

The Mercury Target Shell (Inner Vessel)
The Leak Jacket (Outer Vessel)
Target Unit Main Flange
Supporting Skirt
Mercury Inlet Pipe (two)
Mercury Outlet Pipe

The target with a height of 119 mm, a width of 359 mm, and a length of 650 mm is connected with two mercury inlet pipes and one outlet pipe. The leak jacket is designed as a barrier for mercury leakage prevention to helium vessel in case of the target beam window failure. SUS316 is employed as the target structural material.

3. Structural Analysis

3.1 Structural Analysis of Target Inner Vessel

Structural analysis has been performed to determine the basic design specification of target inner vessel. The tentative design criteria for the stress and the displacement of the vessel is assumed as follows:

Stress < $1.5S_m$ (206MPa at 100 deg.C, 179MPa at 300 deg.C for SUS316)
, where S_m is the design stress intensity limit.

Displacement < 1mm

Parametric survey was carried out step-by-step from a simple vessel model to a reinforced model with ribs and webs. The shell model was used for the calculation. The result is summarized in Table 2.

<u>Model-A</u>

The thickness (t_1 and t_2 in Table 2) and the length (L_1 and L_2) of upper & lower walls are parameters. Among Model-A calculations, A-3, with a thickness t_1, t_2 of 10mm showed a rather good result that the maximum displacement and the maximum stress are 1.6mm and 229Mpa,

respectively. However, the thickness of 10mm is too thick to realize better neutronics performance, and the result did not satisfy the design criteria, therefore the model was withdrawn.

Model-B

Ribs (with a height of h in Table 2) on the upper and lower walls and two webs between upper and lower walls were added to improve Model-A. The wall thickness is fixed as 5mm. In all cases (h=0mm, 15mm and 30mm), this model satisfied the design criteria. The ribs on the upper and lower walls are not always necessary to install, but two webs shall be essential to prevent large displacement of both walls.

Model-C

In this case only two ribs between upper and lower wall exist as reinforcement member to Model-A. The head part and bottom part thickness (t_a and t_b in Table 2) of the upper & lower walls are the parameters. When the head part thickness is 5 mm and the bottom part thickness is 15 mm (C-1), the maximum displacement is 0.69mm and the maximum stress is 168Mpa, which satisfy the stress and displacement criteria. Therefore Case C-1 is adopted for further design study.

3.2 Lifetime Estimation

Lifetime of the beam window due to the thermal cycle fatigue was estimated by using the design fatigue limit curve for SUS316. There are two types of thermal cycles to be considered:

(1) Thermal Cycle due to Normal/Off-normal Beam Shut Down Incident
(2) Thermal Cycle due to 50 Hz Pulse Operation

Figure 3 shows the relationship between the wall temperatures (the maximum temperature in the wall, Hg side temperature and D_2O side temperature) and the wall thickness obtained by 1-D thermal calculation of the beam window. The result shows that the temperature difference within the beam window is 71 degrees at the target beam window and 110 degrees at the leak jacket. The strain of the leak jacket is 0.00282 and the fatigue limit is estimated to be 1×10^5 cycles. Because the frequency of the occurrence of beam shutdowns more than 1 minute is anticipated to be 200 times a week, the 1×10^5 cycles corresponds to approximately 10 years operation.

The energy deposition rate per pulse in the target beam window and the leak jacket window is estimated to be 2.77kcal/s/mm^3. So the maximum temperature rise during one pulse is about 3 deg.C. Hence the thermal fatigue effect due to 50Hz-pulse operation on both beam windows is negligible by small.

The result of the lifetime estimation is summarized in Table 3. For more precise estimation, radiation damage of the wall material and the fatigue due to pulsed pressure wave should be considered.

4.Thermal-hydraulic Analysis

A three-dimensional thermal-hydraulic analysis has been carried out. The purpose of this analysis is to design flow configuration of the RFT target and to confirm that the RFT target can remove the generated heat effectively and, as the result, can assure its structural integrity. The following values were used as tentative judgement criteria for this thermal-hydraulic analysis:

(1) No boiling in mercury(bulk): $T_{Hg} < 358$ deg.C (at 0.1MPa)
(2) Structural material temperature limit: $T_{st} < 400$ deg.C

Criteria (2) requires that the maximum mercury temperature near the target beam window should be below 330 deg.C because 1-D thermal calculation result (Figure 3) showed that the temperature

difference between the maximum temperature in the beam window and the mercury temperature is approximately 70 deg.C. However more detailed analysis should be required to confirm this value.

SALE-3D [3] computer code, which is a simplified ALE computer program originally developed by Los Alamos National Laboratory, is use. The structure surface is treated as adiabatic, therefore no heat conduction between mercury and target structure is considered. Velocity constant and pressure constant condition are used for the coolant inlet and outlet, respectively. The heat deposition profile calculated by LCS is used.

Figure 4 shows the design approach of the flow configuration of the RFT target. As described in section 1, the RFT target design has some potential advantages such as smaller target size and simple flow pattern. Here, we tried to find feasible solution for the thermal-hydraulic problem for the compact FRT target design.
The result of the analysis is summarized in Table 4.

CASE-1
This reference case has a symmetric flow configuration. Mercury enters the beam reaction zone from both sides and bottom of the inlet channel, returning at the beam window. Figure 5 shows the calculated temperature profiles on the vertical and horizontal planes where the maximum temperature occurs. Although the flow pattern of this case is very simple, that is a potential merit of RFT target, the stagnant flow region occurs near the target beam window, and therefore hot zone exceeding mercury boiling temperature occurred in the center line near the beam window.

CASE-2
In CASE-2, flow configuration was modified to give asymmetric flow to reject a stagnant flow region near the center of the beam window. As shown in Figure 6, the stagnant flow near the beam window is diminished but the re-circulating flows occurred inside the outlet channel. As the result, hot zone occurred (Tmax=380 degree C) in the outlet channel.

CASE-3
To prevent the formation of re-circulating flow in the outlet channel, side holes are installed on the outlet channel box of CASE-2. As shown in Figure 7, the re-circulating flow still remains, but the effect is rather mitigated. In this case the maximum mercury temperature is below the boiling point (358 deg.C at 0.1MPa).

CASE-4
This case is the same configuration as CASE-3, but the flow rate is increased from 40 m^3/h to 44 m^3/h (10% up). The result (Figure 8) shows that the maximum temperature of the re-circulation flow regions well decreased to marginal value.

As the result of a series of analyses, it was demonstrated that the modified RFT target, which employs asymmetric flow and side holes, could keep maximum mercury temperature below boiling point. Therefore, we concluded that the modified RFT target is also a feasible candidate for JAERI's 5MW mercury target.

5. Conclusions

As a first step of the JAERI's 5MW mercury target development, the basic structure of the Return Flow Type (RFT) target has been investigated.
The structural analysis showed that the target structure with 2 mm thickness beam window and 5 mm thickness upper and lower walls is feasible by incorporating two webs between upper and lower walls of the target.

Thermal-hydraulic analysis showed that hot zone exceeding mercury boiling temperature occurred in the centerline near the beam window of reference RFT target. The modified RFT target, which employs asymmetric flows and side holes, can keep maximum mercury temperature below boiling point. Therefore, we concluded that the modified RFT target is also a feasible candidate for JAERI's 5MW mercury target.

REFERENCES

[1] R.Hino et al, "Spallation Target Development at JAERI", ICANS-XIV, 1998

[2] M.Kaminaga et al., "Thermal and Hydraulic Design of Mercury Target - Cross Flow Type-", ICANS-XIV, 1998

[3] A.A.Amsden and H.M.Ruppel, "SALE-3D: A Simplified ALE Computer Program for Calculating Three-Dimensional Fluid Flow", NUREG/CR-2185 LA-8905, 1981

Table 1 Proton Beam Parameters

Proton beam	Energy (GeV)	1.5
	Profile	uniform rectangular
	Size	$6.88cm^H \times 10.0cm^W$
	Current	3.33 mA

Table2 Result of Structural Analysis

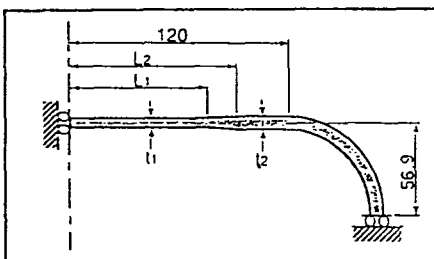

Case	t_1 [mm]	t_2 [mm]	L_1 [mm]	L_2 [mm]	Max. Disp. [mm]	Max. Stress [MPa]
A-1	5	5	—	—	10.7	687
A-2	3	10	70	110	5.0	475
A-3	10	10	—	—	1.6	229

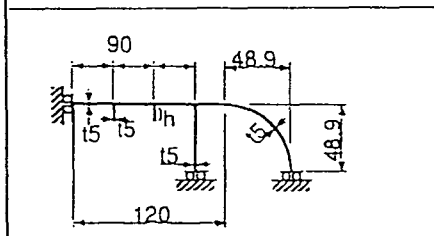

Case	Rib Height h [mm]	Max. Disp. [mm]	Max. Stress [MPa]
B-1	0	0.25	86.7
B-2	15	0.15	86.0
B-3	30	0.11	64.7

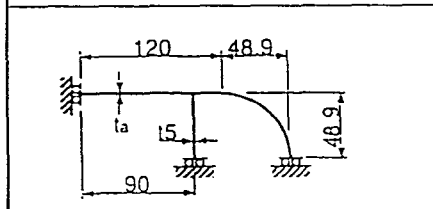

Case	Head t_a[mm]	Bottom t_b[mm]	Max. Disp. [mm]	Max. Stress [MPa]
C-1	5	15	0.69	168
C-2	3	15	2.62	497
C-3	5	5	1.10	236

Table 3 Estimated Lifetime

	ΔT[°C]	T_{max}[°C]	Strain ε	Life Time
Target Beam Window	71	210	0.00178	$>1\times10^6$
Leak Jacket Window	110	260	0.00282	$>1\times10^5$

$$\varepsilon = \frac{\alpha\Delta T(1+\nu)}{2(1-\nu)}q$$

α: thermal expansion coefficient μ: Poisson ratio q=1.5

Table4 Result of Thermal Hydraulic Analysis

Model		Flow Rate [m³/h]	Maximum Mercury Temperature[°C]		Remarks
			Whole Region	Near Beam Window	
Case 1	Reference	40	474	474	×
Case 2	Asymmetric Flow without side holes	40	380	260	×
Case 3	Asymmetric Flow with side holes	40	356	283	○
Case 4	Up Flow Rate of Case 3	44	343	228	○

○ acceptable × not acceptable

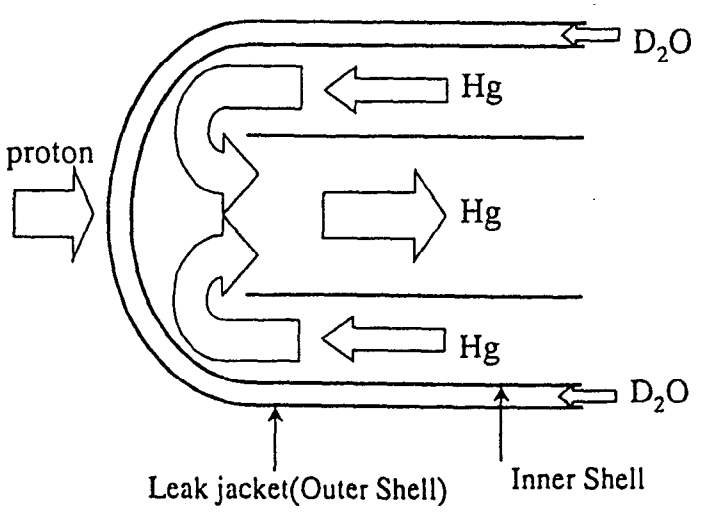

- Mercury(Hg) flows along the proton beam direction and returns at the beam window
- Mercury Coolant
  - Flow rate: 40m³/h
  - Velocity < 1m/s
  - Pressure : 0.5MPa
  - Inlet temperature : 70 °C
  - Outlet temperature: 200 °C
- Target cross section: 119mm^{H} 359mm^{W}
- Leak jacket : Mercury leakage prevention to helium vessel in case of mercury beam windows failure
  - Inlet temperature: 45 °C
  - Outlet temperature: 56 °C
- Structural material : SUS316

Figure 1 RFT Target Concept

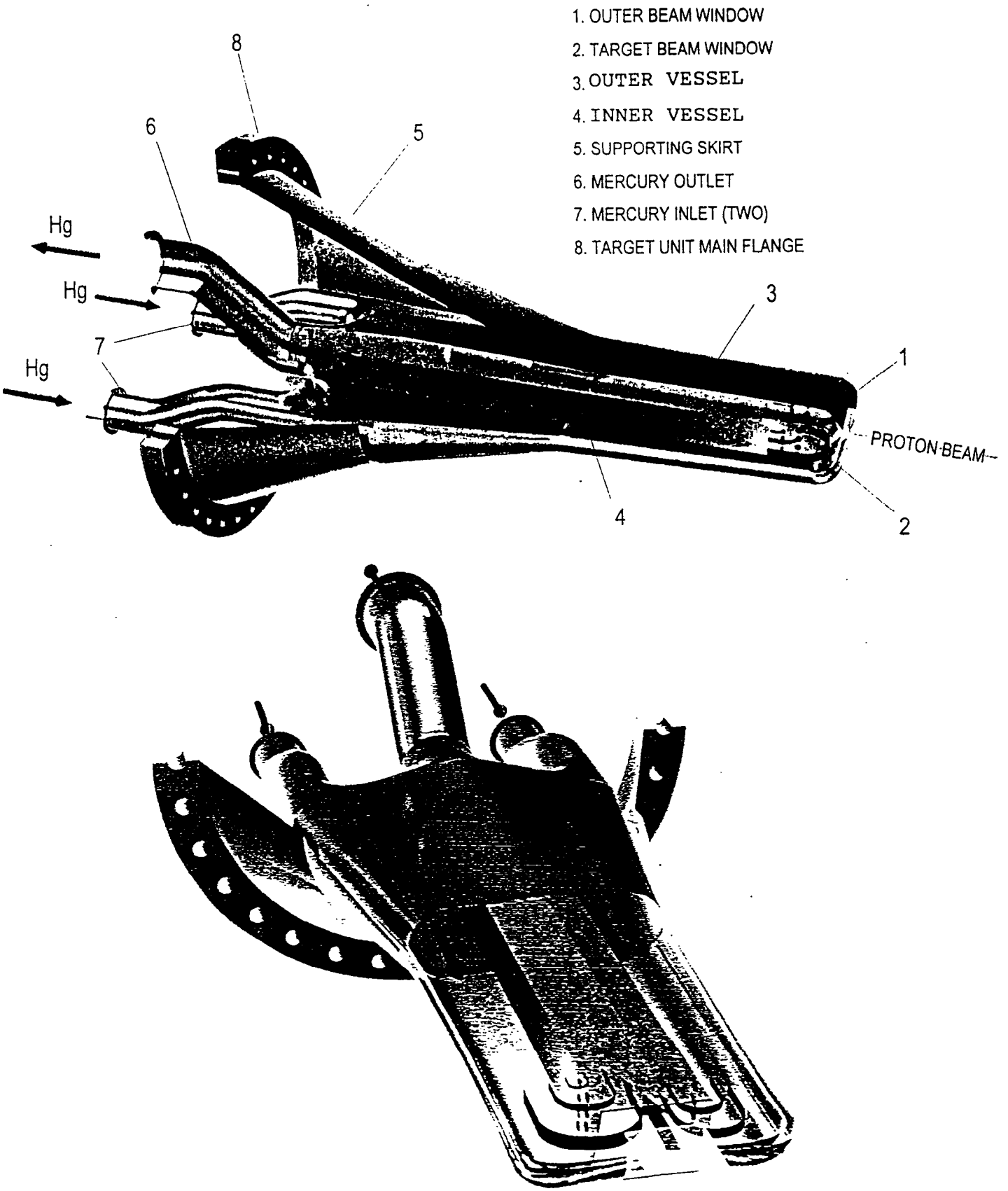

Figure2 View of Return Flow Type Target

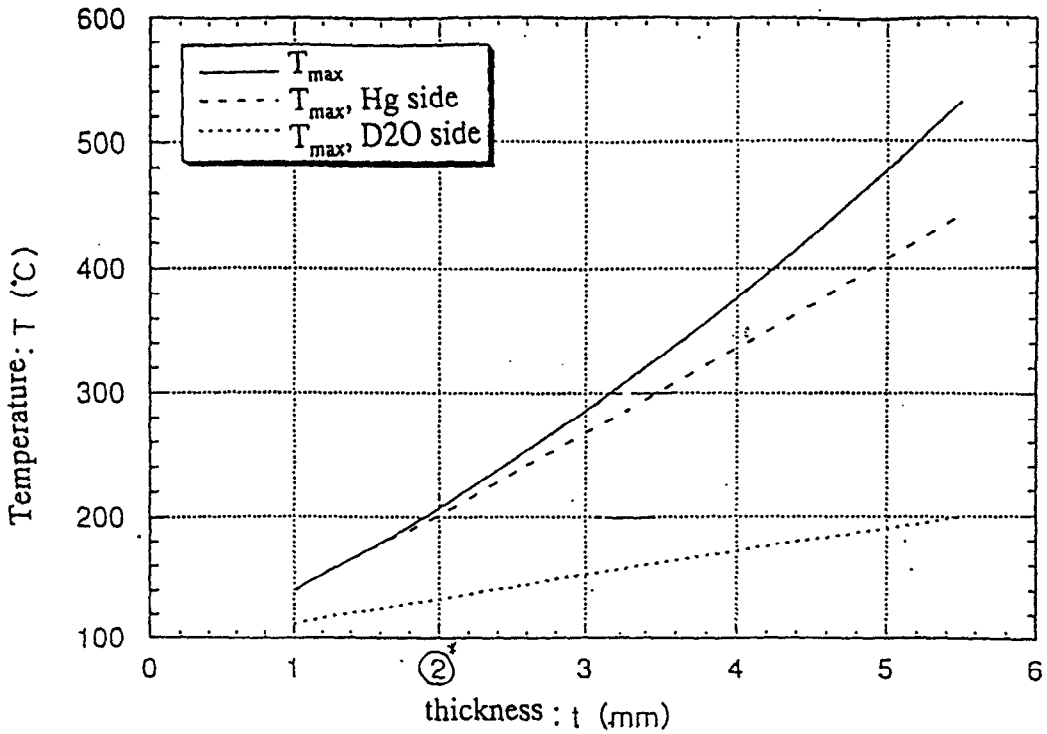

T_{Hg}=135 °C, α_{Hg}=5000kcal/m2·hr·°C (mercury cooling)
T_w=80 °C, α_w=25000kcal/m2·hr·°C (D_2O cooling)
1.2kW/mm/mA (energy deposition at beam window)

Figure 3 Beam Window Temperature vs. Its Thickness

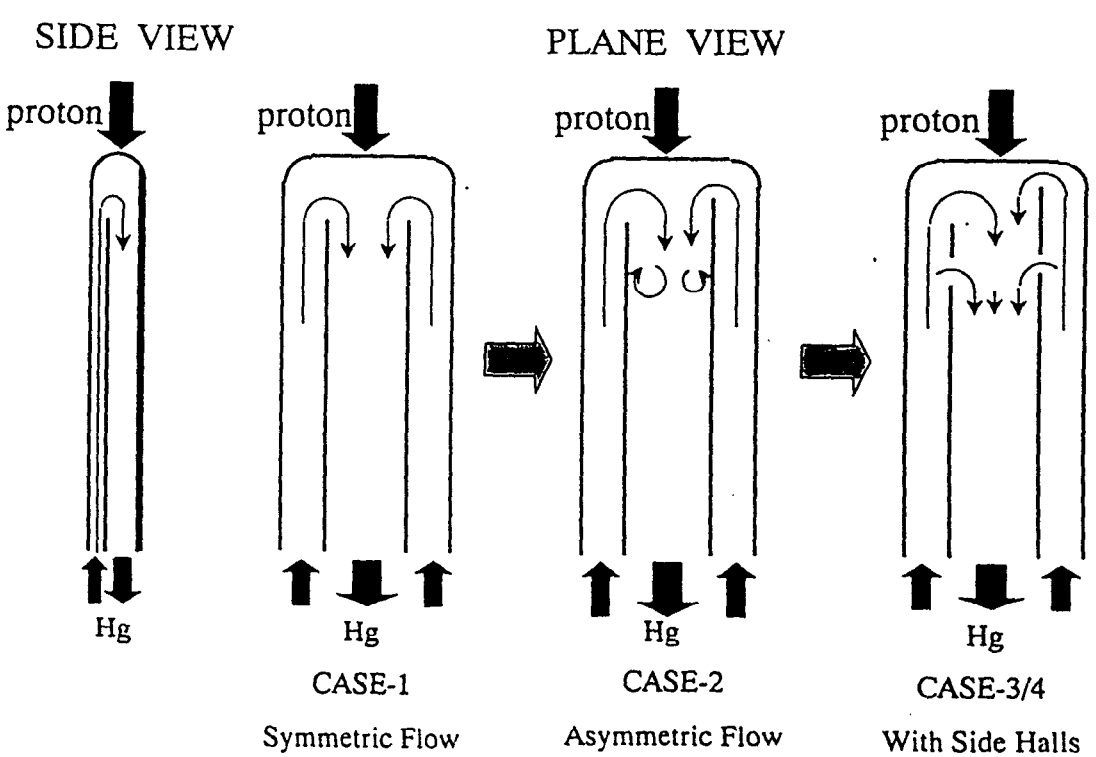

Figure 4 Design Approach of RFT Target Flow Configuration

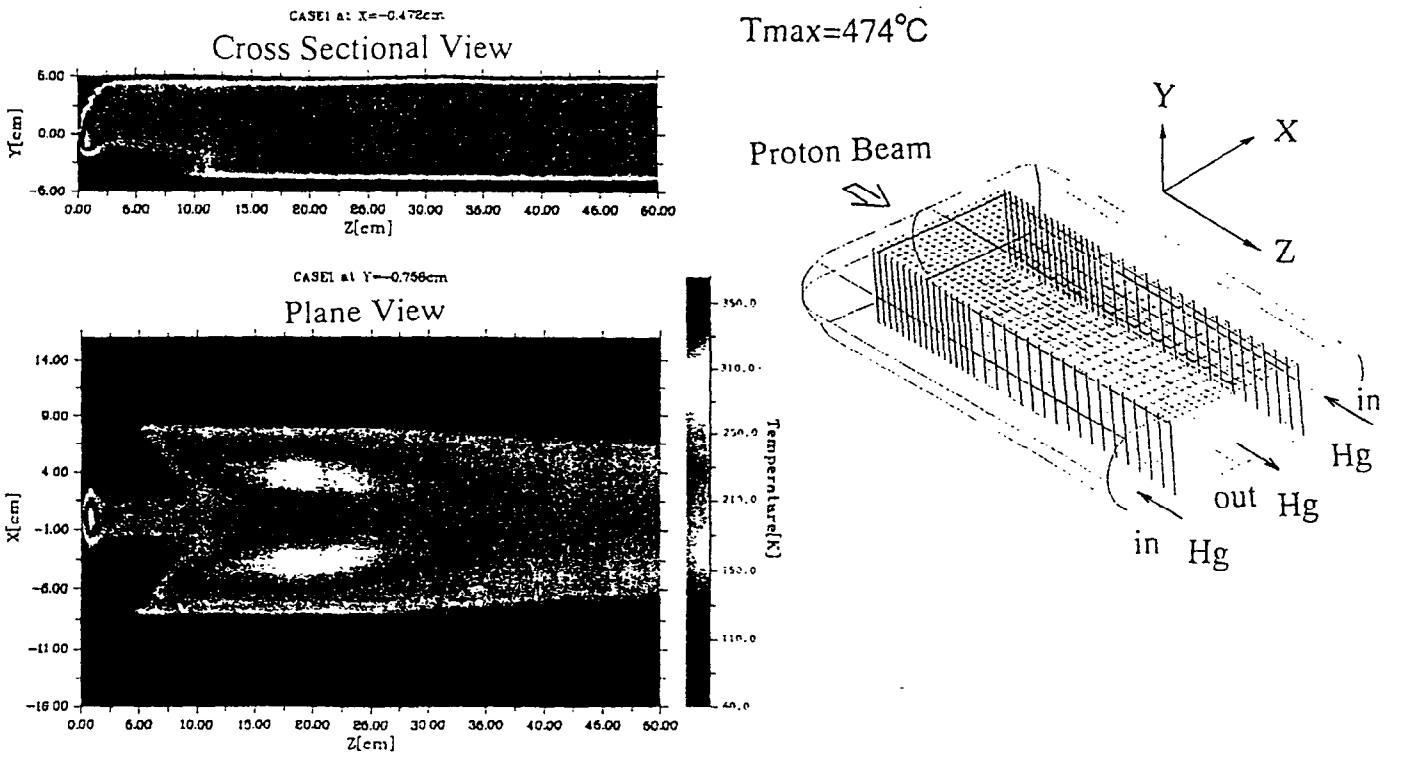

Figure 5 Temperature Profile of CASE-1

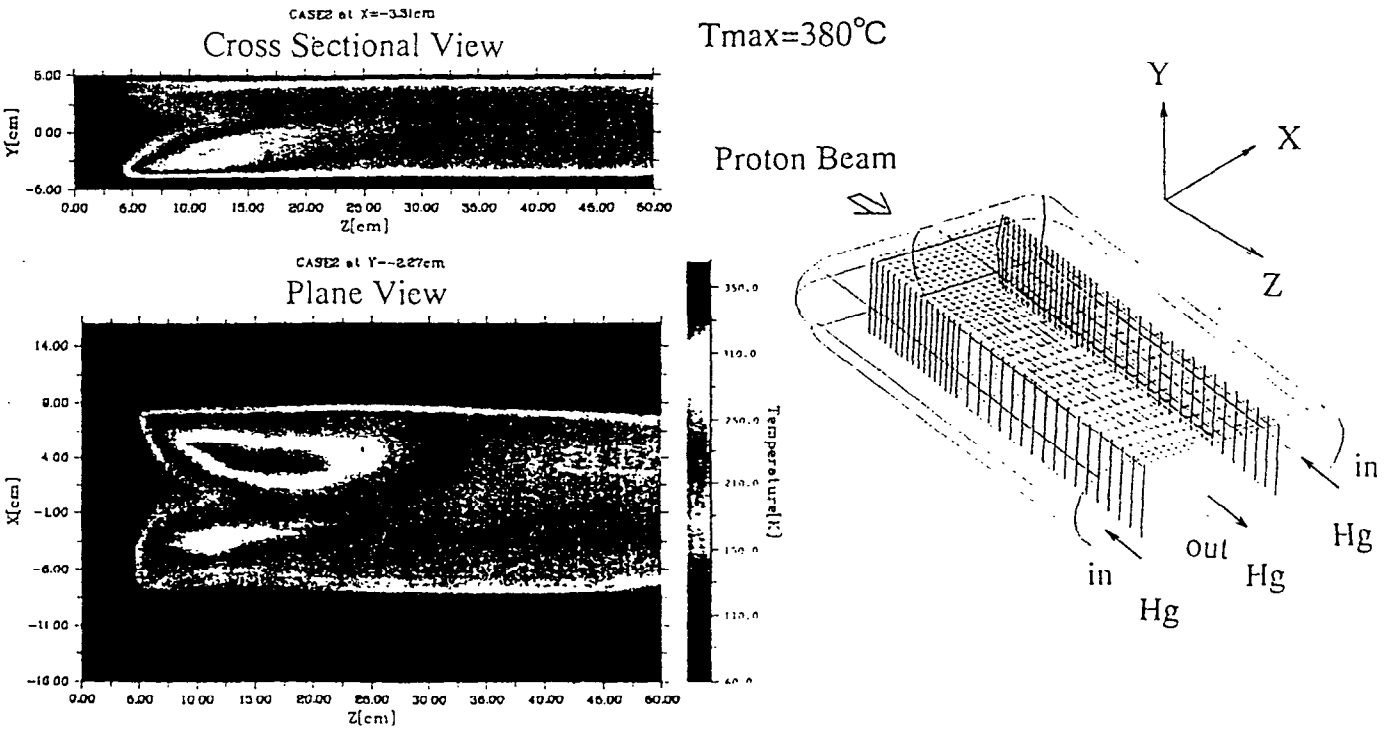

Figure 6 Temperature Profile of CASE-2

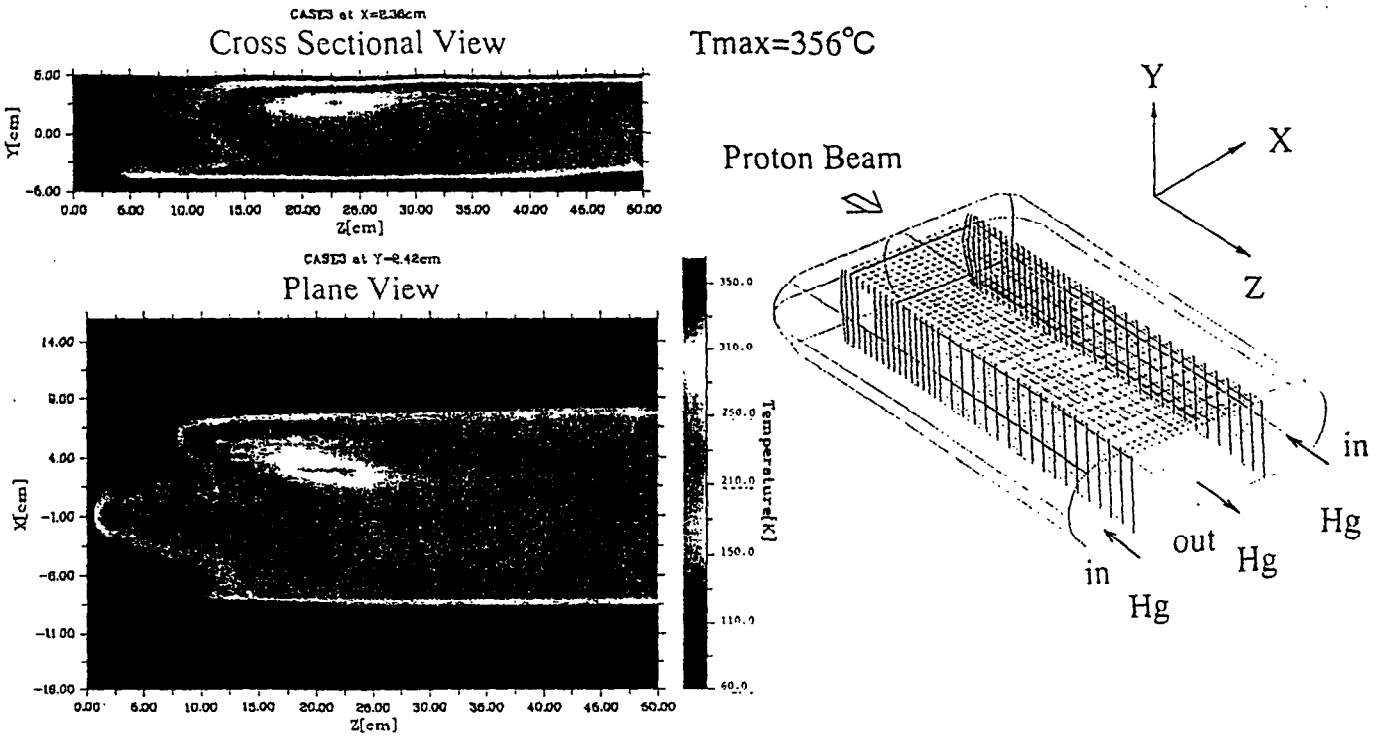

Figure 7 Temperature Profile of CASE-3

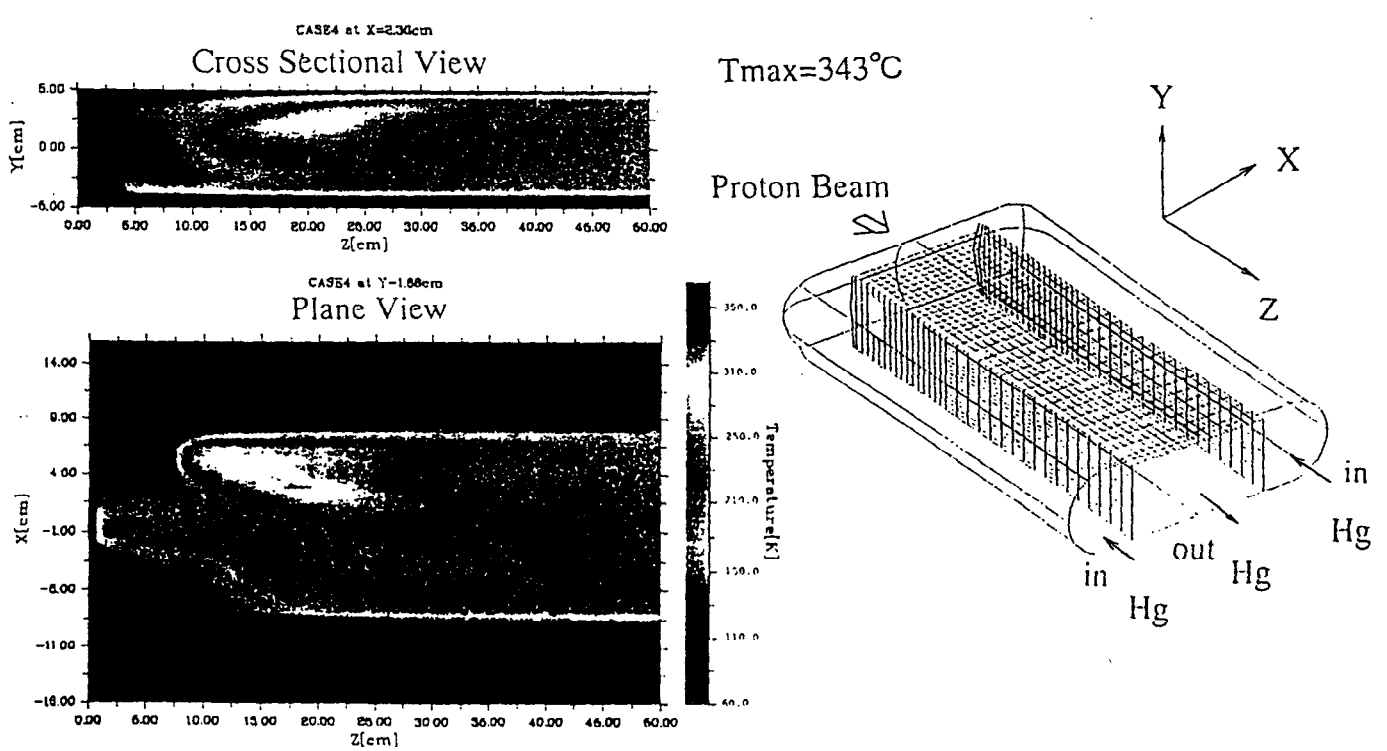

Figure 8 Temperature Profile of CASE-4

ICANS-XIV
14th Meeting of the International Collaboration on
Advanced Neutron Sources
June 14-19,1998
Starved Rock Lodge Utica,IIIinois,USA

Analyses on Pressure Wave Propagation and Dynamic Stress in Mercury Targets

Syuiti Ishikura, Masanori Kaminaga, Akira Susuki, Ryutaro Hino
Japan Atomic Energy Research Institute,JAPAN
Iwao Harada, Kosuke Kamba and Motoaki Sakashita
Hitachi Ltd.,JAPAN

ABSTRACT

Stress and pressure are analyzed for solving the main design problem in the JAERI 5MW liquid mercury target. Two different codes are used to evaluate the stress and pressure waves under a single pulsed heating. They are the structural analysis code and a developed liquid mercury program. Stress waves are computed in an axisymmetric target container coupled with liquid approximated as solid with compressibility. Pressure waves are computed in the target liquid treated as a purely liquid mercury extending TVD(Total Variational Diminishing) in gas to liquid.

The maximum stress 170MPa appears as the meridional stress at the window center, because the bending stress increases for a rectangular beam profile. As beam profiles change from rectangular to parabola, the meridional stress decreases at the value of 100MPa which is smaller than the circumferential stress value 110-130MPa.

The developed program well shows generation, propagation and reflection of the pressure wave. Pressures become 100MPa at the window center and 60 MPa at the cylinder surface.

1 Introduction

A major design problem in neutron spallation source is how to design the structure of the target in consisting with complicated dynamic load generated by pressure waves. A liquid mercury target has been expected as a next generation liquid metal target to produce much more neutrons than a solid target. They are

planning as SNS(Spallation Neutron Source), ESS(European Spallation Source) and NSF(Neutron Spallation Facility) of JAERI using the 5MW liquid mercury target.

From a view point of physical understanding, elastic or stress waves generated in solid have been well known by Love's famous study [1] . Also, stress waves can be computed by the structural analysis code such as ANSYS or ABAQUS. A solid target can be designed within structural dynamics.

A few means exist to know the pressure wave mechanism generated in liquid, because liquid state is not clarified comparing with solid and gas. Skala and Bauer[2] computed the pressure wave using the extension from the structural analysis. The PSI developed KASKA program[3] based on the Lagrange/Finite Difference Method. However, the equation of state is not given such as an equation of perfect gas so that the lack of the equation of state causes a difficulty of liquid metal target design. Solving this difficulty, the liquid program based on TVD (Total Variational Diminishing) have been developed reconstructing TVD theory in gas dynamics to apply the liquid mercury target.

In this report, stress and pressure are independently analyzed for the JAERI 5MW liquid mercury target under a single pulsed heating by using ABAQUS-Explicit code and the developed program. Stress waves are computed in an axisymmetric target container coupled with liquid approximated as a solid with compressibility. Pressure wave is computed in detail as the process of generation, propagation and reflection of the compression and rarefaction waves.

2 Analysis models of 5MW mercury targets

Fig.1 shows analysis models of the JAERI 5MW liquid mercury target used for computations. A basic profile is a rectangular flat beam of 93.6mm diameter. Profiles are changed other parabolic, Gaussian distributions in the radial direction as a computational parameter. The energy deposition varies with both axial and radial positions. The axial beam profile is expressed by an approximate function obtained from Monte Carlo code NMTC/JAERI[4]. The energy deposition per one pulse is shown in fig.1 as a time average of 50Hz. The target is composed with a dome-shaped window and a cylinder of 200mm diameter, 1100mm length and 2.5mm thick. Liquid mercury is kept at 52°C until the first pulse arriving. After the pulse, the temperature difference reaches the maximum 19.5°C at the axial distance 15mm from the window center.

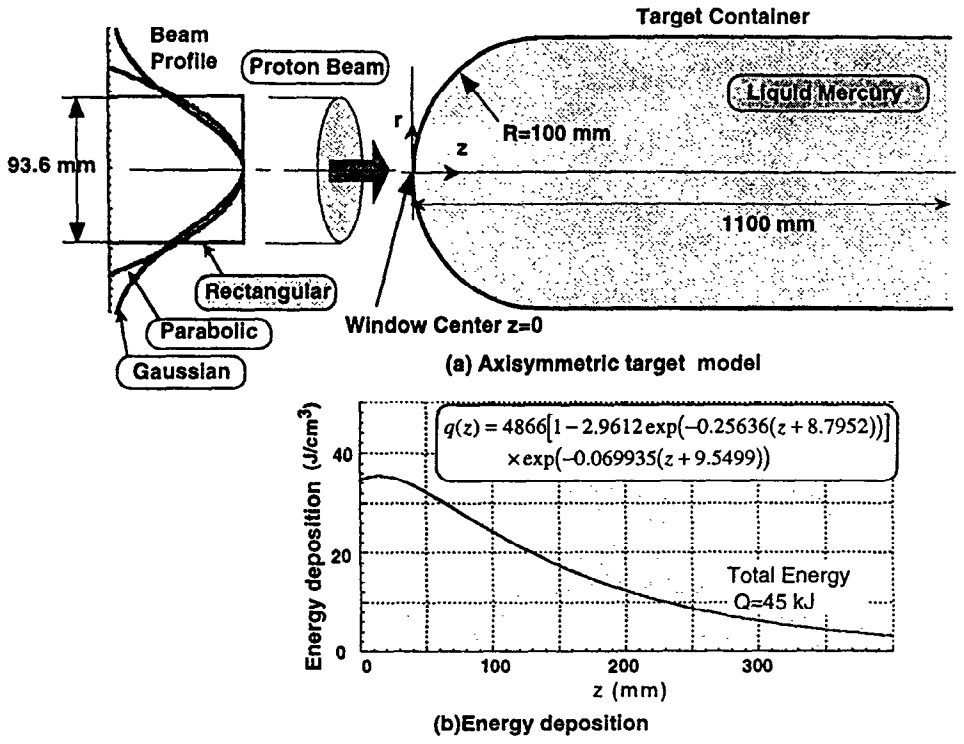

Fig.1 Stress wave analysis model of 5MW mercury targets

3 Structural analysis

3.1 Computational parameters

An axisymmetric co-ordinate system r and z is used through both analyses, where r and z are coordinates in the radial and axial direction, respectively. The window center locates at $z = 0$. Computations are made on the shell container coupled with liquid mercury by using ABAQUS-Explicit FEM code. Liquid mercury is modeled as an incompressible solid, where modulus of elasticity 6.6MPa is small enough and the Poisson's ratio 0.49995 is close to 0.5. Numbers of elements are 235 and 11125 in the container and liquid mercury, respectively. The size of elements is 2mm in the radial direction, and is from 2mm to 10mm in the axial direction.

3.2 Stress on a target container

Fig.2 shows a schematic diagram of the generation and propagation of the stress and pressure waves at early time. In a liquid target, two pressure wave fronts are generated at an interface between cold and heated liquids due to thermal expansion of liquid. One is formed at the intersection between window and cylinder

of beam diameter near the window center. The other is the liquid surface of the cylinder which has the same beam diameter. The first wave continuously acts on the window wall in the axial direction from an initial time. The second wave reaches lately to the cylinder surface of the container traveling the cold liquid in the radial direction. Fig.3 shows the time history of the meridional stress at various

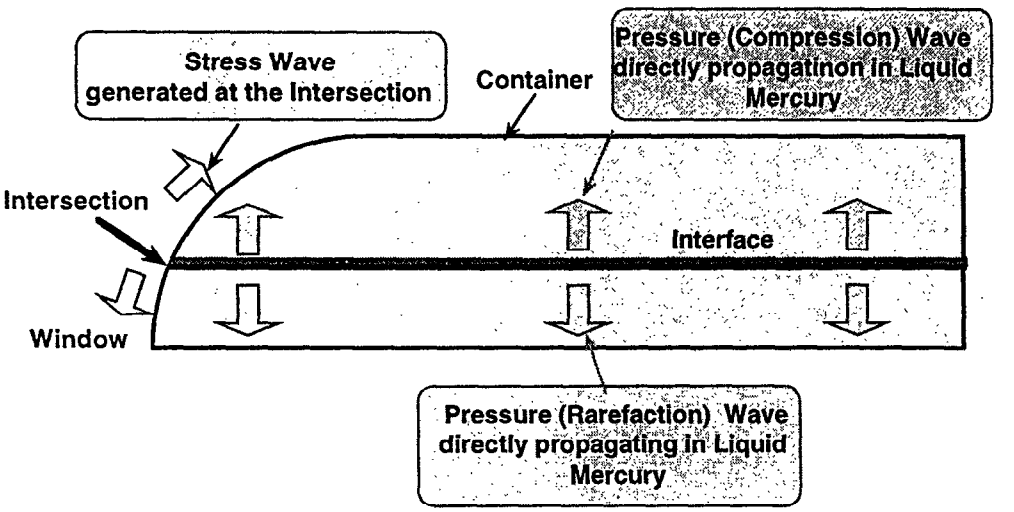

Fig.2 A schematic diagram of generation and propagation of stress and pressure waves

axial positions of the container. It seems that stress at the window center z=0mm behaves differently from these at other positions z=10-50cm in the cylinder. The essential difference is caused by other reason where the tip location is a singular point of the doom-shape container. Fig.4 shows the time history of the meridional stress at the window center. It is easily understood that the bending moment is added to the membrane force. As shown in fig.3, the same stress wave travels from forward (the intersection) to backward (z=10-50cm). The delayed time agrees with a propagation time 20 μ s in which the elastic wave travels the distance 10cm at sound velocity 4890m/s. Then, the meridional stress attains the maximum value 170MPa at the window center z=0mm.

Fig.5 shows the time history of the circumferential stress at various axial positions of the container. It is seen that stress at the positions z=10cm increases firstly and after the time, the stress at other positions z=20-50cm changes simultaneously. The time difference corresponds to the difference of sound velocities of solid and liquid. It takes 20 μ s the stress wave in solid arriving at z=10cm,but the pressure wave in liquid can arrive at the same position in 45 μ s. Then, the the circumferential stress at z=10cm is produced by the stress wave traveling from the

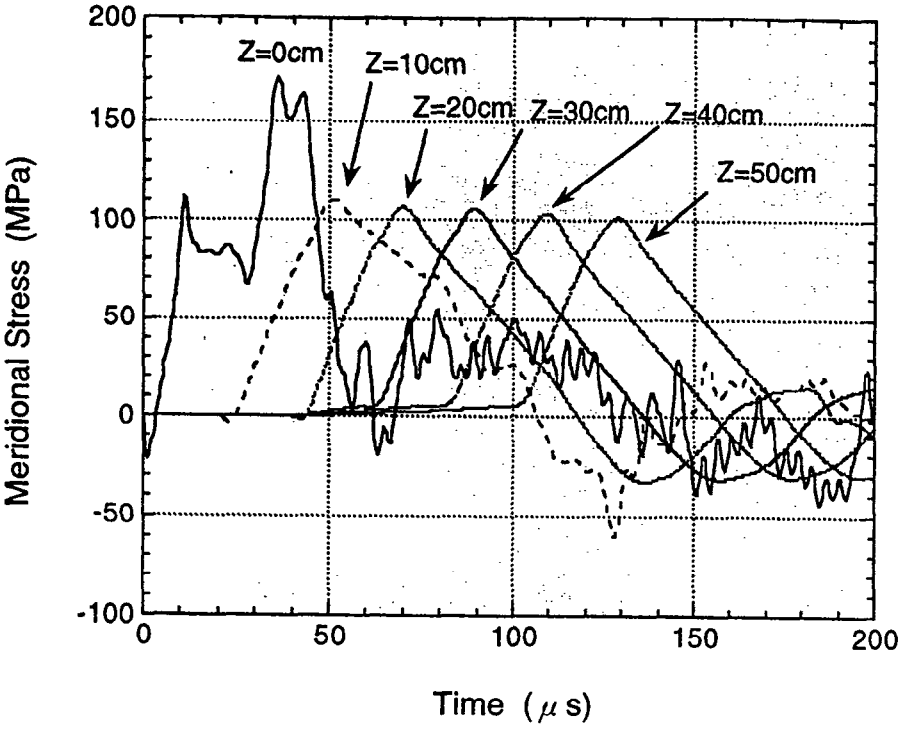

Fig.3 Meridional stress in the target container

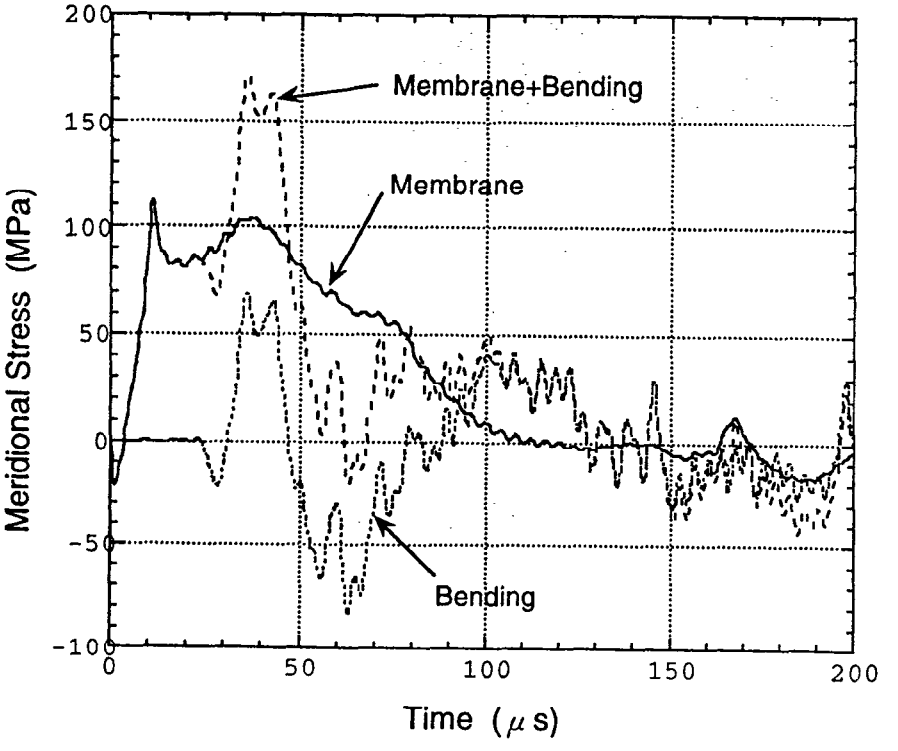

Fig.4 Meridional stress at the window center

intersection. The stress at z=20-50cm is directly produced by the pressure wave traveling from the cylindrical liquid surface of the beam diameter. The stress appears as the maximum stress 130MPa for the different wave pass. The energy deposit affects the strength and profiles of stress which decrease to backward.

Next, the beam profiles are changed expecting the reduction of meridional

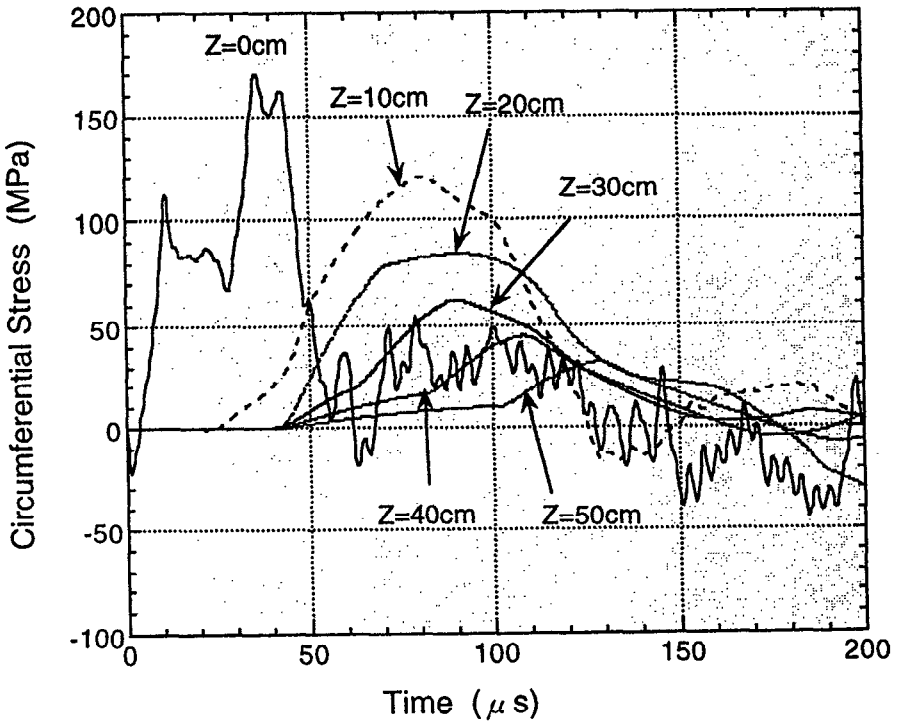

Fig.5 Circumferential stress in the target container

stress,especially, bending moment at the wind center. These profiles are parabolic and Gaussian distributions. Fig.6 shows the effects of beam profiles on meridional stress. It can be seen that the maximum stress 100MPa for both beam profiles is much smaller than the value 170MPa for the rectangular beam profile. This is because the force of the pressure wave decreases at the interface due to the small temperature gradient between cold and heated liquids.

4 Liquid target analysis

4.1 Numerical method and parameters

An axisymmetric compressible Euler equation are employed as the governing equations. The TVD scheme with Roe's flux difference splitting [5] is

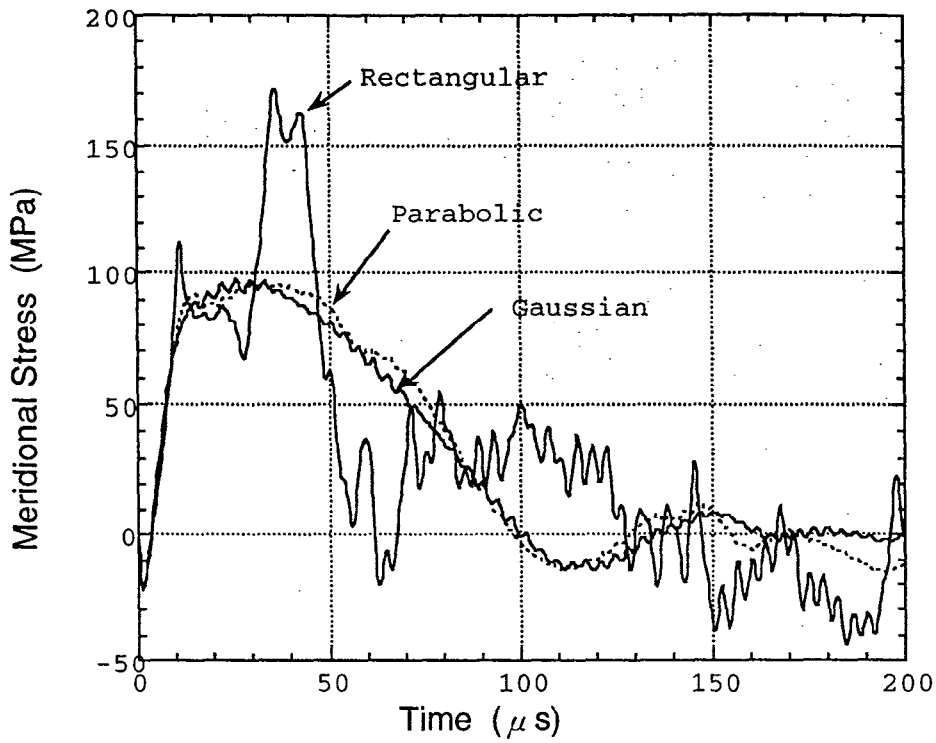

Fig.6 Beam profile effects on meridional stress at the window center

reconstructed for the state equation of liquid (which is the Tait equation, not the Mie-Grüneisen equation), because the original Roe's scheme is derived from the state equation of a perfect gas. The liquid target program is developed on the basis of TVD/Finite Volume Method.

Fig.7 shows the pressure wave analysis model of the JAERI 5MW liquid mercury target. The rectangular beam case is only computed in detail to investigate the generation and propagation process of the pressure waves in the liquid mercury. It is assumed that the wave fully reflects on the wall. The slip condition is adopted on the wall. Fig.8 shows a grid system used for pressure wave computation. The computational region is divided into 600 × 100 cells in the radial and axial directions, respectively. The cell size is about 1 mm square near the target window as shown in fig.8.

4.2 Pressure wave propagation in targets

Fig.9 shows the time history of the pressure in the liquid mercury of the wall. The tracer points are located at z =0 mm, 30 mm, and 100 mm, where z is a coordinate in axial direction and $z = 0$ representsat the center of the target window. In fig.9 the time **a**~**m** correspond to the peaks of the pressure history curves. In the following paragraphs, we will describe the propagation process of

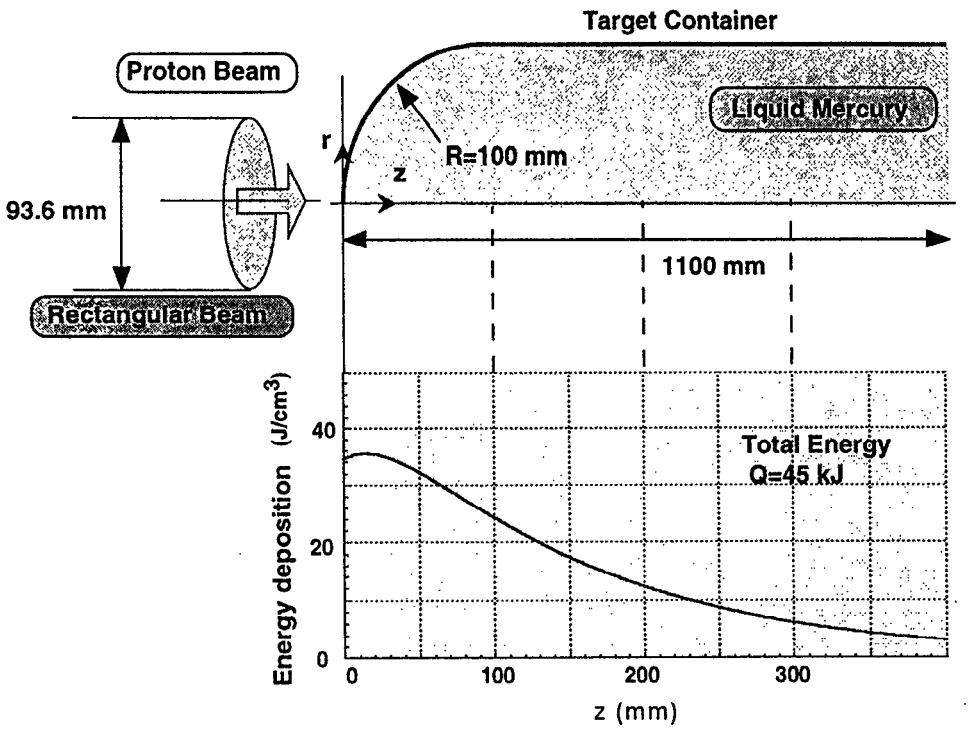

Fig.7 Pressure wave analysis model of 5MW mercury targets

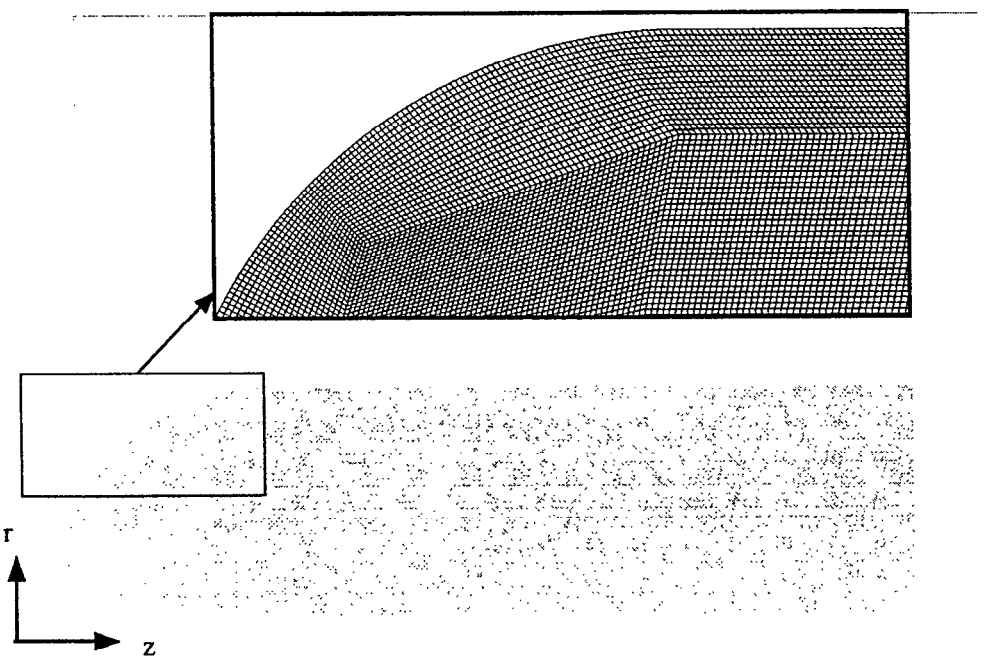

Fig.8 A grid system used for pressure wave computations (100 X600 cells)

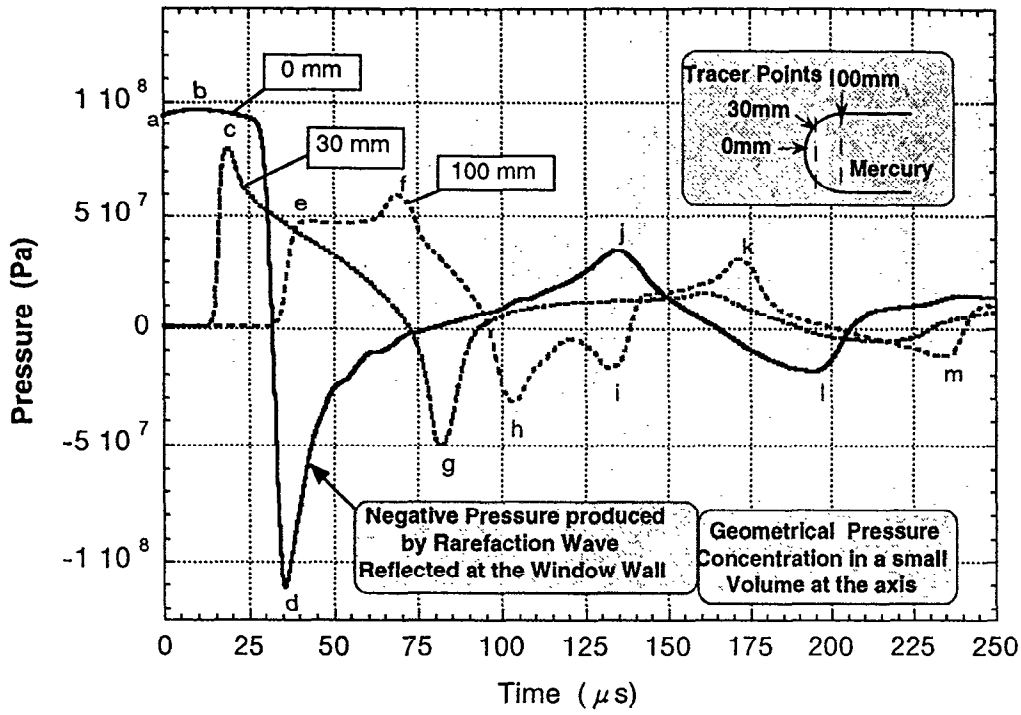

Fig.9 Time history of pressure waves on the mercury surface

pressure waves at each time **a**~**m**. For the help of the comprehension, fig.10 shows the pressure wave propagation in the mercury target represented by the pressure contours at the time **a** ($t = 0$ μs), the time **c** ($t = 26$ μs), the time **f** ($t = 50$ μs) and after. Fig.11 gives the schematic diagram of pressure wave propagation at the time **f**.

To begin with, we will classify pressure waves in a usual way. When a proton beam is pulsed, two types of pressure waves— compression wave and rarefaction wave — generate at the same time. From the path waves have traveled along, another category — direct wave and reflected wave —comes, namely,a direct wave is the wave that has come directly from the point of generation whereas a reflected wave is the wave that has come after it has reflected by walls. Pressure waves are classified with the combination of these two categories. For example, a direct compression wave is defined by the condition that it is a compression wave and it has come directly from the point of generation. The classification may be unworkable if those waves have reflected many times, but at the initial stage, it is very useful to describe the propagation process of waves. At the time **a** (the initial condition), the deposited heat determines the pressure distribution, and the pressure at the point 0 mm becomes high. The highest pressure is, then, observed at z =15 mm. Assuming the sound speed to be equal to 1450 m/s in the liquid mercury, it takes 0.015(m)/1450(m/s) = 10 μs for the highest pressure 95MPa to

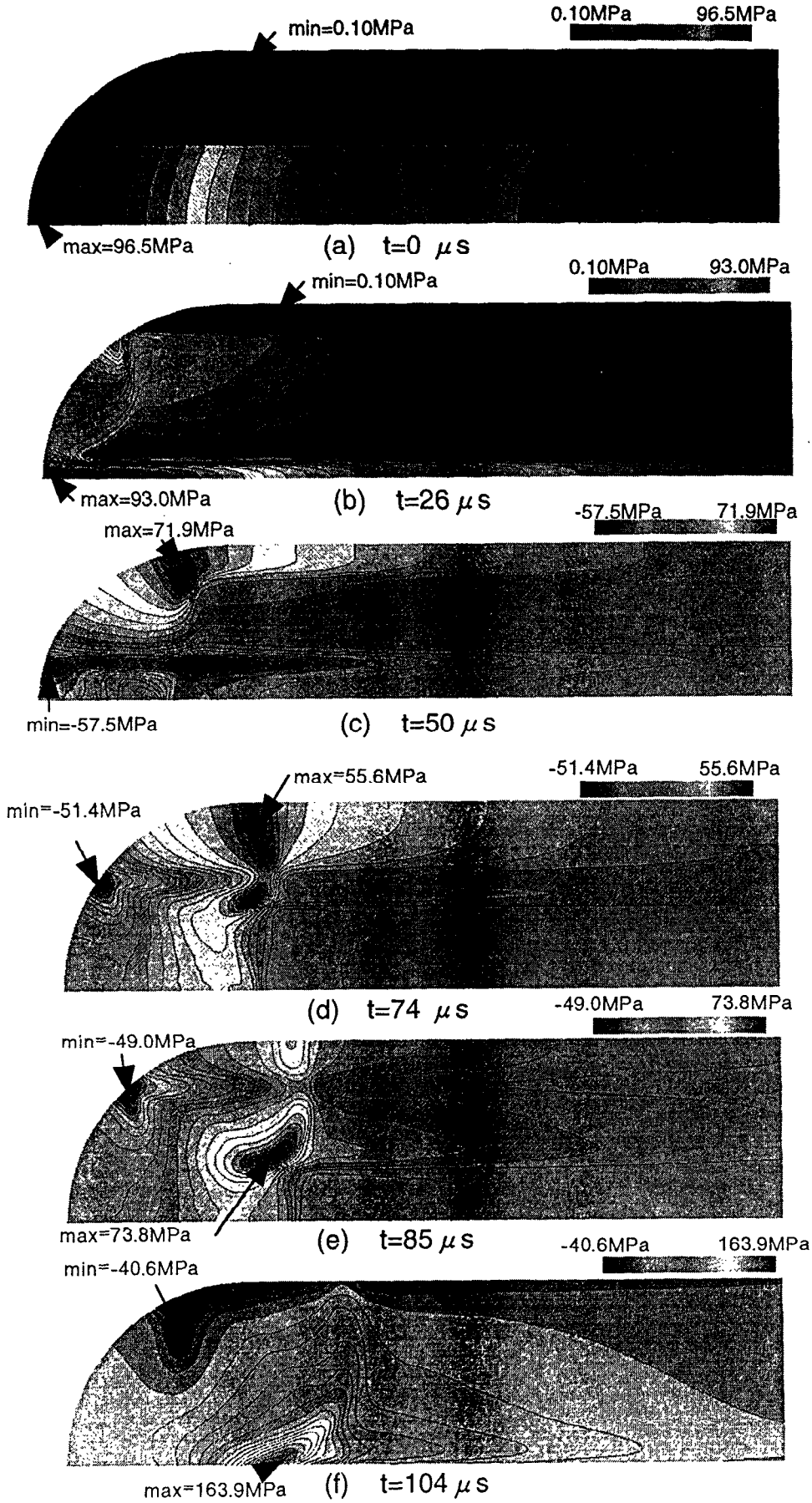

Fig.10 Pressure wave propagation in the mercury target

travel to the target window (z =0 mm). The time 10 μs agrees with the peak time **b** (13 μs) in fig.9.

At the time **c**, the pressure at the point 30 mm increases because two compression waves — the direct compression wave which has come directly and the reflected compression wave which has reflected by the target window wall— reach the point 30 mm at the same time. The pressure at the point 100 mm changes in a different way, because the direct compression wave reaches there ahead of the reflected compression wave at the time **e**, whereas the reflected compression wave reaches the point of the pressure 60MPa at the time **f**. The different time **e** and **f** correspond to the different distance which each wave has traveled. The direct compression wave has traveled the distance between the beam radius 46.8 mm and the target cylinder radius 100 mm, and it reaches the point 100 mm at $(0.1 - 0.0468)(\mathrm{m})/1450(\mathrm{m/s}) = 37$ μs, which agrees with the time **e** (39 μs). On the other hand, the reflected compression wave has traveled 109 mm which is measured along the target wall, and it reaches the point 100 mm at $0.109(\mathrm{mm})/1450(\mathrm{m/s}) = 75$ μs,which agrees with the time **f** (74 μs).

The direct compression wave travels across the target cylinder before it reaches again the point 100 mm after the time **e**. It takes $0.2(\mathrm{m})/1450(\mathrm{m/s}) = 140$ μs, then it reach the point at t =180 μs, which agrees with the time **k**. The rarefaction

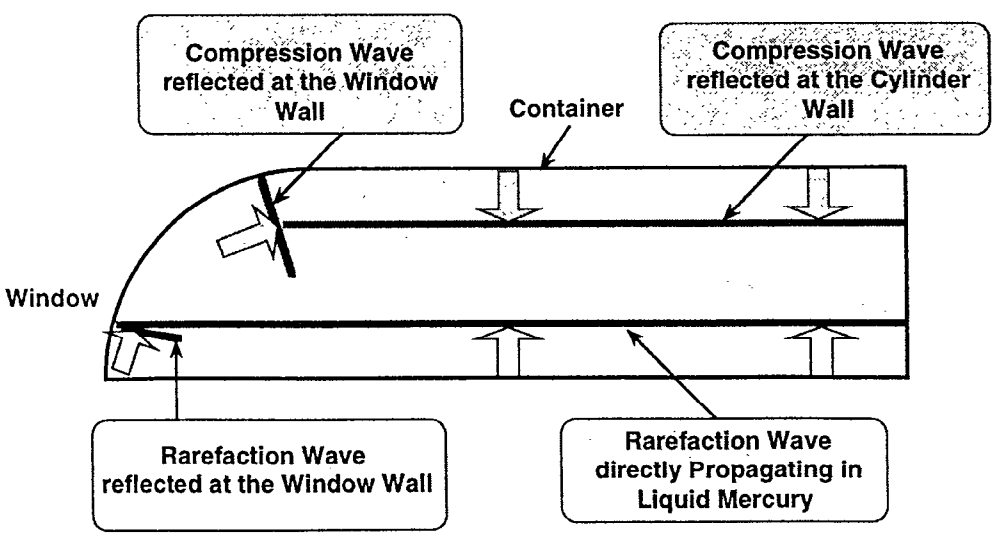

Fig.11 A schematic diagram of pressure wave propagation at t=50 μ s

waves propagate similarly. At the time **d**, the liquid mercury on the axis suffers severe negative pressure because the rarefaction wave are focused there (although such severe negative pressure does not occur in the real liquid mercury). At the

time **g**, the pressure at the point 30 mm become negative because two rarefaction waves — the direct rarefaction wave which has come directly and the reflected rarefaction wave which has reflected by the target window wall—reach there at the same time. The direct rarefaction wave reaches the point 100 mm ahead of the reflected rarefaction waves at the time **h**, and the reflected rarefaction wave reaches the point at the time **i**. Like the case of compression waves, the different time **h** and **i** correspond to the different distance each wave has traveled, though the difference 31 μs is shorter than the difference 37 μs observed in the case of compression waves.

The direct rarefaction wave reaches the point 100 mm at 140 μs after the time **h**, i.e., at t =250 μs, which agrees with the peak at the time **m**.

In the later stage, compression waves and rarefaction waves discussed above go on propagating. The time histories of the pressure become complicated because more reflected waves are generated at the target window and they interfere each other,but they still oscillate in the same cycle 140 μs.

5 Summary

Stress and pressure are analyzed for solving the main design problem in the JAERI 5MW liquid mercury target. Two different codes are used to evaluate the stress and pressure waves under a single pulsed heating. They are the structural analysis ABAQUS-Explicit code and a developed liquid mercury program. Stress waves are computed in an axisymmetric target container coupled with liquid approximated as a solid with compressibility. Pressure waves are computed in target liquid treated as a purely liquid mercury extending TVD(Total Variational Diminishing) in gas to liquid.

The maximum stress 170MPa appears as the meridional stress at the wind center, because the bending stress increases for a rectangular beam profile. As beam profiles change from rectangular to parabola, bending stress decreases at the tip. Then meridional stress decreases at the value of 100MPa which is smaller than the circumferential stress value 110-130MPa.

The developed program well shows generation, propagation and reflection of the compression and rarefaction waves. Pressures become 100MPa at the window center and 60 MPa at the cylinder surface.

In the present analyses, the stress is not so high, but this is the first step to evaluate the dynamic stress generated in liquid metal target. The next steps have to be considered are to predict accurate stress values. First, it is necessary to combine liquid and structure analyses for comparing numerical results with exper-

iments. Secondly, the target is approximated as an axisymmetric container that is a suitable geometry to experiments. The practical shape is between two and three dimensional, so that three dimensional analysis is required to make practical design.

References

[1] A.E.H. Love, "A Treatise on the Mathematical Theory of Elasticity" Dover Publications, New York,(1963)

[2] K.Skala and G.S.Bauer, "On the pressure wave problem in liquid metal targets for pulsed spallation neutron sources ", ICANS-XIII, Vol.2, Switzerland, (1995)

[3] L.Ni, (private communication)

[4] H.Takada, N.Yoshizawa, K.Kosaka and K.Ishibashi, "An Upgrade Version of the Nucleon Transport Code:NMTC/JAERI97", JAERI-Data/Code, 98-005 in Japanese, (1998)

[5] P.L.Roe, "Approximate Riemann Solvers, Parameter Vectors, and Difference Schemes", *Journal of Computational Physics* **43**, p.357-372, (1981)

ICANS-XIV
14th Meeting of the International Collaboration on Advanced Neutron Sources
Starved Rock Lodge, Utica Ill., USA
June 14-19, 1998

Opportunities for Irradiation Studies of Structural Materials for Neutron Sources at the Proton Beam-Stop of Moscow Meson Factory

S.F. Sidorkin[a], G.S. Bauer [b], Y. Dai [b], M.I. Grachev[a], L.V. Kravchuk [a], Y.I. Orlov [c]

[a] Institute for Nuclear Research of the Russian Academy of Sciences, 117312 Moscow, Russia
[b] Paul Scherrer Institut, CH-5232 Villigen-PSI, Switzerland
[c] State Scientific Center of Russian Federation „Institute of Physics and Power Engineering, Obninsk, Kaluga District, Russia

Abstract

In order to be able to investigate experimentally the effect of simultaneous irradiation and stress on solid-liquid metal reactions at widely different temperatures, a modification to the existing irradiation facility at the beam stop of the Moscow Meson Factory (MMF) is examined. The facility would allow to irradiate tubular specimens under internal pressure in a liquid metal environment. Even at its current performance level (50 μA at 500 MeV) the proton beam intensity is sufficient to generate in a suitably large spot peak power densities in the specimens that correspond to the highest loads anticipated in spallation targets currently under study. The installation could be realised in such a way that use can be made of existing equipment both at MMF and nearby laboratories that operate hot cells. Particular attention is being paid to safe and simple handling operations when replacing the specimens and preparing them for shipment.

1. Introduction

Structural materials of neutron sources are subject to a number of load factors, which are known to give rise to the temporal degradation of materials properties. This includes variable internal and external stresses caused by mechanical loads and temperature gradients, structural changes under proton and neutron irradiation of high intensity and corrosion effects. In the case of liquid metal cooling also surface interactions with liquid metals and related phenomena [1] may play a role.

In view of the very limited information available on liquid metal - solid metal interactions in a radiation environment, studying these effects has become particularly important because of increasing R&D activities world wide in related fields such as:

Keywords: Liquid metal, embrittlement, radiation effects, structural materials

- targets for a new generation of high intensity proton accelerators (for neutron sources, electro-nuclear and transmutation facilities with use of lead-bismuth, mercury or gallium in the liquid state [2-13]);
- materials for fusion reactors (questions of the first wall and blanket cooling by lithium, lithium-lead and gallium [14]);
- fast sodium-cooled reactors [15];
- safe power and transport reactors of a new generation with liquid lead and lead-bismuth as coolants [16,17];.

The above mentioned factors may significantly influence the processes of vacancy void swelling, radiation embrittlement and cracking of materials. Liquid metals, through the Rebinder effect [1,18], may reduce the strength (toughness) of materials and give rise to erosion and various kinds of corrosion [1,18,19,20]. A number of other concomitant factors exist [19,20], which defy theoretical or numerical analysis because of the complexity of the problem. In this situation experimental testing is important, and a special experimental facility that allows to investigate all the relevant factors and their complex interaction is highly desirable.

A particular task of near term importance is the experimental assessment of anticipated lifetimes for target windows of high current proton accelerators and the related verification of basic engineering solutions, because several such systems are imminent [2-7].

For this purpose, a special installation based on the beam-stop of the Moscow Meson Factory is proposed. A schematic of the current design of this beam stop is presented in Fig. 1a [21]. The installation consists of a water cooled thermal shield, an aluminium alloy body, a cassette with tungsten plates and the upper plug with channels for coolant (water). It is equipped with a water cooled insert for irradiation of samples in mixed proton and spallation neutron fields. In the present paper possible modifications to this installation are considered which would make it suitable for irradiating specimens under stress and in contact with liquid metals. The necessary requirements and conditions for such irradiation experiments are discussed and it will be shown that appropriate conditions can be generated at the facility.

2. Requirements to the proton beam, the irradiated samples and the installation

2.1 Load levels

The facility should allow to subject the samples to the following load levels:

- continuous mechanical pressure of 0.3 – 2.0 MPa,
- liquid metal at temperatures of 100 – 250°C (Hg), 150 – 400°C (Pb-Bi), 500 – 600°C (Na, Pb);
- heat release density in a steel sample not less than 1.5 10^9 W/m^3. (This heat release density corresponds to the expected thermal loading in materials of neutron target windows for high

current proton accelerators like SNS or ESS and will be sufficient also for the study of structural materials for fission and fusion nuclear reactors.)

2.2 Beam conditions and power deposition

The high intensity linear proton accelerator of the Moscow Meson Factory (Institute for Nuclear Research, RAS) is designed for 600 MeV proton beam energy and a current of 500 μA. Presently a proton current of 70 μA at an energy of 500 MeV is available.

For a Gaussian current density distribution in the beam the power density in the specimens can be represented as::

$$q_v(r) \cong k\rho \frac{dE}{d(\rho x)} \cdot \frac{J_0}{2\pi\sigma^2} \exp\left(-\frac{r^2}{2\sigma^2}\right) = q_{v\max} \cdot \exp\left(-\frac{r^2}{2\sigma^2}\right), \qquad (1)$$

and the standard deviation of the beam, σ, required to obtain a certain maximum power density $q_{v\max}$ becomes (cf. Fig 2):

$$\sigma = \sqrt{\frac{k\rho J_0}{2\pi q_{v\max}} \cdot \frac{dE}{d(x\rho)}}, \qquad (2)$$

Where, the coefficient k takes into account the excess heat release over ionisation losses due to secondary particles in the cascade-evaporation process and from neutron and γ-absorption. This coefficient may be in the range from 1.2 to 1.4 depending on the energy of the primary proton beam, materials used and the design of the target. ρ is the density of the material; $dE/d(x\rho)$ represents the linear ionisation losses.

According to equ. (2), even for a current of 50 μA, the radius of the irradiated area which contains 40% of the proton beam current is equal to $r = \sigma \cong 3.5$ mm. Such dimension is acceptable for physical and mechanical studies.

The radiation damage in steel generated by this beam was estimated and is shown as a function of beam diameter in Fig.3. For a current of 50 μA with σ of 3.5 mm we expect about 1.2×10^{-6} dpa/s, i.e. roughly 0.1 dpa/day.

2.3 Test specimens

For testing of reactor materials under the influence of pressure, tubular samples are used (Fig. 4a). They have diameters of 0.5 – 2 cm and thickness 0.3 - 0.5 mm and are filled with argon at 15 – 20 MPa. This provides a relatively simple way of subjecting the specimens to tensile stress during

irradiation. The irradiated samples are cut into ringlets with a height of 4 – 5 mm for physical studies and mechanical testing (Fig. 4b). A suitable specimen holder for tensile testing is shown in Fig 4d.

Reactor irradiation provides uniform radiation damage in tubular samples with a height of about of 0.1 m. If the same method is to be used in proton irradiation experiments, it is necessary to fix exactly the orientation of samples during physical investigations because of the small area of the proton spot (8 – 20 mm in diameter for currents of 50 – 500 μA). So, initial marking of the samples and corresponding positioning in post-irradiation studies is necessary (Fig. 4a and d).

The tubular samples may be naturally put together as hexagonal or cylindrical assembly similar to fuel elements of nuclear reactors (Fig. 4c). The hydrodynamics and heat transfer for such an assembly are well understood, including critical parameters [22,23]. Moreover, the assembly cover may be used as reference sample irradiated without mechanical stresses.

For other existing methods of testing under stress it would be more difficult to maintain a continuous mechanical load under irradiation (cf. also section 5). This would require additional equipment and will therefore be only considered if there is a sufficiently strong case for it.

2.4 Requirements to the irradiation rig

The proposed layout of the installation takes into account the following requirements:

- a reasonably simple and quick change of samples;
- precise control of the beam position;
- power density of the order of 1.5×10^9 W/m^3 as anticipated e.g. for the ESS beam window [4,7];
- control and stabilisation of temperature;
- an external liquid metal coolant for heat transfer;
- height limitations of the liquid metal insert and sample holders as imposed by the hot cell facilities to be used for post irradiation examination, in case the whole insert has to be taken into a hot cell[1];
- a minimum amount of a liquid metal, especially in the case of mercury or sodium;
- a conversion of radioactive mercury after the experiment into solid solutions (Pb-Hg, Cu-Hg) or complexes like Hg_2Cl_2 in the device for easier handling and waste management.

A double walled stainless steel container with the interspace filled with argon will be provided in order to ease control of the temperature in the liquid metal and for safety. Argon is chosen because helium can easily escape through micro-cracks in welded joints. The space between the container walls will be controlled for leakage.

[1] It would be possible to utilise the existing technology and equipment of laboratories of SSC IPPE, RFC Kurchatov Institute, and Institute of Atomic Reactors (RIAR), thereby avoiding significant expenses that might have to be faced if PIE was carried out abroad.

3. Basic layout of the installation

3.1 Overall Design

The dimensions given below for some of the components are for a beam current of 50 μA as presently available. They may be increased as higher currents become available to irradiate more or larger specimens at the same current density.

For the liquid metal irradiation experiment most of the existing outer plug of the beam stop of the Moscow Meson Factory (Fig. 1a), including the water cooled stainless steel thimble for the irradiation insert will remain essentially unchanged, with possibly minor modifications to accommodate the new liquid metal irradiation insert (Fig. 1a and 5). This will be a double walled stainless steel container which will be inserted into the water cooled aluminum thimble inside the tungsten beam stop. The interspace between the two walls will be filed with circulating argon and will be surveyed for leakage from either one of the two walls which will have water on the outside and liquid metal on the inside. Apart from monitoring the pressure and composition of the argon, there will be electrical sensors in the interspace to indicate any ingress of water or liquid metal. The outer diameter of this container will be ≈ 4 cm in the irradiation area and will widen further up. The walls will be about 1 mm thick and will have spacers between them.

The tubular specimens will be arranged in a cassette with a diameter of about 3-4 cm which is suspended from a cylindrical bar and held against a hollow steel cylinder which separates the downward from the upward liquid metal flow. Heaters for temperature control are located at the cylinder surface.

The upper part of the container is surrounded by a magneto-hydrodynamic (MHD) induction pump. This pump is designed as a tight stator of an asynchronous motor with a short-circuited rotor and pumps the liquid metal in a spiral channel. Due to the centrifugal effect, the spiral MHD pump gives higher values of pressure than a linear motor at the same energy consumption. For ease of manufacturing the helical flow guides of the pump are assumed to be attached to the inner cylinder, although it might be preferable to have them fixed to the container for tightness. The liquid metal will be pumped downwards in the annulus between the cylindrical insert and the inner container wall and will rise between the specimens in the cassette and through the bore in the cylinder. Above the level of the pump the liquid metal flows from inside the cylinder to the outside through bores. A free surface is maintained with a gas atmosphere above it.

The upper part of the container will be an expandable bellows in order to be able to raise the whole assembly of the inner cylinder and the specimen cassette above the level of the liquid metal (which then collects in the bottom of the container) without having to open the system at that stage (see section 4).

Transverse dimensions of the installation in its upper part will be determined by different boundary conditions, such as standard tube diameters and the internal diameter of a suitable stator of a standard asynchronous electrical motor. Such values as clearances for liquid metal passage

and height of the pump stator remain to be determined in alloy body, tungsten plates that would be behind the liquid metal insertion for full stop of the optimisation calculations. Anyhow, the height of the insert should not exceed the limitations imposed by the dimensions of available hot cells and the elements of the existing tungsten beam-stops (aluminium proton beam).

There is no system foreseen for coolant purification, because the irradiation times are sufficiently short (3-6 months). This simplifies the design and operation of the installation.

As a whole, the technical and design solutions chosen satisfy the requirements listed above. Some other important features are:

- The amount of water in the beam is minimised which keeps the radioactivity in the cooling loops low and avoids uptake of hydrogen by the samples in the form of secondary protons that are created in the water coolant by the high current proton beam;
- A large temperature difference can be supported between the liquid metal in the ampoule interior and the water coolant in contact with the external surface of the ampoule;
- The possibility exists to ensure sufficient cooling of proton beam windows by a jet system (see 3.2.2);
- Mostly axis-symmetric parts are used, which simplifies fabrication of the liquid metal insert and the control of the process;
- Existing external parts of the beam-stop that are made of aluminium alloy and the cassette with tungsten plates can be used with minimum changes (the shield plug above the cassette would be fabricated newly, as it completely changes in shape due to MHD pump and supply and control lines);
- The MHD pump that is fabricated on the basis of a serial industrial motor can be reused repeatedly with new cylindrical inserts for different experiments.

3.2 Some detailed considerations

While the whole liquid metal irradiation facility is still in a very conceptual stage of design we would like to give a few details to show that the concept is technically feasible.

3.2.1 The liquid metal pump and loop

As a whole, the design scheme of the liquid metal irradiation insert is similar to the scheme of rotary induction pump and existing designing experience may be used. An available electric rotary pump in Russia is the VIN-5/1.5 [24], it is used in the system of sodium coolant loading in BOR-60 reactor. The pump has an external diameter of 260 mm and can produce a pressure rise of ~ 0.5 MPa at the nominal flow of 1.5 m^3/h. These parameters make available a liquid metal flow of ~1m/s for window and sample cooling. To optimise the coolant flow near the window and keep hydraulic losses along the liquid metal path low, local narrowing of the flow cross section should be provided for near the window. According to one-dimensional estimates, the final pressure gradient along the path will not exceed ~ 0.1 MPa. The pump efficiency will

depend, in the first place, on the dimension and shape of the gap between the stator and the liquid metal layer and on the presence of a core of electrotechnical steel in the inner cylinder. It is expected to be of the order of 3-8%. The electrical power consumption of the pump will be 3 - 4 kW, which is to be compared to the heat release in the proton beam-stop of 22.5 – 30 kW (for 450 – 600 MeV and 50 μA).

During the pre-irradiation tests dependencies of velocities and liquid metal flow rate on the electrical power of the pump should be measured. Without irradiation the flow rate can be obtained from the measured temperature rise upon passage of the fluid through the pump and its power consumption (heat input). At low and moderately high temperatures also the contact-free ultrasonic technique developed at PSI [25] can be used for calibration. For this purpose, a test section with a well defined liquid metal layer of about 8 to 10 mm thickness would be employed.

3.2.2 Cooling of the beam windows

In terms of operational safety the most critical point is the window, i.e. the position where the proton beam enters into the irradiation insert, which has the highest heat load and most be cooled very efficiently.
The temperature gradient across the wall at the maximum of heat release, taking into account transverse heat conduction in the wall material, was estimated by using the following expression:

$$q_{s\max} = -\lambda \frac{\partial T(0,\delta)}{\partial z} = 2q_{v\max}\delta \sum_{k=1}^{\infty} \frac{\sin^2(\gamma_k\delta)\cdot\eta_k \exp(\eta_k)E_1(\eta_k)}{\left(1+\frac{Bi}{Bi^2+(\gamma_k\delta)^2}\right)(\gamma_k\delta)^2} \qquad (3)$$

$$T(0,\delta)-\vec{t}_f = \frac{q_{s\max}}{\alpha} = \frac{2q_{v\max}\delta^2}{\lambda}\sum_{k=1}^{\infty}\frac{\sin(\gamma_k\delta)\cos(\gamma_k\delta)\cdot\eta_k\exp(\eta_k)E_1(\eta_k)}{\left(1+\frac{Bi}{Bi^2+(\gamma_k\delta)^2}\right)(\gamma_k\delta)_k^3} \qquad (5)$$

$$\Delta T_{\max} = \frac{2q_{v\max}\delta^2}{\lambda}\sum_{k=1}^{\infty}\frac{\sin(\gamma_k\delta)[1-\cos(\gamma_k\delta)]}{\left(1+\frac{Bi}{Bi^2+(\gamma_k\delta)^2}\right)(\gamma_k\delta)^3}\eta_k\exp(\eta_k)E_1(\eta_k) \qquad (4)$$

$$\eta_k = \left(\frac{x_k\sigma}{\sqrt{2}\delta}\right)^2 = \left(\frac{\gamma_k\sigma}{\sqrt{2}}\right)^2, \quad x_k = \gamma_k\delta, \quad (\gamma_k\delta)\,tg(\gamma_k\delta) = \frac{\alpha\delta}{\lambda} = Bi \qquad (6)$$

Here, q_s and q_v are the surface and volume heat densities respectively; δ - the thickness of the wall, λ - heat conductivity coefficient, α - heat transfer coefficient, ΔT_{max} - maximum temperature drop along the beam direction (z - direction), $T(0,\delta)$ - the maximum temperature drop between cooling surface and coolant and t_f - the lateral temperature drop along surface between points $r = 0$ and $r = \infty$.

This expression is an exact analytical solution of the two-dimensional equation of heat conduction. For a flat wall (Fig. 6) with the heat release density determined by equ. (1) it shows that the temperature rise across the wall at the maximum of the heat release density (~1.5 MW/m^3) is ~ 32 - 36 ^{0}C for stainless steel (δ = 1 mm) and ~15 ^{0}C for aluminum alloy (δ = 5 mm).

Efficient cooling of the beam windows will require a local water velocity of about 4-5 m/s, while the total flow needed to remove all of the heat dissipated in the irradiation insert is of the order of 8-10 m^3/h, which results in a flow velocity of about 0.5 m/s between the walls of the thimble. We are, therefore, contemplating to design a water feeding system that would take the water immediately down to the proton window region into a manifold with openings facing the beam windows of the beam stop insert and the irradiation insert. The water would then be directed as jets onto the two most heated walls and would generate a high velocity and turbulent flow at the beam windows. The concept is shown schematically in Fig. 7. While providing efficient window cooling, this concept also minimises the amount of wall material in the beam. The return flow would be cooling the outer wall of the irradiation insert.

If it proves feasible, this design would:
- avoid additional layers of structural materials and the corresponding beam widening;
- efficiently prevent the formation of a vapour boundary layer near the windows and ensure efficient heat exchange at the most strongly heated position;
- establish axial symmetry of window cooling;
- keep the total water flow rate at ~10 m^3/h as required to provide a reasonable thermal regime on the external surface of the liquid metal irradiation insert and the tungsten plates;
- be very space efficient, in line with the inner dimensions of the MHD pump, and the existing aluminum body;
- essentially retain the overall cylindrical symmetry of the insert;
- generate a relatively low flux of recoil protons to the samples;

3.3.3 Temperature control

Depending on the liquid metal used, the temperature should be kept constant at widely different levels. Since there will be a more or less constant heat source from the beam and the pump, this may require additional possibilities of heat input by heating elements located on the surface of the central cylinder. For Ga, Hg and PbBi (cf. 2.1) this may not be required, but may become a necessity if irradiations above 350°C shall be performed. For temperatures below that level it may be sufficient to vary the heat flow resistance across the double walled steel container by adjusting the gas pressure in the interspace to keep the temperature at the desired level. A detailed analysis is still pending, since it requires exact dimensions of the design. In any case, it should be possible to maintain the desired temperature level in the liquid metal while cooling the outer

surface of the stainless steel container with moderately pressurised water only. Heat losses towards the top of the insert will have to be minimised by a system of baffles and a design with high heat flow resistance along the walls.

4. Ancillary equipment and handling procedures

Safe and relatively uncomplicated handling of the specimens and the irradiation insert after the end of the irradiation was an essential aspect in conceiving the whole system.

After irradiation the assembly (central cylinder and cassette) with the samples is lifted to allow the liquid metal to collect under the cassette in order to avoid damage of the samples if the metal solidifies (such as Pb-Bi) or to enable sealing its surface, if it stays liquid with a non-radioactive layer, for example Gallium[2] but possibly also simply water. This is done in hermetically sealed conditions (except for gas admission to fill the volume) by expanding the bellows at the top of the container. With the metal solidified or/and covered with an inert layer, the gas space can be vacuum dried and flushed to capture all volatile contamination in a filter system. This process can be assisted by activating the heater system on the central cylinder.

After unscrewing the top flange the central cylinder, together with the sample cassette, can then be pulled into a transfer cask with a shield gate at its bottom (Fig.8). This cask can be mounted on top of a smaller transport flask into which the cassette is lowered by means of the bar from which it is suspended (Fig. 5d). After detaching the bar from the cassette and closing the shielding gates of the transfer cask and the transport flask, the specimens are ready for shipment. Alternatively, the whole transport cask could be shipped to the hot cells and the specimens removed from it there (Fig. 8). In this case it is important that the cask dimensions meet the size requirements imposed by the hot cells.

In principle, a new cassette with a set of specimens can be loaded onto the support cylinder and inserted into the container for irradiation again. In this case the container would be positioned in such a way that the previous beam "window" is now located at an angular position out of the proton beam.

At the end of the container's service life, the metal in it can either be solidified by cooling (Pb, PbBi) or will be converted into a solid amalgam or compound in the case of Mercury. It will the be covered by an inert solid layer (PbBi) before being sent off to the radioactive waste disposal.

While the sample transport flask may be of the usual simple design of a shielded transport container - with provisions to fix the cassette in such a way that it can be detached from and attached to handling bar, the transfer cask should be able to serve a number of purposes:

- It should be possible to hook up the vacuum drying and flushing system to the transfer cask in order to remove residual contamination from any objects in it.

---

[2] For temperatures ~ 30 – 40 ^{0}C, gallium has low solubility in mercury ~ 1 – 2 % and low vapour pressure10^{-5} - 10^{-4} Pa [26,27]. A layer of 2 - 4 cm can safely isolate mercury during handling operations above its surface.

- The cask should be suitable to handle the central cylinder with the sample cassette alone or the irradiation container or the whole assembly (Fig 8). In the latter two cases drying off the residues of cooling water must be possible.
- The cask must, of course, be of sufficient thickness to provide for safe working conditions in its vicinity in all situations. Probably a steel thickness of about 30 cm will be sufficient, which can be added to the outside of the cask according to actual needs. A gate valve with sufficient shielding capability and with provisions to solidify residues of liquid mercury when the inner part of the insert alone is handled should be provided at the bottom of the cask.
- The height of the cask should be sufficient to accommodate the irradiation container with the bellows expanded (Fig 8b). At least it should be possible to mount a suitable extension at its top.
- The transfer cask should allow to melt solidified metal in the bottom of an irradiation container
- It should allow encapsulation of remaining radioactive metal and its additional isolation before delivering to a storage after irradiation;
- The transfer cask should also be used to place a new irradiation insert in the beam stop.
- It must be possible to fix the irradiation container safely inside the cask also for long distance transport.

So, the transfer cask is a working place for the number of technological operations and must be designed with enough flexibility. The question, whether it should have its own hoist or whether the overhead crane can be used for all lifting operations has yet to be decided.

The system for vacuum drying, which is equipped with filters for holding back radioactive vapors, will decontaminate the ampoule surface and inner walls of the container. It should also be suitable to dry off the outer wall of the container which, during operation, are exposed to water. Mercury vapors shall be converted into solid amalgams or compounds.

5. Options

As noted above, the proposed installation can be deigned in such a way that it allows irradiation in a variety of different liquid metals and in a large temperature range, as well as under widely different load (internal tube pressure and power density) conditions. The dimensions mentioned in parts of the paper are rather tentative and chosen for the case where a peak power density in steel of 1.5 GW/m^3 is desired, which is a very high value. For lower power density the irradiated volume can be larger and so can be the dimensions of the test tubes. In this case it may even be possible to cut more or less "standard" test specimens from the tube walls and to examine them with usual tensile testing techniques. The necessary equipment, and relevant experience exist in IPPE and RIAR.

Standard practice in reactor irradiation is to fill the test tubes with the right amount of gas in such a way that the desired internal pressure is reached at the temperature of irradiation. In the case of

proton irradiation heating is very non-uniform and most of the tube surface is at the average temperature of the surrounding liquid metal with only a hot spot at the position of the beam. In this case the uncertainty in temperature determination is, to a first approximation, proportional to the ratio of the part of the tube volume irradiated by the primary proton beam to the total gas volume in the tube. It may, therefore, be preferable to fill most of the volume inside the tube with liquid metal. This can either be the same material as the one used at the outside, or a different one whose behaviour towards the test tubes is known. Partial filling of the tube with liquid metal has three advantages: (1) it will enable a more definite temperature and hence gas pressure control; (2) it will enhance the neutron generation in the test volume and hence reproduce more closely the expected cascade-evaporation particle spectrum in a real target; (3) there is a smaller amount of gas in the volume, which results in less stored energy.

Hermetically sealed tubular samples partially filled by liquid metal and a gas filled cavity in the upper part (for pressure and temperature maintenance) would also allow chemical and spectroscopic analysis for spallation products in the liquid metal and in the gas .

With tubular specimens much longer than the beam dimensions, it will be possible to investigate ringlet samples, which were irradiated in different positions relative to the beam axis and, consequently, have different damage levels as well as different ratios of gas generation to defect production. For tubes irradiated in the geometrical shadow of the front tube, different effective proton energies and flux levels of cascade neutrons can be utilised.

If sodium (or another alkaline metal), is to be used as the liquid component, safe separation from the cooling water of the container is of prime importance. In this case the tubes can be filled with sodium, while their outside is surrounded by Pb-Bi, Ga or another easily melting alloy, serving as an additional barrier to separate the sodium from the water coolant. This will allow also safe use of sodium while , at the same time, keeping its amount at a minimum (~ 50 – 70 g).

In principle it should also be possible to carry out mechanical testing of samples in a liquid metal under irradiation and in situ straining (constant force, constant strain, or even cyclic) by using a technology similar to the one implemented a PIREX at PSI [28] and taking advantage of the fact that the sample cassette is only suspended from the central bar and that this assembly could be replaced by a differently designed one.

6. Conclusions

The above considerations show that the it is possible to realise a facility at the beam stop of the Moscow Meson Factory which, even at the current performance levels of the accelerator would allow important irradiation experiments with regards to liquid metal-solid metal interactions. Most of the technical solutions of this concept have been realised elsewhere in the past and calculations show that they can be adopted to the prevailing conditions. The installation as conceived is rather flexible and may be adopted in order to operate with different coolant or spallation target metals. Dimensions and shapes of samples can be varied, as can be temperature and pressure (mechanical load). Furthermore, the system would be rather cost effective, since it is possible to use existing technologies and equipment of research laboratories at IPPE, Kurtchatov

Institute, and RIAR, and also, where possible, parts and existing designs of equipment of the present beam-stop.

7. Acknowledgements

The details given in this papers are the result of intense interaction with a large number of people. Instead of trying to enumerate all of them, we would like to enlist the institutions from which we received most of the advice that lead to the proposed concept. We are grateful to

- the experts of IPPE,
- the experts of Laboratory of Asynchronous Drives of Institute of Electromechanics,
- the experts of OKB Hydropress,
- the experts of Inst. of Rare Metals,
- the experts of OKB Prometey,
- the experts of Kurchatov Institute,
- the experts Bochvar Institute of Inorganic Materials

for useful discussions and recommendations for problems in connection with the work presented.

Special thanks also go to our colleagues and the management of INR Troitsk and Paul Scherrer Institut for supporting this work. One of us (S.F.S.) would particularly like to thank PSI for making possible several stays as a guest scientist in order to carry forward this work.

8. References

[1] Yu.F. Balandin, V.G. Markov. Structure materials for reactors with liquid metal coolants. Leningrad, Ship industry, 1961.

[2] G. Bauer. SINQ - Status report Oct. 1990. ICANS-11, p.41, KEK, TSUKUBA, Oct. 22-26, 1990.

[3] H. Lengeler. Study of a European Spallation Source. ICANS-12, p-1.

[4] G.S. Bauer. Mercury as a Target Material for Pulsed (Fast) Spallation Neutron Sources. Proceeding of the Meetings ICANS-13 and ESS-PM4, p. 547.

[5] B. Appleton. Status of Oak-Ridge Spallation Neutron Source (ORSNS) Project. ICANS-13, p.814.

[6] M. Furusaka, H. Ikeda. Current status of JHP N-arena. ICANS-13, p.836.

[7] G.S. Bauer. The European Scene regarding Spallation Neutron Sources. Workshop on the Technology and Thermal-Hydraulics of Heavy Liquid Metals. Schruns, Austria, March 24-29. 1996. P. 1-1.

[8] S. Wender. High Power Neutron Production Targets. (The same) p. 1-35.

[9] J.R. Haines et al. Mercury target R&D For The Oak Ridge Spallation Neutron Source. (the same), p.10-39.

[10] Proceedings of the International Workshop Nuclear Methods for Transmutation of Nuclear Waste. Problems, Perspectives, Cooperative Research. Dubna, Russia. 29-31 May 1996.

[11] C. Rubbia. Status Report on Energy Amplifier. Geneva, CERN, 1994.

[12] C. Bowman, E. Arthur, M. Cappiello e.a. Nuclear Energy Generation and Waste Transmutation Using an Accelerator-Driven Intense Neutron Source. Rep. LA-UR-91-2601, 1991.

[13] V.G. Miroshnichenko, S.F.Sidorkin, Y.Y.Stavissky et al. Multiplying Target for a High-Intensity Spallation Neutron Source. ICANS-13, p.454.

[14] V.N. Tebus, B.V. Petrov, P.V. Romanov et al, A Metal Tritium Breeder Materials for ITER Blanket. Atomic Energy, v.81, p.372, 1996.

[15] F.A. Kozlov, V.N. Ivanenko. Sodium as Coolant for Fast Reactor NPPs. Atomic Energy. V.80, issue 5, p.337, 1996.

[16] B.F. Gromov, Yu.I. Orlov, G.I. Toshinskiy, V.V. Chekunov. Nuclear Power Facility with Lead-Bismuth Coolant. Atomic Energy v.81, p.340, 1996.

[17] V.V. Orlov et al., Unconventional Concepts of NPPs with Inherent Safety, Atomic Energy, V.72, I.4,(1992) pp.317-328, in Russian.

[18] Corrosion in Nuclear Application. By Warren E. Berry, 1971.

[19] International Workshop on Spallation Materials Technology. April 23-25. 1996. Oak-Ridge, Tennessee.

[20] Y. Dai, G.S. Bauer. Static Corrosion of Martensitic and Austenitic Steels in Mercury at 300 ^{0}C. Symposium on Materials for Spallation Neutron Sources. Feb. 9-13, 1977, Orlando.

[21] M.I. Grachev, et al. Pulsed and quasistationary neutron sources based on proton beams of Moscow Meson Factory. ICANS-11, KEK, Tsukuba, October 22-26, 1990, p.454.

[22] P.L. Kirilov, Yu.S. Yuryev, V.P. Bobkov, Handbook on Thermal-hydraulic Calculations (Nuclear Reactors, Heat Exchangers, Steam Generators). Energe-atomizdat, Moscow (1984) in Russian.

[23] V.I. Subbotin et al., Hydrodynamics and Heat Transport in Atomic Power Plants. Atomizdat, Moscow (1975), in Russian.

[24] V.A. Gluchich, A.V. Tananaev, I.R. Kirillov. MHD in Atomic Energy. Moscow, 1987, in Russian.

[25] Y. Takeda. Velocity Profile Measurement by Ultrasonic Doppler Method. Experimental Thermal and Fluid Science 1995;10:444-453.

[26] V.S. Chirkin, Thermal properties of nuclear technics materials. Atomizdat, Moscow (1968), in Russian.

[27] S.P. Yatsenko, Gallium, Interaction with metals. Nauka, Moscow (1974), in Russian.

[28] M. Victoria, D. Gavillet. An Overview of the PIIREX Proton Irradiation Facility and its Research Program. International conference on accelerator-driven transmutation Technologies and Applications. Las Vegas, NV July, 1994, p.891.

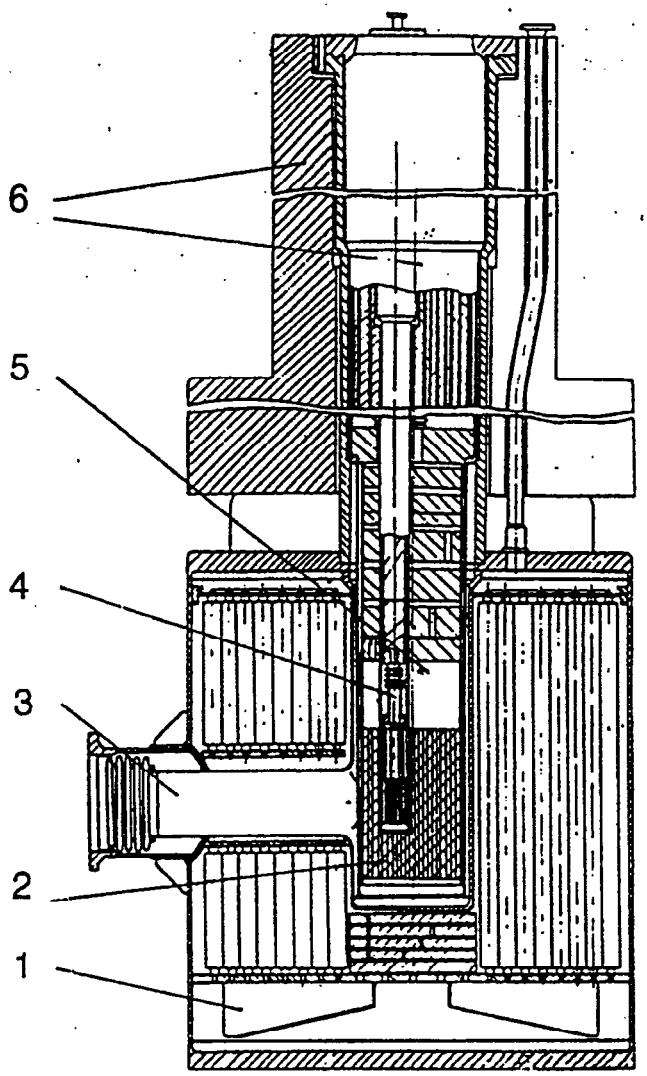

Figure 1a: Sketch of the present beam stop at the MMF:

1 water cooled shielding.
2 beam stop insert made of tungsten plates.
3 proton beam channel.
4 irradiation insert in thimble.
5 aluminium vessel.
6 removable top shield (steel plugs).

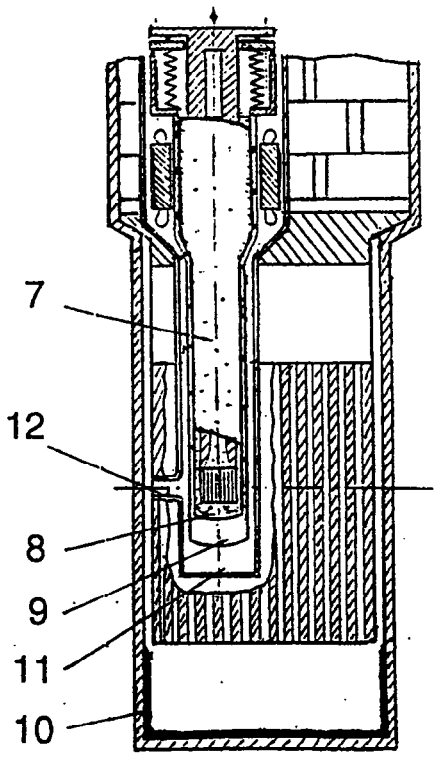

Figure 1b: Sketch of the proposed LM-irradiation insert that would replace the present irradiation insert, requiring only minor modifications to the tungsten plate assembly:

7 liquid metal container.
8 liquid metal
9 outer container of stainless steel with gas atmosphere.
10 Al_2O_3 cover of the bottom part of the aluminium vessel for corrosion protection in case of a LM leak.
11 receptacle for irradiation insert with water filled catcher volume.
12 jet forming manifold for window cooling

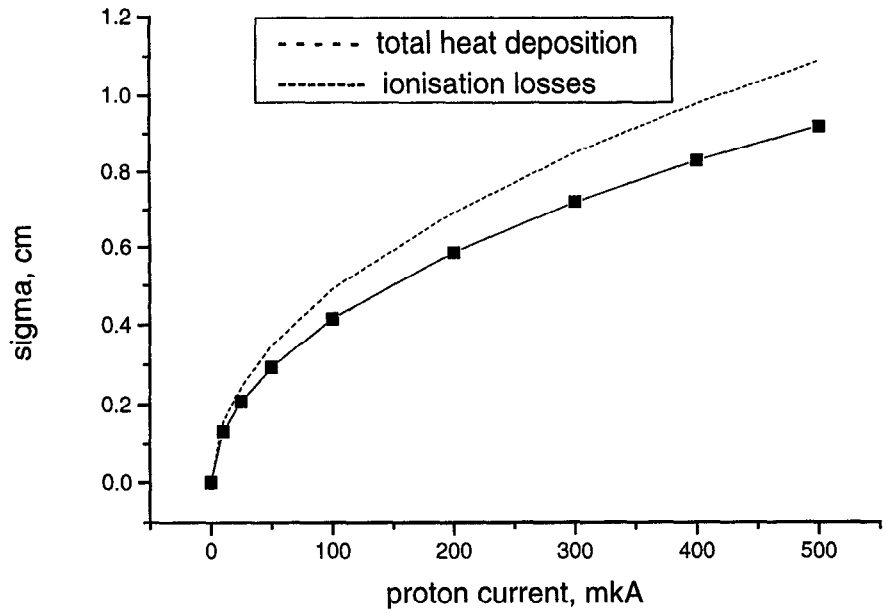

Figure 2: Dependence of the standard deviation σ of a beam with Gaussian intensity profile on the proton current for a stainless steel sample with required maximum heat deposition of 1.5 kW/cm^3. The solid line corresponds to ionisation losses only, the dashed line is the total heat deposition.

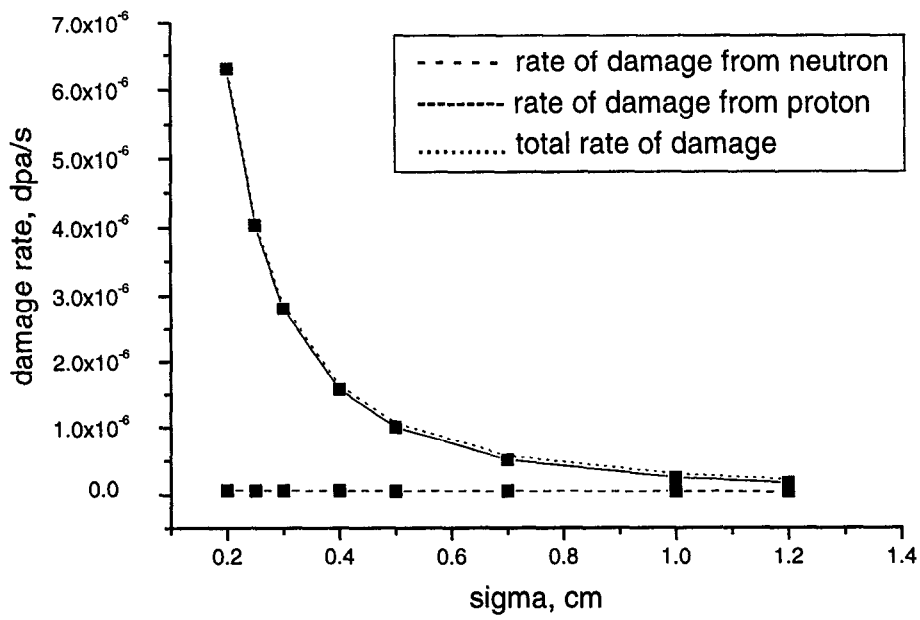

Figure 3: Estimated radiation damage rate due to the proton beam (450 MeV) and the spallation neutron flux as a function of beam width at 100 μA

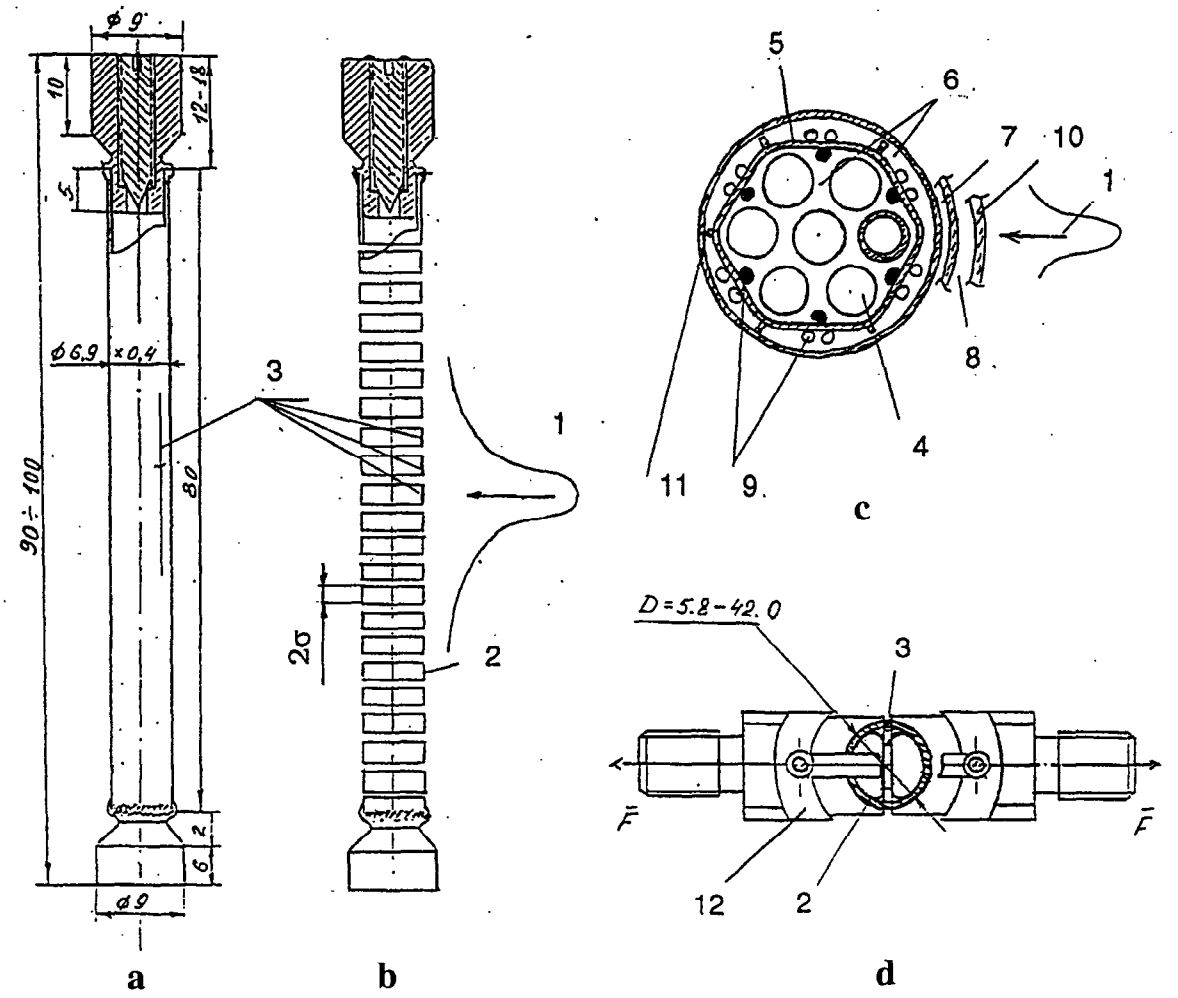

Figure 4: Scheme of samples:

a - tubular sample with sealing plug at the top
b - sample cut up into rings for post irradiation examination
c - specimen cassette with 7 tubular samples
d - typical ring holder for mechanical test of ring samples

1 proton beam
2 sample ring
3 mark
4 tubular sample in cassette
5 cassette body (non stress samples)
6 liquid metal (Hg or Pb-Bi) under the temperature of 150-250°C
7 He or Ar thermal barrier
8 water coolant
9 thermocouples in the protective covering and displacers
10 outside body
11 spacers
12 clamps on testing device

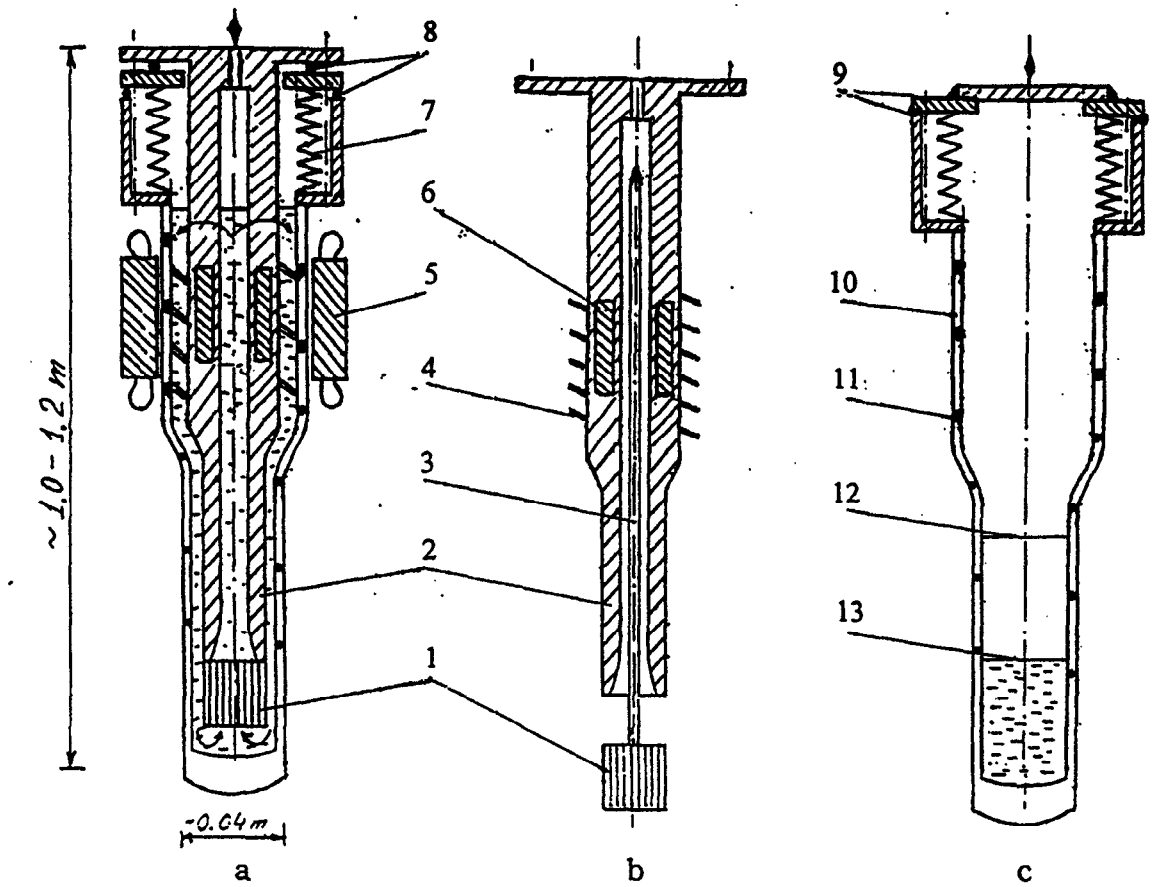

Figure 5: Sketch of the assembly and the main elements of the LM irradiation insert:

a - assembled insert;

b - flow guide and displacement body with specimen cassette suspended from its support bar and pushed down from the flow guide

c - liquid metal irradiation hull ready for shipment to disposal: the liquid metal has been solidified and a top plate welded in place for permanent sealing;

d - specimen cassette in transport flask.

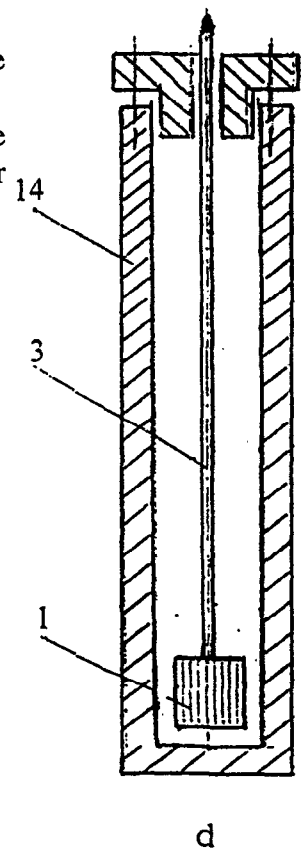

1 cassette with tubular specimen
2 cylindrical flow guide and liquid metal displacement body
3 cassette support bar (holding diagnostics and supply leads)
4 helical flow guide for pumping
5 rotating field EM-pump
6 low permeation steel core to increase EM-pump efficiency
7 bellows for concealed lifting of sample cassette
8 seals
9 welds
10 double walled stainless steel hull
11 spacers
12 level after mercury has been solidified
13 liquid metal level before solidification

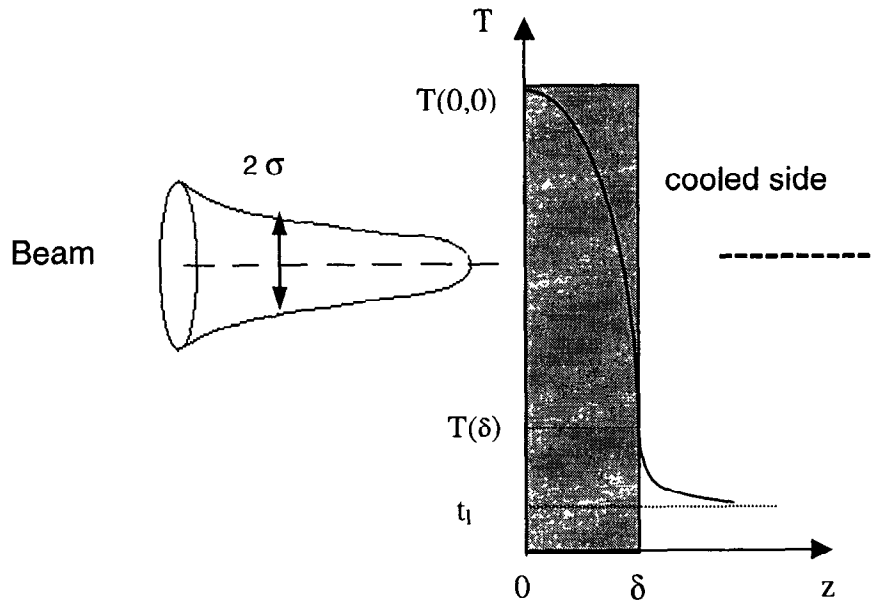

Figure 6: Configuration assumed for calculating the temperature gradient in the walls.

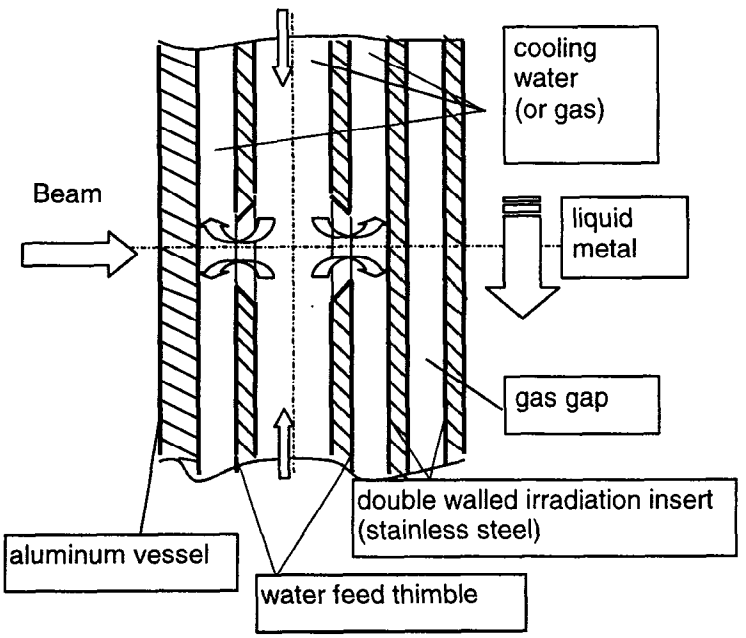

Figure 7: The concept of jet cooling of the beam windows.

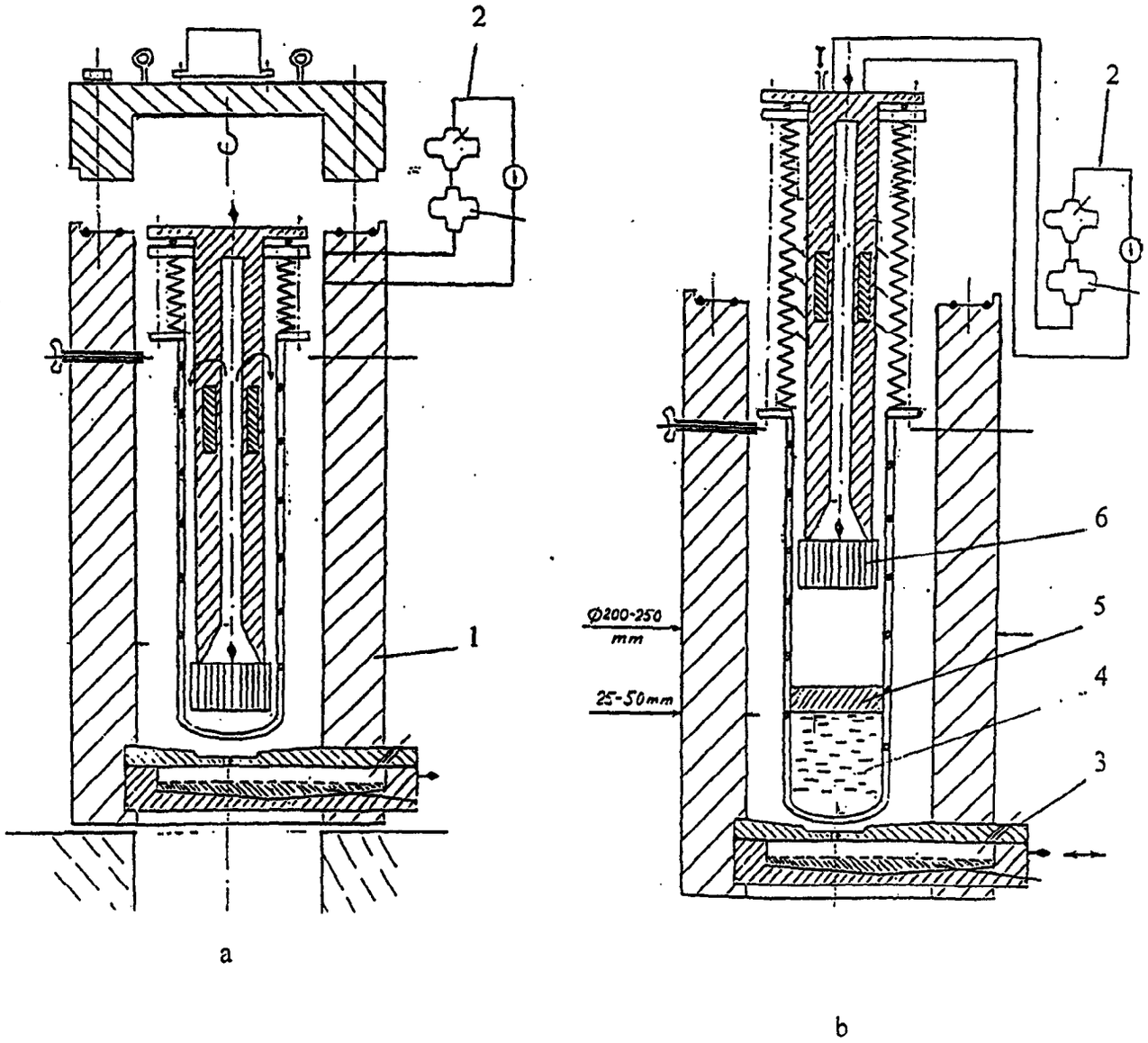

Figure 8: Sketch of additional equipment and possible alternative removal procedures
a - LM-insertion in the transfer container and cleaning of outside surface
b - the cleaning of holder with samples

1 transfer container
2 vacuum drying system
3 removable bottom with Pb or Cu
4 LM level after lifting of the samples
5 Ga-plug (~3 cm)
6 cassette with samples

ICANS XIV
14th Meeting of the International Collaboration on
Advanced Neutron Sources
June 14-19, 1998
Starved Rock Lodge, Utica, IL

Flow Study of JHF N-arena Liquid Target

Jun Sakakibara[1], Takashi Ino[2], and Yasushi Takeda[3]

University of Tsukuba[1]
High Energy Accelerator Research Organization (KEK)[2]
Paul Scherrer Institute[3]

We have been studying the flow of water to design the JHF N-arena liquid metal target using a half size model, and we have found that a cross flow geometry, where the flow is at a right angle to the proton beam axis, is quite suitable for our mercury target design.

The flow was measured for three different test channels. Each had a 200 mm wide U-shaped part following the straight inlet section with a width of 70, 145, or 200 mm. The velocities of water in the U section with a 70 mm inlet were measured to be highest at the outside in the channel and became lower toward the inside while the other two showed the opposite tendency, higher velocities at the inside and lower at the outside. With a consideration of the target heat removal, the optimum channel width at the inlet section was estimated to be approximately 100 mm.

The Reynolds number at the U section of the model was about 1×10^5, one order smaller than the real mercury target. It, however, is considered that there are no significant differences in the time-averaged velocities between the model and the real since the turbulent flows in the channels are fully developed at such high velocities.

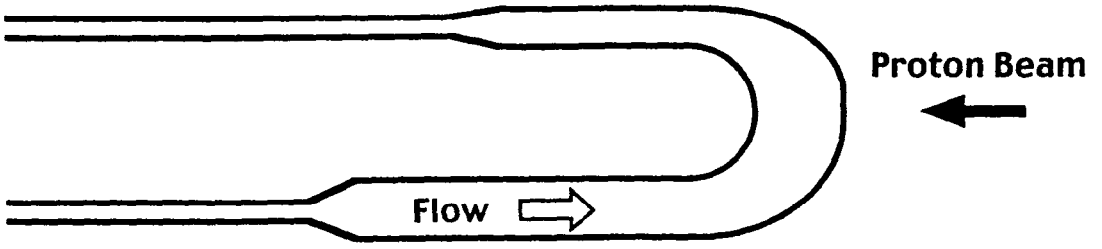

Cross flow geometry of the liquid metal target. The test channel was 200 mm wide on the proton beam axis and tapered down to 70 mm. The width in the straight inlet section was either 70, 145, or 200 mm.

ICANS XIV
14th Meeting of the International Collaboration on
Advanced Neutron Sources
June 14-19, 1998
Starved Rock Lodge, Utica, IL

FLOW MEASUREMENT IN A SINQ MOCKUP TARGET USING MERCURY

Y.Takeda, H. Kikura & G. Bauer
Paul Scherrer Institute, Switzerland

ABSTRACT

An investigation on a flow behaviour of SINQ target is under progress. The experiment is performed using mercury as a model liquid in a mockup target geometry. Measurement is by using ultrasonic Doppler method and one- and two-dimensional stationary flow has been in fully investigated for the hemispherical geometry in the form of velocity profiles and flow maps. Effects of gap geometry and flow rate was investigated. The velocity level was found to be quite low in a deep pocket region of the window, but the flow field is quite symmetric to the beam axis as a time-averaged behaviour.

INTRODUCTION

Flow behaviour around the beam entry window is of utmost importance in relation to heat transport in liquid metal target and to cooling of window by target liquid itself. Design criteria has not yet been clarified and it is an urgent need to investigate flow and temperature behaviour in this region. However, measurement of a flow, a velocity at any point or its spatial and temporal distribution, has been one of the most difficult tasks in using liquid metals and, because of it, its application to the study in physics and to industrial devices has been largely limited.

For overcoming such difficulties, the ultrasonic Doppler method has been developed at PSI and is established after a long development effort [1-3]. This method uses a pulsed echography of ultrasonic beam. From the echo signal, a position information is derived from a time difference between pulse emission and echo reception, and velocity information is from instantaneous frequency at each instant of echo reception. By processing the echo signal such that the instantaneous frequency is obtained as a function of time after pulse emission, instantaneous velocity profile can be obtained.

In this paper, we present our latest results of the measurement of mercury flow in the SINQ mockup target geometry. The investigation is only about flow behaviour and the use of mercury in a forced convection loop can be justified because the investigation is about local flow behaviour and mercury has very similar physical and thermal properties to Lead-Bismuth Eutectic which is a target material of SINQ.

EXPERIMENTAL SET-UP

Mercury loop

The mercury loop of IPLU (Inst. Physics Latvian University) consists of an electromagnetic (EM) pump, two coolers, EM flow meter, a reservoir tank and SINQ target test section. The total mercury inventory is 4.6 m^3 (6 tons) and the maximum flow rate by this EM pump is 4.2 *l*/s. The loop is operated under the room temperature.

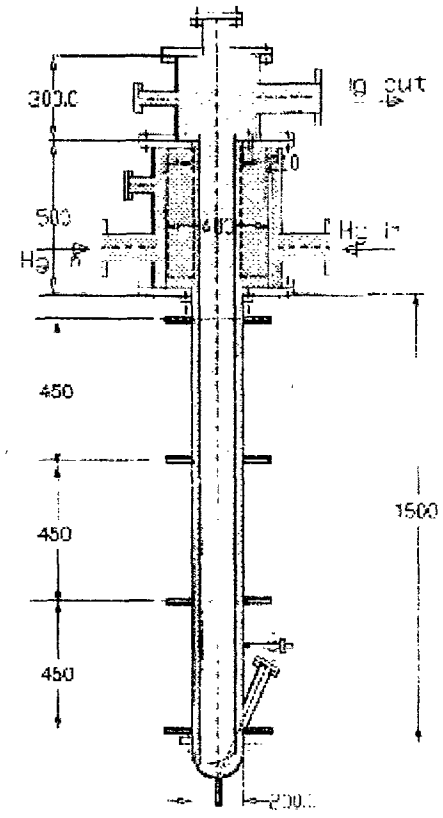

Figure 1 Test section (SINQ Target geometry)

Geometry of SINQ at Riga

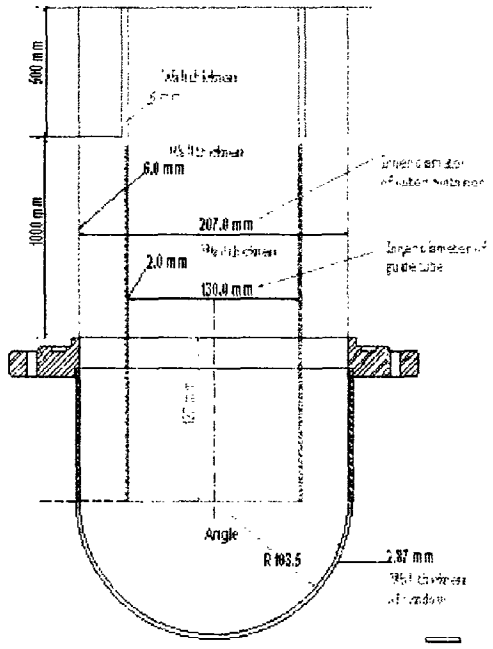

Figure 2 Geomtry of SINQ target window region

Test section

The SINQ target test section is illustrated in Fig.1 and 2. It consists of double coaxial cylinders and has two buffle chambers at the top for inlet and outlet flow respectively. The mercury is fed into this chamber through 6 inlet tubes connected to it. It then flows down in the annular channel toward the bottom part called "window". The fluid turns there into a inner circular channel inside the inner guide tube and flows up to the second chamber for outlet. The diameter of the outer tube is 207 mm and the total length of the test section including these chambers is ca. 2.3m.
We have prepared two kinds of windows having different shapes. The one is a hemispherical window and another has a so-called Kloepperboden shape. The hemispherical window is, however, a reference shape in this study. The radius is 103.5 mm with its center at the exact edge of the guide tube. The geometry of the flow channel is given in Fig.2 and Fig.3 shows this window mounted on the test section.

The Kloepperboden is a structural element and has a flatter structure. Due to a space limitation, the results would be reported separately, and only the result of hemispherical window is reported. All the components and windows are made of stainless steel.

Instrumentation

Flow measurement was made using ultrasonic Doppler method (UVP). The device was developed at PSI aiming at the measurement of flow velocity of liquid metal. In order to be able to measure the flow from

Figure 3 SINQ target window mounted on test section

outside the container wall, the wall thickness was selected as 2.87mm. The standard normal temperature transducer was set on the wall using a positioning device.

For the UVP to work successfully, it is a condition that the fluid includes tiny particles as a reflector of ultrasound wave with fairly high concentration. Due to a large density of mercury, most of impurities and gas bubbles are segregated before the loop is started. Therefore, nitrogen gas was injected prior to startup of the loop to mix small bubbles in the liquid as a reflector of ultrasound.

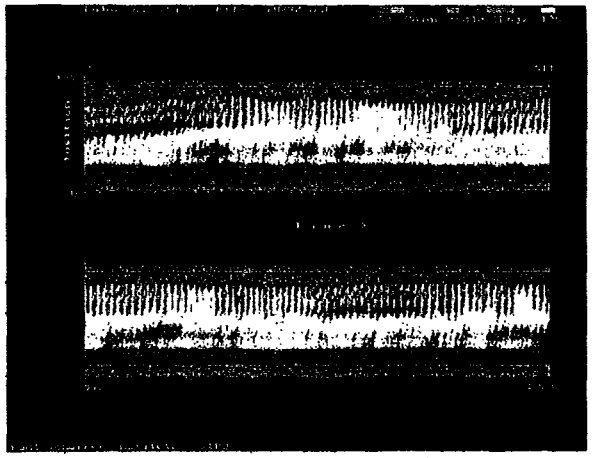

Figure 5 Color density plot of spatio-temporal behavior of the Mercury flow.

One of the worries supposed before the experiment was a problem of wetting of Mercury to the stainless steel wall. It is well known that Mercury has a poor wetting to stainless steel. If the wetting is poor and there remains a thin gas layer between Mercury and the wall, ultrasonic pulse cannot be transmitted to the liquid and measurement might be failed. However no such problem was encountered during the experiment. The ultrasonic beam was transmitted through the stainless wall to Mercury and back-scattered echo signal of sufficient amplitude was received from the beginning of the experiment.

Measurements

We performed series of measurements. The first one was aimed at obtaining one dimensional velocity profiles covering as wide area as possible in the window area. This series was done basically for confirming all the experimental elements such as a loop, a test section and instrumentation to be successfully prepared. And thus, measuring lines of UVP were set rather freely.

The second one was to obtain vector flow maps in the region of returning flow near the edge of the guide tube.

The third one was to study the effects of geometry and flow rate. The effect of the geometry was investigated mainly for the hemispherical window in terms of the gap distance between the edge of the guide tube and the bottom surface. Three gap distances were studied for 2, 4 and 8 cm. The flow rate was changed for 0.6, 1.2 and 2.4 *l*/s.

Experimental condition

The mercury was first well mixed in the reservoir tank by injecting gas from the bottom and then filled into the loop. After starting the EM pump, the flow rate was increased gradually. Temperature was not regulated and it was more or less room temperature around 15°C. It was however observed that it increased slightly when the power of EM pump was increased.

RESULTS AND DATA ANALYSIS

Instantaneous Velocity profiles

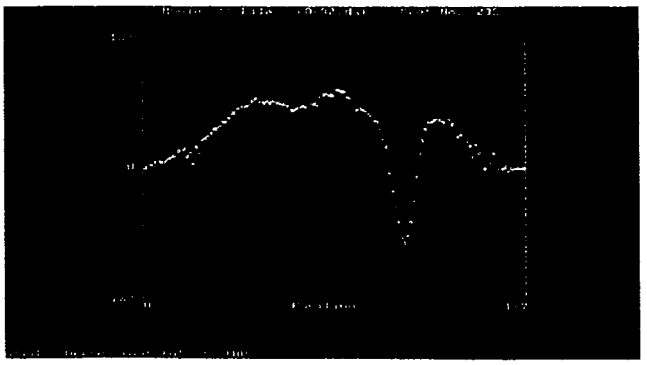

Figure 4 is a typical example of an instantaneous velocity

Fig.4 is a typical example of an instantaneous velocity profile. It shows a successful application of UVP to the mercury flow. As seen in this example, there is a large vortex structure in the flow, which shows a typical chaotic fluctuation as displayed on the color density plot in Fig. 5. The typical time resolution for one instantaneous velocity profile is 100-150 msec. When the profiles are displayed continuously on the computer screen, it reproduces the measurement in motion. However, the display in color density reveals the spatio-temporal behaviour of the flow field more clearly.

Average profiles

A typical data set consists of 1024 instantaneous velocity profiles. For investigating a stationary flow field, the time-averaged velocity profiles were computed. Fig. 6 shows averaged profiles on the center line. It should be noted that the velocity obtained by this method is a component of the velocity vector projected onto the measuring line. In this example, it is therefore a distribution of the axial component as a function of axial position on the center line; Vz(z, r=0).

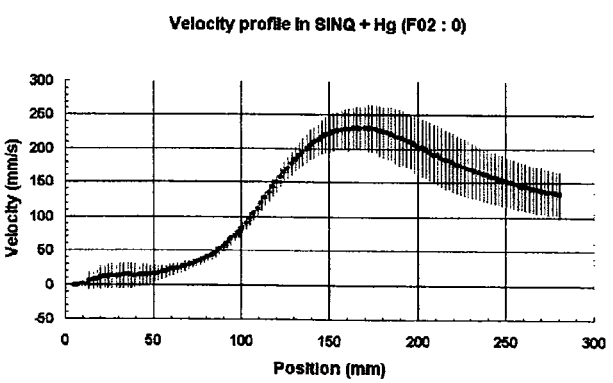

Figure 6 Time-averaged velocity profile on the center line.

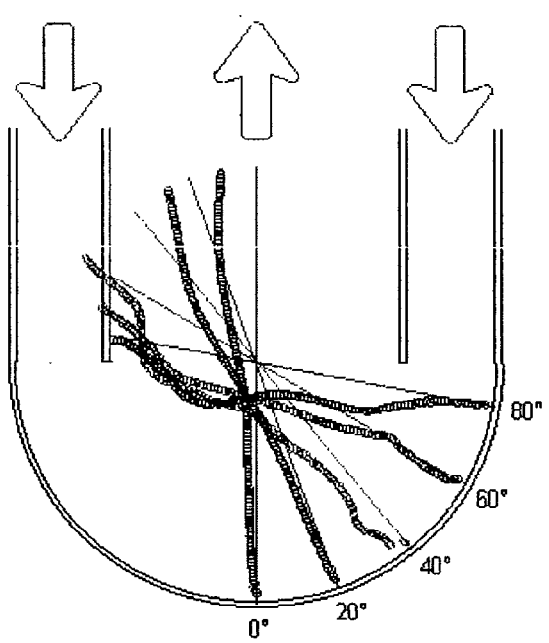

Figure 7 One-dimensional velocity profiles.

Two series of measurements were made for obtaining a one-dimensional distribution. The one is for the interior region, shown in Fig. 7. Simply it shows that the velocity is pretty low near the wall, namely inside the deep pocket of the spherical window (up to ca. 80mm) but then it is high beyond this point. Fig. 8 is a similar plot of the measurements fanned from the center of the window. It shows a fairly good (axial) symmetry and a good agreement with the nature shown in Fig.7.

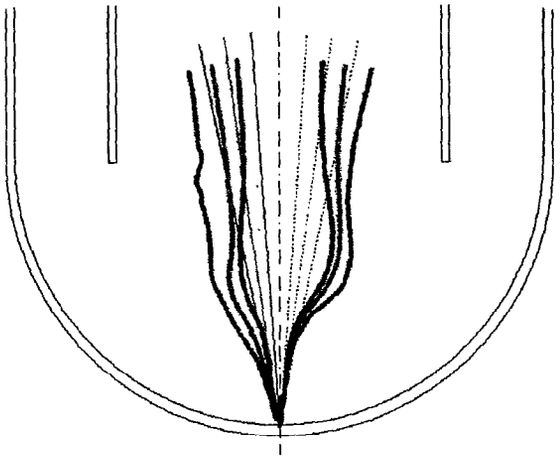

Figure 8 Flow around the centerline. (The sign of velocity coordinate is opposite for plus and minus inclination for display purpose.)

Vector map

Since all the measuring lines are aligned non-parallel, it is possible to obtain two velocity components at the crossing points of measuring lines. Even if these two components are not orthogonal, it is still possible to form a velocity vector on the crossing point from them. The second series of measurement was made for this vector map measurement, in such a way that all the measuring lines are organized suitably for forming the vectors. The details of the method to form the vector in this data analysis is given in [4].

The vector field was computed for the second series of measurement which consists of 36 measuring lines (Fig.9a). This generates in total 379 vectors in the field, when eliminating the points where two crossing angle is less than 15°. The computed vector field is plotted in Fig.9b.

The vector maps thus obtained for different gap distances and flow rate for the third series measurements are shown in Fig.10.

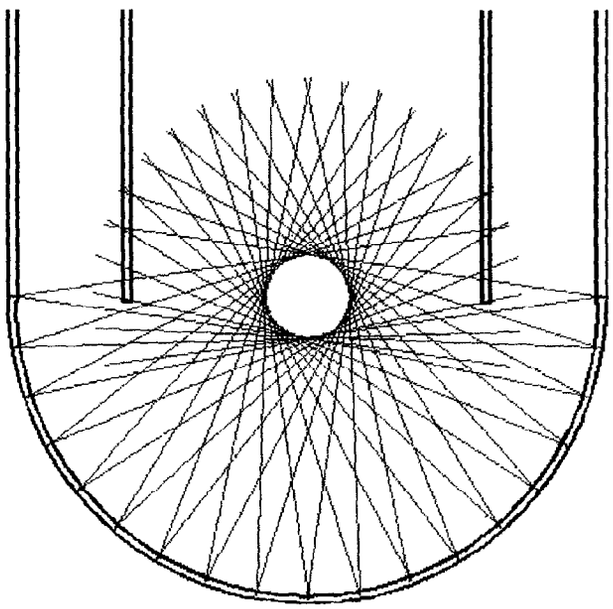

Figure 9a Measuring lines for vector map measurement

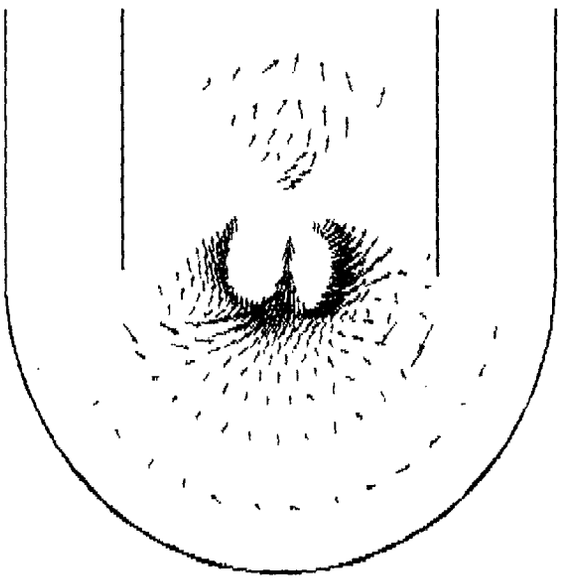

Figure 9b Obtained vector field

DISCUSSION

Flow field

As observed in Fig. 8 & 9, the velocity is very small deep inside the spherical region, especially near its top, although it is not stagnant. Since the measured velocity is a component along the measuring line, it may not be easy to read the result. The easiest case is for the angle of 0° of Fig.8 (same as Fig.6). The axial velocity is low from the bottom of the window until 100mm, namely the center of the sphere. From other measurements we know that there is a recirculation zone just behind the edge of the inner tube. This makes an effective flow area smaller in this region for a main circulation. The position where the velocity distribution shows its maximum value is roughly corresponding to this recirculating region.

When observing a flow on the color density plot or in motion picture, a typical chaotic structure could be recognized in this region; near the edge of the inner guide tube (see Fig. 5). This is a significant flow structure especially for the gap distance of 8 cm. For the smaller gap distance, independent of the flow rate, such chaotic motion is weakened.

We can observe on the plot in Fig.8 a fairly strong jet behavior of the flow exiting from the annular channel. The velocity profiles at the angle from 80° down to 40° have a portion of a flat velocity distribution near the window wall, showing an evidence of jet flow. The width of this jet becomes smaller for approaching to the angle of 40° and it disappears at the angle of 20°.

Axial symmetry

In Fig. 7 and 8, it is clearly seen that the flow field is not necessarily symmetric for the spherical window with gap distance of 8 cm. This seems to be due to the spatio-temporal chaotic flow which is generated near the edge of the inner guide tube. The large eddy is generated in this region, which is totally spatio-temporal. Time characteristics has to be studied in more detail, but it seems that our total measurement time is not sufficient to smear out this characteristics. It may be also due to a non-symmetric inlet condition in the annular channel.

Effects of flow rate

The effect of flow rate is seen in Fig.10 such that it becomes more symmetric for the large flow rate, although it is not a strong effect. A feature in the vector fields appears similar for three flow rates studied here when the gap distance is constant. Again the flow is very non-symmetric for 8 cm gap distance, but it ii similar for other cases.

Effects of gap distance

The effect of gap distance is significantly large as seen in Fig. 10. Even for the smallest flow rate with gap distance 2 mm, the flow appears quite symmetric. It is also seen that the region of very low velocity (dead layer) becomes smaller. It is obvious because the inlet flow velocity at the exit of the annular channel is high.

CONCLUSION

Flow behaviour has been investigated for a window region of SINQ target geometry using mercury and ultrasonic Doppler method. The geometry is still axisymmetry but flow rate and gap distance between the edge of the inner tube and window bottom has been studied. Following conclusions are drawn.

The Ultrasonic Doppler method was successfully applied to mercury flow contained in a stainless steel wall. The system used in this experiment works fine and needs no special modification for this kind of measurement. The ultrasonic transducers can be set outside the stainless steel wall. It enables us to use multiple transducer system for very efficient flow mapping. As a reflector of ultrasonic pulse, gas bubbles and/or impurities included in the mercury might be used. No wetting problem arose for the transmission of ultrasound pulse through the wall to mercury.

Time dependent one-dimensional velocity profiles were successfully measured, which show a strong vortex shedding behind the edge of the guide tube for 8 cm gap distance. The time-averaged profile on the centerline indicates that the recirculation inside the guide tube near the edge is strong.

The flow field is globally axisymmetric on the time-averaged profiles except for the case with gap distance of 8 cm. The effect of the gap distance is much stronger than that of the flow rate for the range studied in the work.

It is, however, proved that the inflow from the annular channel is still weak and may not be sufficient to cool down the central part of the window directly where the temperature is supposed to be highest. This is mainly due to a large dead zone in this region arising from a deep pocket of the hemispherical window and the symmetrical geometry of the total configuration. This requires us to study further in a three-dimensional configuration.

ACKNOWLEDGEMENT

We gratefully acknowledge the support work given by Mr. F. Barbagallo. Participation of IPLU staff, especially Dr. Platacis and Dr. Kolesnikov and the operation crew of the mercury lab of IPLU is greatly appreciated.

References

[1] Y. Takeda, Velocity profile measurement by ultrasonic Doppler method, Exp. Therm. & Fluid Sci., 10, 444-453, (1995)

[2] Y.Takeda, Instantaneous velocity profile measurement by ultrasonic Doppler method, (Invited paper), JSME International Journal, Fluids and Thermal Engineering, Vol.38, No.1, (1995) p8 - 16

[3] Y.Takeda, Ed., First International Symposium on Ultrasonic Doppler Methods for Fluid Mechanics and Fluid Engineering, PSI, Switzerland, 9.-11. Sept., 1996

[4] H.Kikura & Y. Takeda., Flow mapping using ultrasonic Doppler method, Proc. of ASME FED Summer Meeting, Washington DC, 98

Fig. 10 Vector flow fields for different gap distances and flow rates

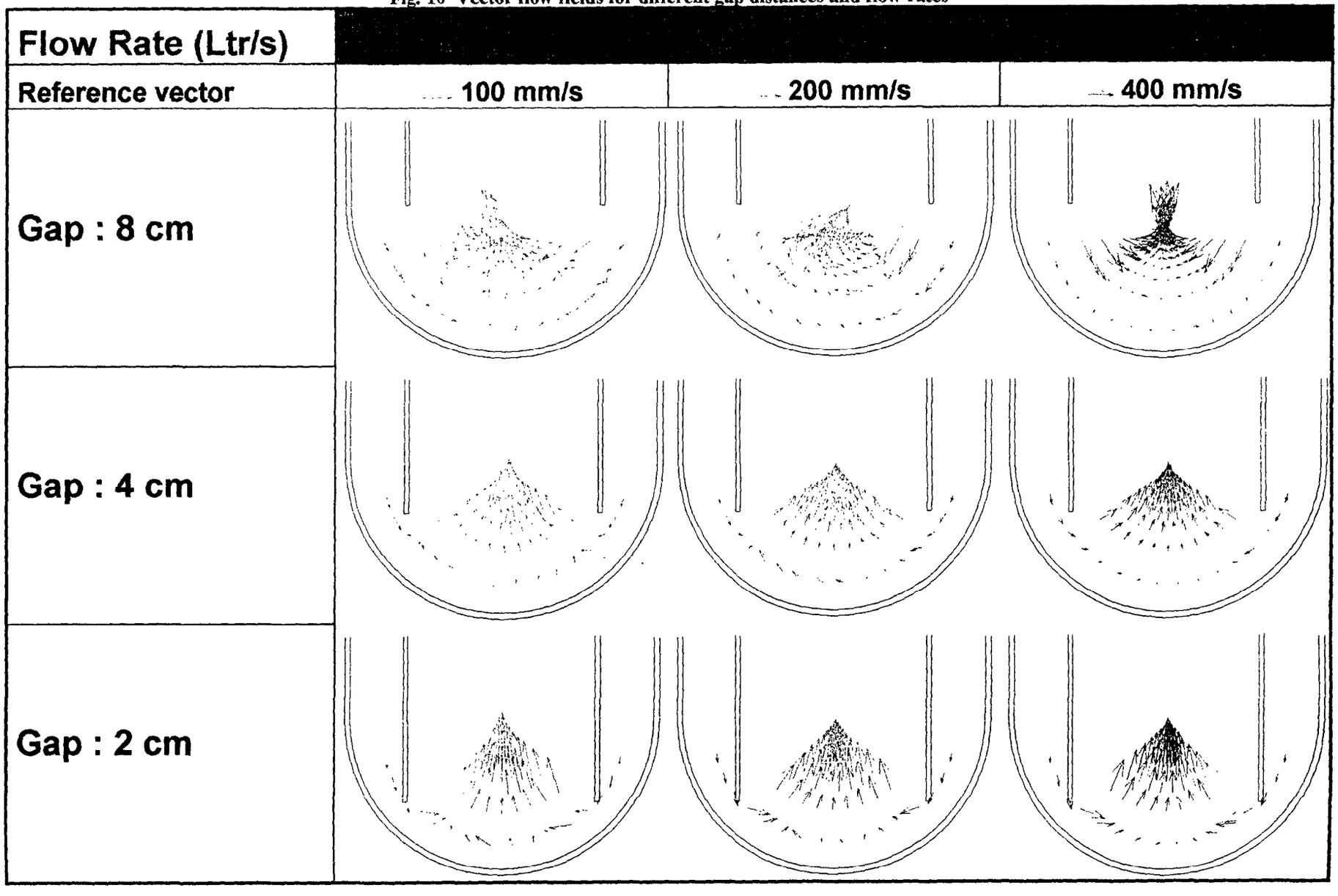

Flow Study on the ESS target water model

K.Haga[1], Y.Takeda, G. Bauer / Paul Scherrer Institute
B. Guttek / Forschungzentrum Jülich

INTRODUCTION

The liquid target of ESS has a configuration of horizontal channel flow. The target container is partitioned into two channels, the lower one is for inflow and the upper one for outflow. The liquid turns at the end where the proton beam is impinging. Detail is given elsewhere [1].

For this configuration, the behaviour of flow in these channels and turning pocket is very important for a secured heat transport out of the reaction zone. Since the flow is bent in the most critical region, occurrence of any recirculation in this region may lead to a boiling of mercury.

The hydrodynamic study is under way to investigate experimentally general behavior of the flow in the configuration of ESS liquid target. The study was performed by two-dimensional model and three dimensional mock up test is under progress. The liquid used is water at this stage. The mercury experiment is under preparation.

We always start the investigation of this kind by using a two-dimensional (2D) model with water. This is because of easiness of preparation and handling the liquid, for enabling flow visualization technique to be used, and good for understanding the flow phenomena.

In this paper the results of 3D experiment is mainly given, while the results of 2D experiment is briefly presented, since all the work and detail of the results can be found elsewhere [2].

Two-dimensional Model

Experimental set-up

Flow measurement for flow mapping was made using ultrasound Doppler method [3,4]. This technique has been developed at PSI for the target R & D program, and we established the method to obtain two-dimensional-two-components (2D2C) velocity vector filed. [5].

The test section, as illustrated in Fig.1, is made of plexiglas, 55 cm long, 20 cm wide and 10 cm height, which follows an entry region of ca. 100 cm. At the position of 3 cm high from the bottom plate a separation plate (2 mm thickness) is placed. An inflow liquid flows in a lower channel (30 mm x 200 mm channel cross sectional area) toward the hemicylindrical top (radius 50 mm) and after bending 180° there, it flows out in an upper channel (70 mm x 200 mm area). This test section is set in a water loop which has a maximum flow rate of ca. 2 *l*/s. The one measurement was focused on the recirculation zone in the upper channel, while the other on the returning flow in the hemicylindrical top. Ultrasound transducers are assembled in special mounting devices, which are attached to the outer wall of the test section. For the measurement of the upper channel, eight transducers are mounted in a block with a regular separation distance of 15 mm having a constant inclination angle of 15° to the normal line. Together with the measurements where the inclination angle is changed to -15°, we have 96 velocity profiles, from which we can form a two dimensional vector field. For the measurement of hemicylindrical region, 14 transducers are set with 12° separation angle and with constant inclination of 15°to the normal line on and at the outer wall. This configuration generates 28 velocity profiles. (on the method for the flow

[1] On leave from JAERI

mapping, ref [5].) More detail of the experimental setup and experimental method can be found in [5].

Flow map

The vector field obtained (361 vectors) is given in Fig. 2 for the upper channel. It is clearly seen that a flow is recirculating in the lower part of the channel (on the separation plate). On the two lowest lines, directions of vector are leftward for X<210 and rightward beyond this point, although vectors are quite small. On the third lowest line, it is more clearly seen that it flows leftward with significant velocity levels, ca. 10 cm/s. The thickness (height) of the recirculation zone is ca. 30 mm at x=50 mm and it extends to the point x=ca.200 mm (250 mm from the top of the cylinder). Beyond this point, the flow is more or less parallel and directed to the exit and no structure was seen.

Fig. 3 shows a result of the measurement for the hemicylindrical region, where 705 vectors are plotted. This shows clearly a returning flow along the end wall as generally anticipated. Since we plotted only time average velocity field, the flow is smooth and no significant small structure is displayed.

Spanwise motion

From the UVP measurements as well as from visual observation, we found that a spanwise motion is not negligibly small. The velocity profiles of the spanwise direction were measured at the top position of the hemicylindrical part along the wall. The Fig. 4 is a time averaged profile. It shows clearly a large spanwise circulation; a pair of large vortices which is observed from the result that the flow direction is opposite from the center of the channel toward outside. By using the orthogonal decomposition of the space-time velocity profile, we found that there are four rolls to the spanwise direction. There is a large scale motion forming one pair of large vortices and secondary two pairs of vortices, which are superposed to the larger one. It is yet to be studied whether this roll structure is intrinsic in this flow configuration or due to an inflow condition of this experimental setup.

Three-dimensional Model

Experimental set-up

Fig.5 shows the water loop used in this experiment. Water is supplied to the test section through three inlet channels. Flow meters are installed at each inlet pipes and the flow rates are regulated by the valves below the flow meters. The maximum achievable total flow rate is 2.5 L/s with the present system. Electrodes for electrolysis are also installed just above the flow meters to generate tiny gas bubbles that makes seeding better for UVP.

Fig.6 shows a cut-out view of ESS model showing the interior geometry. The manifold is made of stainless steal to be used in mercury experiments in future. Three lower pipes are the inlets of water and the upper one the outlet. The rectangular flange seen in the middle allows insertion of the gas injector system to simulate the gas injection into mercury for the pressure wave attenuation, which was not used in this study. Several projections fixed on the outlet pipe are reinforcements to sustain the weight of the manifold.

The model was made with plexiglass which also enables UVP measurement as well as flow visualization experiments. To minimize the reflection effect of ultrasound within the wall, the wall thickness was made thin to be 3mm. The outer width of the model is 306mm. The height is 156mm at the rear edge and 106mm at the front. The window has a round shape with the radius

of 53mm at the center. The side walls are also rounded. Fig.7 shows the flow direction of water in the model. Water flows into three channels of the model through three inlet pipes of the manifold. Two of the channels are placed at the side of the model, and one is at the bottom. The experimental results obtained with the two dimensional model showed the tendency that the recirculation region becomes larger and stronger as the inlet flow rate from the bottom channel is increased. The two additional side channels were installed with intention of making the recirculation region small while keeping the enough cooling of the target window. They are also expected to shift the recirculation region out of the reaction zone. The water passing through the side channels flow into the main channel of the target at the front edge. Three water flows collide each other inside the target window so that the flow structure must be very complicated there. Thereafter the water flows backward to the outlet.

Flow Vector Mapping

The vector maps we can obtain is a time averaged flow field in the model. The flow vector components are calculated with average velocity profiles of 1024 profiles on each measuring lines. It takes about 90 seconds to collect the data of 1024 velocity profiles for one measuring line. Designing an arrangement of measuring lines is important for flow mapping. The angle of the measuring lines to the line normal to the surface of the model must be less than the critical angle of 32.9 degrees, while the distribution of the crossing points should cover whole the flow field of interest. Fig.8 shows a typical arrangement of the measuring lines used in this experiment. True velocity vectors are obtained at 193 crossing points on one plane. These measuring lines are inclined 10 degrees right and left to the perpendicular line, which makes the crossing angle between two measuring lines as 20 degrees. Four perpendicular measuring lines placed on both sides cross with slanted measuring lines at the angle of 10 degrees. These angles were determined to minimise the reflection effect. The maximum depth of the vector field from the top of the target window is 30cm.

Experiment Conditions

Table 1 shows the experiment conditions. One data set corresponds to one vector map. There are 22 data sets with different combinations of flow rate and the height of measuring plane. The MP height in the second column means the height of measuring plane. The base level is at the center of the model, as is shown in Fig.9, and the MP height is expressed by the height from the base level. The MP angle in the third column is the inclination of the measuring plane to horizon, that means, the MP angle of 0 degree corresponds to a horizontal measuring plane. The data sets from Nr.1 to Nr.6 are trial cases to decide the best measuring line arrangement. After the measuring line arrangement was decided as Nr.7, the measurement of the flow field was started systematically. The flow velocity fields in the horizontal plane were measured at three different heights. The items, A, B, C in the flow rate column correspond to the inlet channels as is shown in Fig.7. The ratio of flow rates of three inlet channels were changed as 1:0:1, 2:1:2, 1:1:1, 1:2:1, 0:1:0 with keeping the total flow rate constant at 0.88L/s. Flow velocity at the front edge means the average water velocity at the exit of each channels. The last data set, Nr.22, is of the measuring plane inclined 10 degrees upward.

Experimental Results

It should be noted that the flow velocity vectors shown here are the projection of real vectors to the measuring plane. Since the flow structure is highly three dimensional, the water flow in the model cannot be expressed perfectly on a two dimensional plane, but the general behavior of the total flow can be understood with two dimensional vector maps.

Comparison of vector maps of different flow rate ratios at the base level

The vector fields obtained with the data set Nr.9,11 and 7 are shown in Fig.10, 11, and 12. These data sets can be compared to know the change of a flow field with a relative increase of the lower channel (channel B). The recirculation region can be clearly seen on both sides of the center line in all of these cases. The flow direction at the center line is slightly shifted and inclined to the right, which makes the recirculation region on the left side larger. The reason of the asymmetry flow is not clear; it depends on the accuracy of the flow meter of inlet channels, the symmetry of the target window, or the inlet flow condition. When the flow rate of channel B is small (Fig.10), the recirculation region is small and the flow velocity is also small, which means the flow in these region is almost stagnant. The left side recirculation region begins from the depth of ca. 90mm and continues to ca. 200mm. As the flow rate of channel B increases (Fig.11 and 12), the recirculation region becomes larger and stronger. The starting depth of the region is almost the same with the case of Fig.10, but the end depth extends to ca. 300mm in Fig.11 and further (undetectable) in Fig.12. Fig.13 shows the profile of x component of flow velocity along the x-axis ($V_x(x)$). This shows the peculiar pattern of one dimensional velocity profile across the channel. The plot indicates that there are two counter-rotating vortices along the x-axis, and it also indicates that the border between the two vortices is shifted to the right of the center line. In the case of equal inlet flow rate, the peak of V_x is small compared to the case of large flow rate of B channel, which shows the vortex became weak. In the case of small B channel flow rate, the sign of V_x is opposite to other two cases on the right side, which shows the contraction of vortex, that is, the center of the vortex shifted crossing the x-axis and the flow direction on the x-axis was reversed.

Comparison of vector maps at different levels with equal flow rates

The vector fields obtained with the data set Nr.15 and 18 are shown in Fig.14 and 15. Together with the Fig.11, the vector maps at equal flow rates can be observed at different level. The flow going to the center from side channels just inside the target window become strong as the measuring plane goes up. This shows the flow from side channels is directed upward by the flow from channel B. The flow at the center line is inclined to the right also in these cases. The recirculation region on the left side begins from the depth of ca. 50mm in Fig.15 and it shifts backward in Fig.11 and 14, which indicates that the recirculation region is three dimensional and the interface between the recirculation region and the stream going back in the main channel is inclined. A small vortex seems to be generated behind the edge of the side channels.

Comparison of vector maps of different levels with the inlet flow from bottom channel

Fig.16, 17 and 18 show the flow field in which water was supplied only through the bottom channel. This is the same case with the experiment of two dimensional model. The large vectors inside the target window in Fig.18 correspond to the direct stream from the bottom channel. The vectors near the center line of the model show there is a backward stream in the upper measuring plane. As the measuring plane goes down, the backward stream disappears in Fig.16 and 17 and only the frontward and sideward stream becomes dominant. This shows there is a large vertical recirculation ranging from the bottom to the top of the main channel, just the same with the flow observed in two dimensional model. But in this case, the side wall is rounded and it generates spanwise flow making the total flow field more complicated.

CONCLUSIONS

Using water as the model fluid, average flow behavior in the ESS target model was studied experimentally by UVP method for 2D and 3D structures.

In 2D experiments, it was found that a large recirculation zone is generated in the upper flow channel where most of the beam energy is deposited. It consists of two counterrotating vorticies, but the spanwise motion is relatively small compared to the axial motion. The shape and size of the vortices are supposed to be dependent on flow geometry and flow conditions of the target liquid.

The ESS target geometry has three inlet channels generating cross-flow on the surface of the target window, which was expected to prevent the creation of the recirculation region in the main channel or at least to reduce the effect. But, the results of the 3D mockup water experiments showed that the recirculation region is still generated on the reaction zone with a more complicated flow pattern, at least, under the low flow rate conditions applied here. A pair of recirculation are observed on both sides of the center line of the model. Since the shape of two counterrotating vortices is clearer and spanwise motion is stronger than in 2D model, they are considered to be generated by the side channel flows. As the flow rate ratio of three inlet channels changed, the size and intensity of the recirculation region also changed, but it never disappears. It would be expected that different pattern of flow fields may appear with higher flow rates, but generally the large vortex structure seen with the low flow rate does not change even with higher flow rate. In order to decide the optimum target geometry and flow conditions, further studies have to be done experimentally and numerically.

Reference

[1] H. Lengeler, Ed., Third General ESS-Meeting, Baden, March 22-25, 1995, ESS 5-24-M

[2] Y. Takeda, T. Dury, and G.S. Bauer, "Liquid metal target for spallation neutron sources" Proc. of NURETH-8, Vol.2, pp1252 (1997)

[3] Y. Takeda, Velocity profile measurement by ultrasonic Doppler method, Exp. Therm. & Fluid Sci., 10, 444-453, (1995)

[4] Y.Takeda, Ed., First International Symposium on Ultrasonic Doppler Methods for Fluid Mechanics and Fluid Engineering, PSI, Switzerland, 9.-11. Sept., 1996

[5] H. Kikura & Y. Takeda, ASME Fluid Engineering Division, Summer Meeting, Washington DC, July 98

Table 1 Experimental Conditions for the Water Experiments of the ESS Target Model

Data-Set Nr.	MP Height [mm]	MP Angle [deg]	Flow Rate [L/s]				Velocity at the Front Edge [mm/s]			ML Set Nr.
			A	B	C	Total	A	B	C	
1	0	0	0.33	0.33	0.33	0.99	456	413	456	1
2	0	0	0.33	0.33	0.33	0.99	456	413	456	2
3	0	0	0.33	0.33	0.33	0.99	456	413	456	3
4	0	0	0.33	0.33	0.33	0.99	456	413	456	4
5	0	0	0.33	0.66	0.33	1.32	456	825	456	5
6	0	0	0.22	0.22	0.22	0.66	304	275	304	6
7	0	0	0.22	0.44	0.22	0.88	304	550	304	7
8	0	0	0.44	0	0.44	0.88	608	0	608	7
9	0	0	0.35	0.18	0.35	0.88	483	225	483	7
10	0	0	0	0.88	0	0.88	0	1100	0	7
11	0	0	0.29	0.29	0.29	0.88	401	363	401	7
12	+10	0	0.22	0.44	0.22	0.88	304	550	304	7
13	+10	0	0.44	0	0.44	0.88	608	0	608	7
14	+10	0	0.35	0.18	0.35	0.88	483	225	483	7
15	+10	0	0.29	0.29	0.29	0.88	401	363	401	7
16	+10	0	0	0.88	0	0.88	0	1100	0	7
17	−10	0	0.22	0.44	0.22	0.88	304	550	304	7
18	−10	0	0.29	0.29	0.29	0.88	401	363	401	7
19	−10	0	0.44	0	0.44	0.88	608	0	608	7
20	−10	0	0.35	0.18	0.35	0.88	483	225	483	7
21	−10	0	0	0.88	0	0.88	0	1100	0	7
22	−20	+10	0.29	0.29	0.29	0.88	401	363	401	7

MP : Measuring Plane
ML : Measuring Line

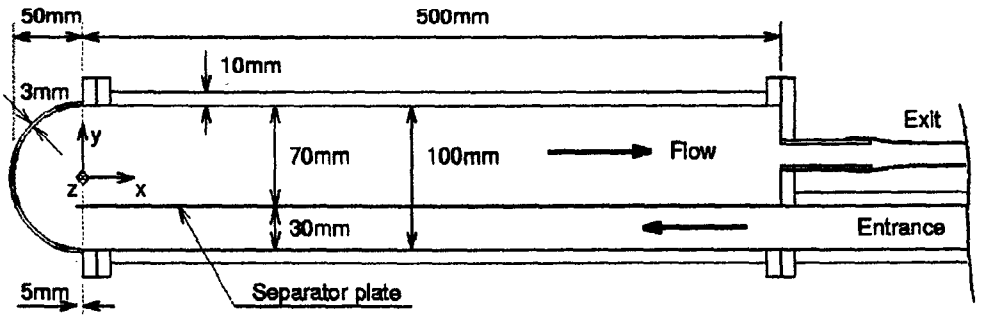

Figure 1 Test section for ESS 2D flow measurement

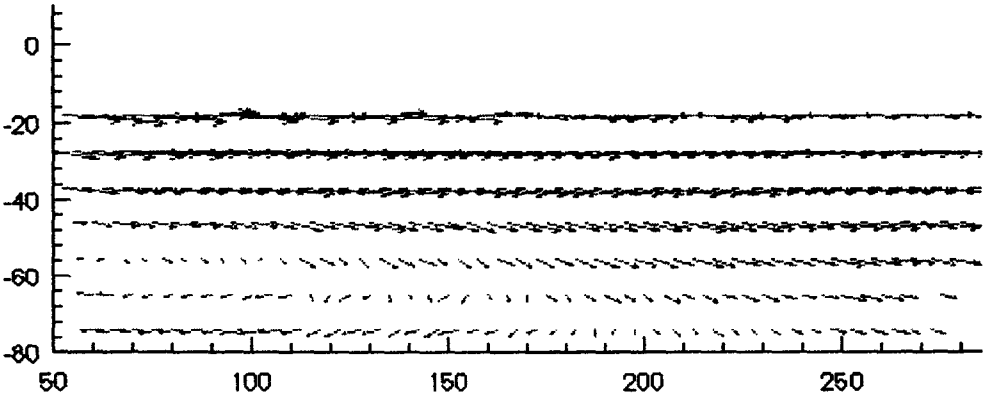

Fig.2 Time-averaged vector field (experimental) for the upper channel near the top.

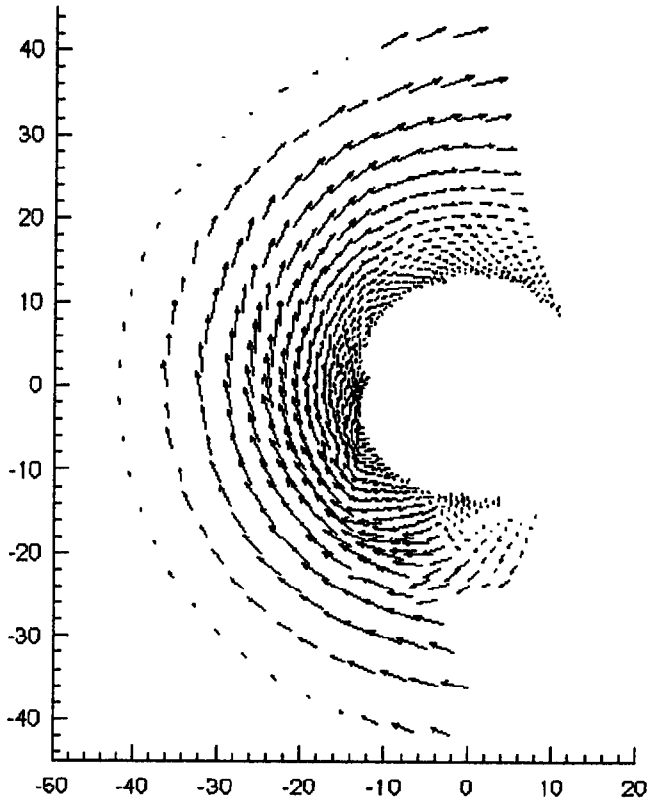

Figure 3 Time-averaged vector field for the hemicylindrical region.

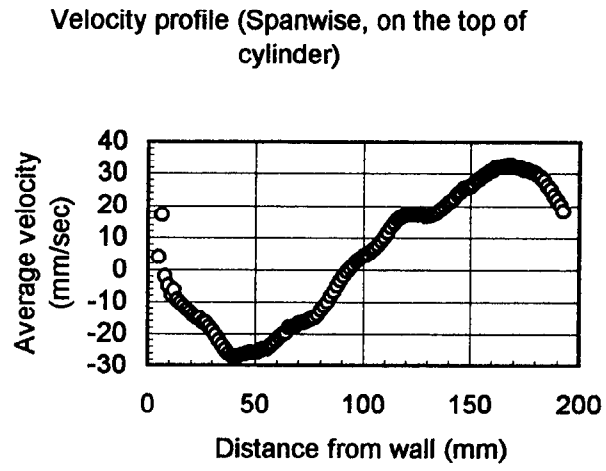

Figure 4 Spanwise velocity distribution (time averaged profile)

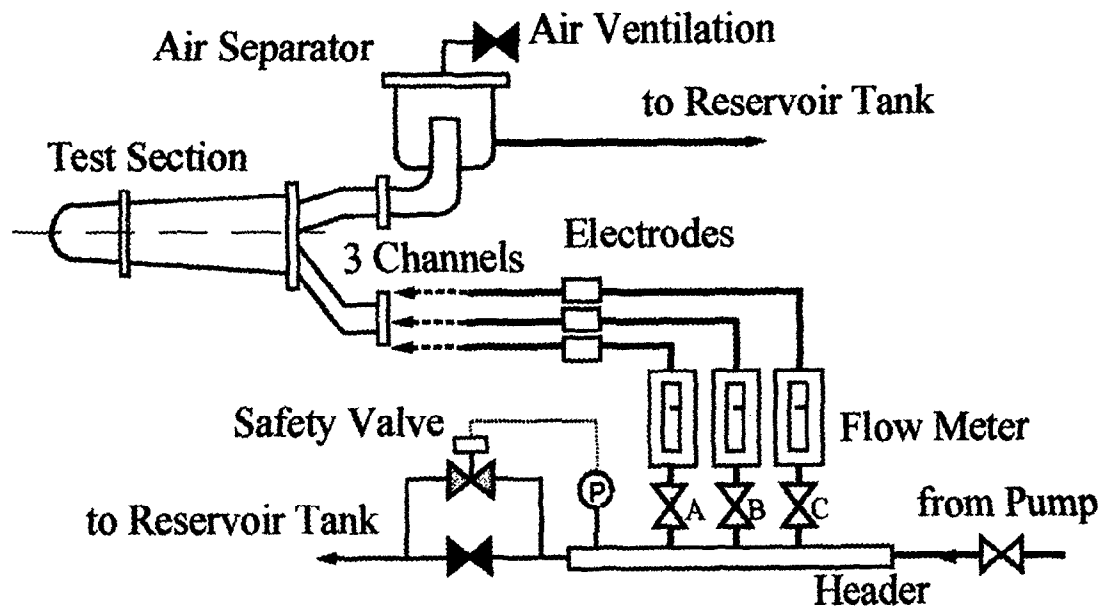

Fig. 5 Water Loop for ESS Experiment

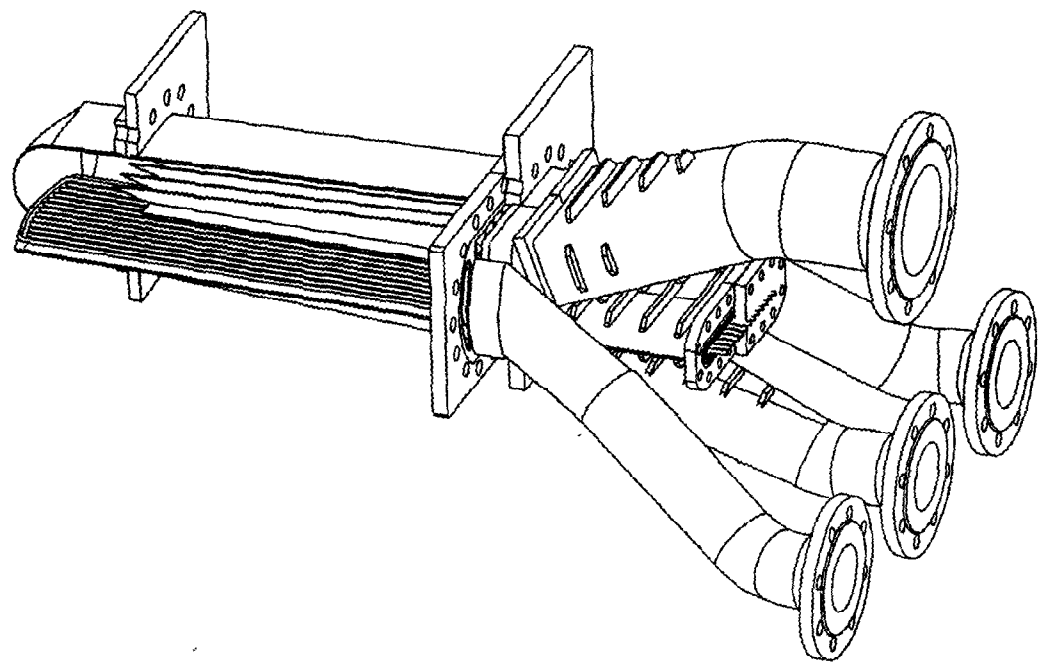

Fig. 6 Cut-out View of the ESS Model

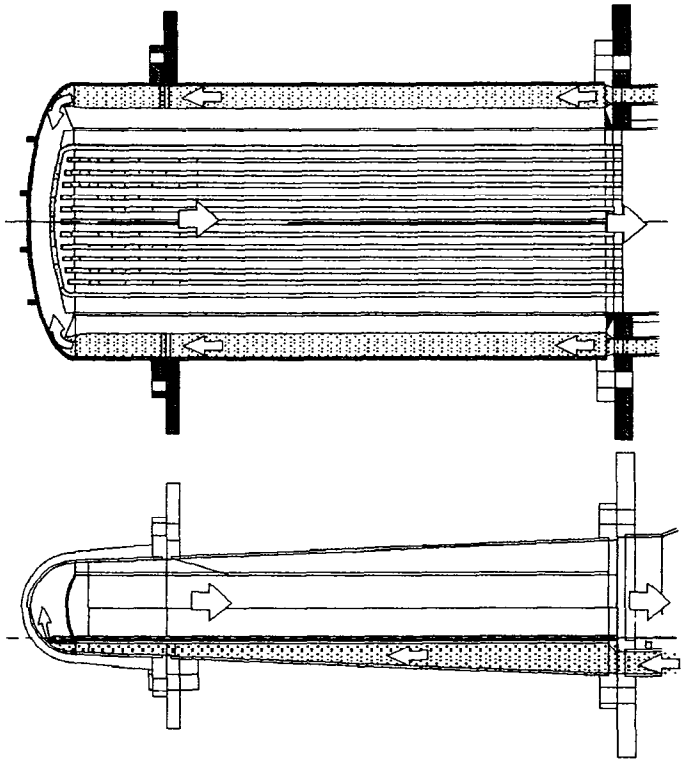

Fig.7 Flow Direction in the ESS Model

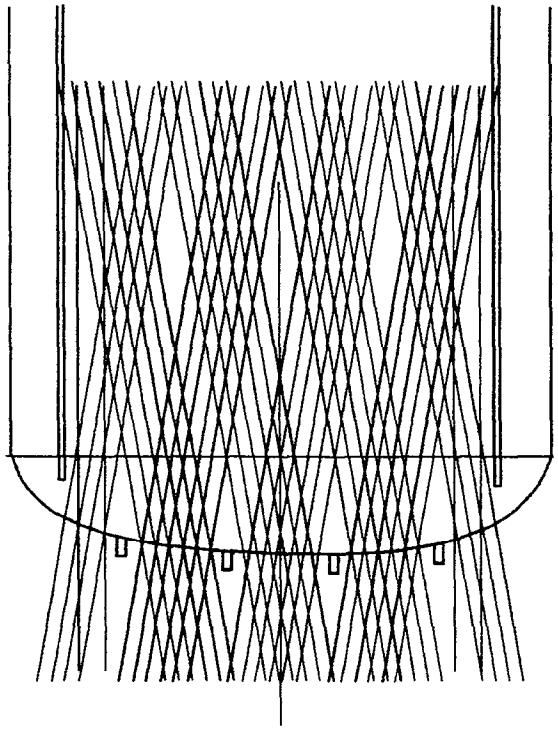

Fig.8 Arrangement of Measuring Lines for Vector Mapping

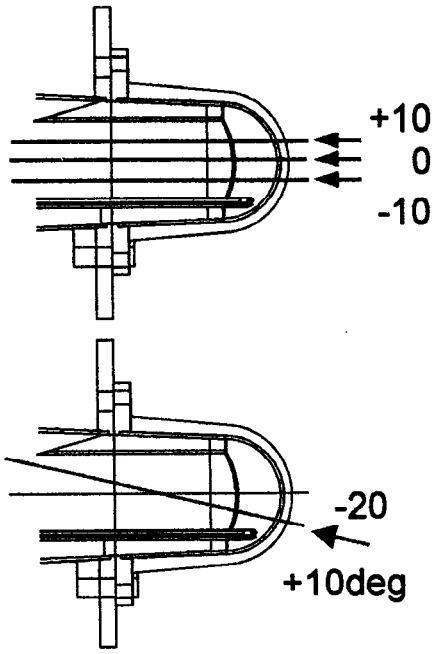

Fig.9 Position of Measuring Planes

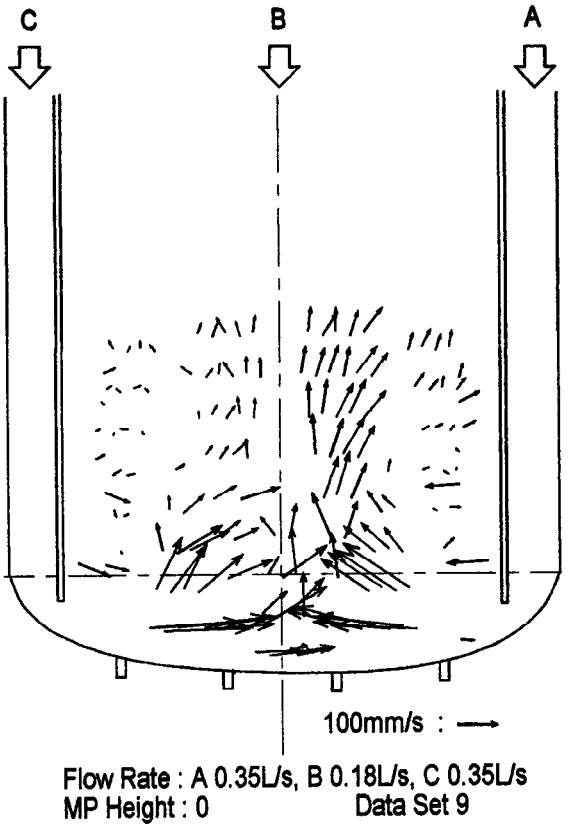

Fig.10 Vector Flow Field (2 : 1 : 2)

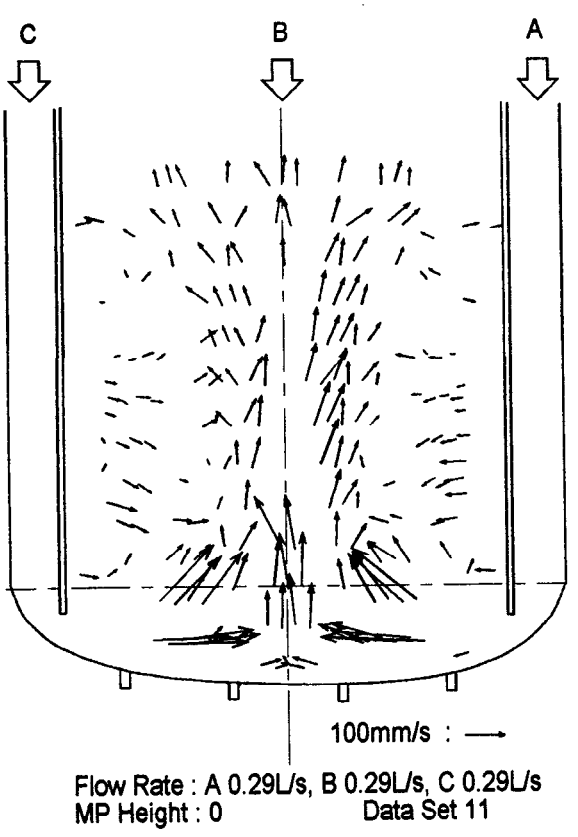

Fig.11 Vector Flow Field (1 : 1 : 1)

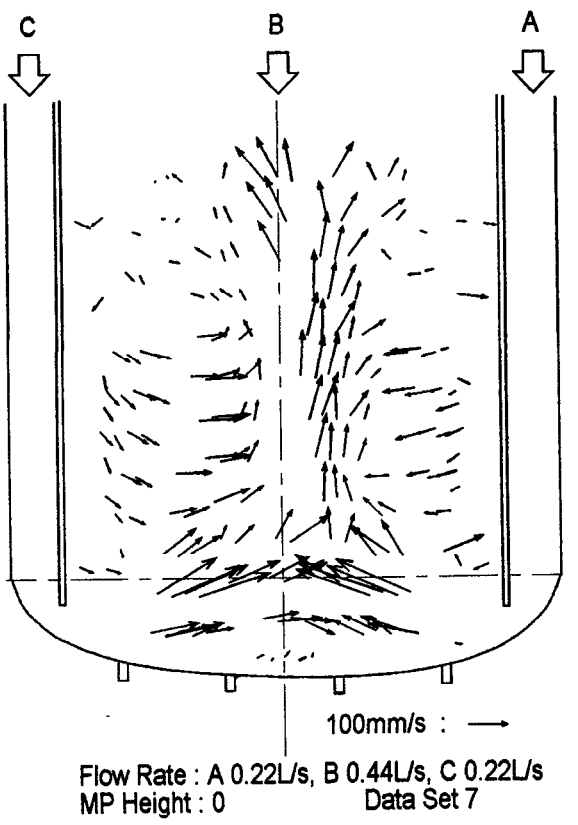

Fig. 12 Vector Flow Field (1 : 2 : 1)

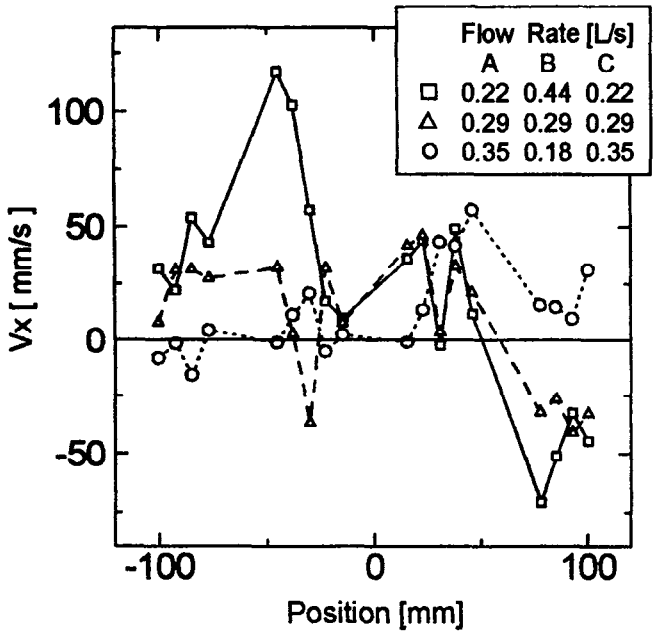

Fig. 13 Vx Profile along X Axis

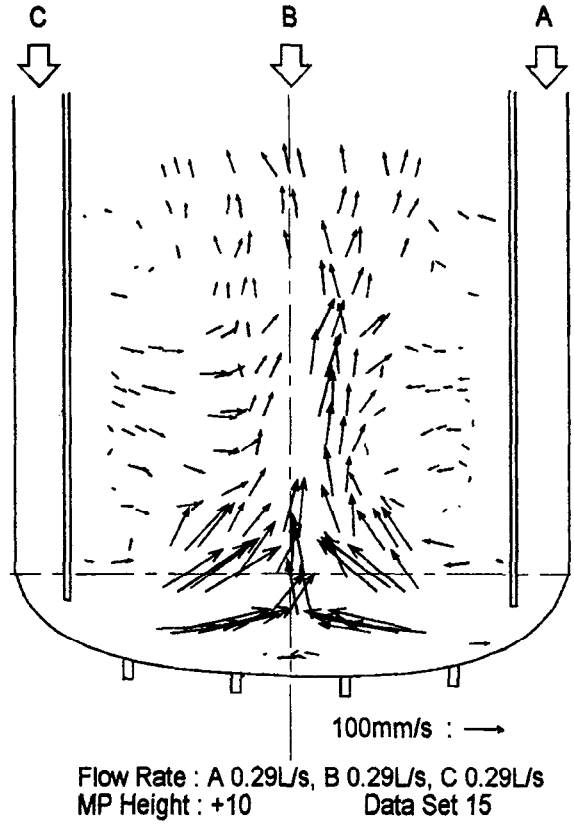

Fig.14 Vector Flow Field (1 : 1 : 1)

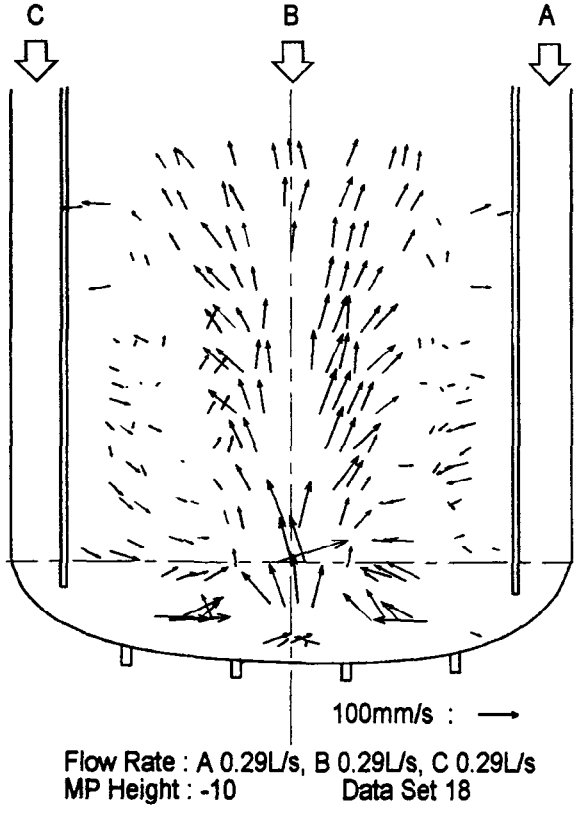

Fig.15 Vector Flow Field (1 : 1 : 1)

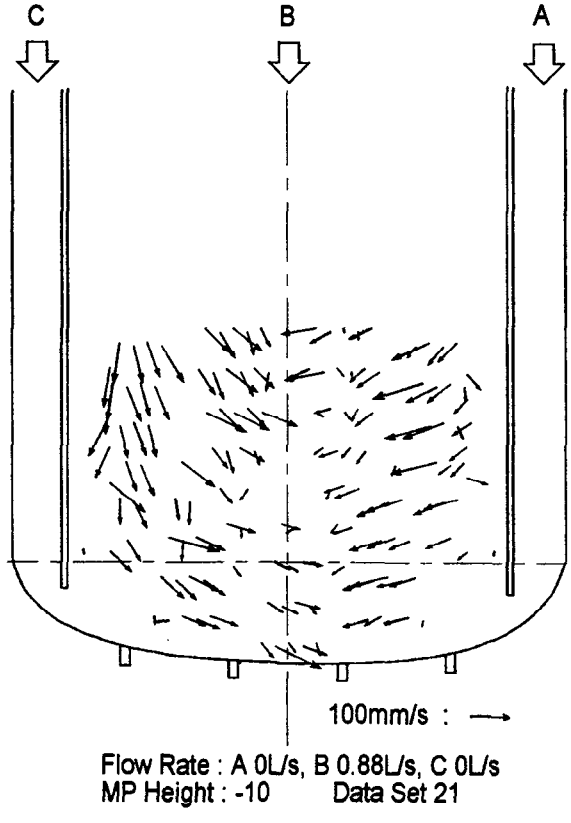

Fig.16 Vector Flow Field (0 : 1 : 0)

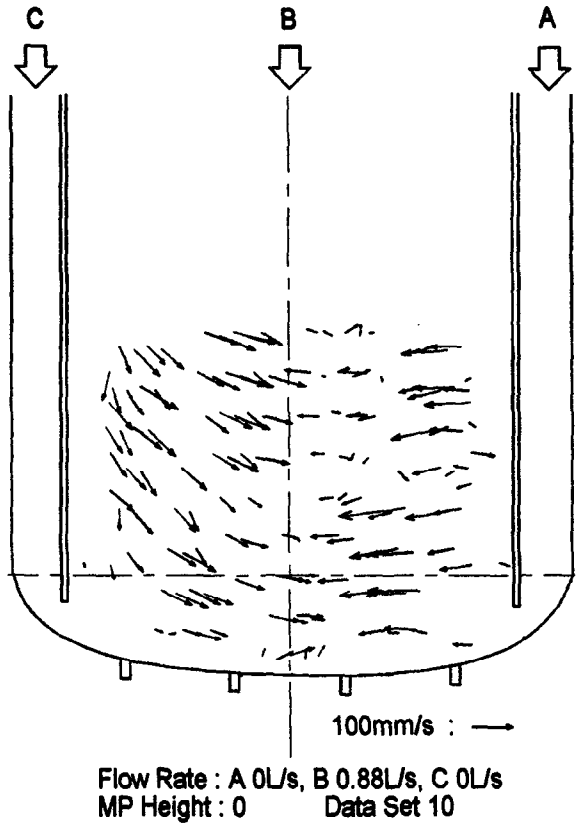

Fig. 17 Vector Flow Field (0 : 1 : 0)

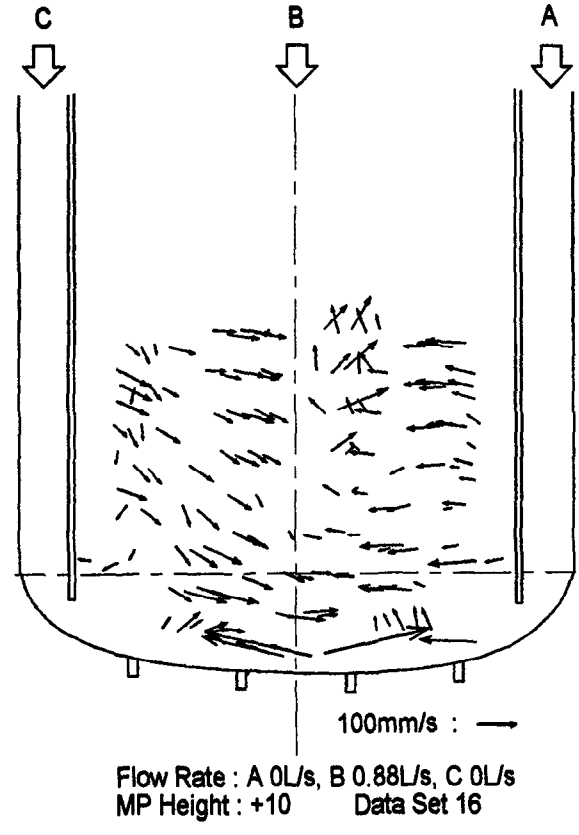

Fig. 18 Vector Flow Field (0 : 1 : 0)

Neutron Scattering Instruments

SOLID TARGET SYSTEMS

ICANS XIV
14th Meeting of the International Collaboration on
Advanced Neutron Sources
June 14-19, 1998
Starved Rock Lodge, Utica, IL

Engineering Design of the Lujan Center Target

Presented by
Nathan K. Bultman
Los Alamos National Laboratory

1. System Overview and Design Objectives

There are two primary engineering design objectives for the new Lujan Center Target System:

1. Provide increased thermal capacity of the tungsten target assembly to allow safe and reliable operation of the target at average proton beam currents up to 200 μA.
2. Increase system availability and access to critical components for replacement as required.

We believe that this engineering design provides a balanced approach that meets these objectives while maximizing overall system performance. The design provides for critical component access and replacement within a maximum three-week down period. Items defined as critical components include the proton beam diagnostic, the proton beam vacuum isolation window, the tungsten targets, and the neutron moderator assemblies.

2. Design Philosophy

The general philosophy of the design approach is one of modularization of critical components into easily accessible coaxial-nested inserts or modules. The objective is to reduce handling time and personnel radiation exposure for target replacement activities and to provide access at the component level for eventual disposal of used target modules. Target replacement will normally be accomplished during a standard maintenance period, however, if an unexpected component failure causes unplanned replacement, minimizing system downtime is critical. The target system must be designed to allow for safe and rapid handling, consistent with the goal of minimizing personnel radiation exposure. Eventual processing of spent target modules will involve separation of the modules into sections of like material and/or activation level (i.e. lead and beryllium reflectors, tungsten target etc.) This design incorporates key features that accommodate remote handling operations as required for this disassembly and disposal process.

3. Target Facility Configuration

The layout of the target system is largely unchanged from the basic configuration that has been in service since 1985. The tungsten target and moderator components are located in the center of a large evacuated vessel (target crypt vessel) that is surrounded by a large biological shield assembly. The biological shield is cylindrical in shape, with a diameter of about 10 meters, and is composed of layers of steel and concrete. The top of the biological shield is enclosed within a hot-cell type structure refered to as the target cell. An artist concept of a target change operation is shown in Figure 1. Note the relative position of the instrument flight paths, the target cell and the external bridge crane with its cover building as shown.

The proton beam leaves the Proton Storage Ring (PSR), inside a horizontal 4-inch diameter beam-tube, about 7.5 meters above the plane of the lower moderators. The beam is bent through a radius of roughly 4.3 meters and is injected vertically downward into the target crypt vessel where it strikes the tungsten targets. Inside the crypt vessel, surrounding the tungsten target region, is a group of steel plates and rings that provide immediate high-energy neutron shielding around the target-moderator section. Figure 2 is a cross-section view through the target crypt vessel and its contents. The elements of the target insert (targets, moderators and reflector components) are visible as well as the surrounding steel shielding.

During a target change or installation activity, water, instrumentation, and cryogenic connections to the target insert are made inside the target cell enclosure at the level of the large square closure plate on the top of the crypt vessel (Figure1). The target cell contains a small, 5-ton bridge crane (not shown in Figure 1) and a pair of remote manipulators. An access port through the roof of the target cell has been installed as part of the upgrade project to allow vertical access to the target module during installation and replacement operations. In the past, access to the target assembly has been through a large hinged shield door in the target cell wall. A large 30-ton bridge crane mounted above the target cell roof (external to the target cell) will provide lifting capability for the target insert and its shielding cask.

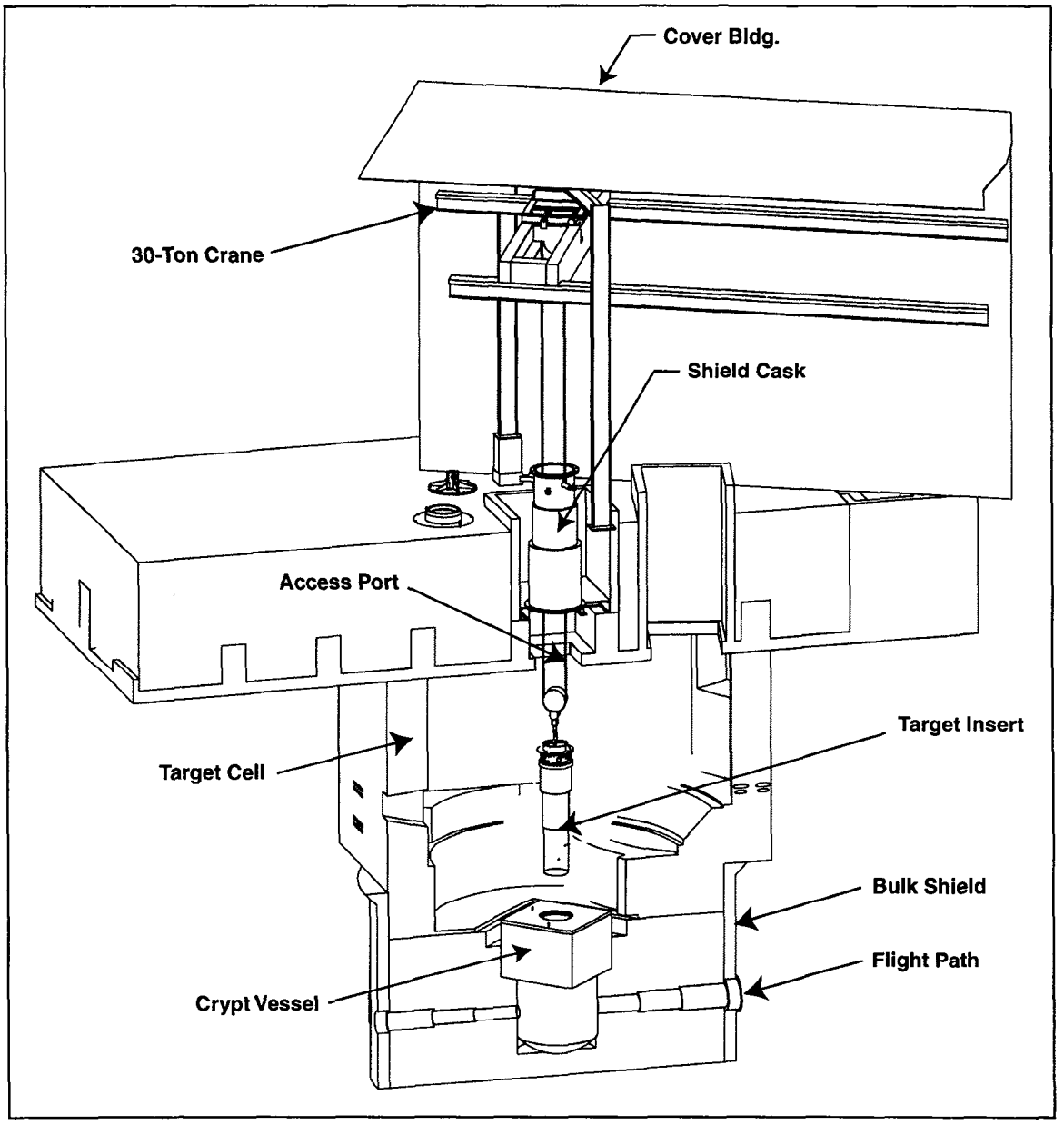

Figure 1. Target change operation

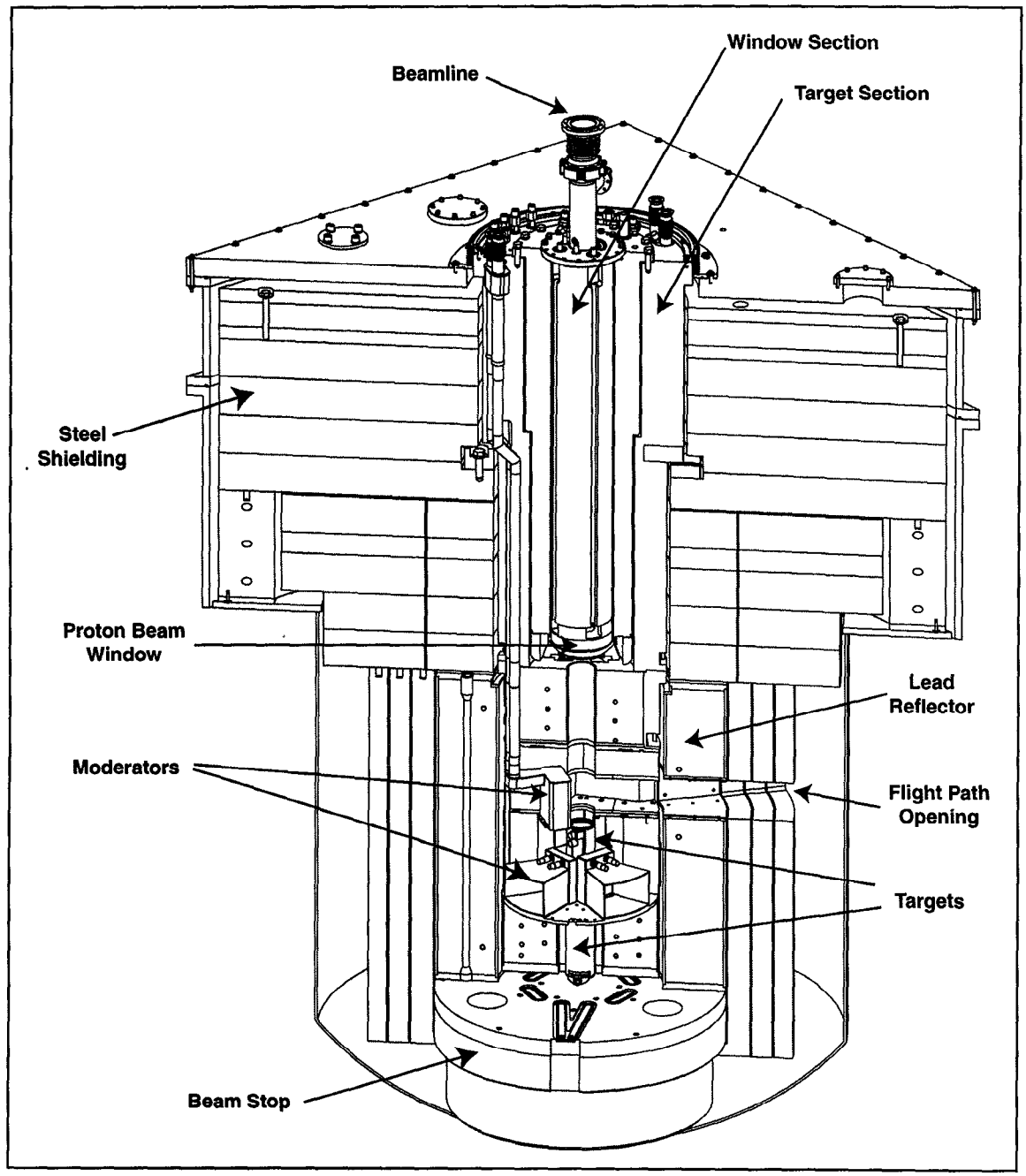

Figure 2. Section view of the target crypt region

The cover building incorporates air-handling equipment and provides atmosphere containment and weather protection during access to the target cell area.

A total of 16 radial ports extend horizontally from the target crypt vessel to the outer diameter of the biological shield, and neutron flight path tubes extend on outward to various neutron-science instruments in the experiment hall. The flight paths are arranged to allow viewing of the various moderators in the target assembly. Figure 3 shows the layout of the 16 flight paths in the experiment hall. Flight paths 12 through 15 were installed in 1991 but were not able to view a moderator until now. These new ports will be activiated as instruments are designed installed.

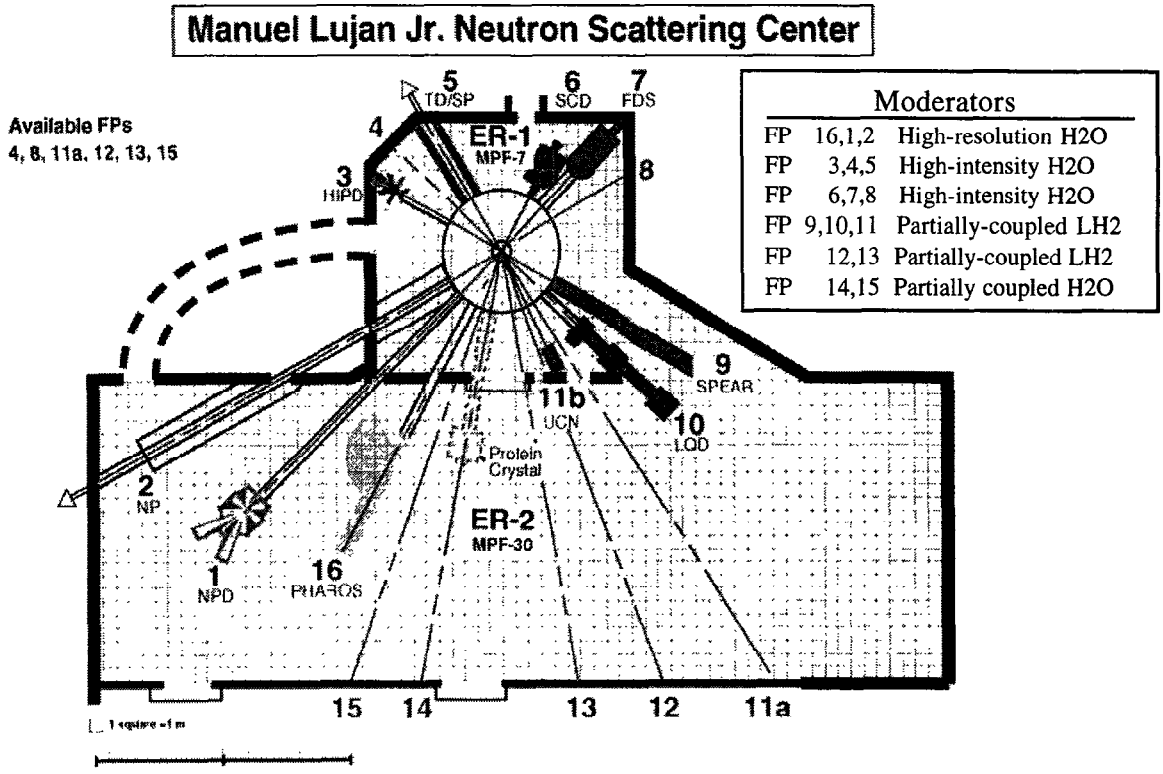

Figure 3. Flight Path Layout in the Experiment Hall

4. Target Insert Configuration

The target insert assembly is comprised of three separately manufactured elements that are assembled in a coaxial nested configuration. Each element is supported and mechanically sealed to its outer neighbor. The inner element is the diagnostic element, the center element is the proton beam window, and the outer portion is the target-moderator-reflector. For simplicity and ease of handling the diagnostic element and the window element are always handled together and refered to as simply the window section. The target-moderator-reflector element is likewise simply called the target section. Figure 4 shows the target and window sections side-by-side, as they would appear before final assembly of the target insert unit. The window section nests inside the target section and can be removed from the crypt separately if required. Removal of the target section however, requires either prior or concurrent removal of the window section. The expectation is that both sections will normally be handled together as a unit (target insert) unless a failure occurs in the window section early in a service cycle. In such an event, the window section would be replaced separately, saving the expense of replacing the entire unit. The diagnostic element carries an electrical device (harp) that provides operational information about the shape and location of the proton beam as it enters the upper tungsten target. The harp requires a high vacuum environment for proper operation and reasonable lifetime so it resides in the high vacuum of the beam transport line. The window section separates the high vacuum environment of the proton beamline (10^{-6} torr), from the low vacuum environment (~1 torr) inside the target crypt vessel. The target section is composed of the upper and lower tungsten-targets, the 6 neutron moderators, the beryllium inner reflector, and two sections of lead reflector. The whole target insert assembly is supported by a steel plate attached to the main shielding blocks inside the crypt vessel. This support plate is installed and aligned to the instrument flight paths and proton beam delivery system during installation of the crypt steel. Precise and repeatable alignment of the moderators to the flight-paths and instruments is assured for all subsequent target insert units (see Figure 1).
Cooling lines and thermal diagnostics for each section of the assembly are routed through the top flange of

that section in order that each be fully self-contained. A more detailed design description of each element follows in the next section.

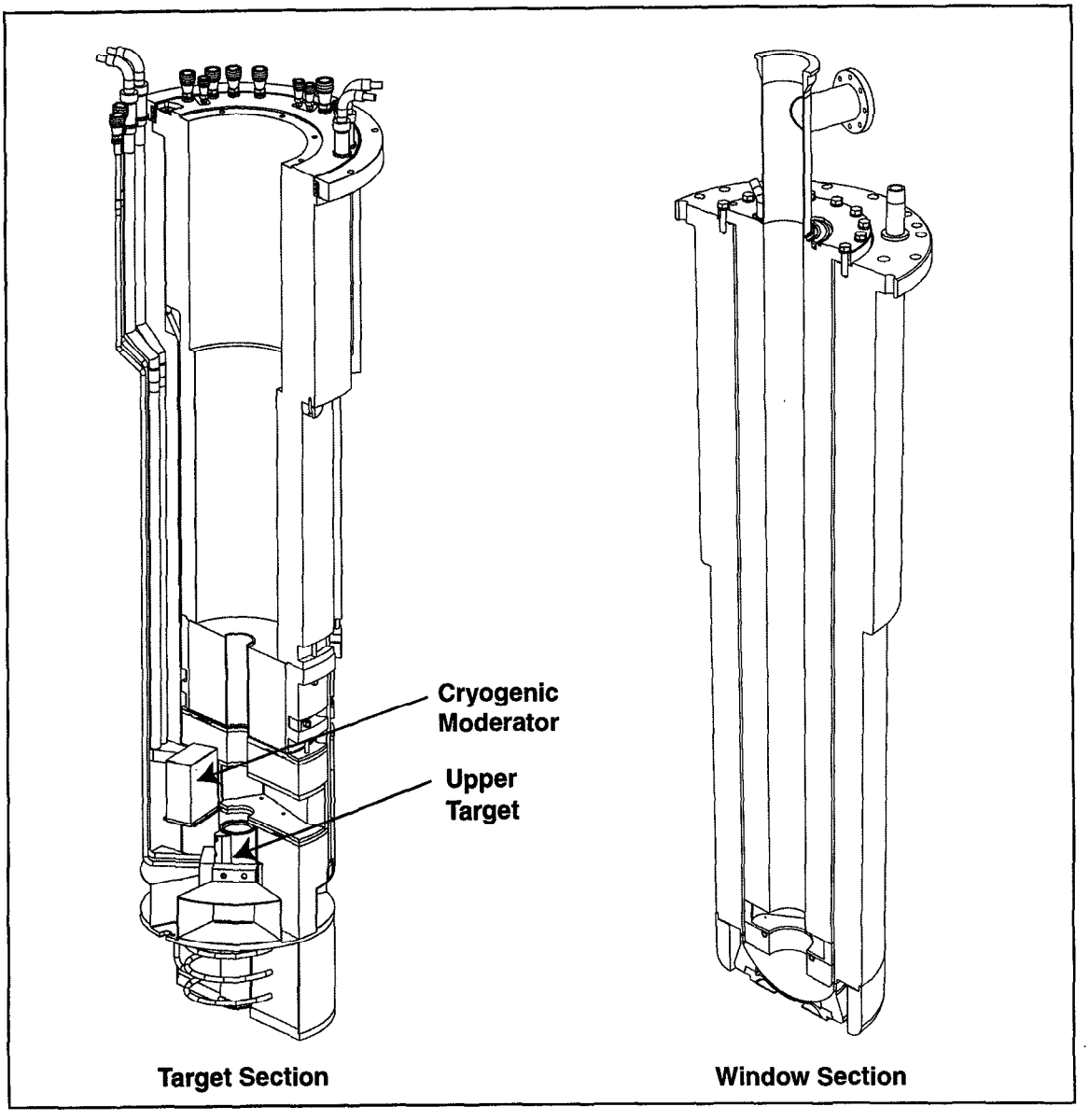

Figure 4. Target Section & Window Section

5. Target Component Design Description

5.1. Proton Beam Design Parameters

Table 1 lists the proton beam characteristics for the design beam current of 200 μA. These parameters were used to generate neutron performance data and component energy deposition rates through the LAHET-MCNP code sets. The heating data were used in the finite element design code ABAQUS v5.6 to estimate component temperature and stress levels during operation.

Table 1. Proton Beam Parameters at 200 μA

Average Proton Beam Current	200 μA
Pulse Length	250 nsec
Average Pulse Rise/Fall Time	125 nsec
Pulse Repetition Rate	30 Hz
Average Particles per Pulse	4.16×10^{13}
Average Charge per Pulse	6.67 μC
Average Current During Pulse	26.7 A
Peak Current During Pulse	53.3 A
Beam Shape	Circular Gaussian
Beam Standard Deviation	1.5 cm, radius
Beam Size, FWHM	3.532 cm
Average Current Density at Beam Center	14.15 $\mu A/cm^2$
Peak Current Density at Beam Center	1.89 A/cm^2

It should be noted that the exact operational proton beam shape varies slightly during operation due to varying beam transport tune conditions. However, the chosen set of beam focus parameters bound the worst case heating conditions in the window and target components. The data are felt to represent a maximum possible focus intensity based on optics calculations for the transport line. This maximum intensity is not necessarily the exact tune that will be used. In practice, the beam diagnostic harp will provide real time measurement of beam focus and current density parameters to allow verification of proper settings (primarily beam steering) of the beam transport optics. This is especially important during the initial comissioning.

5.2. Window Section Assembly

The window section assembly consists of the proton beam diagnostic section and the proton beam window section. These two sections are bolted together at their top flanges using metal seals and are normally handled as a single assembly unit refered to as the window section (Figure 4). This bolted arrangement allows for independant construction and testing of the two sub-assemblies before final assembly of the combined unit. The combined unit weighs about 3400 pounds and is roughly 86 inches long.

5.2.1. Beam Diagnostic Section

The proton beam diagnostic section is the inner section of the window insert assembly. It is roughly 9.25 inches in diameter, 83.4 inches long, and weighs about 945 pounds including the harp and cables. The diagnostic section interfaces to the proton beamline at its top flange using a metal-seal Helicoflex-type quick disconnect flange. It interfaces to the window section through a bolted face-seal connection, also using a metal Helicoflex seal. The harp consists of several planes of individual electrically-isolated

tungsten-carbide wires, attached to ceramic holder plates, and streached across the beam path. The mechanical aperature through the ceramic holder plates of the harp is about 2 inches larger than the inside diameter of the steel insert. The harp is thus shielded both from above, by the body of the insert, and from below by a tungsten shield ring that slides over the harp assembly (Figure 5). Both the body of the insert and the tungsten shield ring are actively cooled to prevent damage to the ceramic holder if the beam should be accidentally mis-steered during initial tuning.

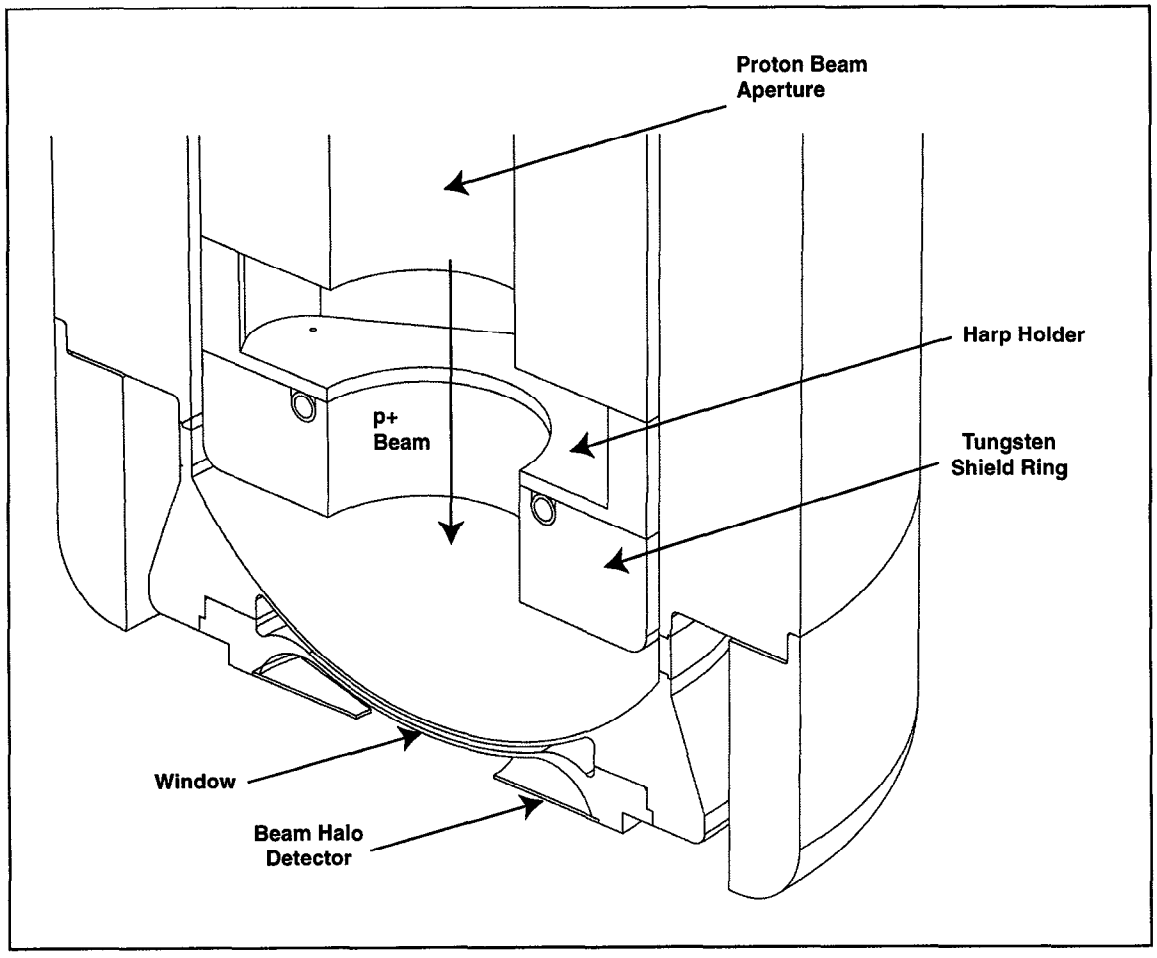

Figure 5. Proton Beam Diagnostic Section Cutaway Diagram

5.2.2. Proton Beam Window Section

The proton beam window section of the window insert (Figure 4) is roughly 17.5 inches in diameter, 66 inches long, and weighs about 2465 pounds. The window is a double-walled hemi-spherical Inconel 718 shell with water cooling between the two layers. The Inconel shells are each 2 mm thick with a 2 mm water-cooling space between. The design basis is a similar window used for vacuum isolation of the A6-beamstop at the LANSCE accelerator facility. Figure 5 is a close-up view of the lower section of the window insert showing the window, harp holder and other items as noted. We believe that the service interval for the window at 200 μA beam current is roughly 4 to 5 years based on performance of the LANSCE window at the same energy but at roughly 5 times higher current. The LANSCE accelerator window is normally replaced yearly. Thermocouples are mounted on the crypt side of the window to provide operational thermal data including a general indication of beam-spot position. The required coolant flow and calculated operational average thermal/stress conditions in the Inconel shell are listed in Table 2 below.

Table 2. Window Operational Parameters (200 μA Beam)

Maximum Beam-Center Heating Rate (based on 200 μA Beam, 1.5 cm σ)	350 W/cm^3
Coolant Type	Water (20 deg. C)
Minimum Allowed Coolant Pressure	60 psia
Maximum Allowed Coolant Pressure	200 psia
Minimum Allowed Coolant Flow Rate	10 gpm
Calculated Steady Operational Temperature, High Vacuum Side	105 C
Calculated Steady Operational Temperature, Water Side	58 C
Maximum Steady Operational Stress Level in Beam Area (von Mises Stress)	30 ksi (208 MPa)

5.3. Target Section Assembly

The target section is composed of many elements and subassemblies that are bolted together in a long, cylindrical unit (Figure 6). At the top of the assembly is a large steel cylinder that acts as neutron shielding for the target system. Attached to the bottom of the steel are the various components of the target, moderator and reflector system.

The target section is assembled from the bottom up, beginning with the lower target and lower moderators. The lower subassembly is then joined to the steel portion from below. To perform this operation, the upper steel portion is suspended vertically from a special assembly scaffold/work area, and the lower subassembly is raised to join from below. The cooling lines from the lower components slide up through holes bored in the top flange of the steel body and are seal-welded at the top surface. When the welding is complete, the window section is lowered into the target section and the entire assembly is leak tested using a specially designed test vessel. The whole target insert assembly is then fully tested to operational pressure, with the lower region in the test vessel under vacuum, before it is transported to the target cell for installation.

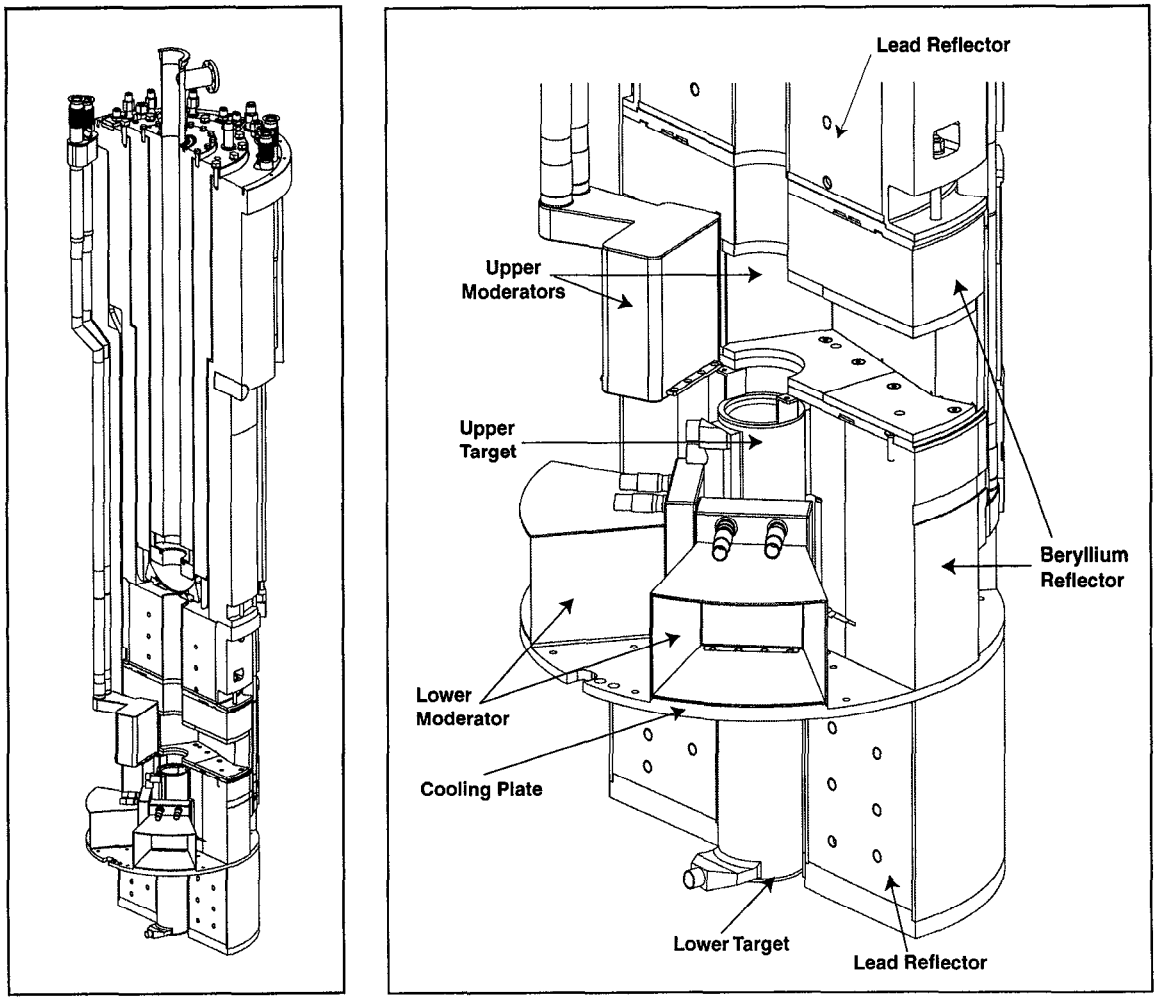

Figure 6. Target Section Cutaway Diagram

5.3.1. Tungsten Targets

The tungsten target consists of two separate sections with a flux trap region between. The top section is a plate-type design and consists of a cylindrical enclosure made of Inconel Alloy 718 containing 7 tungsten disks lying perpendicular to the proton beam. The disks vary in thickness from 8 to 19 mm, top to bottom. Light-water coolant flows between the disks, entering at the top between the container lid and disk 1, and exiting at the bottom of the assembly in a similar manner. Figure 7, shows a section diagram through the top target assembly. Plenna welded to the sides of the target vessel collect and redirect the water flow through each plate gap. The entrance plenum to the top gap has a special transition nozzle to allow a smooth flow transition from the round tube to the thin slot as the water enters the target container. The return pipe is a standard size stainless steel tube that welds directly to the side plenum.

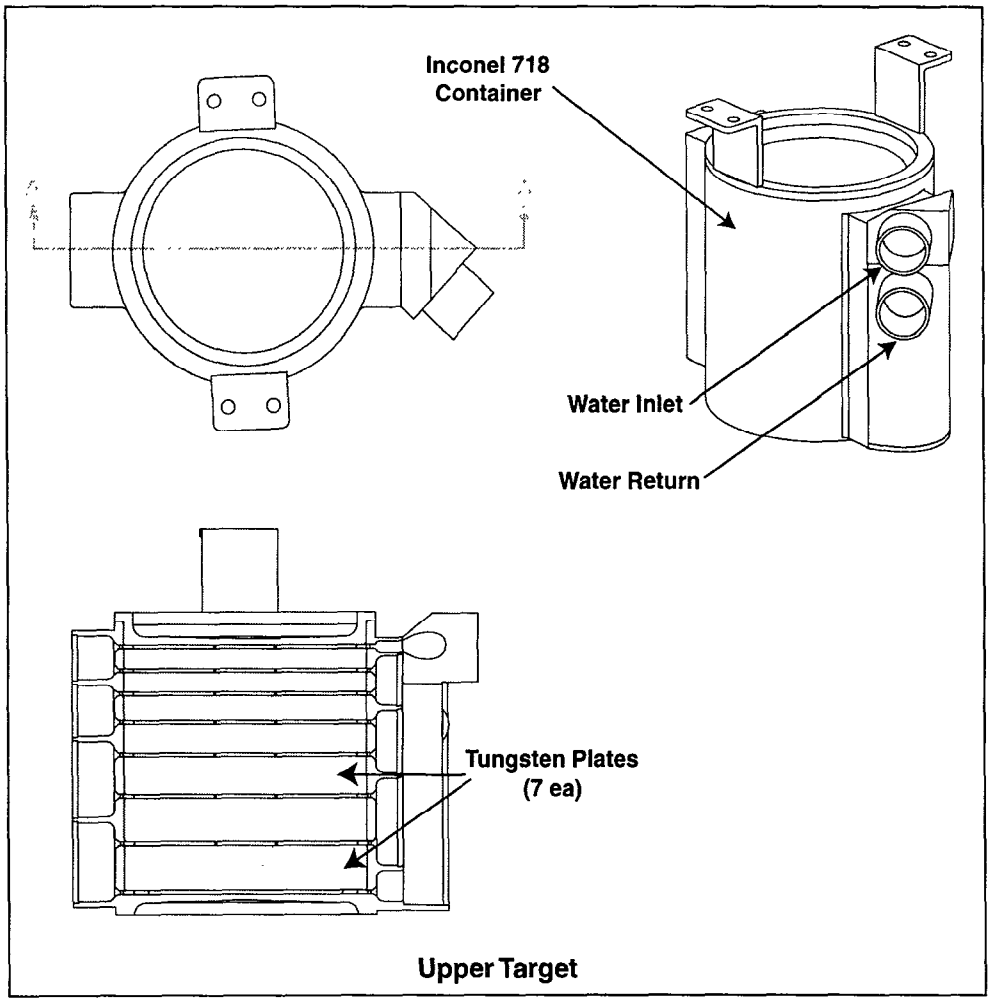

Figure 7. Top and Bottom Target Section Views

Table 3. Upper-Target General Operational Parameters

Target Configuration	Plate-type, light-water cooling
Thermal Load, Total Unit	64.2 kW
Coolant Type	H_2O
Inlet water pressure	1.38 Mpa (200.0 psi)
Total Coolant Mass Flow Rate	38 liter/min
Coolant Temperature Rise	24.3 C
Peak. Time-Averaged Power Density, Plate 1	596 W/cm^3
Peak. Time-Averaged Power Density, Plate 7	272 W/cm^3
Peak Tungsten-Surface Temperature (Plate 5)	134 C
Minimum Tungsten-Surface Sub-Cooling (Plate 6)	35 C

The lower target section (Figure 8) is a solid, bare, tungsten cylinder enclosed within an Inconel 718 cylindrical shell. The tungsten is edge-cooled with water that flows in an annular space between the tungsten and the cylindrical shell. This configuration is slightly more efficient in neutron production than the plate-style discussed because it has less water in the path of the proton beam. This arrangement is possible in the lower target because the peak volumetric heat loading in the bottom target is about 10 times lower than in the top target. The objective in using two different target styles is to more closely match maximum tungsten volume fraction with the heat load requirements at each location.

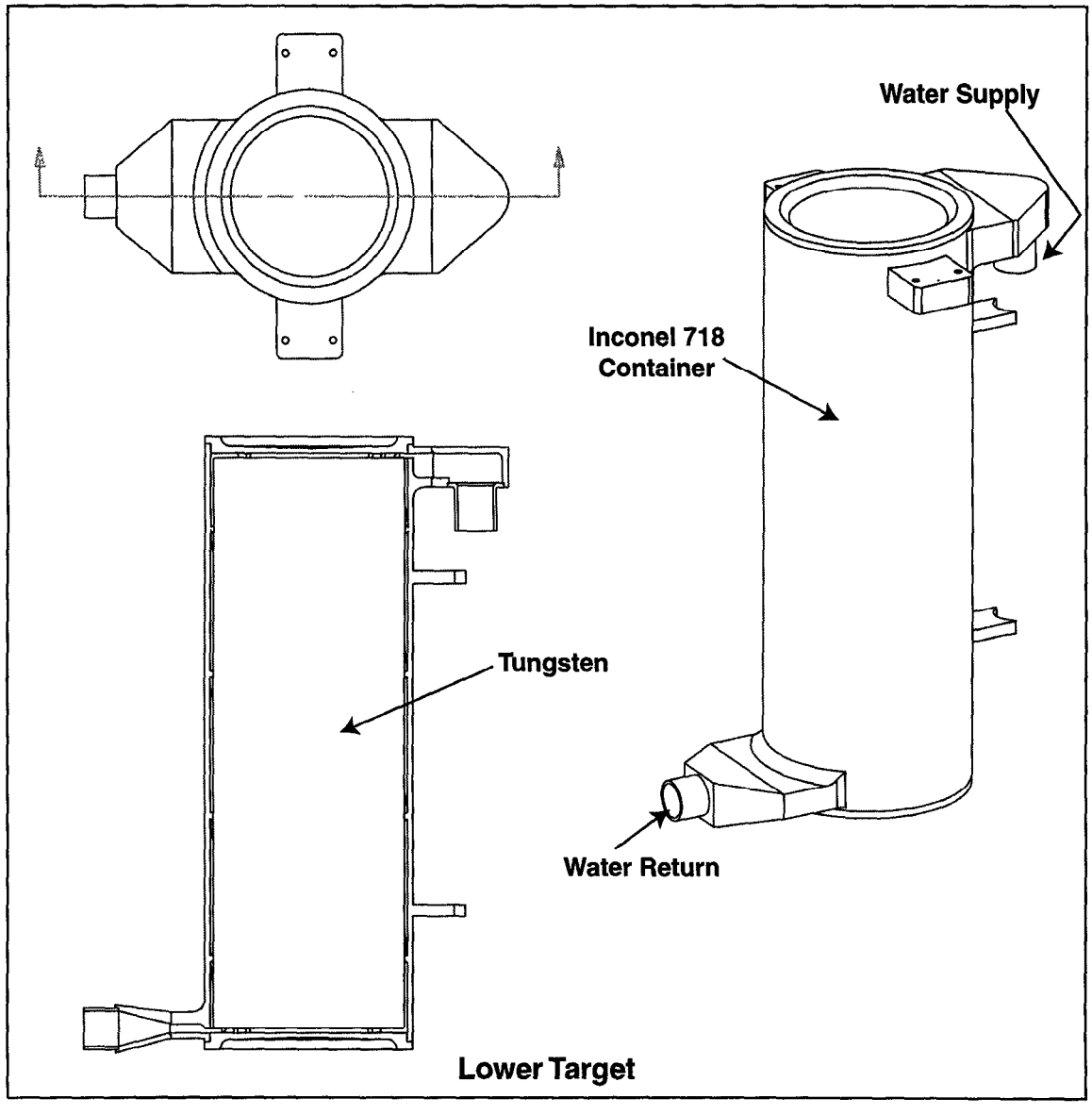

Figure 8. **Lower Tungsten Target**

Table 4. Lower Target General Operational Parameters

Target Configuration	Solid-type, light-water cooled
Tungsten Length	298.45 mm
Tungsten diameter	101.6 mm
Total Tungsten Heat Flux	25.9 kW
Peak Volumetric Heat Flux in the Tungsten	51.0 W/cm^3
Average Heat Flux in the Tungsten	10.8 W/cm^3
Water channel side (gap)	1.5 mm
Water channel top and bottom gap	2.5 mm
Pressure vessel wall thickness	3.0 mm
Inlet water pressure	1.38 Mpa (200.0 psi)
Design water flow rate	0.76 liter/sec (12 gpm)

5.3.2. Moderators

The suite of moderators is divided into a lower tier with four moderators and an upper tier with two moderators. The lower tier services 12 flight paths (1-11 and 16) and the upper tier, services 4 flight paths (12-15). There are three ambient-temperature water moderators in the lower tier and one in the upper tier. Each tier also has one cryogenic liquid-hydrogen moderator that operates at about 20 K. Characteristics of the 6 moderators are listed in Tables 5 and 6 below. Note that all of the lower tier moderators are viewed in transmission whereas the top tier moderators are viewed in back scattering. The upgrade target system has been designed so that no significant adjustments to the present instrument collamation or view-angle are required. The new moderators in the lower tier region are positioned as close as possible to the same locations as the previous moderators. In most cases, this is within 2 mm of the previous position.

Table 5. Moderator Specifications

Flight Path	Moderator Type	Flux-Trap Decoupler	Reflector Decoupler	Poison	Be Flight Path Liner	Lead Flight Path Liner
1,2,16	Water, High Resolution	0.002 inch Gd	0.032 inch Cd	0.002 inch Gd	0.032 inch Cd	0.032 inch Cd
3,4,5	Water, High Intensity	0.032 inch Cd	0.032 inch Cd	none	0.032 inch Cd	0.032 inch Cd
6,7,8	Water, High Intensity	0.032 inch Cd	0.032 inch Cd	none	0.032 inch Cd	0.032 inch Cd
9,10,11	Liquid Hydrogen	none	none	none	none	0.032 inch Cd
12,13	Liquid Hydrogen	none	none	none	none	0.032 inch Cd
14,15	Water, High Intensity	none	none	none	none	0.032 inch Cd

Table 6. Moderator dimensional information

Flight Path	Pre- moderator Thickness (mm)	Moderator Thickness (mm)	Operational Pressure (MPa)	Operational Temperature (K)	Temperature Uniformity Rqm't (+/- K)
1,2,16	21.2	16.1	0.41	293	1
3,4,5	N/A	25.0	0.41	293	1
6,7,8	N/A	25.0	0.41	293	1
9,10,11	N/A	50.0	1.38	20	1
12,13	N/A	40.0	1.38	20	1
14,15	N/A	50.0	0.41	293	1

Water Moderators

The water moderators consist of a one-piece machined body with electron beam welded top and bottom cover plates (see Figure 9).

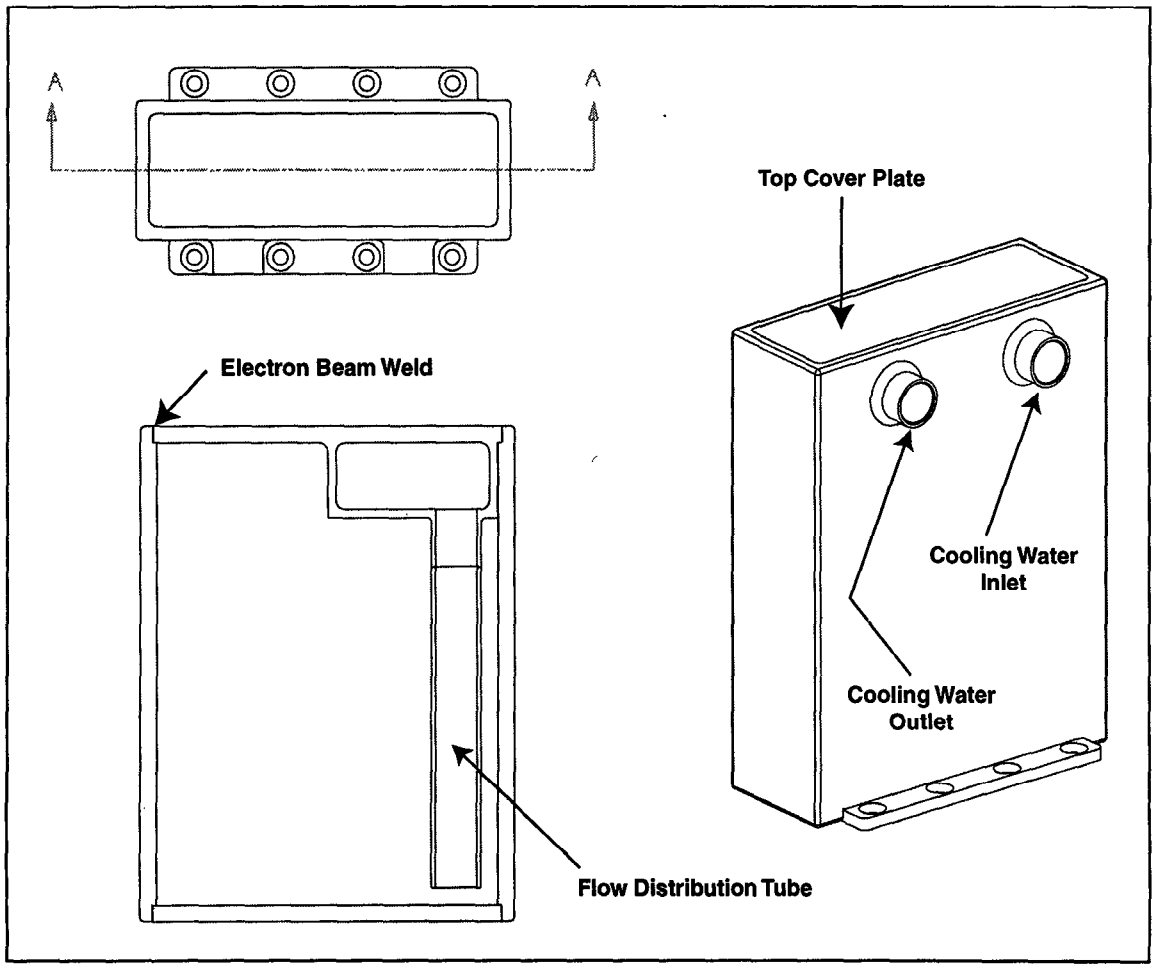

Figure 9. Water Moderator Design

Alloy 6061 aluminum was chosen for it's neutronic properties as well as corrosion resistance in water and it's strength. Electron beam welding the covers provides the best closure process to minimize the heat affected zone and overall distortion. The cooling lines are stainless steel 304 alloy and are joined to the aluminum vessels with a special Bi-Braze transition fitting that has been used successfully at LANSCE on the previous target systems. The fitting is TIG welded to the vessel and piping by hand at assembly. Welding procedures including heat-sinking instructions are provided by BI-Braze to prevent damage to the fitting during installation.

The liquid hydrogen moderators (Figure 10) consist of an internal pressure vessel and an external vacuum vessel. The pressure vessel operates at 20 K and the vacuum vessel at about 25 C. The gap between the pressure vessel and vacuum vessel provides the thermal insulation for the pressure vessel. The vacuum space is actively pumped and monitored for the hydrogen during operation. If hydrogen is detected in the space, the hydrogen safety system vents to prevent an explosive condition from existing in the moderator units or in the vacuum insulated transfer lines that supply liquid to the pressure vessel.

Heat transfer in this assembly is somewhat uncharacteristic of cryogenic systems; nuclear heating in the vessels and piping is significantly higher than either conduction or infrared radiation heating in the region of the moderator vessels near the target. As a result, the typical cryogenic superinsulation normally used in a 20 K unit is omitted in the vessel region, and used only in the upper section of the vacuum transfer line.

The moderators in both tiers are fastened to aluminum cooling plates that serve as an alignment and fixturing base as well as a primary heat sink for the vacuum jackets on the cryogenic moderators and a backup heat sink for the water modertors. The design allows for cooling of the containers without liquid inside, if required. The cooling plates also serve as heat sinks for the flight path liners in the decoupled lower tier as shown in Figure 11. The liners are 0.090 inch thick aluminum shells welded to the lower cooling plate and electroplated with cadmimum metal 0.04 inch thick. Cadmimum metal is also electroplated 0.040 inch thick on the surfaces of the water moderators in the lower tier to provide reflector and flux-trap decoupling. The high resolution moderator serving flight paths 1,2&16 has gadolinium 0.002 inch thick as a flux trap decoupler and also as an internal gadolinium poison divider plate. The gadolinium is plasma deposited on a 0.032 inch thick 1100 aluminum alloy plate that is electron beam welded to the wall of the vessel, this provides good mechanical positioning and good heat transfer to the cooled wall of the vessel.

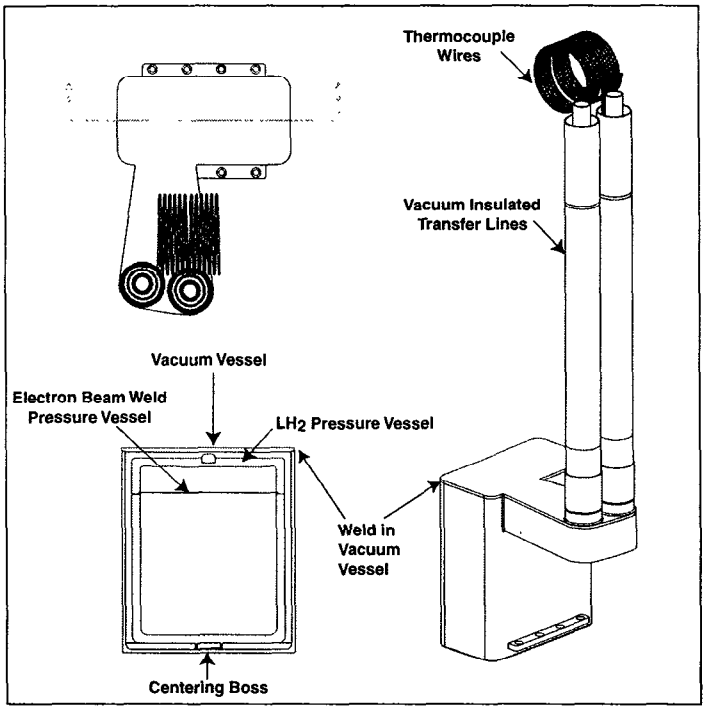

Figure 10. Cryogenic moderator section view

5.3.3. Beryllium Inner Reflector and Cooling Plates

The target and moderator vessels are surrounded by solid sections of beryllium metal that is assembled into a large cylindrical section. The beryllium reflector extends from near the target outside surface to a diameter of 60 cm. Cut-outs arc provided for instrument view ports as well as cooling line routing from all the cooled components. The beryllium itself is cooled by mechanical attachment the cooling plates mentioned above. Heat energy is conducted through the bolted interface and into the aluminum plates. The amount of energy deposited in the beryllium reflector total is about 2.5 kw, requiring a coolant flow of about 2 to 3 gpm at 25 C in the cooling plates. The beryllium is assembled in three main sections with cooling plates to sandwich the assembly together (see Figure 11). The cooling plates serve to locate the beryllium and keep it cool as well as to position the moderators with respect to the reflector. The assembly was fabricated from beryllium shapes on hand at Los Alamos and the geometry was designed to utilize this material. The multiple sections of beryllium shown in the figure partially result from piecing together the available material as needed to produce the required geometry. An attempt was made to position most of the mechanical interfaces (bolted seams) in the unit parallel to the heat flow in the cooled assembly to allow most the effective heat removal by the cooling plates. Thermal analyses were done to insure that adequate cooling exists at 200 μA.

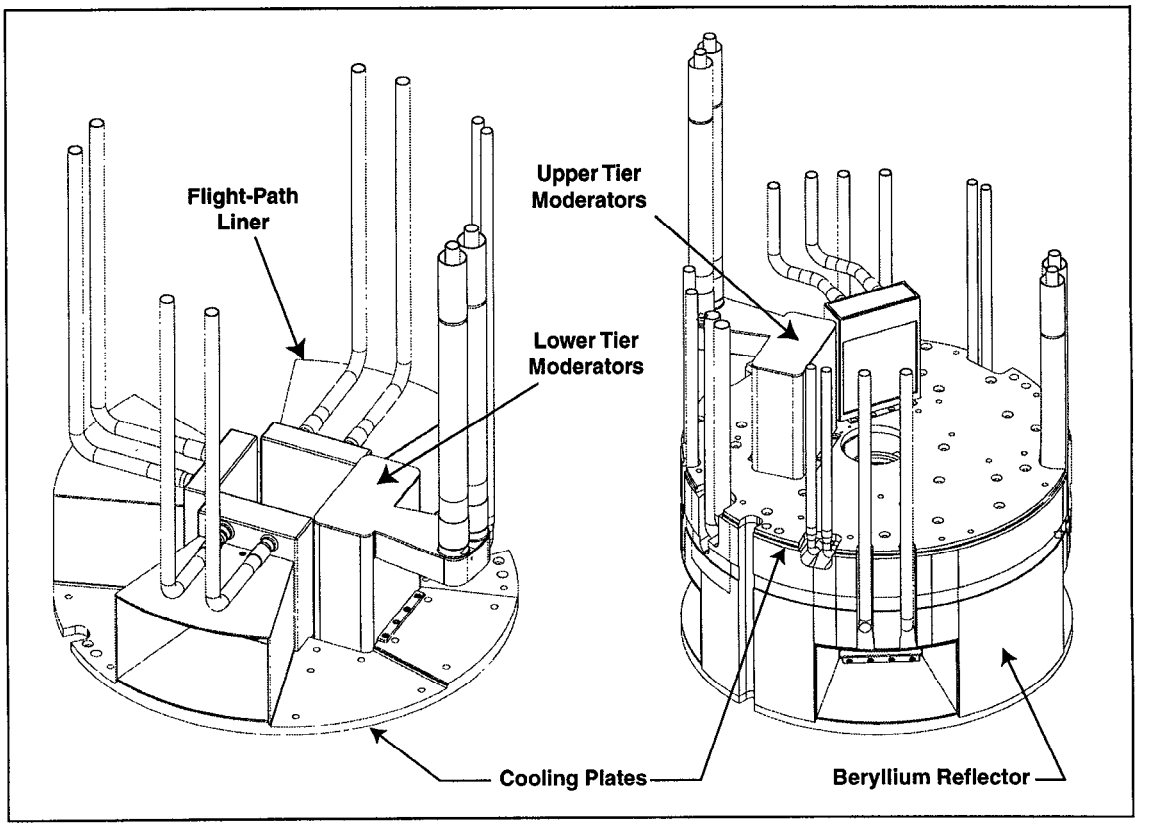

Figure 11. Aluminum Cooling Plate and beryllium inner reflector

6. Lead Outer Reflector

The outer reflector is composed of lead contained in a steel vessel that surrounds the beryllium section and extends out to a diameter of roughly 1.14 meters. The unit weighs about 17800 lb. and is supported from the main structural frame, see Figure 2. The lead is cast into a welded steel container that has an integral water cooling tube. The entire unit was produced as an assembly, complete with piping and lifting features.

It is sized to allow installation through the roof access port using the 30 ton overhead bridge crane. The total heat load is estimated at about 2 kW and it requires 2 to 3 gpm cooling water at 25 C.

7. Beamstop

The beamstop used for the upgraded target system is nearly identical to the present geometry except that a slight reduction in outer diameter will allow roof-port access. The Beamstop is composed of a water-cooled stainless steel top plate that is bolted a larger mild-steel lower section, see Figure 2. The cooled section will carry heat from the uncooled section across the bolted interface. The cooled plate is built from 304 stainless steel and the lower, larger, section is made from regular carbon steel to reduce cost of the assembly. The heat load in the combined volume is estimated at less than 1 kW, and it requires about 2 gpm of cooling water at 25 C.

8. Steel Shielding and Crypt Vacuum Vessel

The bulk shielding (see Figure 1) that resides in the crypt vessel surrounds the outer reflector and extends to the vacuum vessel wall, about 3 meters in diameter. The shielding is composed of flame-cut steel cylindrical rings and plates bolted together in some areas and stacked around the outside of the target-moderator-reflector assembly. The bulk shielding is not actively cooled and is not meant to require maintenance of any sort.

9. Present Status of the System

At the time this document was prepared, all of the crypt contents are installed except for the target insert, which is still in final assembly and testing. Final installation of the target insert is planned for early July 1998.

ICANS-XIV
14th Meeting of the International Collaboration on Advanced Neutron Sources
June 14-19, 1998
Starved Rock Lodge, Utica Ill, USA

Target Materials Development for SINQ and Out of Beam Testing

A. Malik, G. S. Bauer and G. Heidenreich
Paul Scherrer Institut, 5232 Villigen PSI, Switzerland

Abstract

In investigating possibilities to make use of lead as an efficient low absorption target material in the solid rod target of SINQ in a way that would ensure sufficient mechanical stability and corrosion resistance, two routes were investigated: generating stronger compounds or alloys with high lead content and developing a suitable cladding material for the lead. While the first route was, so far, not successful, it could be shown that sufficient bonding can be achieved between an AlMg3 tube and its lead filling that overheating of the lead and softening of the cladding would not be expected under normal operating conditions of SINQ. A larger safety margin can, however, be obtained - albeit on the expense of a slightly lower neutron flux - if steel cladding is used. The plasticity of lead at the temperatures in question was measured and found to be sufficiently high to keep stresses in the cladding in tolerable limits, if space for expansion of the lead is provided anywhere in the enclosing tubes. Thermal cycling under more stringent conditions than expected in SINQ showed no observable damage on the cladding, if the target elements were prepared properly.

1. Introduction

The continuous spallation neutron source SINQ is currently running on the target design which was conceived for its commissioning phase with maximum simplicity in mind. This is a zircaloy-2 rod bundle target which is cooled by heavy water. The neutron flux achieved at 0.25 m distance from the target is $0.3*10^{14} n^0/cm^2/s/mA$ (value as calculated by LAHET and confirmed by scaling from a measurement at a different position [Tob98]). A target development program was initiated with the goal to increase the neutron yield and to design for a target lifetime of at least one year. An enhancement of the neutron flux by more than a factor of two should be possible, if lead can be used instead of zircaloy-2 [Bau98]. Besides the option of a liquid lead target one can also use solid lead rods with a cladding material which ensures mechanical and corrosive stability. To obtain a significant enhancement in the neutron flux at least 50% of the material in the beam must be lead. For the realisation of such a target the following points must be considered:

a heat transfer between target material and cladding;
b mechanical and thermally induced stresses in the cladding material;
c the influence of thermal cycling on the target material as well as on the cladding.

Keywords: Lead, Lead alloys. Cladding, bonding, solid target

A close look at target materials other than pure lead seemed to be useful, since the proton beam deposits up to 300 W/cm^3 in the target. With lead having a comparatively low melting point of T_m=600 K, the maximum temperature of approximately 423 K in the target is significantly higher than $T_m/2$. A target material with a high melting point and good mechanical properties as well as a low neutron absorption cross section would be ideal. In parallel to searching for such a material also the heat transfer properties between lead and low absorption cladding materials, in particular aluminium and ways to improve it were examined.

2. Target material development

2.1. Lead alloys with a high melting point

Lead zirconium alloys have been investigated as neutron multipliers for the fusion reactor technology. All of these investigations were done on the zirconium rich part of the phase diagram which, even there, is not well known. This means that there are no publications, which could be used as a basis. A fairly recent publication [Aria96] of thermodynamic data in the region of 50 at % Pb gave no reasonable values for extrapolations into the lead rich regions [Hall96]. Zr_5Pb_3 produced by hot isostatic pressing had a melting point of more than 1673 K but was very brittle [Dal86].

Based on this information, several process techniques to alloy Pb_5Zr_3 were tried. Using an arc melting furnace, one obtains samples which show a good mixing of lead and zirconium, but due to the different melting points of lead and zirconium one has a high rate of lead evaporation and the sample size and shape are very much restricted. The composition of the samples showed a maximum value of Pb-50 wt% Zr. The samples obtained showed a significant increase in hardness by a factor of four compared to pure zirconium. The melting point of the samples was more than 1400 K. These values can be explained by the formation of intermetallic phases. Scanning electron microscopy revealed lead rich regions and regions with a lower lead content.

Using a sintering technique in a tantalum crucible at 1250 K did not result in a complete reaction and the concentration gradient within any one sample was very high. Furthermore, the samples did not show any increase in the melting point.

To decrease the evaporation rate of lead a pre-alloy was produced consisting of Zr-29 wt% Cu. This pre-alloy had a melting point of ~1299 K. Afterwards an alloy was cast in the induction furnace under vacuum with a nominal composition of Pb and 20 wt% of the pre-alloy. One obtains an alloy with a melting point of more than 1400 K. Investigations by SEM again showed a two-phase system with the copper atoms at the phase boundaries. The evaporation of the lead could be reduced but still a marked temperature rise was observed when the zirconium chemically reacted with the lead and a significant amount of lead was evaporated. All samples showed a strong tendency to embrittle in air, and extended observation in the SEM resulted in radiation damage.

2.2 Dispersion strengthened lead

Conventional lead alloys do not show improved mechanical properties over lead beyond 373 K. Therefore, possibilities were investigated to use a dispersion strengthened lead alloy. The samples used were Pb-0.05 wt% Cu - 0.02 wt% Sn which were produced by a melt-spinning technique at the University of Braunschweig [Fox96, Mos95]. The samples were thermally cycled between room temperature (293 K) and 373 K and then between RT and 410 K. In all cases 501 cycles were run. Measurement of the Brinell hardness showed a decrease of about 14% compared to the untempered sample and the hardness was even lower than that of a conventional Pb-0.1 wt% Ca sample which was submitted to the same heat treatment.

3. Bonding procedure between target material and structural material

With respect to thermal neutron absorption zircaloy and aluminium seem to be the ideal candidates for the structural material. Aluminium is preferable since it has a higher thermal conductivity. Also, its coefficient of thermal expansion is closer to that of lead and thus the resulting absolute stress in the target material is lower. Furthermore, there is some uncertainty about the hydrogen embrittlement in the case of zircaloy and more data are needed. Using aluminium - or one of its alloys - one has to take care that an ideal heat transfer between target material and structural material is obtained because otherwise the temperature of the lead might run too high and expansion might result in a rupture of the cladding. Since aluminium and lead do not bond, an additional bonding layer must be used. For this bonding layer copper seemed to be the right material because of its very good heat conductivity and its low solubility in aluminium as well as in lead.

To produce the final target rod the following steps were performed: In the first step a very thin coating of copper was deposited on the inside of the AlMg3 tubes by electroplating. To achieve a perfect bonding between the copper clad inside of the aluminium tubes and lead, a specially designed filling station was used (Fig. 1). This equipment allows to reduce any oxide layer either on the copper or on the molten lead by rinsing the tubes and the liquid lead container with a gas mixture of 95%N_2 and 5%H_2. This is done while heating-up the target rod and the lead to ~750 K. Then the inlet for the liquid lead is opened and the tube is filled. Cooling from bottom to top allows to avoid formation of cavities due to the shrinking of lead (~3%) during solidification. A picture of a tube filled by this method is given in Fig. 2. In Fig. 3 the excellent wetting behaviour of lead on the copper surface is clearly shown.

4. Out of beam testing

4.1 Mechanical properties of lead

For the finite element calculations [Ni98] the stress strain curves for lead at temperatures beyond 373 K had to be measured. The measurements were done in the "Laboratorium für Sicherheits- und Unfallforschung" at PSI. A picture of the samples and some of the results of these measurements are shown in Fig. 4 and Fig. 5 [Kal97].

4.2 Test of the mechanical strength and the thermal stability of the copper layer

To guarantee the mechanical strength and stability under elevated temperatures of the bonding between target material and structural material tensile tests as well as heat treatments were carried out. The samples were produced by bonding two AlMg3 plates which had been coated with copper by electroplating to a 10 mm thick lead layer, using a similar procedure as given above. The plate was then cut into 5 mm wide slices (Fig. 6) which were used in a tensile testing experiment at room temperature and for the heat treatments.

In the tensile testing experiments no failures were observed at the lead-copper or copper-AlMg3 interface The evaluation of the data reflected the mechanical properties of pure lead. From this experiment it can be concluded, that the mechanical bonding of the copper layer to both materials is much stronger than the expected stress rates in the target.

The same sample geometry was used to determine if any diffusion of copper into lead or aluminium occurs at temperatures, which are expected in SINQ. The copper layer thickness was determined by scanning electron microscopy before and after ageing the sample first at 423 K for ten days and then for another ten days at 473 K. No decrease in the average copper layer thickness was found (Fig. 7-8). Both temperatures are higher than the expected temperatures for this target geometry.

4.3 Examination of the heat transfer between target material and cladding

With the methods given above the mechanical and the thermal stability of the bonding layer was shown. To prove the effectiveness of the layer in improving the heat transfer, ultrasonic as well as thermographic investigations were carried out. Three different AlMg3 tubes where provided for this test: the first tube (No. 1) was empty, the second tube (No. 2) was not electroplated with copper but otherwise the same filling procedure was applied as described above and, finally, the third tube (No. 3) was electroplated with copper but the copper layer was deliberately damaged at one spot.

In order to examine the quality of the bonding the specimens were examined by ultrasonic techniques. The results are shown in Fig. 9. By comparing to the image obtained for the empty tube it can be seen that for sample No. 2 bonding between target material and structural material is found on about 40% of one side, while there is no bonding at all on the second side. The partial bonding is probably due to the presence of magnesium in the alloy since the phase diagram of aluminium-lead shows a miscibility gap. Technically the bonding occurs at the side closest to the heating element along the tube (cf. Fig. 1). Sample No. 3 shows the expected perfect bonding on both sides with the exception of the purposefully damaged region. These results were confirmed fully in the thermographic studies.

As a conclusion from these measurements one might consider not to electroplate the AlMg3 tubes (which is rather tedious and costly) and to still achieve a satisfying heat transfer between lead and cladding with some optimisation of the filling process. These findings are supported by [Sna84] who quote a heat flux resistance of 10^{-4}-10^{-5} m^2K/W.

4.4 Cyclic Testing of tubes filled with lead

Since about 20000 load cycles occur per year in SINQ, resulting from accelerator trips, the resistance of the target rods and their cladding material to this cyclic stress must be investigated. In order to simulate exactly the conditions in SINQ one would need to be able to deposit about 350 W/cm^3 in the target material and about 2/3 of this in the cladding. This is beyond the existing experimental possibilities except for the use of the proton beam itself. A substitute test was set-up using a high frequency generator of two megahertz for the heating and a water loop for the cooling. The samples were heated only in the central 3.5 cm of the target rod simulating in this way to some extent the radial distribution of the proton beam profile. In SINQ the maximum power deposition will be also in this range of the target rods.

Due to the skin-effect, the penetration depth of the high frequency field is of the order of 0.1 mm compared to the wall thickness of the cladding material which is in the range of 0.5-1 mm. Thus, the heating will always be from the outside, contrary to the volume heating that will prevail in SINQ. The experimental set-up was chosen in a way that made it possible to control the surface temperature of the cladding material: Unlike in a previous experiment [Häb97] the target rod was heated outside the cooling bath and the rod was then quenched into the water (Fig. 10). This method simulates mainly the effect of the tripping of the proton beam, when a heated rod is cooled down by the water flow (which is the more relevant phase of the thermal cycle, because its rate cannot be controlled in the target). The cladding material is cooled while the target material is still hot and thus hinders shrinking of the cladding material. In this way the mechanical stress in the cladding material is simulated properly.

Tests were performed on the following samples:

a. two oval AlMg3 tubes (samples No. 1 and 2) with a copper layer as bonding material.
b. one oval AlMg3 tube without a bonding copper layer (sample No. 3).
c. six circular steel tubes (samples No. 4-9).

The AlMg3 tubes were filled in a nitrogen-hydrogen atmosphere as described above. All other tubes with exception of two steel tubes (No. 4 and 5) where filled using a set-up slightly modified from the one shown in Fig. 1. Samples No. 4 and 5 were prepared by filling the liquid lead into cold steel tubes. In this case there is no bonding between the steel tubes and the target material. The lead rods can be easily removed from the tubes because there is a small gap between the lead rod and the steel tubes after cooling down.

Heating the lead inside the aluminium tube to T_{Pb1}=350°C (sample No. 1) and quenching it into water the cladding was visibly deformed after 40 cycles (f_1=0.02 Hz) as can be seen in Fig. 11. The test was stopped after 70 cycles to avoid rupture of the cladding material. The lead inside sample No. 2 was heated up to T_{Pb2}=150°C only for 10000 cycles (f_2=0.04 Hz) and no deformation due to the expansion of the lead was found. This rod was then used for another 10000 cycles at T_{Pb2}=200°C. Again no deformation was found. Sample No. 3 was heated up to T_{Pb3}=150°C for 10000 cycles (f_3=0.04 Hz) and again no deformation due to the expansion of the lead was found.

To understand the failure mechanism in the case of sample No. 1 one has to consider on one hand that upon melting of the lead a volume expansion of 6% relative to room temperature occurs. On the other hand, since the temperature in the cladding is at least 50°C higher than in the lead, the mechanical properties of AlMg3 are drastically reduced ($T>T_m/2$). Thus no conclusion can be drawn of this failure of the cladding material, since in SINQ the temperature of the cladding will not exceed 100°C due to continuous water-cooling. For a relevant testing of the aluminium tube, the temperature in the cladding should not exceed 200°C. Samples No. 2 and 3 where investigated under conditions that would prevail if the heat transfer between target material and cladding was always fairly good, which can be assumed according to the results of the ultrasonic scanning and to FEM calculations [Ni98] of the pressure on the cladding. Those rods did not show any permanent deformation, which means that only elastic deformation occurred during the tests.

Concerning the steel tubes, the lead inside sample No. 4 was heated to T_{Pb5} = 400°C for 10000 cycles (f_4=0.025 Hz). No damage could be observed. The same sample was then used for another few cycles to determine the surface temperature of the steel tube. During these tests a crack of about 1.7 mm length developed in the cladding and a small amount of lead evaporated. The temperature measured on the topside of the steel tube was more than T_{Steel1} = 600°C, which is, of course, far beyond the operating conditions of a water-cooled target. In case of sample No. 5 the end caps of the rods were not welded to the tubes but simply glued on. Heating the lead to 400°C lead to an expansion of the lead to which one of the end caps could not stand up. The glue yielded and the loose lead was partially extruded from the tube. Samples No. 6, 7 and 9 were cycled 10000 times (f_7=0.01 Hz) to T_{Pb7}=400°C and no damage was observed. No. 9 was cycled for another 10000 times but this time the rod was held at 390 degrees for 23 seconds. Again no damage was observable.

Sample No. 8 with thermocouples placed on the surface and in the middle of the rod is kept as a reference sample in order to be able to set up the desired experimental conditions any time.

Concerning the results of the steel tube tests, several observations were made: First the failure of sample No. 4 was solely due to the fact that the temperature of the steel cladding was much higher than in the lead. This can be directly related to the fact that there existed no bonding at all between cladding and target material and heating was only via the cladding. In fact, when the tube was placed in the high frequency coils, an air gap of about 1 mm existed between the topside of the lead rod and the tube (Fig. 12). Since most of the induced heat was in the cladding this lead to a considerable overheating of the tube's upper side (T_{Steel1}>600°C compared to T~500°C on the lower side), which then resulted in the cracking. As in the case of the failed aluminium tube this case cannot happen in SINQ since the cladding will always be cooled.

Fig. 12 may also be used to explain why the testing of sample No. 6 had to be stopped. As one can see small air gaps exists also at the ends of the lead rod. This allows directional expansion of the lead during the heating [Ni98]. If this gap is not present, there will be stress on the end caps due to the plastic deformation of the lead. Since in this case the end caps were only glued and not welded in place the pressure was too large and the lead was pushed out.

With the samples No. 6, 7 and 9 no damage was observed and X-ray examination showed no gaps between target material and cladding.

5. Conclusions

While we were not successful, so far, in developing an alloy with high lead content and satisfactory mechanical and corrosion properties for the SINQ target rods, the work reported here clearly showed the clad lead rods can be used to improve the neutronic performance of SINQ. Under normal operating conditions both, AlMg3 and steel seem to be practicable. While the use of aluminium relies on being able to obtain good heat contact between the target material and the cladding and on maintaining the temperature below 250°C at all times, the use of steel seems to be more fault tolerant. Neutronically, using steel cladding will result in about 15% less neutron flux than aluminium [Bau98]. But, on the other hand, steel would probably also be the structural material of a liquid metal target, which makes it desirable to accumulate experience with this material in the SINQ environment before embarking on that final step. Thus, the decision between steel and aluminium as cladding material will also depend on what the prospects are to proceed towards a liquid metal target. Finally, it should be noted that also zircaloy would be a favoured candidate, if hydrogen uptake and embrittlement turns out not to be a problem. Relevant information is expected already from the examination of the first SINQ target which was operated for 500 mAh in 1997 and which will be taken apart and examined in the second half of 1998.

6. Literature

Aria96 D. Arias, J. Abriata and L. Ribaudo, J. Nuclear Materials, 229, 24 (1996).

Bau98 G.S. Bauer, A. Dementyev, E. Lehmann, "Target Options for SINQ" this conference

Dal86 M. Dalle Donne, S. Dorner and D. F. Lupton, J. Nuclear Materials, 141-143, 369 (1986).

Fox96 B. Fox, Diploma thesis "Entwicklung einer Bleilegierung mit verbesserter Hochtemperaturbeständigkeit" Universität Braunschweig (1996).

Häb97 P. Häberli, private communication (1997)

Hall96 B. Hallstedt, private communication (1996).

Kal97 D. Kalkhof and J. Kamber, PSI TM-49-97-09 (1997).

Mos95 L. Mosler, PhD thesis "Eigenschaften rasch erstarrter Bleilegierungen mit Kupfer-Zinn-Dispersoiden" Universtität Braunschweig (1995)

Ni98 L. Ni G. S. Bauer and Y. Dai "Thermal Structure Analyses on the Test Rods in the SINQ Target Mark 2 with Irradiation Test Samples" this conference (1998)

Sna84 B. Snaith, P. W. O'Callaghan and S. D. Probert, Appl. Energy 16, 175 (1984).

Tob98 Tobler, "Neutronenflussbestimmung in der Rohrpostanlage (1rp) für die Neutronenaktivierungsanalyse" internal report PSI TM-32-98-01 (1998)

Fig. 1: Picture of the lead filling station. The lead container on top of the AlMg3 tube is heated by two heating elements while the other two heater are along the tube and at the bottom. The gas inlet is mounted on the back side.

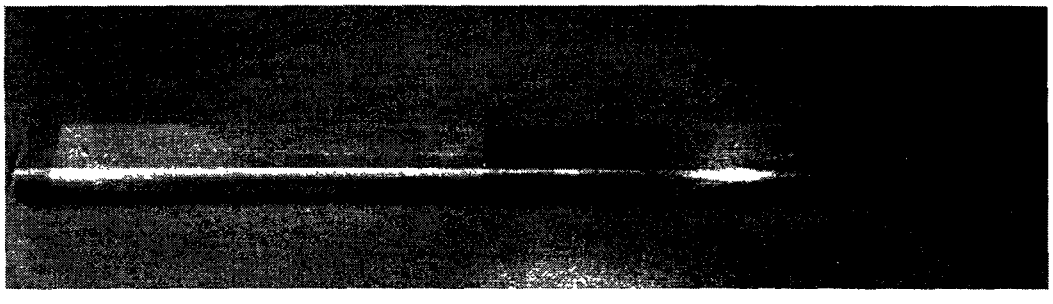

Fig. 2: AlMg3 tube filled with lead.

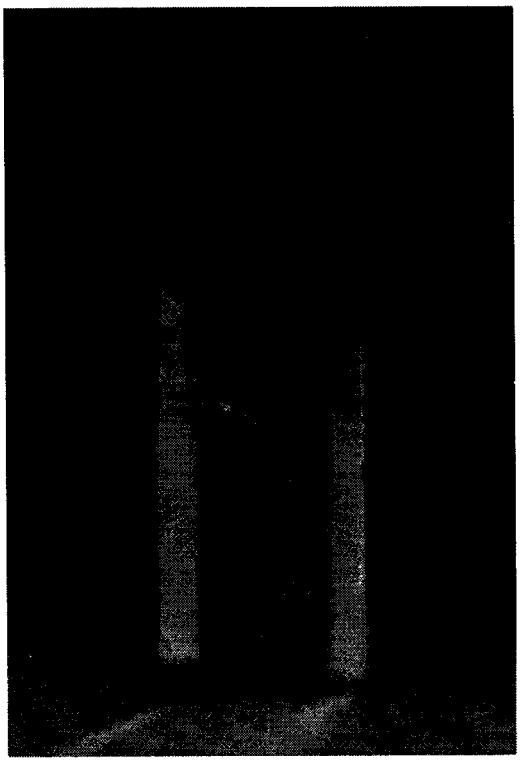

Fig. 3: The good wetting behaviour of lead on the copper surface is seen on this cut through an AlMg3 tube.

Fig. 4: Tensile testing specimens, on the left side for elevated temperatures and on the right for room temperature measurements.

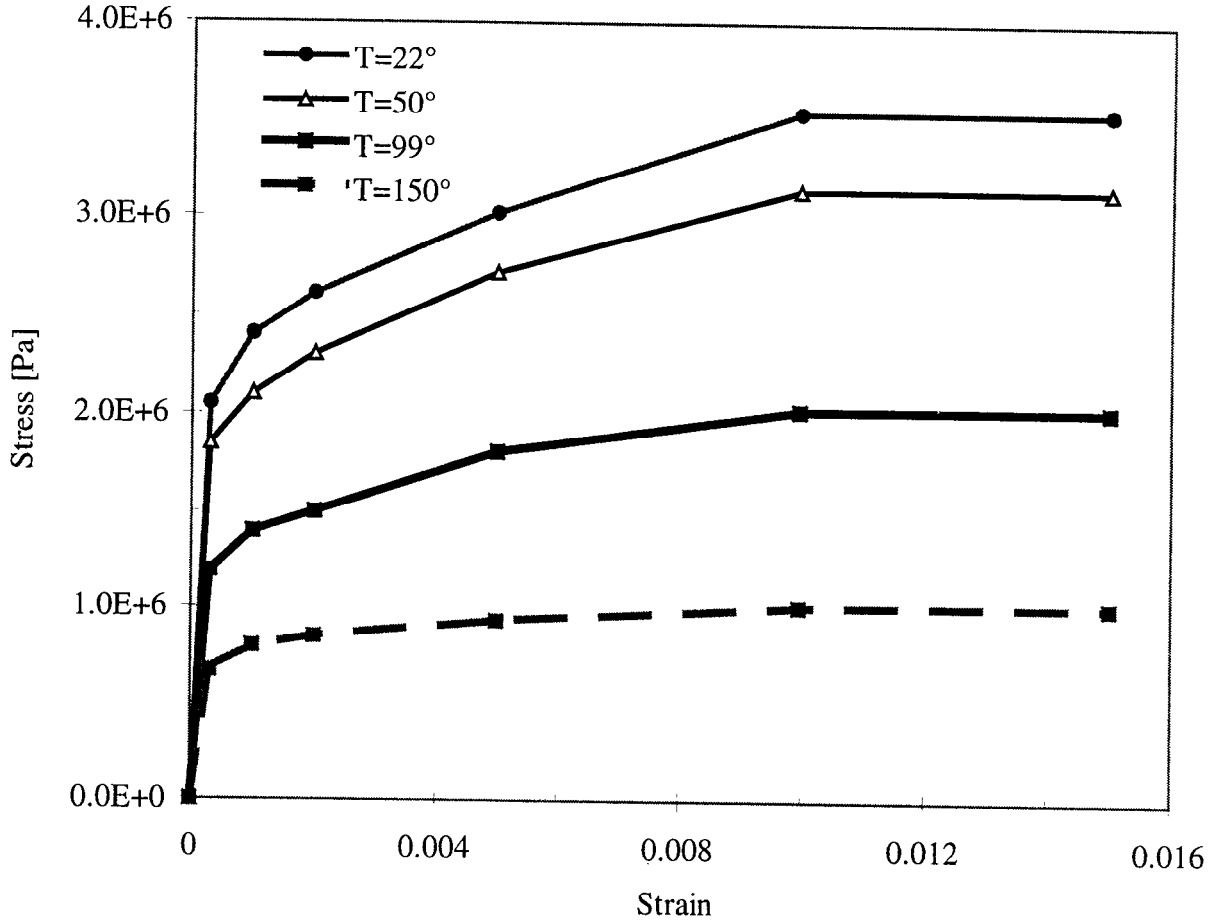

Fig. 5: Measurements of the stress-strain curves at different temperatures [Kal97].

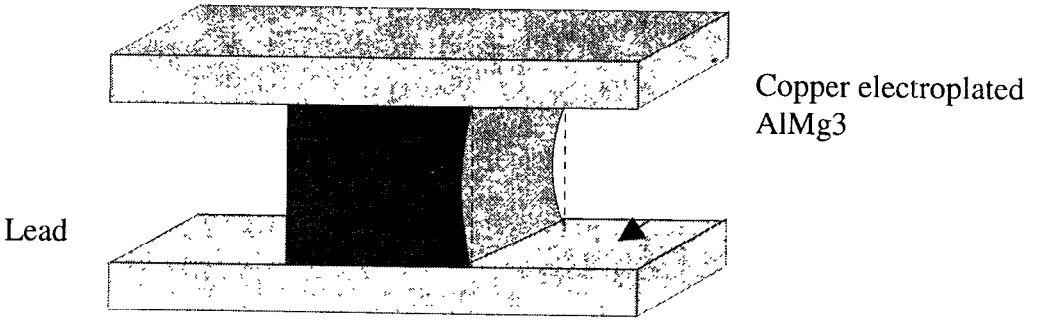

Fig. 6: Sample for the testing of the mechanical and thermal stability of the electroplated copper layer.

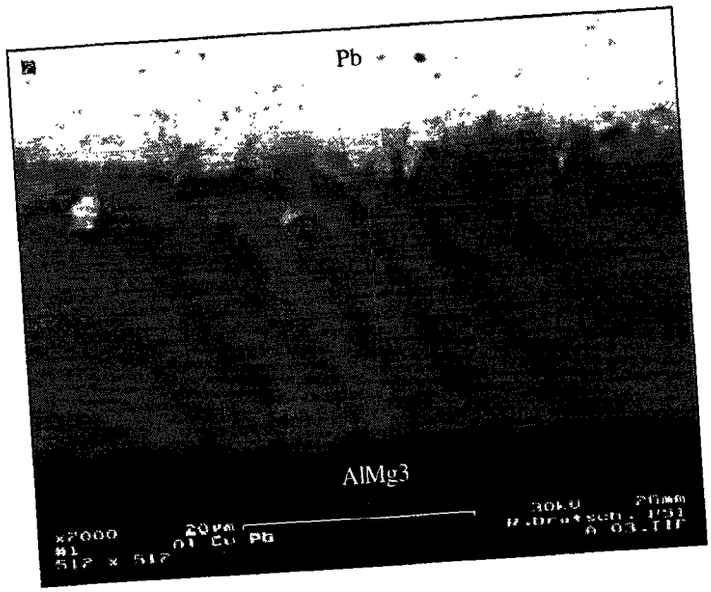

Fig. 7: SEM picture of the AlMg3-20 µm Cu-Pb interface (30 kV, 2000x).

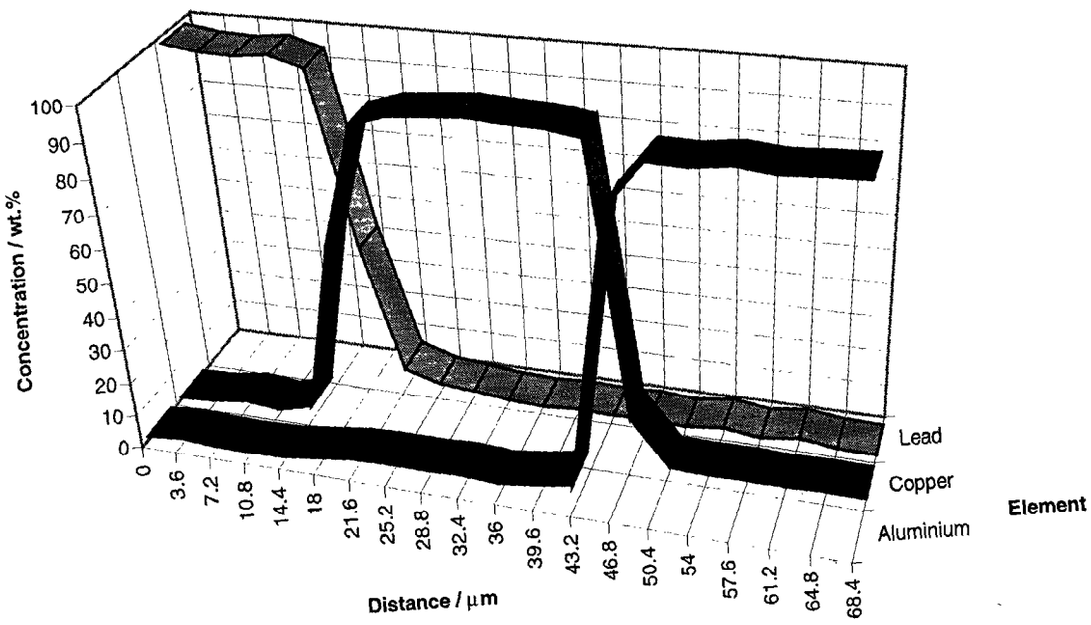

Fig. 8: Profile of the interface lead-copper-aluminium after the heat treatment.

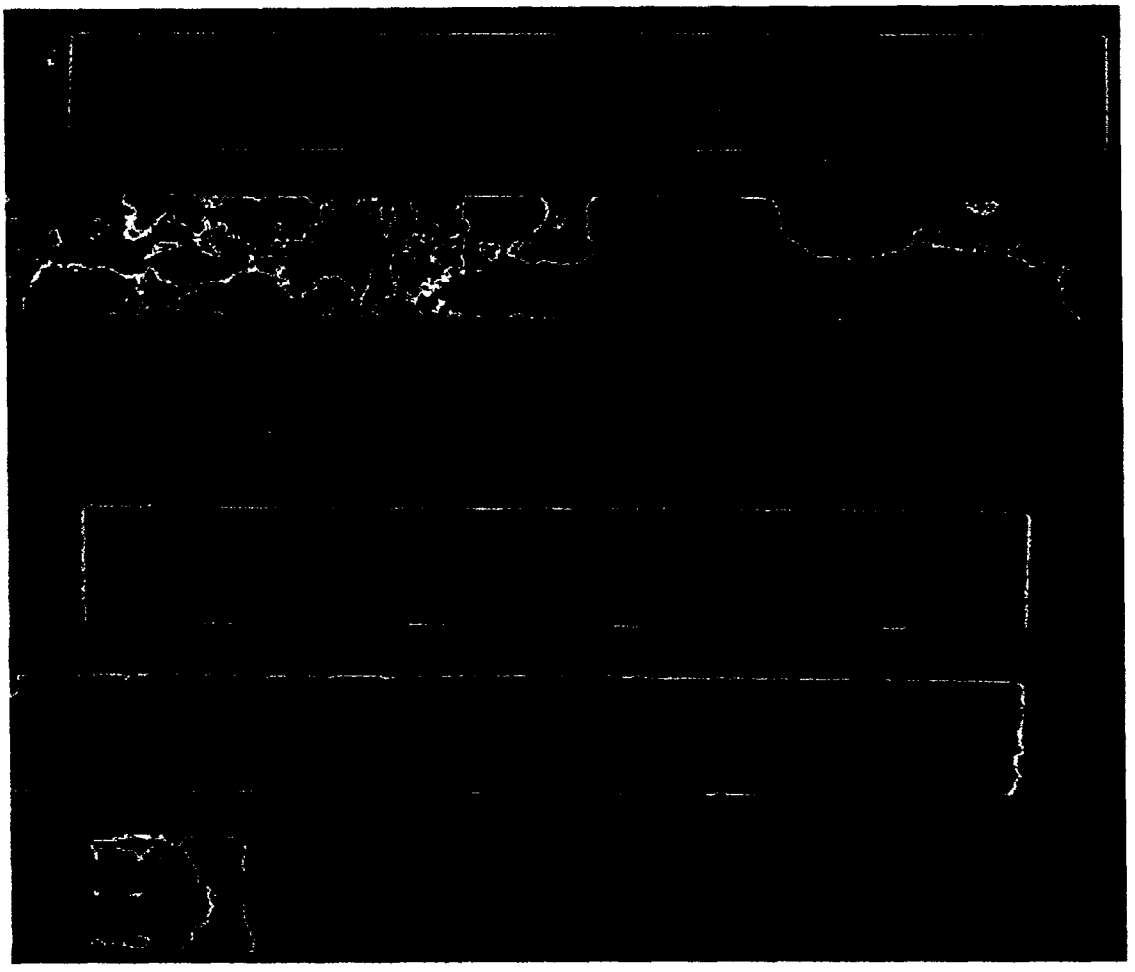

Fig. 9: Ultrasonic investigation of the bonding quality in the AlMg3 tubes. From top to bottom:

a. Empty tube.
b. AlMg3 tube with no electroplated copper layer showing partial bonding (blue areas).
c. AlMg3 tube with a electroplated copper layer showing perfect bonding.
d. Empty tube second side.
e. Second side of b. showing no bonding.
f. Second side of c. showing perfect bonding with exception of the purposely damaged area.

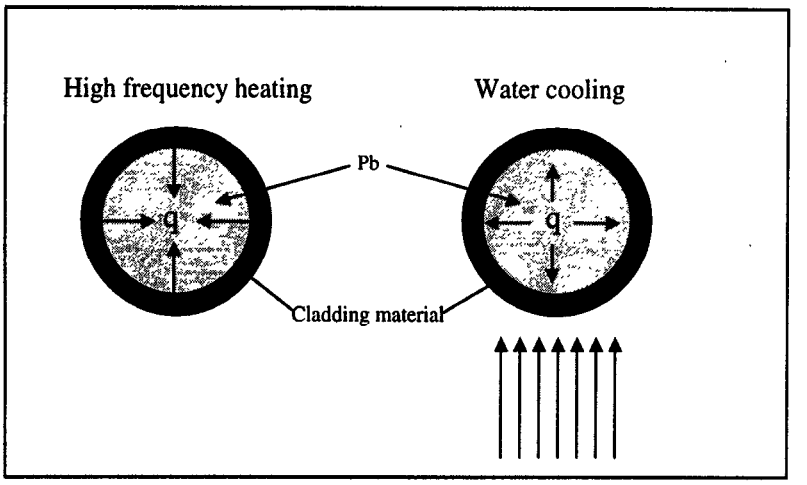

Fig. 10: Heat flux q during heating and cooling.

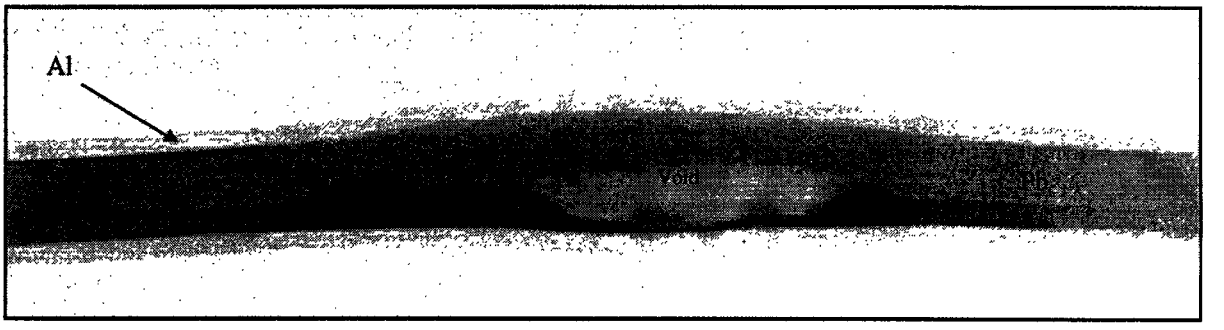

Fig. 11: Neutron radiography of a plastically deformed aluminium tube with a thin copper layer of about 20 μm which is filled with lead.

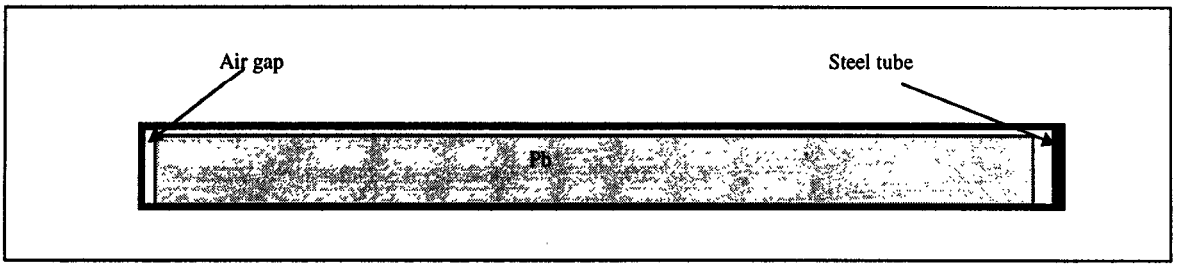

Fig. 12: Schematic outline of the target rod.

ICANS-XIV
14th Meeting of the International Collaboration on Advanced Neutron Sources
Starved Rock Lodge, Utica Ill., USA

Lessons learned from the First 500 mAh of Beam on SINQ

H. Heyck, B. Amrein, G.S. Bauer, K. Geissmann

Paul Scherrer Institut, CH-5232 Villigen-PSI, Switzerland

Abstract
First operational experience was gained at the PSI's spallation neutron source SINQ after commissioning in the end of 1996 and almost a half year of routine operation in 1997. The radiological consequences of a water cooled target could be investigated, allowing to develop measures to improve health physics conditions.

The irradiated first day target was successfully replaced by a new target with test rods for various target materials with higher neutron yield. The target storage facility and the target handling equipment was put in operation after test runs and improvements of the handling concepts.

1. Introduction

The spallation neutron source SINQ [1], [2] replaced the swimming pool reactor SAPHIR, which had provided neutrons for the Swiss and international users communities from 1957 to 1994. SINQ was connected to the proton beam line of PSI's accelerator in 1996 [3]. The accelerator has been in operation and under continuous development since 1972. An important improvement of SINQ over SAPHIR is its cold moderator of liquid D_2 in a vessel of 25 litres volume near the target in the D_2O reflector, which is viewed by a system of supermirror coated neutron guides. Data on the performance of SINQ can be found in ref. [4]. The deposition of radiation energy in the liquid D_2, allows SINQ to be run only with the cold neutron source in operation.

After commissioning and testing in the first half of the year, SINQ's first routine operational phase was from July 1 to the end of November 1997. During this period, neutron production was mainly determined by the users' demand for commissioning their instruments. It resulted in a total of 500 mAh of protons on the target.

The normal weekly operational schedule allowed about 56 hours of production of cold and thermal neutrons for various experiments. Operation time of SINQ was limited by the shut down time for accelerator maintenance problems that had arisen with a beam splitter further upstream in the proton beam, supplying PSI's cancer therapy facility with protons. This made it necessary to run low current on the accelerator to secure reliable beam delivery when this facility was used. The splitter region was completely rebuilt in 1998 and should no work with lower losses. Another

Keywords: SINQ-operational experience, Coolant activation, Change of target

limitation was the availability of operating personnel, because the control system was not yet working . Availability and regulatory restrictions did not allow unmanned operation.

Figure 1 shows the monthly integral proton current on SINQ, giving both, the scheduled and the achieved values for 1997. After the end of the major shutdown of the accelerator during the first half of 1998, also SINQ's systems will have been improved and the neutron source will be available for an extensive user programme in July 1998.

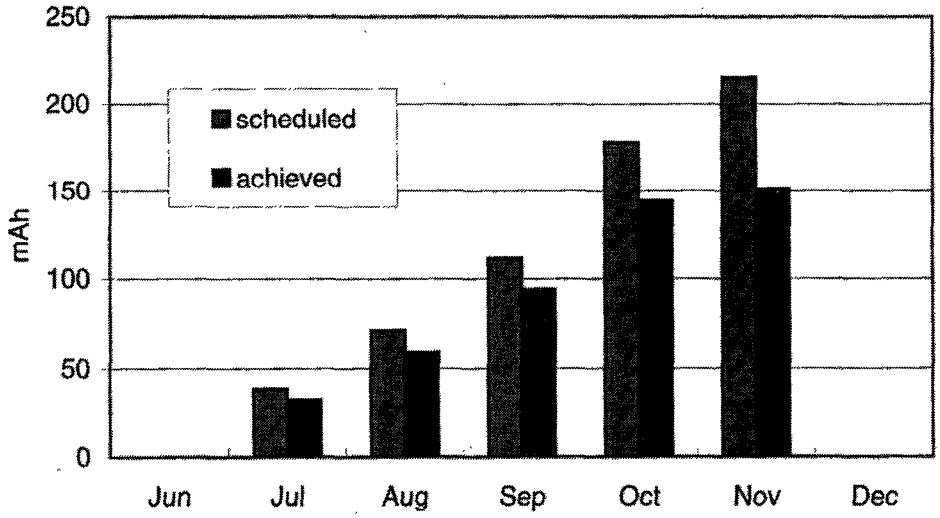

Figure 1: Integral proton current on SINQ, scheduled and achieved in the second half of 1997

2. Operational conditions of SINQ's cooling systems

The start up target is made of solid rods of Zircaloy, because of its low neutron absorption and the experience existing with this material from reactor uses. Zircaloy has, however, a relatively low neutron yield, compared to a PbBi eutectic liquid target, for which SINQ was originally conceived, but due to its low absorption, a similar neutron flux was expected as for W or Ta in SINQ [5]

The heat generated by the radiation in the target, in the target hull (window) and in the moderator is removed by separate D_2O cooling systems. The water jacket of the moderator tank and the various cooling devices of shieldings and enclosure systems in the target block are H_2O-cooled.

The most severe consequence of operating SINQ with the present solid state target is the activation of the water in the target cooling system by high energy protons and neutrons. This activation cannot be avoided with the concept of a water cooled solid target and would require a liquid metal target to improve. Anyhow the activation of the moderator and the target hull cooling water is independent from the target cooling concept.

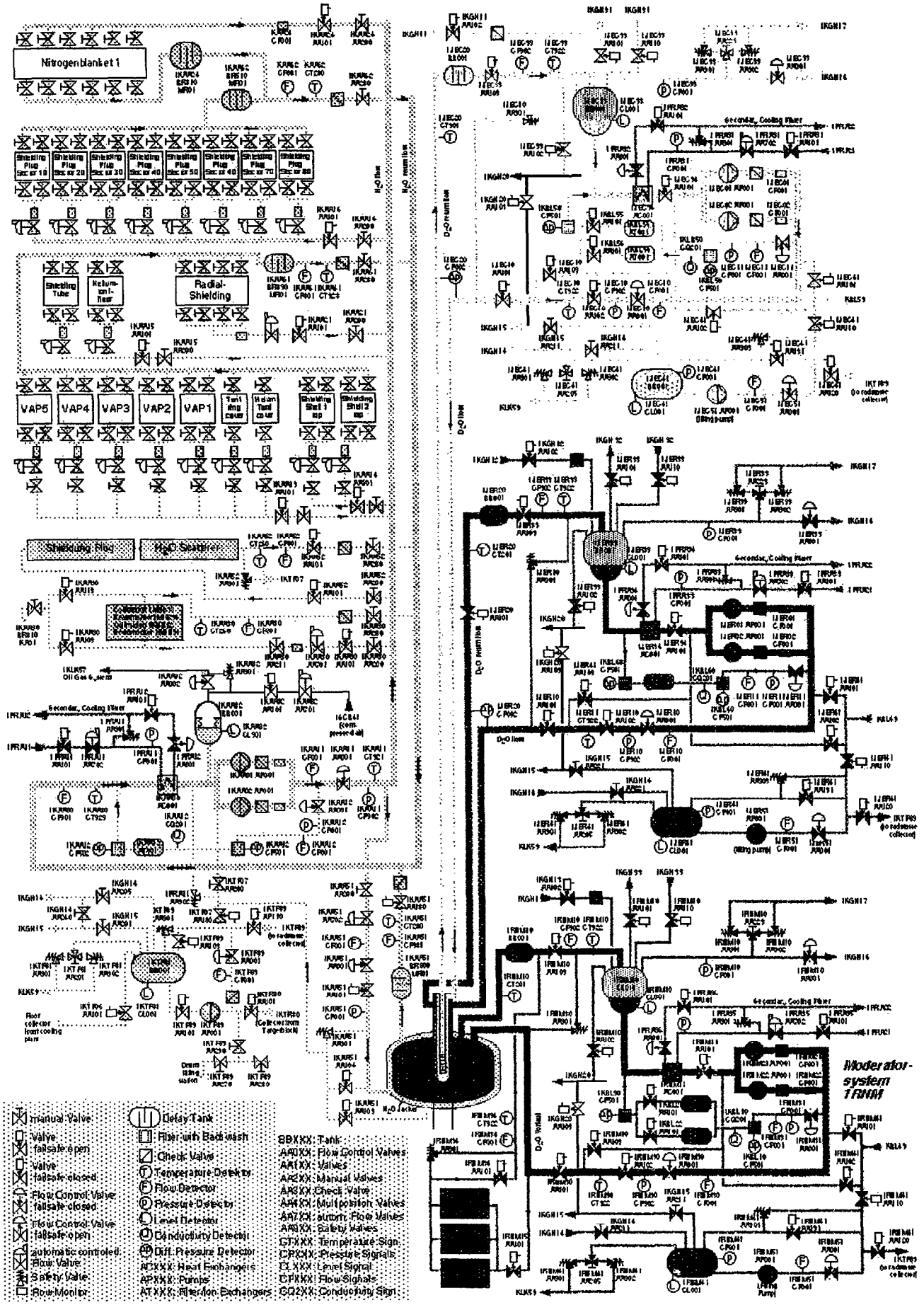

Figure 2: Overview over SINQ's cooling systems

The main characteristics of these cooling loops are given in Table 1 and a schematic diagram of the four loops is shown in Fig. 2.

Table 1: Characteristics of cooling circuits at SINQ

Cooling system / Parameter	Target	Target hull	Moderator	Shielding
Medium	D_2O	D_2O	D_2O	H_2O
Forward flow temperature(°C)	40	40	40	40
Return flow temperature (°C)	55	44	49	46
Forward flow pressure (bar_{abs})	7-11	7-11	3.5	4
Return flow pressure (bar_{abs})	5	5	2	2
Mass flow (kg/sec)	10-15	2	2.9	8.4
clean up bypass (kg/sec)	0.4	0.08	0.55	0.28
coolant volume (litres)	3400	460	5710	2480
Nominal power rating (kW)	650	35	111	210

During operation with full proton beam current of about 0,9 mA, the activation of the cooling water and moderator results in an average dose rate of about 1 Sv/h (100 Rad/h) in the rooms of the cooling plant. This radiation makes the rooms inaccessible during operation with beam on target and several hours after shut down and requires radiation hard materials to be used throughout the loops.

A typical time history of the dose rate in a representative position inside the cooling plant is shown in Fig. 3. An accelerator shut down of about one hour occurred before noon, and caused the drop in the curve of the dose rate history. The main activities, which cause the high radiation level during operation, are only short lived isotopes like C-11, O-15, N-13, N-11 and reach saturation after a short time. Their fast decay after shut down allows to enter the rooms of the cooling plant after a few hours. During the first periods of running this became necessary in order to take water samples from the different cooling circuits, especially from the target cooling system.

Whereas the continuous build up of Tritium, being α β^--emitter, does not contribute to the dose rate, Beryllium-7 with its half life of 53 days accounts for most of the residual radiation level in the cooling plant when it is not operated.

Beryllium-7 is a spallation product of oxygen in water and plates out on the walls of components like pipes and especially in heat exchangers, due to their large surface and temperature gradient. The bypass flow through the clean up systems is not sufficient to hold back the majority of the Be-7 before it plates out.

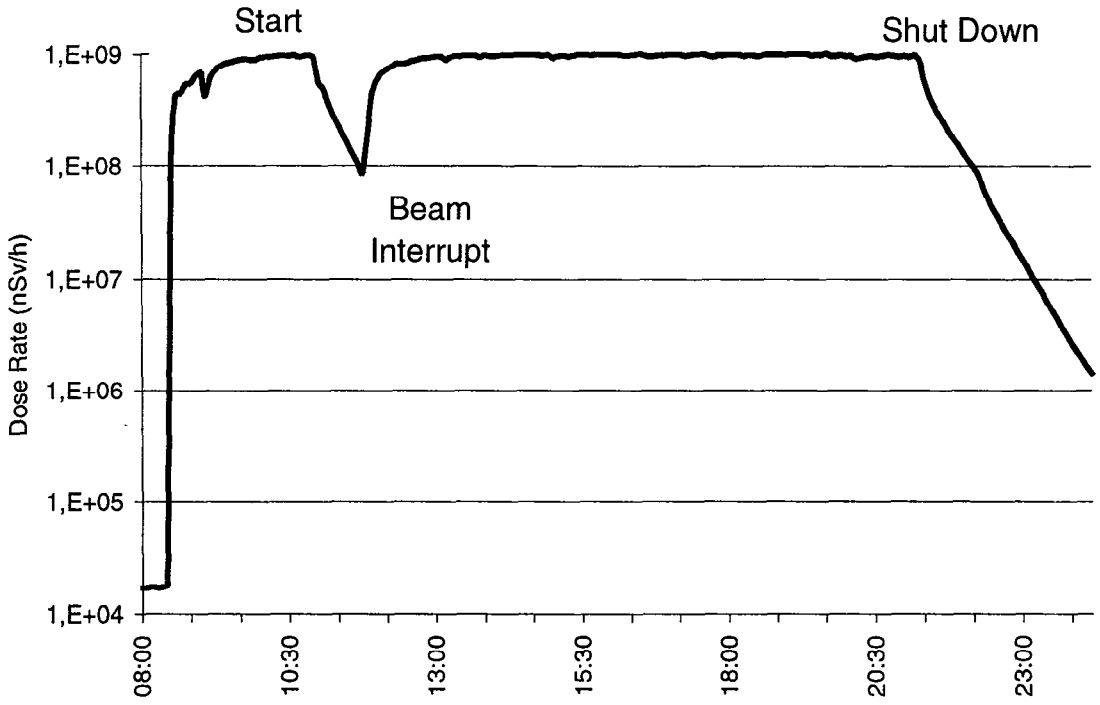

Figure 3: Dose rate in the cooling facility during two shifts of operation of SINQ

The residual activity, dominated by Be-7, increases continuously, due to the build up of activity with significantly longer half lives until saturation of these activities is reached. Such isotopes were measured in water samples from the four systems. Some typical isotopes are shown in Table 1.

Table 2: Long lived activities in the SINQ cooling loops after the end of the 1997 irradiation period. These values represent the situation in the water five days after the end of the irradiation. While showing the relative values for the loops, they do not allow to derive the true production rates for Be-7, because most of it had already plated out on the walls.

	Cooling system	**Target**	**Target hull**	**Moderator**	**Shielding**
Parameter					
Medium		D_2O	D_2O	D_2O	H_2O
Istope	**Half Life**				
3-H	12,35 a	140 MBq/kg	30 MBq/kg	2910 MBq/kg	10 MBq/kg
7-Be	53 d	1500 kBq/kg	30 kBq/kg	320 kBq/kg	60 kBq/kg
22-Na	2.6 a	50 kBq/kg			

Two days after the last operation period, the average dose rate in the cooling system room was 50 µSv/h. A maximum of 3,3 mSv/h was measured on the surface of the heat exchanger of the target cooling system. This heat exchanger will now be shielded as a measure to reduce the dose rate in the room, when SINQ is not in operation.

After a cool down period of half a year with the water clean up systems in operation, the cooling systems were emptied into their dump tanks. Almost no activity was found in the dumped water, except for the Tritium. A increase of the dose rate level was registered in the rooms of the cooling plant after draining the water, because the Be-7 plated out in pipes and heat exchangers was not shielded any more by the water in these components (Fig. 4).

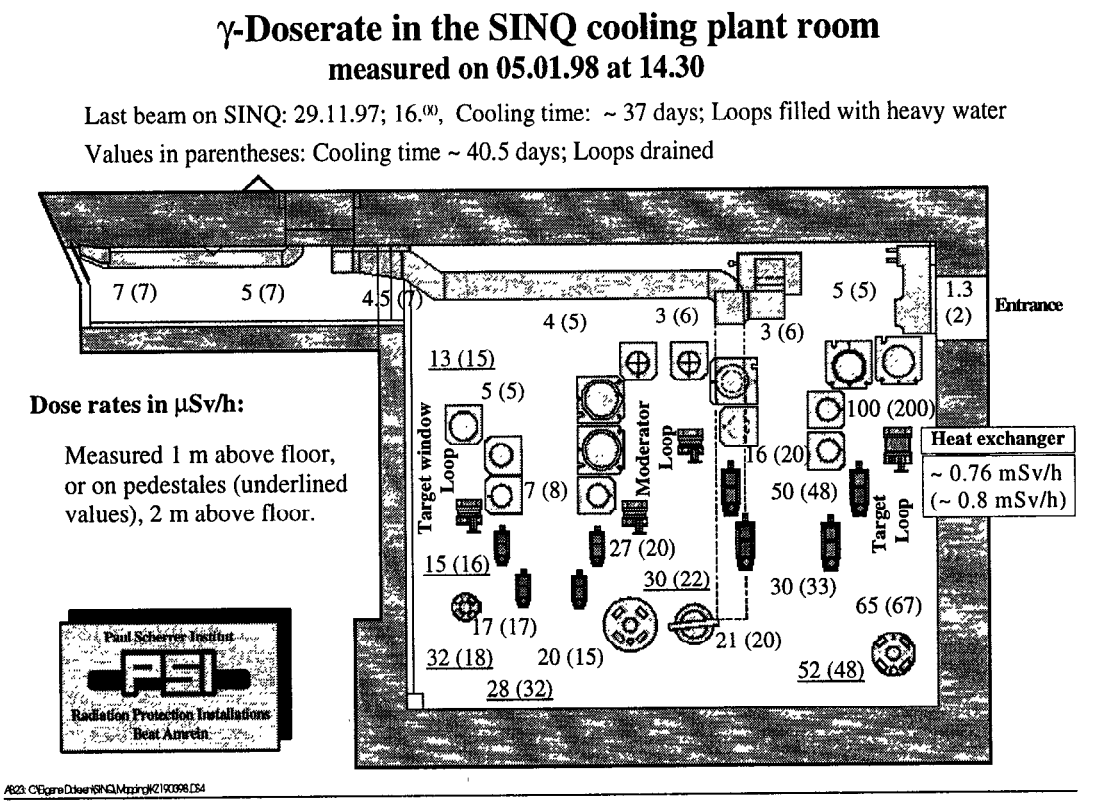

Figure 4: Dose rate levels measured at various points of the SINQ-cooling plant room nearly 1000 hours after SINQ had been shut down for the 1998 maintenance period before and after (in parentheses) draining the cooling loops.

It can be estimated that the equilibrium dose rate from Be-7 in the cooling plant room of SINQ will be about 10 times higher than those given in Fig. 4. Because of the expected increase of the residual dose rate, a sample taking system will be installed, which allows to take water samples from the target cooling loop during operation. This is important for the surveillance of the target integrity since almost no other indicator exists for a degradation of the target.

3. Exchange of the target

The first solid Zircaloy target used has been exposed to a total of 500 mAh of beam only, but was removed for inspection and examination during the next operation period in order to check for any radiation damage on target material and target window as part of the SINQ target development programmes [5].

The new target is basically of the same design as the previous one, but incorporates temperature measurements in selected Zircaloy rods and several test rods for the development of the next target with higher neutron yield but based on the same general design as of the present target type [6].

The target exchange flask design is derived from a refueling machine of a reactor. Since its shielding should be adequate for solid and liquid targets alike, the strongest shielding is in the bottom region at the level of the target material of a solid target. The top end of the flask has a connector to the 60 ton payload crane of the SINQ-target hall.

After drying the target insert and removing the upper shielding from the target block, the piping was disconnected from the top flange of the target insert and was plugged. During this phase a temporary lid with rubber lips closes the gap between the flask and the opening of the target head room. By extracting the air from the target head room into the ventilation system of the target block, an effective air lock was established.

With the ventilation system in target exchange mode, the adapter to the target exchange flask was installed and the flask was docked on to the target head. The 4,5 meter long target insert was then pulled into its transport jacket inside the flask with the flask's own hoist. With the shielding gate at the bottom end closed, the flask was lifted to the target storage pit in the target hall.

After docking the flask onto an adapter on top of the storage position, the shielding gate could be opened and the target was lowered into its storage pipe. An air lock is established by a hose, extracting air from the inside of the adapter into the radioactive offgas system.

The sealed storage position was filled with inert gas at a pressure lower than atmosphere, allowing surveillance of the enclosure. Furthermore, temperatures and humidity inside the enclosure are continuously monitored.

The spent target will be transferred with the target exchange flask from the storage pit into a hot cell for dismantling during the next operation period. Whereas the shielding plug of the target insert can be reused, the target will be prepared for final storage after removal of some of its rods for post irradiation examination. To this end the target will be placed in a steel container and embedded in molten lead-bismuth, which, after solidification, provides safe enclosure for final storage.

Samples from the Zircaloy rods of the target and the target hull material will be taken to the hot lab for investigation.

4. Conclusions

The experience from the first five month of SINQ operation confirmed the validity of the design and operation concept. Improvements will be made by installing a water sampling system and some additional shielding in the cooling plant room.

Filters and ion exchangers will be modified in the next shut down period for better efficiency. The fractions of the ion exchange resins will be increased to lower the pH value. A coarser filter mesh will be used to increase the bypass flow through the purification system.

The implementation of a new PC-based process control system is now complete and will allow unmanned routine operation 24 hours per day with an operator on duty for day time service and checks only. The new control system will allow remote monitoring and surveillance by a service engineer, which is on call 24 hours a day.

With these measures in effect, SINQ's availability will hopefully be, , determined exclusively by the availability of the accelerator. The anticipated running time is about 5000 hours/year.

5. References

[1] W.E. Fischer for the project team "SINQ - The Spallation Neutron Source, a new Research facility at PSI", Application of Accelerators in Research and Industry, J.L. Duggan and I.L. Morgan, eds. AIP Press, New York (1997) pp 1119-1122

[2] G.S. Bauer "Medium Power Spallation Neutron Sources for Research Applications" Proc Int Conf on Neutrons and Their Applications; SPIE Vol. 2339 pp 156-169

[3] G.S. Bauer, W.E. Fischer, U. Rohrer, U. Schryber "Commissioning of the 1 MW Spallation Neutron Source SINQ" PAC'97 Vancouver 12.-16.05 1997

[4] W. Wagner, G.S. Bauer, J. Duppich, S. Janssen, E. Lehmann, M. Lüthy and H. Spitzer "Flux Measurements at the New Swiss Spallation Neutron Source SINQ" J. Neutron Research, Vol 6, pp. 249-278 (1998)

[5] F. Atchison "The Neutronic Performance of Solid-Target Alternatives for SINQ" Proceedings of the 11th Meeting of International Collaboration on Advanced Neutron Sources ICANS XI, Tsukuba 22.-26.10 1990.

[6] G. Heidenreich and G.S. Bauer "The PSI-SINQ Target Development Programme"; in PSI-Proceedings 92-03 (1992) p. C1

[7] G. Bauer, Y. Dai and L. Ni "Experience and research on Target and Structural Materials at PSI" International Workshop on JHF Science (JHF98), Tsukuba, Japan, March 4-7, 1998

ICANS-XIV
14th Meeting of the International Collaboration on Advanced Neutron Sources
Starved Rock Lodge, Utica Ill., USA
June 14-19, 1998

Measurements of Heat Transfer at the Beam Window in a Mockup Target for SINQ Using Mercury

I. Platnieks[a], G.S. Bauer[b], O. Lielausis[a] and Y. Takeda[b]

[a]Institute of Physics of the University of Latvia,
[b]Paul Scherrer Institut, Ch-5232 Villigen-PSI, Switzerland

Abstract

Efficient window cooling will be crucial, if a liquid metal target is to be used in the 1 MW spallation source SINQ at some stage, and may have a profound effect on the design of the whole target system. In order to study the wall-to-liquid heat transfer, a Heat Emitting Temperature Sensing Surface (HETSS) was developed and used to measure the temperature difference between the fluid and the wall under different geometric and flow conditions. Turbulence generated by the expanding flow path at the end of the guide tube was found to be efficient even in a geometrically symmetric situation, while thermal convection only plays a role at very small flow rates. Cutting the bottom edge of the guide tube at an angle did not result in any noticeable improvement. Although the results suggest that a hemispherical beam window might be properly cooled without special measures, more controllable configurations will be examined, too.

1. Introduction

One of the main problems in liquid metal target development for high power spallation neutron sources is cooling the beam entrance window. The temperature will, in general, be too high for direct water cooling; at the very minimum it will require a high pressure water system which not only is a source of additional stress on the walls, but also carries the risk of water ingress into the liquid metal in case a leak develops. It would, therefore be highly desirable to be able to cool the window directly by the liquid metal. In order to evaluate this option, knowledge of the flow structure and of the wall-to-fluid heat transfer coefficient is necessary. Although Computational Fluid Dynamics methods have made great progress in recent years in predicting the situation even in complicated geometries, it is still indispensable to perform certain code validation experiments. For this reason a full scale mockup experiment for the SINQ liquid metal target was installed at the large Mercury loop operated by the Institute of Physics of the Latvian University at Riga. In the present paper we report on measurements that aim at determining the heat transfer in the hemispherical cap of the target under different flow conditions which were examined in parallel by an ultrasonic flow mapping technique [1].

Keywords: Liquid metal target; heat transfer, turbulence, Mercury

2. The SINQ target test stand

A schematic drawing of the SINQ target mockup installed at the Mercury loop in Riga is shown in Fig. 1. The lower half of the SINQ target with a diameter of 20 cm and a height of 1500 cm is reproduced in full, while the upper half, which has a diameter of 40 cm and will contain the heat exchanger etc. is only built with reduced height and is meant essentially to serve as a flow distribution and rectification system. The lower part of the inner guide tube and the hemispherical cap can be exchanged to vary the geometry in the cap region and to perform different kinds of measurements. The Mercury flow rate can be varied up to 3.8 l/sec, which is more than what is considered necessary for removing 1 MW of beam power from the SINQ target. Although the operating temperature of the Mercury loop is lower than that of a PbBi target would be, using Mercury for the tests is considered a good choice because it is technically easier than PbBi and all heavy liquid metals are rather similar in their properties. For the present experiments a specially built cap was used which, on its inside, was equipped with a system of Heat Emitting Temperature Sensing Surfaces (HETSS)

3. The Heat Emitting Temperature Sensing Surface

HETSS is a boundary surface between the solid wall and the liquid which is constructed in a way to allow to generate a well defined heat flux density in a selected area and to record the resulting temperature distribution. Technically this is accomplished by forming the surface as an electrically heated resistor for which it is possible to measure the electrical resistance as well as the power dissipation with spatial resolution. By measuring the voltage drop U and the current I in each HETSS element, the dissipated power can be determined from the product U*I of the two quantities, while their ratio U/I gives the resistance, which is temperature dependent. This makes it possible to record the local temperature average over the area of the HETSS. The surface-resistor must be thin enough to have large heat resistance along their length and must be backed by material with poor heat conductivity in order to direct all the heat into the liquid perpendicularly to wall, i.e. with minimum lateral dissipation.

Depending on whether and in what way U and/or I are controlled, the HETSS can be operated in different modes. Ideally, keeping U*I constant would result in a fixed heat flux density and would allow to determine the heat transfer directly as a function of heat flux density. Alternatively, U/I could be kept constant which would mean constant surface temperature and would allow to determine the heat transfer as a function of temperature. In practice it is, of course, easiest to work with a constant current source, which means that the heat flux will depend on the temperature.

Practically the HETSS is produced as a continuous structure of thin copper strips made by the etching technique. Leads for picking up the voltage drop are arranged at suitable positions, while a controlled current is supplied to a larger area for reasons of practicality. In our case (Fig. 2) an area of 21x4 cm^2 was subdivided into three groups with seven units of 4x1 cm^2 each and a separate current source was used to feed each group. This results in

a measuring mode somewhat in between the two limiting cases given above, because only the current rather than the power is controlled.

As an example, Fig 3 gives the measured resistance in the 21 sectors with and without heat flux and the temperature distribution deduced from the measured change in resistance. From top to bottom Fig 3 shows:
- the resistance per surface unit without heat generation
- the resistance measured with the heat flux distribution shown in the frame below
- the heat flux averaged over the respective surface unit
- the temperature distribution deduced from the measured change in resistance.

It is obvious that very precise resistance measurements are required, but several tests have shown that the method gives trustworthy results.

The quantity to be determined for each HETSS unit is the temperature rise per unit heat flux, h (in K/(W/cm^2)), which is the inverse of the heat transfer coefficient:

$$h = \Delta T_s / q \tag{1}$$

The temperature increase on the surface is calculated as

$$\Delta T_s = k_{af} (\Delta T_{Cu} - q \cdot d_i / \lambda_i), \tag{2}$$

where ΔT_{Cu} is the temperature of the copper foil forming the HETSS, k_{af} is the area factor of copper in the HETSS layout (0.8 in the present case) , d_i is the thickness of insulation between the copper and the mercury (75 µm), λ_i is the heat conductance of the insulation (0.39 W\mK for glass textolite as used).

The heat flux density is calculated as

$$q = Q / S, \tag{3}$$

where Q denotes the electrical power supplied to the HETSS element (≈28 W in the present experiment), S is the area of the HETSS element (4 cm^2).

The copper temperature increase is then obtained as

$$\Delta T_{Cu} = (R - r) / r \cdot \alpha, \tag{4}$$

where R is the electrical resistance of the heated HETSS element at full power, r is the electrical resistance of the same element at the temperature of the incoming fluid , α is the temperature coefficient of resistance for copper (0.0044 1/°K).

Both the values of R and r for each HETSS element n were calculated as the ratio of potential drop to the current in the corresponding section at the respective power loads. This current was obtained by means of measuring the potential difference on an instrumental shunt included in the current path. The shunt coefficient equals $k_m = 0.0075$ V/ A.

$$R_n = (U_n / U_m) \cdot k_m \text{ and } r_n = (u_n / u_m) \cdot k_m \tag{5}$$

with $n = 1....21$, $m = 1....3$.

The electrical resistance r of HETSS element at the temperature of the incoming flow was obtained at the beginning of the experiment by applying an electrical power which causes a negligible temperature increase (0.0015 W/ cm^2). The changes in the incoming flow temperature are taken into account by means of a continuos measurement of the voltage drop on a special copper resistor. This resistor was connected to a stabilized current source and fixed on the outer pipe of the Mockup where the incoming flow temperature can be determined. The ratio of the actual voltage drop on the resistor to that measured at the beginning of the experiment φ_r / φ_{r0} was used in the computer evaluations as a correction coefficient. (The temperature of the incoming flow was in range 18 ± 1 C° during the experiments.)

The heat flux from a single HETSS element is

$$Q_n = U_n \cdot U_m / k_m \tag{6}$$

The final formula for computer calculations is then

$$h_n = k_{af}\left(\frac{\frac{U_n}{U_m} - \frac{u_n \cdot \varphi_r}{u_m \cdot \varphi_{r0}}}{\alpha \frac{u_n \cdot \varphi_r}{u_m \cdot \varphi_{r0}}} - \frac{U_n \cdot U_m \cdot d_i}{S[m^2] \cdot k_m \cdot \lambda_t}\right) / \frac{U_n \cdot U_m}{S[cm^2] \cdot k_m}. \tag{7}$$

Inserting the fixed quantities for the present experiment, we have

$$h_n = 0.8\left(\frac{\frac{U_n}{U_m} - \frac{u_n \cdot \varphi_r}{u_m \cdot \varphi_{r0}}}{0.0044 \frac{u_n \cdot \varphi_r}{u_m \cdot \varphi_{r0}}} - 64.1 \cdot U_n \cdot U_m\right) / 33.3 \cdot U_n \cdot U_m \tag{7a}$$

For the experiments we are reporting on here, the 21 HETSS elements of 4x1 cm^2 surface area each were arranged in the form of a 4 x 21 cm^2 ribbon imbedded in the hemispherical surface of the bottom cap of the SINQ target mockup. Fig. 4 shows the general arrangement. The bottom cap was produced by arranging the HETSS on a hemispherical dome and casting epoxy on their back side for thermal insulation. After removing the mold the epoxy block was placed into a steel pot with a flange that could be mounted to the bottom end of the outer target tube in different angular positions. The outer surface of the HETSS was covered with a thin layer (0.75 µm of glass textolite) for electrical insulation from the Mercury. As shown in Fig. 4, the labeling of these positions was with respect to the Mercury loop, with 0° being in the loop plane and counting clockwise when viewed from the top. Fig. 4 also shows how the HETSS were numbered from 1 to 21.

The electrical connections and the link with the computerized data acquisition system (cf. Fig. 2) are build to have suitable signal levels for the electronics and to avoid high voltages on the HETSS insulation. The simplification of electrical circuit by going from separately controllable power supplies for each HETSS element to the grouping mentioned above creates some non-uniformity of heat flux density distribution which was found not to have exceeded 8%, as can be deduced from Fig 3.

4. Experiments

Since the present measurements form part of a code validation experiment as well as a flow optimization procedure aiming at establishing good cooling conditions for the SINQ liquid metal target window, he same flow geometry and flow rates used in local velocities measurements [1] were used in the test matrix for the HETSS measurements. So far two different geometric arrangements were examined, namely one in which the bottom end of the central guide tube was cut horizontally (referred to as "flat") and one where the tube was cut at an angle (referred to as "slanted"). In both cases the clearance between the guide tube and the hemispherical cap was varied. The "gap width" quoted is the distance between the bottom edge of the guide tube and the hypothetical line of its intersection with the cap (vertical distance). In the case of the slanted cut the average distance, i.e. the distance at half height of the slanted cut is quoted (cf. Fig. 5)

4.1 Guide tube with horizontal bottom edge

For a flat bottom edge of the central guide tube one intuitively expects a stagnant zone and hence a peak in the wall temperature at constant heat flux density near the center of the cap. The fluid is expected to heat up on its way to that zone and, therefore, an increase in wall temperature is expected from both ends of the HETSS ribbon. The latter is actually observed, in particular for small gap widths, as can be seen from Fig. 6, which gives the 50 second time average of the temperature rise in the wall per unit heat flux for different flow configurations (gap widths and flow rates in the loop as defined above). Contrary to intuition, there is no peak in the center of the ribbon. This may be attributed to the combination of two effects: (1) since the ribbon has constant width while the flow channel effectively narrows as the fluid moves down the cap, cold fluid flows over the HETSS from the side and contributes to a lower wall temperature in the measuring geometry than would be obtained in a real axisymmetric configuration and (2) there is not real stagnation of flow at the apex of the cap, at least not when averaged over the area of one HETSS unit and over reasonable amounts of time. While the first effect is an artifact of the present HETSS geometry, the second one may be important in a real situation.

Since the heaters in the HETSS are extremely thin they have practically no thermal inertia. The temporal stability of flow can, therefore, be estimated by using different averaging times. The signals were integrated over nine different time periods between 0.1 and 50 seconds. As can be seen from Fig. 7, where the third dimension in the plots is averaging time, the difference between long and short averaging is more pronounced for high flow rates and large gaps. The instantaneous temperature can exceed the averaged value significantly. In our observations we found up to a factor of two, even though our spatial average is 4 cm^2. In a real situation with a thick wall the fluctuations would probably be significantly smaller due to thermal inertia.

The assumption that cooling in the cap is considerably more efficient than in a stagnant situation is also corroborated by the observed level of temperature increase, which is of the order of 3K or less in all cases. According to calculations, the heat flux density of

$7W/cm^2$ would create about 80K of temperature drop in a stagnant layer of 1 cm of mercury. This was also verified experimentally: In the configuration shown in Fig. 8 the bottom temperature of a 1 cm thick horizontal mercury layer was stabilized by flowing water, while the top surface was heated with 7 W/cm^2. The single HETSS element which was used to generate the power reached a temperature of 76K above the bottom temperature.

The experiments thus confirm that, instead of an axis-symmetrical, two-dimensional flow structure there exists a more complicated one which is more beneficial for cooling the wall. The differences in temperature distribution along the HETSS at short and long averaging times suggest the presence of large scale turbulent perturbations. The expansion of flow cross section after the gap is, of course, a very powerful turbulization mechanism. If the bottom end of the guide tube is below the center of the hemispherical cap, the possibly slightly turbulent flow coming down the ring space between the two tubes passes though a zone of narrowing cross section, which is an effective laminarization mechanism. The thermal boundary layer accumulates heat in this local laminar area and is attacked by turbulence when the laminar jet loses its power. This laminar jet is less pronounced at large gap width, and hence the measured wall temperature is more dominated by the turbulent flow and is, therefore, lower. Also the absence of a central peak at small gap widths is attributed to the effect of turbularization at the edge of the guide tube

Since this turbulent fluctuations prevail on a short time scale and the velocity vector at any position can change sign, the averaged velocity field for such an unsteady flow structure can well show a stagnant area in the central part of the cap. Another possible mechanism which can result in the same cooling effect might be connected with azimuthal velocities in the system. The two configurations are sketched in Fig. 9. Effective cooling of the bottom area could be caused by the vertical vortex which usually arises in center-directed velocity flows (in the bath tub, for example). It is observed in MHD experiments that the axes of such vortices change their positions chaotically. Again, the HETSS strip will be very sensitive to such cooling.

4.2 Guide tube with slanting bottom edge

The purpose of cutting the bottom edge of the inner guide tube at an angle was to destroy the axial symmetry and by this token move any flow stagnation zone away from the apex of the hemispherical cap, where heating would be most intense in the real situation in SINQ.

Examples of our results shown in Fig. 10, which were taken with the HETSS arranged in the plane of the slanted cut (cf. Fig. 5), do not indicate any drastic non-symmetry in the temperature distribution. The narrow gap was at the side of the HETSS units with the low index numbers. Although the two peak structure is not as pronounced as in the case of the flat bottom edge guide tube, no indication of any flow structure improvement by sloping the guide tube end is obvious from these experiments. If any, the temperatures in the cap center seem to be even slightly higher, especially at high flow velocities. The reason

might be the destruction of some favorable flow structure by the asymmetry, because significant azimuthal velocity structures will not be able to develop in this geometry.

4.3 Importance of thermal convection

An alternative explanation to the one given above for the existence of the two peak structure involves the role of thermal convection, assuming that a stagnation zone in the forced flow exists at all times near the bottom of the hemispherical cap. In order to estimate its importance, measurements were carried out at three different heat flux densities, namely 7, 3 and 1 W/cm^2. If thermal convection contributes to the heat removal to any significant extent, varying the heat flux density should destroy the proportionality between temperature and heat flux density. If the wall temperature per unit heat flux is the same at different heat flux densities, thermal convection plays no role even for the highest heat flux. The data reproduced in Fig. 11 show that the normalized temperature distribution is indeed independent of the heat flux density used for the 2 cm gap case and at flow rates of 1.2 l/s and more, where the temperature peaks are most prominent. This shows that the characteristic temperature maxima cannot be explained by thermal convection. It is, however, observable at low flow rates and at large gap widths where the normalized temperature can be seen to decrease with increasing heat flux.

5. Conclusions

The measurements reported here are the first extensive application of the newly developed HETSS technique. The results clearly show that the technique, although so far limited to rather low heat flux, is useful in measuring heat transfer coefficients.

The fairly effective cooling of the cap observed even for the flat bottom edge of the flow guide tube can be explained either by chaotic turbulence or by the development of a vortex that changes its orientation chaotically around the tube axis. Special vorticity measurement techniques could be developed to get better information about the instantaneous flow structure. For this purpose electric potential sensing in locally created magnetic field appears to be suitable.

The peak heat flux density at the SINQ beam window is expected to be about 10 times higher (70 W/cm^2) than the highest value generated by the HETSS. Since the measured normalized temperature jump is in the range of 1.5 - 2 K/(W/cm^2), this would mean that, if scaling is valid, the inner window surface would take on a temperature which is about 100 to 140 K higher than the temperature of the forward flowing liquid metal (ca 180°C). While this would not put the window temperature in a regime that is in any way dangerous for steel, it might be good to have more control over the situation than just rely on chaotic fluctuations. Therefore, a controllable jet will be directed across the beam window area by a special bypass pump in the next stage.

For this investigation we are considering a layout of the HETSS better matched to the real geometric situation and allowing to imitate the real distribution of heat flux in the SINQ beam window. In order to be able to use the existing equipment, the new arrangement is designed such that its units have the same area and the same electrical data as the present ones.

6. References

Y. Takeda, H. Kikura and G.S. Bauer "Measurements of Flow Configurations in a Mockup Target for SINQ", this conference

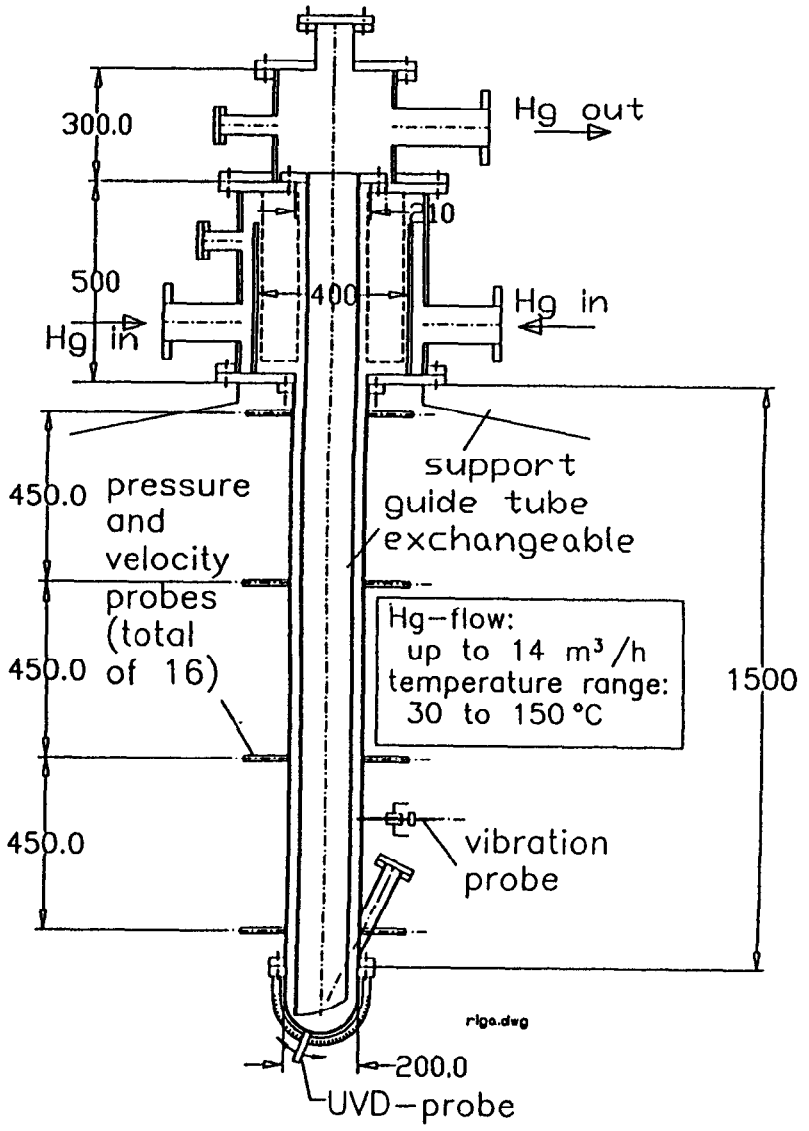

Figure 1: Schematic of the full scale SINQ target mock up installed at the mercury loop of the University of Latvia in Riga. The top half is only simulated with reduced height for flow rectification. The bottom cap and lower part of the guide tube can be exchanged.

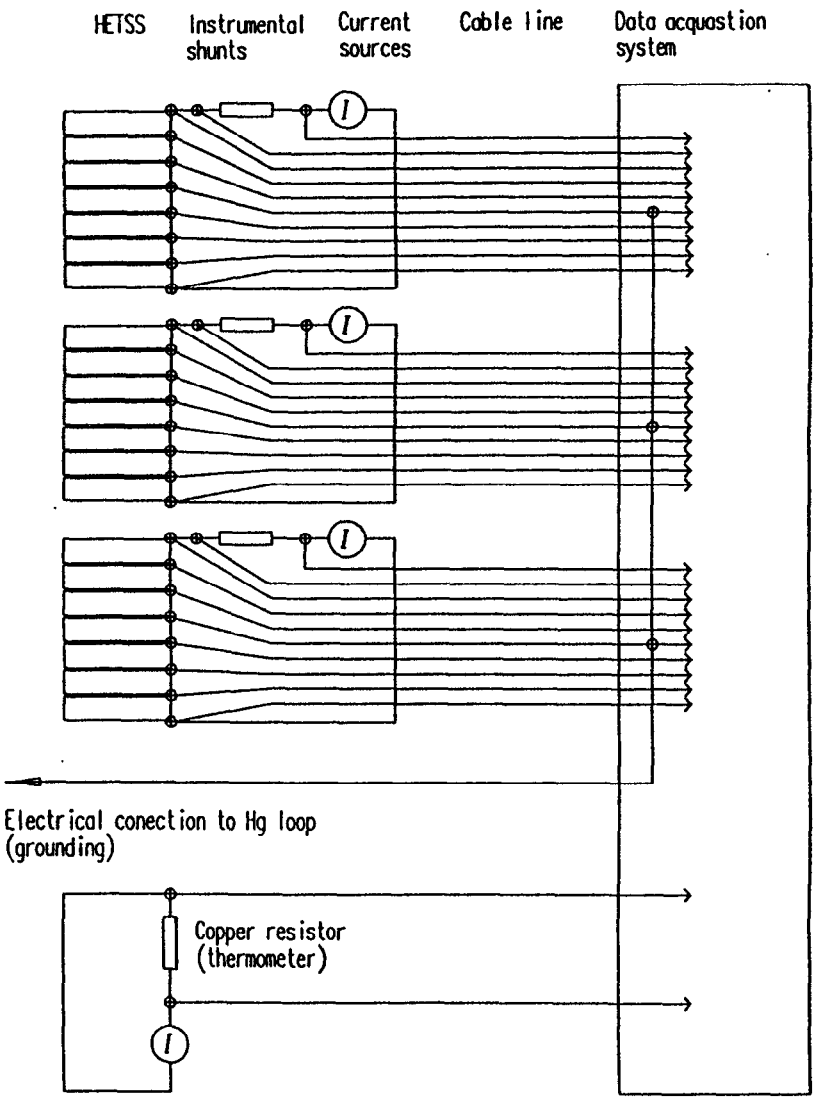

Figure 2: Power supply and voltage measuring scheme of three group of seven HETSS each used in the present experiment.

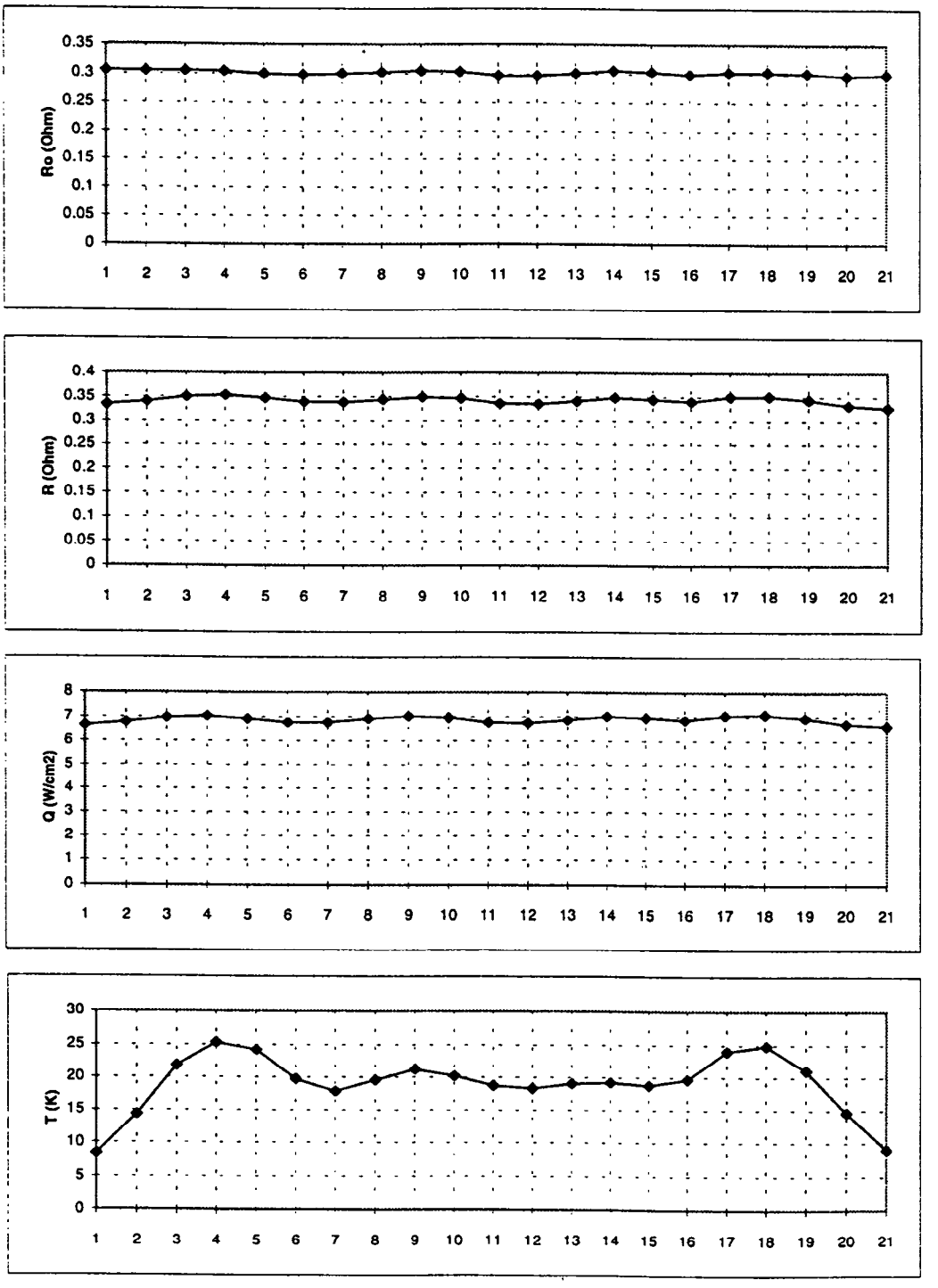

Figure 3: Top to bottom: resistance measured for the 21 HETSS with virtually no heat generation; - resistance measured at the heat flux distribution shown in the frame below; -- - measured heat flux distribution; - temperature above the inflowing fluid deduced for the 21 HETSS from the measured change in resistivity. Gap width was 2cm and flow rate was 0.6 l/sec.

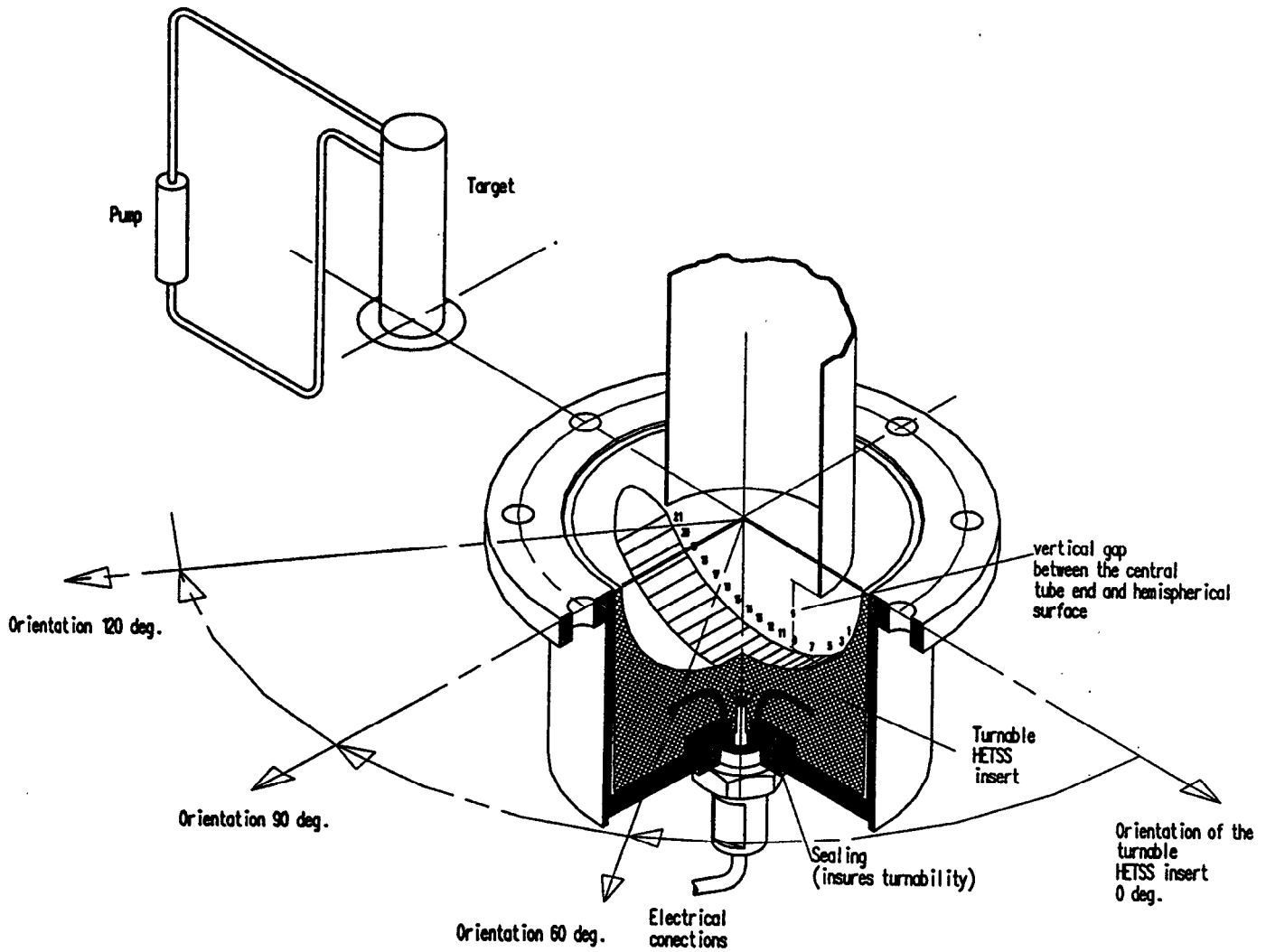

Figure 4: Sectional view of the HETSS-cap used for the heat transfer measurements and nomenclature for the orientation of the HETSS.

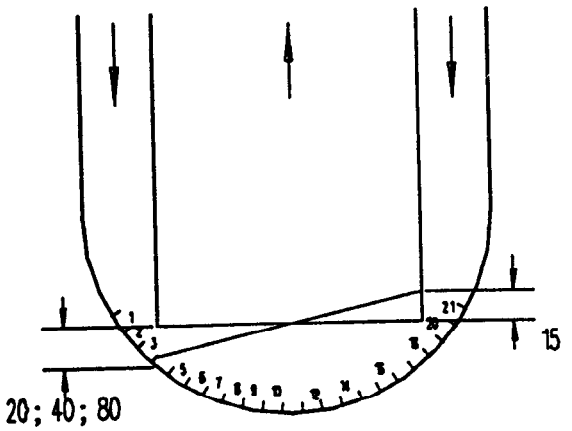

Figure 5: Schematic of the "flat" and "slanted" guide tubes and measure used for the "gap width" in the present experiments.

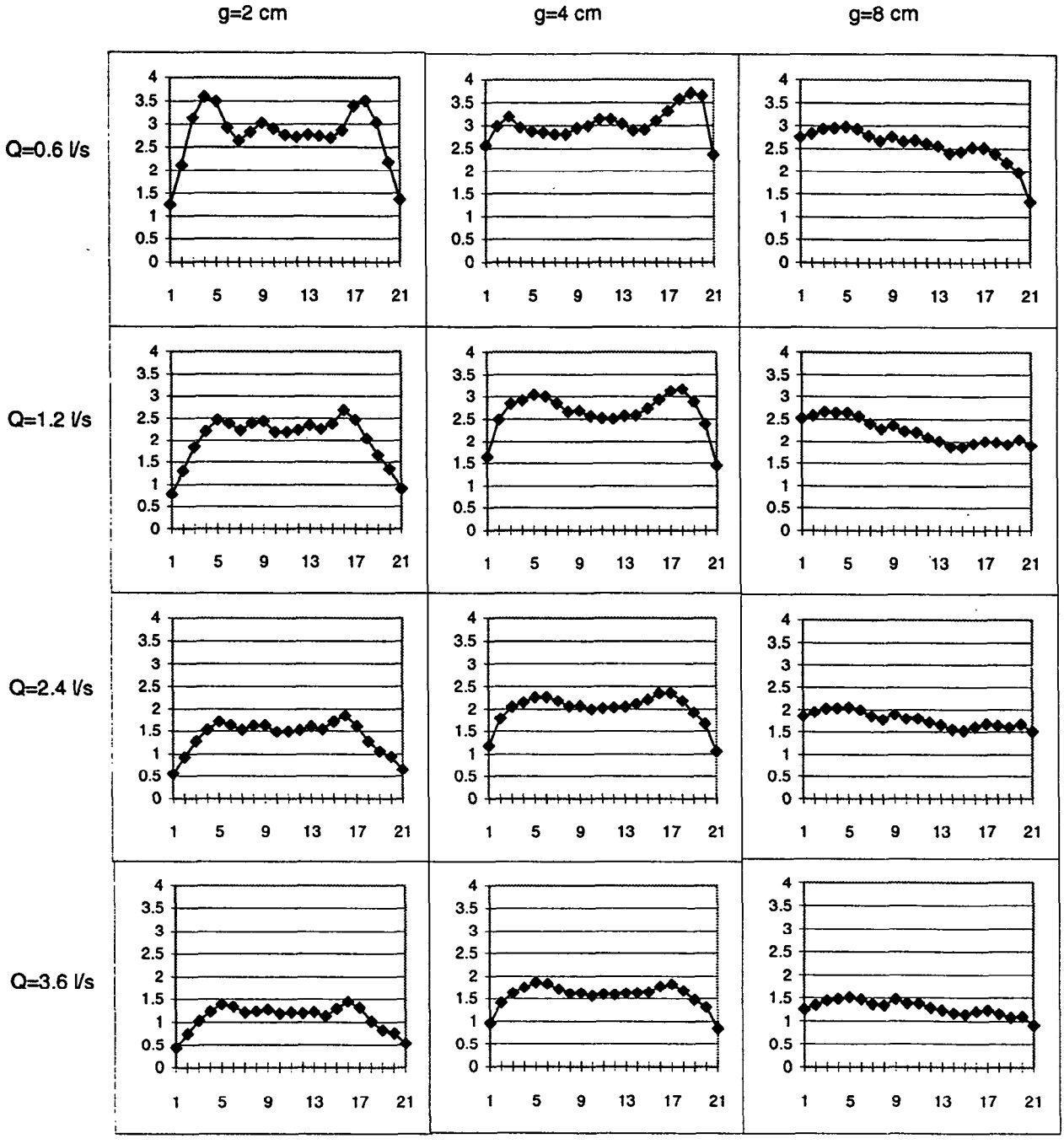

Figure 6: Local normalized temperature, in units of K/(W/cm^2), relative to the inflowing fluid as derived for the 21 HETSS elements at a heat flux density of 7 W/cm^2 for the 0° orientation according to Fig. 4 and for a flat bottom end of the guide tube. Q is the mercury flow rate and g is the gap width. Averaging in the measurement is over 50 seconds.

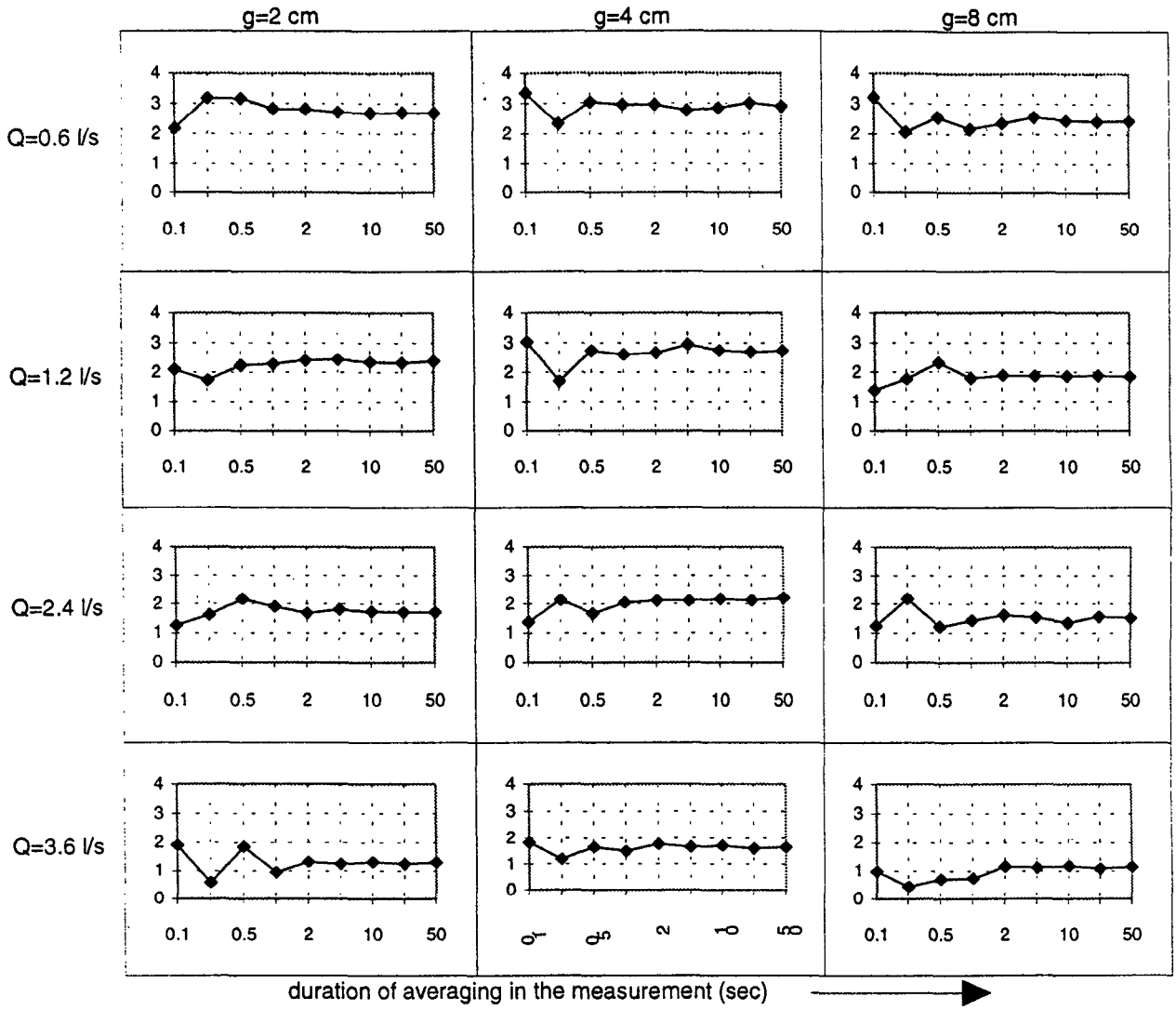

Figure 7: Local thermal temperatures deduced for the HETSS element Nr. 15 for different times of averaging. Measuring conditions are the same as in Fig. 6

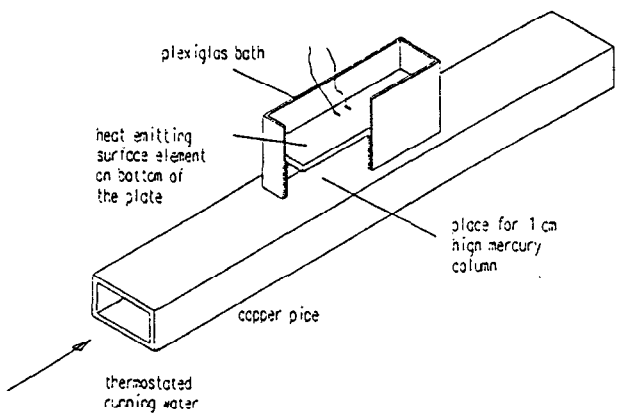

Figure 8: Arrangement used to determine the temperature rise of the HETSS for a stagnant layer of mercury.

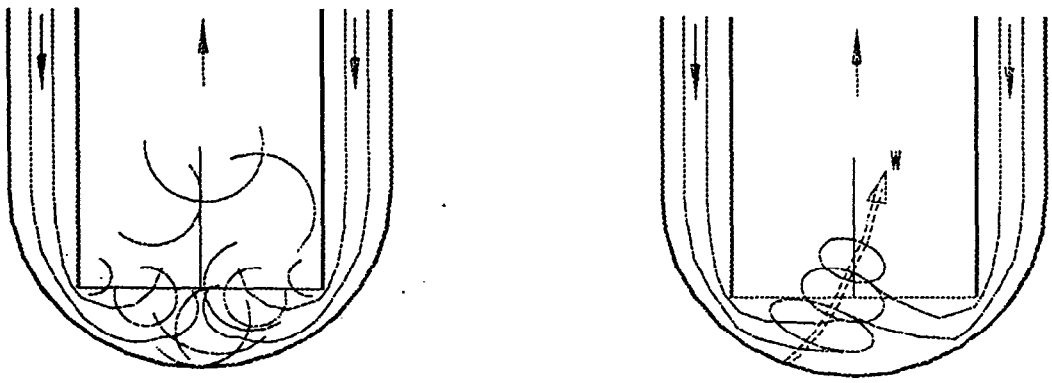

Figure 9: Schematic visualization of chaotic turbulence or vortex flow in the cap, both of which might be responsible for the observed good wall cooling.

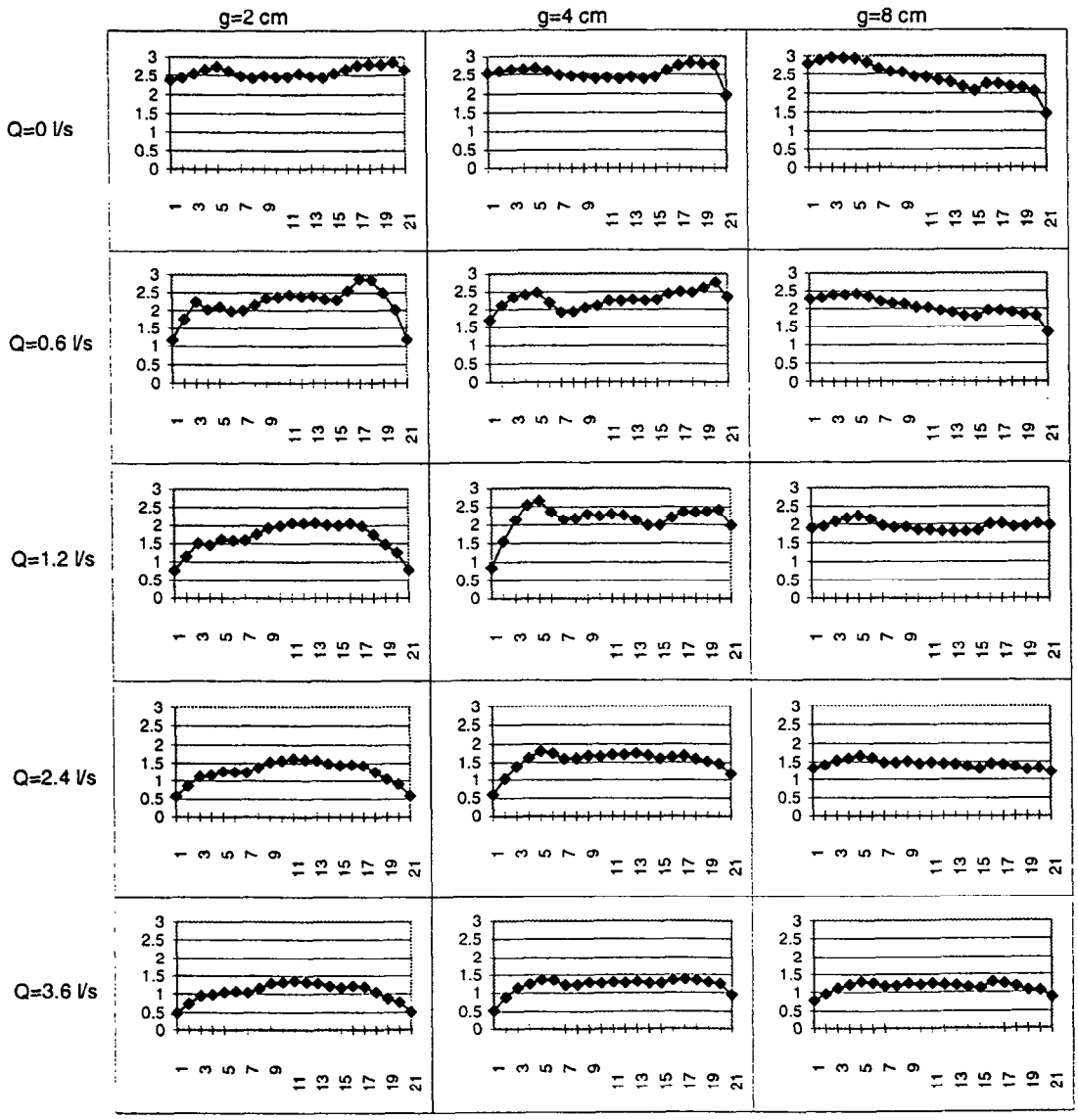

Figure 10: Local temperature distribution per unit heat flux density derived from measured resistance change in the 21 HETSS elements for a slanted cut of the guide tube as shown in Fig. 5a for different flow rates Q and nominal gap widths g.

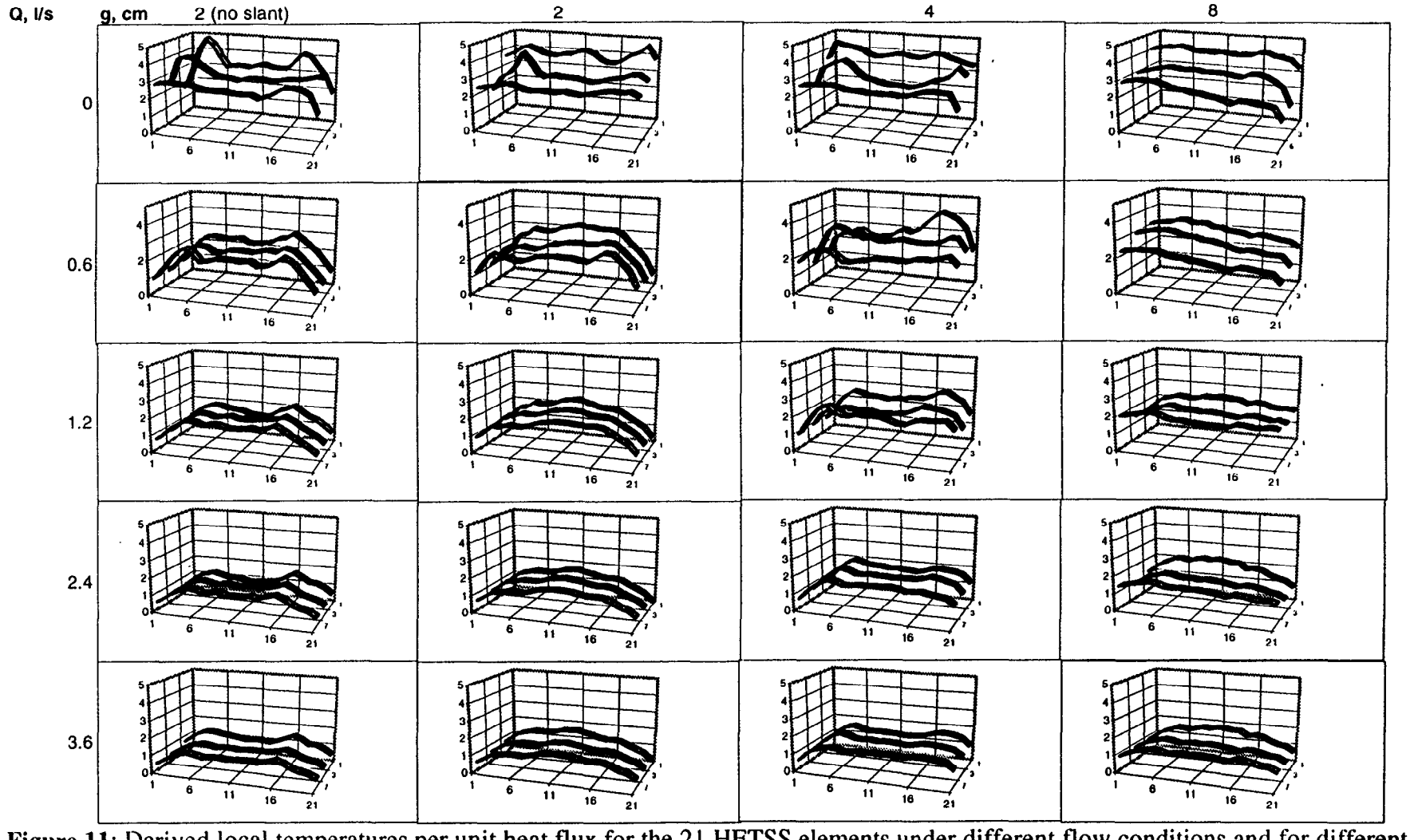

Figure 11: Derived local temperatures per unit heat flux for the 21 HETSS elements under different flow conditions and for different heat flux densities of 1, 3 and 7 W/cm^2 (parameter of the curves in each plot). At high flow rates above 1.2 l/s the temperatures are independent of heat flux density, showing that thermal convection plays no role. The first row of data is for the flat guide tube, the others are for a slanted bottom edge.

ICANS XIV
14th Meeting of the International Collaboration on Advanced Neutron Sources,
Starved Rock Lodge, Utica, Ill, USA
June 14-19, 1998

Heat Transfer and Thermomechanic Analyses on the Test Rods in the SINQ-Target Mark 2

L. Ni and G S. Bauer
Paul Scherrer Institute, CH-5232 Villigen-PSI, Switzerland

Abstract

The thermal and mechanical loads anticipated on the experimental target elements filled with test samples (Zircaloy cladding) or Lead (steel cladding) of the SINQ target Mark 2 were examined by means of a coupled thermomechanical analysis. It could be shown that in no case stress levels are to be expected on the cladding that would be near the engineering limits of the materials in question, in particular if the plasticity of the Lead and the gaps between the test specimens in the experimental rods are accounted for. Also, the temperature levels anticipated in the test specimens are relevant for future practical applications. The validity of using average heat transfer correlations for the water cooled surfaces was demonstrated by a sample calculation using coupled fluid-structure analysis in one case.

1 Introduction

Since December 1996 the continuous spallation neutron source SINQ has been producing neutrons at Paul Scherrer Institute. The first target which is designed for a beam power of 1 MW, was made up of Zircaloy rods and is cooled by heavy water. In order to investigate radiation damage and thermomechanical behaviour of materials under irradiation in a realistic spallation environment, test rods will be put into SINQ-Target Mark 2 [4]. Among them are ten test sample rods containing more than 1500 specimens from different materials enclosed in Zircaloy-2 (Zy) tubes. Furthermore, some test elements relevant for the intended lead filled target (Mark 3) will be induced, as well as four solid steel rods. The test elements are 10.75mm diameter steel tubes, with 0.875mm wall thickness and filled with lead.

The temperature field and resulting mechanical load in the irradiated material is governed by the amount of heat deposited by the proton beam [6]. The thermal stress must be kept at reasonably low level to avoid surface and subsurface cracking of the material and hence a degradation of its performance. A thermal hydraulic analysis with conductive and convective heat transfer and a coupled structure mechanic examination is therefore indispensable.

The present paper describes the temperature and thermal stress analysis on the test rods, including heat transfer coefficient as well as the fluid velocity field through the rod bundle under conditions of a spallation environment. The calculations have been carried out by using the ANSYS-code with finite element method [2]. Special features such as material non-linearity, like plasticity, and contact resistance, have been taken into account.

Keywords: Rod target, Thermal stress, Lead plasticity, Heat transfer, Target cladding

2. Modelling for Coupled Heat Transfer and Thermomechanical Analyses

Fig. 1 shows part of the rod bundle arrangement in the experimental SINQ target. The test rods will be placed along the central axis of the target so that they will be exposed to different proton energies and intensities. According to the calculations by A. Dementyev et. al. [6], most energy will be deposited on the rods at the front of the target where the proton beam enters. So these rods will be examined first. Candidate tube materials for the lead filled rods are stainless steel HT-9, AlMgSi and Zircaloy.

The model used for the calculation is schematically shown in Fig.2. Energy conservation is applied for the steady state thermal conduction and convection calculation. Inside the rod (Fig. 2), the heat transfer process is governed by conduction, so that Fourier's law was used to relate the heat flux vector to the thermal gradient. The deposited power density q was taken from ref. [6] and was used here as an input parameter. On the rod surface, convective cooling by water prevails over the whole surface (with a water temperature T_b=50°C* and a velocity of 0.5m/s of the incoming flow). Therefore Newton's law of cooling was applied to determine the unknown surface temperature T_s.

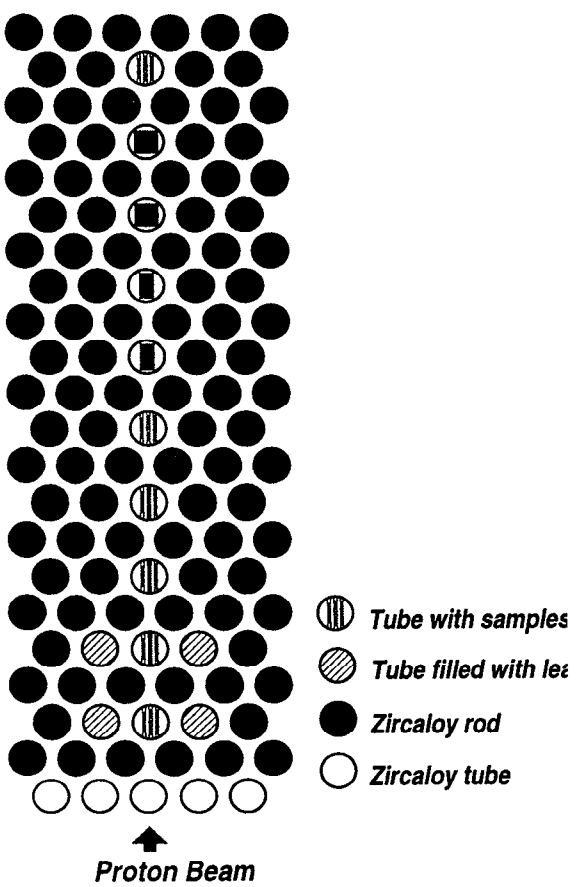

Fig. 1: *Arrangement of test rods in the SINQ Mark 2 (after [4])*

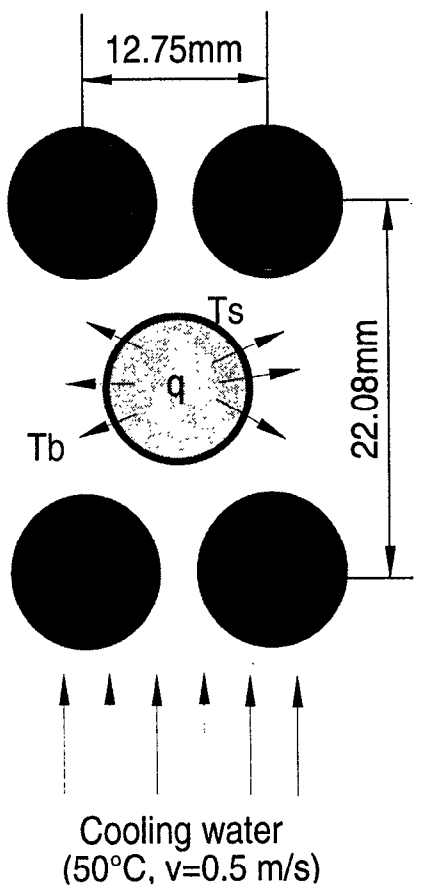

Fig. 2: *Computational model for heat transfer analysis*

* actually 40°C ;10°C safety margin

The average value of the wall heat transfer coefficient is determined from Nusselt and Reynolds number correlations for the staggered rod bundle according to [9]. For detailed studies it is, however, necessary to take into account that the wall heat transfer coefficient changes along the rod surface because of different local flow situations. This can be done by a fluid flow calculation. An example will be discussed in Section 5.

Having obtained the temperature field and the heat flux distribution, a steady state structure analysis could be applied to give detailed information on thermal stresses and deformations. A coupled thermal-structure analysis (Fig. 3) was performed in ANSYS, in which the coupling effects of the structural deformation on the thermal expansion are accounted for. The structural deformation may be plastic, such as in case of lead. Also the heat conduction resistance may have to be considered when the materials are not in perfect contact. Examples are treated in Section 4.

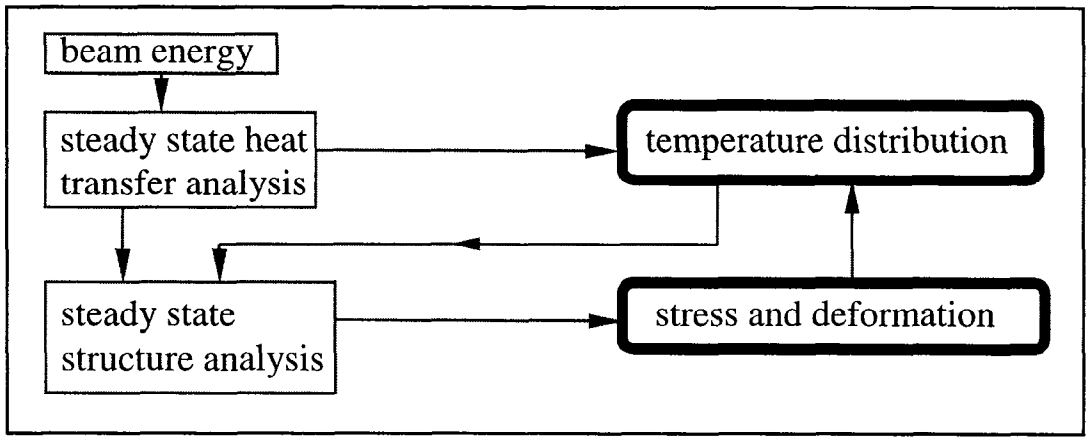

Fig. 3: *Coupled heat transfer and thermomechanic analysis procedure in ANSYS*

3. Thermomechanics of the Lead Filled Test Rods with and without Plasticity

Figure 4 shows the geometry of the test element. The possible maximum power density distribution along the length has been taken from the calculation by A. Dementyev et. al. [6] and is plotted in Fig. 5. The energy deposition over the rod cross-section was considered as uniform, because actual variations are small.

Since lead is quite a soft material, the stress-strain relation is very plastic, especially at high temperatures. Measured stress-strain curves for lead at 4 different temperatures, 22°C, 50°C, 99°C and 150°C, are given in ref [7] (Fig. 6). A plastic module was used in ANSYS, so that plasticity becomes active (i.e., plastic straining occurs) when the stress in the material exceeds its yield stress. Because of the symmetric geometry and power density distribution, only a quasi three-dimensional model was applied.

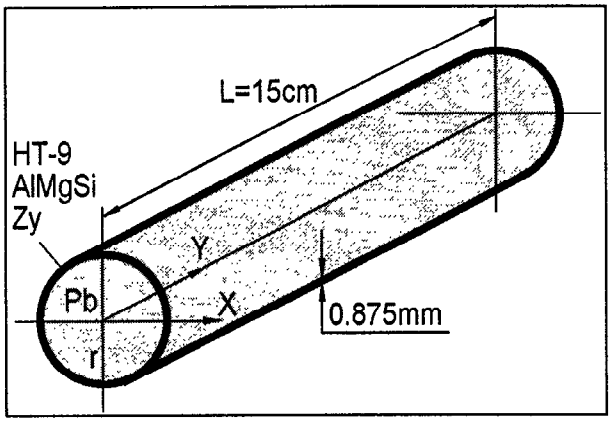

Fig. 4: *Geometry of the test rod*

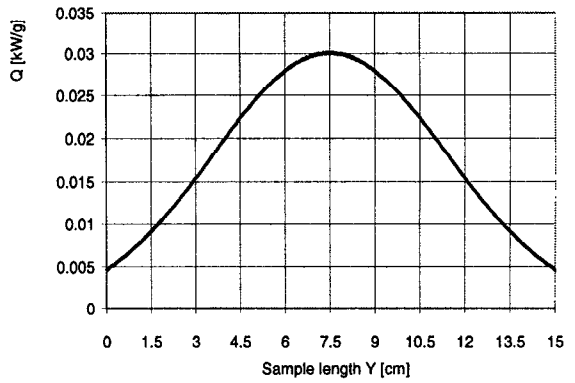

Fig. 5: *Power density distribution along the length of a lead filled rod*

In order to create a case for comparison the plasticity of lead was not taken into account in a first run. Figure "r98.ps46a" shows temperature and stress results on the HT-9 tube filled with lead, in which lead is assumed to be elastic only and both ends of the sample are free. In this picture, window "1" depicts the temperature distribution (TEMP in [°C]) in the rod, and window "2" the "equivalent" von Mises stress (designated as SEQV in [N/m^2]).The scale in horizontal direction, x, is five-fold enlarged to show the details. A maximum temperature of 167°C is found in the rod centre, where the highest energy deposition exists. The maximum von Mises stress of 377 MP appears in the middle part of the steel tube. DMX stands for the maximum total displacement (0.125mm) in the selected co-ordinate system (shown in the figure). Its main contribution comes from the axial component.

When the temperature dependent elastic-plastic stress-strain relations of the lead are taken into account, which is more realistic, the thermal stress decreases considerably due to plastic deformation. This case is presented in Figure "r98.ps46", where the maximum von Mises stress is now only 187 MP while the maximum total displacement, which now occurs at the free end, is increased to 0.557mm.

Results of the calculations for all three tube materials are listed in Table 1. As a general feature, the maximum temperature T_{max} occurs in the rod center, while the maximum von Mises stress $\sigma_{Mis,max}$ and the maximum hoop stress $\sigma_{\theta,max}$ (which is the important quantity for the safety of the target design) are found in the middle section of the tubes. It can be seen that, both HT-9 and Zy cladding result in relatively high temperature levels, while the moderately high stress occurs in the Zy tube. The rod with AlMgSi tube shows the lowest temperature level since AlMgSi has a much better thermal conductivity than the other two materials. With allowance made for plasticity of lead (the case with elastic behaviour only is not relevant in practice), the highest hoop stress is still found for HT-9 but is well below the design limit for this material. It should also be noted that, even when allowing plastic deformation of lead, perfect mechanical contact between the two metals is assumed and no slipping is allowed, which would further reduce the stress. The lowest rod surface temperature $T_{s,min}$ and the maximum total displacement U_{max} are also given in Table 1 for reference.

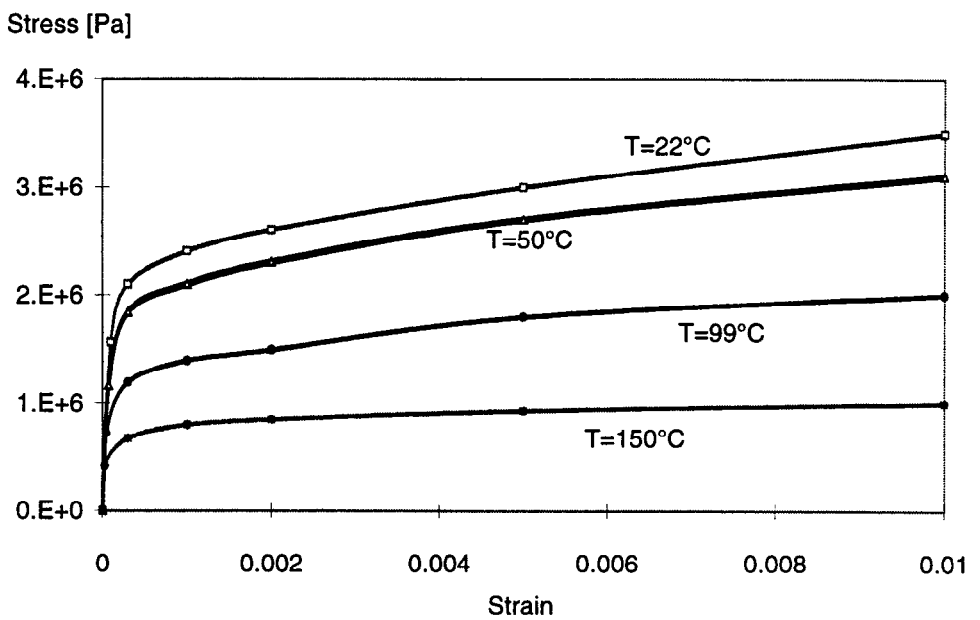

Fig. 6: *Stress-strain relations for lead (after [7])*

The role of the plasticity of lead can also be seen for the case shown in Fig. "r98.ps41b", where the HT-9 tube is not completely filled, leaving a gap of 1.1mm before heating. Because the temperature level (window "1") is highest at the free surface, the deformation shown in window "2" is mainly plastic (USUM stands for total displacement). The gap has narrowed by 0.0819mm. Without allowance of the plasticity the maximum displacement is only 0.0357mm and the stresses are much higher.

Table 1: *Thermomechanics results for test samples filled with lead*

Rod Design	Allowance for plasticity of lead	T_{max} [°C]	$T_{s,min}$ [°C]	$\sigma_{Mis,max}$ [MPa]	$\sigma_{\theta,max}$ [MPa]	U_{max} [mm]
HT-9 tube filled with Pb	no	167.32	59.25	377.	432.	0.125
HT-9 tube filled with Pb	yes	167.17	59.57	187.	215.	0.557
Al tube filled with Pb	no	144.09	59.78	61.9	68.8	0.151
Al tube filled with Pb	yes	144.10	59.78	60.8	70.6	0.136
Zy tube filled with Pb	no	170.23	59.26	237.	269.	0.12
Zy tube filled with Pb	yes	170.14	59.5	157.	185.	0.421

4. Experimental Rod with Perfect and Imperfect Internal Contact

In practice it is impossible to assemble a structure as complicated as our experimental rods without leaving any gaps inside. It is therefore important to examine the effect of such gaps on the temperature and stress levels in the specimens. For the time being only the middle cross-section of the rods where the highest energy deposition occurs has been examined for the ten experimental rods with test samples. A plane strain module was used to show the maximum possible stress. The input power density q [W/m^3] for the specimens inside the rod was again taken from Dementyev et. al. [6]. It is uniform for the same material but the value depends strongly on the heated material and on the position of the rod. We only present results here for the most heated -and hence most critical- rod. In particular we also examine the case where the specimens are imperfect in thermal contact among each other and with the fillers, i.e. interfacial gaps exist between two mating surfaces.

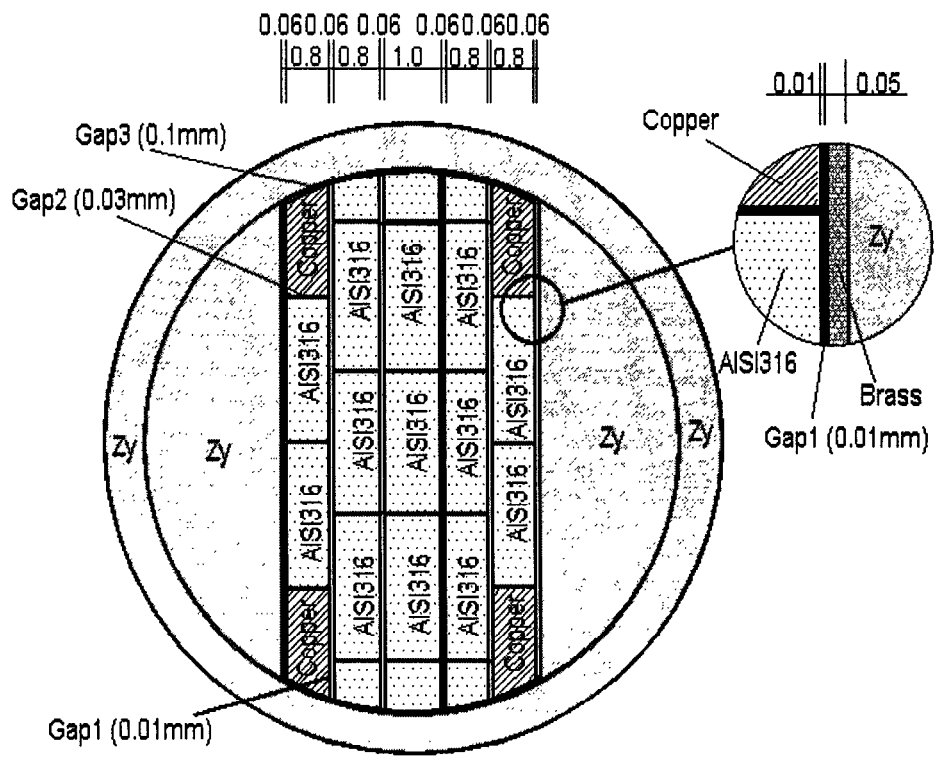

Fig. 7: *Cross-section of the rod with several layers of test specimens*

In Figure 7 the cross-section and the gap distribution of the test sample are displayed schematically. Boundary and water cooling conditions are the same as in Section 3. One quadrant of the cross-section was modelled only, because of symmetry. First the case with perfect contact (i.e. without gaps) was calculated. Figure "r98.ps37" shows distribution of the temperature (TEMP in window "1"), the total displacement (USUM in window "2"), the hoop stress σ_θ (SY in window"3") and the out-of-plane stress σ_z (SZ in window "4"). As can be seen, the maximum temperature T_{max} occurs in the rod centre. Although the maximum out-of-plane stress $\sigma_{z,min}$ runs

high (412MP), it occurs in the innermost material (AISI316) and is of no concern because it is compressive. In this case, both the maximum tensile hoop stress $\sigma_{\theta,max}$ (155MP) and the total displacement U_{max} appear at the top part of the Zy-tube. The maximum values for this case (designated as Nr. 1) are listed in Table 2 in order to compare with the cases of imperfect thermal contact.

Although the thermal stress values are clearly under the irradiation stress limit, it should be noted that this is for a hypothetical gap-free case. In practice such a situation cannot prevail, since it is impossible to mount the tiny specimens in an exact fit because of the manufacturing tolerance. Therefore, thermal contact resistance to heat flow exists between two mating surfaces. This resistance manifests itself in a sudden temperature drop at the interface which must not be ignored.

Thermal contact resistance depends not only on the material properties (such as hardness and conductivity), contact pressure and surface roughnesses, but also mainly on the sizes of interfacial gaps which are usually filled with gas [8]. In our case, the surface irregularities due to machining imperfections can be quite large, so that significant temperature jumps at the interfaces must be anticipated.

In our analysis with interface contact resistance, we assumed an equivalent gap thickness which is constant over the whole contact surface and Helium or air to be present in the interfacial gaps. Conduction in the gas phase was assumed as the dominant mode of heat transfer across the gaps. Observations [8] showed that convective heat transfer can be considered as negligible for gap widths up to a few millimetres. Also radiation was neglected because the temperatures at the both sides of the gaps are not very different. Besides, since the thermal conductivity of a gas is independent of its pressure [1], the conductance of a gas gap is insensitive to decreases in gas pressure until a certain "threshold pressure" is reached when the mean free path of the gas molecules λ becomes comparable in magnitude to the average gap width, which is beyond our consideration for the time being (for Helium: λ = 0.186μm and for air: λ = 0.064μm at atmospheric pressure). Under these circumstances, Fourier's law of heat conduction still applies to the gas layer which can then be treated as a continuum.

In Figure "r98.ps15", the temperature and the von Mises stress for the standard case (No. 3) with Helium in the gaps are plotted in window "1" and window "2", respectively. The maximum temperature in the rod centre rises from 166.7°C (without gap) to 258°C (with the most realistic gap widths: Gap1:Gap2:Gap3 = 10μm : 30μm : 100μm, cf. Fig 7). This temperature rise and the existence of contact resistance result in a higher stress level up to 641MP, which is (once again) compressive and occurs at the rod centre. The maximum hoop stress on the Zy-tube, $\sigma_{\theta,max}$=63.1 MP, is of no concern with respect to the stress design limit.

The temperature distribution along the horizontal radial direction without gaps and with He or air gaps is plotted in Fig. 8. The maximum temperature in the rod with air gaps (case No. 2) rises to almost 600°C because of the low thermal conductivity of air! This results in a very high stress level ($\sigma_{Mis,max}$ = 1690MP, cf. Table 2) which exceeds the allowable limit. From the point of view of heat transfer and cooling, Helium in the gaps is clearly to be preferred to air.

Table 2 lists the results of all calculations for this sample rod with different gap widths. In all cases, the temperature level increases due to gaps and the maximum temperature T_{max} occurs in the rod centre. The maximum von Mises stress $\sigma_{Mis,max}$ as well as the minimum out-of-plane stress $\sigma_{z,min}$ (which is compressive and contributes the main component to $\sigma_{Mis,max}$) also appear in the rod centre. It can also be seen that the rod is very sensitive to the width of "Gap1", since changing it from 5μm (case No. 4) to 20μm (case No. 5), has a strong effect on the temperature jump and therefore on the stress levels. By comparison, changing the width of "Gap 2" (from 10μm in case No. 6 to 50μm in case No. 7) and "Gap3" (from 20μm in case No. 8 to 200μm in case No. 9) makes no big difference on the temperature and stress levels. So we can conclude that it is very important to keep the width of "Gap1" as small as possible.

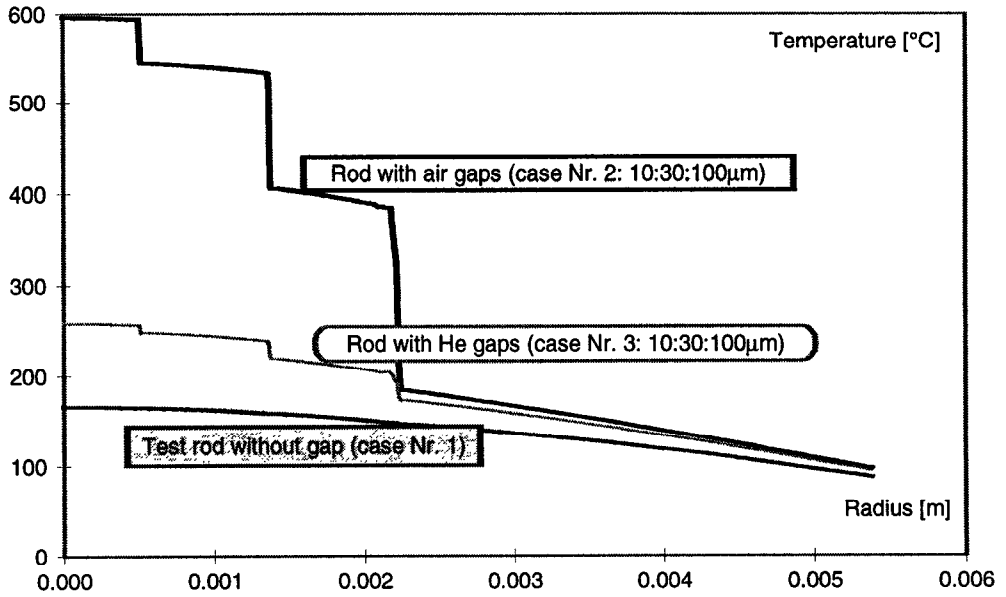

Fig. 8: *Temperature jumps in radial direction with and without gap*

It should be noted that the existence of the gaps affects the temperature and stress levels inside the test specimens but does not pose a risk to the integrity of the surrounding Zircaloy tube. The maximum tensile hoop stress on the Zy-tube $\sigma_{\theta,max}$ (not the maximum value inside the rod) which is also listed in Table 2 is found to decrease upon introduction of the gaps relative to case No. 1 ($\sigma_{\theta,max}$ =155MP). This is because "Gap3" allows the heated specimens inside the rod to expand freely and therefore the induced hoop stress on the tube becomes lower. The maximum total displacement occurs at the rod top (and bottom) where the largest gap width ("Gap3") was assumed. Even for case No. 2 which corresponds to an air filled gap of 100μm before heating, where U_{max} is found to be 56.5μm, the gaps have narrowed but are still not closed, which would improve the heat transfer, of course.

Table 2: *Results for the sample rod with perfect and imperfect interface contact*

Case number	No. 1	No. 2	No. 3	No. 4	No. 5	No. 6	No. 7	No. 8	No. 9
$q_{AISI316}$ [W/m^3]	2.7e8	2.7e8	2.7e8	2.7e8	2.7e8	2.7e8	2.7e8	2.7e8	2.7e8
q_{Zy} [W/m^3]	2.e8	2.e8	2.e8	2.e8	2.e8	2.e8	2.e8	2.e8	2.e8
q_{Brass} [W/m^3]	2.7e8	2.7e8	2.7e8	2.7e8	2.7e8	2.7e8	2.7e8	2.7e8	2.7e8
q_{Copper} [W/m^3]	2.7e8	2.7e8	2.7e8	2.7e8	2.7e8	2.7e8	2.7e8	2.7e8	2.7e8
Gap filling	no gap	Air	He	He	He	He	He	He	He
Gap1 [μm]	0.	10.	10.	5.	20.	10.	10.	10.	10.
Gap2 [μm]	0.	30.	30.	30.	30.	10.	50.	30.	30.
Gap3 [μm]	0.	100.	100	100.	100.	100.	100.	20.	200.
T_{max} [°C]	166.69	596.17	258.01	228.08	313.24	257.65	257.88	230.83	267.63
$T_{s,min}$ [°C]	87.6	70.47	74.34	73.02	76.61	74.51	74.2	85.99	70.25
$\sigma_{Mis,max}$ [MP]	323.	1690.	641.	549.	812.	640.	641.	558.	671.
$\sigma_{\theta,max}$ [MP]	155.	61.7	63.1	58.8	59.4	46.9	51.5	51.9	56.5
$\sigma_{z,min}$ [MP]	-412.	-1690.	-643.	-551.	-814.	-642.	-643.	-559.	-673.
U_{max} [μm]	7.82	56.5	20.9	17.8	26.6	20.8	20.9	15.9	30.6

5 Simulation of the Coolant Flow through the Heated Rod Bundle

While the foregoing calculations were made under the assumption of a constant heat transfer coefficient along the rod surface, the actual local wall heat transfer coefficient depends on the flow pattern around the rod surface. In order to estimate this effect, the flow field around the rods and the local heat transfer were modelled by using the ANSYS submodule FLOTRAN. At the same time, the heat transfer within the rod and the corresponding stress distribution were investigated by means of a coupled ANSYS/ FLOTRAN and ANSYS/MULTIPHSICS analysis. Details of this analysis will be reported elsewhere. Here we only show the main features and the first results of the coupled thermal hydraulic and thermomechanic approach by ways of an example.

Lines in Fig. "r98.p72" show the modelled section of the rod bundle including fluid and non-fluid (solid rods) regions . The incoming flow from bottom was assumed to be uniform (with a velocity of 0.5m/s at a temperature of 50°C) and the exit pressure was set to zero. Periodic boundary conditions were applied on both right and left boundary lines. In the solid rods, the case of lead filled, 0.875mm thick Zy-tubes was considered, and an uniform power density with a maximum value of 280 W/cm^3 was used. Contrary to Section 3, the convective heat transfer around the rod surface is now considered as a function of position.

Figure "r98.p72" gives the velocity and pressure distributions of the flow field around the rods. There is very little temperature rise in the fluid. The left picture of Fig. "r98.p75" (window "1") displays the temperature field in the left half of the central rod. As can be seen, the maximum temperature in the central rod changes marginally to 169°C, (as compared to 167°C in the uniform cooling case, Fig. "r98.ps46"), and it is slightly asymmetric between the upstream (bottom half of the rod) and downstream (top half of the rod) side because of the different local flow status. Hot spots occur at both stagnation points where the temperature reaches a maximum value of 132°C. The difference between the highest and lowest temperature on the surface is 46K (Fig "r98.p75" and Fig. 9).The calculated flow-dependent heat transfer coefficient is shown in Fig. 9, in comparison to the average value obtained from an empirical relation in ref [9].

In order to examine the effect on the stress in the cladding we used the case of no plastic deformation in the lead since we were working in a plane stress model only. As noted before, this results in higher stress levels than expected in reality, but the effect of local variation should be roughly the same. The right picture in Fig. "r98.p75" depicts the von Mises stress in the central rod as calculated, accounting for the local variations of the heat transfer. The comparison with the corresponding results based on the average heat transfer coefficient in window "1" and window "2" of Fig. "r98.p76" shows that the maximum von Mises stress on the tube is slightly higher in the "local" case (319MP), than in "average" case (311MP). These results show that in the present situation the precision of predictions based on the average heat transfer are well within usual engineering safety margins. However, if the safety margin becomes small or the local properties, such as hot spots, are of special interest, a coupled fluid-structure analysis shall be used.

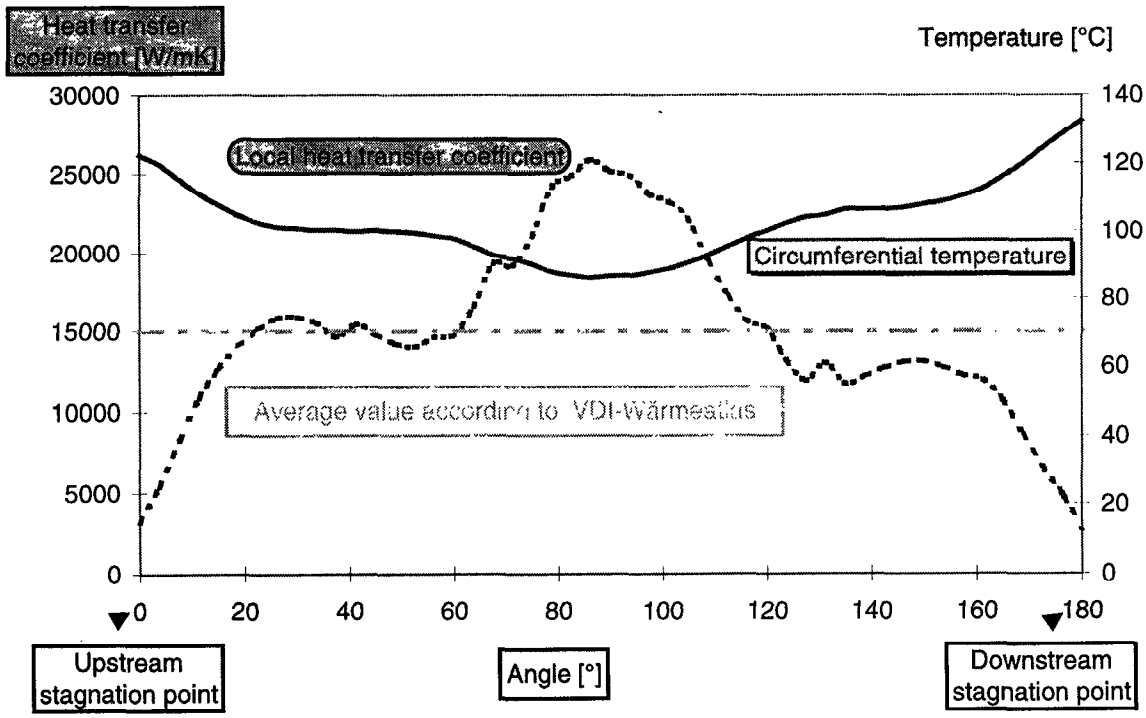

Fig. 9: *Local heat transfer coefficient and temperature distribution along the rod surface*

6. Conclusions

A sample calculation of the coupled fluid-structure analysis based on the local flow pattern, which is time-consuming, demonstrated that this procedure need only be applied if stress safety margins are very small or if the local properties such as hot spots are of special interest.

The coupled heat transfer and thermomechanic analysis, although carried out under the somewhat simplifying assumption of a constant heat transfer coefficient over the rod surface, showed that

- temperature and stress levels in the test samples of the SINQ target Mark 2 are in the range where they would also be anticipated in a real application of the tested materials;
- stress levels on the enclosure tubes (Zircaloy) are not a problem for this material;
- using Helium to fill the gap between test specimens and fillers will lead to significantly lower temperature levels in the specimens than having air in the gaps.
- for the lead filled HT-9 tubes moderate hoop stress levels can be expected if the plasticity of the lead is accounted for and the tubes are not completely filled;

While the cases with and without gap are clearly limiting cases not possible in the real specimen arrays because neighbouring layers will always touch at some points and develop a gap in other regions, it is comforting to see that all cases lead to stress levels within the safe range of application of the materials concerned, especially those used for the enclosure tubes.

References

[1] Aaron, R.L.: "A Theroretical Study of the Thermal Conductance of Joints with Varying Ambient Pressure" MS Thesis, Southern Methodist University, Dallas, 1963

[2] ANSYS Revision 5.3, 1997, Swanson Analysis Systems, Inc.

[3] Bauer, G.S. & Dai, Y., PSI Annual Report 1996/Annex IIIA, p.5.

[4] Bauer, G.S., Dai, Y. and Ni, L.: "Experience and Research on Target and Structural Materials at PSI", The International Workshop on JHF Science (JHF98), High Energy Accelerator Reasearch Organization (KEK), Tsukuba, Japan, March 4-7, 1998.

[5] Dai, Y., PSI Annual Report 1997/Annex IIIA

[6] Dementyev , G.S. Bauer Y. Dai and E. Lehmann: "Neutronic Aspects of the SINQ Mark 2 Target with Irradiation Test Samples" this conference

[7] Kalkhof, D & Kamber, J.: "Zugversuche an Bleiproben als Beitrag für die SINQ-Targetentwicklung", PSI-Dokumentation, TM-49-97-09

[8] Madhusudana, C.V.: "Thermal contact Conductance", Mechanical Engineering Series, New York (etc.), Springer, cop. 1996, ISBN 0-387-94534-2

[9] VDI-Wärmeatlas: "Berechnungsblätter für den Wärmeübergang", Springer-Verlag Berlin Heidelberg, 1997

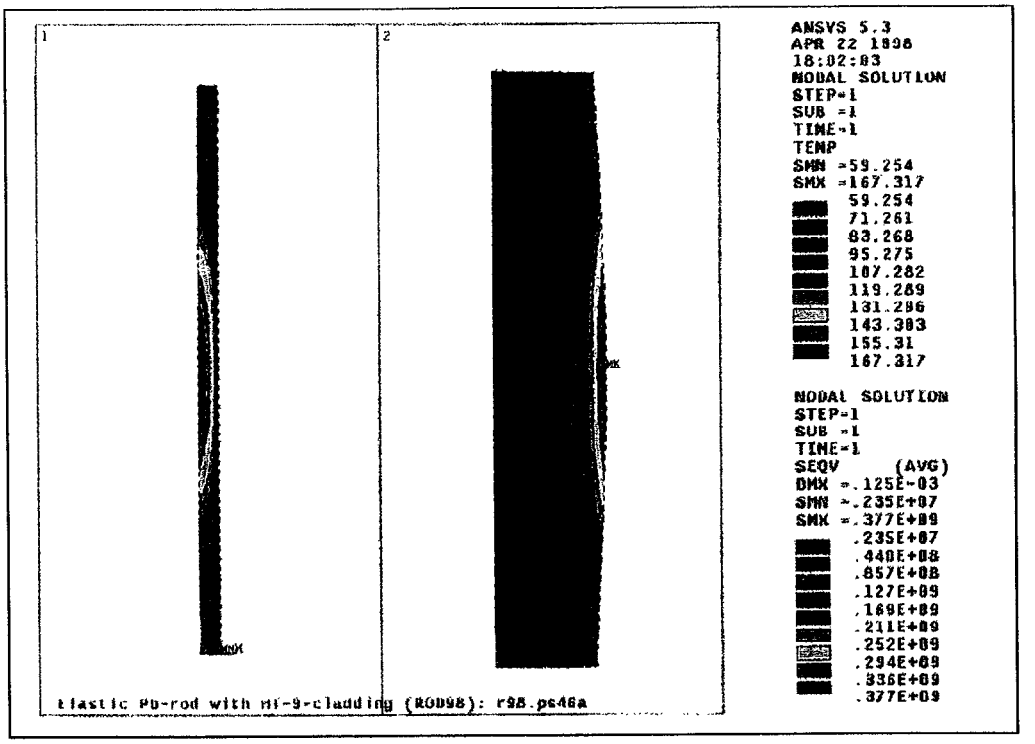
1
2
ANSYS 5.3
APR 22 1998
18:02:03
NODAL SOLUTION
STEP=1
SUB =1
TIME=1
TEMP
SMN =59.254
SMX =167.317
59.254
71.261
83.268
95.275
107.282
119.289
131.296
143.303
155.31
167.317
NODAL SOLUTION
STEP=1
SUB =1
TIME=1
SEQV (AVG)
DMX =.125E-03
SMN =.235E+07
SMX =.377E+09
.235E+07
.440E+08
.857E+08
.127E+09
.169E+09
.211E+09
.252E+09
.294E+09
.336E+09
.377E+09
Elastic Pb-rod with Hf-9-cladding (ROD98): r98.ps46a

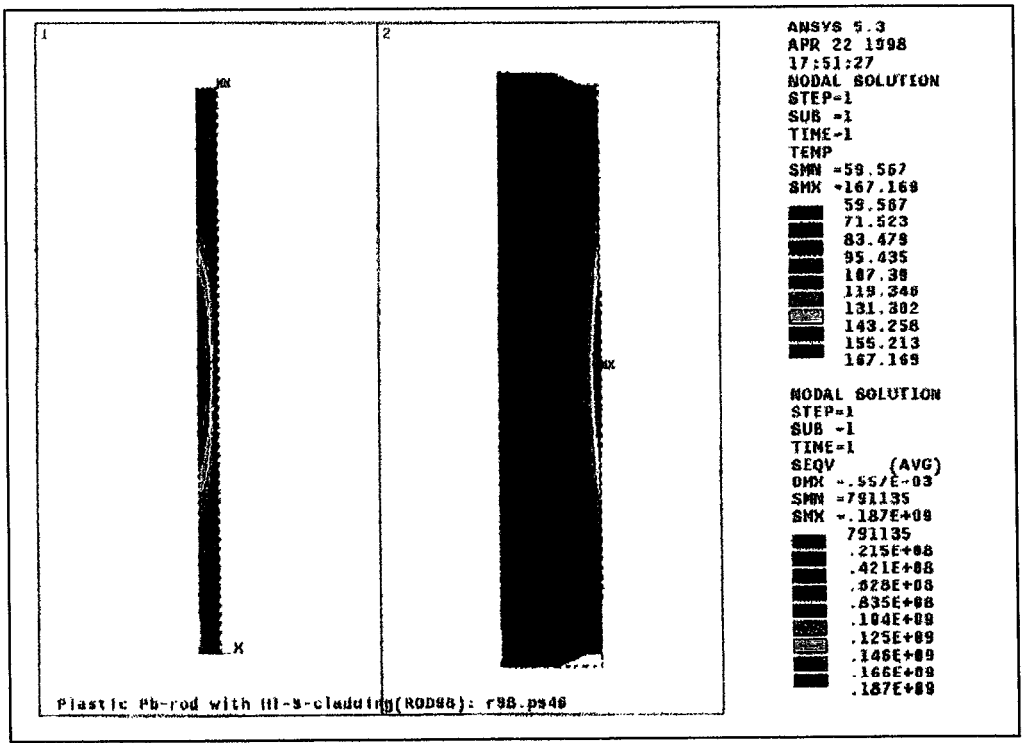
1
2
ANSYS 5.3
APR 22 1998
17:51:27
NODAL SOLUTION
STEP=1
SUB =1
TIME=1
TEMP
SMN =59.567
SMX =167.169
59.567
71.523
83.479
95.435
107.39
119.346
131.302
143.258
155.213
167.169
NODAL SOLUTION
STEP=1
SUB =1
TIME=1
SEQV (AVG)
DMX =.557E-03
SMN =791135
SMX =.187E+09
791135
.215E+08
.421E+08
.628E+08
.835E+08
.104E+09
.125E+09
.146E+09
.166E+09
.187E+09
Plastic Pb-rod with Hf-9-cladding(ROD98): r98.ps46

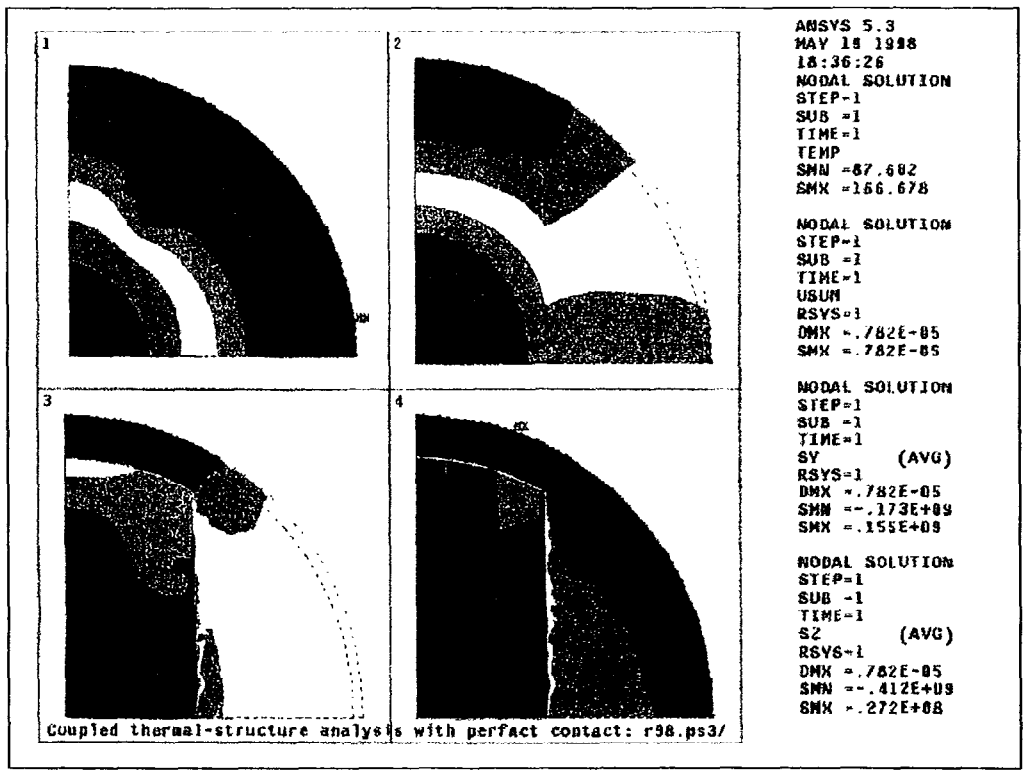
1
2
3
4
ANSYS 5.3
MAY 18 1998
18:36:26
NODAL SOLUTION
STEP=1
SUB =1
TIME=1
TEMP
SMN =87.602
SMX =166.678
NODAL SOLUTION
STEP=1
SUB =1
TIME=1
USUM
RSYS=1
DMX =.782E-05
SMX =.782E-05
NODAL SOLUTION
STEP=1
SUB =1
TIME=1
SY (AVG)
RSYS=1
DMX =.782E-05
SMN =-.173E+09
SMX =.155E+09
NODAL SOLUTION
STEP=1
SUB =1
TIME=1
SZ (AVG)
RSYS=1
DMX =.782E-05
SMN =-.412E+09
SMX =.272E+08
Coupled thermal-structure analysis with perfect contact: r98.ps3/

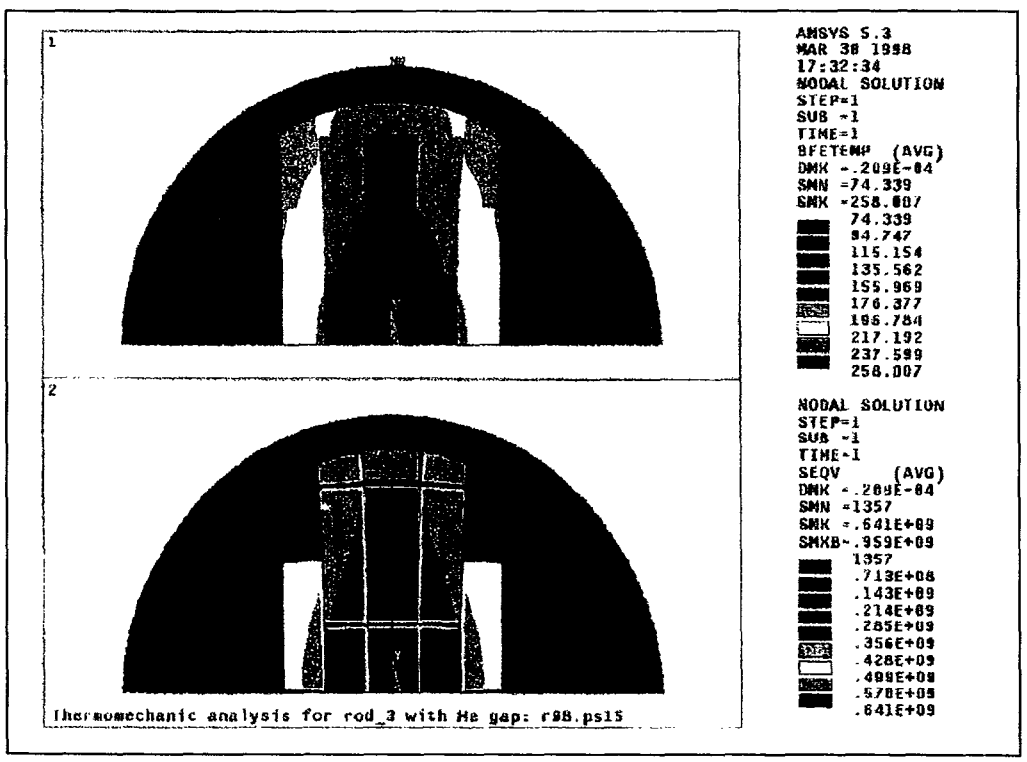
1
2
ANSYS 5.3
MAR 30 1998
17:32:34
NODAL SOLUTION
STEP=1
SUB =1
TIME=1
BFETEMP (AVG)
DMX =.209E-04
SMN =74.339
SMX =258.007
74.339
94.747
115.154
135.562
155.969
176.377
196.784
217.192
237.599
258.007
NODAL SOLUTION
STEP=1
SUB =1
TIME=1
SEQV (AVG)
DMX =.209E-04
SMN =1357
SMX =.641E+09
SMXB=.959E+09
1357
.713E+08
.143E+09
.214E+09
.285E+09
.356E+09
.428E+09
.499E+09
.570E+09
.641E+09
Thermomechanic analysis for rod_3 with He gap: r98.ps15

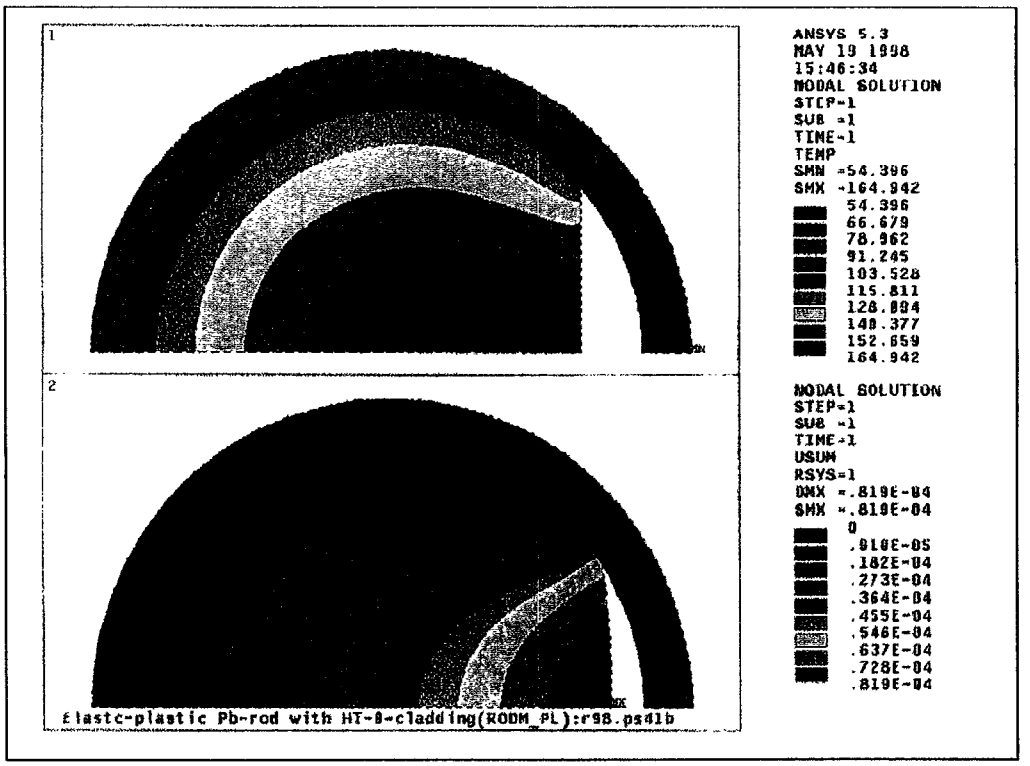
1
2
ANSYS 5.3
MAY 19 1998
15:46:34
NODAL SOLUTION
STEP=1
SUB =1
TIME=1
TEMP
SMN =54.396
SMX =164.942
54.396
66.679
78.962
91.245
103.528
115.811
128.094
140.377
152.659
164.942
NODAL SOLUTION
STEP=1
SUB =1
TIME=1
USUM
RSYS=1
DMX =.819E-04
SMX =.819E-04
0
.910E-05
.182E-04
.273E-04
.364E-04
.455E-04
.546E-04
.637E-04
.728E-04
.819E-04
elastc-plastic Pb-rod with HT-9-cladding(RODM_PL):r98.ps41b

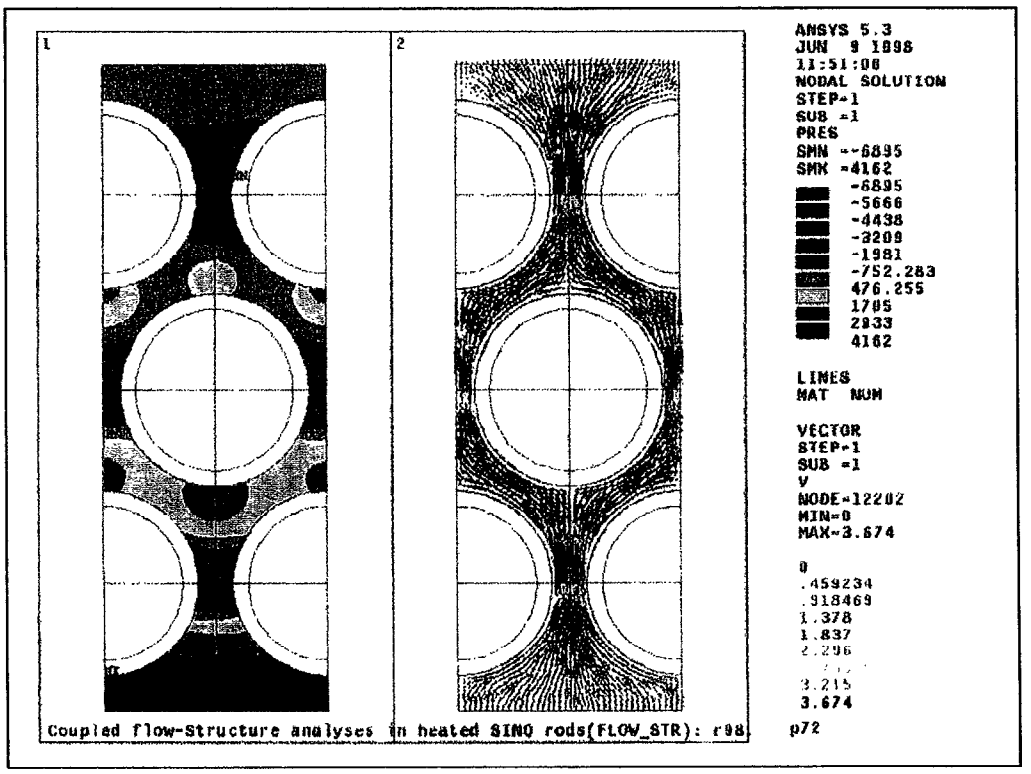
1
2
ANSYS 5.3
JUN 9 1998
11:51:08
NODAL SOLUTION
STEP=1
SUB =1
PRES
SMN =-6895
SMX =4162
-6895
-5666
-4438
-3209
-1981
-752.283
476.255
1705
2933
4162
LINES
MAT NUM
VECTOR
STEP=1
SUB =1
V
NODE=12202
MIN=0
MAX=3.674
0
.459234
.918469
1.378
1.837
2.296
3.215
3.674
Coupled flow-Structure analyses in heated SINQ rods(FLOW_STR): r98
p72

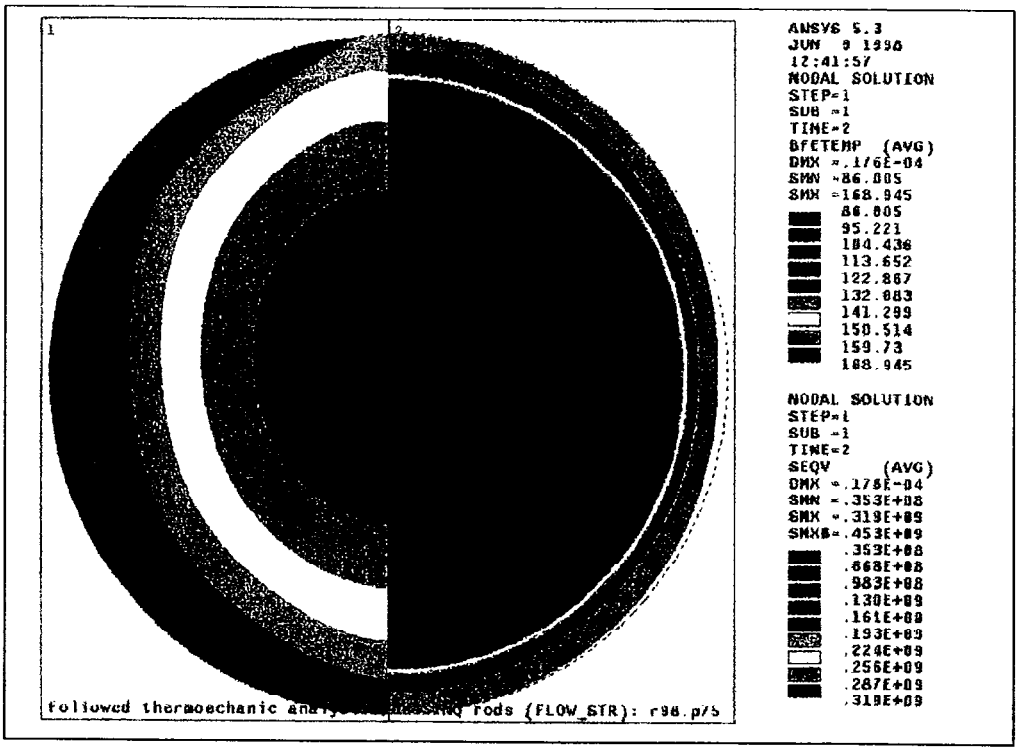
1
2
ANSYS 5.3
JUN 9 1998
12:41:57
NODAL SOLUTION
STEP=1
SUB =1
TIME=2
BFETEMP (AVG)
DMX =.176E-04
SMN =86.805
SMX =168.945
86.805
95.221
104.436
113.652
122.867
132.083
141.299
150.514
159.73
168.945
NODAL SOLUTION
STEP=1
SUB =1
TIME=2
SEQV (AVG)
DMX =.178E-04
SMN =.353E+08
SMX =.319E+09
SMX6=.453E+09
.353E+08
.668E+08
.983E+08
.130E+09
.161E+09
.193E+09
.224E+09
.256E+09
.287E+09
.319E+09
followed thermoechanic
rods (FLOW_STR): r98.p75

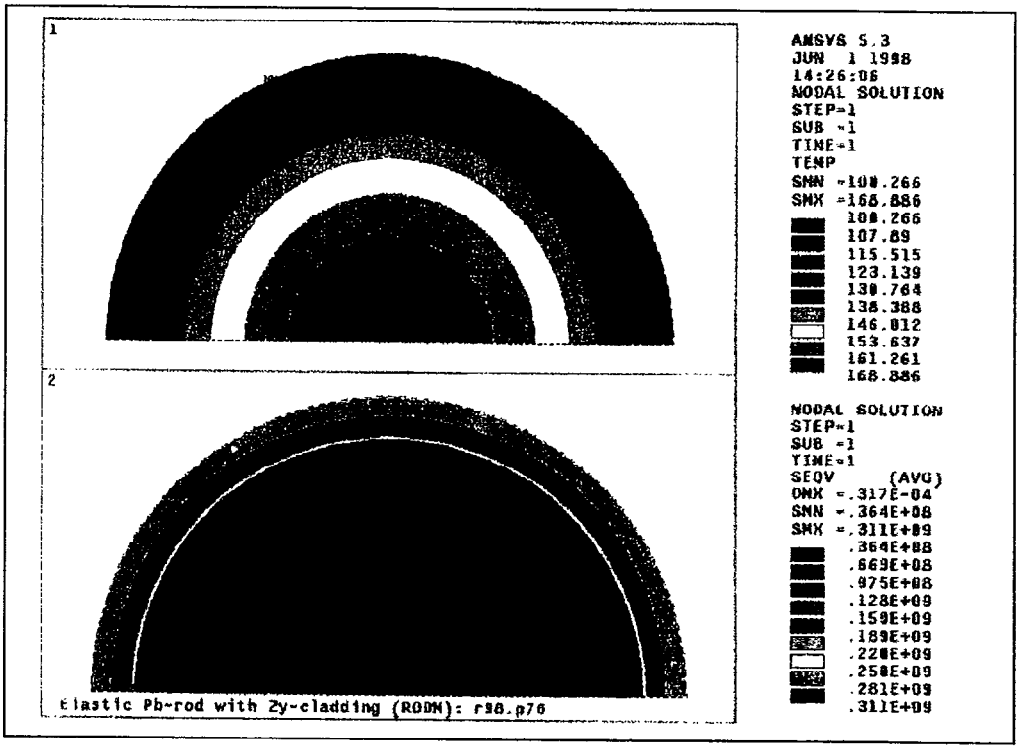
1
2
ANSYS 5.3
JUN 1 1998
14:26:06
NODAL SOLUTION
STEP=1
SUB =1
TIME=1
TEMP
SMN =100.266
SMX =168.886
100.266
107.89
115.515
123.139
130.764
138.388
146.012
153.637
161.261
168.886
NODAL SOLUTION
STEP=1
SUB =1
TIME=1
SEQV (AVG)
DMX =.317E-04
SMN =.364E+08
SMX =.311E+09
.364E+08
.669E+08
.975E+08
.128E+09
.159E+09
.189E+09
.220E+09
.250E+09
.281E+09
.311E+09
Elastic Pb-rod with Zy-cladding (ROOM): r98.p76

Thermal-Hydraulic Design Concept of the N-Arena Solid-Target System

Kaichiro Mishima, Yasushi Saito and Takashi Hibiki
Research Reactor Institute, Kyoto University

ABSTRACT

In relation to thermal-hydraulic design of the proposed spallation neutron source of the N-Arena of the Japan Hadron Facility (JHF), the basic concpet of solid target, criteria for thermal-hydraulic design, and subjects to be clarified are discussed. Next, the outline of R & D on the target design is described, and finally some results of feasibility study on the maximum beam power which can be attained with a solid target are presented.

1. INTRODUCTION

In relation to thermal hydraulic design of the proposed spallation neutron source of the N-Arena of the Japan Hadron Facility (JHF), a joint study between the High Energy Accelerator Research Organization (KEK) and research groups including Hokkaido University, Tsukuba University, Kyoto University and Kobe University started in 1997. Several research meetings were held to discuss the basic concept of the target and cooling system design, to define the subjects to be solved, to plan, to perform and to assess the results of the R & D on the thermal-hydraulic design as well as material problems.

In this paper, the basic concpet of solid target, criteria for thermal-hydraulic design, and subjects to be clarified are discussed. Next, the outline of R & D on the target design is described, and finally some results of feasibility study on the maximum beam power which can be attained with a solid target are presented.

2. THERMAL-HYDRAULIC DESIGN CONCEPT AND DESIGN CRITERIA

2.1 Target Design Concept

The geometrical arrangement of the solid target could be as shown in Fig.1. In the present design, parallel plate geometry was chosen because of its simplicity and experience.

2.2 Target Design Criteria

The following criteria are imposed on the thermal-hydraulic design of the solid target and the cooling system.

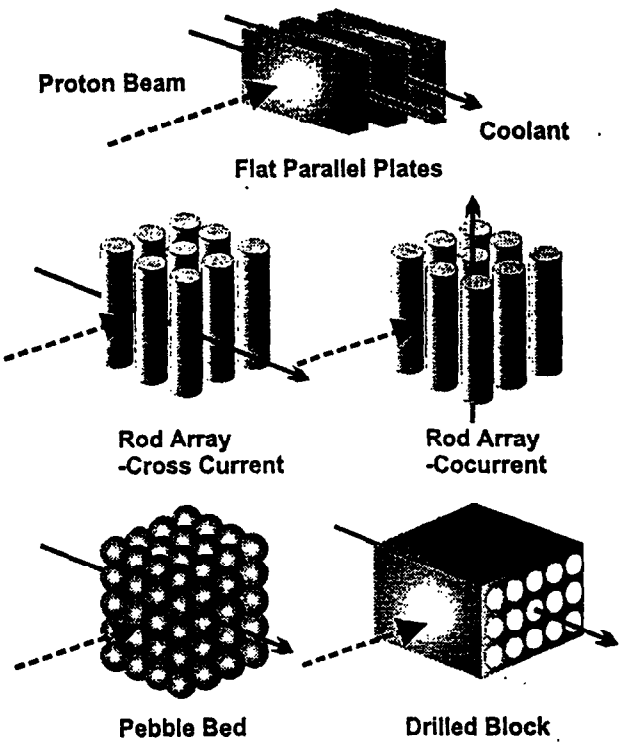

Fig.1 Basic concept of the solid target.

(1) Generally coolant boiling has undesirable effects on the solid (the target and the beam window) surface and maybe on the neutronics. For this, no boiling should be allowed in the target coolant channels under normal operating conditions, therefore:

$$T_w < T_{ONB} - \text{(safety margin)}$$

(2) To maintain the integrity of the solid target and the beam window, the temperatures in the solid, i.e.the target and the beam window, should be below the maximum permissible temperature of the material at any time and anywhere, so that

$$T_{solid} < T_{max}$$

The valued of T_{max} should be determined taking account of the melting temperature, the effects of temperarure on mechanical strength, etc. Temporarily,

T_{max} is set at 573K.

(3) If the boiling crisis occurs on the solid surface, the solid temperature may rise beyond the maximum permissible temperature of the material. Therefore, the critical heat flux for the occurrence of boiling crisis should not be reached under normal and abnormal operating conditions:

$$q_w < q_{CHF}/(\text{safety margin})$$

Note that under some special conditions, no sharp increase of solid temperature is observed even if CHF is reached. If this happens in the solid target cooling, this criterion can be ignored.

(4) The coolant flow should not cause any significant vibration, deformation, erosion of the solids, therefore:

$$v < v_{crit}$$

where V_{crit} denotes the critical velocity to initiate significant vibration which may cause deformation or damage of the solid target. The critical velocity can be estimated to be, for example, one half of Miller's velocity [1].

(5) Temperature gradient and transients in the solid should not cause excessive thermal stress, thermal shock and fatigue during the lifetime of the solid material, therefore:

$$\sigma_{solid} < \sigma_{max}$$

where σ_{solid} and σ_{max} denote the stress in the solid and the maximum permissible stress for the solid material, respectively.

(6) In addition, all the above criteria should be met even under the influence of radiation damage, radio-isotope production and chemical reaction throughout the life time of the solid material. Therefore, care should be taken for the effects of swelling of the slid target and beam window, accumulation of ^7Be and ^3H in the solid and the cooling system, as well as hydrogenation and embrittlement of the solid material.

2.3 Cooling System Design Criteria

(1) Primary cooling system (PCS) should have enough cooling capacity not to cause any damage of the target and the beam window under normal and abnormal operating conditions as well as in the decay heat removal after shut down of the beam.

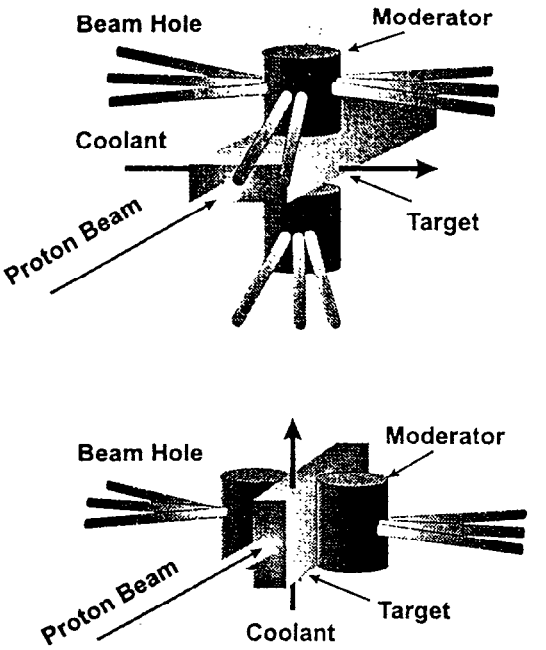

Fig. 2 Arrangement of the solid target and moderator assembly.

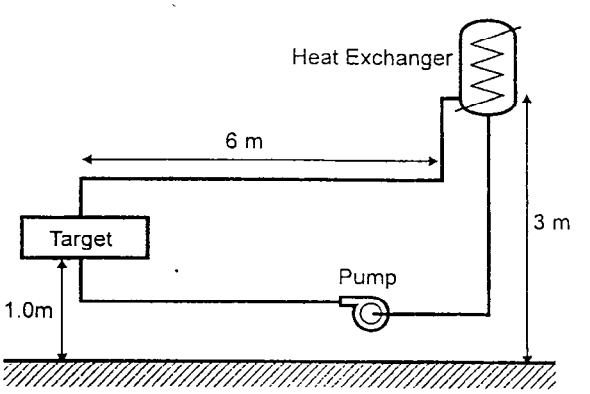

Fig.3 Skeleton of the primary cooling system.

(2) PCS should fit in the available space but should not interfere with the accessories, so that the arrangement of the target, moderator and PCS is chosen as the one on the top in Fig.2 because of the convenience for the arrangement of beam tubes, and the coolant flow direction should be horizontal. The skeleton of the PCS should be as shown in Fig.3.

(3) Adequate seismic design should be applied to PCS, namely, the system should stand for earth quakes of 0.3G, for example.

(4) PCS should be accessible or can be remote handled for maintenance and repairment throughout in-service.

(5) Care should be taken for radiation from radio-isotopes and corrosion products accumulated in PCS. For example, to cope with ^{3}H and ^{7}Be production, ^{3}H handling system, filtration and purification system, cold trap should beprepared and the biological shielding should be applied to PCS.

3. THERMAL-HYDRAULIC DESIGN CONDITIONS AT PRESENT

(1) Heat generation

The power density in the solid (target and beam window) was calculated by the Monte Carlo method. The resultant power density profile along the center axis of the solid target is as shown in Fig.4. The vertical axis denotes the power density per unit beam power. From this, the maximum heat generation density at the beam power of 0.6MW is estimated to be 840 MW/m^3.

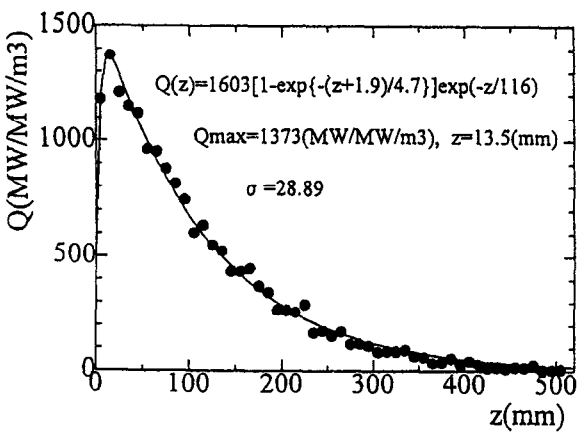

Fig. 4 Heat generation density per beam power along the center axis of the target

(2) Target material and dimensions are tabulated as follows:

material	: Ta-coated W, W, (U)
target shape	: flat plates
dimensions	: 167mm×60mm, 5 mm thick
supporting	: welded, swaged, inserted, spring-supported

(3) Heavy water was selected as primary coolant because of its neutronics characteristics. Some additives in the coolant maybe necessary to suppress certain kind of corrosion or chemical rea

(4) The conditions in the coolant channel which faces to the hottest target is as follows:

gap ×width	: 1.5 mm×60 mm
flow direction	: horizontal
inlet temp.	: 30℃ or 20℃ if necessary
inlet pressure	: atmospheric pressure or elevated pressure to suppress onset of nucleate boiling

4. SUBJECTS AND R & D RELATED TO THERMAL-HYDRAULIC DESIGN

4.1 Loop Tests

The loop test is being performed by Kobe University for the following purposes:

(1) To obtain data on flow distribution and pressure drop in the target coolant channels, which results are reflected to the distributor design,

(2) To test the proposed target design against flow induced vibrations and deformations,

(3) To study parallel channel flow instability under boiling conditions,

(4) The loop characteristics under natural circulation during decay heat removal.

The explanation of this test will be presented in the separate paper. It should be noted also that the flow visualization study is being performed by University of Tsukuba in relation to the thermal-hydraulic design of liquid metal target.

4.2 Heat Transfer Experiments

The heat transfer experiments are being conducted or planned by Kyoto University as follows:

(1) To obtain the data and to propose correlations to be used in the design calculations for heat transfer coefficient, conditions for onset of nucleate boiling (ONB) and critical heat flux (CHF),

(2) To find a way to heat transfer enhancement if necessary for heat removal from the solid target with very high heat flux.

The results from this experiment will be presented in the separate paper.

4.3 Material Problems

The following subjects are anticipated concerning the materials of the target and the beam window.

(1) Water chemistry, such as ^{7}Be-production and

deposition rate, ^3H-production and its handling, release of ^3H into environment and its influence is being studied by KEK.

(2) Effects of radiation damage, such as swelling, change in target material properties, i.e. thermal condutivity, mechanical strength, thermal expansion coefficient, etc. are being studied by Kyoto University.

(3) The impact of chemical reactions, such as the compatibility of the target material with D_2O, the formation of oxidation layer on the solid target and its effect, for example, small thermal conductivity, etc., and hydrogenation and embrittlement of the solid materials should be investigated.

4.4 Target Design and Calculations

The following target design and calculations are being performed by the participating research groups.

(1) Target design, such as material selection, i.e. Ta-coating of W, target dimensions, flow distributor and target holder desing is being performed by Kobe University.

(2) Heat generation rate was derived from neutronics calculations performed by Hokkaido University.

(3) Design calculations are being performed by the participating research groups, i.e. HokkaidoUniversity, Kobe University, Kyoto University, and KEK, such as: finite element calculation of temperature profile and thermal stress in the solid, estimation of margins to ONB and CHF, optimization of target design, maximum beam power which can be attained with a solid target.

4.5 Cooling System Design

Concerning the design of PCS, the following subjects are being or to be investigated: pressure and heat balance in PCS and the secondary system, design of natural circulation loop for decay heat removal, consideration of emergency cooling or heat sink under LOCA conditions, filtration and purification system to remove raio-isotopes and corrosion products in PCS, biological shielding for PCS, safety system, i.e. interlocks, pump trips, emergency power supply, etc, if necessary.

5. FEASIBILITY STUDY ON MAXIMUM POWER WITH SOLID TARGET

5.1 Limiting Factors (except material properties)

In view of thermal-hydraulic design, the following factors may limit the maximum beam power which can be imposed on the solid target.

(1) If no boiling is allowed in the coolant channel, the condition for the onset of nucleate boiling may be a major limiting factor for beam power. The temperature for onset of nucleate boiling T_{ONB} increases as the coolant velocity and the pressure increases. The onset of nucleate boiling can be delayed by decreasing the inlet coolant temperature T_{in}.

(2) Critical heat flux limits the maximum power because it indicates the limit of heat removal from the solid surface. CHF increaseas the heated length decreases, the coolant velocity increases, the pressure increases, and the inlet coolant temperature T_{in} decreases.

(3) Maximum temperature in the solid can be a limiting factor to repvent the melting or damage of the solid target. The maximu temperature increases as the cololant velocity decreases and the target thickness increases. The maximum teperature also increases if the thermal conductivity decreases due to radiation damage and if an oxide layer is formed on the surface

(4) The thermal stress and the fatigue can be a limiting factor if the temperature difference and the thickness of the solid target is large.

(5) Flow induced vibrations can be also a limiting factor if a very high coolant velocity is required for target cooling. The critical velocity for significant vibrations v_{crit} depends on holder design, and increases as the target thickness increases and the target widthdecreases. The critical velocity is higher for curved plates, and if support comb is applied to the leading edge of the target plates.

(6) Embrittlement of the solid material can be a limiting factor if the effect of radiation damage and hydrogenation is significant.

5.2 Tentative Results of the Feasibility Study

The calculations were peformed with the following conditions:

(1) The heat transfer coefficient for single-phase flow was calculated by the Dittus-Boelter correlation [2].

(2) The heat transfer coefficient for boiling region was calculated by the Thom's correlation [3].

(3) Condition for the onset of nucleate boiling was calculated by the intersect between Thom's correlation and the Dittus-Boelter correlation.

(4) CHF was calculated by the Bernath correlation [4].

(5) The bulk coolant temperature was calculated by the half of the total heat generation per one target plate at the peak power density, but the coolant channel recceived the heat from both of the target plates adjacent to the channel, and the target temperature was calculated with this bulk coolant temperature and the peak power density obtained from Fig.4.

The results of the calculations are shown in Figs. 5, 6 and 7 where the maximum heat flux in the target, CHF, and the onset of nucleate boiling point, surface and peak temperatures of the target are shown as functions of the beam power for the target thicknesses 3, 5 and 7 mm, respectively. The other conditions are: the coolant gap was 1.5 mm, coolant velocity 10 m/s, system pressure 0.1 MPa and the inlet temperature 30 ℃. From these figures, it can be seen that the most severe condition to limit the beam power is the onset of nucleate boiling, although sufficient margin to CHF exists, and when the target thickness is 7 mm, the maximum temperature also bcomes a limiting factor.

Fig. 8 shows the effect of changing the coolant velocity from 10 m/s to 15 m/s. From this, it can be seen that CHF is increased, the onset of nucleate boiling is supressed by increasing coolant velocity.

Fig. 9 shows the effect of system pressure. From this figure, it can be seen that CHF is increased and the onset of nucleate boiling is supressed by increasing system pressure.

Fig.10 shows the effect of swelling. If the channel gap is decreased to 1.0 mm due to swelling, then CHF decreases and ONB occurs at lower beam power, because of reduced coolant flow rate and as a consequence increased coolant bulk temperature.

Fig.11 shows the effect of oxide layer on the target temperarure. Here the thermal conductivity of the oxide layer is assumed to be reduced to one tenth.

Fig. 12 shows the effect of assumption that the peak heat flux location. Here it is assumed that the peak heat flux occurred at the outlet of the heated channel, i.e. location of highest bulk coolant temperature. In reality, if one uses realistic power profile along the coolant channel, the result may be in between Figs. 5 and 12.

6. SUMMARY

In relation to thermal-hydraulic design of the proposed spallation neutron source of the N-Arena of the Japan Hadron Facility (JHF), the basic concpet of solid target, criteria for thermal-hydraulic design, and subjects to be clarified were discussed. Next, the outline of R & D on the target design was described, and finally some tentative results of feasibility study on the maximum beam power which could be attained with a solid target were presented. The result indicated that the condition for the onset of nucleate is the most significant limiting factor to the maximum beam power. The results also indicated that the maximum beam power can be as high as 1 MW. The final conclusion should be drawn by more detailed and reliable calculations.

REFERENCE

1. D.R. Miller, "Critical Velocities for Collapse of Reactor Parallel-Plate Fule Assemblies," Trans. ASME, J. Engng. for Power 82 (1960) 83.
2. F.W. Dittus and L.M.K. Boelter, "Heat Transfer in Automobile Radiators of the Tubular Type," Univ. Calfornia Publs. Eng., 2 (1930) 443-461.
3. R.S. Thom, "Boiling in Subcooled Water during Flow up Heated Tubes or Annuli," Proc. Inst. Mech. Eng., 180, Pt3C (1965) 226-246.
4. L. Bernath, "A Theory of Local-Boiling Burnout and Its Application to Existing Data," Chem. Eng. Prog. Symp., Ser. 56 (1960) 95-116.

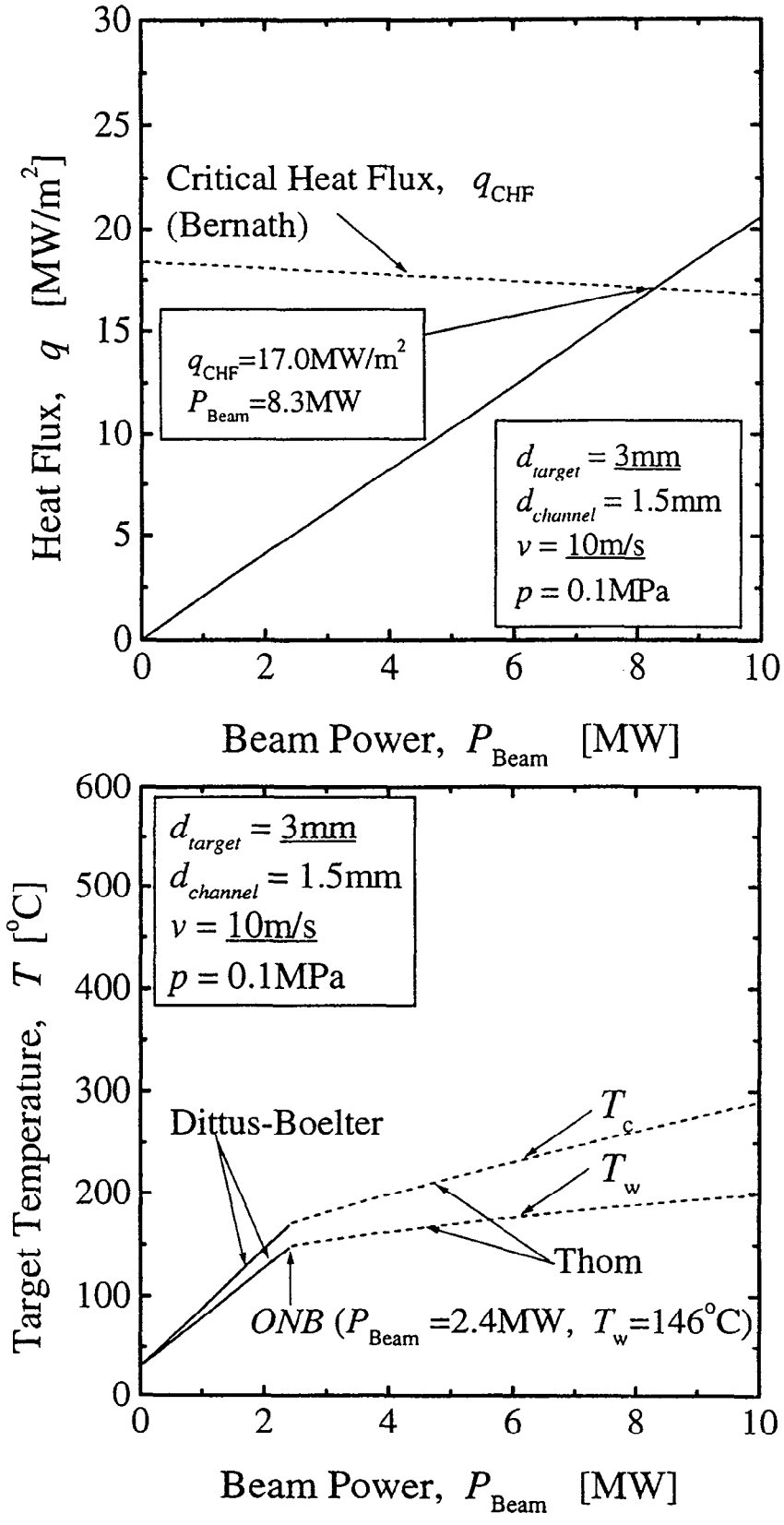

Fig.5 Maximum heat flux, CHF and target temperature vs. beam power for **target thickness 3mm**, gap 1.5mm, coolant velocity 10m/s at 0.1MPa and inlet temperature 30 °C.

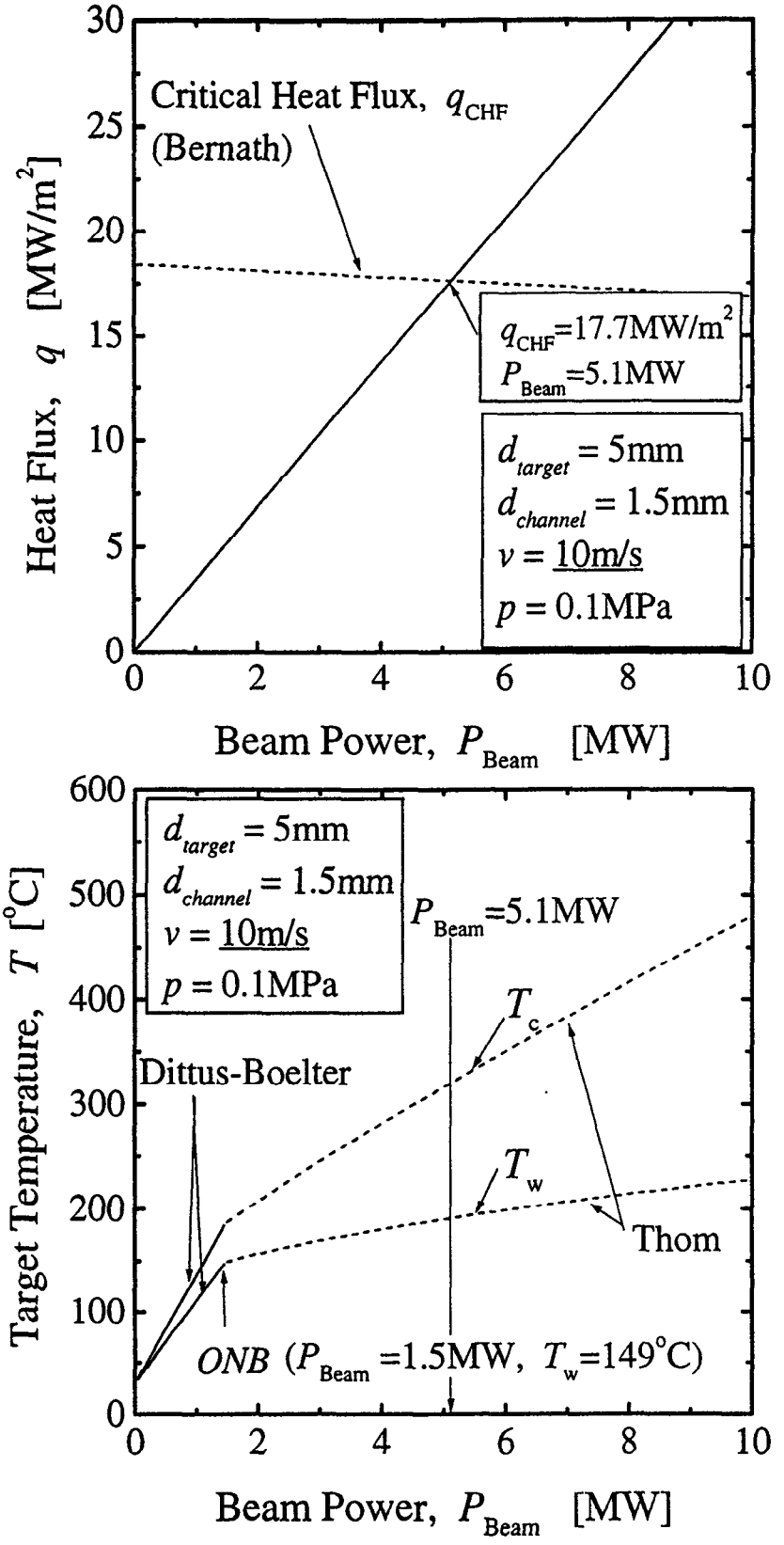

Fig.6 Maximum heat flux, CHF and target temperature vs. beam power for target thickness 5mm, gap 1.5mm, coolant velocity 10m/s at 0.1MPa and inlet temperature 30 °C.

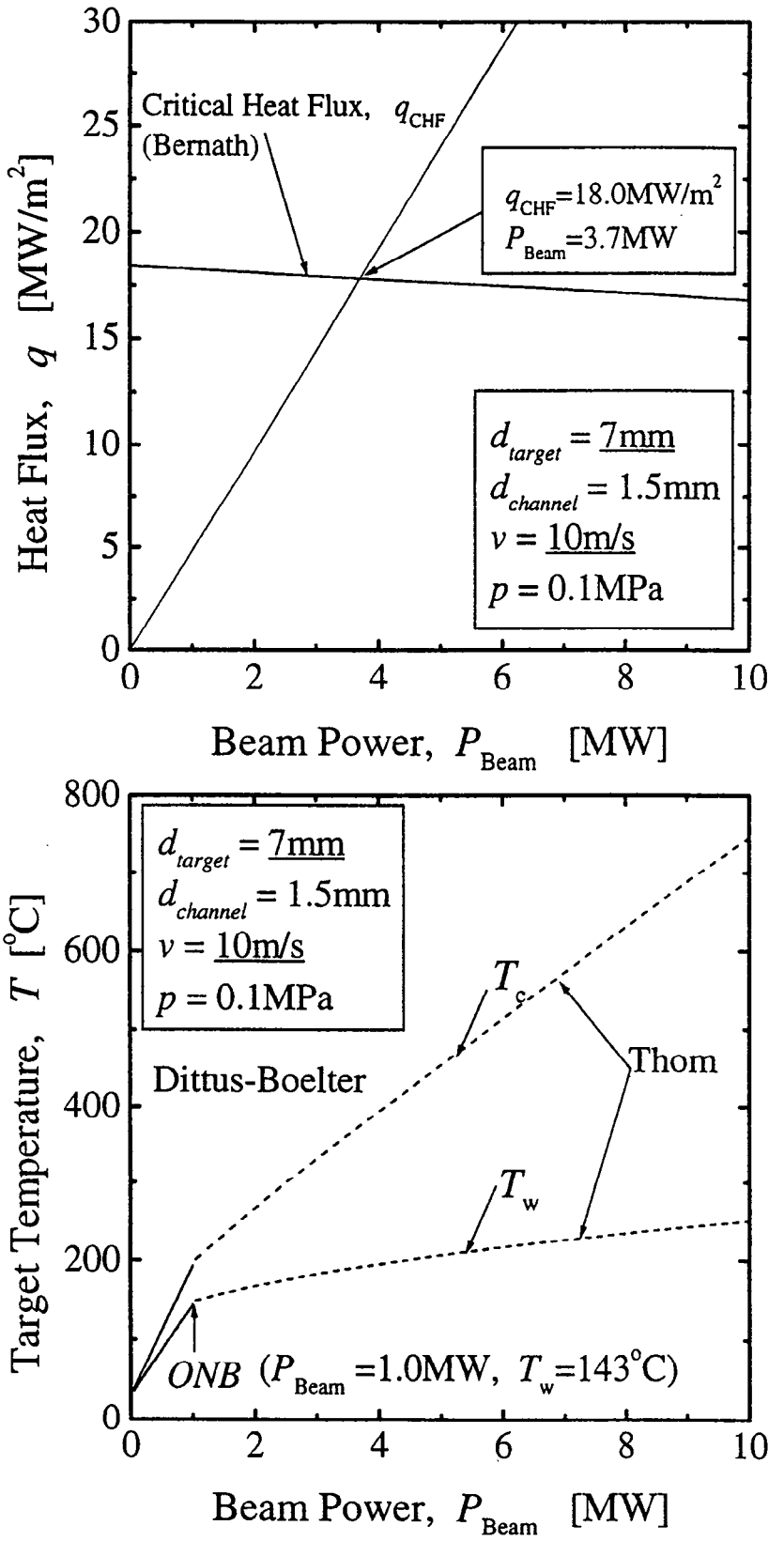

Fig.7 Maximum heat flux, CHF and target temperature vs. beam power for **target thickness 7mm**, gap 1.5mm, coolant velocity 10m/s at 0.1MPa and inlet temperature 30 °C.

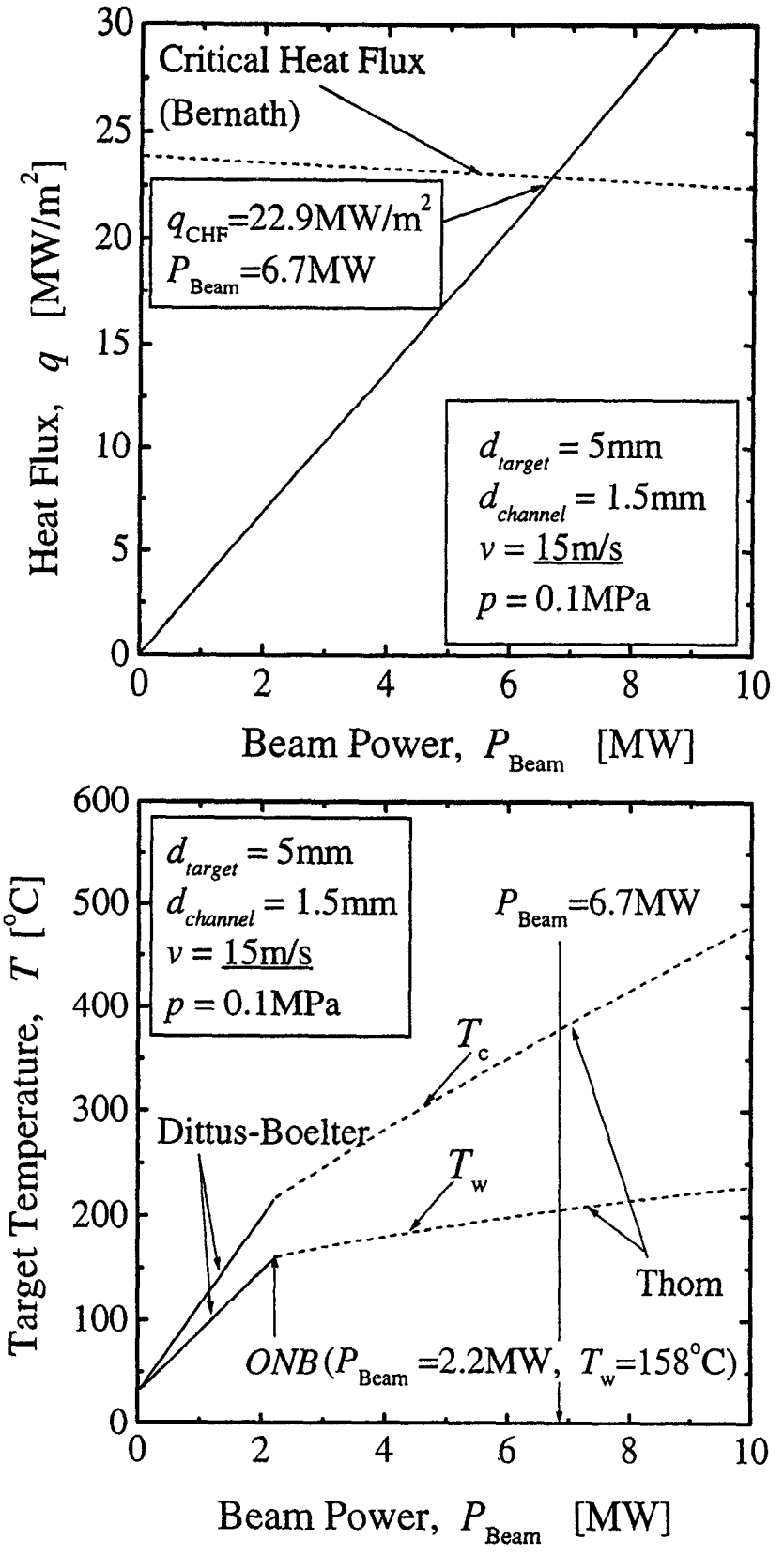

Fig.8 Maximum heat flux, CHF and target temperature vs. beam power for target thickness 5mm, gap 1.5mm, **coolant velocity 15m/s** at 0.1MPa and inlet temperature 30 °C.

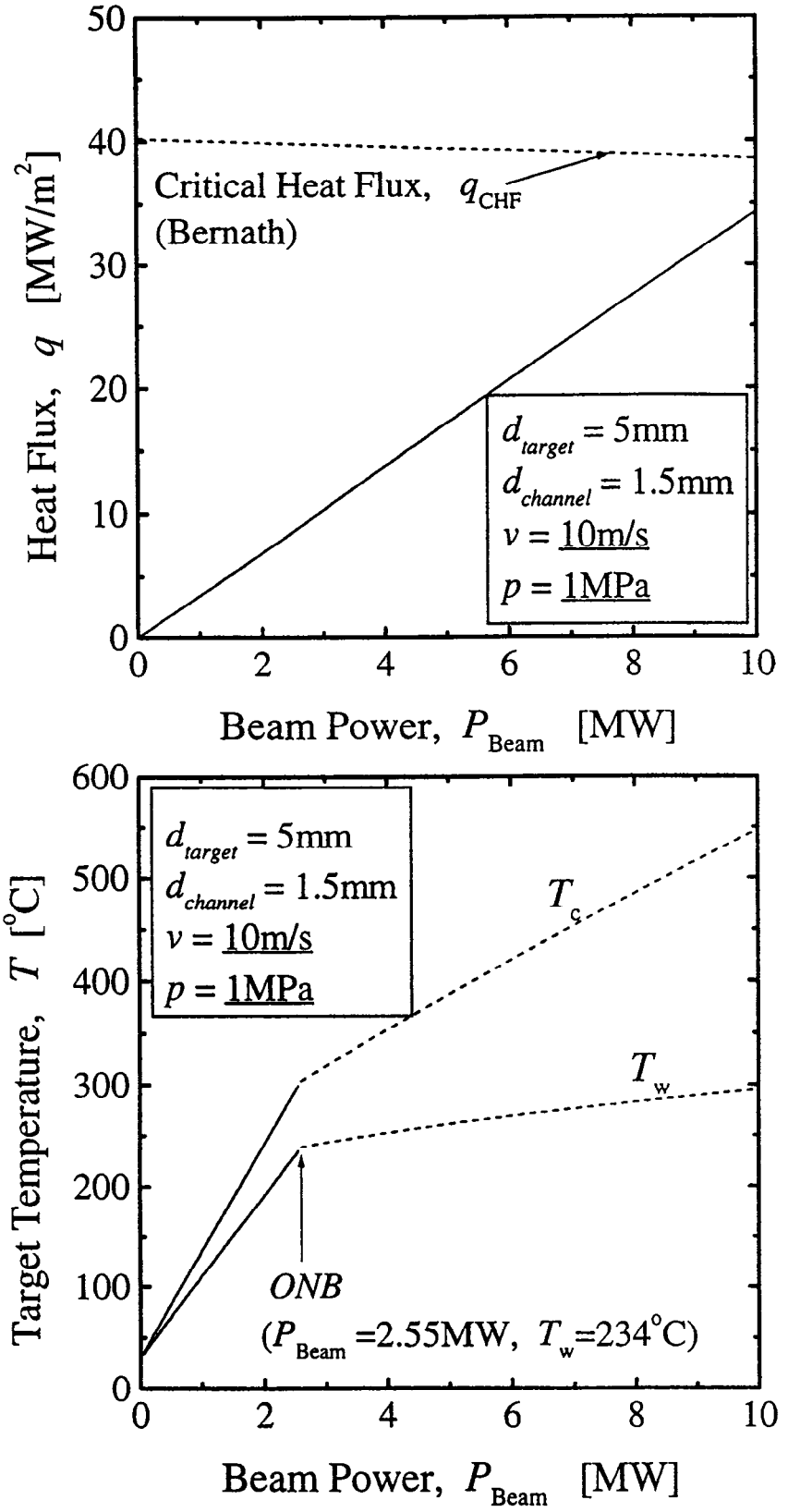

Fig.9 Maximum heat flux, CHF and target temperature vs. beam power for target thickness 5mm, gap 1.5mm, coolant velocity 10m/s at **1 MPa** and inlet temperature 30 °C.

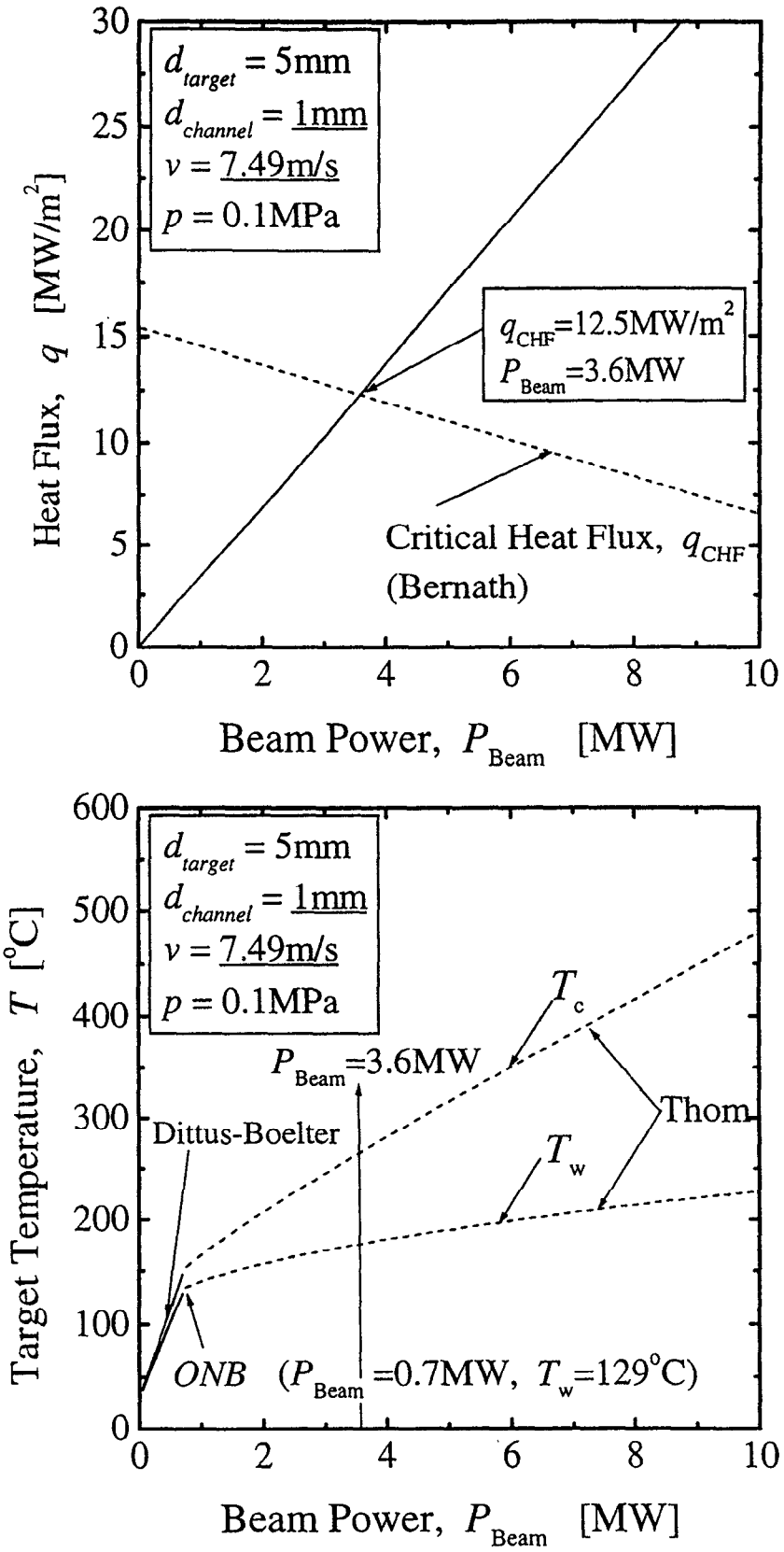

Fig.10 Maximum heat flux, CHF and target temperature vs. beam power for target thickness 5mm, **gap 1mm**, **coolant velocity 7.49m/s** at 0.1Mpa and inlet temperature 30 °C.

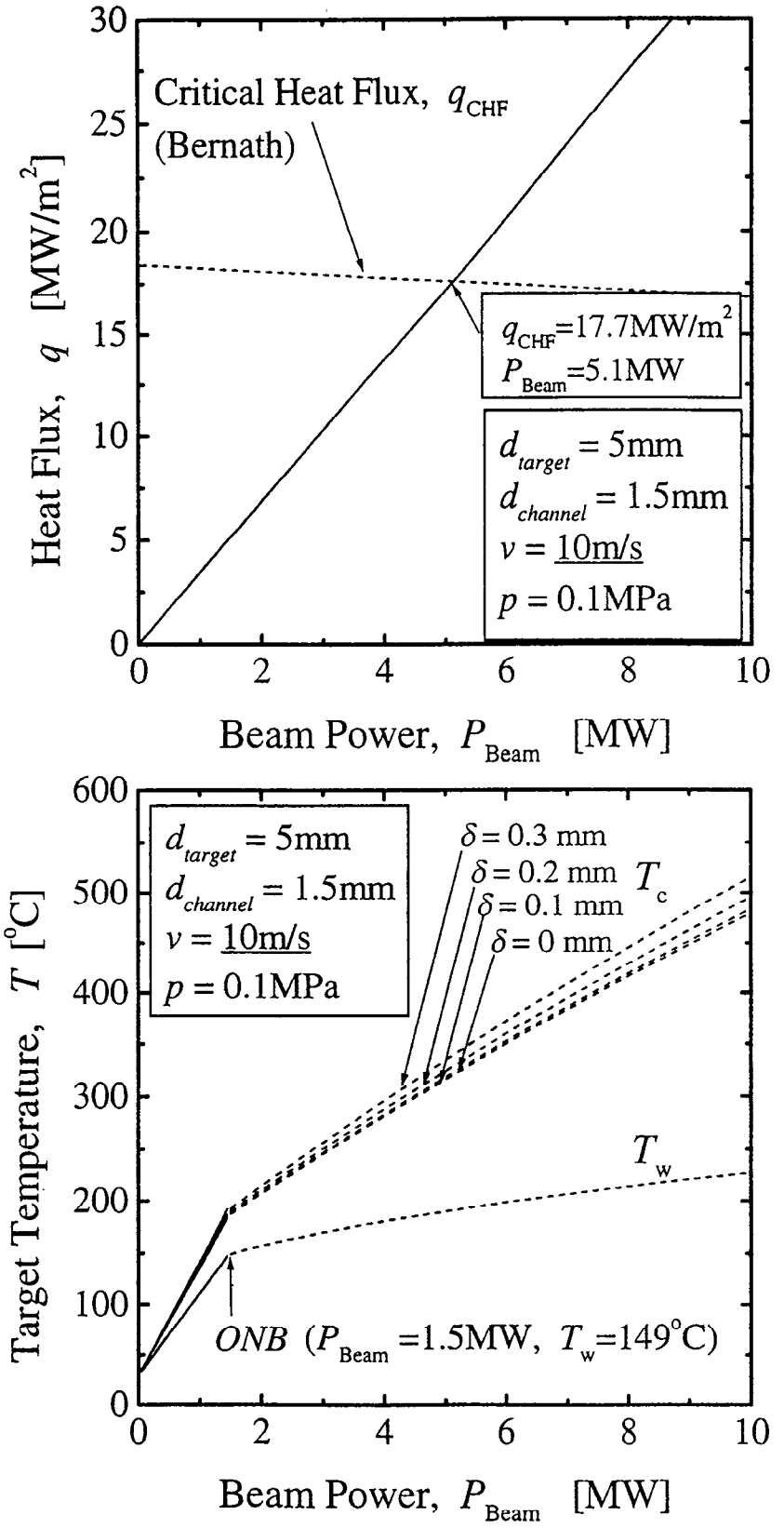

Fig.11 The effect of oxide layer on the target temperature for target thickness 5mm, gap 1.5mm, coolant velocity 10m/s at 0.1MPa and inlet temperature 30 °C.

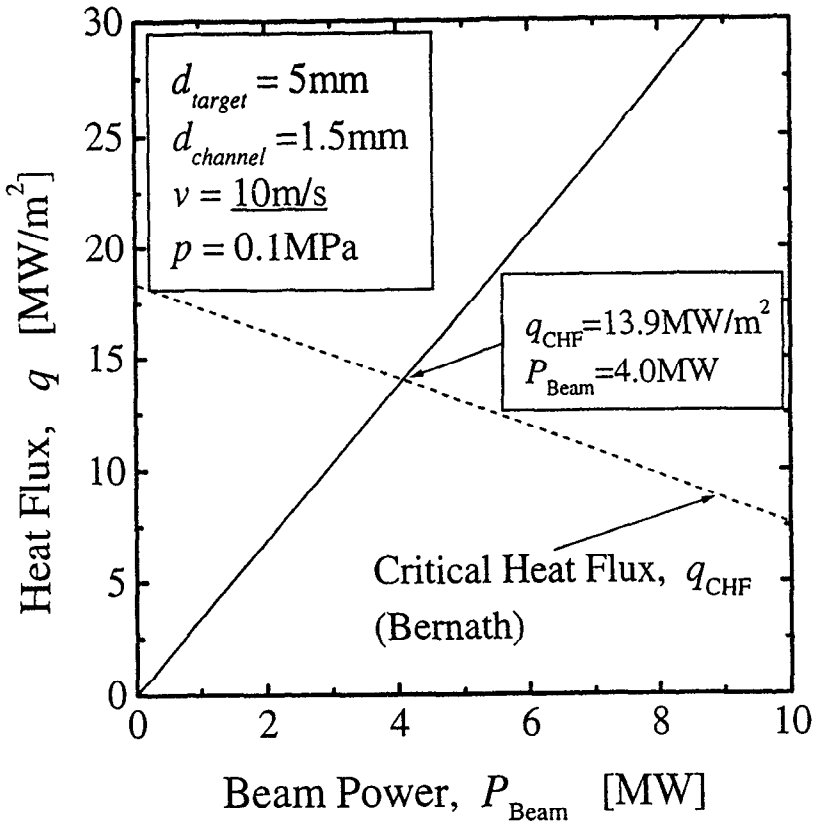

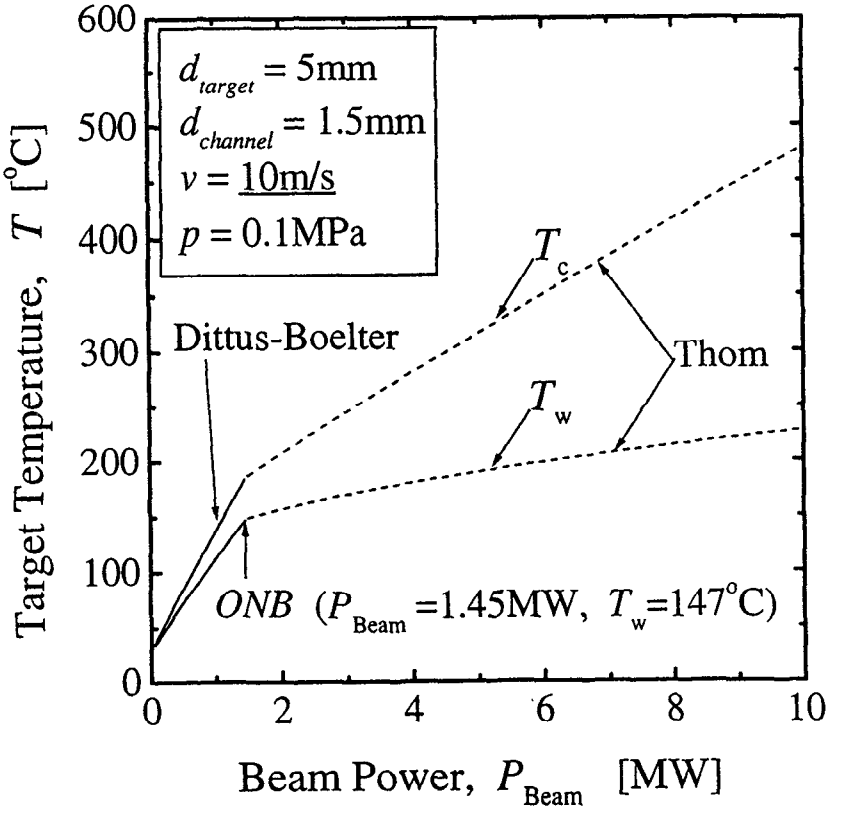

Fig.12 The results obtained assuming peak heat flux occurred at the outlet otherwise the same conditions as Fig.6 for target thickness 5mm, gap 1.5mm, coolant velocity 10m/s at 0.1MPa and inlet temperature 30 °C.

ICANS-XIV
14th Meeting of the International Collaboration on
Advanced Neutron Sources
June 14-19, 1998
Starved Rock Lodge, Utica, Illinois, USA

Discussion on the thickness optimization of the water-cooled solid target for N-arena

N.Takenaka [1], Y.Hayashida [1], R. Yasumura [1], T.Fujii [1], N.Hata [2], Y.Ogawa [2], Y.Kiyanagi [2]

1: Dept. Mechanical Engineering., Kobe Univ.,
1-1 Rokkodai, Nada, Kobe 657-8501 Japan
e-mail takenaka@mech.kobe-u.ac.jp
2: Division of Quantum Energy Engng., Graduate School of Engng., Hokkaido Univ.
Kita-13, Nishi-8, Kita-ku, Sapporo 060-8628, Japan

Abstract

Analytical results of one-dimensional (1-D) design on the thermal hydraulics of the water cooled solid target for the preliminary design of the target system in N-arena of JHF were presented. The target systems with plate disks, 60 mm x 166.6 mm in cross section with various thicknesses placed parallel with the gaps of 1.5 mm for the coolant channels were designed. The target material was tungsten. The water and the heat deposition fraction were defined and calculated for each design conditions. It was shown that the water irradiated by the beam is the least when the target thickness is designed as the intersection point in d-Q diagram is moved to the maximum heat deposition rate point by pressurizing the coolant or the heat transfer augmentation if possible.

Keywords; solid target, water cooled, thermal hydraulics, water fraction, optimization

1. Introduction

The purpose of this study is the thermal hydraulics designs of target systems in the spallation reactor to produce neutrons in N-arena of Japan Hadron Facilities.

The target systems with plate disks, 60 mm x 166.6 mm in cross section with various thicknesses placed parallel with the gaps of 1.5 mm for the coolant channels were designed. The target of N-arena is now designed to be divided into a front and a rear target. Neutrons generated mainly in the front target are moderated. The rear target is considered as the beam dump. The effective length of the front target is 300 mm.

Preliminary design of the target system to make rough sketches of the target plate designs for the N-arena were discussed. The analyses of one-dimensional (1-D) design on the thermal hydraulics of the water cooled solid target in the single coolant channel were carried out. The water fraction and the heat deposition fraction were defined and calculated to discuss the design for decreasing the water irradiated by the beam. The methods of the analyses, some results on heat transfer of the window and the target and the fractions are discussed

2. Analyses of 1-D design on the thermal hydraulics of the water cooled solid target

The heat deposition rates of a proton beam irradiated to a pure Tungsten target were calculated with a Monte-Carlo method. The beam shape was an ellipsoid 40 mm and 140 mm in diameters and the intensity distribution was assumed to be parabolic. The target was a block 60 mm x 166.7 mm in rectangular cross section and 500 mm in depth. The distributions of the heat deposition rates along the beam line averaged in the whole cross section (axis) and in a cylinder 20 mm in diameter at the center of the cross section (center axis) were obtained. The both calculated results were fitted with an empirical equation are shown in Fig.1, respectively. The heat deposition rates in the beam window made from stainless steel 304 and Inconnel 600 were also calculated in the same methods.

The wall and the maximum temperatures are highest at the center of the target plate. To estimate the highest temperatures in a target plate by 1-D equations, they were calculated with an assumption that the heat deposition rate over the target is uniform at the value obtained by center axis shown in Fig.1(b). The predicted temperatures were low, i.e., had some safety margin comparing with those by the 3-D results.

The thermal hydraulics conditions from the safety considerations for the water cooled target plate are as follows:

(a) The heat flux at the target surface is below the critical heat flux.
(b) The temperature at the target surface is below the saturation temperature of the water to avoid boiling.
(c) The maximum temperature in the target is below a certain temperature much lower than the melting point of the target material.
(d) The thermal stress in the target is below a certain value smaller than the yield stress or the stress which causes the deformation of the coolant channel.
(e) Water irradiated by the proton beam, i.e., water fraction of the target is as little as possible.

The conditions for the beam window are the same as (a)-(d).

The conditions of (a) and (b) are based on the heat convection in the coolant and those of (c) and (d) on the heat conduction in the target. The equations used for these conditions are summarized in Table 1. The configurations of the target and the coolant channel are shown in Fig.2. The coolant temperature in the channel can be calculated by the enthalpy conservation.

The wall surface and the maximum temperatures are mainly discussed in this report. Since the critical heat fluxes for the coolant conditions are estimate to be much higher than the heat fluxes estimated by the conditions (b) and (c), they are not discussed in this report. The details of the thermal stress should be discussed for the 3-D geometry and 1-D calculations on the thermal stress were made for the estimation in this paper.

The thickness of the target plate which allow the conditions from (a)-(d) can be calculated at a given heat generation rate. The thickness of the target which agree with the conditions (a) and (b) is proportional to the heat deposition rate while that with the conditions (c) and (d) proportional to its square. Therefore, the relation between the heat deposition rate and the thickness of the target plate is illustrated by a d-Q diagram as shown in Fig.3. The minimum target thickness d_{min} is determined by the maximum heat deposition rate Q_{max} as shown in the figure. It can be seen that the target thickness is determined by the conditions (a) or (b) in high heat deposition conditions and by the conditions (c) or (d) in low heat deposition conditions. The former conditions are based on the heat convection where the target thickness is determined by the heat transfer at the wall surface without the effects of the target material. The limit of the wall temperature can be changed by the system pressure and the wall temperature can be decreased when the heat transfer augmentation is carried out. Two or three times heat transfer augmentation may be possible if the target wall surface was machined to certain shape. The latter are based on the heat conduction in the target material. The

limit of the maximum temperature was determined by the material strength and the target shape and was not much changed by the thermal hydraulic condition.

For the discussion on the condition (e) water fraction f_w and heat deposition fraction f_Q were defined. The target of N-arena is divided into front and rear target. Neutrons generated mainly in the front target are moderated. The rear target is considered as the beam dump. The effective length of the front target L_{eff} is 300 mm in the present calculation.

These fractions are defined in the front target as

$$f_w = n\,\delta / L_{eff}\,, \quad f_Q = \Sigma Q_i d_i / \int Q(z)dz$$

where suffix i means the i-th target plate counted from the beam side and n is the number of the target plates in the effective length.

2-1. Calculated results on the target design

Examples of the calculated results for the target at the position where the heat deposition rate is the highest for the proton beam power 0.6 and 1.2 MW in N-arena. The target material was tungsten and the width of the coolant channel was fixed at 1.5 mm.

The temperatures at the target wall surface and the maximum temperatures of the target at the center are shown in Figs.4 and 5 against the velocity for the target thickness from 3 to 10 mm. C in Table 1 is a parameter to estimate the entrance region. C=4 is the most realistic for the target assembly. C=0 is the most safety design and was used in this calculation.

The wall surface and the maximum temperatures of the beam window are shown in Figs.5 and 6 for 3 and 5 mm thick stainless steel 304 and Inconnel 600, respectively. Since the beam window was cooled at one side by water and the other side was adiabatic, the maximum temperature is at the beam side surface.

The thickness of the target is determined by the heat convection or the heat conduction depending on the heat deposition rate as described before. The target thickness distributions along the beam line were determined for the heat deposition rate distribution shown in Fig.1(b). The width of the coolant channel and the coolant inlet temperature were fixed 1.5 mm and 30 C, respectively.

The distributions of the heat deposition rate, the target thickness, the heat flux, the wall and the maximum temperatures and the maximum thermal stress are shown in Fig.8 where W_p, u_{ch}, T_{max}* and T_w* are the beam power, the coolant velocity in the channel and the limit of the maximum and wall surface temperatures for the design, respectively. The thicknesses of the target were calculated based on the heat convection near the beam window where the wall temperature was kept to the designed value and the heat flux was also constant. After the cross point shown in the d-Q diagram in Fig.3, they were calculated based on the heat conduction where the maximum temperature was kept to the designed value and the thermal stress was also constant. The designed values of the wall surface and the maximum temperature, T_w* and T_{max}*, should be determined by the pressure and the strength of the target material, respectively.

2.2 Water and heat deposition fractions

The water and the heat deposition fractions as defined above, f_w and f_Q are shown by the lines against the limit of the wall temperature T_w* for T_{max}* of 200, 250 and 300 C in Figs.9 and 10 where the minimum target plate thicknesses are also plotted by the symbols. With increasing T_w*, f_w decreases, f_Q and d_{min} increase at first, and then they keep constant values after certain values of

T_w*. The conditions on d-Q diagram at the points (a)-(c) in this figure are shown and the certain point is at where the maximum heat deposition rate is at the value of the intersection points of two lines in d-Q diagram. It can be seen that the water irradiated by the beam is the least when T_w* can increase up to the value at the point (b) with pressurizing the coolant. Or it can be seen further increase of T_w* after the point (b) is meaningless to decrease the water fraction and there is the limit to decrease the water fraction by the pressurization of the coolant.

The effects of the heat transfer augmentation rate, h_A/h, on the fractions are shown in Figs. 11 and 12, where h_A and h means the augmented and the normal heat transfer coefficient, respectively. More augmented is the heat transfer, f_w decreases and f_Q increases but the rates of the increase and decrease become very small after certain values of T_w*. The reason is just the same as above. So it can also be seen that there is a limit to decrease the water fraction effectively by the heat transfer augmentation.

It was shown that the water irradiated by the beam could be decreased by the pressurization or the heat transfer augmentation but there were limits to decrease the water fraction. The limits is determined when the target thickness is designed as the intersection point in d-Q diagram is moved to the maximum heat deposition rate point, i.e., the target thicknesses are determined in the heat conduction region.

3. Conclusions

Analytical results with 1-D model are presented as the preliminary designs for the thermal hydraulic of the solid target for N-arena in JHF. Water and heat deposition fractions were defined and the design conditions to decrease the water irradiated by the beam were discussed.

The water irradiated by the beam could be decreased by the pressurization or the heat transfer augmentation but there were limits to decrease the water fraction. The limits is determined when the target thickness is designed as the intersection point in d-Q diagram is moved to the maximum heat deposition rate point.

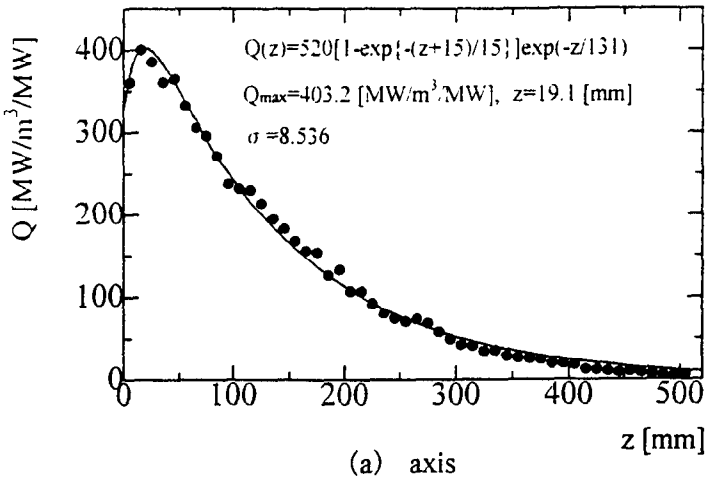

(a) axis

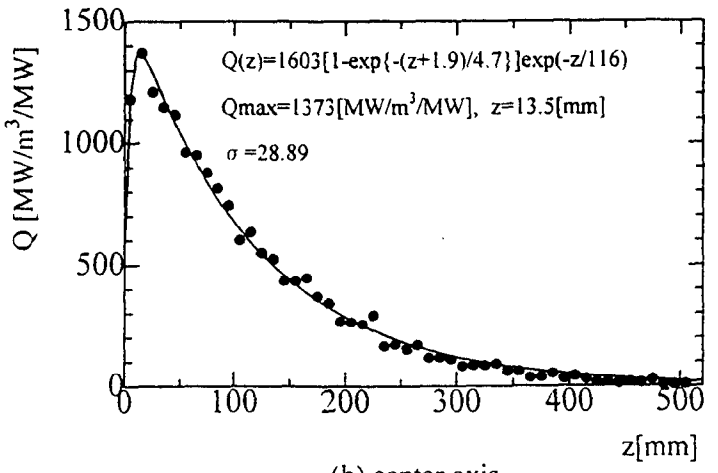

(b) center axis

Fig.1 Heat deposition rate in target

Equations for One-dimensional Design

Critical Heat Flux and Wall Temperature

$$q = \frac{Qd}{2} = h(T_w - T_L)$$

$$Nu = 0.023 Re^{0.8} Pr^{0.4} (1 + \frac{C}{z/D}), \quad Nu = \frac{hD}{\lambda_L}, \quad Re = \frac{uD}{\nu_L}$$

$$q < q_{crit}, \quad T_w < T_{sat}$$

Maximum Temperature and Wall Stress

$$T_{max} - T_w = \frac{1}{8\lambda_s} Qd^2$$

$$T_{max} << T_{m.p.}$$

$$\tau_s = \frac{\alpha E}{12\lambda_s(1-\nu)} Qd^2 = \frac{2\alpha E}{3(1-\nu)}(T_{max} - T_w)$$

$$\tau_s < \tau_{max}$$

Design Results

T_w, q_{crit} ; $Qd <$ Designed Value

T_{max}, τ_{max} ; $Qd^2 <$ Designed Value

Table 1. Equations used for the calculation

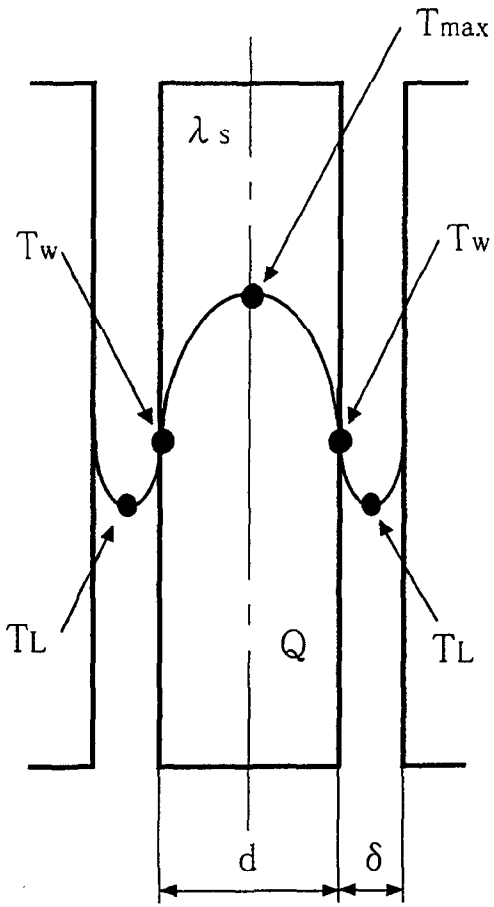

Q: heat deposition rate [W/m³]
Tw: target wall sarface temperature [℃]
Tmax: target maxmum temperature at center [℃]
TL: coolant temperature [℃]
d: target thikness [m]
δ : coolant channel width [m]
λs: thermal conductivity of target material [W/mK]

Fig.2 Target and coolant channel

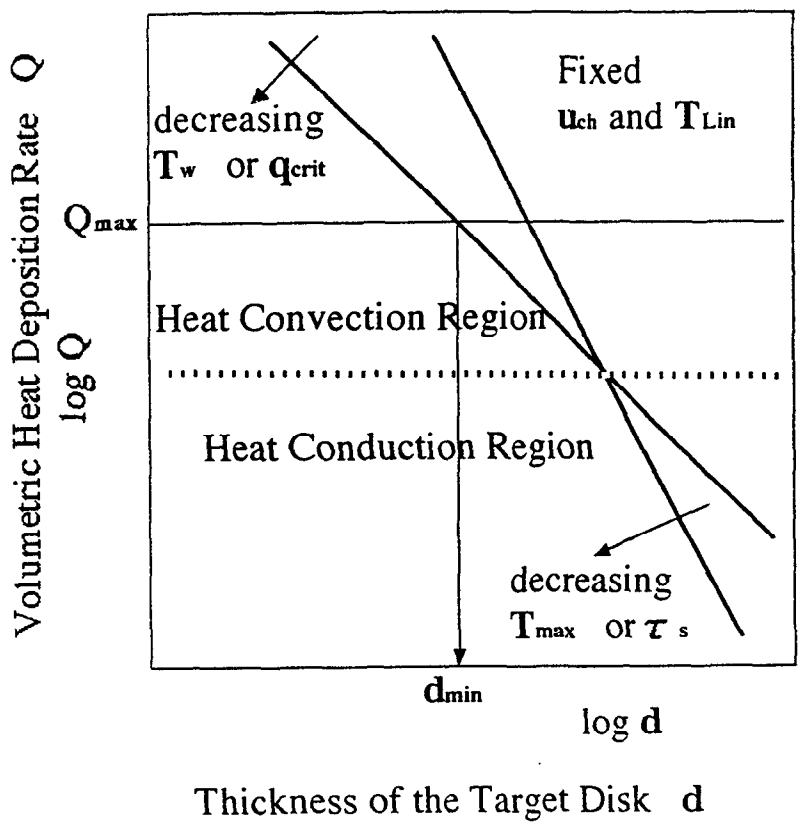

Fig.3 Relationships of thickness of target d and volumetric heat generation rate Q, d-Q diagram

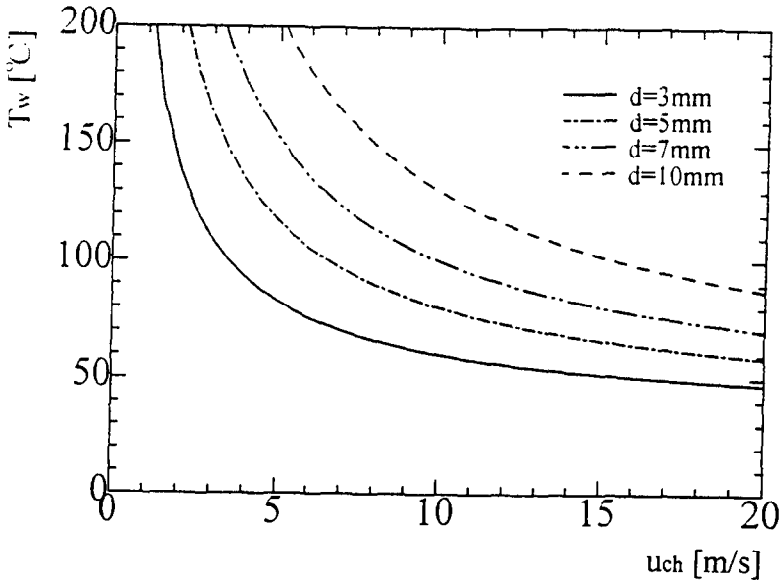

(a) Wp=0.6MW

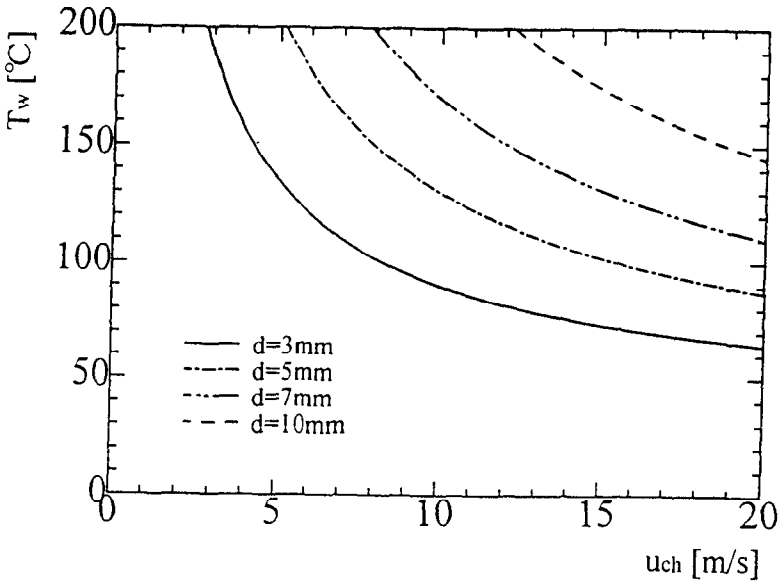

(b) Wp=1.2MW

Fig.4 Wall surface temperature of target

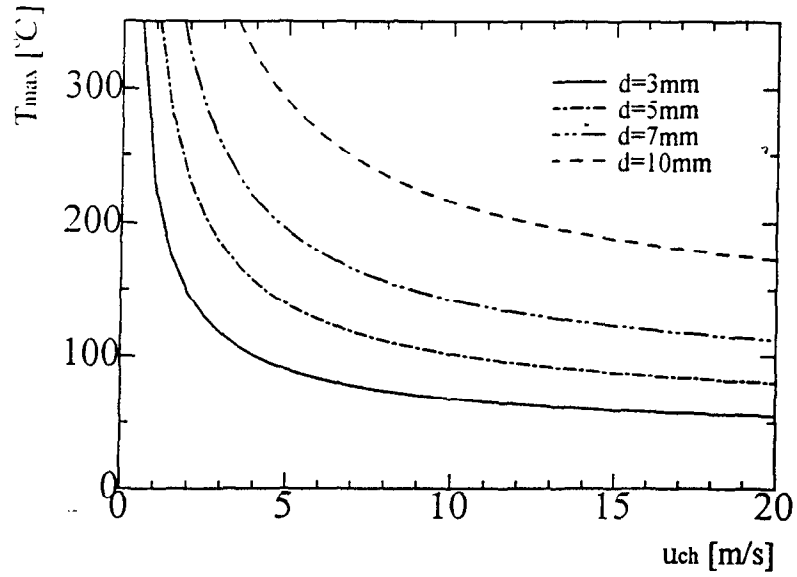

(a) Wp=0.6MW

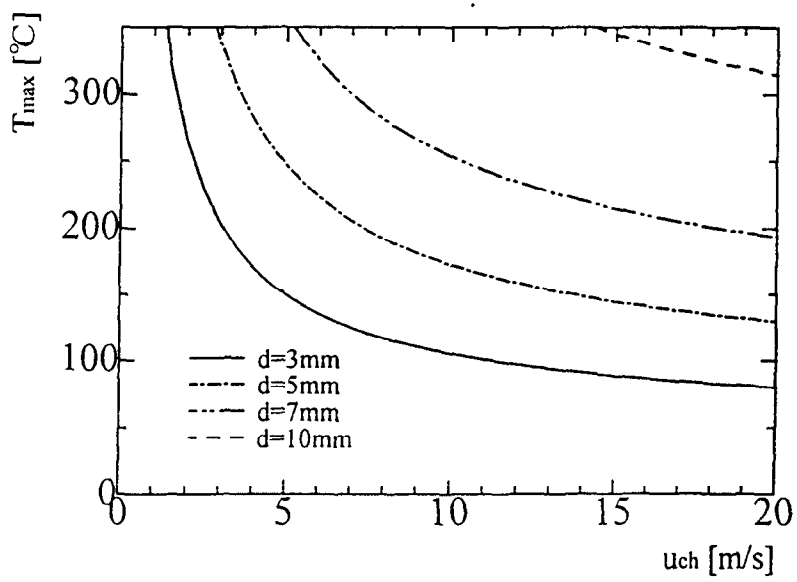

(b) Wp=1.2MW

Fig.5 Maximum temperature of target

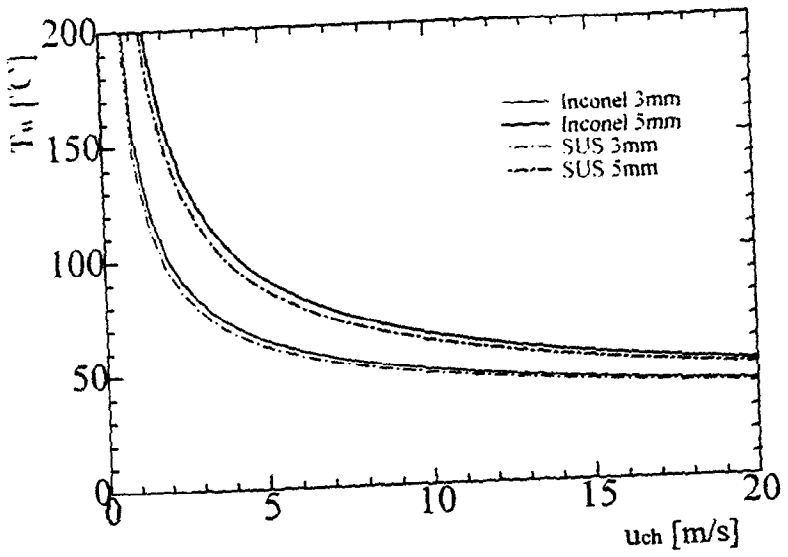

W_p=0.6MW, C=0, T_{Lin}=30℃, δ =1.5mm, L=167mm

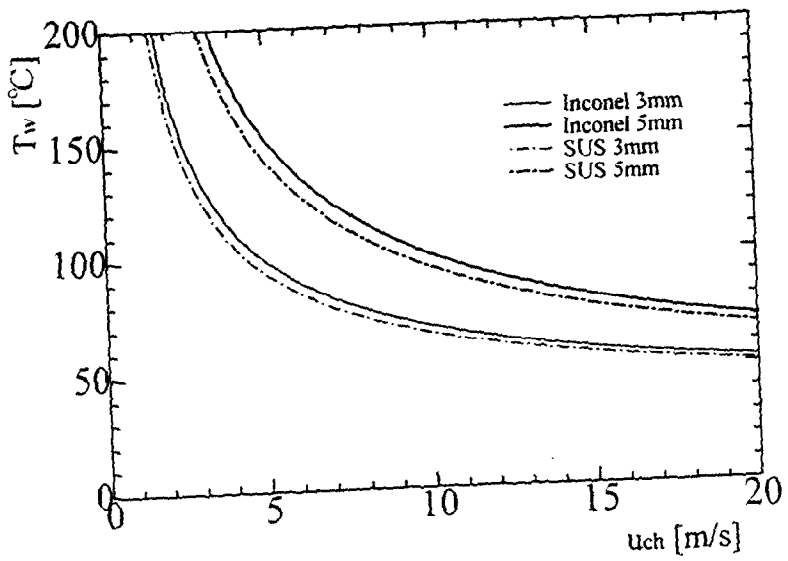

W_p=1.2MW, C=0, T_{Lin}=30℃, δ =1.5mm, L=167mm

Fig.6 Wall surface temperature of window

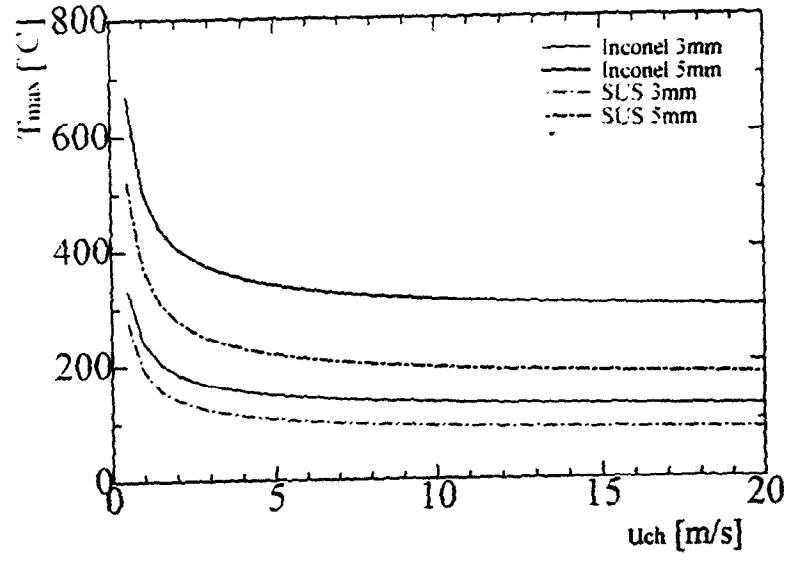

W_p=0.6MW, C=0, T_{Lin}=30℃, δ =1.5mm, L=167mm

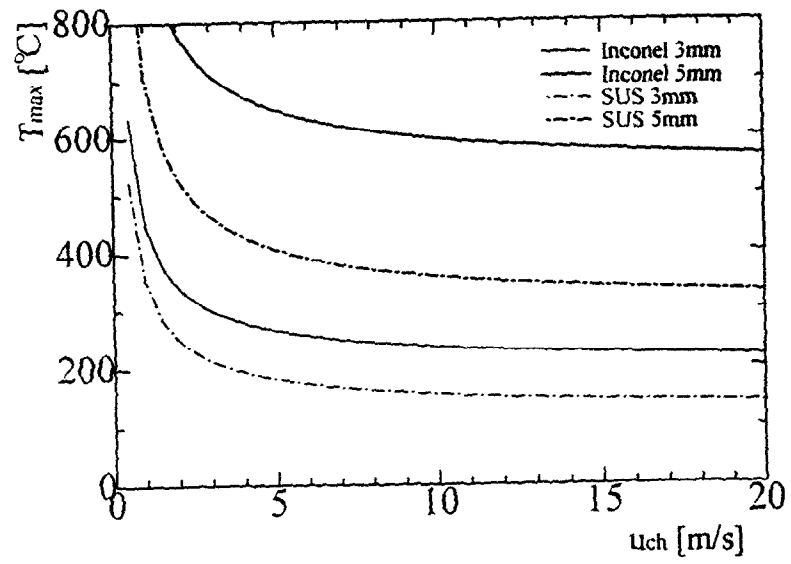

W_p=1.2MW, C=0, T_{Lin}=30℃, δ =1.5mm, L=167mm

Fig.7 Maximum temperature of window

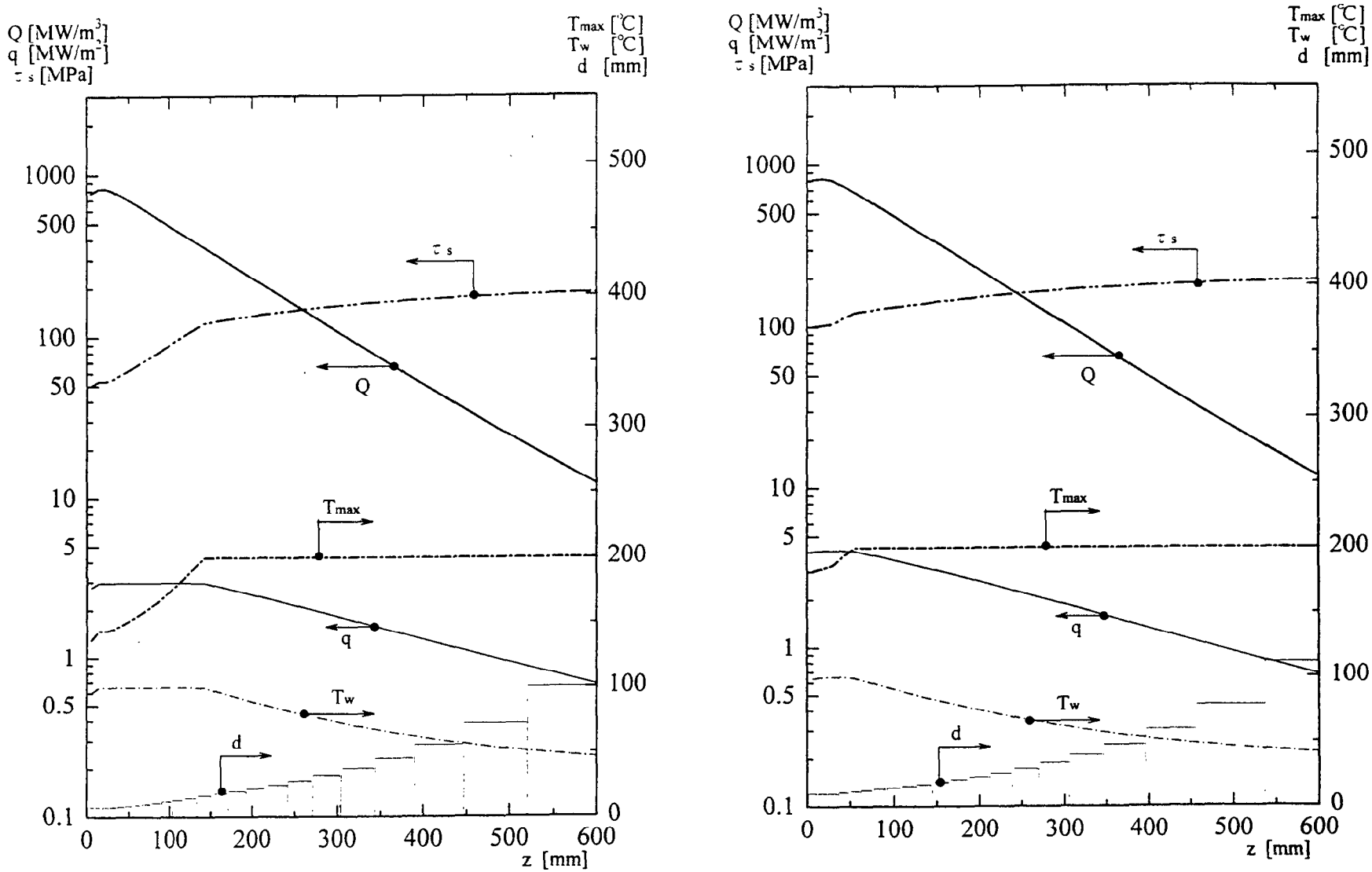

W_p=0.6MW, u_{ch}=10m/s, T_{max}*=200℃, T_w*=100℃

W_p=0.6MW, u_{ch}=15m/s, T_{max}*=200℃, T_w*=100℃

Fig.8 Target design results

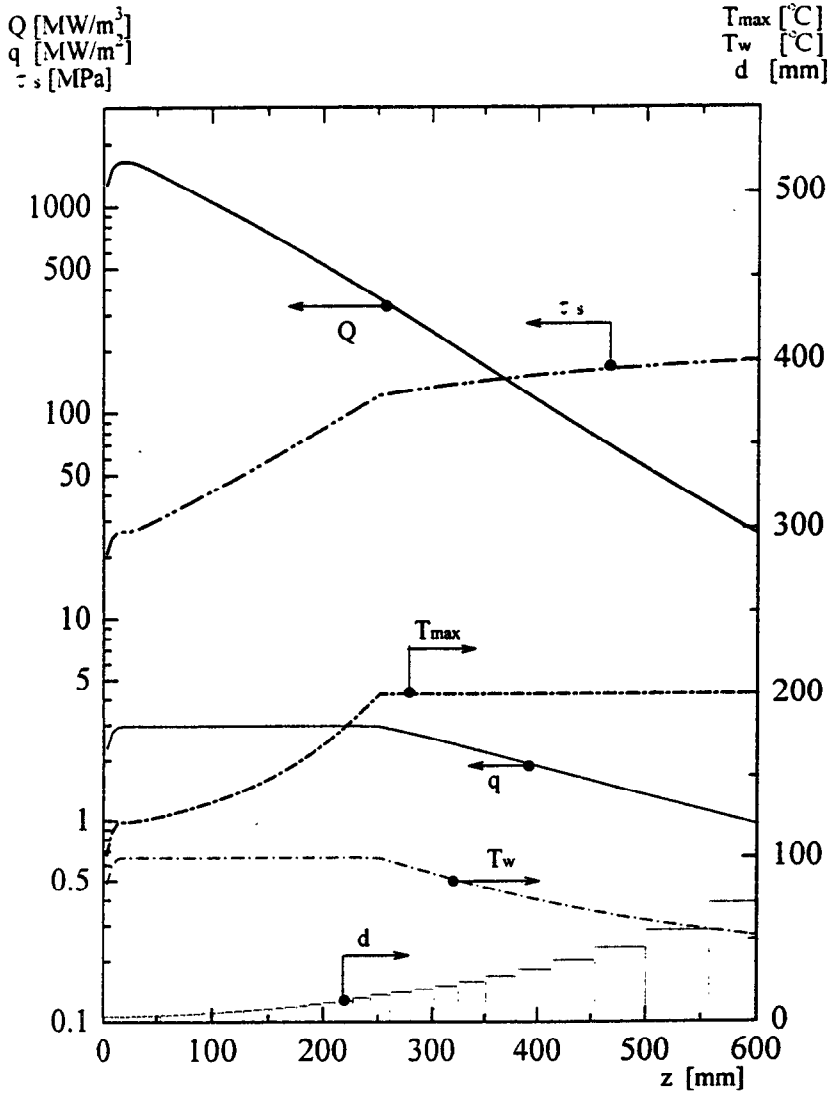

W_p=1.2MW, u_{ch}=10m/s, T_{max}*=200℃, T_w*=100℃

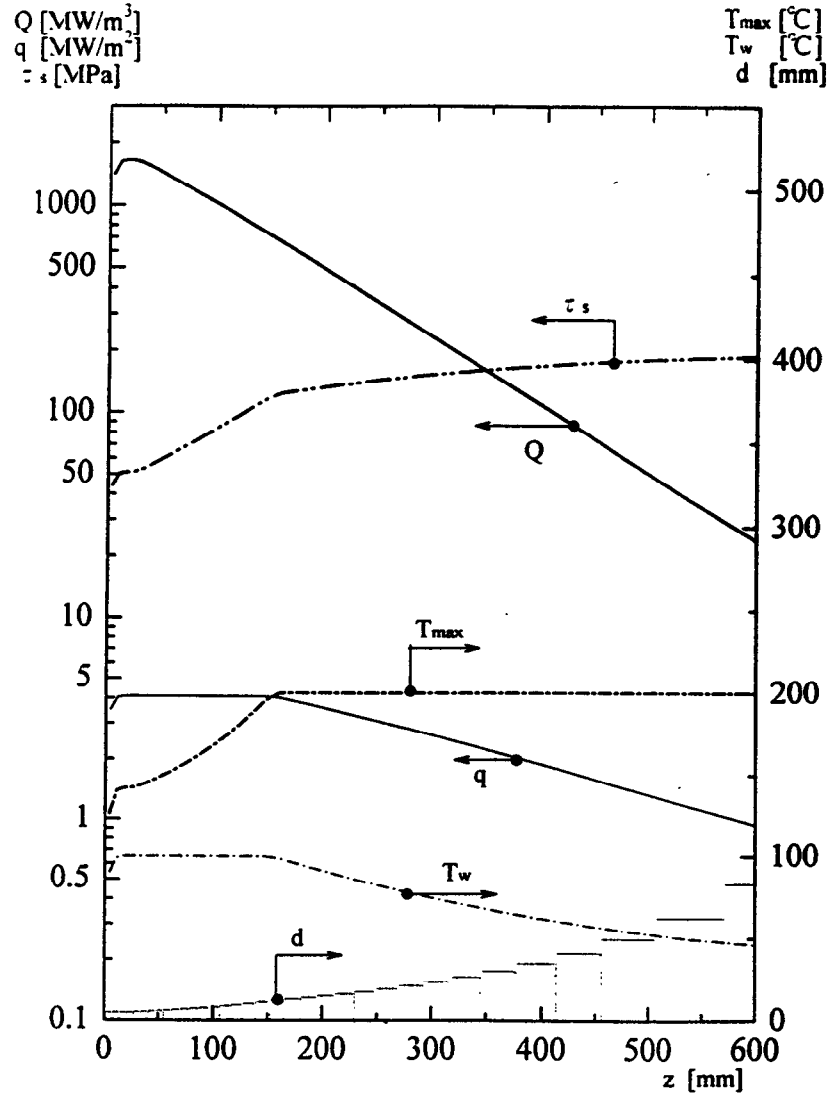

W_p=1.2MW, u_{ch}=15m/s, T_{max}*=200℃, T_w*=100℃

Fig.8 Target design results

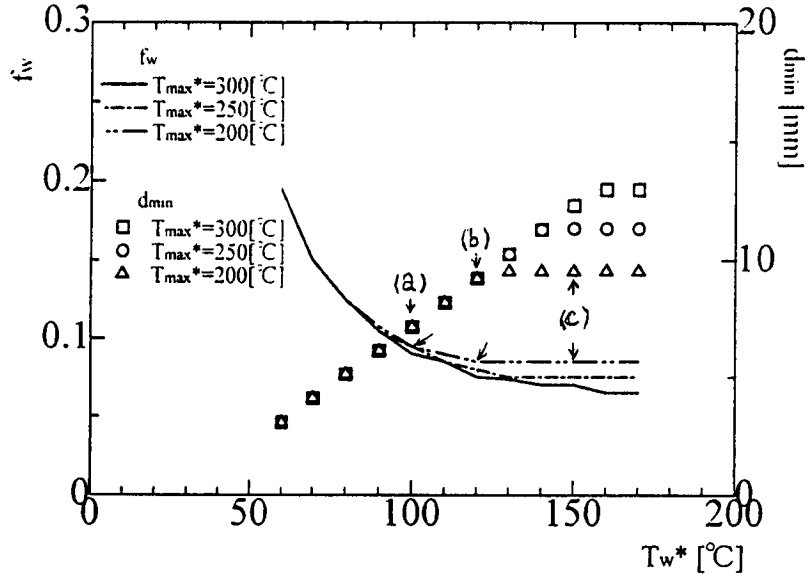

W_p=0.6MW, u_{ch}=10m/s, C=0, T_L=30℃, δ=1.5mm, L=167mm

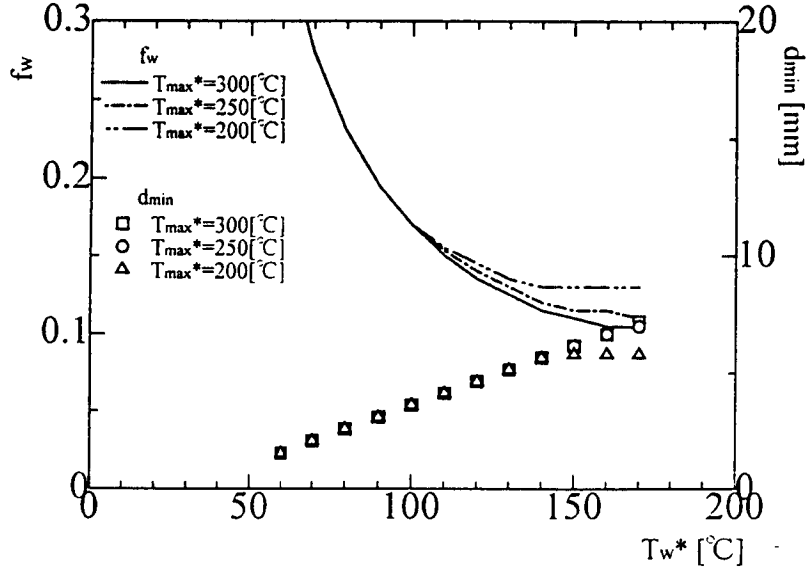

W_p=1.2MW, u_{ch}=10m/s, C=0, T_L=30℃, δ=1.5mm, L=167mm

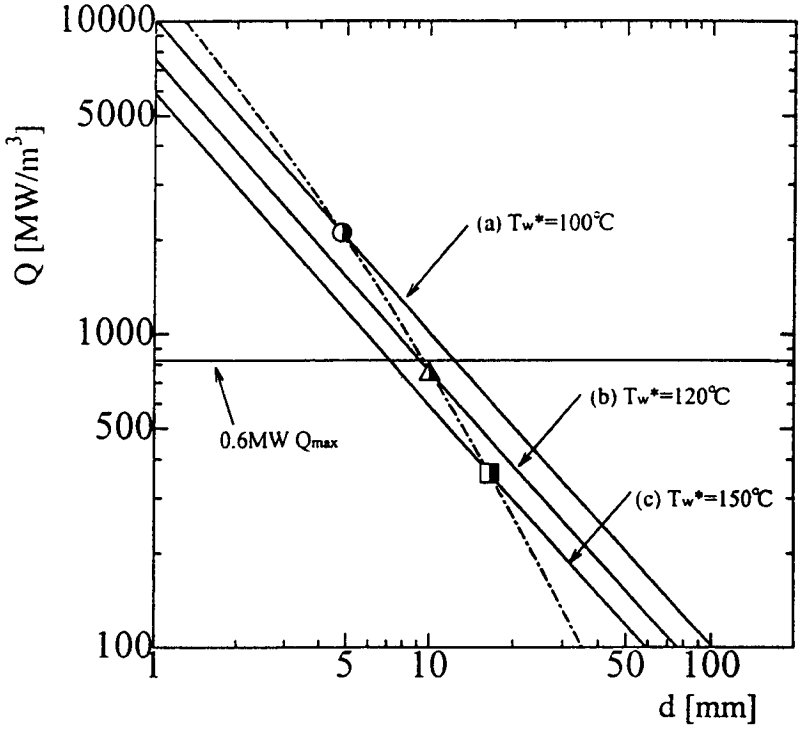

T_{max}*=200℃, T_L=30℃, u_{ch}=10m/s, C=0, δ=1.5mm, L=167mm

Fig.9 Water fraction f_W and d-Q diagram for wall temperature limit T_W*

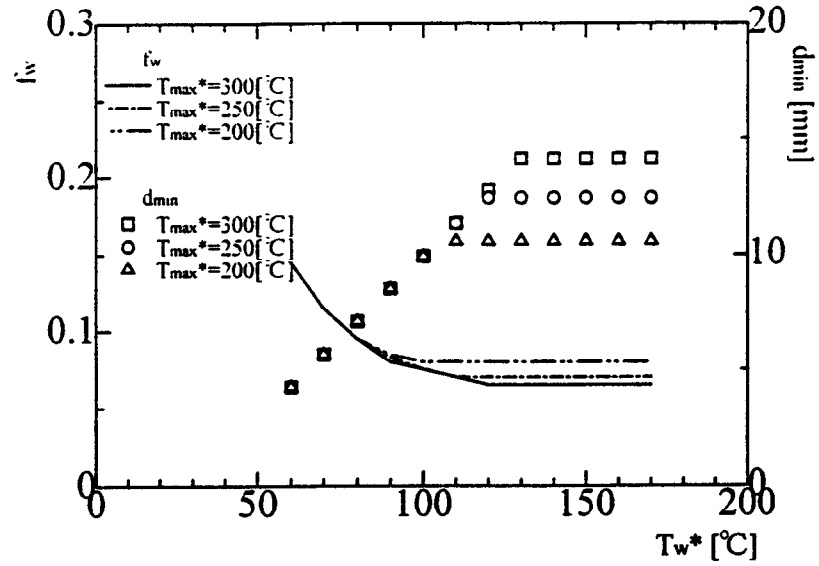

W_p=0.6MW, u_{ch}=15m/s, C=0, T_L=30℃, δ =1.5mm, L=167mm

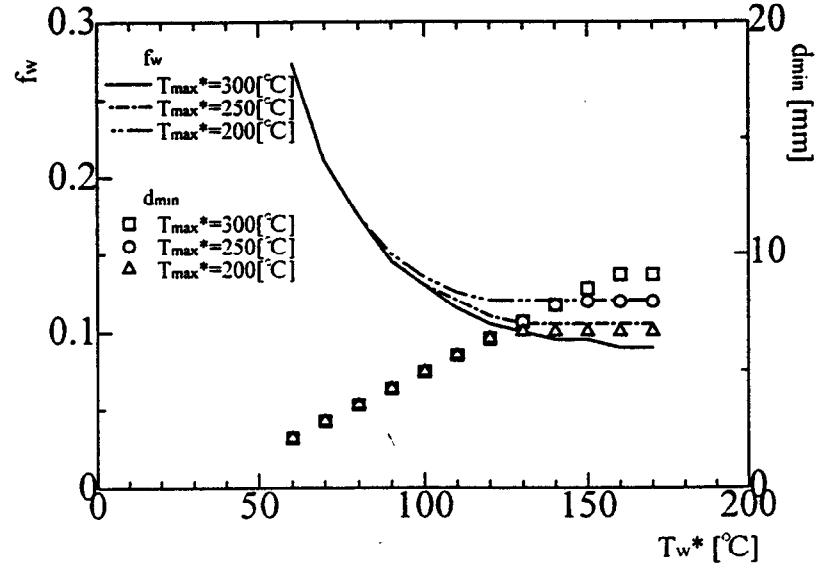

W_p=1.2MW, u_{ch}=15m/s, C=0, T_L=30℃, δ =1.5mm, L=167mm

Fig.9 Water fraction f_W and d-Q diagram for wall temperature limit T_W*

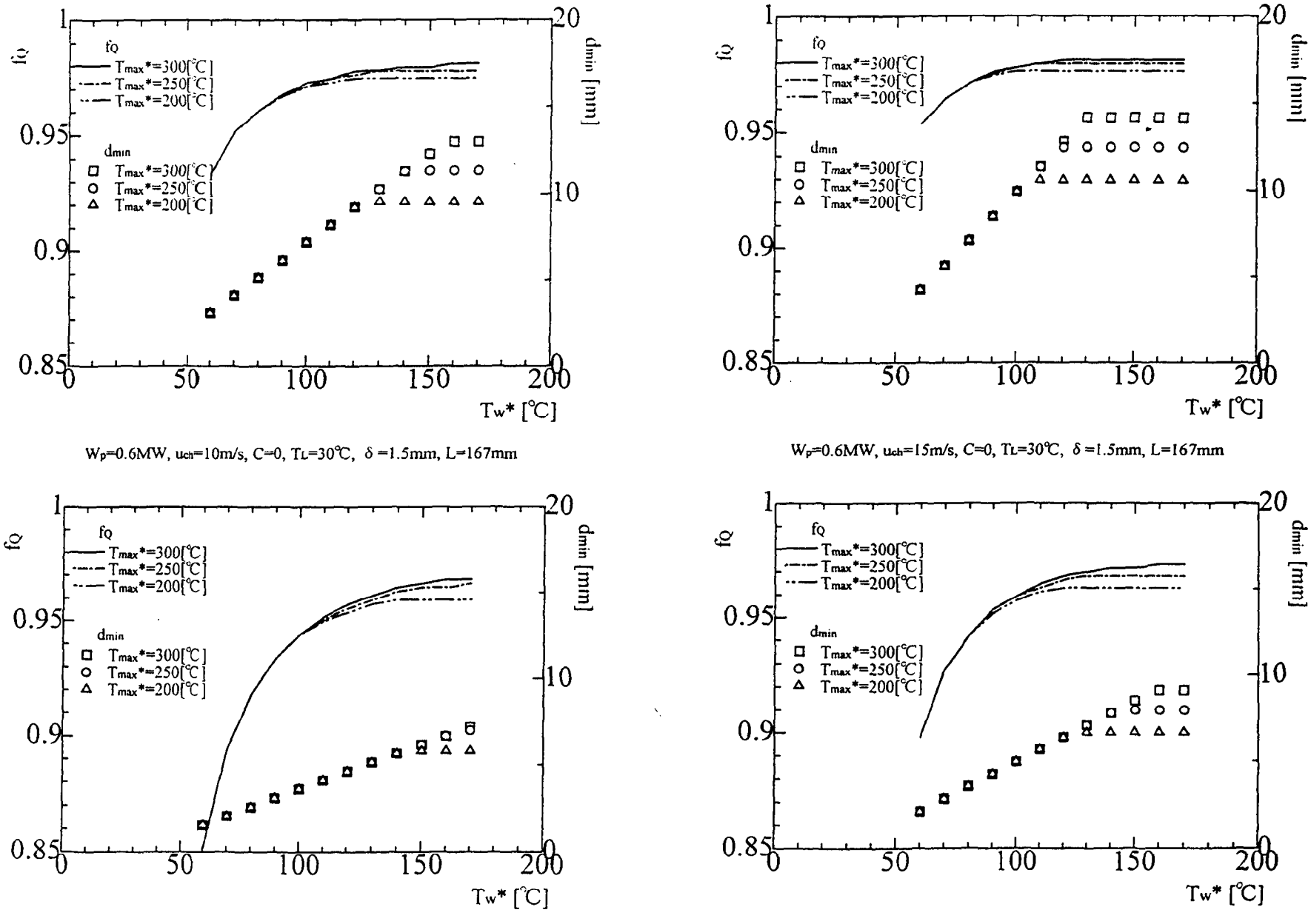

Fig.10 Heat deposition rate fraction for wall temperature limit T_w*

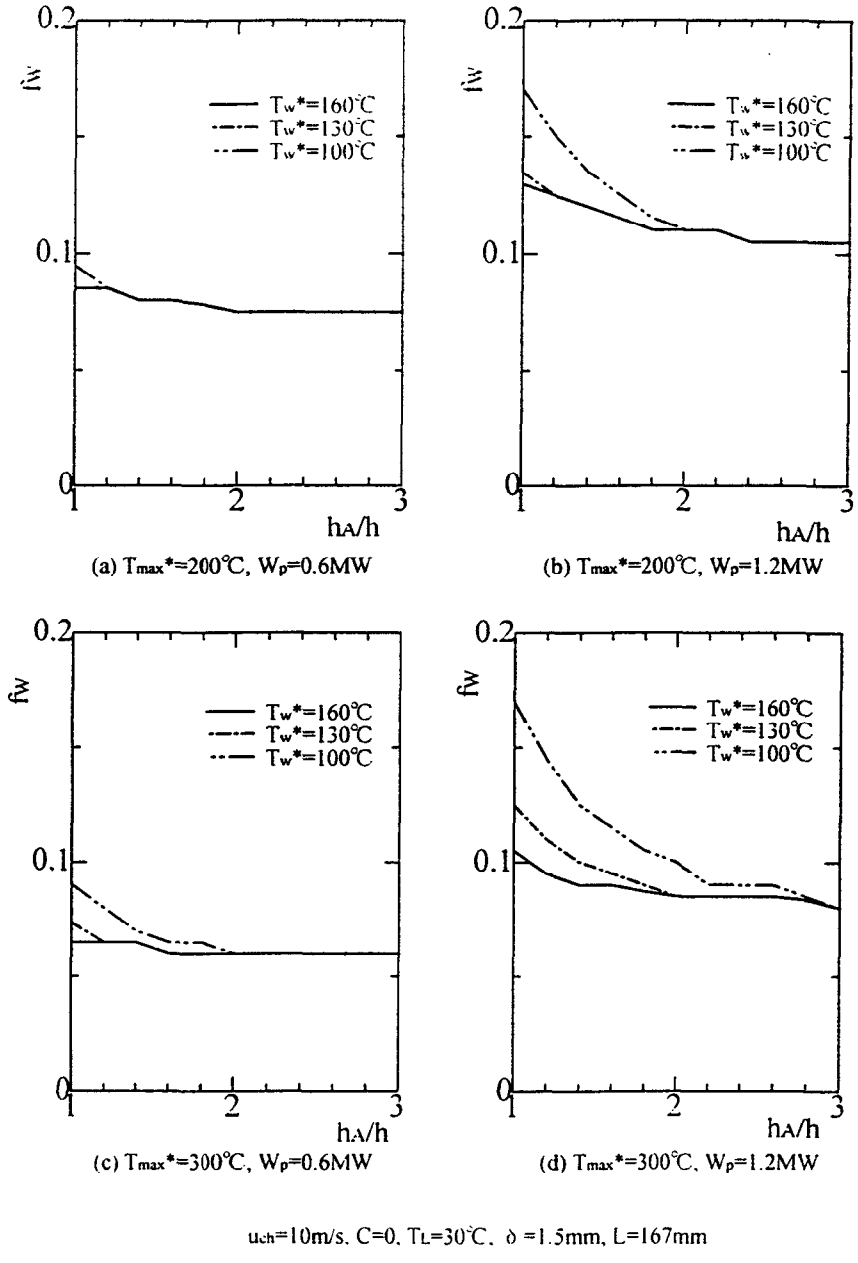

Fig.11 Water fraction f_W for heat transfer augementation rate h_A/h

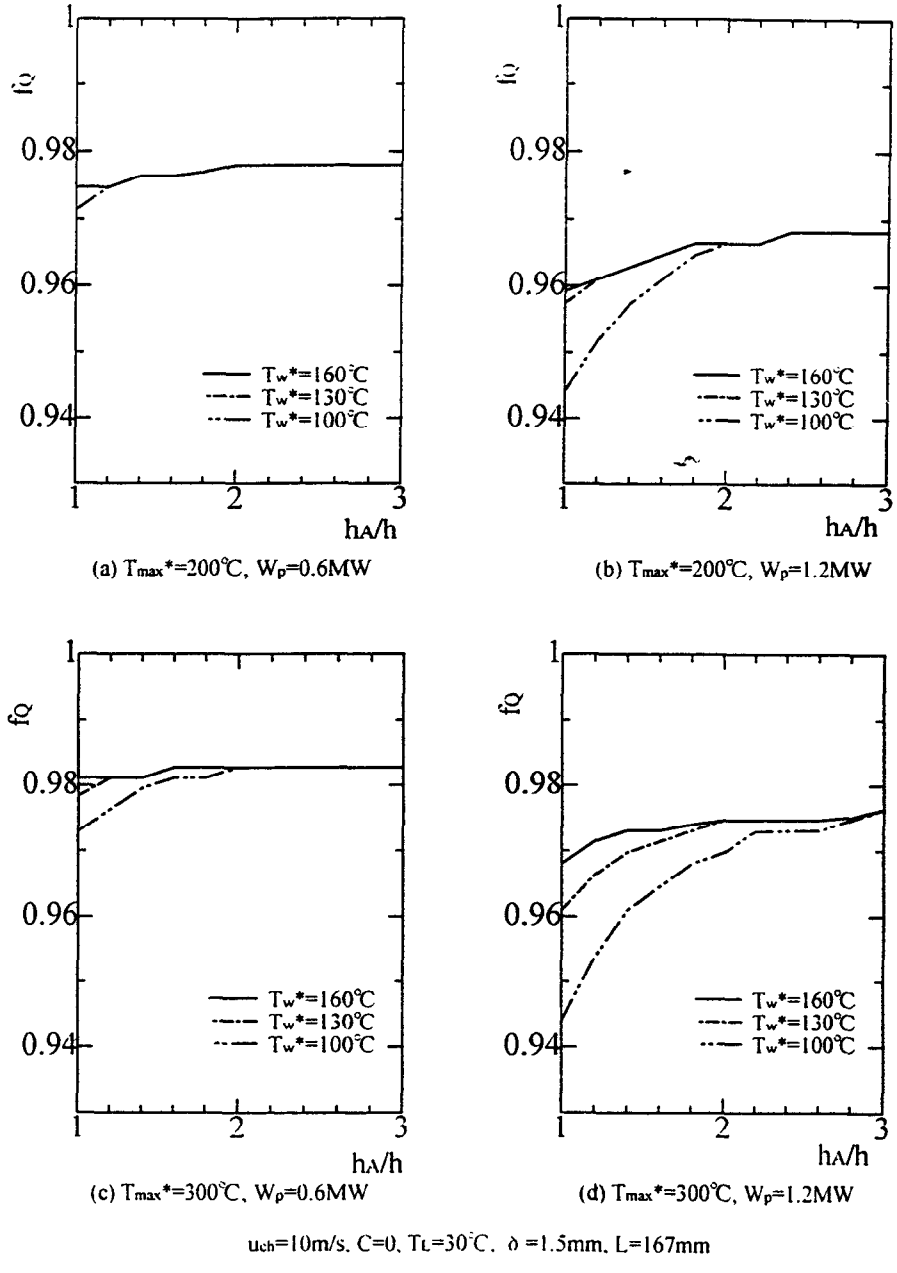

Fig.12 Heat deposition rate fraction f_Q for heat transfer augementation rate h_A/h

AUTHOR INDEX

Author	Page Number
Adams, M.A.	761
Aeppli, G.	598
Aksenov, V.L.	41
Alonso, J.	71
Amrein, B.	374
Ananiev, V.D.	41
Appleton, B.R.	32
Arai, M.	468
Argyriou, D.N.	813
Aso, T.	252, 804
Assoufid, L.	628
ASTE Collaboration	244, 457, 468
Balagurov, A.M.	650
Balchin, J.J.P.	761
Barnert-Wiemer, H.	557
Barnes, J.M.	678
Bauer, G.S.	10, 101, 229, 301, 321, 329, 361, 374, 382, 396, 703, 717
Belch, H.A.	764, 829, 864
Belushkin, A.V.	41, 768
Bertolini, L.R.	628
Betzold, H.	907
Bewley, R.I.	581
Beynon, T.D.	669
Bohringer, D.E.	773, 783
Bowden, Z.	791
Broholm, C.	598
Broome, T.A.	669, 761
Brown, B.S.	3
Brun, T.O.	586
Bull, M.	642
Bultman, N.K.	345
Carlile, C.J.	761
Carpenter, J.M.	3, 98, 144, 507, 751, 764, 864
Charlton, L.	678
Chen, D.	829
Conrad, H.	244
Cragg, D.A.	761
Crawford, R.K.	3, 201, 221, 764, 829, 864, 881
Czirr, J.B.	792
Daemen, L.L.	202, 586
Dai, Y.	301, 717
Dementyev, A.	703, 717
Donley, L.I.	829, 864
Döring, K.	557
Eccleston, R.S.	184, 581
Eckert, J.	586

Endoh, Y. 855
Ferguson, P.D. 489, 524, 890
Fornek, T. 221
Foster, S. 581
Frost, C.D. 184
Fujii, T. 424
Fult, B. 598
Furusaka, M. 56, 569, 823, 891
Futakawa, M. 244, 830
Gabriel, T.A. 678
Geissmann, K. 374
Gillette, V.H. 533
Grachev, M.I. 301
Granada, J.R. 533
Guttek, B. 329
Haga, K. 252, 329
Hagen, M. 642
Hammonds, J. 829, 864
Harada, I. 288
Harris, M. 642
Hastings, J.B. 57, 229, 836
Hata, N. 424
Haumann, J.R. 864
Hayashida, Y. 424
Heidenreich, G. 361
Herwig, K.W. 221
Heuser, B. 628
Heyck, H. 374
Hibiki, T. 411
Hino, R. 22, 252, 269, 278, 288, 804, 830
Hjelm, R.P. 202, 628
Hodges, J.P. 813
Iijima, K. 823
Ikeda, H. 46, 56
Ikeda, K. 278
Ikeda, Y. 457, 468, 728
Ino, T. 320
Ioka, I. 830
Ishikura, S. 252, 278, 288, 804
Ishiyama, W. 132
Itoh, S. 823
Iverson, E.B. 507, 751
Iwasa, H. 125, 569
Jericha, E. 61
Johnson, J.O. 678
Jorgensen, J.D. 813
Kai, T. 728, 743, 804
Kamba, K. 288
Kaminaga, M. 252, 269, 278, 288, 804

Kamiyama, T. 125, 569
Kasugai, Y. 457, 468
Kato, H. 125
Keimer, B. 598
Kern, S. 598
Kikuchi, K. 244, 830
Kikura, H. 321
Kinoshita, H. 252
Kiyanagi, Y. 125, 424, 468, 478, 569, 823
Kleb, R. 764, 829
Kogawa, H. 252, 830
Konno, M. 569
Kosako, K. 728, 743
Kravchuk, L.V. 301
Ku, C. 864
Kurosawa, K. 278
Larese, J.Z. 57, 586
Leach, D. 864
Lehmann, E. 703, 717
Lielausis, O. 382
Littrell, K. 864
Loong, C.-K. 829, 894
Lucas, A.T. 687
Ludewig, H. 57, 836
Macek, R. 84
Malik, A. 361
Mason, T.E. 598
McEwen, K. 642
McMichael, G.E. 3
Meigo, S. 448, 457
Mezei, F. 113, 119
Miller, M.E. 751
Mishima, K. 411
Miura, T. 823
Mizumoto, M. 22
Montanez, P. 57, 836
Mook, H.A. 598
Mukaiyama, T. 22
Murakami, K. 132
Nagao, T. 728, 743
Nagler, S.E. 598
Nakagawa, H. 125
Nakamura, F. 269
Nakashima, H. 457, 468, 728, 743
Neef, R. 441
Ni, L. 229, 396
Nipko, J.C. 829
Norris, J. 184
Ogawa, Y. 125, 424, 569, 823

Oku, T. 125
Orlov, Y.I. 301
Osborn, R. 598
Ostrowski, G.E. 829, 864
Oyama, Y. 22, 457, 468, 728, 743
Pepe, M.E. 533
Pepyolyshev, Y.N. 768
Perrott, L.C. 852
Peters, L.D. 751
Petrillo, C. 642
Picton, D.J. 669
Pitcher, E. 489, 524, 895
Platnieks, I. 382
Radaelli, P.G. 159, 884
Rauch, H. 61
Regler, M. 61
Rhodes, N.J. 184
Richardson, Jr., J.W. 813
Robinson, R.A. 598, 657
Russell, G.J. 489, 524, 895
Ruzicka, W. 3
Sacchetti, F. 642
Saito, Y. 411
Sakakibara, J. 320
Sakashita, M. 269, 288
Sasa, T. 448
Sasaki, S. 823
Sbaffoni, M.M. 533
Schlueter, M.W. 751
Schorr, S. 119
Scott, T. L. 751
Seeger, P.A. 202, 586, 628, 887
Shabalin, E.P. 497
Shimizu, H.M. 125
Short, S. 813
Sidorkin, S.F. 19, 301
Smith, G.C. 57
Soyama, K. 132
Spitzer, H. 229
Stechemesser, H. 244, 557
Steigenberger, U. 642
Suda, Y. 125
Susuki, A. 252, 269, 288
Suzuki, Y. 847
Tagawa, H. 269
Takada, H. 448, 457, 468, 728, 743
Takagi, R. 478
Takeda, M. 855
Takeda, Y. 320, 321, 329, 382, 889

Takenaka, N. 424
Takeuchi, K. 829
Taylor, A.D. 51
Temple, S.A. 852
Terada, A. 252, 804
Teshigawara, M. 728, 743, 804
Thelliez, T.G. 202
Thiyagarajan, P. 628, 864
Thomas, G. 852
Todosow, M. 57, 836
Toeller, J. 864
Tomkinson, J. 761
Toyoshima, N. 855
Tsujimoto, K. 448
Uchida, S. 278
Uden, C.N. 761
Urban, V. 864
Uzawa, M. 278
Vinogradov, A.V. 41, 768
Vitt, R. 864
Volin, K. J. 773, 783
von Holzen, G. 229
Wakabayashi, T. 125
Watanabe, N. 22, 457, 468, 569, 728, 743, 804, 890
Weber, H. 61
White, D.J. 184
Williams, W.G. 51, 169
Worlton, T.G. 195
Wozniak, D.G. 864
Yanagisawa, I. 278
Yasui, S. 823
Yasumura, R. 424
Yocum, D. 829
Zsigmond, G. 113